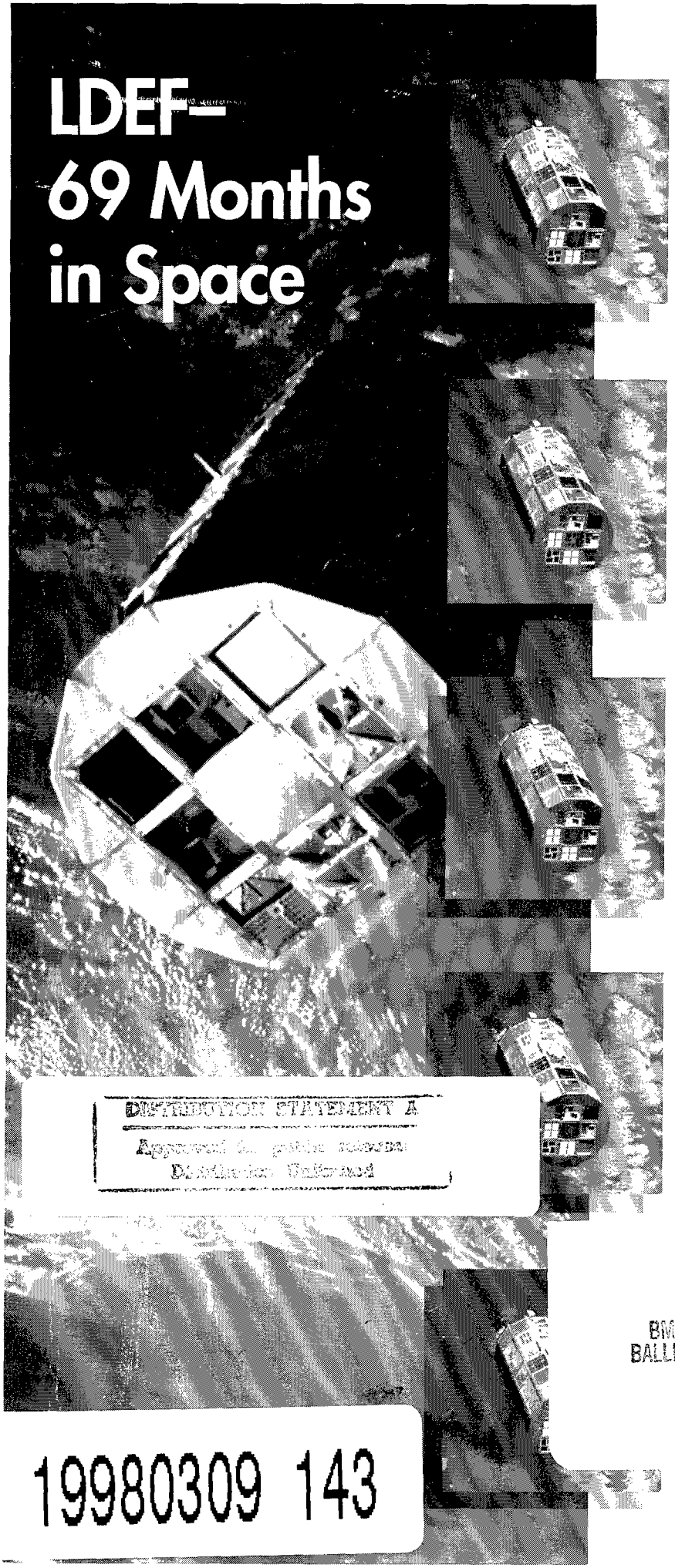


LDEF–69 Months in Space

Second Post - Retrieval Symposium

June 1-5, 1992
San Diego, California

Sponsors:

LDEF Science Office
NASA Langley Research Center

American Institute of
Aeronautics and Astronautics

NASA Conference Publication 3194
Part 2

DISTRIBUTION STATEMENT A
Approved for public release;
Distribution Unlimited

BMD TECHNICAL INFORMATION CENTER
BALLISTIC MISSILE DEFENSE ORGANIZATION
7100 DEFENSE PENTAGON
WASHINGTON D.C. 20301-7100

19980309 143

Aeronautics and Astronautics

U5680

2/18/98 3:57:01 PM

Accession Number: 5680
Publication Date: Jun 01, 1992
Title: 69 Months in Space Second LDEF Post-Retrieval Symposium
Corporate Author or Publisher: AIAA, NASA Washington, DC
Report Number: NASA CP-3194, Part 2
Descriptors, Keywords: Space Experiment
Pages: 00476
Cataloged Date: May 04, 1995
Copyrighted or Not: Y
Document Type: HC
Number of Copies in Library: 000001
Record ID: 29993

LDEF–
69 Months
in Space

NASA Conference Publication 3194
Part 2

Second Post - Retrieval Symposium

Edited by
Arlene S. Levine
NASA Langley Research Center
Hampton, Virginia

Proceedings of a symposium sponsored by the National Aeronautics and Space Administration, Washington, D.C., and the American Institute of Aeronautics and Astronautics, Washington, D.C., and held in San Diego, California
June 1-5, 1992



National Aeronautics and
Space Administration

Office of Management

Scientific and Technical
Information Program

1993

FOREWORD

Nineteen hundred ninety-two, designated The International Space Year (ISY), coincided with the 35th anniversary of the International Geophysical Year (IGY). The International Space Year honored space exploration and the planet Earth and also marked the 500th Anniversary of Christopher Columbus's discovery of the New World. Langley Research Center, the home of the Long Duration Exposure Facility (LDEF), celebrated its 75th anniversary. In addition, 1992 marked the second anniversary of the LDEF retrieval. Since publication of the First LDEF Post-Retrieval Symposium Conference Publication in January 1992, the LDEF principal investigators, co-investigators, and collaborating investigators have had an additional 12 months to analyze and interpret the data from LDEF's 57 onboard experiments and to reach a better understanding of the space environment (ionizing radiation, meteoroids, space debris, and atomic oxygen in the upper atmosphere) and the effects that prolonged exposure in this environment will have on future spacecraft such as large low-Earth orbit (LEO) platforms, Earth-orbiting spacecraft, and on future manned and unmanned spacecraft to the Moon and to other planets.

Results of the second year LDEF studies were presented at the Second LDEF Post-Retrieval Symposium, held at the Town and Country Hotel, San Diego, California, June 1 to 5, 1992. This symposium was co-sponsored by NASA Langley Research Center and the American Institute of Aeronautics and Astronautics. This document contains the full-length papers presented at the second symposium. The collection includes invited review papers on ionizing radiation, meteoroids and debris, environmental effects on materials, environmental effects on systems, and archiving of the LDEF data. Contributed papers on ionizing radiation, meteoroids and debris, space effects on materials and systems, the LDEF mission and induced environments, microgravity, and life science are also included. The document organization is very similar to that of the symposium.

LDEF Mission and Induced Environments
Space Environments - Ionizing Radiation
Space Environments - Meteoroid and Debris
Space Environments - Microgravity
Space Environmental Effects - Materials
Space Environmental Effects - Systems
Space Environmental Effects - Biology
The Future

During the symposium William H. Kinard chaired the first half of the general session containing the invited review papers, and Bland A. Stein chaired the second half of the general session containing the invited review papers, plus the Mission and Induced Environments papers, and a Microgravity paper. Thomas Parnell chaired the Ionizing Radiation sessions; J.A.M. McDonnell, Jean-Claude Mandeville, Dale R. Atkinson, Michael Zolensky, and Donald Humes chaired Meteoroid and Debris sessions; Joan Funk and John Davis chaired the Data basing session; Ann Whitaker and Bruce Banks chaired the Coating session; Philip Young chaired the Polymer session, and R.C. Tennyson chaired the Polymer Matrix Composites session. Roger Linton chaired the Metals and Metal Matrix Composites session. Gale Harvey and Bland Stein chaired the Contamination session. James Mason, Joel Edelman, and Harry Dursch chaired the Systems sessions. William H. Kinard chaired the closing general session containing papers on biology and future activities.

I wish to thank the contributing authors whose research greatly enhanced the knowledge of space environments and their effects on materials, systems, and biology. The papers contained in this volume underwent a technical review by peer reviewers and an editorial review. I also wish to thank the technical reviewers for their time and effort in making this collection as current and accurate as it is. I would like to thank Maureen Sgambelluri, who assisted with the symposium logistics, and who cheerfully reformatted some of the papers contained in this publication. I would like to gratefully acknowledge Susan Hurd, Mary Edwards, Lisa Levine, Alisa Hollins, and Jeanne Gordon, for their support in editing this document.

This conference publication is the second in a series of three LDEF Post-Retrieval documents. In June 1991, over 400 LDEF investigators and data users convened in Kissimmee, Florida for the First LDEF Post-Retrieval Symposium. The results of the symposium (130 papers) are printed in a three-part NASA Conference Publication, ***LDEF-69 Months in Space: First LDEF Post-Retrieval Symposium,*** January 1992, (NASA CP-3134.) The LDEF Science Office plans to hold a third symposium in November 1993, in Williamsburg, Virginia. Published abstracts for the third symposium will be available at the meeting. Additional information on these symposia may be obtained by contacting:

Arlene S. Levine
LDEF Science Office M/S 404
NASA Langley Research Center
Hampton, Virginia 23681-0001
Telephone: 804 864-3318
Fax: 804 864-8094

The use of trade names or manufacturers in this publication does not constitute an official endorsement of such products or manufacturers, either expressed or implied, by the National Aeronautics and Space Administration.

CONTENTS

FOREWORD.....iii

Part 1*

Mission and Induced Environments

Refinements on the Pinhole Camera Measurements of the LDEF Attitude.....3
Palmer N. Peters, Paul L. Whitehouse and John C. Gregory

LDEF Microenvironments, Observed and Predicted.....13
R.J. Bourassa, H.G. Pippin, and J.R. Gillis

A Generalized Approach to the Thermal Analysis of the Long Duration Exposure Facility's Flight Experiments.....27
Thomas R. Sampair*

ENVIRONET: On-Line Information for LDEF.....51
Michael Lauriente

Space Environments - Ionizing Radiation

Status of LDEF Ionizing Radiation Measurements and Analysis.....69
Thomas A. Parnell

Sensitivity of LDEF Foil Analyses Using Ultra-Low Background Germanium Vs. Large NaI(Tl) Multidimensional Spectrometers.....79
James H. Reeves, Richard J. Arthur, and Ronald L. Brodzinski

Radioactivities Induced in Some LDEF Samples.....87
Robert C. Reedy, Calvin E. Moss, S. George Bobias, and Jozef Masarik

A Photon Phreak Digs the LDEF Happening.....97
Alan R. Smith and Donna L. Hurley

Charged Particle Activation Studies on the Surface of LDEF Spacecraft.....107
Ilhan Olmez, Forest Burns, and Paul Sagalyn

Collection, Analysis, and Archival of LDEF Activation Data.....111
C.E. Laird, B.A. Harmon, G.J. Fishman, and T.A. Parnell

---

* Part 1 is presented under separate cover.

Induced Activation Study of LDEF 125
B.A. Harmon, G.J. Fishman, T.A. Parnell, and C.E. Laird

Revised Prediction of LDEF Exposure to Trapped Protons 137
John W. Watts, T. W. Armstrong, and B. L. Colborn

A Measurement of the Radiation Dose to LDEF by Passive Dosimetry 147
J. B. Blake and S. S. Imamoto

LDEF: Dosimetric Measurement Results (AO 138-7 Experiment) 157
J. Bourrieau*

Absorbed Dose Measurements and Predictions on LDEF 163
A.L. Frank, E.V. Benton, T.W. Armstrong, and B.L. Colborn

LET Spectra Measurements of Charged Particles in P0006 Experiment of LDEF 171
E.V. Benton, I. Csige, K. Oda, R.P. Henke, A.L. Frank, E.R. Benton, L.A. Frigo, T.A. Parnell, J.W. Watts, Jr., and J.H. Derrickson

Light-Heavy Ion Measurements in CR-39 Located on the Earth Side of LDEF 181
I. Csige, E.V. Benton, S. Soundararajan, and E.R. Benton

Three-Dimensional Shielding Effects on Charged Particle Fluences Measured in the P0006 Experiment of LDEF 187
I. Csige, E.V. Benton, L. Frigo, T.A. Parnell, J.W. Watts, Jr., T.W. Armstrong, and B.L. Colborn

Development and Application of a 3-D Geometry/Mass Model for LDEF Satellite Ionizing Radiation Assessments 195
B.L. Colborn and T.W. Armstrong

Radiation Model Predictions and Validation Using LDEF Satellite Data 207
T.W. Armstrong and B.L. Colborn

Future Directions for LDEF Ionizing Radiation Modeling and Assessments 221
T.W. Armstrong and B.L. Colborn

Cosmogenic Radionuclides on LDEF: An Unexpected ^{10}Be Result 231
J.C. Gregory, A. Albrecht, G. Herzog, J. Klein, R. Middleton, B. Dezfouly-Arjomandy, and B.A. Harmon

Heavy Ion Measurement on LDEF 239
D. Jonathal, R. Beaujean, and W. Enge

Progress Report on the Heavy Ions in Space (HIIS) Experiment 247
James H. Adams, Jr., Lorraine P. Beahm, Paul R. Boberg, and Allan J. Tylka

Progress Report on the Ultra Heavy Cosmic Ray Experiment (AO 178) 261
A. Thompson, D. O'Sullivan, J. Bosch, R. Keegan, K.-P. Wenzel, F. Jansen, and C. Domingo

Author Index 269

Part 2

Space Environments - Meteoroid and Debris

Interim Report of the Meteoroid and Debris Special Investigation Group 277
Michael E. Zolensky, Herbert A. Zook, Fred Hörz, Dale R. Atkinson, Cassandra R. Coombs, Alan J. Watts, Claire Dardano, Thomas H. See, Charles Simon, and William H. Kinard

Micrometeoroids and Debris on LDEF 303
Jean-Claude Mandeville

Continued Investigation of LDEF's Frame and Thermal Blankets by the Meteoroid and Debris Special Investigation Group 313
Thomas H. See, Kimberly S. Mack, Jack L. Warren, Michael E. Zolensky, and Herbert A. Zook

Predicted and Observed Directional Dependence of Meteoroid/Debris Impacts on LDEF Thermal Blankets 325
Gerhard Drolshagen

3-D Crater Analysis of LDEF Impact Features from Stereo Imagery 339
Clyde A. Sapp, Thomas H. See, and Michael E. Zolensky

Further Analysis of LDEF FRECOPA Micrometeoroid Remnants 347
Janet Borg, Ted E. Bunch, Filippo Radicati di Brozolo, and Jean-Claude Mandeville

Long Duration Exposure Facility (LDEF) Experiment M0003 Meteoroid and Debris Survey 357
M.J. Meshishnek, S.R. Gyetvay, K.W. Paschen, and J.M. Coggi

Derivation of Particulate Directional Information from Analysis of Elliptical Impact Craters on LDEF 417
P.J. Newman, N. Mackay, S.P. Deshpande, S.F. Green, and J.A.M. McDonnell

Characteristics of Hypervelocity Impact Craters on LDEF Experiment S1003 and Implications of Small Particle Impacts on Reflective Surfaces 431
Michael J. Mirtich, Sharon K. Rutledge, Bruce A. Banks, Christopher De Vries, and James E. Merrow

Hypervelocity Impact Survivability Experiments for Carbonaceous Impactors 453
T.E. Bunch, Luann Becker, Jeffrey Bada, John Macklin, Filipo Radicati di Brozolo, R.H. Fleming, and Jozef Erlichman

Hypervelocity Impact Facility for Simulating Materials Exposure to Impact by Space Debris 479
M.F. Rose, S. Best, T. Chaloupka , B. Stephens, and G. Crawford

Analysis of LDEF Micrometeoroid/Debris Data and Damage to Composite Materials 493
R. C. Tennyson and G. Manuelpillai

SIMS Chemical Analysis of Extended Impacts on the Leading and Trailing Edges of LDEF Experiment AO187-2 513
S. Amari, J. Foote, P. Swan, R.M. Walker, E. Zinner, and G. Lange

Cratering in Glasses Impacted by Debris or Micrometeorites 529
David E. Wiedlocher and Donald L. Kinser

Scanning Electron Microscope/Energy Dispersive X-Ray Analysis of Impact Residues in LDEF Tray Clamps 541
Ronald P. Bernhard, Christian Durin, and Michael E. Zolensky

Projectile Compositions and Modal Frequencies on the "Chemistry of Micrometeoroids" LDEF Experiment 551
Ronald P. Bernhard, Thomas H. See and Friedrich Hörz

Asteroidal Versus Cometary Meteoroid Impacts on the Long Duration Exposure Facility (LDEF) 575
Herbert A. Zook

Interplanetary Meteoroid Debris in LDEF Metal Craters 577
D.E. Brownlee, D. Joswiak, J. Bradley, and F. Hörz

Origin of Orbital Debris Impacts on LDEF's Trailing Surfaces 585
Donald J. Kessler

Damage Areas on Selected LDEF Aluminium Surfaces 595
Cassandra R. Coombs, Dale R. Atkinson, Martha K. Allbrooks, Alan J. Watts, Corey J. Hennessy, and John D. Wagner

LDEF Data: Comparisons with Existing Models 619
Cassandra Coombs, Alan Watts, John Wagner, and Dale Atkinson

New Meteoroid Model Predictions for Directional Impacts on LDEF 665
Neil Divine and Rene Agüero

Long Duration Exposure Facility (LDEF) Attitude Measurements of the Interplanetary Dust Experiment 667
Philip C. Kassel, Jr., William R. Motley III, S. Fred Singer, J. Derral Mulholland, John P. Oliver, Jerry L. Weinberg, William J. Cooke, and Jim J. Wortman

Elemental Analyses of Hypervelocity Microparticle Impact Sites on Interplanetary Dust Experiment Sensor Surfaces 677
C.G. Simon, J.L. Hunter, D.P. Griffis, V. Misra, D.A. Ricks, J.J. Wortman, and D.E. Brownlee

Long-Term Microparticle Flux Variability Indicated by Comparison of Interplanetary Dust Experiment (IDE) Timed Impacts for LDEF's First Year in Orbit with Impact Data for the Entire 5.77-Year Orbital Lifetime 693
C.G. Simon, J.D. Mulholland, J.P. Oliver, W.J. Cooke, and P.C. Kassel

The Interstellar Gas Experiment: Analysis in Progress 705
F. Bühler, D.L. Lind, J. Geiss, and O. Eugster

Space Environments - Microgravity

Follow Up on the Crystal Growth Experiments of the LDEF 725
K.F. Nielsen and M.D. Lind

Author Index 733

Part 3*

Space Environmental Effects - Materials

LDEF Materials Overview 741
Bland A. Stein

Oxygen Isotopes Implanted in the LDEF Spacecraft 791
J.M. Saxton, I.C. Lyon, E. Chatzitheodoridis, P. Van Lierde, J.D. Gilmour, and G. Turner

Silizane to Silica 797
Gale A. Harvey

---

* Part 3 is presented under separate cover.

Stability and Reactivity of Dimethylethoxysilane 811
Richard E. Johnson and Douglas I. Ford

LDEF Polymeric Materials: 10 Months Vs. 5.8 Years of Exposure 827
Philip R. Young, Wayne S. Slemp, and Alice C. Chang

Viscoelastic Characterization of Thin-Film Polymers Exposed to Low-Earth Orbit 849
Alan Letton, Allan Farrow, and Thomas Strganac

A Study of the UV and VUV Degradation of FEP 867
Graeme A. George, David J.T. Hill, James H. O'Donnell, Peter J. Pomery, and Firas A. Rasoul*

Outgassing and Dimensional Changes of Polymer Matrix Composites in Space 877
R.C. Tennyson and R. Matthews

High-Toughness Graphite/Epoxy Composite Material Experiment 889
David K. Felbeck*

LDEF Fiber-Composite Materials Characterization 905
C.J. Miglionico, C. Stein, R.E. Roybal, and L.E. Murr

Space Environmental Effects on LDEF Composites: A Leading Edge Coated Graphite Epoxy Panel 923
Pete E. George, Harry W. Dursch, and Sylvester G. Hill

The Effects of Long-Duration Space Exposure on the Mechanical Properties of Some Carbon-Reinforced Resin Matrix Composites 941
Richard F. Vyhnal

An XPS Study of Space-Exposed Polyimide Film 957
Myung Lee, William Rooney, and James Whiteside

Surface Analyses of Composites Exposed to the Space Environment on LDEF 963
Joseph J. Mallon, Joseph C. Uht, and Carol S. Hemminger

Thermal Expansion Behavior of LDEF Metal Matrix Composites 977
Tuyen D. Le and Gary L. Steckel

Spectral Infrared Hemispherical Reflectance Measurements for LDEF Tray Clamps 1001
B.K. Cromwell, Capt. S.D. Shepherd, C.W. Pender, and B.E. Wood

Surface Characterization of Selected LDEF Tray Clamps 1015
T.F. Cromer, H.L. Grammer, J.P. Wightman, P.R. Young, and W.S. Slemp

Contamination on LDEF: Sources, Distribution, and History 1023
Gary Pippin and Russ Crutcher

Contamination Measurements on Experiment M0003 1033
Eugene N. Borson and F. Barry Sinsheimer

Optical Characterization of LDEF Contaminant Film 1035
Brian K. Blakkolb, Lorraine E. Ryan, Howard S. Bowen, and Thomas J. Kosic

Evaluation of Seals, Lubricants, and Adhesives Used on LDEF 1041
Harry Dursch, Bruce Keough, and Gary Pippin

The Continuing Materials Analysis of the Thermal Control Surfaces Experiment (S0069) 1061
Donald R. Wilkes, Edgar R. Miller, James M. Zwiener, and Richard J. Mell

Thermal Control Paints on LDEF: Results of M0003 Sub-Experiment 18 1075
C.H. Jaggers, M.J. Meshishnek, and J.M. Coggi

LDEF Thermal Control Coatings Post-Flight Analysis 1093
Wayne S. Slemp and Philip R. Young

Selected Results for LDEF Thermal Control Coatings 1099
Johnny L. Golden

Fluorescence Measurements of the Thermal Control Experiments Coatings on LDEF S0069 and AO114 1111
J.M. Zwiener, R.J. Mell, P.N. Peters, J.C. Gregory, D.R. Wilkes, and E.R. Miller

Atomic Oxygen Effects on LDEF Experiment AO171 1125
Ann F. Whitaker, Rachel R. Kamenetzy, Miria M. Finckenor, and Joseph K. Norwood

Monte Carlo Modeling of Atomic Oxygen Attack of Polymers with Protective Coatings on LDEF 1137
Bruce A. Banks, Kim K. de Groh, Bruce M. Auer, Linda Gebauer, and Jonathan L. Edwards

Second LDEF Post-Retrieval Symposium Interim Results of Experiment AO034 1151
Roger C. Linton and Rachel R. Kamenetzky

The Interaction of Atomic Oxygen with Copper: An XPS, AES, XRD, Optical Transmission and Stylus Profilometer Study 1169
Ganesh N. Raikar, John C. Gregory, Ligia C. Christl, and Palmer N. Peters

LDEF Materials Data Analysis: Representative Examples 1187
Gary Pippin and Russ Crutcher

Materials and Processes Technical Information System (MAPTIS) - LDEF Materials Data Base 1201
Joan G. Funk, John W. Strickland, and John M. Davis

Data Bases for LDEF Results 1223
Gail Bohnhoff-Hlavacek

Long Duration Exposure Facility Experiment M0003 Deintegration Observation Data Base 1235
S.R. Gyetvay, J.M. Coggi, and M.J. Meshishnek

Color Photographs 1247

Author Index 1249

Part 4*

Space Environmental Effects - Systems

Overview of the Systems Special Investigation Group Investigation 1257
James B. Mason, Harry Dursch, and Joel Edelman

Post-Flight Analyses of the Crystals from the M0003-14 Quartz Crystal Microbalance Experiment 1269
W.K. Stuckey, G. Radhakrishnan, and D. Wallace

Radiation Sensitivity of Quartz Crystal Oscillators Experiment for the Long Duration Exposure Facility (LDEF)--Part II 1285
J.S. Ahearn and J.D. Venables

The Effect of the Low Earth Orbit Environment on Space Solar Cells: Results of the Advanced Photovoltaic Experiment (S0014) 1291
David J. Brinker, John R. Hickey, and David A. Scheiman

LEO Effects on Candidate Solar Cell Cover Materials 1303
Paul M. Stella

New Results from FRECOPA Analysis 1315
Christian Durin

Degradation of Electro-Optic Components Aboard LDEF 1333
M.D. Blue

---

* Part 4 is presented under separate cover.

LDEF Space Plasma-High Voltage Drainage Experiment Post-Flight Results 1343
J.Y. Yaung, B.K. Blakkolb, W.C. Wong, L.E. Ryan, H.J. Schurig, and W.W.L. Taylor

In Orbit Degradation of EUV Optical Components in the Wavelength Range 10-140 nm AO 138-3 1355
J.P. Delaboudinière, Ch. Carabétian, and J.F. Hochedez

Degradation of Optical Components in a Space Environment 1361
Linda L. DeHainaut, John R. Kenemuth, Cynthia E. Tidler, and David W. Seegmiller

Studies of Effects on Optical Components and Sensors: LDEF Experiments AO-147 (ERB Components) and S-0014 (APEX) 1375
John R. Hickey, David J. Brinker, and Philip Jenkins

Effects Of Long Term Space Environment Exposure on Optical Substrates and Coatings (S0050-2) 1389
Keith Havey, Arthur Mustico, and John Vallimont

LDEF Space Optics Handbook 1399
Robert J. Champetier, Dale R. Atkinson, and William T. Kemp

Ruled and Holographic Experiment (AO 138-5) 1401
Francis Bonnemason

Holographic Data Storage Crystals for the LDEF 1403
W. Russell Callen and Thomas K. Gaylord

Characterization of a Space Orbited Incoherent Fiber Optic Bundle 1413
Stephen A. DeWalt and Edward W. Taylor

Analyses of Space Environment Effects on Active Fiber Optic Links Orbited Aboard the LDEF 1425
E.W. Taylor, T.W. Monarski, J.N. Berry, A.D. Sanchez, R.J. Padden, and S.P. Chapman

Radiation and Temperature Effects on LDEF Fiber Optic Samples 1439
A.R. Johnston, R. Hartmayer, and L.A. Bergman

Long Duration Exposure Facility (LDEF) Low-Temperature Heat Pipe Experiment Package (HEPP) Flight Results 1455
Roy McIntosh, Craig McCreight, and Patrick J. Brennan

Space Environmental Effects - Biology

Final Results of Space Exposed Experiment Developed for Students 1479
Doris K. Grigsby

Continued Results of the Seeds in Space Experiment 1493
Jim A. Alston*

The Future

LDEF Archival System Plan 1499
Brenda K. Wilson

Retrievable Payload Carrier -- Next Generation Long Duration Exposure Facility: Update '92 1511
A.T. Perry, J.A. Cagle, and S.C. Newman †

Next Generation Optical Instruments and Space Experiment Based on the LDEF Thermal Control Surfaces Experiment (S0069) 1521
Donald R. Wilkes

An LDEF II Dust Instrument for Discrimination Between Orbital Debris and Natural Dust Particles in Near-Earth Space 1535
A.J. Tuzzolino, J.A. Simpson, R.B. McKibben, H.D. Voss, and H. Gursky

Future Radiation Measurements in Low Earth Orbit 1551
James H. Adams, Jr.

Color Photographs 1563

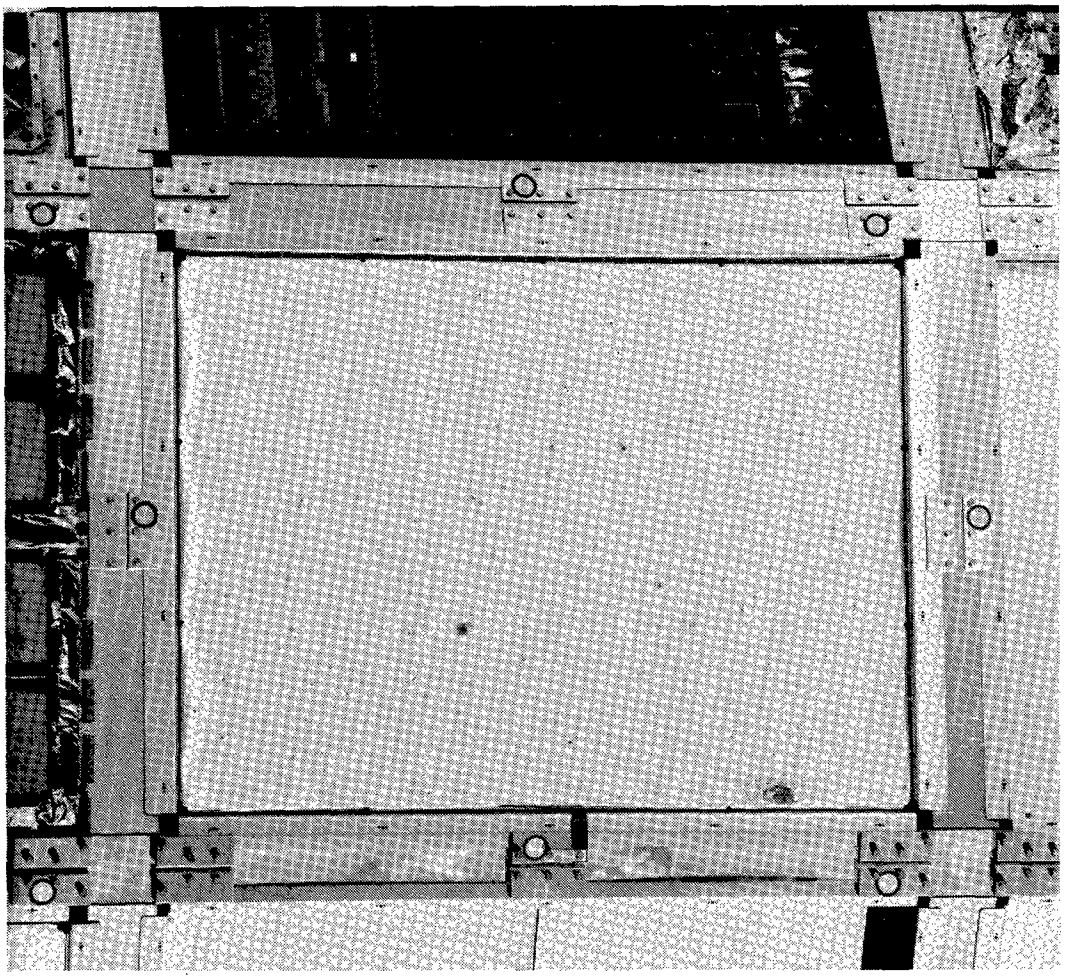
Author Index 1565

*Poster Presentation
† Oral and Poster Presentation

Part 2

SPACE ENVIRONMENTS

METEOROID AND DEBRIS



L-90-10447

INTERIM REPORT OF THE METEOROID AND DEBRIS SPECIAL INVESTIGATION GROUP

Michael E. Zolensky, Herbert A. Zook and Fred Horz
SN2, NASA Johnson Space Center, Houston, TX 77058
Phone: 713/483-5129, FAX: 713/483-5347

Dale R. Atkinson, Cassandra R. Coombs and Alan J. Watts
POD Associates Inc., 2309 Renard Place SE, Suite 201, Albuquerque, NM 87106
Phone: 505/243-2287, FAX: 505/243-4677

Claire B. Dardano and Thomas H. See
Lockheed ESCO, C23, 2400 NASA Rd. 1, Houston, TX 77058
Phone: 713/483-5329, FAX: 713/483-5347

Charles G. Simon
Institute for Space Sciences & Technology, 1810 NW 6th St., Gainsville, FL 32609
Phone: 904/371-4778, FAX: 904/372-5042

William H. Kinard
404, NASA Langley Research Center, Hampton, VA 23665
Phone: 804/864-3796, FAX: 804/864-3769

SUMMARY

The LDEF Meteoroid and Debris Special Investigation Group (hereafter M&D SIG) was formed to maximize the data harvest from LDEF by permitting the characterization of the meteoroid and space debris impact record of the entire satellite. Thus, our work is complementary to that of the various M&D PIs, all of whom are members of the SIG. This presentation will summarize recent results and discussions concerning five critical SIG goals: 1) classification of impactors based upon composition of residues, 2) small impact (microimpact) features, 3) impact cratering and penetration data to derive projectile sizes and masses, 4) particulate flux estimates in low-Earth orbit, and 5) the LDEF Meteoroid and Debris database.

INTRODUCTION

A meeting of the Meteoroid and Debris Special Investigation Group (M&D SIG) was held in March of 1992. We reviewed progress towards the M&D SIG goal of using the entire LDEF satellite to define the meteoroid and space debris environment in low-Earth orbit. M&D SIG members are at work on numerous projects, including use of 3-D impact feature images to derive precise crater depth and diameter information, detailed examination of the impact record of the LDEF frame (which provided common material exposed in all pointing directions), examination of impact damage on aluminum panels, characterization of impactor residues, and modelling of the Near-Earth particulate environment using M&D SIG data. All of these activities are reported separately in this conference proceedings document.

One determination of the recent M&D SIG meeting was that consensus should be met by the membership on five key activities; these are (a) establishment of standard criteria for distinguishing natural from man-made impactors, (b) characterization of same for very small impact features (<10 um diameter), (c) use of laboratory simulations for calibration of impactor properties from observed impact features, (d) use of LDEF results to calculate particulate flux in low-Earth orbit, and (e) use of a standardized database for M&D results. This report is a first attempt to address these critical issues in a forum accessible to other LDEF investigators and the community at large, both for information purposes and also to invite critique from the larger community. Consensus on these issues has not always been achieved, as will become obvious. However, we are able to delineate the scope of disagreements and suggest ways of resolving them. For example, we recognize that much future work will necessarily concern calibration of craters in aluminum (the most common material on the LDEF), and cratering and penetration processes in the Teflon thermal blankets.

As the reader has now discovered, this paper is not a global overview of M&D SIG activities, but is narrowly focussed. We discuss each critical issue below, in the order in which presented above.

CRITERIA FOR DISTINGUISHING NATURAL FROM MAN-MADE IMPACTORS

Introduction

Since different capture experiments on LDEF employed different collection schemes and different analysis techniques, it has proved difficult to establish universal criteria for distinguishing between natural and man-made impactors. The situation becomes more complex for the entire LDEF with its myriad of experimental surfaces and analytical investigations. However, in the interest of promoting the comparisons of results from many laboratories, we propose the following classification scheme. This scheme has been employed for some LDEF studies already (ref. 1).

Contamination

Clearly, the level and composition of contamination must be carefully established before analysis of residues should be attempted. Also, supposedly well-understood LDEF materials often contain impurities which, though minute on a gross scale, are important at the scale necessary for analysis of impactor residues. LDEF surfaces are sprinkled with particles of alkali-halide salts (from oceanic spray and human waste), paint flakes containing high concentrations of Ti and/or Zn and/or Mg (from LDEF paints that were shed due to the action of atomic oxygen and ultraviolet radiation, flakes of Al from blankets and antenna arrays, and other less characterized materials.

Because of ubiquitous Si contamination on LDEF (from outgassing RTV?) particular care must be employed in use of this element for establishing criteria. This is particularly unfortunate since Si is an important element in meteoroids. Other elements found within this particular contaminating material include O, C, H, Na, K and Ca.

Criteria For Natural Impactors

Any of these constitute sufficient conditions:

A Chemical Criteria
- (1) Mainly Fe with minor S and/or Ni
- (2) Various proportions of Mg, Fe and Ca + minor S, Ni, and/or Al
- (3) Fe+Cr only if O is also present in same residue grains and outgassed RTV contamination is not locally evident
- (4) Non-terrestrial isotopic compositions
- (5) Presence of solar wind implanted He or Ne
- (6) Given that impact residues are frequently fractionated, comparisons between ratios of refractory to volatile elements can also be employed to establish criteria for origin. Useful ratios are Al/Mg, Ca/Mg and Ti/Mg (see ref. 2 for application of these ratios).

B Physical Criteria
- (1) Presence of solar flare tracks

C Mineralogical Criteria
- (1) Contains olivine, pyroxenes, ferromagnesian phyllosilicates (serpentines, smectites) and/or Fe-Ni sulfides

Criteria For Man-made Impactors

Not any of the above criteria; also:

D General Criteria
- (1) Mainly Al or Al_2O_3 + minor Fe, Ni, Cr, Cl, Na or C
- (2) Mainly Fe with accessory Cd, Ti, V, Cr, Ni, Mn, Co, Cu or Zn with the latter elements present in abundances greater than to be expected for common minerals. A common man-made material is stainless steel consisting of Fe, Cr and Ni.
- (3) Various proportions of Ca, Al, Si, Ti, K, Zn, Co, Sn, Pb, Cu, S, Cl, Au or Ag.

Surface Specific Criteria

Au- No change
Ge- No change
Al- Expect Al contamination to affect criteria A1, A2 and D2. Criteria D1 will not apply
Steel- Expect Fe and Cr contamination to affect criteria A1 and A2. Be careful when applying criteria A3 or D2.

MICROIMPACT FEATURES

A subcommittee of the M&D SIG has summarized all data gathered on micro-craters or perforations (features nominally <10 μm in diameter) found on LDEF surfaces. The goal is to issue a final summary report that will include all reported impact flux data in several formats in

order to allow maximum utilization by the various communities. The M&D SIG practice of reporting all primary data along with any interpretive data will be followed. The final report will also include summaries of information reported in the literature or directly to the M&D SIG concerning micro-impactor chemical compositions and developments and new insights into the theoretical and semi-empirical prediction of micro particle fluxes and velocity distributions in low-Earth orbit (LEO).

This interim report lists the LDEF cumulative micro particle crater/penetration fluxes reported to date in the literature (refs. 3-9, ft notes 1-4)* or directly to this committee (ref. 10, ft notes 5-6). Table 1 lists the flux data (number/m^2/s) along with LDEF experiment numbers and bay locations, the time periods of exposure, the types and amounts of surface materials scanned, the scanning methods, the minimum detectable crater diameters (>90% confidence) as reported by the individual investigators, and the number of impact features counted. Data is grouped by LDEF locations and exposure times and listed in order of increasing minimum feature size. The sources for the tabulated data are listed at the end of the table. Data for micro-craters and penetration holes in Teflon thermal blankets are not included at this time, but will be added along with other data for the next interim report. These blankets are a valuable source of impact data, but the size of micro craters that can be observed will be limited by the surface texture of the Teflon blankets, which is highly variable and results from atomic oxygen and ultraviolet radiation damage.

The LDEF community is encouraged to contribute new information on small impact features. Several of the investigators who supplied information for this report have undertaken the difficult task of converting data from different LDEF surfaces (metals, foils, ceramics) into a common format. Most notably, Horz et al. (ref. 3), Mandeville et al. (ref. 4, ft note 1) and especially McDonnell, et al. (refs. 5-7) have discussed and applied conversion formulae extensively. Interested readers are referred to these sources for more information. Further refinement in these procedures can be expected as more data is collected and correlated. The committee's final report will contain the latest versions of these investigators' formulae.

There are numerous empirical and semi-empirical relationships developed to convert impact crater and penetration hole morphology in metals, crystalline materials and thin films (metal and polymeric) to particle mass or size, or equivalent crater size in aluminum, or equivalent penetration thickness for aluminum film. All such methods are dependent on general assumptions about impactor density and velocity and interaction with the target. Velocity and density assumptions can be applied unilaterally to all features on a given LDEF side and provide an acceptable level of comparison for a statistically large sample set. Average velocities for micro-particles striking the various sides of LDEF can be calculated from reported flux data with modest accuracy. In addition, as data on impactor chemical composition is reported, greater insight into the range and average densities of micro impactors can be gained.

The portions of conversion formulas that involve terms dependent on the physical properties of the target materials as they relate to interaction with hypervelocity micro-impactors can be accurately determined in many cases by empirical evaluation. Van de Graaff accelerators are useful for determining material response to hypervelocity micro-particle impacts. While there is some test data on Fe and Al metals and foils, much more data is needed for these as well as for micro-particle impacts into crystalline materials such as Si and Ge. However, a thorough review of the literature concerning micro-particle hypervelocity impacts into these materials may provide enough data to determine the cratering characteristics of these events under orbital conditions.

* See footnote section that follows the reference list.

Table 1. Cumulative particulate impact fluxes observed on LDEF surfaces for small craters (<10 μm).

LDEF Exp.	Tray	Time Period	Material Scanned	Total Area Scanned (cm^2)	Scanning Method	Min. Detectable Crater dia. (μm)	Number of Impacts	Cumulative Flux ($m^{-2}s^{-1}$)	Ref. or *Ft note*
ROW 1									
Clamp 8	A01	5.77 yrs	Al	2	SEM[9]	4	8	$2.2x10^{-4}$*	*8*
ROW 3									
A0201	C03	Day 1-8	MOS[1]	942	electron.[2]	0.4[3]	64	$9.8x10^{-4}$	*4*
A0201	C03	Day 1-8	MOS[4]	629	electron.[2]	1.0[5]	3	$6.9x10^{-5}$*	*4*
A0138	B03	Day 10-280	Au[13]	2.1	SEM[9]	1	[1]	$2.0x10^{-4}$	11
A0201	C03	Day 9-346	MOS[1]	942	electron.[2]	0.4[3]	391	$1.4x10^{-4}$	*4*
A0201	C03	Day 9-346	MOS[4]	619	electron.[2]	1.0[5]	183	$1.0x10^{-4}$	*4*
A0138	B03	Day 10-280	Al[14]	25	SEM[9]	2	5	$8.6x10^{-5}$*	11
A0138	B03	5.77 yrs	Al[15]	4	SEM[9]	1	15	$2.1x10^{-4}$	4,11
A0138	B03	5.77 yrs	Al[15]	2	SEM[9]	1	[8]	$2.2x10^{-4}$*	4,11
A0138	B03	5.77 yrs	Al[15]	8.6	SEM[9]	2	6	$3.8x10^{-5}$*	4,11
A0138	B03	5.77 yrs	Al[15]	9.9	SEM[9]	3	4	$2.2x10^{-5}$*	4,11
A0023	C03	5.77 yrs	Al[12]	53	optical	4	[22]	$2.3x10^{-5}$	6
A0201	C03	5.77 yrs	MOS[4]	570	optical	1.0[5]	275	$2.7x10^{-5}$	*6*
A0023	C03	5.77 yrs	Al[11]	53	optical	5	[6]	$6.2x10^{-6}$*	6
A0023	C03	5.77 yrs	Al[7]	203	optical	7	26	$7.0x10^{-6}$	6
A0201	C03	5.77 yrs	MOS[4]	294	optical	14	12	$2.2x10^{-6}$	6
ROW 6									
A0201	D06	Day 1-8	MOS[1]	942	electron.[2]	0.4[3]	17	$2.6x10^{-4}$	*4*
A0201	D06	Day 1-8	MOS[4]	629	electron.[2]	1.0[5]	2	$4.6x10^{-5}$*	*4*
A0201	D06	Day 9-346	MOS[1]	860	electron.[2]	0.4[3]	3012	$1.2x10^{-3}$	*4*
A0201	D06	Day 9-346	MOS[4]	622	electron.[2]	1.0[5]	1198	$6.6x10^{-4}$	*4*
A0201	D06	5.77 yrs	MOS[4]	59	optical	1.0[5]	411	$3.8x10^{-4}$	*6*
A0201	D06	5.77 yrs	MOS[4]	59	optical	1.0[5]	114	$1.1x10^{-4}$	*6*
A0023	E06	5.77 yrs	Al[10]	107	optical	3	[1158]	$6.0x10^{-4}$	6
A0023	E06	5.77 yrs	Al[12]	53	optical	4	[218]	$2.2x10^{-4}$	6
A0023	E06	5.77 yrs	Al[11]	53	optical	5	[187]	$1.9x10^{-4}$	6
A0023	E06	5.77 yrs	Al[7]	203	optical	7	570	$1.1x10^{-4}$	*6*

Table 1. Continued

LDEF Exp.	Tray	Time Period	Material Scanned	Total Area Scanned (cm^2)	Scanning Method	Min. Detectable Crater dia. (μm)	Number of Impacts	Cumulative Flux ($m^{-2}s^{-1}$)	Ref. or *ft note*
ROW 7									
Clamp 1	C07	5.77 yrs	Al	2	SEM[9]	2	10	$2.7x10^{-4}$	2
ROW 8									
A0187	E08	5.5 yrs	Ge[16]	2.2	SEM[9]	0.25	184	$4.8x10^{-3}$	5
A0187	E08	5.5 yrs	Ge[16]	7	SEM[9]	1	389	$3.2x10^{-3}$	5
A0187	E08	5.5 yrs	Ge[16]	7	SEM[9]	2	189	$1.6x10^{-3}$	5
A0187	E08	5.5 yrs	Ge[16]	7	SEM[9]	4	56	$4.6x10^{-4}$	5
ROW 9									
A0201	C09	Day 1-8	MOS[1]	923	electron.[2]	0.4[3]	232	$3.6x10^{-3}$	4
A0201	C09	Day 1-8	MOS[4]	629	electron.[2]	1.0[5]	72	$1.7x10^{-3}$*	4
A0201	C09	Day 9-346	MOS[1]	874	electron.[2]	0.4[3]	4308	$1.6x10^{-3}$	4
A0201	C09	Day 9-346	MOS[4]	599	electron.[2]	1.0[5]	1470	$8.1x10^{-4}$	4
A0201	C09	5.77 yrs	MOS[4]	59	optical	1.0[5]	934	$8.7x10^{-4}$	6
A0023	C09	5.77 yrs	Al[7]	102	optical	7	435	$2.3x10^{-4}$	6
A0023	C09	5.77 yrs	Al[8]	26	optical	8	110	$2.3x10^{-4}$	11
ROW 12									
A0201	B12	Day 1-8	MOS[1]	942	electron.[2]	0.4[3]	59	$9.1x10^{-4}$	4
A0201	B12	Day 1-8	MOS[4]	629	electron.[2]	1.0[5]	4	$9.2x10^{-5}$*	4
A0201	B12	Day 9-346	MOS[1]	874	electron.[2]	0.4[3]	2408	$8.6x10^{-4}$	4
A0201	B12	Day 9-346	MOS[4]	605	electron.[2]	1.0[5]	1077	$6.1x10^{-4}$	4
A0201	B12	5.77 yrs	MOS[4]	59	optical	1.0[5]	430	$3.9x10^{-4}$	6
A0201	B12	5.77 yrs	MOS[4]	39	optical	14[6]	66	$9.3x10^{-5}$	6
A0023	D12	5.77 yrs	Al[10]	53	optical	3	[361]	$3.7x10^{-4}$	6
A0023	D12	5.77 yrs	Al[11]	107	optical	5	[298]	$1.5x10^{-4}$	6
A0023	D12	5.77 yrs	Al[7]	203	optical	7	467	$1.3x10^{-4}$	6

Table 1. Continued

LDEF Exp.	Tray	Time Period	Material Scanned	Total Area Scanned (cm^2)	Scanning Method	Min. Detectable Crater dia. (μm)	Number of Impacts	Cumulative Flux ($m^{-2}s^{-1}$)	Ref. or *ft note*
EARTH-FACING									
A0201	G10	Day 1-8	MOS[1]	943	electron.[2]	0.4[3]	16	$2.5x10^{-4}$	*4*
A0201	G10	Day 1-8	MOS[4]	629	electron.[2]	1.0[5]	0	$<2.3x10^{-5}$*	*4*
A0201	G10	Day 9-346	MOS[1]	893	electron.[2]	0.4[3]	28	$1.1x10^{-5}$	*4*
A0201	G10	Day 9-346	MOS[4]	619	electron.[2]	1.0[5]	29	$1.6x10^{-5}$	*4*
A0201	G10	5.77 yrs	MOS[4]	354	optical	1.0[5]	185	$2.9x10^{-5}$	*6*
A0201	G10	5.77 yrs	MOS[4]	354	optical	14[6]	1	$1.6x10^{-7}$*	*6*
SPACE-FACING									
A0201	H11	Day 1-8	MOS[1]	688	electron.[2]	0.4[3]	33	$6.9x10^{-4}$	*4*
A0201	H11	Day 1-8	MOS[4]	472	electron.[2]	1.0[5]	5	$1.5x10^{-4}$*	*4*
A0201	H11	Day 9-346	MOS[1]	677	electron.[2]	0.4[3]	347	$1.8x10^{-4}$	*4*
A0201	H11	Day 9-346	MOS[4]	461	electron.[2]	1.0[5]	150	$1.1x10^{-4}$	*4*
A0201	H11	5.77 yrs	MOS[4]	157	optical	1.0[5]	171	$6.0x10^{-5}$	*6*
A0201	H11	5.77 yrs	MOS[4]	177	optical	14[6]	55	$1.7x10^{-5}$	*6*
A0023	H11	5.77 yrs	Al[7]	310	optical	7	193	$3.4x10^{-5}$	6
A0023	H11	5.77 yrs	Al[8]	0.5	SEM[9]	2	20	$2.2x10^{-3}$	2
A0023	H11	5.77 yrs	Al[8]	0.5	SEM[9]	4	15	$5.8x10^{-4}$	2

Notes

Values in brackets [ ] are subject to verification.
Fluxes marked with an asterisk * were calculated from undersized sample sets (<10 impacts).

[1]0.4 μm SiO_2 on Si
[2]Electronic signals
[3]Equivalent to 1 μm in Al
[4]1 μm SiO_2 on Si
[5]Equivalent to 3 μm in Al
[6]Spall diameter
[7]4.8 μm foil
[8]25 μm foil
[9]Scanning Electron Microscopy
[10]2 μm foil
[11]3.7 μm foil
[12]3.1 μm foil
[13]125 μm foil
[14]5 μm foil
[15]Plate
[16]200 μm wafer

Data from penetrations and cratering in aluminum foils on LDEF can provide the means for calibration of the crater size relationship between Al and other materials. This data can also be used to calibrate the sensitivity of the Interplanetary Dust Experiment (IDE) sensors (A0201). Crater-size distributions in these materials can also be compared. Additional information is highly desirable on micro-crater densities and size distributions on other materials on LDEF, especially optically-smooth surfaces.

Several important observations are immediately evident from the data in Table 1. Singer, Mulholland and co-workers (refs. 8-9, ft note 4), have reported a short-term increase in micro-particle debris impacts on LDEF following deployment and attributed the source to Shuttle activities. Electronic data from the A0201 high-sensitivity sensors located on the Earth, Space and West (anti-ram) sides of the satellite showed a greatly increased flux of micro-particle impacts during the first 8 days following deployment. The impact fluxes on the low sensitivity A0201 sensors on these same locations were the same or less than their respective first year fluxes, indicating that the vast majority of the particles must be submicron. The impact fluxes (for the initial 8 days) on both types of A0201 sensors mounted on the east (ram) side of LDEF were approximately double their first year fluxes. Further examination of this data combined with refined IDE sensor sensitivity relations derived from orbital data and from archived ground test data should define a narrower size range for these debris particles.

There is fairly good agreement of the density of small crater densities for all surfaces on a particular side of LDEF that were exposed for the entire 5.77 year mission. Comparison of Al foil and plate data from the West and North sides of LDEF (trays C03 and D-12, respectively) with the IDE (Exp. A0201) sensor data from the same locations (ref. 10) indicates that the 1.0 μm metal-oxide-semiconductor (MOS) sensors were triggered by particles that would leave an ~3 μm diameter crater in Al. This is based on the determination of McDonnell, et al. (ref. 6), that the marginal perforation limit, f, for the A0023 thin foils was given by:

$$f = (0.59)(1.15)D_c = 0.68D_c$$

where D_c is the crater diameter at the foil surface. While no 5.77 year flux data is available for the IDE 0.4 μm MOS sensors (due to power loss), a first order estimate of the sensitivity factor can be derived from the ratio of the insulator thickness:

$$(0.4/1.0) \times 3\ \mu m = 1.2\ \mu m \text{ equivalent Al crater size}$$

There is much to be said (and much that has been said) about the reported flux distributions listed in Table 1. These tasks are appropriately left to the community and a summary of their efforts will appear in the committee's final report. However, a question of long term micro-particle impact flux variation on the West side of LDEF by factor of 2 is raised by the temporal data reported to this committee by Mulholland, et al. (ref. 9, ft note 4), and Mandeville (ft note 6). According to these investigators, a higher particulate flux rate occurred during the first year of LDEF's orbit compared to the 5.77 year average flux. Mulholland also reported first year fluxes on LDEF's space-facing and North (row 12) sides that were about twice as great as the 5.77 year average fluxes for these locations (ref. 10). The East (ram) sensors showed no significant variation in the first year and 5.77 year impact fluxes. South (row 6) side sensors have not been evaluated yet. Earth-facing panel IDE sensors showed a 5.77 year flux rate that was twice as high as the rate during the first year, and no large particle impacts were noted on these sensors. These are interesting results that may eventually be correlated with orbital or natural events by the community.

Because of the reported long term temporal variations in micro-particle impact fluxes, it is imperative to correlate all other temporal impact data available from surfaces that were only

exposed during the first year of LDEF's orbit. Data from optically smooth surfaces are preferred to other surfaces because of a reduced crater-size detection threshold.

Another question of interest to this committee is: what are the smallest size primary impacts observed on LDEF? Walker and Swan (ft note 5) have reported results from high magnification (1000X) SEM scans of their optically-smooth Ge capture cells located on row 8 (Table 1). In general, all craters on row 8 Ge wafers had associated spall zones. The exposure time for these surfaces is given as ~5.5 years because they were initially covered with 2 μm thick metallized Mylar films that apparently failed during the first few months of orbit. The smallest craters found by the researchers were ~0.1 μm in diameter. In most cases the surface texture of metal samples precludes identification of such small features.

In summary, this interim report of the M&D SIG Micro Crater Committee has

(1) listed the micro-particle cumulative flux data reported to date,
(2) noted general consistency among the 5.77 year flux rates reported from different surfaces,
(3) identified long term temporal variations in the reported "average" flux rates,
(4) listed the cumulative flux data for the smallest features identified on LDEF (0.1 μm craters in Ge) to date.

The following tasks are required to develop a comprehensive data base on micro-particle impacts on LDEF:

(1) More ground test data are needed on hypervelocity (10-20 km/s) micro-particle impacts into crystalline materials such as Si and Ge. A thorough review of the literature should define the needs for additional test data.
(2) Additional information is highly desirable on micro-crater densities and size distributions on other materials on LDEF, especially optically-smooth surfaces.
(3) It is imperative to correlate all other temporal impact data available from surfaces that were only exposed during the first year of LDEF's orbit.
(4) Chemical analysis information on particle sources should be collected.

Although the fourth point listed has not been discussed in detail in this interim report, a significant data base on micro-particle residue analyses is under development (see refs. 2 & 11, ft note 1). Several hundred impact sites have been analyzed by various investigators, and significant new data was presented at the Second LDEF Post-Retrieval Conference in June 1992.

CONVERSION OF IMPACT FEATURE DIMENSIONS INTO PROJECTILE PROPERTIES: CALIBRATION OF LDEF FEATURES

Introduction

An important goal of the M&D SIG is to reconstruct the initial impact conditions for individual impact craters and penetration holes, as well as the average conditions characterizing any given population of impact features. Of specific interest is the derivation of projectile properties, such as size, mass, and kinetic energy, and their relative and absolute frequencies typical for a given population of impact features, and ultimately for the entire LDEF. These frequencies constitute first order information for the reconstruction of possible sources and source mechanisms for both natural and man-made particles. They also form the basis for any predictive capabilities regarding collisional hazards to operations in LEO. As a consequence, the

dimensional analysis of impact features and the conversion of these dimensions into projectile properties constitutes a high priority activity of the M&D SIG.

Such efforts are frequently also referred to as "calibrations" because they utilize craters and penetration holes produced under known laboratory conditions. The latter reveal significant dependency on impact velocity, angle of incidence and diverse physical properties of both the target and projectile materials, such as density, compressive strengths, porosity, and material-yield criteria under high dynamic compressive and tensile stresses. As a consequence, results obtained under a specific set of laboratory conditions are not readily applied to another set of conditions. Substantial efforts by many workers, both experimentalists and theoreticians, are underway to understand the effects of absolute projectile size (dimensional scaling), velocity (velocity scaling) and material properties (strength scaling) that control the size of an impact feature, including combined parameters such as kinetic energy (energy scaling). Proper interpretation of LDEF impact features depends on the correct scaling of all parameters, yet improved dimensional scaling and velocity scaling rank foremost in the goals of LDEF workers, because the current experimental data base suffers from a paucity of information at appropriate projectile sizes (1-1000 μm) and velocities (>10 km/s).

This report reviews some of the existing experimental data and their generalizations to permit interpretation of LDEF craters and penetration holes. It does not intend to provide a complete overview of the extensive impact literature. We will also demonstrate that computer based impact simulations have evolved into powerful tools to permit extrapolation of laboratory results to conditions beyond those actually simulated.

Experimental Calibration

All calibration activities begin with well-controlled experiments, combined with standardized measurement techniques. For example, when measuring the diameters of craters or perforation-holes several different diameter measurements can be made. The diameters can be measured at the original surface of the impacted material (this is the preferred measurement), or they can be measured at the center of the crater/perforation lip, or they can be measured at the outer lip edges. These diameters can differ by factors of two to four from each other for the smallest craters. If the type of measurement is well-documented, and if the impactor and target materials are well-characterized and the impact characteristics (i.e. velocity, angle of incidence) are known, it may be possible to convert these measurements to equivalent diameters at the original surface of the impacted materials. For calibration, the better characterized the laboratory conditions, the more useful the data. The impactor and target materials should have well-known physical properties, including knowledge of how these properties vary with the extreme temperatures and pressures characteristic of hypervelocity impacts. If the impact data will be used to calibrate or benchmark a hydrodynamics computer code, the materials' equations of state must also be well known. For these reasons, initial calibration experiments typically use such materials as aluminum, stainless steel, or lexan. In addition, initial calibration experiments often use the same material (e.g. aluminum) for both target and impactor.

Several experimental techniques are available for performing calibration tests. All of these techniques have positive and negative features, and there is not currently one which directly simulates all aspects of the meteoroid and debris impact environments. For determining material properties and equations of state, flat-plate impact experiments at the velocities of interest are the best technique. The capability to get the appropriate velocities with the correct types of materials is the primary issue in calibration testing. Various types of accelerators (e.g. Van de Graaff electrostatic accelerators, plasma-drag accelerators or light-gas guns) can achieve different velocity regimes, but with a limited range of particle sizes, shapes and materials. For

example, two-stage, light-gas guns are available which can launch almost any material larger than ~50 μm, of many different shapes, to velocities typically <8 km/s. On the other hand, Van de Graaff accelerators can launch particles at velocities exceeding 20 km/s, yet only for submicron-sized, surface-conducting and highly-charged projectiles. This is why these particular experiments typically employ iron particle projectiles, and why experiments with silicates and other interplanetary dust analogues are lacking. These limited launch capabilities have led to a paucity of data on various materials and impact conditions which are nonetheless critical to LDEF data analysis.

Analytical Calibration

Calibration is completed when analytical models have been checked to ensure they correctly reproduce impact phenomenology and once they include predictive capabilities of impact effects and damage. Analytical models can be in the form of either semi-empirical equations for first-order analysis or hydrodynamic computer codes for more precise analysis and a better understanding of the physical processes involved.

Semi-Empirical Equations

Semi-empirical equations can be curve-fits to limited experimental laboratory data sets or can be derivations from physical equations, but with empirical constants or exponents. Both approaches are highly dependent on the size and quality of the data set. In addition, the second type of equation is highly dependent on the assumptions which were used to perform the derivations. The derived equations can be much more accurate than pure curve fits, but can suffer due to the assumptions. For example, it is common practice to include only target material properties in these equations. This is a poor practice, because material properties of the impactor are just as important.

Many semi-empirical equations have been proposed. However, the equations which have been most widely used in analyzing space exposed surfaces include: Pailer and Grun (ref. 12) and Carey et al. (ref. 13) for marginal perforations; Cour-Palais (14) for cratering in metals, specifically in aluminum targets; and Gault (ref. 15) and Mandeville (ref. 16) for brittle glass or ceramics. With the increased data from the last several years, the semi-empirical equations have been improved somewhat, yet there is still no overwhelming concensus regarding improved utility to cases beyond those simulated in the laboratory, as discussed by Humes (ref. 17), for example.

Currently, the recommended equations are as follows. For marginal perforations of Al we use the McDonnell and Sullivan (M&S) equation (ref. 7):

$$f_{max}/d_P = 1.023 d_P^{1.056} (\rho_P/\rho_T)^{0.476} (\sigma Al/\sigma_T)^{0.134} V_P^{0.664}$$

where f_{max} is the equivalent thickness of foil for the ballistic limit, d is diameter (measured in cm), T stands for the target, P for the particle, ρ is density, σ is strength, and V is impact velocity (in km/sec). For craters in aluminum use the formula of Cour-Palais (ref. 14) as updated by Humes (ref. 17):

$$P = 0.42 m^{0.352} \rho_P^{1/6} V^{2/3} (\cos\theta)^{2/3}$$

where P is crater depth measured down from the ambient surface, m is particle mass, and θ is the

impact angle. For craters in brittle materials use the equation of Mandeville (ref. 16):

$$\log D_c = 0.48 + 0.36 \log m$$

where D_c is crater diameter.

The biggest shortcoming of most of these equations is the limited data set used for derivation. Also, in many cases we are not yet smart enough to properly synthesize the data, and the processes are extremely complex, defying treatment via a few simple terms.

New efforts underway by LDEF PIs and SIG members will attempt to combine data sets and revise equations for marginal perforation and cratering based on the increased quantity of data. Of particular interest in their work is the transition from cratering to penetration, such that small craters and relatively large penetration holes from a single experiment surface may be converted to internally consistent distributions of projectile sizes; this is not currently the case, as described by Warren et al (ref. 18) for Solar Max and by Humes (ref. 17) for LDEF surfaces. In addition, McDonnell, Mandeville, Watts and Atkinson are continuing their individual developments of the current marginal perforation, cratering, and brittle cracking equations. Horz et al. (ft note 8) suggest that the marginal penetration limits can possibly be replaced by unique solutions for projectile size from the measurement of hole diameter and foil thickness (at unit velocity). Much more experimental data is still needed, particularly for the brittle cracking of ceramics and the behavior of composites in order to define good semi-empirical equations for major classes of materials employed in spacecraft.

Hydrodynamics Codes

Hydrodynamics codes are based on physical principles. These computer codes require long run times and large computer memories, and are typically used on computer workstations or supercomputers. These codes are very useful for predicting specific cases, or for looking at how impact phenomena vary with changes in material properties. However, their long run times (which lead to high costs) make them of little use for first-order predictions.

These codes are very dependent on the degree of characterization of the materials' equations of state, properties, property variations with temperature and pressure, and pre-impact states. If these are not known, then specific impact cases cannot be predicted. In addition, because of material variations, the codes require benchmarking against actual experiments. This benchmarking consists of making predictions, comparing the predictions against actual experimental data, and "tweaking" material properties within the acceptable physical ranges to consistently match the data.

Many hydrodynamics codes are currently in existence. In the past, HULL and CSQ were widely used for impact predictions. Currently, the best codes for impact predictions are the CTH code from Sandia National Laboratory and the MESA code from Los Alamos National Laboratory. All of these codes are undergoing continual improvements. In addition, a new Smoothed Particle Hydrodynamics (SPH) code is in development at the Phillips Laboratory in Albuquerque, NM.

The biggest drawbacks in using hydrodynamics codes are the lack of equation of state data for many of the materials of interest, and the codes' problems in modeling ceramics and composites. The latter problems will be slowly reduced with future codes and further code improvements. However, the lack of equation of state data can only be fixed by collecting additional data.

Example Of An LDEF-Related Calibration

The following is an example of a calibration performed for interpretation of LDEF cratering data and for selecting the "best" marginal perforation equation. First, the CTH code has been benchmarked against experimental data. Then the CTH code has been used to predict marginal perforations in typical satellite materials. These predictions have then been compared against predictions made using the Pailer and Grun or the McDonnell and Sullivan equations. We present here results of a preliminary study, which concentrates on the issue of marginal perforations (penetrations). The emphasis on aluminum for both impactors and targets is based upon the wide availability of data for this metal. Fortunately, both the frame of LDEF and most space debris are composed of aluminum. Because symmetric modelling avoids the issue of material strengths and densities this aspect was not well studied, except in the context of matching Horz's data.

A series of calculations have been made using the CTH code to investigate the penetration of typical satellite walls with typical space debris, which were then compared to LDEF observations. For these calculations the walls were assumed to be Al 6061-T6 alloy. For the CTH calculations, the impactors were spherical aluminum bodies, and both impact speed and size were varied to determined a matrix of penetration conditions. The matrix was bounded with the upper impact speed of about 20 km/s for debris (head-on collisions), and with a maximum particle size of 0.5 cm (the largest crater observed on LDEF about 0.5 cm diameter). Table 2 lists the results of these preliminary runs.

The first task with the CTH code was to perform some type of validation between experimental results and reproducible computer simulations. The data and results from a series of gas gun experiments was provided by Fred Horz (NASA JSC) (Table 3; also ft note 8).

The data provided by Horz contained many combinations of materials that were used for the impactor and the projectile. In order to get reasonably accurate results with the CTH code the materials chosen had to have material properties that were readily available and well characterized. Complex compound materials were ruled out, leading to a choice of an aluminum target and an impactor made of soda-lime glass.

Several models were available in CTH code to permit thermodynamic formulation of an equation of state; however, the one chosen was the Mie-Gruneisen. We caution that this is largely a thermodynamic parameter, related to shock isentropes, that may have little to do with affecting the material flow. The CTH code has an enormous number of options for both equations of state and constitutive relations. These calculations concentrated on simple elastic-plastic models and simple fracture (spall) models. The plastic compressive yield strengths were varied for both the soda lime impactors and the aluminum targets. The spall strengths were similarly varied. Yield and spall strength data were obtained from the literature and soda-lime manufacturers; for aluminum the data were based solely upon "best fit", since aluminum can have grossly varying properties depending upon composition and tempering history. By inspection of the literature we found that the closest fit for the aluminum targets of Horz was Al 1100 alloy with a temper of H16. The final best fit data and information entered into the code were the following:

Aluminum:

yield = 1.3 kbars, spall = 1.6 kbars; density = 2.70g/cm^3;
sound speed = 5.31 x 10^5 cm/sec; Gruneisen = 2.25; heat capacity = 1.04 x 10^{11} erg/cm^3/eV; constant in linear Hugoniot = 1.34

Soda-lime Glass (Horz Experiments):
yield = 10 kbars, spall = 1.2 kbars; density = 2.20g/cm^3;
sound speed = 5.91 x 10^5 cm/sec; Gruneisen = 0.40; heat capacity = 8.744 x 10^{10} erg/cm^3/eV; constant in linear Hugoniot = 1.50

TABLE 2 Results of preliminary runs

Plate Thickness (mm)	Proj. Diam. (mm)	Proj. Veloc. (km/s)	Penetration	Comments
2.5	5.0	1.3	Yes	Spall
2.5	1.0	4.4	Yes	Spall
2.5	1.0	4.3	No	Spall
2.5	0.75	8.0	Yes	Spall
2.5	0.75	7.5	No	Spall Layers
2.5	0.50	17.0	Yes	Clean Hole
2.5	0.5	16.0	No	Spall Layers
2.0	1.0	3.5	Yes	Spall
2.0	1.0	3.0	No	Crater
2.0	0.75	5.3	Yes	Spall
2.0	0.75	5.0	No	Spall Layers
2.0	0.50	11.3	Yes	Spall
2.0	0.50	11.0	No	Spall Layers
2.0	0.25	20.0	No	Vapor Prob
1.5	1.0	2.2	Yes	Spall
1.5	1.0	2.0	No	Crater
1.5	0.75	3.2	Yes	Spall
1.5	0.75	3.0	No	Spall layers
1.5	0.50	7.0	Yes	Spall
1.5	0.50	6.5	No	Crater

TABLE 3: Data from F. Horz on Soda-Lime Glass Impact Experiments

Shot Number	Projectile Diameter (mm)	Aluminum Thickness (mm)	Velocity (km/s)	Hole Diam. (mm) Test	Hole Diam. (mm) CTH
786	3.175	9.02	5.8	3.62	10
787	3.175	8.64	5.81	7.31	12.5
788	3.175	7.62	5.79	10.19	12.5
789	3.175	1.6	5.87	8.76	10
791	3.175	10.94	5.84	13.73*	11.00*
785	3.175	9.525	5.91	2.24	9.8

*Crater diameter, not a penetration

Data/Model Fit

Workers at POD, Assoc., have tried to fit the penetration data with analytic equations. The CTH data is approximately fitted by the function:

$$V_P = k\, d_P^{\alpha}\, T^{\beta}$$

where k is a constant, V_P is the projectile velocity, d_P is the projectile diameter and T is the wall thickness. A large number of CTH runs were required to identify the actual penetration conditions. The resulting matrix of CTH data is, however, somewhat sparse. The best fits give:

$$\alpha = -1.5\ (\pm 0.2) \text{ and } \beta = 1.6\ (\pm 0.2)$$

Thus:

$$V_P = 1.4 d_P^{-1.5}\, T^{1.6}$$

with v_P in km/s when d_P and T are in cm. Rearranging, we have

$$T = 0.81 d_P^{0.9375}\, V_P^{0.62}$$

which should be compared to the Pailer and Grun (P&G) (ref. 12) equation:

$$T = m_P^{0.4}\, V^{0.833}\, \rho_P^{0.333}/(\varepsilon^{0.06} \rho_T^{0.5})$$

where ε is a material-specific strain value, ρ_T and ρ_P are wall and particle densities, m_P is the particle mass, and V is the normal impact speed. For a symmetric Al/Al impact this becomes:

$$T = 1.13 d_P^{1.2}\, V_P^{0.833}$$

We note that, although of similar form, the two equations differ in the values of the power indices. It is not clear whether these differences are real or merely a consequence of limited data. The Pailer & Grun formulation is not based on either theory or computation, but rather on experimental data for a variety of impactor and target materials, sizes or velocities; it is a "global" best fit for all their data.

Another equation utilized and compared is that of McDonnell and Sullivan (M&S) (see above). The M&S equation has power indices closer to those obtained from the CTH data, and lies between the CTH formulation and that of P&G. Again, the M&S equation is mostly derived from experimental data. For a symmetric Al/Al impact, the M&S formulation reduces to:

$$T = 1.023 d_P^{1.056}\, V_P^{0.644}$$

Taking a closer look at the three penetration equations quoted above, the following estimates are derived for predictions of penetrations as a function of satellite wall thickness. Although the CTH calculations were specific to only three wall thicknesses, extrapolations have been made using the derived equations. Each of the equations is inverted to give particle size. Thus we have:

CTH: $d_P = 1.2520 T^{1.067}\, V_P^{-0.666}$
P&G: $d_P = 0.9032 T^{0.833}\, V_P^{-0.6942}$
M&S: $d_P = 0.9769 T^{0.947}\, V_P^{-0.6288}$

Although the three equations differ in their constants and power indices, they predict very similar values of particle diameter for given values of T and V, as shown below in Table 4. We note that the predicted particle diameters agree within <17%, with the greatest errors occurring at the smallest sizes. These particles and wall dimensions, and the impact speed, are within the range of existing impact facilities, and experiments form part of the data base upon which scaling laws are founded. The above close agreements with differing laws illustrate why such differences exist, since unambiguous results are not easily obtained.

TABLE 4: Penetration Particle Diameters for Debris

Wall Thickness	d_P (mm)			Ratio
	P & G	M & S	CTH	max/min
1.0 mm	0.313	0.299	0.268	1.17
1.5 mm	0.439	0.438	0.414	1.06
2.0 mm	0.558	0.576	0.563	1.03
2.5 mm	0.672	0.711	0.713	1.06
3.0 mm	0.782	0.845	0.867	1.11
3.175 mm	0.819	0.892	0.92	1.12

Summary Of Future Requirements

Several requirements still exist in order to complete calibration for LDEF. Completing these requirements will also benefit other impact data calibration projects and any future flights of meteoroid and debris experiments. As previously stated, the current data sets need to be combined. This will allow refinement of semi-empirical cratering, marginal penetration, and brittle cracking equations. It will also allow identification of gaps in the data.

Much data still needs to be collected for use in developing semi-empirical equations. This is particularly true for impacts in brittle materials. Data also needs to be collected to better define equations of state for materials of interest to LDEF, other spacecraft, and future meteoroid and debris experiments. In addition, data needs to be collected on the total damage (e.g. spallation, delamination, and deformation) caused by impacts, not just cratering, cracking and perforation.

Currently, no good models exist for first-order total-damage prediction. These types of semi-empirical equations and models need to be developed. These models then need to be associated with environment models for complete calibration of the LDEF data.

Finally, while not previously addressed, there is a problem with calibration of the small crater (<100 μm diameter) data on anodized materials. The thickness of the anodization layer can be of great significance to the size of crater formed by different impactors, if the layer thickness is greater than ~20% of the crater diameter. The aluminum oxide in the anodized layer has a higher density and is much harder than Al 6061-T6 alloy. This can change the calibration of cratering and penetration equations, and alter the conclusions which will be made from subsequent analysis, such as environment model comparisons. This feature could also explain the trend, reported by several LDEF workers (see above), for cumulative impact feature number

densities to "roll-off" at smaller sizes (e.g. <50 μm), and thus be well below the Kessler predictions and IDE results (ft note 4).

PARTICULATE FLUX ESTIMATES

Spacecraft in Earth orbit produce clouds of debris when they spontaneously explode or collide with one another. The first satellite explosion was observed by NORAD radar in 1961 and there have been over 90 satellite fragmentations since that time (ref. 19). That mutual collisions between spacecraft might produce a hazard to future space travel became clear in publications in the early 1970's (see ref. 20 for early work on collisions and for reference to yet earlier publications). Investigation of the space debris phenomenon has greatly intensified since that time to extend knowledge of the space debris population down to well below the 10 cm diameter objects that NORAD has been able to detect.

Meanwhile, meteoroid investigators attempted to determine the flux-versus-mass distribution of meteoroids by examining surfaces that had been exposed to space for extended periods (including lunar rocks) and then returned to Earth for laboratory examination; this determination was to be made by observing the number and size distributions of impact craters on the returned surfaces. By the mid 1970's these investigators started to detect, to their annoyance, impacts by aluminum and paint particles on the retrieved surfaces (ref. 18). That this was a problem meteoroid investigators would simply have to live with was shown quite clearly when about three square meters of the surface area of the Solar Max satellite was brought back to the Earth during a repair mission (see ref. 18 for some of this work and for references to earlier work). Hundreds of impacts by both meteoroids and orbital debris were detected on the Solar Max surfaces.

LDEF, because it was stabilized with its long axis continuously pointed radially to the Earth and fixed in rotational orientation about this axis so that one surface always faced in the direction of orbital motion of LDEF, is adding greatly to our knowledge of the flux of meteoroids and orbital debris. In addition to the large area-time of space exposure (two orders of magnitude greater than previously returned spacecraft surfaces), LDEF also affords the opportunity to obtain information about the directionality of the meteoroid and debris fluxes. This information can then be related, it is hoped, to the sources of meteoroids and orbital debris. Perhaps the asteroidal versus cometary abundance of impacting meteoroids can be deduced.

Well before LDEF recovery, Zook (ref. 21) theoretically deduced, under a "randomness" assumption, that from 6 to 9 times more meteoroids per unit area were expected to strike an LDEF leading edge surface than would impact a trailing edge surface; and, further, that this ratio depended on the velocity distribution with which meteoroids approached the Earth. These leading-to-trailing edge ratios of fluxes were due solely to LDEF orbital motion. When meteoroid impact velocities and a penetration equation are also taken into account, relative areal densities--leading to trailing edge--of meteoroid impact craters on LDEF can also be calculated (refs. 17 & 22); these ratios are found to range from 10 to 30, depending on the meteoroid velocity distribution and the meteoroid size distribution used. Kessler et al. (ref. 19) similarly deduced theoretical ratios to be expected for orbital debris.

LDEF Results To Date

We summarize here only the most salient findings concerning the separate meteoroid and debris impact populations, and their directionalities, that have been derived from LDEF investigations and published to date.

First there is clear evidence of impacts by both orbital debris and meteoroids on LDEF. By far the best means to separate the two populations is to determine the composition of the residue, if any, in the impact craters. Most spacecraft debris particles consist of aluminum fragments of spacecraft structures, of aluminum oxide from the burning of solid rocket fuel, or of paint particles (shown by the elements zinc, titanium, and aluminum, whose oxides commonly provide the white pigments in thermal paints). Impacts by organic particles--often human waste--are also seen quite often (usually dominated by the elements phosphorus, sodium, and potassium in EDX analyses). Such analyses are being carried out by several groups (see, especially, articles in "LDEF--69 Months in Space"). These analyses are far from completed and are essentially all still in progress; determining the composition of the residue in each of thousands of craters is no small task!

Analyses of residues in impact craters on gold surfaces that were facing the trailing direction of LDEF (refs. 1 & 3, ft note 8) have produced a very interesting result: Of 187 craters that had been analyzed for residue, 30 were found to result from impacting space debris while 57 were identified as of meteoritic origin; 111 craters had no identifiable residue in them and so an origin could not be assigned. This result was surprising because before LDEF recovery it had been predicted (ref. 19) that almost no debris would hit the backward-facing LDEF surfaces. The only way these surfaces can be struck is for particles to catch up to LDEF from behind. This, in turn, implies that LDEF must be near the perigee of particles in highly elliptical orbits; debris in geosynchronous transfer orbits would appear to be responsible.

On an aluminum surface facing about 50 degrees from the leading edge, Horz et al. (ref. 3, ft note 8) found that orbital debris impacts start to become more numerous than meteoroid impacts for impact craters smaller than about 100 microns in diameter. Below 50 microns in diameter, orbital debris appears to dominate the crater populations on leading-edge LDEF surfaces. Although several investigator groups (see LDEF-69 Months in Space) are doing compositional analyses, that by Horz et al. (ref. 3, ft note 8) is probably the most complete to date and is therefore quoted here.

Second, the time variation of the flux striking LDEF is also a strong indicator of the origin of the impacting particles. The only "active" meteoroid experiment on LDEF was the "IDE" experiment flown by Singer et al. (ref. 8, ft note 4) which electrically recorded when each impact occurred that penetrated one of many MOS detectors placed around LDEF. This experiment recorded over 15,000 impacts that penetrated either 0.4 μm or 1.0 μm thick dielectric layers of MOS capacitors.

The IDE sometimes sensed multi-orbit "streams" of particles, where the impact rate would greatly increase for a few minutes on every orbit. A very strong stream of this type was seen on June 4, 1984, where the stream was seen every orbit for about 25 orbits; 131 impacts occurred in 2 minutes on the first passage of this stream. The only reasonable interpretation of such a multi-event sequence is that LDEF was passing through the orbit plane of the debris cloud associated with some satellite (not yet identified). Also, the impact rate on IDE was elevated for the first few days of the mission. Presumably this was caused by contaminant particles from the Shuttle that had launched LDEF.

IDE also detected "beta meteoroids". These meteoroids are dust grains that are leaving the solar system on hyperbolic orbits to become interstellar grains, and their apparent flux should be at a maximum when a sensor faces toward the Sun. The beta's were best, and most clearly, detected by rearward-facing IDE sensors when they faced the Sun.

Third, the spatial density of impact craters is much greater on surfaces close to the leading edge of LDEF than it is on surfaces near, or at, the trailing edge. Leading edge-to-trailing edge ratios of spatial densities of craters depend on crater size and range from about 10 for craters smaller than about 50 microns in diameter (ref. 6) to about 20 for impact craters larger than about 500 microns in diameter (refs. 17 & 23). Although there are probably a number of debris impacts in the population of large (diameter >500 microns) impact craters, the ratio of leading-to-trailing crater spatial densities also appears consistent with meteoritic impacts alone (ref. 22). The best fit to the observed LDEF results is obtained when the meteor velocity distributions of Kessler (ref. 24) and of Erickson (ref. 25) are used to give particle velocities relative to the Earth.

In summary, analyses of impact craters (and holes in thin films and plastic) and the time history of impacts on LDEF are giving us a much better picture of both the meteoroid and space debris populations in near-Earth orbit. We have become especially aware of new features of the orbital debris populations: some debris clouds are concentrated into orbital planes and do not dissipate into the background as fast as one might have expected; more debris is impacting trailing-edge surfaces than was expected, probably implying that geosynchronous transfer orbits are well populated with debris.

Implications Of Results And Further Studies Needed

The largest impact crater on LDEF was 0.57 cm in diameter and was probably caused by an object about a millimeter, or a little less, in diameter. This is greatly helping to bridge the observational gap between the radar data (now estimated to reach down to about 1 cm diameter) obtained from ground stations and data returned from direct observations in space on orbital debris, or to make it possible to more confidently calibrate atmospheric meteor data. This means that shielding against meteoroids and debris to protect satellites from damage can now be better estimated; this is especially important for Space Station Freedom where many millions of dollars will be spent for impact shielding. It is also very important to establish an impact cratering rate at one point so that it may be compared with cratering rates at some time in the future; thus the growth of the orbital population with time can be monitored and compared with theoretical models and thereby validate (or invalidate) them.

Work for the future includes the following: 1) Much more needs to be learned about the chemistry of residues in impact craters--especially as it applies to separating the meteoroid and orbital debris populations into two distinct groups. 2) In theoretical modeling, all investigators need to understand the assumptions involved and what the implications are of changing the assumptions. That includes the "randomness" assumption for meteoroids, as well as trying out different meteoroid velocity distributions than the ones that have been tried. That is, how unique is the Erickson-Kessler distribution? Can we put in a larger asteroidal component and still fit the data?

LDEF METEOROID AND DEBRIS IMPACT DATABASE

The LDEF M&D database maintained at Johnson Space Center consists of five data tables containing information about individual features, digitized images of selected features, and inventory data for LDEF hardware controlled at JSC. About 4000 features were identified during the disassembly of the satellite at Kennedy Space Center, and an additional 4500 have subsequently been identified at Johnson Space Center. The database also contains a small amount of information which has been submitted by members of the PI community. Location information and other data for about 950 samples which are controlled by JSC are also included in the database.

Images for about 4500 features have been digitized. Although these images are not stored on-line because of the large amount of disk space required, the database contains the names (left and right image) and the removeable disk designation on which they reside. These images can be made available for downloading at the user's request.

Data Tables

The five data tables in the M&D database are named Primary Surfaces, Features, Cores, Digital Images, and Allocation History. The Primary Surfaces, Cores, and Allocation History tables are primarily used for keeping track of the samples controlled by JSC, although they do contain other information about the nature of the samples. The Features Table represents the focus of the database on which the other tables are based. It contains one record for every feature which has been identified either at KSC, JSC, or by contributing investigators. The Digital Images Table represents an index for retrieving digitized images of the features.

Sample Numbering Scheme

The feature numbers recorded in the database represent a combination of the surface ID and a unique feature number for that surface. The surface ID consists of four parts: the LDEF Bay and Row number, the component type, and the component number. The bay and row numbers are the same as those initially assigned to the satellite grids. The component type is a one-letter code which translates to a particular piece of hardware. Examples of common component-type codes are "E" for experiment trays, "C" for clamps and "F" for frame pieces (intercostals and longerons). The component number is a sequential number assigned to differentiate separate pieces of the same component type taken from the same bay and row. (NOTE: Subsequent divisions of components after the initial KSC scan are assigned 2-letter subsurface designations for purposes of maintaining uniqueness of individual surface pieces.) Specific feature numbers are assigned sequentially as they are identified; numbers begin with 1 for each surface.

Cores, which represent features that have been removed from a surface with part of the surrounding substrate, are numbered sequentially as they are removed regardless of the surface number. All cores taken from LDEF are prefixed with the characters "LD-" to differentiate LDEF cores from those taken from other satellites.

Primary Surfaces Table

The Primary Surfaces Table contains one record for each surface (and subsurface) on which features have been identified. The table contains fields for the origin, shape, orientation,

surface area, substrate, location, and comments. These fields contain the following types of information:

Origin	LDEF Experiment Number, Intercostal, Longeron, Thermal Blanket
Shape	Rectangle, Dimensions
Orientation or Position	Left, Right, Center
Surface Area	Area of the surface in mm^2 (excluding overlaps and penetrations for bolts)
Substrate	Aluminum, Teflon, Steel, Gold
Location	JSC Location, PI (Locations are recorded only for those surfaces controlled by JSC)

Features Table

The Features Table contains one record for each feature which has been identified. It contains fields for the site of identification, X and Y coordinates, diameters, depth, impact type, and the presence of material. These fields contain the following types of information:

Site of Identification	KSC, JSC, or PI Name
X and Y Coordinates	Two sets of coordinates are recorded; one set represents the coordinates relative to an arbitrary origin assigned when the surface was originally scanned at KSC The other set represents the coordinates as recorded during any subsequent scanning of the surface at other facilities; offsets are calculated so that the data can be converted to the KSC values.
Diameters	Diameters for both major and minor axes are recorded for non-circular features. The diameters currently recorded in the database represent measurements made from lip to lip. Analysis of the digital images is now underway at JSC which will provide diameters of the features as determined at the original target surface.
Depth	Depth information is now recorded for only a very few features; this information was provided by Don Humes. Analysis of the digital images will also provide depth data for digitized features.
Impact Type	Crater, Hole or Penetration, Other (spray pattern, etc.)
Material Presence	Yes, No, and sometimes the quantity of material

Cores Table

The Cores Table contains one record for every unique Feature/Core combination. In some instances, there may be more than one feature present on a core because close proximity of the features makes it difficult to separate them. In such cases, there are two (or more) records entered; both records have the same core number but different feature numbers. Additionally, there may be several records for different core numbers with the same feature number. This situation usually arises when the surface is made up of more than one layer of material, and the feature is present on several layers.

This table contains fields for the core number, feature number, sub-surface, layer, substrate, and location. These fields contain the following types of information:

Core Number	Sequentially assigned unique integer, prefixed by the characters "LD-". Core numbers are assigned in order, regardless of the surface on which they were identified.
Feature Number	Corresponds to the number of the feature (or features) physically present on the core.
Sub-Surface	Additional designator for surfaces physically separated from original surfaces.
Substrate	Aluminum, Steel, Teflon, Gold
Location	JSC Lab or PI Name

Digital Images Table

The Digital Images Table contains one or more records for each left image filename. Duplicate records with the same image filename are allowed to accommodate images recorded at KSC and later recorded at JSC with the same name. It contains fields for left and right image filenames, feature number, magnification, station no., disk no., and image date. These fields contain the following types of information:

Left Image File and Right Image File	The names of the image filenames are constructed so that the feature number is contained in the name of the file and so that they conform to DOS file naming convention of an 8-character name followed by a 3-character extension. For the first image produced of a feature, the first character of the left image file is "L" and the first character for the right image file is "R". Subsequent files are identified by consecutive alphabetic characters; for example, the second set is prefixed by "A" and "B" for the left and right images respectively, the third set by "C" and "D", and so forth. Characters 3-5 of the filename represent the component and component number of the surface ID, characters 6-9 represent the specific feature number (with imbedded zero's for numbers less than 1000). The file extension represents the LDEF Bay and Row grid location.
Feature Number	The Feature Number is included for the convenience of the user. It corresponds to the feature number in the Features Table, and may be derived from the image filenames.
Magnification	This field represents the magnification at which the feature was imaged.
Station Number	There were several scanning and imaging stations set up at KSC, and each one was assigned a separate number. All images recorded at JSC are Station 7.
Disk Number	Represents the disk # on which the image resides. The characters A and B represent the front and back of the disk respectively.
Image Date	Represents the date the image was acquired.

Allocation History Table

The Allocation History Table is used for recording the history of the movement of primary surfaces and cores controlled by JSC. Every time a surface or core changes custody, an

entry is made in this table. It contains fields for surface number, core number, investigator or site, and the date allocated. These fields contain the following types of information:

Surface Number	Corresponds to the surface ID recorded in the primary surfaces table. Data is contained in this field only if the sample represents a primary surface.
Core Number	Corresponds to the core number (not the feature number) recorded in the cores table. Data is contained in this field only if the sample represents a core.
Investigator/Site	Either a NASA site or an investigator's name.
Date Allocated	Date the sample was allocated or returned to JSC.

Database Access

The LDEF database may be accessed via SPAN, Internet, or modem. The capability for downloading results of searches to users' local computers via FTP, Kermit, or Mail is being developed and will be available within the next few months. Image files may be downloaded via FTP and, less efficiently, via Kermit. The image files do not stay on-line, but may be made accessible on request.

ACCESS VIA DECNET:

1) Log onto host computer.
2) Type SET HOST 9300.
3) Type PMPUBLIC at the Username: prompt.

ACCESS VIA INTERNET:

1) Type TELNET 146.154.11.35
   or
   TELNET CURATE.JSC.NASA.GOV
2) Type PMPUBLIC at the Username: prompt.

ACCESS VIA MODEM:

The modem may be 300, 1200, or 2400 baud; no parity; 8 data bits; 1 stop bit. The area code is 713 for long distance calls.

1) Dial 483-2500.
2) Type SN_VAX in response to the Enter Number: prompt.
3) Hit <CR> 2 or 3 times after the CALL COMPLETE message.
4) Type J31X in response to the # prompt.
5) Type C CURATE in response to the Xyplex> prompt.
6) Type PMPUBLIC at the Username: prompt.

ACKNOWLEDGEMENTS

The M&D SIG members not listed as authors of this report are: Martha Allbrooks (POD Associates, Inc.), Don Brownlee (University of Washington), F Buhler (University of Bern), Ted Bunch (NASA ARC), Vladimar Chobotov (Aerospace Corp.), Gunther Eichhorn (Space Telescope Science Institute), Miria Finckenor (NASA MSFC), Donald Humes (NASA LaRC), Don Kessler (NASA JSC), J-C Mandeville (CERT-ONERA), J A M McDonnell (University of Kent), Michael Mirtich (NASA LaRC), J D Mulholland (Institute of Space Science & Technology), Robert Walker (Washington University), Jerry Weinberg (Institute of Space Science & Technology), and Ernst Zinner (Washington University). All of these individuals have contributed significantly to the results and discussions reported here.

REFERENCES

1 Horz, F. and Bernhard R.P. (1992) Compositional Analysis and Classification of Projectile Residues in LDEF IMpact Craters. NASA Tech. Memorandum 104750, 150p.

2 Amari, S, Foote, J., Simon, C., Swan, P. Walker, R. and Zinnerm E. (1991) SIMS Chemical Analysis of Extended Impact Feature from the Trailing Edge Portion of Experiment A0187-2, NASA CP 3134, 503-516.

3 Horz, F., Bernhard, R.P., Warren, J., See, T.H., Brownlee, D.E., Laurance, M.R., Messenger, S., and Peterson, R.B. (1991), Preliminary Analysis of LDEF Instrument A0187-1: Chemistry of Micrometeoroids Experiment, NASA CP 3134, 487-501.

4 Mandeville, J.C., and Borg, J, (1991) Study of Cosmic Dust Particles on Board LDEF: The FRECOPA Experiments A0138-1 and A0138-2, NASA CP 3134, 529-548.

5 McDonnell, J.A.M, Deshapande, S.P., Green, S.F., Newman, P.J., Paley, M.T., Ratcliff, P.R., Sullivan, K., and Stevenson, T.J. (1991) First Results of Particulate Impacts and Foil Perforations on LDEF, Adv. Space Res., Vol. 11, No. 12.

6 McDonnell, J.A.M. and Stevenson, T.J (1991) Hypervelocity Impact Microfoil Perforations in the LEO Space Environment (LDEF MAP A0023 Experiment), NASA CP 3143, 443-457.

7 McDonnell, J.A.M., and the Canterbury MAP Team (1992) Impact Cratering from LDEF's 5.7 Year Exposure: Decoding of the Interplanetary and Earth-Orbital Populations, LPSC Proceedings, Vol. 22, 185-193.

8 Singer, S.F., Stanley, J.E., Kassel, P.C., Kinard, W.H., Wortman, J.J., Weinburg, J.L., Cooke, W.J., and Montague, N.L. (1991) First Spatio-Temporal Results from the LDEF Interplanetary Dust Experiment, Adv. Space Res., Vol. 11, No. 12, 115-122.

9 Mulholland, J.D., Singer, S.F., Oliver, J.P., Kassel, P.C., Kinard, W.H., Wortman, JJ., Weinburg, J.L., Cooke, W.J., and Montague, N.L. (1991) IDE Spatio-Temporal Impact Fluxes and High-Time Resolution Studies of Multi-Impact Events and Long-Lived Debris Clouds, NASA CP 3134, 517-528.

10 Simon, C.G., Data Presented by Mulholland at Second LDEF Symposium.

11 Simon, C.G., Hunter, J.L. Griffis, D.P., and Wortman, J.J. (1991) Ion Microprobe Elemental Analysis of Impact Features of Interplanetary Dust Experiment Sensor Surfaces, NASA CP 3134, 529-548.

12 Pailer N. and Grun E. (1980) The penetration limit of thin films. Planet. Space Sci., 28, 321-331.

13 Carey W.C., McDonnell J.A.M. and Dixon D.G. (1985) An empirical penetration equation for thin metallic films used in capture cell techniques. In Properties and Interactions of Interplanetary Dust (R.H. Giese and P. Lamy, Eds.), Reidel Publ. Co., pp. 131-136.

14 Cour-Palais B.G. (1987) Hypervelocity impact in metals, glass and composites. International J. Impact Engineering, 5, 681-692.

15 Gault D.E. (1973) Displaced mass, diameter and effects of oblique trajectories for impact craters formed in dense crystalline rocks. The Moon, 6, 32-44.

16 Mandeville J.C. (1975) Microcraters observed on 15015 breccia and micrometeoroid flux. In: Proceedings of the 6th Lunar Science Conference (R.B. Merrill, Ed.), pp. 3403-3408.

17 Humes D.H. (1991) Large craters on the meteoroid and space debris impact experiment. In: LDEF--69 Months in Space, NASA Conference Publication 3134 (A.S. Levine, Ed.), pp. 399-418.

18 Warren J.L., Zook H.A., Allton J.H., Clanton U.S., Dardano C.B., Holder J.A., Marlow R.R., Schultz R.H., Watts L.A., and Wentworth S.J. (1989) The detection and observation of meteoroid and space debris impact features on the Solar Max satellite. In: Proc. 19th Lunar and Planet. Sci. Conf., pp. 641-657. Lunar and Planetary Institute, Houston.

19 Kessler D.J., Reynolds R.C., and Anz-Meador P.D. (1989) Orbital debris environment for spacecraft designed to operate in low Earth orbit. NASA TM 100 471. 21 pp.

20 Kessler D.J. and Cour-Palais B.G. (1978) Collision frequency of artificial satellites: the creation of a debris belt. J. Geophys. Res. 83, 2637-2646.

21 Zook H.A. (1987) The velocity distribution and angular directionality of meteoroids that impact on an Earth-orbiting spacecraft. In: Lunar and Planetary Science SVIII, pp. 1138- 1139. Lunar and Planetary Institute, Houston.

22 Zook H.A. (1991) Deriving the velocity distribution of meteoroids from the measured meteoroid impact directionality on the various LDEF surfaces. In: LDEF--69 Months in Space, NASA Conference Publication 3134 (A.S. Levine, Ed.), pp.569-579.

23 See T.H., Horz F., Zolensky M.E., Allbrooks M.K., Atkinson D.R., and Simon C.G. (1991) Meteoroid and Debris Special Investigation Group preliminary results: size-frequency distribution and spatial density of large impact features on LDEF. In: LDEF--69 Months in Space, NASA Conference Publication 3134 (A.S. Levine, Ed.), pp. 477-486.

24 Kessler D.J. (1969) Average relative velocity of sporadic meteoroids in interplanetary space. AIAA J., 7, 2337-2338.

25 Erickson J.E. (1968) Velocity distribution of photographic meteors. J. Geophys. Res., 73, 3721-3726.

FOOTNOTES

1 Mandeville, J.C., and Berthold, L., Hypervelocity Impacts on Retrieved Surfaces: LDEF and MIR, IAU Colloquium, No. 126, in press.

2 McDonnell, J.A.M., Sullivan, K., Green, S.F., Stevenson, T.J., and Niblett, D.H., Dynamic Modelling Transformations for the Low Earth Orbit Satellite Particulate Environment, IAU Colloquium, No. 126, in press.

3 McDonnell, J.A.M., Sullivan, K. Stevenson, T.J., and Niblett, D.H., Particulate Detection in the Near Earth Space Environment Aboard the Long Duration Exposure Facility LDEF: Cosmic or Terrestrial?, IAU Colloquium, No. 126, in press.

4 Mulholland, J.D., Oliver, J.P., Singer, S.F., Weinburg, J.L., Cooke, W.J., Montague, N.L., Kassel, P.C., Wortman, JJ., Kinard, W.H., and Simon, C.G., LDEF Interplanetary Dust Experiment: A High-Time Resolution Snapshot of the Near-Earth Particulate Environment, Proc. Hyp. Vel. Impacts Space, University of Kent at Canterbury, U.K., in press.

5 Walker, R. and Swan, P (1992) Personal Communications.

6 Mandeville, J.C., (1992) Personal Communication.

7 Bernhard R.P. (1992) Personal Communication.

8 Horz F., Cintala M., Bernhard R.P. and See T.H. Dimensionally scaled penetration experiments: Aluminum targets and glass projectiles 50 μm to 3.2 mm in diameter. International J. Impact Engineering, in press.

MICROMETEOROIDS AND DEBRIS ON LDEF

Jean-Claude Mandeville
CERT-ONERA / DERTS
2, Avenue E.Belin, 31055 Toulouse Cedex (France)
Phone: (33) 61557117, Fax (33) 61557169

SUMMARY

Two experiments within the French Cooperative Payload (FRECOPA) and devoted to the detection of cosmic dust have been flown on the Long Duration Exposure Facility (LDEF). A variety of sensors and collecting devices have made possible the study of impact processes on dedicated sensors and on materials of technological interest. Examination of hypervelocity impact features on these experiments gives valuable information on size distribution and nature of interplanetary dust particles in low-Earth orbit (LEO), within the 0.5-300 micrometer size range. However no crater smaller than 1.5 microns has been observed, thus suggesting a cut-off in the near Earth particle distribution. Chemical investigation of craters by EDX clearly shows evidence of elements (Na, Mg, Si, S, Ca and Fe) consistent with cosmic origin. However remnants of orbital debris have been found in a few craters; this can be the result of particles in excentric orbits about the Earth and of the 8° offset in the orientation of LDEF. Crater size distribution is compared with results from other dust experiments flown on LDEF and with current models. Possible origin and orbital evolution of micrometeoroids is discussed. Use of thin foils detectors for the chemical study of particle remnants looks promising for future experiments.

INTRODUCTION

Interplanetary space contains solid objects whose size distribution continuously covers the interval from submicron sized particles to km sized asteroids or comets. Some meteoroids originate from comets, some originate from collisions within the asteroid belt /1/. In addition to natural particles, a significant and growing number of particles has been added by human activity in near-Earth space. In the vicinity of Earth, gravitational perturbations and the influence of the atmosphere greatly affect the distribution of the particles. In-situ detection and collection of dust by experiments flown on LDEF have already improved our current understanding of this important aspect of the space environment, but many issues are still a matter of debate, namely the relative contribution of natural particles and orbital debris /2/.

Two entirely passive experiments have been flown for the detection of microparticles, as part of the FRECOPA experiment. The first one, Study of Meteoroid Impacts on Various Materials (AO138-1), was composed of a set of thick glass and metallic samples; the second one, Dust Debris Collection with Stacked Detectors (AO138-2), was composed of multilayer thin-foil detectors. The experiment was located inside tray B03, on the trailing side of LDEF. Detailed description of the hardware and preliminary results after retrieval have been given elsewhere /3,4,5 /.

ANALYSIS OF IMPACT CRATERS

The results concerning the largest impact features found in association with the FRECOPA payload were given in a previous paper (ref.5); here we address the size distribution of small-sized (< 100 microns) craters. The initial surveys were conducted with an optical microscope utilizing magnifications of 20X and 100X, while more detailed scanning and examination of peculiar features was carried out with a dedicated Scanning Electron Microscope (SEM). Energy dispersive X-ray analyses (EDX) were performed on the melt residues associated with some craters in order to garner information on the chemical composition of the projectiles.

Crater-Size Distribution

In addition to two large impact features (one full penetration 1.25 mm in diameter and one marginal penetration 1.07 mm in diameter of a 1 mm aluminium shield) about 90 craters larger than 50 microns have been found on a total area of one square meter. Four craters are larger than 500 microns. Most of the large craters are circular in outline, though a few small craters do indicate oblique incidences.

Most of the data about the size distribution of small craters come from two 10 x 10 cm aluminium samples exposed during the entire mission and from samples located inside a canister, exposed only during the first nine months. Four cm^2 of aluminium (sample A54 from AO138-1 experiment) have been thoroughly analyzed in search of microcraters, less than 20 microns in size. A first scanning of the samples at a magnification of 750X allows a selection of events showing typical crater features (circular feature, prominent rim). A typical flux density of 2.1 10^{-4} /m^2/s of craters larger than 1.5 microns has been derived; a similar flux (2.2 10^{-4} /m^2/s) has been found on the surface of other aluminium samples (A21, A22 from AO138-1). Flux mass distributions found for larger craters can thus be extended with very good agreement to small sizes.

Scanning of a few samples (from AO138-2) exposed only during the first nine months of the mission has been made. Preliminary data seem to indicate an impact flux higher than for samples that were exposed during the entire 69 month period - with a flux of 6.1 10^{-4} /m^2/s for craters larger than 2 microns, as compared to 2.1 10^{-4} /m^2/s. This flux value must be confirmed by further investigation, currently in progress, but it seems to be consistent with data from the Interplanetary Dust Experiment (IDE) experiment as given by J.D. Mulholland /6/.

We observed no craters smaller than 1.5 microns in size, thus implying a cut off in the natural particle size distribution. Considering simulation experiments giving a factor of 5 between the crater size and the particle diameter suggest the smallest impacting particles had a mass in the 10^{-13} g range.

The cumulative flux size distribution of craters (in aluminium) larger than 1.5 microns is shown on Figure 1. The upper part of the figure shows the crater size distribution of craters beteween 1 micron and 10 microns as derived from high magnifiaction SEM scanning of small craters on aluminium samples (A54). For comparison we have ploted the size distribution of small craters on a sample (E7.tb), located on the leading side, from the Multiple foil Abrasion Package (MAP) experiment given to us for analysis by J.A.M. McDonnell. The search for craters smaller than 2 microns is not yet finished, but there is some evidence of a cut-off in this size-range.

The figure 2 shows a comparison between the number of craters observed on the MAP experiment and the number of small craters from samples exposed on the MIR space station in 1989 /7/. The flux of small particles is higher on MIR samples than on the leading side of LDEF, and there is evidence of particles smaller than those detected so

far on LDEF. Furthermore the samples on MIR were not always facing the leading side. The present modeling of latitude dependence for orbital debris cannot entirely explain such a difference. A possible explanation for this higher flux is that the environment of a manned station could generate more small debris than an unmanned spacecraft such as LDEF.

Comparison With Models

It is interesting to compare LDEF data with values given by existing models describing the earth particulate environment. Such a comparison has been done for some data avalaible to us (MSDIE, MAP, tray clamps) for three different crater diameters (5, 50 and 500 microns). The modeling has been conducted with the Esabase software developed by ESA /8/. Flux models used in the program are Grün's (1985) polynomial model for meteoroids /9/ and Kessler's 1990 model for orbital debris /10/; depth of penetration formula used for conversion of crater diameter to particle diameter is the one used by D. Humes /11/ and originally proposed by B. Court-Palais /12/ (crater is assumed to be near-hemispherical in shape with a depth/diameter ratio of P/D = 0.55) :

$$P = 0.42\, m^{.352}\, \rho^{1/6}\, V^{2/3}$$

P is given in cm, m in g, ρ in g/cm^3 and V in km/s.

According to the models, average impact velocity for meteroids and for debris is computed with Esabase for each face of LDEF. Results are shown on Figure 3. The flux of particles responsible for the formation of the craters is then computed for each face of LDEF taking into account the fact that craters of a given size are produced by larger particles on the trailing side than on the leading side, due to the differences in impact velocities (see Table 1). Preliminary results given in Figure 4 show good agreement between the observed and computed values. Because of the 8° offset in the orientation of LDEF with respect to the velocity vector, the value of the flux is at a maximum on row 10 and minimum on row 4 (instead of row 9 and row 3, respectively). Morever, this small offset can explain the occurence, on row 3, of impact craters produced by orbital debris in circular orbits. This is shown by the model and confirmed by the chemical identification of man-made debris remnants inside craters (see ref.13 and lower in this paper). Conversely, only debris in highly elliptical orbits could impact samples located on row 4.

Comparison of the flux of particles on the leading and on the trailing sides is shown on Figure 5. The ratio of maximum (row 10) to minimum flux (row 4) is not constant and depends on the size of the crater: the ratio is lowest at 50 microns crater diameter thus indicating a similar spatial density for meteoroids and orbital debris; for small craters the ratio is increasing and implies that the contribution of orbital debris is dominant for particles in the micron-size range.

Marginal Perforation and Cratering Processes

The impact survey yields a crater-size distribution which should be converted to a particle mass distribution by using the relevant relationship between crater sizes and particle mass and velocity. The final results are based upon processes involved during the crater formation. A variety of experimental and theoretical approaches are used and an important goal of the Meteoroid and Debris Special Investigation Group is to provide a common ground for the conversion of penetration and impact features into particle size. However, on experiments such as those flown on LDEF, several assumptions must be made on the nature of the particles and on their impact velocity in order to derive their mass from the size of the craters formed on the exposed targets. As shown by current models for the velocity distribution in the vicinity of the Earth of meteoroids and orbital debris, average impact velocity is different on the various sides of LDEF (consequently a

crater of a given size has been formed by a larger particle on the trailing side than on the leading side).

The characteristic ratio for impacts on thin targets, at marginal perforation, crater diameter/target thickness, (D/f), was measured for aluminium samples exposed on MIR (foil thickness 0.8, 2 and 5 microns) and on LDEF (5 and 25 microns and 1 mm foils). The D/f ratio appears to be sensibly constant at approximately 1.4 (or f/D = 0.71) for the 36 marginal perforation features observed. The impact velocity is unknown, but as shown earlier it should be higher than 10 km/s. Similar results have been obtained by McDonnell /14/ and Hörz /15/ from laboratory experiments (impact velocity: 6 km/s, aluminium target and silica projectile). Under such conditions the value of the foil thickness to particle diameter ratio (f/d) is close to 3.5 and the crater diameter ratio to projectile diameter ratio (D/d) is close to 5.

Chemical Analysis of Particle Remants

A critical problem is the determination of the chemical composition of the impacting particles. In general they are physically destroyed and mixed with target material in the process of crater formation and identification of impactor, even qualitatively, is difficult. The first EDX analysis of 45 small craters has shown the occurence of elements such as Ca, Na, K, Si, Ti, Fe and S.

Table 2 summarizes our results for the craters investigated so far: light elements C and O are present, with a ratio C/O varying from 0.1 to 3. Significant variations appear inside the distribution of individual craters. The other main elements identified in the various craters are usually referred to as "chondritic" elements, as they exist in various proportions and are signatures of extraterrestrial particles: Na, Mg, Si, S, Ca and Fe (samples 8 and 11). For these elements also, important variations are found from point to point inside the crater reinforcing the idea that the particles are truly aggregates bursting apart during the impact. The systematic presence of C and O components in the various residues analyzed is an important result: the occurence of CHON particles detected in P-Halley nucleus would not be a particularity of this comet but could be a constant for extraterrestrial particles of cometary origin, as seems to be the case for such particles /5,16/.

Evidence of elements charateristic of orbital debris (Ti, Zn) has been found only inside two craters.Thus we are highly confident that the majority (95 %) of the craters analysed are of extraterrestrial origin, as expected due to the fixed orientation of LDEF during its flight and to the exposition side of the FRECOPA payload on board LDEF. However, there is still a possibility to record impacts from orbital debris in highly eccentric orbits /13/. Sample 9 (Table 2) located on the leading edge shows conversely the occurence of a large number of craters caused by orbital debris.

Of peculiar interest was the study of impact features on the thin-foil detectors. One of the 5 microns thick aluminium foil (sample AD11) from the AO138-2 detector shows a perforation measuring 55 by 40 microns (oblique impact or elongated projectile). It is a typical "supramarginal perforation" with a crater diameter to foil thickness ratio of D/f=10, diameter of the particle is estimated to be 40 microns. The bottom plate beneath the perforation shows a star-shaped distribution of small secondary craters (sample AD12). The top foil acted as a shield, fragmenting the projectile and spreading the fragments over the surface of the thick plate. The craters range in size from 0.6 to 15 microns and are mostly distributed along two perpendicular axes. An angular particle, 18 mm by 15 microns is visible at the intersection of the axes. EDX analysis has provided evidence of impactor fragments. The elements identified in the central part of impact feature (Si, Fe, Na, Mg) are characteristic of interplanetary dust particles from the mafic silicate family, probably olivine. The variation in chemical composition between and within craters confirms the idea of an aggregate particle which burst apart on impact. None of the above elements was found in the craters far from the center of the impact feature which implies that these were caused by the aluminium fragments from the top foil. Detectors consisting of a thin shield and thick bottom plate appear to offer a

significantly higher return of information concerning chemical analysis of impactor residues than do single plate detectors.

CONCLUSION

LDEF gives us a unique opportunity for the study of the many processes involved in high-velocity impact phenomena and for the comprehensive description of the LEO microparticle population. Crater size distribution has already given us a good description of the actual in situ particulate hazard for spacecrafts. There are still some uncertainties on the mass distribution of the particles mainly due to the different hypervelocity impacts equations; however, comparison with current models shows no large discrepancies. A difficult task remains: the assessment of the contribution of the two populations (natural and man-made particles) through chemical identification of impact residues.

Acknowledgements: Support from CNES for completion of experiment and for data analysis and support from NASA for completion of the mission are greatly acknowledged.

REFERENCES

1. C. Leinert and E. Grün, Interplanetary Dust, in: *Physics and Chemistry in Space*, Springer (1988) p.34.

2. A.S. Levine, ed., LDEF - 69 Months in Space, NASA CP-3134 (1991), pp. 397-584.

3. J.C. Mandeville, AO138-1 and AO138-2 Experiments, in: *LDEF Mission 1 Experiments*, eds. L.G. Clark, W.H. Kinard, D.J. Carter, J.L. Jones, NASA SP-473, (1984) p.121.

4. J.C. Mandeville and J.A.M. McDonnell, Micrometeoroid multiple foil penetration and particle recovery experiments on LDEF, in: *Solid Particles in the Solar System*, ed. I. Halliday and B.A. McIntosh, D.Reidel (1980) p.395.

5. J.C. Mandeville and J. Borg, Study of cosmic dust particles on board LDEF, the Frecopa experiments AO138-1 and AO138-2, in *LDEF - 69 Months in Space,* NASA CP-3134, (1991).

6. J.C. Mandeville, Aragatz Mission Dust Collection Experiment, *Adv.Space Res.* 10, 3, 397, 1990.

7. J.D. Mulholland, G.G. Simon, W.J. Cooke, J.P. Oliver, V. Misra, Long-term particle flux variability indicated by comparison of interplanetary dust experiment (IDE) timed impacts for LDEF first year in orbit with impact data for the entire 5.75 year orbital lifetime, in *NASA CP-10097,* (1992).

8. J. de Kruijf, ESABASE, A most versatile and flexible system engineering tool ESA BR-54, (1988).

9. E. Grün et al., Collisional balance of the meteoroid complex, *Icarus*, 62, 244, (1985).

10. D.J. Kessler, R.C. Reynolds, P.D. Anz-Meador, Orbital debris environment for spacecraft designed to operate in low earth orbit, NASA TM-100471, (1989).

11. D. Humes, Large craters on the meteoroid and space debris impact experiment, in *LDEF - 69 Months in Space,* NASA CP-3134, (1991).

12. Anonymous, Meteoroid damage assessment, NASA SP-8042, (1970).

13. R. Bernhard, and F. Hörz, Compositional analysis of projectile residues on LDEF instrument AO187-1, NASA-CP 10097 (1992).

14. J.A.M. McDonnell, Factors affecting the choice of foils for penetration experiments in space, in *Space Research X,* North Holland pub. (1970).

15. F.Hörz, R.P. Bernhard, T.H. See, D. Atkinson, M. Allbrooks, M and D SIG Progress Report : Laboratory simulations of LDEF impact features, in *LDEF - 69 Months in Space,* NASA CP-3134, (1991).

16. J. Borg, T.E. Bunch, Radicati di Brozolo, Further analysis of LDEF Frecopa micrometeoroid remnants, NASA CP-10097 (1992).

Table 1: Comparison impacts parameters for LDEF and for the Model

Crater size, μm		Mass, gm		Diameter, μm		Impact velocity, km/s		D_c / d_p	
row 3	row 9	row 3	row 9	row 3	row 9	row 3	row 9	row 3	row 9
400	400	$1.2e^{-6}$	$4.5e^{-7}$	133	95	15	25	3	4.2
50	50	$3.2e^{-9}$	$1.3e^{-9}$	18	13	15	25	2.7	3.7
5	5	$2.8e^{-12}$	$1.1e^{-12}$	1.4	1	15	25	3.7	5

Table 2: CHEMICAL ANALYSIS ON LDEF SAMPLES

SAMPLE	MATERIAL	THICKNESS (μm)	CRATER SIZE (μm)	ELEMENTS FOUND ON MATRIX	ELEMENTS FOUND ON CRATER
1. B26	Al	2000	325	Al, Cu, (Mg, Mn)	Cu, Fe, Mg, Mn, C
2. B25	Al	2000	338	Al, Cu, Mg, (Mn, Si)	Fe, Cu, Mn, C, Mg
3. VC-D3-V	glass	1000	940x700 spall	Si, O, Au (coating), Ni	2 part.:Zn, O, Si, C 1 part. : Au
4. B16	glass	1000	180x130 spall	Si, O	Si, O..
5. A2-5	Al	250	190 12.5 (low vel.) 6.5x5 (low vel.)	Al, O, Fe " "	nothing Al, Si, Fe, Ca, C Al, O
6. A2-6	Al	250	4.8	Al, O, (Fe)	nothing
7. A2-1	Al	250	57	n.a.	
8. A2-2	Al	250	14 120 15	Al, O, Fe, Ni " "	Fe, Ca, Cl, K, Si, Na, Mg, O nothing
9. e7tb (MAP)	Al	25	12 craters < 5 μm 3 craters > 5 μm	Al, Fe, Cu, Zn	Si on crater lip, Mg (Fe, Ca, Zn, Mg, C)
10. AD11 (AO138-2)	Al	5 + 150	40 μm perf + ejecta		O, Mg, Si, Al
11. A54-2,4	Al	250	15 craters 1.5>Dc>15 μm		C, O, Na, Mg, Si, S, Ca, Fe
12. A54-3	Al	250			
13. E13 (AO138-2)	Au	150	3 craters < 4 μm		

Figure 1: Crater distribution on LDEF Comparison of data from FRECOPA and MAP.

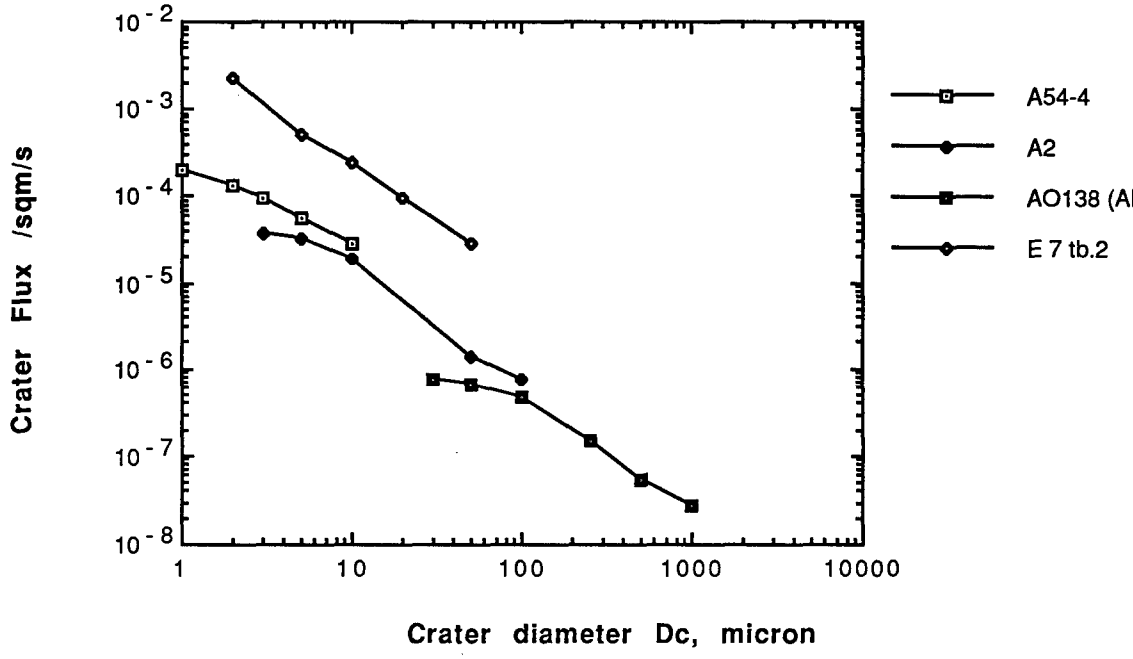


Figure 2: Comparison of crater flux on LDEF (leading edge) and on MIR.

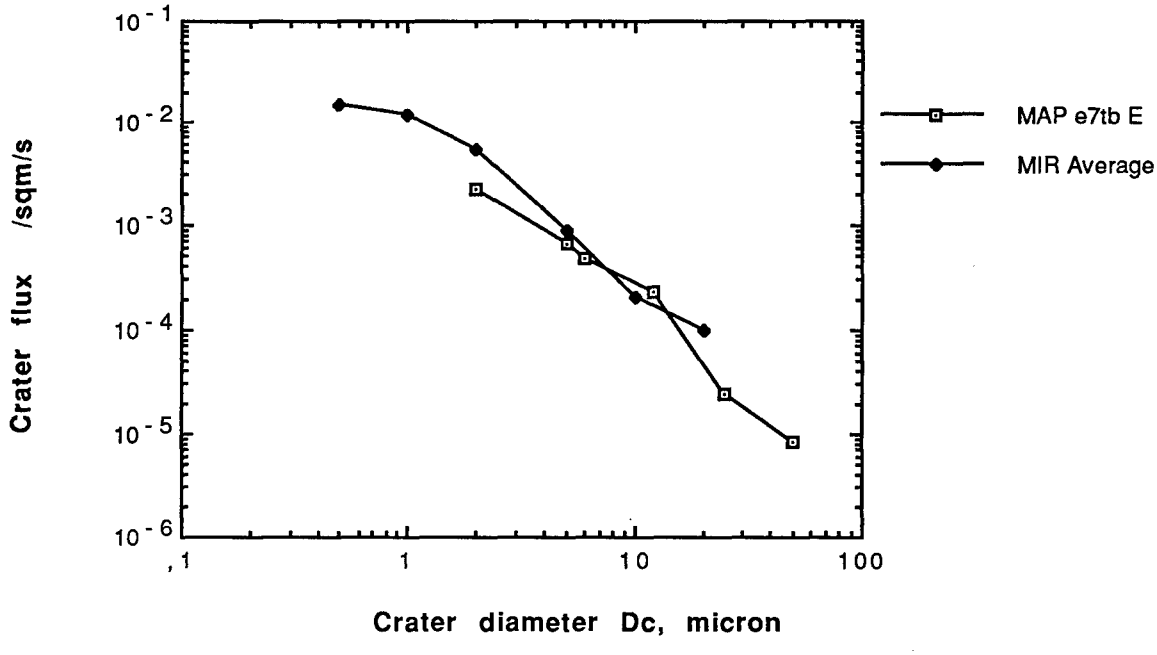


Figure 3: Impact velocity on different faces of LDEF.

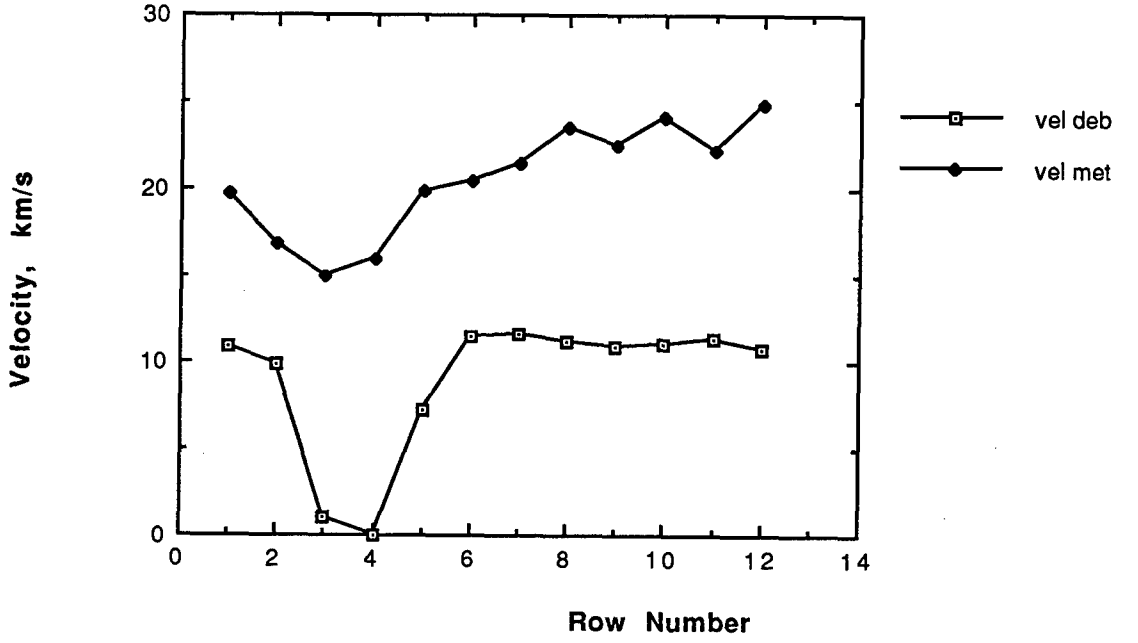


Figure 4: Comparison of crater flux on LDEF with model (Esabase) (crater diameter 5, 50, 500 microns).

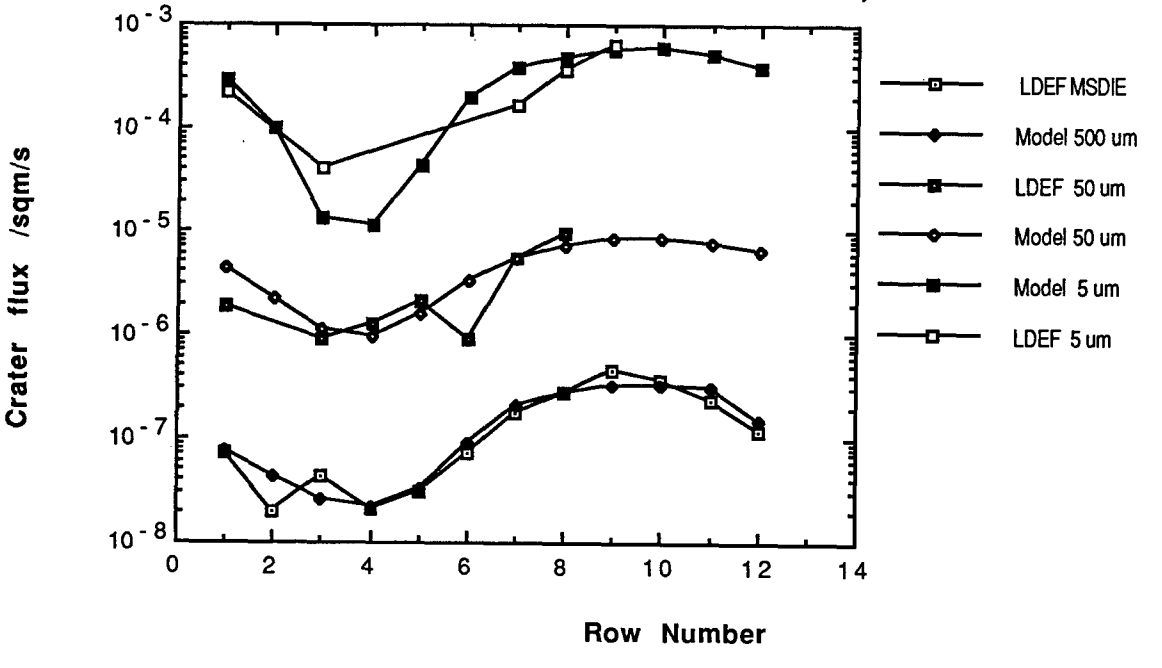
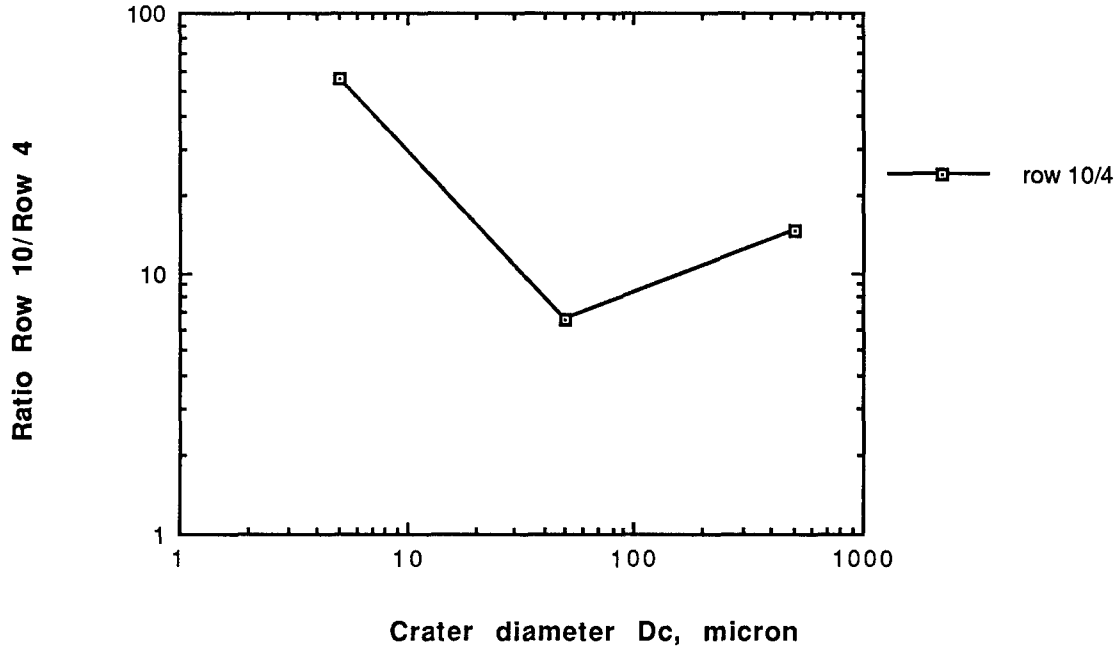


Figure 5: Comparison of flux on leading edge and on trailing edge of LDEF.



CONTINUED INVESTIGATION OF LDEF'S STRUCTURAL FRAME AND THERMAL BLANKETS BY THE METEOROID & DEBRIS SPECIAL INVESTIGATION GROUP

Thomas H. See
Lockheed Engineering & Science Co.
Houston, Texas 77058
(713) 483-5027 / FAX (713) 483-5347

Kimberly S. Mack
Lockheed Engineering & Science Co.
Houston, Texas 77058
(713) 244-5919 / FAX (713) 483-5347

Jack L. Warren
Lockheed Engineering & Science Co.
Houston, Texas 77058
(713) 483-5122 / FAX (713) 483-5347

Michael E. Zolensky
NASA / Johnson Space Center
Houston, Texas 77058
(713) 483-5128 / FAX (713) 483-5347

Herbert A. Zook
NASA / Johnson Space Center
Houston, Texas 77058
(713) 483-5058 / FAX (713) 483-5276

INTRODUCTION

Since the return of the Long Duration Exposure Facility (LDEF) in January, 1990, the Meteoroid and Debris Special Investigation Group (M&D SIG) has been examining LDEF hardware (*i.e.*, experiment trays and structural components) in an effort to define the low-Earth orbit (LEO) particulate environment as witnessed by the spacecraft during its 5.7 year stay in orbit. Last year we reported (ref. 1) on the frequency of larger features as determined from data acquired by the M&D SIG's Analysis Team (A-Team) during LDEF deintegration. At that time the A-Team examined every square millimeter of the spacecraft locating and documenting the presence of all impact craters ≥500 μm in diameter and all penetration holes ≥300 μm in diameter (ref. 2). Over the past year M&D SIG members and Lockheed Engineering & Sciences Co. personnel at the Johnson Space Center (JSC) in Houston, Texas have been examining selected LDEF structural frame components (*i.e.*, intercostals) in much greater detail in order to augment this large-particle data with that from smaller particles.

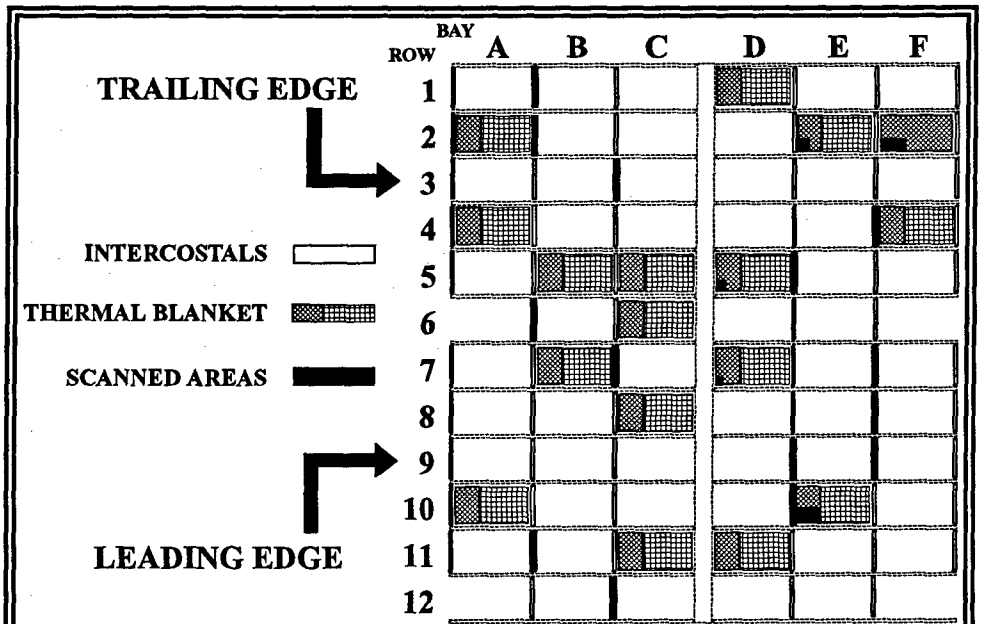


Figure 1. Sketch illustrating the numbering scheme (*e.g.*, C03) utilized in the designation of experiment-tray locations and the nominal leading and trailing edges of the spacecraft. All intercostals, except those from the end rings on Rows 6 and 12, are now in the possession of the M&D SIG at JSC, as is the left third of each of the 16 A0178 thermal blankets and all of the P0004/P0006 (F02) thermal blanket. The other two thirds of each blankets is in the possession of J.A.M. McDonnell at the University of Kent, U.K.. Solid dark areas indicate frame and blanket surfaces that have been scanned and are included in this study.

In all, LDEF exposed

~130 m^2 of surface area to the LEO particulate environment, ~15.4 m^2 of which was occupied by structural frame components of the spacecraft. This report focuses on the data acquired by detailed examination of LDEF intercostals, 68 of which are now in possession of the M&D SIG at JSC (Figure 1). In addition, limited data will be presented for several small sections from A0178 thermal control blankets that were examined/counted prior to being shipped to Principal Investigators (PI's) for scientific study. As was the case in Ref. 1, the data presented here are limited to measurements of crater and penetration-hole diameters and their frequency of occurrence which permits, yet also constrains, more model-dependent, interpretative efforts. Such efforts will focus on the conversion of crater and penetration-hole sizes to projectile diameters (and masses), on absolute particle fluxes, and on the distribution of particle-encounter velocities. These are all complex issues (refs. 3, 4, 5, 6, 7, 8) that presently cannot be pursued without making various assumptions which relate, in part, to crater-scaling relationships, and to assumed trajectories of natural and man-made particle populations in LEO that control the initial impact conditions.

RATIONALE FOR SELECTION OF SURFACES

The size of a crater or penetration hole depends on the physical properties associated with the target and projectile materials, and on the projectile's mass and impact velocity. On LDEF, a given unit impactor generated craters of different sizes depending on the location or pointing direction of the target because of the different effective (mean) encounter velocity, assuming a constant target material. The quantitative relationships for these parameters are known for some LDEF materials, but only over a restricted range and set of initial conditions. In order for the M&D SIG to deduce particle frequencies as a function of directionality it is necessary to characterize impact features on identical target materials so that the physical properties of the target can be accounted for, or remain constant. Furthermore, because of the highly stochastic nature of the collisional environment, it is also necessary to study materials which exposed sufficient surface areas to have accumulated a representative population of impact features. Such factors pointed to LDEF's structural frame as the *only* material that fit all of these criteria.

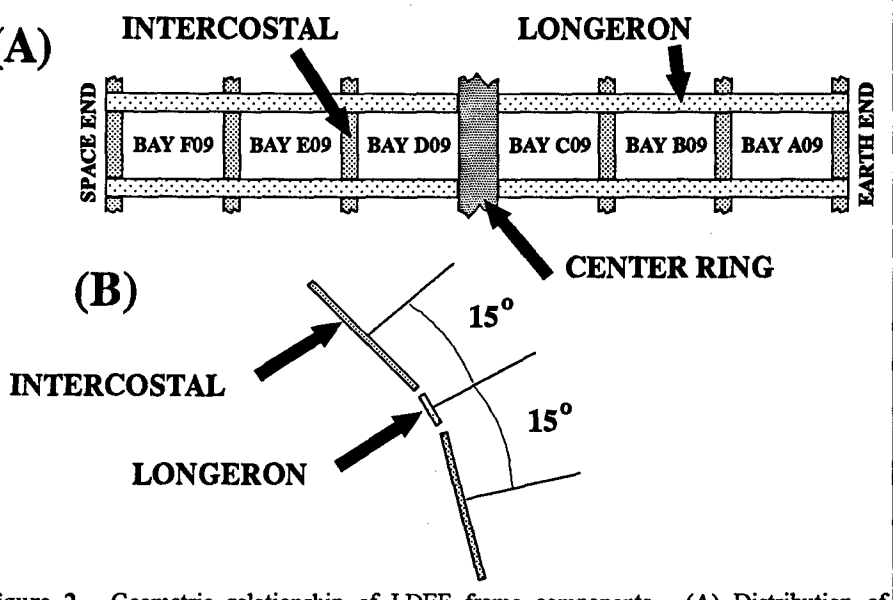


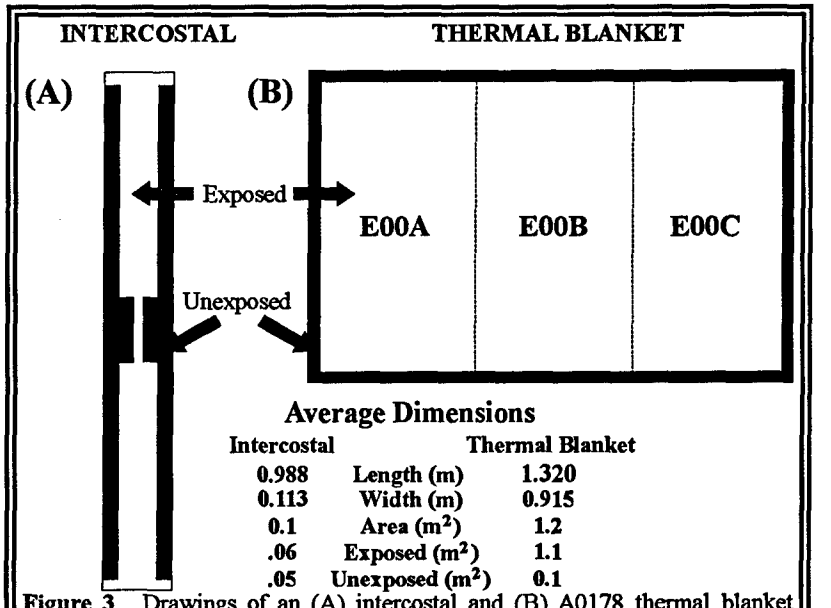
Figure 2. Geometric relationship of LDEF frame components. (A) Distribution of longerons and intercostals in a typical "Row" of LDEF Bays and instrument locations. (B) A view down the axis of the spacecraft illustrating the angular relationship between a longeron and adjacent intercostals (ref. 1.).

LDEF's entire structural frame was fabricated from 6061-T6 aluminum, a commonly used spacecraft material whose response to hypervelocity impact has been

studied in great detail (*e.g.*, refs. 3, 6, and 9). The frame components formed an open-grid, 12-sided structure that produced individual instrument bays (Bays A-F; Figure 1) and provided attachment points for the experiment trays. The longitudinal frame members (~4.6 m long) were termed "longerons" (Figure 2a), while cross members between longerons were called "intercostals" (~1 m in length). Individual rows were assigned sequential numbers (1-12), with Row 9 facing in the nominal velocity vector (leading-edge direction) and Row 3 in the trailing-edge direction. For simplicity, the M&D SIG assigned half-row numbers to the longerons (*e.g.*, longeron 2.5 resides between Rows 2 and 3). The angle between adjacent instrument rows, defined by the intercostals, was 30° (resulting in the 12-sided cylindrical structure), while the angle between adjoining intercostals and longerons was 15° so that one longeron accommodated instruments from two adjacent rows (Figure 2b). The frame components of the Earth- and space-facing ends (*i.e.*, Bays G and H) of the spacecraft were essentially flat. This configuration resulted in LDEF possessing 26 principal pointing directions (*i.e.*, 24 around the periphery plus the Earth- and space-facing ends) and provides an unprecedented opportunity to study impact craters in a fairly well understood infinite halfspace target. Because of their size and mass, and because of their significance to the overall structural integrity of the spacecraft, the longerons and the components from the Earth- and space-facing ends could not be made available for detailed study in the laboratory. On the other hand, the small size and mass of the individual intercostals made them well suited for removal and detailed scanning within the Facility for the Optical Inspections of Large Surfaces (FOILS) laboratory at JSC.

Surface Areas and Procedures

Individual intercostals exposed ~0.06 m^2 of surface area (Figure 3a and Table 1), while a complete row of intercostals, not including the center ring (*i.e.*, the four mid- and two end-ring intercostals; see Figures 1 and 2), totaled ~0.32 m^2; end-ring intercostals exposed only ~0.04 m^2 each. Multiply by 12, and accounting for the two Row 6 and two Row 12 intercostals not included, results in a total exposed surface area of ~3.68 m^2 of LDEF intercostals in our study.



Average Dimensions

Intercostal		Thermal Blanket
0.988	Length (m)	1.320
0.113	Width (m)	0.915
0.1	Area (m^2)	1.2
.06	Exposed (m^2)	1.1
.05	Unexposed (m^2)	0.1

Figure 3. Drawings of an (A) intercostal and (B) A0178 thermal blanket illustrating the areas that were exposed to the LEO particulate environment. Note that the drawings are not to scale with respect to each other.

Although they were not as evenly distributed as the aluminum frame, the Scheldahl G411500 thermal blankets associated with the sixteen A0178 experiment trays and the one P0004/P0006 experiment tray offer another material type that was widespread around the exterior of LDEF (*i.e.*, all rows except 3, 9 and 12 possessed at least one of these blankets; see Figure 1). Each blanket exposed ~1.1 m^2 (Figure 3b) of surface area and consisted of a 200 to 300 Å thick layer of silver-inconel that was sandwiched between a space-facing layer of FEP Teflon (~125 μm thick) and an 80 to 100 μm thick layer of DC1200 primer and Chemglaze Z306 black conductive paint. Unfortunately, the impact/penetration behavior of this composite foil is poorly understood at present and dedicated calibration experiments designed to address such behavior are needed.

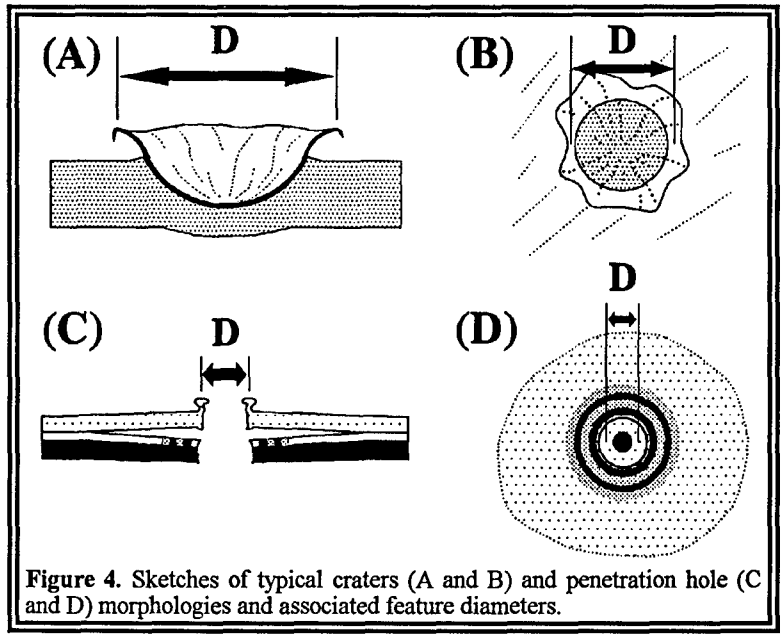


Figure 4. Sketches of typical craters (A and B) and penetration hole (C and D) morphologies and associated feature diameters.

As was the case in the earlier work (ref. 1) that utilized only the larger impact features on LDEF, crater diameters reported here for the intercostals refer to rim-crest-to-rim-crest dimensions (Figure 4a and 4b), while penetration-hole and crater diameters for the thermal blankets refer to center-of-rim-to-center-of-rim measurements (Figures 4c and 4d). For details on the morphology and associated measurement techniques for these, as well as all other impact features documented by the M&D SIG, interested readers should see Refs. 1 and 2. However, unlike the earlier effort, many of the features documented during the detailed examination of the thermal blankets were craters instead of penetration holes (see below). In general, regardless of the feature size or event type, the outer layer (*i.e.*, the Teflon) still delaminated from the silver-inconel/thermal paint backing as illustrated in Figures 4c and 4d. Furthermore, most of these smaller impact features did not exhibit the associated rings that were so common with the larger penetration events into this same material (refs. 2 and 15).

Table 1. Number of individual features documented in each size bin for the LDEF intercostals and thermal blankets, as well as the associated exposed surface area for each component. Size bins are inclusive on the lower end of each bin (*i.e.*, bin 11 contains all particles ≥11 μm and <16 μm in diameter.

	INTERCOSTALS Crater Diameter (μm)																	SURFACE
COMPONENT	<11	11	16	22	31	44	63	88	125	177	250	354	500	707	1000	1414	TOTAL	AREA (m^2)
B01F02				2	1	4	7	7	3	5	2						31	0.0595
B02F02			5	4	2	7	10	10	1	1		1					41	0.0579
C03F02		1		4	5	3	4	3	5	1	2	1		1			30	0.0587
F04F02				1	1	3	4	3	1	2	1	1				1	18	0.0604
E05F02		10	38	14	14	5	7		2	3	2	1					96	0.0587
B06F02		2	10	17	10	11	3	5	3	2	1		1				65	0.0600
C07F02			9	28	34	45	11	19	16	8	5	4	1				180	0.0590
F07F02	40	63	143	148	42	49	16	15	10	7	3	3	2				501	0.0589
F08F02			4	4	40	25	33	19	17	9	6	6	3		1		167	0.0602
E09F02					28	22	52	20	18	12	6	2	4		1		165	0.0588
F09F02		10	32	80	65	77	29	36	22	15	7	4	5		2		384	0.0580
E10F02			19	18	65	38	39	18	14	17	11	1	8	1	2		251	0.0595
B11F02		1	10	15	9	42	23	26	12	8	6	3	1	1		1	158	0.0584
C12F02					1	7	19	12	7	7	4	1	1	1			60	0.0598
TOTAL	40	87	270	335	317	338	257	193	131	97	56	28	26	4	6	2	2147	

	THERMAL BLANKETS Feature Diameter (μm)																SURFACE
COMPONENT	10	14	20	28	40	57	80	113	160	226	320	453	640	905	1280	TOTAL	AREA (m^2)
E02E00AA / F02E00AA		1	1	7	9	19	10	11	6	6	1	2	1			74	0.1615
D05E00AA						2		2	2			2		2		10	0.0411
D07E00AA								4	3	5	3	2	2			19	0.0212
E10E00AA / E10E00AC						2	1	29	60	55	26	17	8	5	2	205	0.1558
TOTAL		1	1	7	9	23	11	46	71	66	30	23	11	7	2	308	

Table 1 lists the number of features, sorted by size, documented on each LDEF row, as well as the exposed surface areas of each intercostal and thermal-blanket section that is included in the study. All scanning was conducted within the FOILS laboratory at JSC; the intercostals were scanned at a 40x magnification which easily permitted identification of all craters >30 μm in diameter on these relatively smooth surfaces. *Thus, below 30 μm the coverage is not complete.* During the scanning of the thermal blankets no attempt was made to document features <100 μm in diameter, except on components E02E00AA and F02E00AA which possessed a relatively small number of impacts to begin with and, therefore, were easily documented down to ~50 μm diameter features. It should be noted that no effort is presently underway to conduct a systematic and comprehensive study of the thermal-blanket materials that are presently in the possession of the M&D SIG at JSC. The only thermal-blankets materials documented thus far at JSC are those that were being processed for shipment to various PI's for scientific study, some of which planned to totally consume the samples. Therefore, the statistics associated with these data are extremely poor and the data are presented here purely as supplementary information. It should be noted that McDonnell is examining sections of the other two thirds of these blankets.

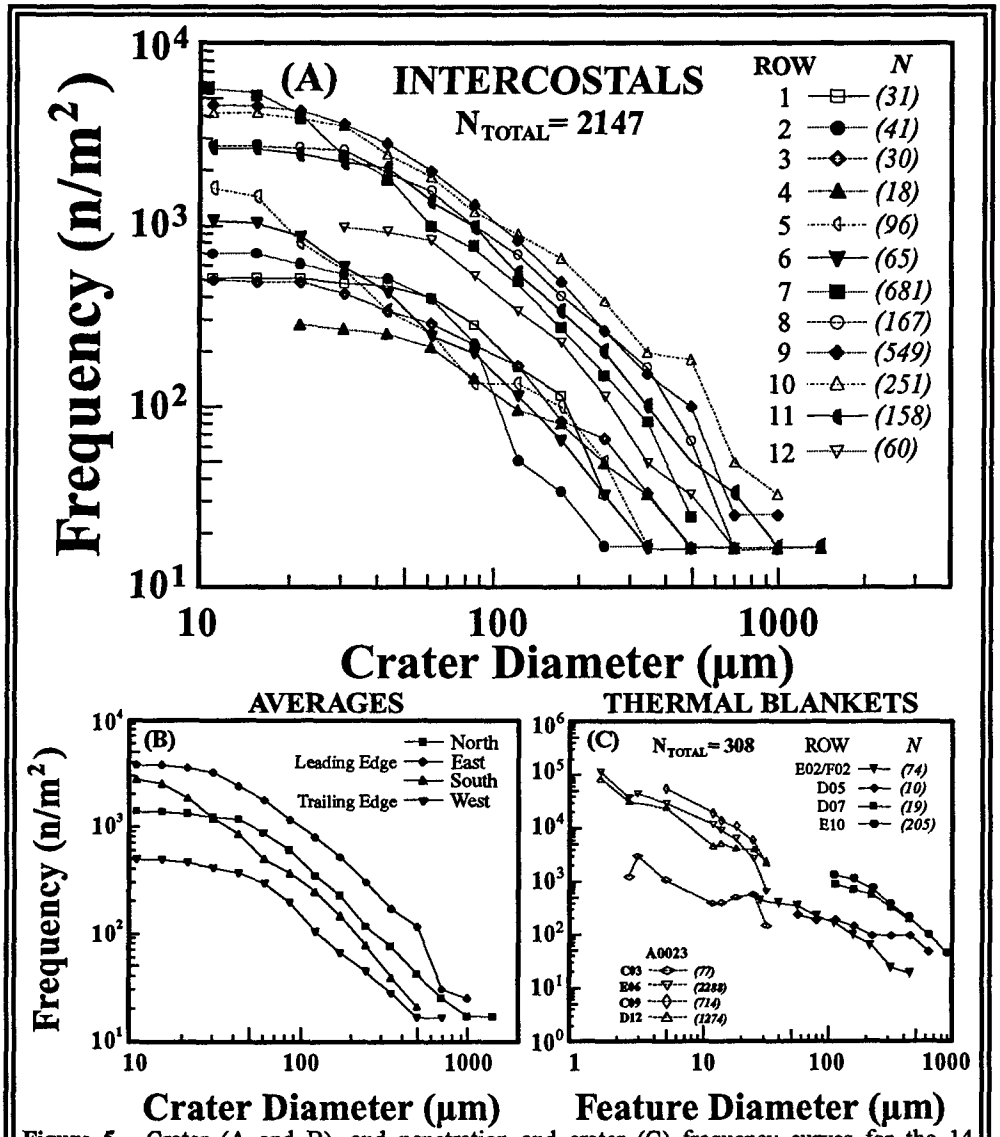


Figure 5. Crater (A and B), and penetration and crater (C) frequency curves for the 14 intercostals (12 different pointing directions) and the small sections from five of the Scheldahl thermal insulation blankets. (A) Crater frequencies for the 6061-T6 aluminum intercostals; the counts below ~30 μm are incomplete and this explains why the curves tend to flatten out below this diameter; see text. (B) Average frequency data for the four primary LDEF pointing directions (*i.e.*, North - 11, 12 and 1; East - 8, 9 and 10; South - 5, 6 and 7, and West - 2, 3 and 4). (C) Penetration-hole and crater frequency flux curves for several small pieces from A0178 thermal blankets along with data obtained from McDonnell *et al.* for the A0023 Multi-Foil Microabrasion Package (MAP) experiment. Note that these curves depict the frequency over the entire 5.7 years LDEF remained in LEO.

RESULTS

The cumulative size frequency distribution and spatial density of craters and penetration holes are illustrated in Figure 5. Note that features ~200 μm in diameter in Figure 5C

generally occurred as craters and not penetration holes, because the increasingly smaller projectiles did not possess adequate size, mass and/or kinetic energy to completely penetrate the ~200 μm thick thermal blanket. In such cases the blanket responds as an infinite halfspace target resulting in a cratering instead of a penetration event.

Figure 5a displays the crater frequencies for the 14 intercostals examined to date (*i.e.*, one intercostal from each LDEF row except for Rows 7 and 9 on which two intercostals have been examined). These data are in good agreement with our earlier results (ref. 1) and with those of others (*e.g.*, ref. 11; not plotted for the sake of clarity), with the highest cratering rates being observed in the forward-facing directions (*i.e.*, Rows 8, 9 and 10) and the lowest frequencies found in association with the rearward-facing surfaces (*i.e.*, Rows 2, 3 and 4). In general, the slope for the various curves are very similar, suggesting overall ratios of large to small particles remaining relatively constant, regardless of pointing direction.

A possible exception to this relation can be seen in the curve associated with Row 7. Intercostal F07F02 possesses an unusually high density of craters <30 μm in diameter (see Table 1). Although no more effort was made to locate and document small features on this intercostal than any of the other 13 intercostals, the number of craters <30 μm in diameter is more than three times greater for F07F02 than for even the Row 9 leading-edge intercostals. In fact, F07F02 has 2.8 times more total craters, and more than 10 times the number of <30 μm diameter craters than does C07F02, an intercostal that was positioned on the opposite end of Row 2. Specifically, of the 681 craters documented on the two Row 7 intercostals, ~74% resided on F07F02, while 57% of the 681 craters were <30 μm in diameter and located on F07F02. Furthermore, the distribution of craters on F07F02 was evenly split between both ends of the intercostal, with 252 craters being located above the center clamp position (see Figure 3a), and 251 craters located below this central clamp position.

Several other surfaces on this same row and end of LDEF have exhibited a similar trend (Figures 5c and 6). At the request of the M&D SIG, Don Humes (personal communications, 1992) examined some of the hardware associated with the experiment trays located on either side of intercostal F07F02, since both bays were occupied by Humes' S0001 experiments. Figure 6 illustrates the results of Humes' investigation and depicts the results of his counts on an experiment-tray lip that resided on the F07F02 intercostal. The two Row 7 intercostals are plotted separately so that the unusual nature of the F07F02 intercostal is visible; also plotted are the frequency curves for the Row 9 and Row 3 intercostals. The Humes data exhibits an excellent match to our intercostal data between ~50 and 400 μm, and reveals an even higher flux below ~50 μm than does our data. The two intercostals from Row 7 are very different below ~30 μm, with intercostal C07F02 displaying a trend that is similar to all other intercostals examined to date. An intercostal from Row 8 (F08F02) is included in this study, yet it does not exhibit the trend observed for F07F02.

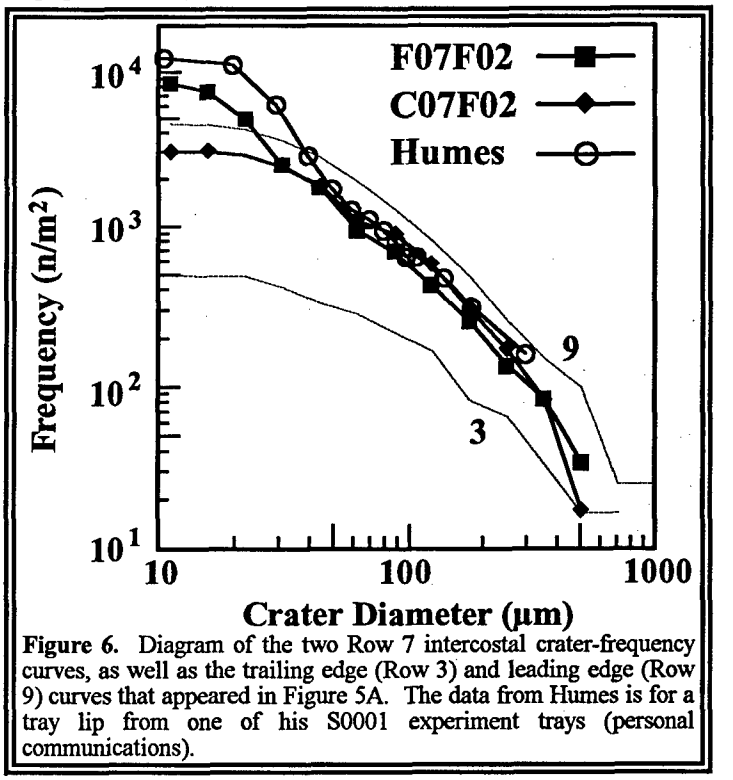


Figure 6. Diagram of the two Row 7 intercostal crater-frequency curves, as well as the trailing edge (Row 3) and leading edge (Row 9) curves that appeared in Figure 5A. The data from Humes is for a tray lip from one of his S0001 experiment trays (personal communications).

There are two possible explanations for the variation of spatial densities of craters seen in the two separated locations on Row 7. The first possibility is that the variations are simply due to different

scanning biases from one location to another. The second and most likely possibility is that the observed variations do not suffer from observational biases and are of real statistical significance and need to be explained.

If the second possibility is true, then the variations must either be due to an extremely great variability in the spatial density of meteoroids or Earth-orbiting debris, or it is due to a source of impacting objects very near LDEF. The highest measured impact rate on LDEF was that by the Interplanetary Dust Experiment (IDE; ref. 7) where 131 impacts were recorded within an approximately two minute time period during LDEF's passage through a debris stream early in the mission. This corresponds to about one impact per second on the ~1 m^2 IDE experiment. Since the orbital velocity of LDEF was ~8 km/s, the spatial density of impacting objects -- even for this most intense stream -- did not exceed about $10^{-4}/m^3$, or about one impact per square meter per second. At such a rate no strong change in the integrated impacting flux at locations separated by several meters should be seen. As for sources very near LDEF, two possibilities come to mind. First, could all, or many of these small craters represent secondary craters? Potential locations of a primary crater have been explored, yet no potential source can be found. Nothing in the vicinity of this intercostal can be found that projects above the surface that could serve as a reasonable location for such a primary. The closest object protruding above the surface of the spacecraft is the Row 6 trunnion pin that was located on the center ring at a distance of more than two meters away and with a 30° angle between the rows. The other possible source might have been the nearby Space Shuttle during rendezvous maneuvers. This potential source can't yet be ruled out.

An alternative cause for the differences noted for Row 7 is some sort of optical scanning bias. We note, in Table 1, that nearly all the difference in crater spatial densities on Row 7 is due to craters smaller than 31 μm in diameter, meaning that most of these craters were smaller than are nominal scanning threshold of 30 μm (only above which are we confident of 100% coverage). It is not a question of statistics; the spatial density variations seen for craters less than 31 μm in diameter are clearly not due to Poisson statistical variations. Some sort of scanning bias -- not yet identified -- could cause the observed variations seen in Rows 7 and 9. We intend to scan selected areas from several intercostals and pointing directions at higher magnifications to help address the issue of possible scanning bias.

During the documentation of intercostal F07F02 it was noted that an unusually high number of these craters contained apparent residues. Therefore, after documentation of this intercostal was completed it was sectioned into 24 smaller pieces that could be examined in a Scanning Electron Microscope (SEM) in hopes of obtaining some qualitative chemical information regarding the projectile(s) responsible for these craters. To date, only 19 of the most promising craters, ranging in size from 10 μm to 95 μm in diameter, have been examined. Of these, four (21%) were found to contain residue of probable micrometeoritic compositions, three (16%) contained man-made (*i.e.*, two paint and one solder) material, two (11%) revealed chemistries that have commonly been associated with contamination on LDEF (*i.e.*, Si and Ca), and the remaining ten (53%) were indetermanent (*i.e.*, either insufficient amounts of residue were present or the resulting compositions could have more than one source). So far, these distributions appear like those observed for LDEF as a whole, and do not support a uniform particulate source for the abundant small craters identified on intercostal F07F02.

Obviously, the source(s) of these craters is (are) of extreme interest to the M&D SIG and further research into possible causes are under investigation. We presently plan on examining more of these features via optical and chemical techniques in hopes of providing more data to address this issue. The chemical distribution of those craters analyzed to date is most likely not representative of the entire intercostal since we purposefully chose craters that optically, at least, appeared to offer the best opportunities in providing chemical information.

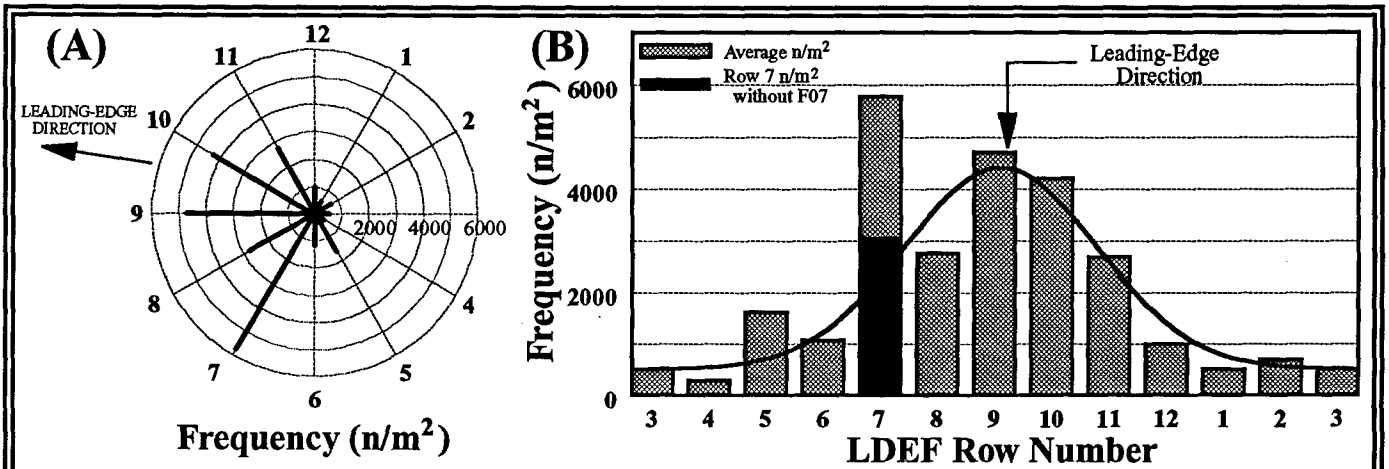


Figure 7. (A) Polar coordinate diagram of the cratering frequencies for the 12 LDEF rows for craters of all sizes. (B) Histogram of the same data as in (A). Two Row 7 bars are represented, one with F07F02 included, and the other depicting where C07F02 would plot by itself. Note that Row 3 is plotted on both ends of the chart. The curve in (B) represent a Gaussian fit to the data with F07F02 not included.

Returning to the general trends within our data, Figure 5b depicts the average frequencies for the four main LDEF pointing directions (*i.e.*, 12 [north], 9 [east], 6 [south] and 3 [west]). Each curve represents the average of the main row from each direction plus the rows on either side (*i.e.*, west represents the average of Rows 2, 3 and 4). Such a plot is useful in revealing the overall trends associated with each of these four pointing directions. As expected, the forward-facing rows reveal the highest cratering frequencies, while the rearward-facing rows exhibit the lowest. Also, not surprisingly, the northern facing rows (1, 12 and 11) display a slightly higher overall flux than do their southern-facing counterparts. Since LDEF's velocity vector was actually skewed ~8° toward Row 12 such a trend is understandable (*i.e.*, the northern-facing rows faced ~8° more into the velocity vector, while the southern-facing rows were ~8° further removed from the velocity vector, ref. 16; see Figure 7a). Again, note the influence of the F07F02 intercostal on the overall average flux associated with the southern-facing rows of Figure 5B.

Figure 7 depicts, in both polar and histogram form, the impact frequency for all sizes of craters (n/m^2) on each of the twelve rows. In our earlier efforts (refs. 1 and 13) that utilized only those craters ≥500 μm in diameter, we found that the highest cratering rates were associated with Row 10. However, now that we have greatly enhanced the data set and added much smaller features to our statistical database we find that the leading-edge or velocity vector did indeed experience the highest cratering rate (*e.g.*, ref. 12), again with the exception of the one Row 7 intercostal. The nearly 50% decrease in the large-cratering frequency for Row 9 versus Rows 8 and 10 that was discussed in Ref. 13 (see Figure 4 of ref. 13) disappears when much smaller craters are included (Figure 7a).

Figure 7b shows the same data plotted in histogram format and again illustrates the effect that intercostal F07F02 had on the average impact frequency for Row 7. The filled bar for Row 7 depicts where the Row 7 would fall if only the C07F02 intercostal was included. Finally, it can be seen that the intercostal data reveals a Gaussian-type distribution around the nominal leading-edge direction (Figure 7b). From a similar fit to the large-crater data in Ref. 13 we reported a leading-edge:trailing-edge ratio of ~20:1, while the Gaussian fit to the new intercostal data suggests a ratio more on the order of 10:1.

Figure 8a depicts the relative production rates for craters ≥44 μm and ≥63 μm in diameter and was generated by normalizing the absolute cratering frequencies for each row (Figure 7b) to that of Row 9 (leading-edge). At these crater sizes, there should be no biases introduced by incomplete scanning. This figure shows that the ratio of the production rate of impacts on the leading edge to that on the trailing edge is on the order of 10:1. Of equal interest is how this ratio varies as a function of crater size, an issue that is addressed in Figure 8b. For the larger craters (*i.e.*, ≥500 μm and ≥707 μm in diameter), Figure 8b indicates

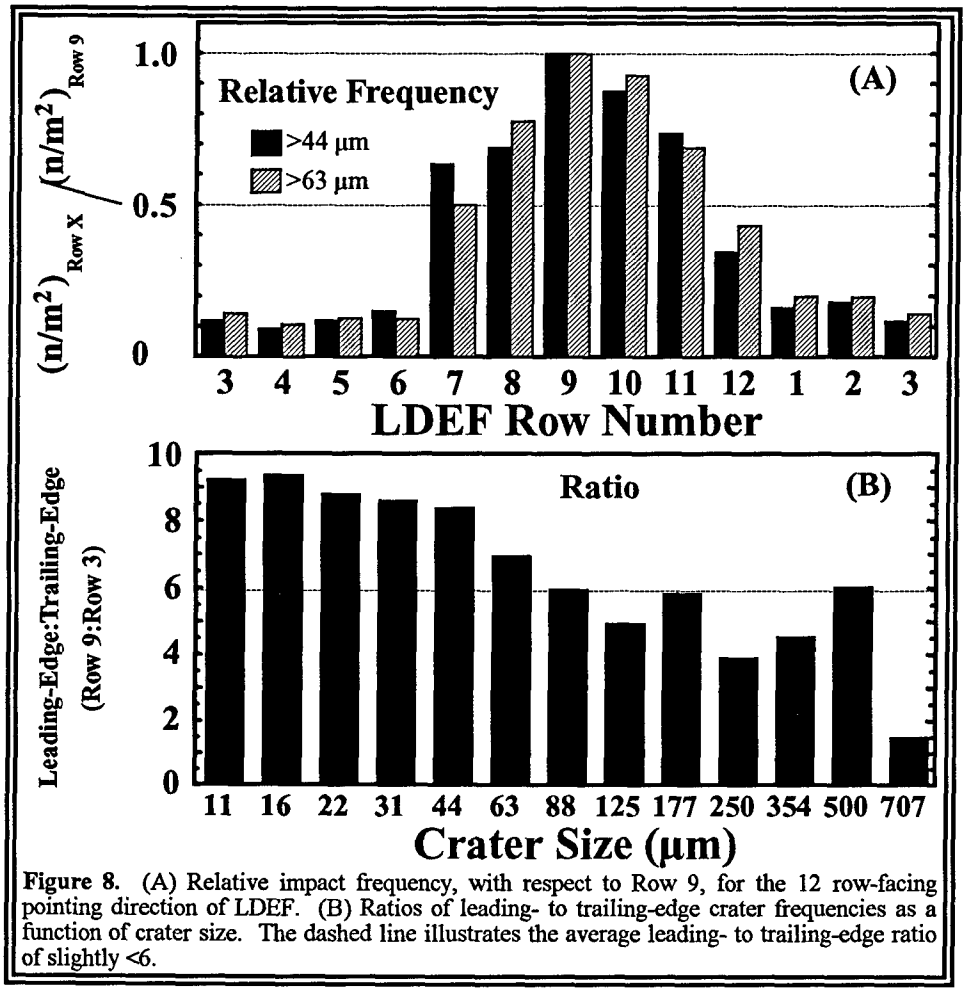


Figure 8. (A) Relative impact frequency, with respect to Row 9, for the 12 row-facing pointing direction of LDEF. (B) Ratios of leading- to trailing-edge crater frequencies as a function of crater size. The dashed line illustrates the average leading- to trailing-edge ratio of slightly <6.

a difference in the crater production rate between the leading- and trailing-edge of ~4 to 1, while for the smaller feature sizes this ratio is ~9:1. It should be noted that only 38 of the 2147 impacts (<2%) included in this study were ≥ 500 μm in diameter, resulting in a relatively large error associated with the 500 and 707 μm size bins. In general, however, there does appear to be a trend for the differences in feature production rate between the leading- and trailing-edge to increase as feature size decreases. Additional evidence for such a change can be found in the thermal-blanket and MAP experiment data illustrated in Figure 5c. For the larger penetration features (~500 μm in diameter) the leading- to trailing-edge ratio is ~10:1, while for the smallest features for which data is available on both Rows 3 and 9 (*i.e.*, ~5 μm in diameter; see Figure 5c) this ratio climbs to ~50:1. Is the large-particle population more isotropically distributed, or are these difference related to the sources, and hence the associated velocities of the different particle-population sizes?

The measured ratios, Row 9 to Row 3, of the spatial density of impact craters do not agree with current theoretically predicted ratios for either meteoroids (ref. 12) or for Earth-orbital debris (ref. 14). Since it is believed that these two sources dominated all others on LDEF, it follows that the present theoretical models are inadequate to explain the data (ref. 17). For meteoroids to produce a front-to-back ratio as low as 6:1, a much larger fraction of high-velocity meteoroids than hitherto modeled seems to be required. If orbital debris is the primary source for the observed impact craters, the data suggest that there is much more debris than is now suspected in geosynchronous transfer orbits -- especially those with orbital inclinations near 28.5° (ref. 14). It may also be necessary to carefully reexamine the modeling for incorrect assumptions.

CONCLUSION

Last year we concluded that the observable impact record had to be expanded to include smaller impact features (ref. 1). Our current efforts are a step in that direction as we have continued to document various LDEF hardware (predominantly the structural frame) in order to better define and understand the LEO particulate environment. Our current results indicate that new theoretical modeling of both meteoroids and Earth-orbital debris needs to be undertaken. Specifically, new models should fit our latest observations of the directionality of crater spatial densities, and explore what these models imply in terms of sources of meteoroids or orbital debris.

Additional theoretical work is also need to address other questions that have remained unanswered with respect to LDEF. What is the relationship between the sizes of the observed penetration holes in the Teflon thermal blankets with that of the observed crater sizes on the intercostals. Obviously, different materials pointing in the same general direction should have, overall, witnessed a similar particle population size over an extended period of time, such as the 5.7 years in which LDEF was in LEO. Questions such as these can only be addressed following a dedicated series of impact experiments into both of these materials. Such an effort will be a high priority of the M&D SIG over the next year. Is the observed 5.7 year average impact frequency representative of what is happening year after year, or is it simply an average of a highly variable particle population? Mullholland *et al.,* (ref. 7) present evidence that suggests the LEO particulate environment is quite dynamic and varies greatly as a function of time and orbital position. However, until additional data can be gathered such an idea remains controversial.

At present, we plan on continuing our scanning and documentation of the LDEF intercostals (at least until we have examined at least three intercostals per row) to improve our statistical database. In addition, it is hoped that the proposed calibration work for the thermal blankets can be conducted so that we can convert our cratering and penetration-hole frequencies into some sort of coherent particle-size population.

REFERENCES

1) See, T.H., Hörz, F., Zolensky, M.E., Allbrooks, M.K., Atkinson, D.R. and Simon, C.G., (1992) Meteoroid and Debris Special Investigation Group Preliminary Results: Size-Frequency Distribution and Spatial Density of Large Impact Features on LDEF. *LDEF - 69 Months in Space, First LDEF Post-Retrieval Symposium, NASA CP-3134*, p. 477-486.

2) See, T.H., Allbrooks, M.A., Atkinson, D.R., Simon, C.G. and Zolensky, M. (1990) *Meteoroid and Debris Impact Features Documented on the Long Duration Exposure Facility, A Preliminary Report, Publication #84, JSC #24608*, p. 583

3) Kessler, D.J. (1991) Orbital Debris Environment for Spacecraft in low Earth orbit, *J. Spacecraft, 28, 3,* p. 347-351.

4) Peterson, R.B. (1989) Instrument Pointing Considerations; *Report to Cosmic Dust Collection Facility Open Forum*, Lunar and Planetary Science Institute, March 1989

5) Zook, H.A. (1987) On cosmic dust trajectory measurements and experiment pointing considerations, in *Progress towards a Cosmic Dust Collection facility on Space Station*, Mackinnon, I.D. and Carey, W.C., eds., Lunar and Planetary Institute, LPI Technical Report 88-01, p. 76-77.

6) Zook, H.A. (1991) Meteoroid directionality on LDEF and asteroidal versus cometary sources (abstract). *Lunar Planet. Sci. XXII*, Lunar and Planetary Institute, Houston, Texas., p. 1577-1578.

7) Mullholland, J.D., Singer, S.F., Oliver, J.P., Weinberg, J.L., Cooke, W.J., Montague, N.L., Wortman, J.J., Kassel, P.C., and Kinard, W.H. (1992) IDE Spatio-Temporal Fluxes and High Time-Resolution Studies of Multi-Impact Events and Long-Lived Debris Clouds. *LDEF - 69 Months in Space, First LDEF Post-Retrieval Symposium, NASA CP-3134*, p. 517-528.

8) Hörz, F., Messenger, S., Bernhard, R., See, T.H. and Haynes, G. (1991) Penetration phenomena in Teflon and aluminum films using 50-3200 ¦m glass projectiles (abstracts), *Lunar Planet. Sci. XXII*, Lunar and Planetary Institute, p. 591-592.

9) Cour-Palais, B.G. (1987) Hypervelocity Impacts in Metals, Glass, and Composites, *Int. J. Impact Eng., 5*, p. 681-692.

10) McDonnell, J.A.M. and Stevenson, T.J. (1992) Hypervelocity Impact Microfoil Perforations in the LEO Space Environment (LDEF, MAP A0023 Experiment). *LDEF - 69 Months in Space, First LDEF Post-Retrieval Symposium, NASA CP-3134*, p. 443-458.

11) Hörz, F., Bernhard, R.P., Warren, J.L., See, T.H., Brownlee, D.E., Laurance, M.R., Messengerm, S. and Peterson, R.B. (1992) Preliminary Analysis of LDEF Instrument A0187-1 "Chemistry of Micrometeoroids Experiment." *LDEF - 69 Months in Space, First LDEF Post-Retrieval Symposium, NASA CP-3134*, p. 487-502.

12) Zook, H.A., (1992) Deriving the Velocity Distribution of Meteoroids From the Measured Meteoroid Impact Directionality on the Various LDEF Surfaces. *LDEF - 69 Months in Space, First LDEF Post-Retrieval Symposium, NASA CP-3134*, p. 569-579.

13) Zolensky, M., Atkinson, D., See, T.H., Allbrooks, M., Simon, C., Finckenor, and Warren, J. (1991) Meteoroid and Orbital Debris Record of the Long Duration Exposure Facility's Frame, *J. Spacecraft and Rockets, 28, #2*, p. 204-209.

14) Kessler, D.J., Origin of Orbital Debris Impacts on LDEF's Trailing Surfaces. *LDEF - 69 Months in Space, Second LDEF Post-Retrieval Symposium, NASA CP-3194, 1993*.

15) Allbrooks, M. and Atkinson, D. (1992) *The Magnitude of Impact Damage on LDEF Materials*. A final report to the M&D SIG under subcontract NAS9-17900, SC-02N0165768 to Lockheed - ESC.

16) Peters, P.N. and Gregory, J.C. (199) Attitude Stability of LDEF: Refinement of Results from the Silver Pinhole Camera. *LDEF - 69 Months in Space, Second LDEF Post-Retrieval Symposium, NASA CP- NASA CP-3194, 1993.*

17) Coombs, C., Watts, A., Wagner, J. and Atkinson, D. (1992) *LDEF Data: Comparisons with Existing Models.* A final report to the M&D SIG under subcontract NAS9-17900, SC-02N0165768 to Lockheed - ESC.

Predicted and Observed Directional Dependence of Meteoroid/Debris Impacts on LDEF Thermal Blankets

Gerhard Drolshagen

ESA/ESTEC
2200 AG Noordwijk, The Netherlands

SUMMARY

The number of impacts from meteoroids and space debris particles to the various LDEF rows is calculated using ESABASE/DEBRIS, a 3–D numerical analysis tool. It is based on recent reference environment flux models and includes geometrical and directional effects.

A comparison of model predictions and actual observations is made for penetrations of the thermal blankets which covered the UHCR experiment.

The thermal blankets were located on all LDEF rows, except 3, 9 and 12. Because of their uniform composition and thickness these blankets allow a direct analysis of the directional dependence of impacts and provide a test case for the latest meteoroid and debris flux models.

Introduction

In this paper the observed number of holes from particle impacts in the thermal blankets covering the Ultra High Cosmic Rays (UHCR) experiment on LDEF is compared to model predictions.

Trays of the UHCR experiment (AO178) were present on all LDEF rows except 3, 9 and 12. No trays were on the space and Earth pointing ends. The distribution of the thermal blankets on most of the 12 LDEF rows allows a detailed study of the directional dependence of impacts from meteoroids and space debris particles.

The LDEF was deployed in space on April 7, 1984 in an almost circular orbit with mean altitude 477 km and inclination of 28.5°. After a total exposure time in space of 5.76 years, it was retrieved on January 12, 1990. By that time the orbit had decayed to about 335 km.

LDEF was gravity–gradient stabilized with the longitudinal axis pointing towards the center of the Earth. After retrieval it was noticed that the flight attitude had been such that row 9 was facing about 8° off its nominal ram direction.

The thermal blankets covering the UHCR experiment were made of a compound of FEP Teflon ($\approx$ 125 μ) followed by thin layers of Silver and Inconel (combined less than 0.5 μ) and Chemglaze Z306 black paint (60 - 100 μ). The thermal blankets covered a total area of about 18 m^2.

In the next section the procedure is presented which is used to calculate the number of impacts and penetrations on the thermal blankets and the results are given. The predicted and observed number of holes is then compared.

Numerical Analysis Procedure

Flux models have been developed for both micrometeoroids and space debris to predict the number of impacts for given mission parameters. The resulting damage can be assessed through empirically derived design equations which give penetration capabilities, crater sizes, etc. as function of the particle parameters.

For a detailed impact risk assessment a fully three dimensional numerical analysis tool was developed which includes directional and geometrical effects and spacecraft shielding considerations. It is based on the latest environment and particle/wall interaction models [1].

This tool is a new application of the ESABASE framework of system level analysis and engineering tools and is supported by enhanced 3–D graphics.

The user specifies the mission parameters, spacecraft geometry, attitude and shielding as well as the particle type, size and velocity range to be analysed. The computed output includes:

- the number of impacts,
- the number of failures, taking into account the spacecraft shielding and damage assessment equations,
- the probability of no failure,
- the mean particle velocity (amplitude and direction),
- the percentage of cratered area.

The new tool was applied to an ESABASE model of the LDEF.

The total average meteoroid flux can be given in terms of the integral flux $F_{M,0}$ which is the number of particles with mass m or larger per m^2 per year impacting a randomly–oriented flat plate under a viewing angle of 2π. The unshielded interplanetary flux at 1 AU distance from the sun can be described analytically [2] as

$$F_{M,0}(m) = 3.15576\ 10^7(F_1(m) + F_2(m) + F_3(m))$$

where:

$$F_1(m) = (2.2\ 10^3 m^{0.306} + 15)^{-4.38}$$

$$F_2(m) = 1.3\ 10^{-9}(m + 10^{11}m^2 + 10^{27}m^4)^{-0.36}$$

$$F_3(m) = 1.3\ 10^{-16}(m + 10^6 m^2)^{-0.85}$$

with m in grams.

It should be emphasized that the meteoroid flux model gives a yearly average. At times of peak activity of a major meteor stream fluxes can be up to 5 times higher for a 1–2 day period.

Relative collision velocities for meteoroids can range from 11 to 72 km/s.

The following velocity distribution is used in the present reference flux model [3]:

$$g(v) = \begin{cases} 0.112 & \text{if } 11.1 \leq v < 16.3 \text{ km/s} \\ 3.328\ 10^5\ v^{-5.34} & \text{if } 16.3 \leq v < 55.0 \text{ km/s} \\ 1.695\ 10^{-4} & \text{if } 55.0 \leq v < 72.2 \text{ km/s} \end{cases}$$

The average impact velocity is about 17 km/s.

The unshielded flux $F_{M,0}$ has to be modified to account for the gravitational attraction (which enhances the meteoroid flux in the Earth proximity) and the geometrical shielding of the Earth (which reduces the flux). The gravitational enhancement factor G_e for the velocity distribution given above is defined as [3]:

$$G_e = 1 + \frac{R_e}{r}$$

where R_e is the mean earth radius and r is the orbit radius.

The meteoroid flux to an earth orbiting spacecraft is then given by: $F_M = F_{M,0} G_e$.

The Earth shielding factor for a given surface depends on the spacecraft altitude above the Earth surface and on the relative orientation of the surface normal with respect to the Earth direction. It is calculated numerically and applied for every surface element of the model.

For a surface with normal pointing towards Earth the flux is reduced by a factor $F = \cos^2\Theta$ relative to a surface pointing exactly away from Earth

(with: $\sin\Theta = (R_e + 100)/(R_e + h)$; R_e =Earth radius, h= spacecraft altitude).

The Earth shielding factor for a surface with normal perpendicular to the Earth direction (like the 12 LDEF rows) is given by:

$$F = 1 - 1/\pi\ (\Theta + 0.5 \sin 2\Theta).$$

According to ref. 3 the average density of micrometeoroids larger than 0.01 g is assumed to be 0.5 g/cm^3. Smaller particles are thought to have a higher density; however, there is still a considerable uncertainty about these densities. In this study a constant value of 1.0 g/cm^3 is used for the penetration analysis of the thermal blankets.

The assumption of spherical shape is made for converting particle diameters to masses.

According to the reference model used [3] the annual averaged meteoroid flux is omnidirectional with respect to the Earth surface. Relative to an orbiting spacecraft with fixed orientation w.r.t. the flight direction the meteoroid flux has a directional dependence.

When performing an impact analysis with the ESABASE/DEBRIS tool the impact flux and the directional dependence is obtained by a Monte Carlo procedure. For each surface element of the spacecraft model a user specified number of rays (typically several hundred) is analysed. Directions and velocities of the rays are selected at random but account for the flux distribution as given by the models (e.g. for meteoroids, isotropic impact direction with the exclusion of the Earth cone and the velocity distribution given above). To account for the spacecraft velocity each ray with given direction and velocity is then weighted by a factor:

$$k = v^3/(v_m^2\ v^*)$$

$$\text{with : } v^* = (v_m^2 - v_s^2 sin^2\alpha)^{0.5}$$

where v is the impact velocity, v_m is the meteoroid velocity, v_s is the spacecraft

velocity and α is the impact angle measured w.r.t. the flight direction.

A surface constantly facing into the flight direction will encounter about 7 times higher fluxes than a trailing surface. In addition, the average impact velocity for leading surfaces is higher as well.

The Earth shielding introduces a directional dependence as well. At an altitude of 470 km (and assuming an atmosphere thickness of 100 km) a surface with normal pointing directly towards Earth will receive about 9 times less impacts from meteoroids than a surface facing in the opposite direction towards space.

Flux Model for Space Debris

A new flux–diameter model, predicting the average space debris environment for low earth orbits, was recently published [3].

According to this model the cumulative flux of orbital debris of size d and larger on spacecraft orbiting at altitude h, inclination i, in the year t, when the solar activity for the previous year was S, is given by the following equation:

$$F = H(d) \cdot k_D \cdot \Phi(h,s) \cdot \Psi(i) \cdot [F_1(d) \cdot g_1(t) + F_2(d) \cdot g_2(t)]$$

where

F = flux in impacts per square meter of surface area per year
k_D = directional factor; = 1 for randomly tumbling surface
d = orbital debris diameter in cm
t = time expressed in years
h = altitude in km (h $\leq$ 2000 km)
S = 10.7 cm–wavelength solar flux in year t − 1
i = inclination in degrees

and $H(d) = \sqrt{10^{exp(-(log_{10}d-0.78)^2/0.637^2)}}$

$$\Phi(h,S) = \Phi_1(h,S)/(\Phi_1(h,S)+1)$$

$$\Phi_1(h,S) = 10^{(h/200-S/140-1.5)}$$

$$F_1(d) = 1.22 \times 10^{-5} \cdot d^{-2.5}$$

$$F_2(d) = 8.1 \times 10^{10} \cdot (d+700)^{-6}$$

$$g_1(t) = (1+q)^{(t-1988)}$$

$$g_2(t) = 1 + p(t-1988)$$

q = the assumed annual growth rate of fragments in orbit.
p = the assumed annual growth rate of mass in orbit.
q = 0.02; p = 0.05, the values recommended by NASA are used in this study.

$\Psi(i)$ = inclination dependence of flux; $\Psi(28.5°) = 0.931$

Impact velocities can range from 0 to about 15.5 km/s with an average velocity of 10 km/s.

For an oriented spacecraft surface the debris fluxes will be different for the various surfaces.

The present debris flux models are based on the approximation that all debris is moving in circular orbits. Relative to a moving spacecraft this implies that all space debris arrival directions are confined to a plane parallel to the surface of the Earth. The model excludes impacts from below (Earth direction) or above (space direction). Furthermore, for a spacecraft in circular orbit, a simple addition of velocity vectors shows that impacts can only occur under angles between 0° and 90° w.r.t. the flight direction and that every impact direction is associated with a unique impact velocity:

$v = 2\ v_s \cos\alpha.$

The velocity distribution for a given orbit is specified as well in ref. 3 and included in the present study. For the LDEF orbit the model gives the following relative impact velocity distribution:

$$g(v) = v(2v_o - v)[18.7e^{-((v-2.5v_o)/0.5v_o)^2} + 0.67e^{-((v-1.3v_o)/0.56v_o)^2}] + 0.01156\ v\ (4v_o - v)$$

with $v_o = 7.27$.

According to the reference model used, for I = 28.5°, most impacts are expected from the sides, between 30° and 80° from the flight direction.

This distribution of space debris fluxes leads to a considerable directional dependence. For the LDEF orbit forward facing surfaces will receive about 2.6 times higher fluxes than randomly oriented surfaces while exactly backwards facing surfaces should encounter no impacts at all.

The average density of particles larger than 0.62 cm in diameter is assumed to be $\rho = 2.8d^{-0.74}$ g/cm^3. The average density of smaller space debris particles is thought to be 4.0 g/cm^3.

These densities were used for the present analysis.

For the calculation of meteoroid fluxes a constant altitude of 470 km was assumed. Given the weak dependence of meteoroid fluxes on the altitude that implies only a minor approximation. Average annual fluxes are used for this long duration mission.

For the space debris analysis the changing LDEF orbit and solar activity were considered. The mission was split into 8 different time periods. For each one of these periods the altitude and the value for the solar activity were kept constant.

The periods, altitudes and solar activity parameters chosen are given in Table 1 together with the relative contributions (last column) of each period to the total number of impacts from space debris. This relative weight is the same for any debris size.

Penetration Analysis

To calculate the number of holes in the blankets a design or damage equation has to be used which gives the ballistic limit for given target thickness and impact parameters. For the specific material compound of the thermal blankets a specific damage equation is not available.

In this study, the number of holes (punctures) is calculated by using the following equation which was derived for single metal plates (thin plate formula) [4]:

$$t = 0.57 m^{0.352} \rho^{0.167} v^{0.875}$$

where:

t : threshold thickness for penetration
m : mass of projectile [g]
ρ : density of projectile [g/cm^3]
v : impact velocity of projectile [km/s]

A puncture occurs whenever the threshold thickness for an impacting particle with given mass, density and velocity exceeds the shielding thickness of the surface under consideration.

Use of this equation for thermal blankets implies several approximations and uncertainties.

This equation was derived for normal impact directions. Impacts from both meteoroids and space debris particles, however, will generally not occur under normal direction. In that case the velocity entering into the equation can either be taken as the total impact velocity, assuming that over a wide range of angles the penetration capability is independent of the impact angle, or the normal component of the velocity can be used. In this study the total impact velocity was used.

The given equation is strictly valid only for Aluminium. Different procedures have been suggested to modify the equation or to derive an equivalent thickness for materials other than metals and for compounds (see e.g. ref.5). However, to avoid the introduction of another uncertainty in this study the equation was used as given above and applied to different effective thicknesses of the blankets: 200 μ, 225 μ and 250 μ.

Using a different equivalent thickness does change the absolute number of penetrations but has only a minor effect on their relative distribution on the various rows.

3–D Results

Predicted Number of Impacts

The predicted number of impacts from meteoroids and space debris particles on the 12 LDEF rows and the space and Earth ends as obtained by the ESABASE/DEBRIS analysis tool is given in Table 2. These results are for particles with a diameter of 100 μ or larger (assuming $\rho = 1$ g/cm^3 and spherical shape for meteoroids). The results are given /m^2 and for the total mission duration of 5.76 years.

According to present models the directional distribution is the same for all particle sizes.

In this size regime the meteoroids are clearly dominating.

The directional dependence is noticeably different for meteoroids and space debris. Meteoroid impacts are predicted on all faces. The flux ratio front/rear is about 7 and the ratio space end/Earth end is about 9. (Note that this result is for constant impacting particle sizes. The ratio for constant crater dimensions will be different.)

Debris impacts are more concentrated on forward and side faces. As a direct consequence of the model assumption of circular orbits no impacts are predicted for the two ends and the very small number on row 3 is a result of the 8° attitude offset.

Observed Number of Holes

After an initial inspection at KSC 2/3 of each thermal blanket from the UHCR experiment was transported to ESTEC while the remaining 1/3 remained with NASA.

In total ESA received about 12 m^2 of thermal blankets from 16 different sections which were located on 9 different rows.

For a preliminary analysis at ESTEC each of the 16 sections was split into 6 subsections and the number of complete penetrations of the blankets was counted [*]. All subsections had roughly the same area of 0.11 m^2. The results for the total number of holes, independent of their size, are presented in Table 3. Given is the absolute count for each subsection and section and then for each section again the average number $/m^2$. In several cases there is a surprisingly large variation over the different samples from the same row. This is especially evident for the sections on rows 2, 7 and 10. Possible explanations for these differences are the encounter of localised clusters of particles or an uneven thickness of the thermal blankets (mainly the paint could vary in thickness). A final conclusion on these findings has not been reached.

Comparison of Predictions and Measurements

The predicted number of penetrations and the actually observed number of holes in the thermal blankets is presented in Table 4. Compared are the values $/m^2$. For the observations the average value is given if several sections were on the same row.

The calculated values in Table 4 are for an effective blanket thickness of 250 μ which gave the best overall agreement with the observations.

The clear majority of holes is predicted to result from meteoroid impacts.

The predicted number of holes is larger than the predicted number of impacts with D > 100 μ (Table 2) showing that smaller particles can penetrate the 250 μ blankets.

The relevance of the predicted absolute numbers should not be overstressed. Some of the main uncertainties in the numerical penetration analysis were mentioned before. For some parameters a sensitivity analysis was performed:

If the effective thickness of the blankets is reduced to 225 μ, the number of holes increases by 20 – 25 %. It increases by 70 – 80 % for a thickness of 200 μ.

For the assumed blanket thickness the predicted number of penetrations from meteoroids increases by 20 –30 % if the density of meteoroids is increased from 1 g/cm^3 to 2 g/cm^3. For a lower density the number is reduced correspondingly.

In all these cases the directional distribution of the holes is relatively little changed.

The measurements indicate some systematic deviation from the predicted directional dependence. The front/rear ratio of observed holes is larger than predicted. Such a discrepancy could have several reasons. It is possible that the directional dependence (especially for meteoroids) is not treated accurately enough in the numerical tool.

* F.Levadou, private communication, ESA/ESTEC, 1991.

Another possible explanation is that the fluxes of Earth orbiting particles which would heavily favor impacts on forward pointing faces are underestimated by the models. The man made debris population could be larger than assumed or a belt of Earth orbiting meteoroids could exist, as was suggested before (see e.g. ref. 5).

In addition there clearly is a North/South asymmetry with more penetrations having occurred on the North side (centered around row 12). Such a North/South asymmetry was reported before, and in the microabrasion package experiment MAP AO 023, it was found to be reversed for crater diameters smaller than 20 μ.

Conclusion

Predicted and observed numbers of holes on LDEF AO178 thermal blankets were compared. The predictions are based on reference flux models which are presently used as standards for spacecraft shielding design and analysis purposes. A recently developed 3–D numerical analysis tool was used for the actual calculations.

The overall agreement is quite good but some systematic differences in the directional dependence are found.

In this study only the number of complete penetrations is compared. A more detailed study of the observed impact features including analysis of crater dimensions, geometries and morphologies is in progress. The measured size distribution of penetration holes in these blankets with diameters > 300 μ has been reported before [6].

It would be highly desireable to distinguish between impacts from meteoroids and man made debris. That would require a chemical analysis of particle residues in the craters. Such an element analysis has been successfully performed for impacts on other LDEF surfaces and structural parts. For most impact features on these thermal blankets, however, such an analysis seems not feasible. As the blankets are very thin few residues are found. In addition the blanket material compound contains a large range of elements which makes it very difficult to distinguish material from the blankets and the impactor.

Despite these shortcomings the blankets (which were not designed for impact analyses) have already provided much new information on the meteoroid and debris environment and more can be expected as results of more detailed analyses become available.

References

1. G.Drolshagen and J.Borde, 'ESABASE/DEBRIS, Meteoroid/Debris Impact Analysis, Technical Description', ref. ESABASE–GD–01/1, 1992.

2. E.Grün, H.A.Zook, H.Fechtig and R.H.Giese, 'Collisional Balance of the Meteoritic Complex', Icarus, Vol. 62, p.244, 1985.

3. CR BB000883A, 'Update of Meteoroid and Orbital Debris Environment Definition', initiated by: B.J.Anderson, NASA/MSFC/ES44, Jan. 1991. The model is also given in: NASA, SSP 30425, Chapter 8, 1991.

4. B.G.Cour–Palais, 'Meteoroid Environment Model – 1969. [Near Earth to Lunar Surface]', NASA SP–8013, 1969.

5. J.A.M.McDonnell and T.J.Stevenson, 'Hypervelocity Impact Microfoil Perforations in the LEO Space Environment. (LDEF, MAP AO 023 Experiment), Proceed. of First LDEF Post-retrieval Symp., NASA CR 3134, Part 1, P.443, 1991.

6. T.H.See, F.Hörz, M.E.Zolensky, M.K.Allbrooks, D.R.Atkinson and C.G.Simon, 'Meteoroid and Debris Special Investigation Group Preliminary Results: Size–Frequency Distribution and Spatial Density of Large Impact Features on LDEF', Proceed. of First LDEF Post-retrieval Symp., NASA CR 3134, Part 1, P.477, 1991.

Table 1: Parameters used for LDEF space debris analysis. The last column gives the relative contribution of each period.

Period	S_{t-1}	h [km]	Δt [years]	$\Phi g_1 \Delta t$
7/4/84 – 31/12/84	120	475	0.73	0.344
1/1/85 – 31/12/85	100	475	1.0	0.557
1/1/86 – 31/12/86	75	470	1.0	0.647
1/1/87 – 31/12/87	75	465	1.0	0.648
1/1/88 – 31/12/88	85	455	1.0	0.595
1/1/89 – 30/6/89	120	415	0.5	0.175
1/7/89 – 31/12/89	160	370	0.5	0.071
1/1/90 – 12/1/90	200	340	0.033	0.002

Table 2: Predicted number of impacts, N_I, from meteoroids (ρ=1.0 g/cm^3) and space debris with particle diameters D > 100 μ on the various LDEF faces. The values given are per m^2 and for the total LDEF mission duration of 5.76 years.

Row	$N_{I,met}$	$N_{I,deb}$	$N_{I,tot}$
	[impacts /m^2/5.76 years]		
1	20.8	2.75	23.6
2	11.3	0.417	11.7
3	7.26	4.40 E−4	7.26
4	8.46	3.90 E−2	8.50
5	15.0	1.26	16.3
6	26.6	4.11	30.7
7	39.2	6.10	45.3
8	47.7	7.46	55.2
9	51.4	8.86	60.3
10	50.4	8.35	58.8
11	44.3	6.75	51.1
12	33.3	5.35	38.7
Space end	42.7	0	42.7
Earth end	4.49	0	4.49

Table 3: Observed number of holes on LDEF thermal blankets.

Location	Number of holes counted		Holes /m^2
	count on 6 subsections	sum	
D1	14,9,9,6,10,8	56	85
A2	0,2,0,6,1,3	12	18
E2	6,6,7,4,7,1	31	47
A4	2,4,4,5,6,1	22	34
F4	1,4,2,2,4,3	16	24
B5	1,5,3,2,5,2	18	27
C5	4,3,2,4,5,3	21	32
D5	5,3,4,2,7,2	23	35
C6	8,7,9,10,4,8	47	70
B7	15,29,25,28,34,23	154	235
D7	17,13,8,20,22,22	102	156
C8	28,23,27,26,26,22	152	232
A10	51,49,53,35,34,45	267	408
E10	28,32,40,30,33,29	192	293
C11	26,25,24,26,23,25	149	227
D11	23,27,24,27,28,33	162	247

Table 4: Comparison of predicted and observed number of holes, N_h, /m^2 on LDEF thermal blankets.

Row	Predicted			Observed
	$N_{h,met}$	$N_{h,deb}$	$N_{h,tot}$	
1	72.1	21.3	93.4	85
2	31.8	1.48	33.3	32.5
4	18.6	0.06	18.7	29
5	41.0	7.17	48.2	31.3
6	92.8	32	125	70
7	156	47.4	203	195.5
8	201	62.8	264	232
10	213	66.6	280	350.7
11	188	58.6	247	237

3-D CRATER ANALYSIS OF LDEF IMPACT FEATURES FROM STEREO IMAGERY

Clyde A. Sapp and Thomas H. See
Lockheed Engineering & Sciences Co., Houston, TX 77058
Phone: 713/483-5141, FAX: 713-483-5347

Michael E. Zolensky
SN2/NASA, Johnson Space Center, Houston, TX 77058
Phone: 713/483-5128, FAX: 713-483-5347

SUMMARY

We report here preliminary results from attempts to derive depth and diameter information from digitized stereo images of impact features on LDEF. Contrary to our prior assumption, we find that impact craters in the T6 Al alloy are not paraboloid in cross section, but rather are better described by a 6th-order polynomial curve. We explore the implications of this discovery.

INTRODUCTION

In expectation of the LDEF return, the requirement for a system to analyze the hyper-velocity impact craters on the space-exposed surfaces of the spacecraft was determined. Ideally, this analysis system would be able to define in three dimensions the surface structure of each crater to a high degree of precision. As a minimum, the system should be able to determine the true depth and diameter of each crater. The 'true' depth is defined as the deepest point in the crater as measured from the level of the ambient surface, and the 'true' diameter is the inside diameter of the crater when measured at the level of the ambient surface (see Figure 1).

A number of constraints were placed upon this system design. The budgetary limitations were fairly severe, and the time frame for technique investigations was short. It was essential that the analysis system use a technique that was non-destructive and remote (i.e., no contact with the material surface permitted). In addition, the system must use a technique that could be incorporated into a portable system to be used at Kennedy Space Center during the deintegration of the LDEF spacecraft.

It was decided to use binocular imagery to analyze the crater morphologies. It was fairly inexpensive to achieve, and made use of some existing hardware to collect the information. A portable system configuration consisted of a portable PC equipped with a color video digitizing board and a color video multiplexer, a binocular microscope, a pair of video cameras, and a pair of optical disk drives with removable media. This system configuration would collect pairs of color digital images and store them to the optical media for later analysis. It was also decided to write software that would automatically register the image pairs on a pixel by pixel basis using a traditional cross-correlation technique. The parallax information in each pixel registration would provide depth data for each pixel, and thereby provide a full three-dimensional representation of the crater surface.

During the three month deintegration of LDEF, the Meteoroid and Debris Special Investigation Group (M&D SIG) generated approximately 5000 digital color stereo image pairs of impact-related features from all space-exposed surfaces. An earlier paper (1) describes the theory and practice of determining this 3-dimensional feature information from stereo imagery.

RECENT WORK

The attempts to analyze the KSC imagery using traditional cross-correlation were unsuccessful due to several problems inherent in the data. There was a significant difference in the photometric responses between the two cameras due to a lack of photometric calibration. In an analog world, this problem could be easily rectified by compensating for the different gains and offsets. In the digitized images, however, the data has already been quantized and truncated making it impossible to recover much of the information. There was also a problem with a lack of detail in many of the images due to depth of field limitations and lack of focal calibrations between cameras. Most of the craters digitized displayed a high degree of specular reflectivity, which is incompatible with cross-correlation techniques. Specular reflections are strongly viewing angle dependent, which means that high contrast details seen from one camera are likely to be very low contrast, or even invisible from the other camera. These problems, combined with a poor initial understanding of the task complexity, caused the planned approach of automated registration via cross-correlation to be unsuccessful.

Due to the problems encountered in attempting to implement the fully automated software, the decision was made to get an interactive (man-hour intensive) method working, and then come back later and continue the development of a fully automated capability as time permitted. The interactive approach was to allow an analyst to select a series of tie-points from an image pair, and use the three-dimensional information of the tie-points to perform a least-squares parametric fit to define the crater's geometry. (A tie-point is a pair of points, one from each of the two images, which represent the same point on a surface, i.e., a tie-point 'ties' the two images together at a single point.) The initial approach required that a few basic assumptions be made. The assumptions were that 1) the craters are basically paraboloid, 2) the craters are central-symmetric to an axis which is perpendicular to the ambient plane, and 3) there was liable to be some inherent error in the tie-point selections.

The interactive data collection software was set up so that the analyst would select tie-points in three sets, one each for the ambient surface, the crater interior, and the lip of the crater. (Note: the lip tie-points were collected just for statistical information. No attempt was made to parametrically define the lip geometry.) The first step in the analysis was to first calculate the distance from the focal plane for each tie-point in all three data sets. The analysis software would then calculate a least-squares fit for the ambient plane and compensate for rotations and offsets of the crater surface with respect to the camera's focal plane in all three data sets. A least squares fit of a paraboloid to the interior crater points was then performed. The intersection of the ambient plane with the paraboloid then determined the ideal crater depth, and the width of the paraboloid at the intersection with the ambient plane defined the ideal crater diameter.

In order to test the accuracy of the interactive analysis software, three craters were selected which were large enough to perform fairly accurate manual depth and diameter measurements. The manual measurements were performed resulting in measured depths of 147, 455, and 933 microns and diameters of 279, 1254, and 2426 microns. Binocular images of each crater were digitized, and the interactive data collection of tie-points was completed. The tie-point data was analyzed using the parametric fit software, and the outputs were compared to the manual measurements. There was an expected error in the manual measurements of

approximately 2%, but for this accuracy test, the manual measurements were accepted as 'true.' The results were somewhat disappointing. The average error in the estimated crater depth was 15.5%, and the average error in the diameter estimate was -11.9%. Both of these errors were significantly larger than was considered acceptable.

In attempting to determine the source of the encountered errors, three possible causes were isolated and tested. The possibilities were defined as 1) software 'bugs,' 2) an algorithm which was overly sensitive to input errors, and 3) a false basic assumption regarding paraboloid crater geometry. The error sources were tested in the order listed above, as this was deemed to be the order of their likelihood.

In order to test the software integrity, several 'perfect' paraboloid craters were computer generated, and corresponding tie-points were generated. The analysis resulted in 0% error. The tie-point collection, and initial depth calculations were also tested separately using holes drilled in aluminum as test cases. These two tests combined demonstrated that the software was performing as expected.

To test the algorithm's sensitivity to input errors, the previously generated 'perfect' craters were again used. A Monte Carlo technique was applied to generate randomized errors in the tie-point data prior to being input to the analysis software. The magnitude of the induced errors was greater than or equal to the maximum expected input errors. Numerous runs were performed in batch mode with statistical analysis of the resulting outputs. This analysis resulted in an average error in the depth estimate of 2.5%, and an average error in the diameter estimate of 7.5%. These errors were larger than desired, but still not large enough to account for the errors encountered in the analysis of the real craters.

It was decided then to test the basic assumption of the crater geometry. In order to test this assumption, five impact craters were generated in T6 aluminum alloy, which is the most common exposed material on the LDEF. These craters were large enough to be easily cross-sectioned; the sizes ranged from 3.1 to 7.0 mm in depth and 7.0 to 19.8 mm in diameter. Each crater was then carefully cross-sectioned through its center. Digital monocular images of the cross section of each crater were generated, and a high resolution two-dimensional digitization of the interior surface structure of each crater was then performed. The digitizations contained 66 to 111 data points each to attempt to minimize the errors. A series of two-dimensional polynomials were then fitted to the digitized points. Second order (Eq. 1), fourth order (Eq. 2), and sixth order (Eq. 3) polynomial curve fits were each performed. No odd order polynomials were used because the assumption that a crater is central symmetric was still in effect. A first order term (***bx***) was left in the fit equations in order to compensate for any axial rotations incurred during the initial digitization.

$$y = a + bx + cx^2 \qquad \text{(Equation 1)}$$
$$y = a + bx + cx^2 + dx^4 \qquad \text{(Equation 2)}$$
$$y = a + bx + cx^2 + dx^4 + ex^6 \qquad \text{(Equation 3)}$$

The results of these curve fits compared to the raw data were somewhat surprising. The 2nd order curve fits were consistently deeper and wider than the actual craters. The 4th order curve fits were consistently shallower and wider than the actual craters. The 6th order curve fits, however, resulted in inconsistent errors in depth and diameter. Figure 2 shows images of the three cross-sectioned craters with the superimposed 2-D curve fits. Figure 3 depicts the total amount of error encountered in the curve fits, and Table 1 summarizes the percent errors in depth and diameter estimates for each of the five test shots from each type of curve fit. The consistency of the magnitude and especially sign of the errors in the second and fourth order curve fits suggests that these errors are not due to random factors, but instead are due to the unsuitability of these equations for defining the crater geometry.

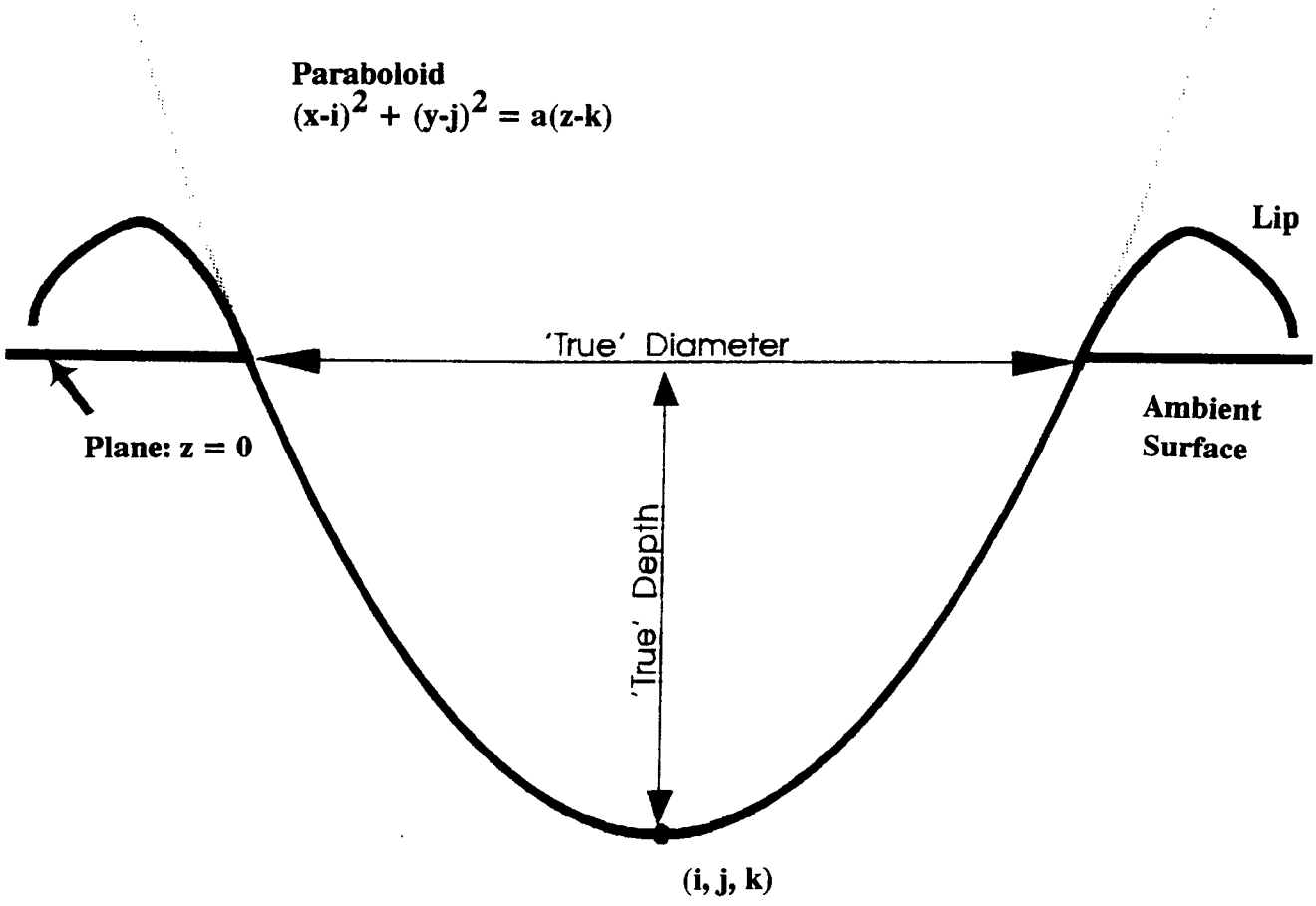


Figure 1 Initial idealized crater geometry assumed for this investigation, employing a paraboloid cross-section. True depth and diameter are indicated.

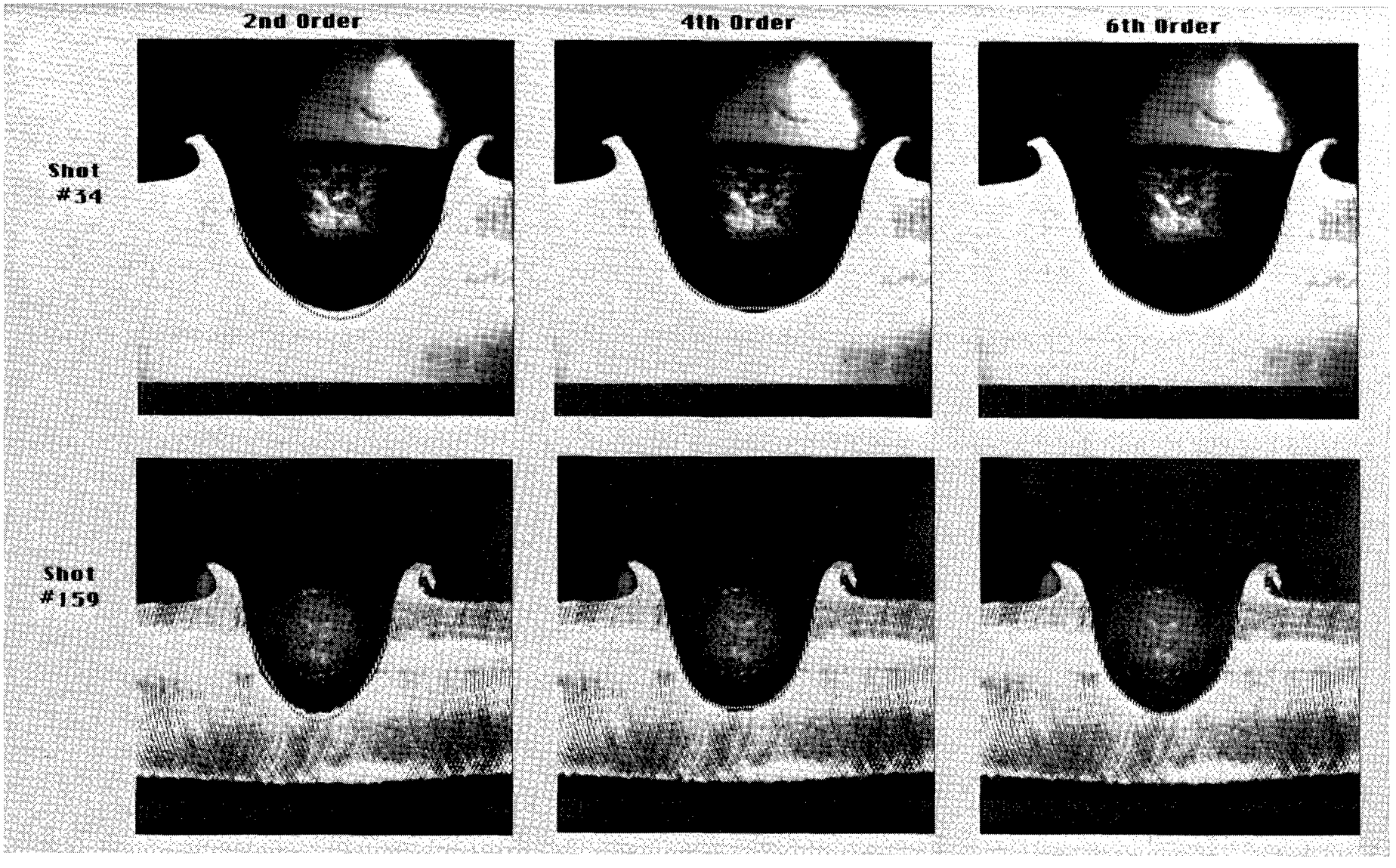


Figure 2 Comparison of polynomial 2-D curve fits for large cross-sectioned test craters in T6 aluminum. For two different craters (#s 34 and 159) fits to 2nd-, 4th- and 6th-order curves are indicated by stippled curves.

Table 1 Errors in Depth and Diameter Estimates For the Five Test Shots From Each Type of Curve Fit

	Depth Error (%)			Diameter Error (%)		
Shot #	2nd Order	4th Order	6th Order	2nd Order	4th Order	6th Order
34	5.57	-3.92	-2.43	9.80	2.07	1.11
148	7.14	-3.63	-1.89	6.29	0.70	-0.06
159	6.79	-3.97	-1.33	9.30	1.88	0.76
160	6.57	-3.39	1.44	8.46	1.47	-0.10
163	8.70	-3.61	1.57	7.69	1.26	0.04

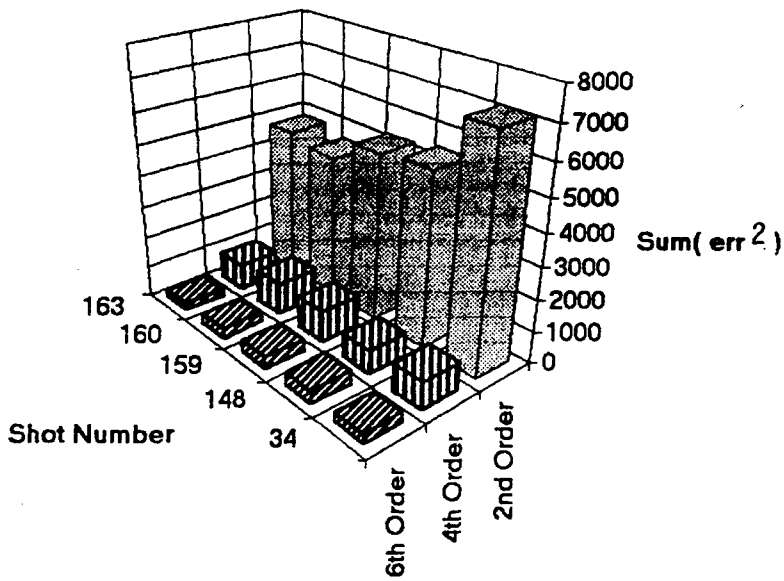


Figure 3 Summary of polynomial curve fits for all 5 large test craters. The vertical axis indicates the sum of square of the errors for diameter and depth.

When comparing the results of the cross-section study to the 3-D paraboloid fits on the three original test craters, a rather puzzling discrepancy arises: the 2-D parabolas were consistently deeper and wider than the actual craters, but the 3-D paraboloids were consistently deeper and *narrower* than the actual craters. The explanation for this discrepancy has not yet been determined. It is possible that findings of the cross-section study hold true only for the size range which was tested (7 - 20 mm, much larger than the LDEF impact craters), or perhaps the overall crater geometry is more a factor of the particle velocity upon impact. What seems more likely though is that the majority of the problem is due to input errors. The initial three (small)

test craters had only 12, 9, and 7 tiepoints, while the five cross-sectioned craters had 66 to 111 data points. The effect that a single pixel of uncertainty has in the vertical is inversely proportional to two times the tangent of the angle of separation between the two cameras. In the cases being looked at here, that proportion is approximately four to one. This means that a single data point has about four times the uncertainty in the 3-D paraboloid analysis as a similar point in the 2-D polynomial curve fits. Also, the initial test crater images suffered from the same focus and depth of field problems, which increases the amount of error in the data point selection.

CONCLUSIONS AND FUTURE WORK

The conclusions based on the work done thus far is that the assumption that impact craters are basically paraboloids is false, at least for the size ranges tested by cross-section. The current algorithm's sensitivity to input errors is also a major concern. Future testing needs to address the issue of algorithm sensitivity versus the number of input data points, as this was not addressed during the initial sensitivity testing. Further cross-section tests are planned for smaller craters to determine if the initial results of the cross-section tests are size related. Investigations will be made into methods for minimizing the effect of input errors to the 3-D analysis. It may also be possible to derive a correction factor from the data which would enable the continued usage of the paraboloid fit to determine a crater's depth and diameter. We also hope to write a semi-automated tie-point selection routine which will use existing manually selected tie-points as 'seeds' to enable a much greater number of input data points. If this venture is successful, we may be able to perform a 6th order 3-D polynomial curve fit to the craters for a much more reliable crater definition.

REFERENCE

(1) See T.H., Allbrooks M.K., Atkinson D.R., Sapp C.A., Simon C.G. and Zolensky M.E. (1992) Meteoroid and Debris Special Investigation Group: Data Acquisition Procedures. LDEF - 69 Months in Space, NASA CP-3134, p.459-475.

FURTHER ANALYSIS OF LDEF FRECOPA MICROMETEROID REMNANTS

Janet Borg
Institut d'Astrophysique Spatiale, Bat.121
91405 Orsay (France)
Phone: (33) 1 6941 5255, Fax: (33) 1 6941 5268

Ted E. Bunch
Planetary Biology Branch, NASA AMES Research Center
Moffett Field, CA 94035 (USA)
Phone: 415/604 6058, Fax: 415/604 6779

Filipo Radicati di Brozolo
Charles Evans & Associates
301 Chesapeake Drive, Redwood City, CA 94063 (USA)
Phone: 415/369 3867, Fax: 415/369 7921

Jean Claude Mandeville
ONERA/CERT Space Technology Department
BP 4025, 31055 Toulouse cedex (France)
Phone: (33) 6155 7117, Fax: (33) 6155 7172

ABSTRACT

In the Al collectors of experiment AO138-1 of the French Cooperative Payload (FRECOPA) payload, we identified a population of small craters (3-9 microns in dia.) induced by the impacts of micron-sized grains, mainly of extraterrestrial origin. Chemical analyses of the Interplanetary Dust Particle (IDP) remnants were made in the bottoms and on the rims of the craters, in addition to immediate off-rim areas. So far, the compositional investigation of the craters by Energy Dispersive Spectroscopy (EDS) has shown evidence of an extraterrestrial origin for the impacting grains. The systematic presence of C and O in the residues has been reported and may be compared with the existence of particles showing high proportions of biogenic light elements and detected in the close environment of P-Halley comet nucleus (called CHON particles). An analytical protocol has been established in order to extract molecular and possible isotopic information on these grains, a fraction of which could be of cometary origin. Although these very small craters may show crater features that are typical of the larger Long Duration Exposure Facility (LDEF) population (> 50 microns in dia.), some show unique morphologies that we have not previously observed. Our initial Laser Induced Mass Spectrometry (LIMS) analytical results show strong signals for nitrogen-bearing ions in craters characterized by high C and O contents; they also suggest that carbon contents in some craters could exceed that known for carbonaceous chondrites.

INTRODUCTION

Since the first NASA U-2 flight collection in 1974 (ref. 1), the collection and analysis of IDPs orbiting around the Earth have been greatly enhanced. This enhancement occurred especially by the analyses of hard collectors that were exposed in Low Earth Orbits, before the impacting grains could have been processed by their entry in the Earth's atmosphere.

Our primary interest in the analysis of IDPs arises from the possibility that an unknown fraction of these particles could be of cometary origin and thus contain information on the early history of the solar system. In addition, asteroidal and interstellar particles may also be present. Cometary material is likely to be the most primitive material accessible for analysis. It is thought that grains once present in the cometary nuclei and now present as individual grains in interplanetary space are the best candidates for having remnant properties that were acquired before and/or during condensation in the protosolar nebula. The smaller size fraction (grains < 10 microns in diameter) is assumed to be enriched in grains of cometary origin (ref. 2). Our collected IDPs have been subjected to various kinds of irradiations, inside the past and present solar system. Bénit and Bibring (ref. 3) have theorized that these different irradiations of grains could result in different physical, chemical and isotopical properties. In particular, carbonaceous material present in some grains could have been synthesized during early periods of intense solar irradiation. Manmade orbital debris is also present and many of these particles had velocities similar to some IDPs (ref. 4). Debris particles are recognizable by their compositional signature (Ti or Zn of paint flakes, aluminium oxide spheres or lack of a "chondritic"composition, etc).

Among all the spacecrafts returned, LDEF was the first one designed to study the effects of space environment and to determine particle flux and orbital parameters. The FRECOPA experiment, in particular, was devoted to the study of dust particles and contained two entirely passive experiments that were flown for the detection of microparticles - AO138-1 and AO138-2. It was located on the west-facing side (location B3) of LDEF directly opposed to the velocity vector. Its position is assumed to have been exposed mostly to grains of extraterrestrial origin (ref. 5). Our primary objective was to gain information on the micron-size fraction of IDPs by hard capture into a high purity Al surface. Even though the impacted paricles were mostly destroyed (some intact grains survived moderate to low velocity impacts), meaningful information on composition, flux and particle size can still be obtained. Moreover, the light elements, particularly the biogenic elements C, H and N, and possibly intact carbonaceous compounds, can be suitably analyzed which is essential for characterizing possible cometary particles.

EXPERIMENTAL APPROACH

We are mainly interested in the analysis of IDP impact residue found in some small craters ($\leq 10\ \mu m$ in diameter) that formed in thick (250 microns) Al targets of the FRECOPA experiment AO138-1. During an impact, the impacting particle (impactor) is melted to partially melted and/or vaporized. Some of the target material (Al) is admixed with the impactor during the time of crater formation. Cratering by light gas gun hypervelocity impact experiments have shown that meaningful biogenic element and organic compound information may be obtained from IDP residues formed from impacts of ≤ 6 km sec^{-1} , which is the experimental limit (ref. 6). We suggest that most of the

small crater impactors collided with LDEF at velocities equal to or greater than the spaececraft velocity (7.5 km sec^{-1}; ref. 7).

An initial survey of the sample was accomplished by using a scanning electron microscope (JEOL JSM-840A), at low magnification (x750), in order to locate the craters. The JEOL SEM is equipped with an EDS Analysis TRACOR System in which the X ray detector is protected by a very thin (15 μm) carbon window, which allows for semi quantitative analysis down to the element Na, and qualitative detection down to C; N is not detected, due to absorption of its X rays by the C window. Thus, energy dispersive analyses (EDAX) allowed us to characterize the impactor composition including the light elements carbon and oxygen. Aluminium was disregarded because of its incorporation from the target into the impactor residue during impact melting.

The samples were then subjected to an imagery and analytical protocol that includes FESEM (field emission scanning electron microscopy) and LIMS. The FESEM observations were performed by using a HITACHI S-4000, located at NASA AMES. LIMS analyses were performed by using a LIMA-2A instrument at CHARLES EVANS & ASSOCIATES. This instrument was operated in the single laser probe mode, which allows for atomic and molecular identification. At some future time, residues that are characterised by high C/O ratios from EDAX analyses will be analysed by the 2-stage laser mode technique which allows for more complete molecular identification.These samples may be finally analyzed by a CAMECA 4F ionprobe for determination of D/H ratios.

ANALYTICAL AND OBSERVATIONAL RESULTS

Flux and EDAX Measurements

An earlier effort showed that the cumulative flux for impact features smaller than 10 μm in diameter is ~ $5 \cdot 10^{3}$ m^{-2} $year^{-1}$ (ref. 8). These particles consisted mostly of extraterrestrial particles, which was confirmed by EDAX analyses. The measurements were made on ~ 10 cm^2 of exposed surface and are consistent with the previous estimates of the micrometeroid particle mass distribution given in Figure 1, although slightly higher. The extraterrestrial particles show various proportions of chondritic elements (Na, Al, Mg, Si, S, Ca and Fe), intrinsic Al being masked by the Al target. We noticed a strong depletion in Ni which was not observed above the analytical detection limits in our samples. Furthermore, C and O are present in 90% of the cases; the C/O peak height ratio varies from 0.1 to 3 (ref. 9). The systematic presence of low Z elements, associated with other elements whose abundances reflect a chondritic type composition, can be compared to results obtained by the PUMA and PIA experiments (ref. 10). These experiments analyzed grains in the close environment of the Halley comet's nucleus and demonstrated that at least 50% of the grains within the nucleus contain a phase made of C,H,O and N atoms (CHON particles). The existence of grains with similar compositions, close to the nucleus and in terrestrial orbit, means that they are stable and refractory enough to survive long-term irradiation in the intense solar UV field. Such refractory phases may have had an irradiation origin.

FESEM Observations

FESEM images show several characteristics unique to very small craters and impactor residues: i) Some craters have raised rims and depth/diameter ratios (D/d) ~ 0.7 similar to those of larger craters. However, instead of peeled-back rim structures commonly seen in the large craters, these small raised rims have a vermicular appearance (Figs. 2a & b). In addition, the rim is symmetrical with no missing parts which implies a high angle impact. Impactor residue thinly covers the crater cavity; some melt balls or droplets can be seen in the crater bottom (Fig. 2b). These features may be characteristic of high impact velocities (> 10 km sec^{-1}). ii) Other very small craters have no raised rims and are shallower than those in i; D/d = < 0.5. Moreover, the Al within the crater has a peculiar polygonal structure (Figs. 2c & d). Figure 2c shows a crater with gently sloping walls except on the left side of the crater where the wall is vertical. This feature may imply that the crater formed at a low impact angle, impacting from right to left in the figure (P. Schulz; pers. comm.). These craters are subrounded to elongated in shape with or without visible impactor residue. In some craters of this type, C-bearing residue has a puddle-like appearance and, in some areas, has separated from the crater wall (Fig. 2d). Crater features like these have not been reported for larger LDEF craters. The lack of rims in some small craters may be the result of low velocity impacts, low angle impacts and/or spallation. The cause of the polygonal structure in the cratered Al is unknown.

LIMS Analyses

The single laser ionization technique is limited in its ability to identify primary organic molecules. This method uses a high power density pulsed laser irradiation, which tends to fragment most, though not all, parent molecules into smaller fragment ions. Despite this drawback, significant information can be obtained. For example, Fig. 3a shows the LIMS negative ion mass spectrum for crater P6 (shown in Fig. 2c). This spectrum is dominated by carbon clusters (C_2^- and C_{12}^-) and these are accompanied by protonated clusters (C_xH^-). In addition, nitrogen is present as CN^- and CNO^-; sulfur is present either as S^- or as SO_2^-. This carbon cluster pattern is typical of laser fragmentation of a carbon precursor (e.g., graphite or amorphous). Since N and H are present, this suggests that the impactor contained organic species, although no identifiable parent molecules were found up to ionic mass (m/z) 250. The spectrum of crater P10 (shown in Fig. 2d) is even more informative and suggests large amounts of N in the preimpact particle. Figure 3b shows prominent carbon clusters up to C_{15}^-, protonated clusters and very strong CN^-, CNO^- and C_3N^- features, in addition to other unidentified ionized masses. Chlorine, F, and OH^- are also present, although these may be contaminates.

CONCLUSIONS

LDEF was impacted by millions of very small particles that constitute the bulk of extraterrestrial impactors (ref. 11). We have demonstrated that very useful information can be obtained on the carbonaceous chemistry of residual impactors on very small craters. The results of our FRECOPA test cases indicate that craters as small as 3 microns contain particle residues that have "chondritic" signatures as well as carbonaceous material. Although the amount of carbonaceous material is not accurately known, estimates indicate that carbon contents in some craters exceed that

which is known for carbonaceous chondrites with the C/O ratios being more consistent with cometary particles than with bulk CM2 carbonaceous chondrites (ref. 10). In addition, the strong signals for nitrogen-bearing ions in the LIMS analyses suggest concentrations greater than that of carbonaceous chondrites and possibly consistent with Halley CHON particles (ref. 10).

At this time, it is premature to conclude that the particles responsible for the production of the small craters analyzed in our study were cometary in origin. However, the analytical techniques that we used and others that we plan to use in the near future on tens of small craters may allow us to clearly distinguish between cometary and asteroidal particle impactors. The LDEF data base pertaining to composition and origin of particle impactors can be greatly enhanced by detailed characterizations of large numbers of small craters.

AKNOWLEDGEMENTS

Support from CNES for completion of FRECOPA experiment and for data analysis and support from NASA for completion of the mission are greatly acknowledged. We thank the NASA OSSA Exobiology 199-52-12 and OAST 506-48 Programs and NASA SBIR Contract NAS2-13178 for partially supporting this work.

REFERENCES

1. Brownlee D.E.et al.: An atlas of Extraterrestrial Particles collected with NASA U2 Aircraft. 1974 - 1976, *NASA TMX 73*, pp.152-168, 1976.

2. Bell J.F.: Size-dependent composition in the meteroid/asteroid population. *Met.*, vol. 26, no 4, p.316, 1991.

3. Bénit J.and Bibring J-P.: Irradiation effects on the surface of icy bodies. *Lunar Planet. Sci., The L.P.I.* , Houston, pp 65-66, 1990.

4. Humes D.H.: Large craters on the meteroid and space debris impact experiment. *LDEF1 symposium, NASA Publ.3134,* pp. 399-418, 1991.

5. Amari S., Foote J., Simon C., Swan P., Walker R.M., Zinner E., Jessberger E., Lange G. and Stadermann F.: SIMS chemical analysis of extended impact features from the trailing edge portion of experiment AO187-2. *LDEF1 symposium, NASA Publ.3134*, pp. 503-516, 1991.

6. Bunch T.E., Radicati di Brozolo F. and Schultz P.: LDEF crater and impactor simulations by light gun hypervelocity impact experiments. *"H.I.S.Workshop proceedings", University of Kent at Canterbury . ,1992.*

7. Zook H.A.: Meteroid directionality on LDEF: Asteroidal versus cometary sources and how to obtain an effective velocity for beta meteroids. *"H.I.S.Workshop proceedings", University of Kent at Canterbury, 1992.*

8. Mandeville J.C.and Borg J.: Study of cosmic dust particles on board LDEF : the FRECOPA experiments AO138-1and AO138-2. *LDEF1 symposium, NASA Publ.3134*, pp. 419-434, 1991.

9. Borg J. ,' Bibring J-P., Mandeville J-Cl. , Vassent B.and Laval R.: Micrometeroid analysis on board FRECOPA payload. *"H.I.S.Workshop proceedings", University of Kent at Canterbury, 1992.*

10. Langevin Y., Kissel J., Bertaux J-L., and Chassefière E.: First statistical analysis of 5000 mass spectra of cometary grains obtained by PUMA 1 (Vega 1) and PIA (Giotto) impact ionization mass spectrometers in the compressesd modes. *Astron.Astrophys.* vol. 187, pp. 761-766, 1987.

11. Grün E., Zook H.A., Fechtig H. and Giese R.H.: Collisional balance of the meteorite complex. *Icarus 62*, pp. 244-272, 1985.

FIGURE CAPTIONS

Figure 1. The flux of natural objects compared at 1 AU with that of manmade debris. The large black square represents results obtained on Al collectors of the FRECOPA AO138-1 experiment (refs. 8, 9), for events ≤ 10 microns in size, compared with other natural and manmade debris flux measurements.

Figure 2. FESEM images of very small LDEF impact craters. (a) Image of a small crater in Al with a prominent raised rim (~ 3 μm diameter); arrows point to melt ejecta which is mostly Al. (b) Enlarged view of the crater in a showing the vermicular morphology of the rim and a melt ball in the crater bottom. (c) Shallow crater with little residual impactor and no raised rim. Arrows point to contamination grains. Note the peculiar polygonal structure of the Al. (d) Another polygonally textured crater with impactor melt residue. Short arrow points to the seperation of residue from Al; long arrow points to a contaminant.

Figure 3. Laser ion microprobe negative ion mass spectra acquired from inside craters P6 (3a) and P10 (3b) respectively. Each spectrum is produced by a single laser pulse. Estimated power density ~ 10^9 W/cm^2 per pulse. The intensity (vertical) scale is in arbitrary units. Both spectra exhibit intense signals of $C_xH_y^-$ clusters, which follow a pattern consistent with a carbonaceous or organic composition of the analysed area. Other notable peaks include CN^- and CNO^-. A weak signal of S_2^- (or SO_2^-) is observed at m/z 64 in crater P6 (Fig. 3b). Signals of Cl^- (Figs. 3a and 3b), O^-, OH^- and F^- may be contaminants.

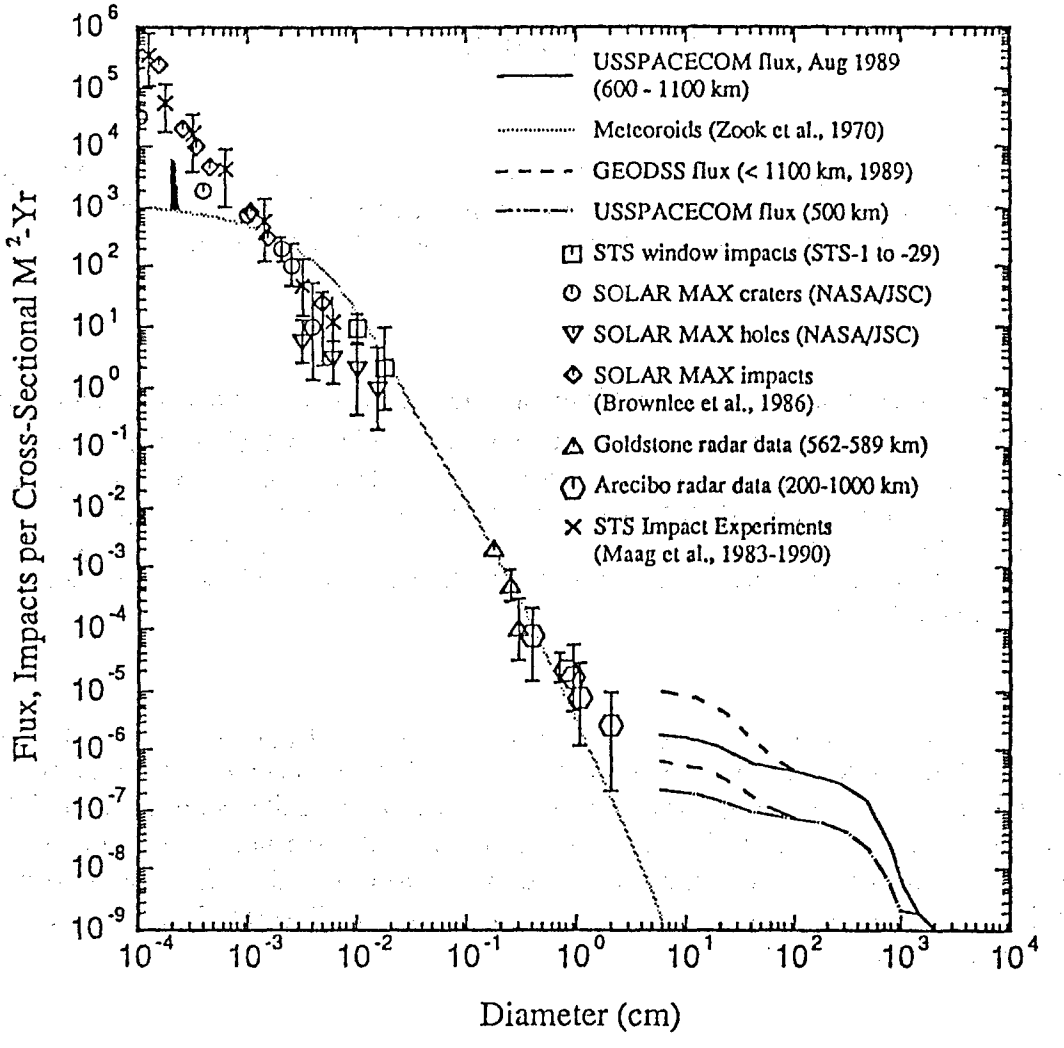


Figure 1. The flux of natural objects compared at 1 AU with that of manmade debris. The large black square represents results obtained on Al collectors of the FRECOPA AO138-1 experiment (refs. 8, 9), for events ≤ 10 microns in size, compared with other natural and manmade debris flux measurements.

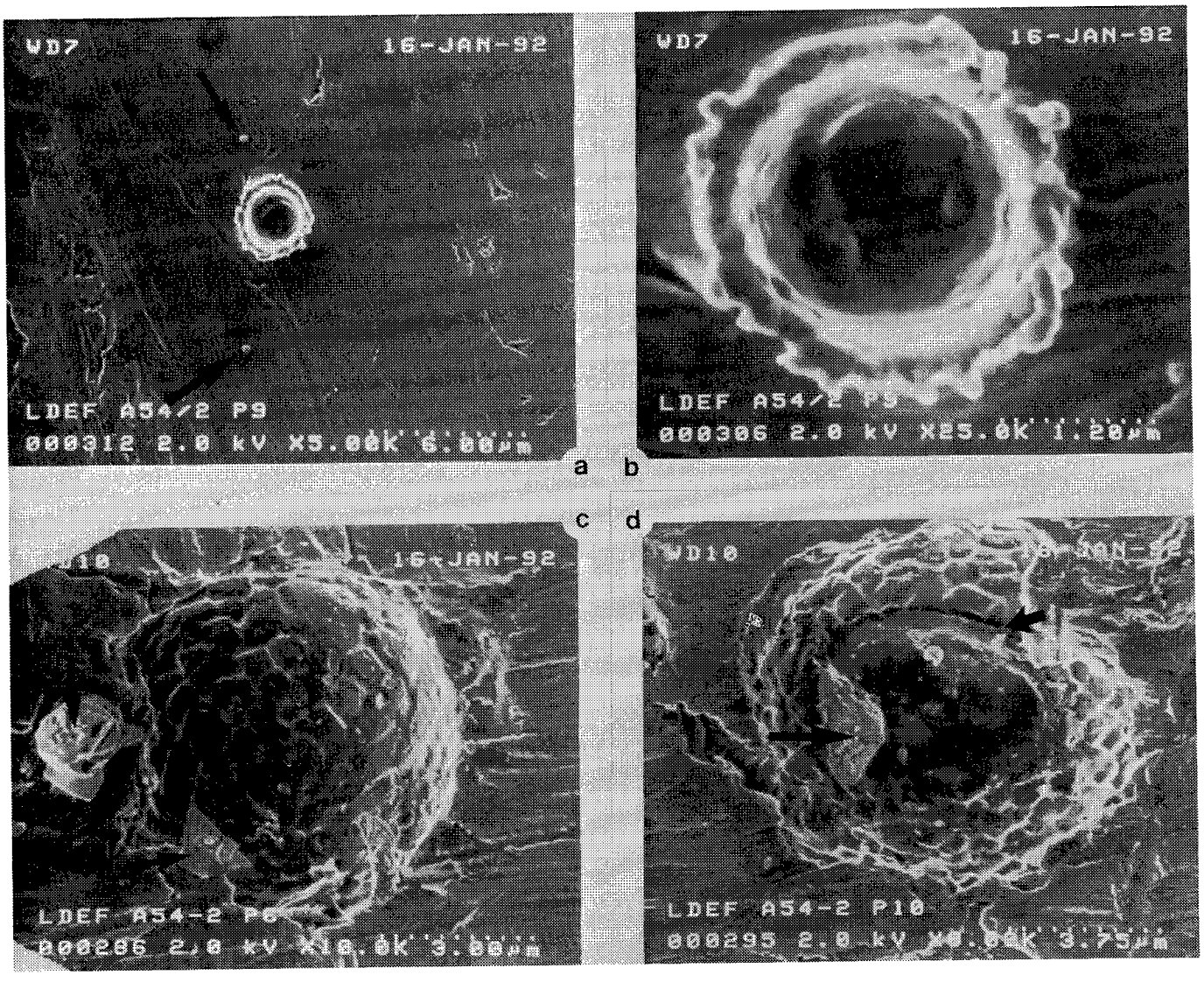


Figure 2. FESEM images of very small LDEF impact craters. (a) Image of a small crater in Al with a prominent raised rim (≈ 3 microns in diameter); arrows point to melt ejecta which is mostly Al. (b) Enlarged view of the crater in a showing the vermicular morphology of the rim and a melt ball in the crater bottom. (c) Shallow crater with little residual impactor and no raised rim. Arrows point to contamination grains. Note the peculiar polygonal structure of the Al. (d) Another polygonally textured crater with impactor melt residue. Short arrow points to the seperation of residue from Al; long arrow points to a contaminant.

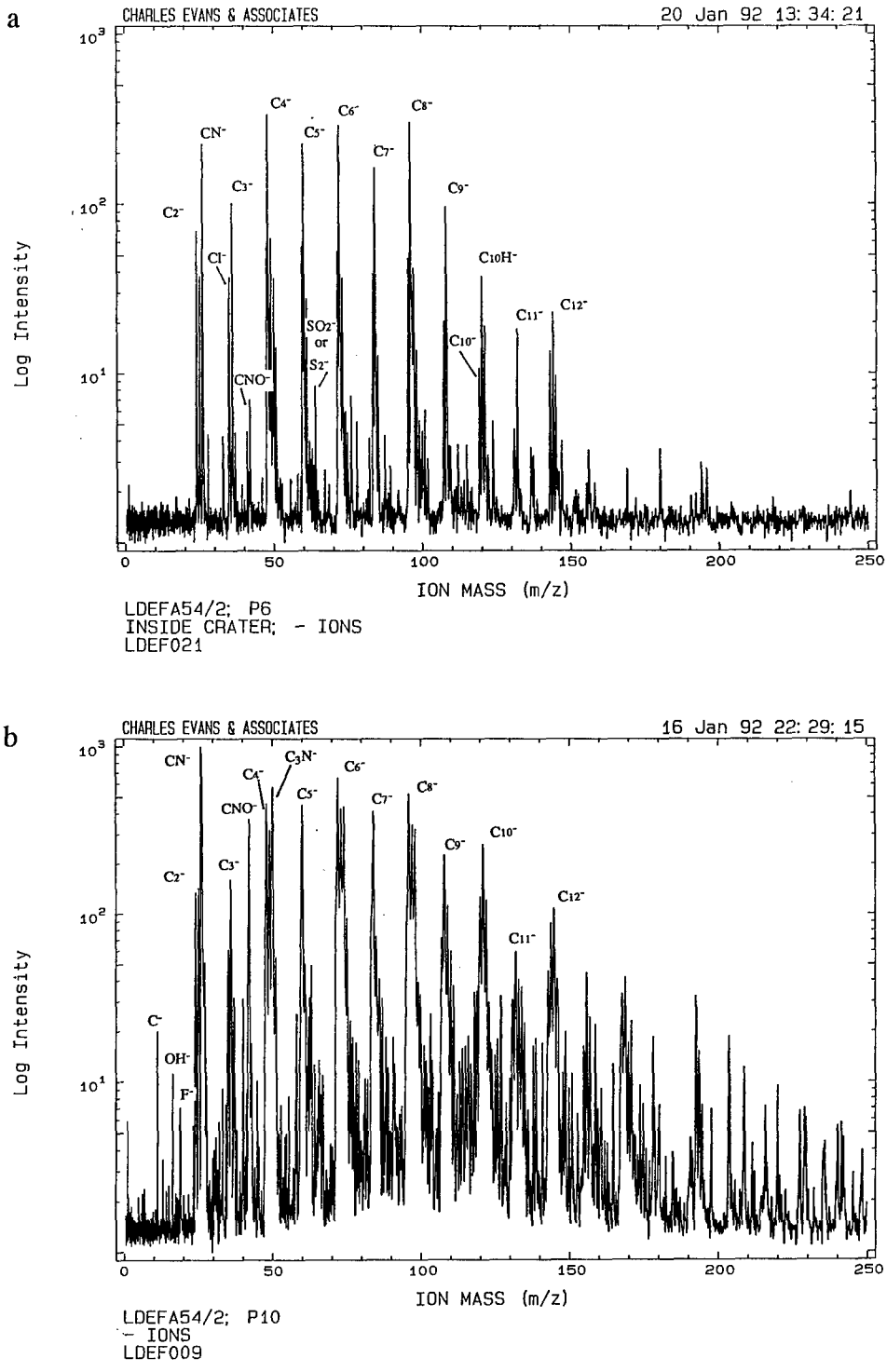


Figure 3. Laser ion microprobe negative ion mass spectra acquired from inside craters P6 (3a) and P10 (3b) respectively. Each spectrum is produced by a single laser pulse. Estimated power density ≈ 10^9 W/cm^2 per pulse. The intensity (vertical) scale is in arbitrary units. Both spectra exhibit intense signals of $C_xH_y^-$ clusters, which follow a pattern consistent with a carbonaceous or organic composition of the analysed area. Other notable peaks include CN^- and CNO^-. A weak signal of S_2^- (or SO_2^-) is observed at m/z 64 in crater P6 (Fig. 3b). Signals of Cl^- (Figs. 3a and 3b), O^-, OH^- and F^- (Fig. 3b) may be contaminants.

LONG DURATION EXPOSURE FACILITY (LDEF) EXPERIMENT M0003 METEOROID AND DEBRIS SURVEY

M. J. Meshishnek, S. R. Gyetvay, K. W. Paschen, and J. M. Coggi
Mechanics and Materials Technology Center
The Aerospace Corporation
El Segundo, CA 90245-4691
Phone: 310/336-8760, Fax: 310/336-1636

SUMMARY

A survey of the meteoroid and space debris impacts on LDEF experiment M0003 has been performed. The purpose of this survey was to document significant impact phenomenology and to obtain impact crater data for comparison to current space debris and micrometeoroid models. The survey consists of photomicrographs of significant impacts in a variety of material types; accurate measurements of impact crater coordinates and dimensions for selected experiment surfaces, and databasing of the crater data for reduction, manipulation, and comparison to models. Large area surfaces that were studied include the experiment power and data system (EPDS) sunshields, environment exposure control canister (EECC) sunshields, and the M0003 signal conditioning unit (SCU) covers. Crater diameters down to 25 microns were measured and catalogued. Both leading (D8) and trailing (D4) edge surfaces were studied and compared. The EPDS sunshields are aluminum panels painted with Chemglaze A-276 white thermal control paint, the EECC sunshields are chromic acid-anodized aluminum, and the SCU covers are aluminum painted with S13GLO white thermal control paint. Typical materials that have documented impacts are metals, glasses and ceramics, composites, polymers, electronic materials, and paints. The results of this survey demonstrate the different response of materials to hypervelocity impacts. Comparison of the survey data to curves derived from the Kessler debris model and the Cour-Palais micrometeoroid model indicates that these models overpredict small impacts (< 100 micron) and may underpredict large impacts (> 1000 micron) while having fair to good agreement for the intermediate impacts. Comparison of the impact distributions among the various surfaces indicates significant variations, which may be a function of material response effects, or in some cases surface roughness. Representative photographs and summary graphs of the impact data are presented.

I. INTRODUCTION

The successful retrieval of the Long Duration Exposure Facility (LDEF) has provided a unique opportunity for the study of micrometeoroid and debris impacts. Originally intended for an 11-month mission, LDEF remained in orbit for nearly six years (69 months). This extended stay in space significantly increased the value of LDEF for the study of micrometeoroid and space debris phenomena. Due to its gravity gradient stabilized attitude, LDEF had each of its surfaces in a constant and known orientation with respect to its velocity vector. Thus, a study of the impacts on various surfaces of LDEF should provide information with respect to the spatial and angular distribution of impactors and provide information on both space debris and micrometeoroid impacts. The large number of impacts observed on LDEF enables meaningful comparisons of this data to current models used for the prediction of such events. In addition, the large number of material types flown on LDEF provides startling examples of various materials' responses to hypervelocity phenomena. Comparison of observed impact damage with laboratory simulations should

also prove fruitful. For these reasons, the LDEF Meteoroid and Debris Special Investigation Group performed extensive examinations of all LDEF experiments and hardware during the deintegration process at KSC.[1]

The Aerospace Corporation LDEF experiment (SSD-802/M0003) housed in four of the 86 LDEF trays and positioned on the leading and trailing edges of the LDEF structure contained well over 1200 samples of over 200 material types. Many of these materials had essentially identical samples on the leading and trailing edges. Moreover, the experiment had some relatively large area sunshields, which provided prime surfaces for impact counts. For these reasons, a meteoroid and debris survey of M0003 was undertaken with the objectives of documenting the impact phenomenology and impact crater statistics.

II. BACKGROUND

The LDEF is a NASA satellite designed to study the effects of prolonged exposure to the space environment. Experiments carried aloft on LDEF numbered 57 and were from the following four categories: materials, coatings and thermal systems; electronics and optics; power and propulsion; and science. These experiments were housed in 86 experiment trays attached to the LDEF structure. The LDEF itself is a dodecahedral cylindrical framework with spaces for 72 trays on the circumference; the remaining 8 and 6 trays are mounted on the space- and earth-facing ends of the structure. The LDEF was designed to orbit the earth in fixed orientation due to gravity gradient stabilization. This three-axis stabilization caused LDEF to have one end pointed toward the earth and the other towards space. Furthermore, one side of LDEF, called the leading edge, was always normal to the velocity vector, while another side, known as the trailing edge, was always in the spacecraft wake. The LDEF was equipped with a viscous magnetic dampener to reduce or eliminate oscillation of the spacecraft. Figure II-1 depicts the LDEF structure together with the numbering

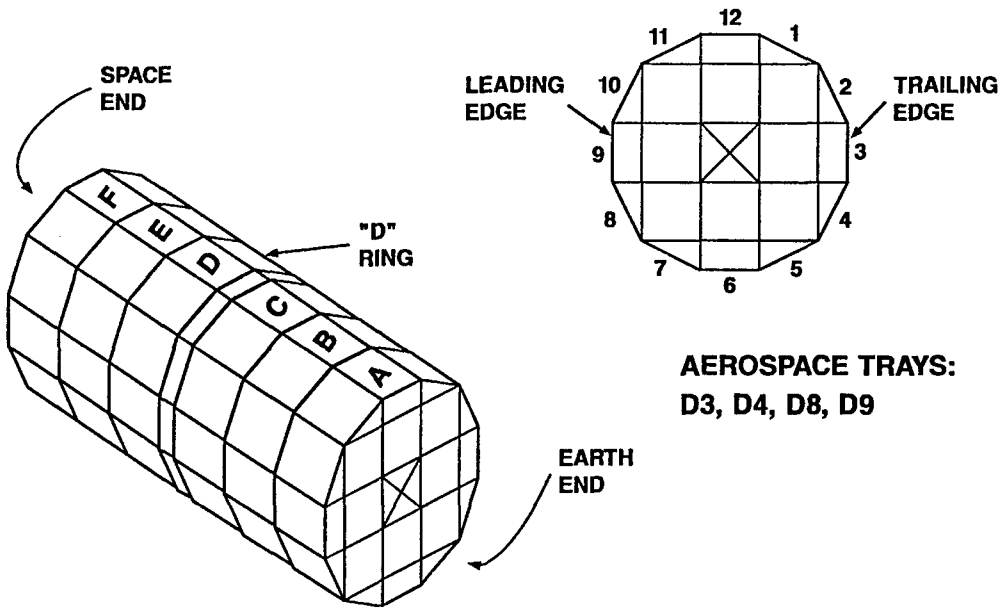


Figure II-1. LDEF surface nomenclature.

scheme for the tray positions and the nomenclature for the various faces of the spacecraft. It is important to realize that, due to its unique structure and orientation, the environment around LDEF varies with location. The principal differences in the environment are the concentration of atomic oxygen, which is highest on the leading edge and diminishes to zero on the trailing edge, and the much larger number of impactors that hit the leading versus the trailing edge of LDEF.[2]

LDEF was deployed on STS mission 41C on 7 April 1984 and was originally intended for an 11- month mission. However, due to problems encountered with the Shuttle schedule and the ensuing Challenger disaster, LDEF was not retrieved until 12 Jan. 1990. This allowed LDEF to remain in orbit for 69 months, increasing by over a factor of six the time during which the spacecraft would encounter micrometeoroids and space debris. During this time, the orbit of LDEF decayed, descending from the deployment altitude of 257 nmi to 179 nmi at retrieval. However, the orientation of LDEF remained stable during this period. The decrease in altitude produced changes in the environment surrounding LDEF, most notably the density of atomic oxygen and the concentration of meteoroids and debris. At the lower altitude, the concentration of atomic oxygen rises dramatically, while the density of meteoroids and debris decreases slightly.[2]

A significant amount of work has been performed by the LDEF Meteoroid and Debris Special Investigation Group and other LDEF experimenters in documenting, analyzing, and modeling the vast number of hypervelocity impacts that occurred on LDEF.[3-11] These hypervelocity impact features are produced by collisions between space debris particles or dust and small meteoroids with spacecraft surfaces. Collision velocities can vary widely and depend upon the constant orbital velocity of the earth, the spacecraft orbital velocity, the impactor velocity, and the direction of impact. The collision velocities for space debris particles range from about 3 to 15 km/s, with average values of 10 to 13 km/s. The distribution of velocities has been given by Kessler.[12] For meteoroids, the collision velocities range from about 3 to 72 km/s with an average velocity of 19 km/s. Zook and Erickson have provided data that give the distribution of meteoroid velocities seen by spacecraft.[11,13-15]

With respect to hypervelocity impacts in materials, different phenomena are observed depending on the impact velocity, relative sizes of the impactor and target, and material properties of the target. For targets that are thick relative to impactor sizes, craters will be formed that generally have lips resulting from plastic flow to molten spatter. However, for very thin targets, such as foils, which are much smaller than the impactor diameter, perforations occur resulting in a hole only slightly larger than the impactor diameter. Secondary or collateral damage can occur from the impactor remnants and the punched-out section. For high-velocity impacts, both the target foil and the impactor are vaporized. However, for lower velocities, the impactor and foil can remain molten or solid, and collateral damage is possible.

Brittle materials, such as glasses or ceramics, often have chonchoidal surface spalls and cracks, and may have star cracks propagating radially from the crater. Layered targets, such as coated substrates, often exhibit delamination around or near the crater. If one averages all impacts, the ratio of crater size to impactor size is generally about 5. For local spall regions, the spall radius to impactor radius ratio is about 20. Star cracks, when formed, can extend outward over 100 times the impactor diameter.

III. EXPERIMENT DESCRIPTION

One of the most comprehensive materials experiments on board LDEF, M0003, was integrated by The Aerospace Corporation Materials Sciences Laboratory as Principal Investigator, and was designed to study the effects of the space environment on current and developmental spacecraft materials. Assembled on two leading-edge and two trailing-edge trays that contained over 1274 specimens, two active data systems, and two timed exposure vacuum canisters, the experiment was a collection of 19 subexperiments from The Aerospace Corporation Laboratories, Air Force and Navy Laboratories, and Department of Defense Contractors. Many of these materials are currently in use on Space and Missile Systems Center (SMC) spacecraft. The Aerospace Corporation, as the integrating agency, was charged with the documentation of the experiment from the earliest stages of retrieval through the complete deintegration of the trays. This included detailed examination and photography of the individual specimens during removal and packaging. Special attention was given to documentation of meteoroid and debris impact phenomenology. Additionally, several surfaces of the experiment hardware, such as the sunshields for the data systems and canisters, were examined in great detail for the size and number of impacts as well as their material response. These surfaces provided large areas for study (> 1.5 m^2) and, therefore, statistically large numbers of craters to count. The surfaces studied were on the leading-edge tray, D8, and the trailing-edge tray, D4. They are referred to as "leading edge" for D8 and "trailing edge" for D4 for simplicity. However, since the leading and trailing edges of LDEF were rows 9 and 3, respectively, it must be recognized that the surfaces in this study were actually 30° off-normal to the leading and trailing edges. Moreover, measurements made on the LDEF and the results from some experiments have determined that the LDEF structure was actually off normal alignment with the velocity vector by about 8°.[16] Thus, tray D8 was 38° from normal to the velocity vector or ram.

The immediate objectives of the experiment were to understand the changes in the structure and properties of materials resulting from exposure to the natural space environment and to compare them to predictions based on laboratory experiments. Ideally, correlation of changes in physical properties will be made with changes in microstructure. The longer-term objectives were to improve the performance and usage of existing materials and to decrease the lead times for application of new materials on DOD space systems. An important outcome expected from this experiment was the understanding and modeling of material degradation. Due to the longer exposure of LDEF to the space environment, the opportunity exists for a deeper and expanded study of material degradation due to meteoroid and debris impacts.

The MOOO3 experiment was a cooperative effort and provided the first opportunity for DOD space programs and laboratories to evaluate materials after long exposure to the space environment. From the recommendations of an advisory group composed of participating organizations, a mix of current and developmental spacecraft materials was chosen for this experiment. An overview of the material categories, the originating agency, and the Principal Investigator is given in Table I.

Table I. Summary of M0003 Experiments

Subexperiment No.	Scope	Experimenter	Agency
-1	Radar camouflage materials and electro-optical signature coatings	Richard Porter	Wright Labs/SNA, Wright Patterson AFB, OH 45433-6533
-2	Laser optics	Linda De Hainaut	Phillips Lab/LTC, Kirtland AFB, NM 87117-6008
-3	Structural materials	Charles Miglionico	Phillips Lab/SUE, Kirtland AFB, NM 87117-6008
-4	Solar power components	Terry Trumble	Wright Labs/POOC, Wright Patterson AFB, OH 45433-6533
-5	Thermal control materials	Charles Hurley	Univ. of Dayton Research Inst., 300 College Park, Dayton, OH 45469-0001
-6	Laser communication components	Randall R. Hodgson	McDonnell Douglas Astronautics Corp., Mail Code 1067267, P. O. Box 516,St. Louis, MO 63166
-7	Laser mirror coatings	Terry M. Donovan	Naval Weapons Center, Thin Film Physics Div. Code 3818, China Lake, CA 93555
-8	Composite materials, electronic piece parts, fiber optics	Gary Pippin	Boeing Aerospace Co., Materials technology Dept., MS 2E-01, P. O. Box J04, Sunnyvale, CA 94086
-9	Thermal control materials, antenna materials, composite materials, and cold welding	Brian C. Petrie	Lockheed Missiles & Space Co., Dept. 62-92, Bldg. 564, P. O. Box 92957, M2/321, Los Angeles, CA 90009
-10	Advanced composite materials	Gary L. Steckel	The Aerospace Corp., P. O. Box 92957, M2/321, Los Angeles, CA 90009
-11, -12	Contamination monitoring Radiation measurements	Eugene N. Borson	The Aerospace Corp., P. O. Box 92957, M2/250, Los Angeles, CA 90009
-13	Laser hardened materials	Randall R. Hodgson	McDonnell Douglas Astronautics Corp., Mail Code 1067267, P. O. Box 516,St. Louis, MO 63166
-14	Quartz crystal microbalance	Donald A. Wallace	QCM Research, 2825 Laguna Canyon Rd., P. O. Box 277, Laguna Beach, CA 92652
-15	Thermal control materials	Oscar Esquivel	The Aerospace Corp., P. O. Box 92957, M2/241, Los Angeles, CA 90009
-16	Advanced composites	Gary L. Steckel	The Aerospace Corp., P. O. Box 92957, M2/321, Los Angeles, CA 90009
-17	Radiation dosimetry	Sam S. Imamoto, J. Bernard Blake	The Aerospace Corp., P. O. Box 92957, M2/260, Los Angeles, CA 90009
-18	Thermal control paints	Christopher H. Jaggers	The Aerospace Corp., P. O. Box 92957, M2/271, Los Angeles, CA 90009
-19	Electronic piece parts	Seymour Feuerstein	The Aerospace Corp., P. O. Box 92957, M2/244, Los Angeles, CA 90009

The M0003 Experiment hardware consisted of four peripheral trays, two experiment power and data systems (EPDSs), two environment exposure control canisters (EECCs), two signal conditioning units (SCUs), and several Li/SO_2 batteries to provide experiment power. The experiment was an active one in that it was equipped to record temperature, strain, solar cell output, quartz crystal microbalance frequency, fiber optics output, circuit interrogation, and various data system parameters. One six-inch-deep tray and one

three-inch-deep tray connected by a wiring harness and containing a data system (EPDS), a canister (EECC), an SCU, and numerous material specimens were located on rows 8 and 9 of ring D on the leading edge of LDEF. A similar configuration was located on rows 3 and 4 of ring D on the trailing edge. The canisters were preprogrammed to provide timed exposures of specimens of 9, 19, and 40 weeks. The canisters closed after these exposure times had elapsed. The design of the trays was modular, allowing samples to be thermally coupled or decoupled from the tray and, therefore, the LDEF structure. Figures III-1 through III-4 illustrate the layout of the four trays, showing the location of the various components and sensors.

The test articles were mounted on black or clear anodized aluminum hardware modules within the trays. Most experiments had duplicate samples on both the leading and trailing edge trays; several had them in the canisters as well. Some experiments also included a set of control specimens that were reverse mounted on the modules, thereby exposing the samples only to thermal vacuum cycling. These test articles included a variety of thermal control coatings, optics, composites, structural materials, solar cells, fiber optics, laser communication components, antenna materials, electronic piece parts, dosimeters, and contamination monitors. The selection of sample complements, multiple locations, and flight controls increased the value and utility of the experiment by allowing differentiation of the environmental phenomena, especially those due to combined or synergistic effects. The most notable effects are the erosion of materials due to atomic oxygen and the impacts due to space debris. These two effects are prominent on the leading edge of LDEF and nearly absent on the trailing edge. Varying degrees of exposure provided by the canisters also aid in the study of these phenomena. Damage to the material samples is shown in the photos taken at Aerospace prior to deintegration of the trays (Figures III-5 through III-8). The damage and its impact on materials performance has been described previously.[17]

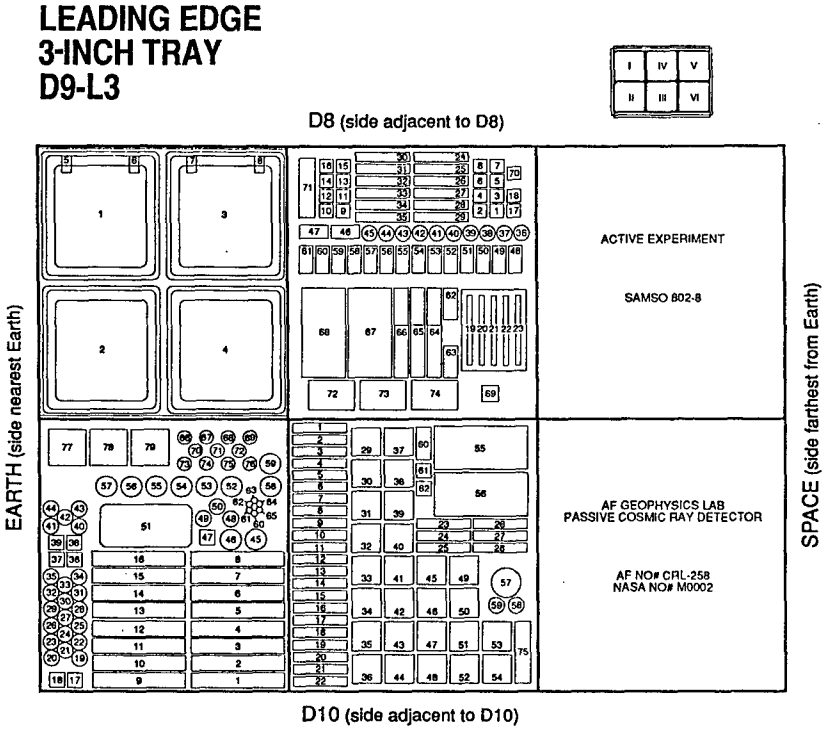


Figure III-1. Layout of D9 leading edge 3-inch-deep tray.

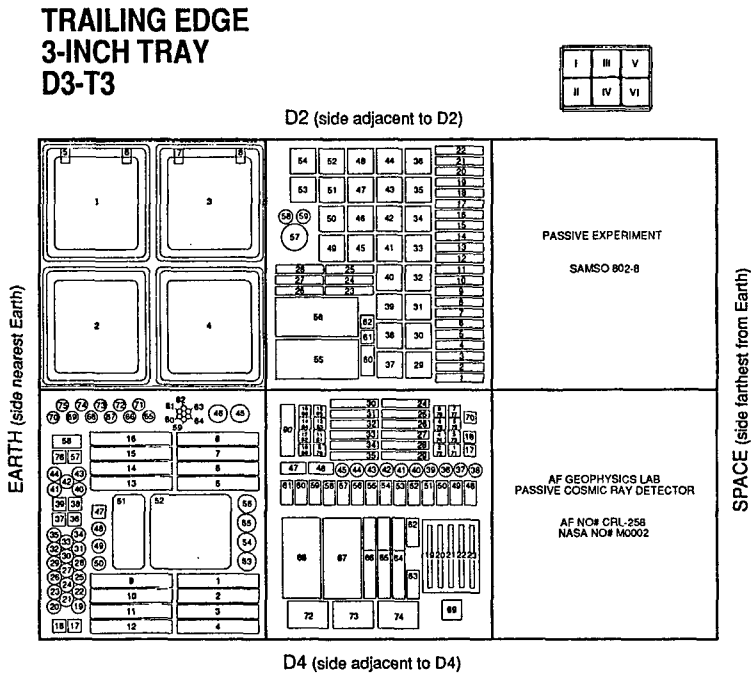


Figure III-2. Layout of D3 trailing edge 3-inch-deep tray.

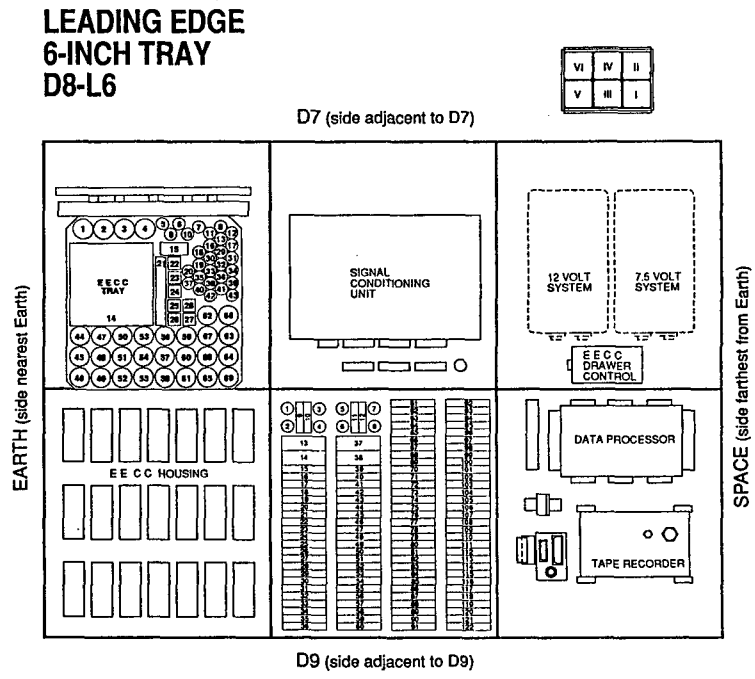


Figure III-3. Layout of D8 leading edge 6-inch-deep tray.

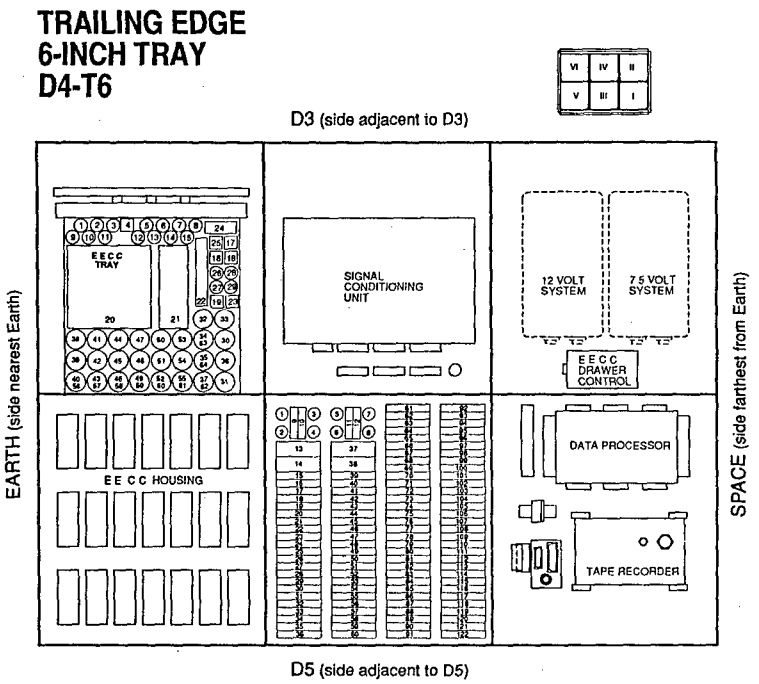


Figure III-4. Layout of D4 trailing edge 6-inch-deep tray.

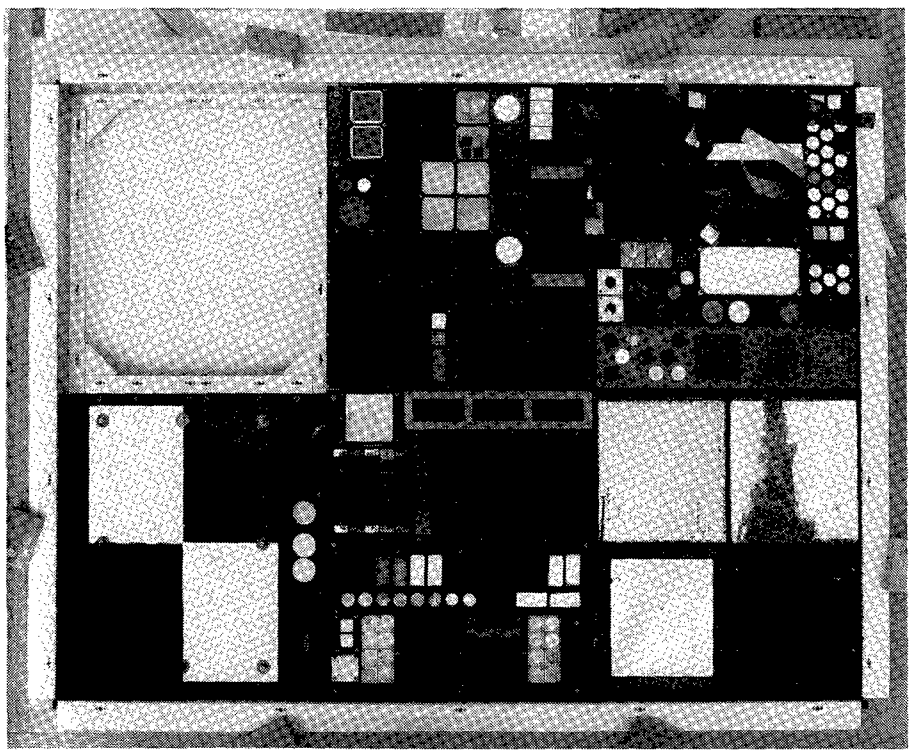


Figure III-5. D9 tray postflight, prior to sample deintegration, in tray holding fixture.

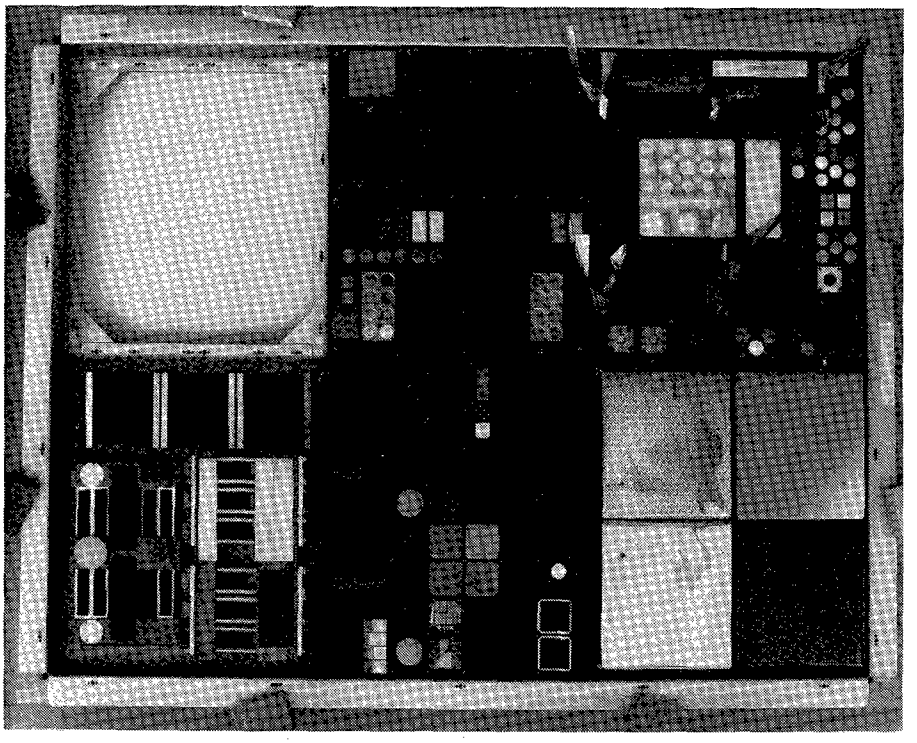


Figure III-6. D3 tray postflight, prior to sample deintegration, in tray holding fixture.

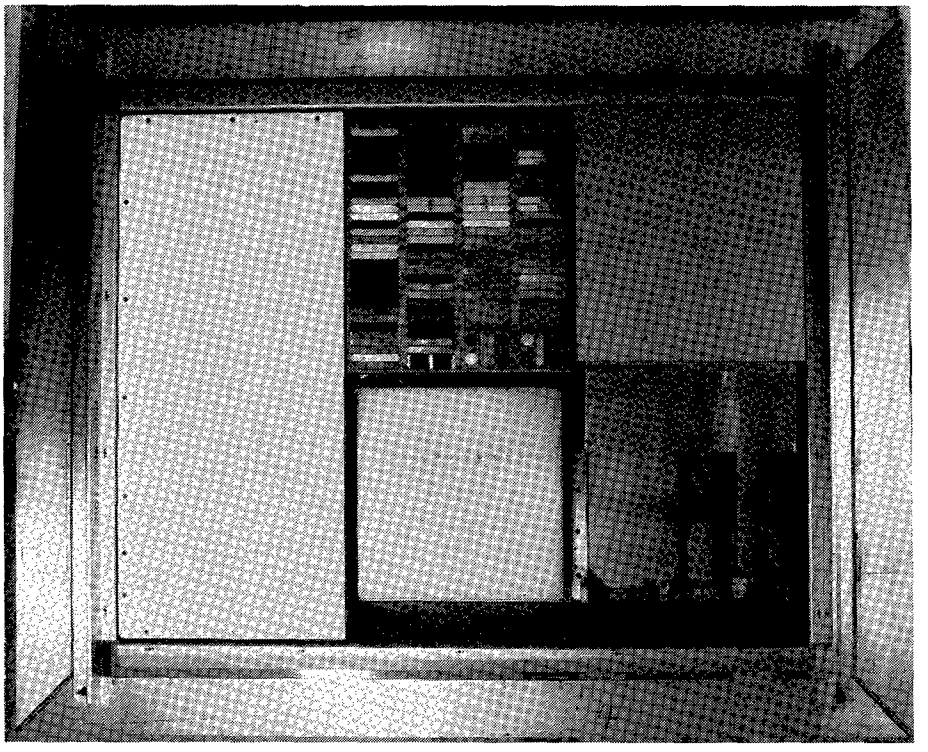


Figure III-7. D8 tray postflight, prior to sample deintegration, in tray holding fixture.

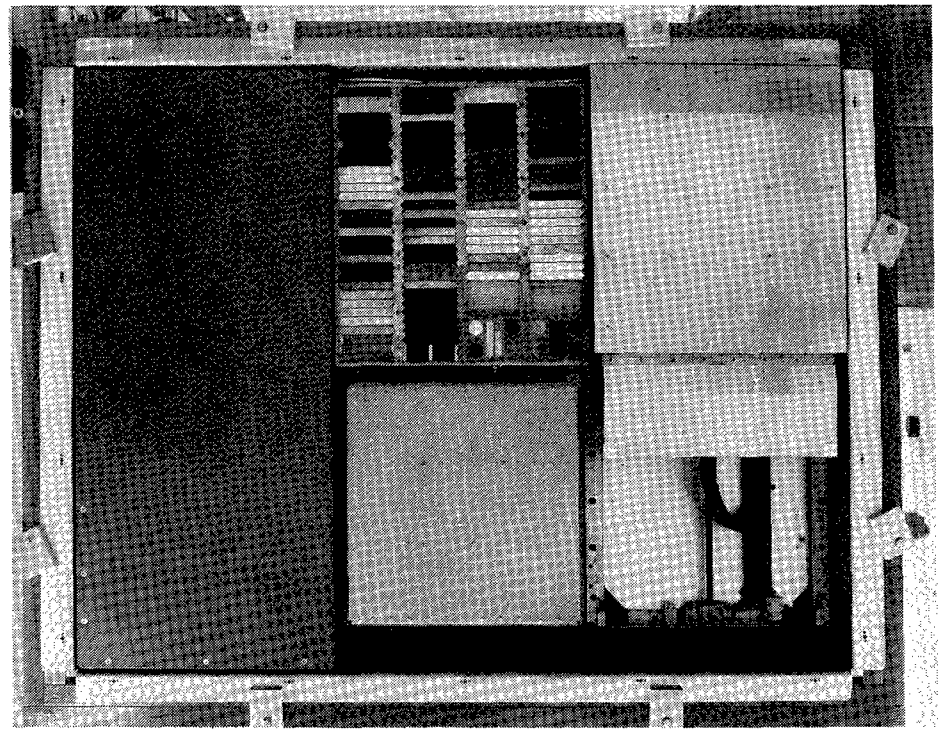


Figure III-8. D4 tray postflight, prior to sample deintegration, in tray holding fixture.

IV. CRATER SURVEY METHOD

Documentation of the impacts on the various sunshields and covers was accomplished by manually scanning the panel with a 10X eyepiece mounted on an x-y translation system. This fixture allowed determination of the crater's position and size. Comparison to a reticule scale allowed measurement of the crater diameter. When possible, three measurements were made on each crater. These corresponded to the actual crater diameter, the melt or spall zone surrounding the crater, and the larger area of delamination or damage. These measurement conventions are shown in Figure IV-1. All craters with diameters of 0.001 in. or greater (25 microns) were recorded. In some cases, data was recorded on impacts where the only feature was the delamination zone of 0.001 in. to approximately 0.004 in. However, data used for modeling consisted only of the craters with diameters 0.001 in. or greater. This survey and the disassembly of the four LDEF trays were performed in a class 10,000 clean room facility at The Aerospace Corporation. As the material specimens were removed from the trays, they were individually examined, preserving the orientation of the samples on LDEF. Each was photographed using brightfield, darkfield, and Nomarski optical microscopy techniques. Typical micrometeoroid and debris damage was carefully photographed and documented. In addition, crater counts were performed on the samples from subexperiment #2, Laser Optics, and subexperiment #19, Electronic

Materials. A Zeiss research microscope was used at 200X to 1000X, allowing observation of craters as small as 1 micron and as large as 782 microns on these samples. No perforations were observed.

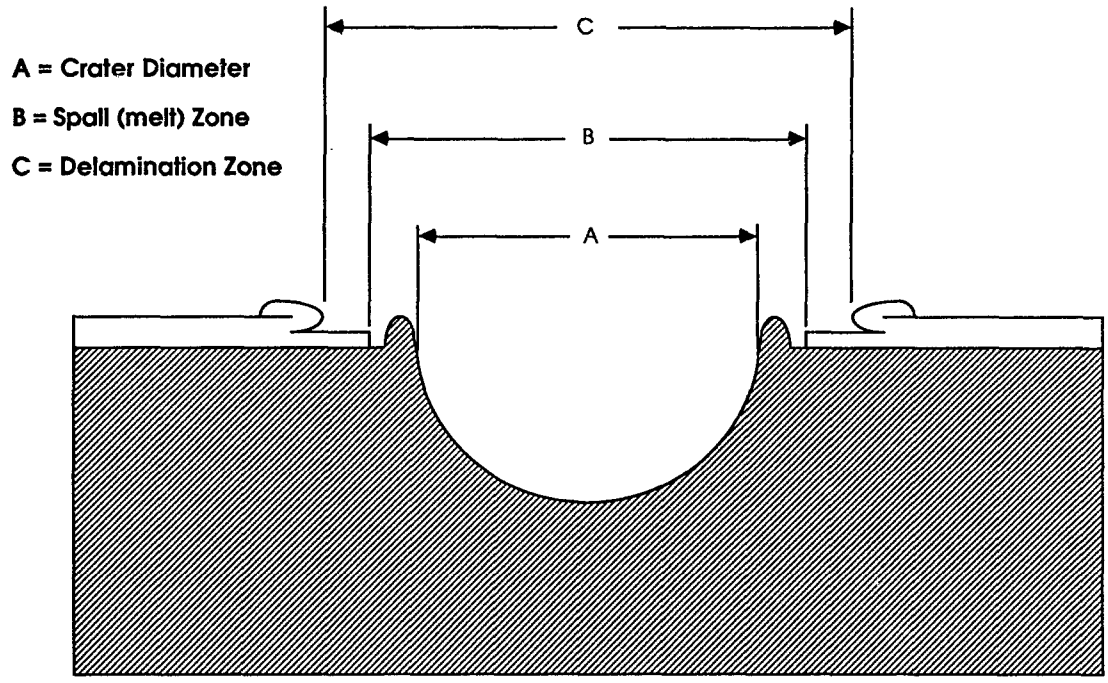


Figure IV-1. Micrometeoroid and debris survey terminology.

V. RESULTS BY SAMPLE

Table II gives a brief synopsis of the surfaces surveyed in this study.

Table II. M0003 Surfaces Surveyed for M + D Damage.

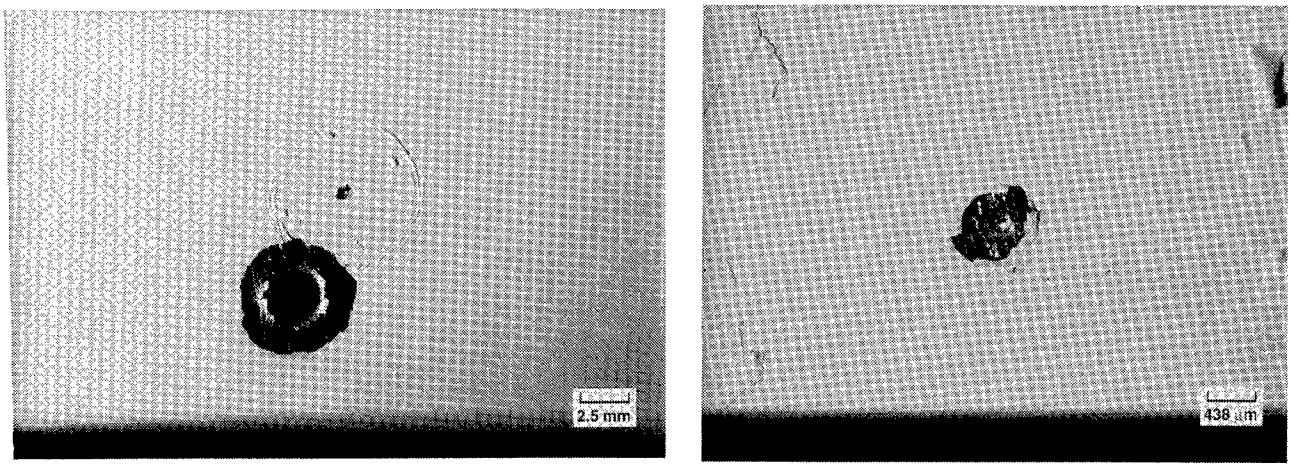
Designation	Substrate	Coating	LDEF Location	Observations
D8 EPDS Sunshield	Aluminum	Chemglaze A-276	Leading edge, D8	Chalky surface; AO eroded binder
D4 EPDS Sunshield	Aluminum	Chemglaze A-276	Trailing edge, D4	Dark brown; UV degraded binder
D8 EPDS Sunshield	Aluminum	Chromic acid anodized	Leading edge, D8	Dull luster from AO exposure
D4 EPDS Sunshield	Aluminum	Chromic acid anodized	Trailing edge, D4	Reddish brown contamination film
D8 Mod VI Panel	Aluminum	Chromic acid anodized	Leading edge, D8	Dull luster from AO exposure
D4 Mod VI Panel	Aluminum	Chromic acid anodized	Trailing edge, D4	Reddish brown contamination film
D8 SCU Cover	Aluminum	S13GLO	Leading edge, D8	Crazed rough surface
D4 SCU Cover	Aluminum	S13GLO	Trailing edge, D4	UV degraded; Darkened

The D8 EPDS sunshield was an aluminum panel 42 by 93 cm having a thickness of 0.1 cm (40 mil), and was painted with a white thermal control paint (Chemglaze A-276) with an underlying primer coat to promote adhesion. The thickness of the paint was approximately 75 microns (3 mil). This paint consists of an inorganic titanium dioxide pigment in an organic polyurethane binder. After the exposure to the space environment, the paint binder at the surface of the paint layer had been eroded away by atomic oxygen, leaving a powdery coating of loose pigment particles. This surface was quite fragile and contained thousands of impact craters varying in size from below 0.001 to 0.093 in. in diameter. The largest crater penetrated through the aluminum. Surrounding most of the craters was an area of delaminated, or spalled paint or an area of roughened texture. The delamination occurred in intermediate layers of paint in which the top layer was folded over the outer edge of the delamination area, leaving a thin layer of paint still adhering to the aluminum substrate. An area of bare metal or melt zone was present between the crater and the delamination area on the larger craters of about 0.005 in. diameter and up. Most of these larger craters had raised rims surrounding the crater cavity, and, in some cases, patches of red or brown primer paint could be seen around the craters or on top of the raised rims. Most of the smallest craters were not visible through the 10X eyepiece, but the impacts were detected by the presence of the delamination zones, which were much larger in diameter than the actual crater by a factor of about 25. Delamination zones of 0.001 in. were observable. Figure V-1 shows photos of representative impacts in this sunshield.

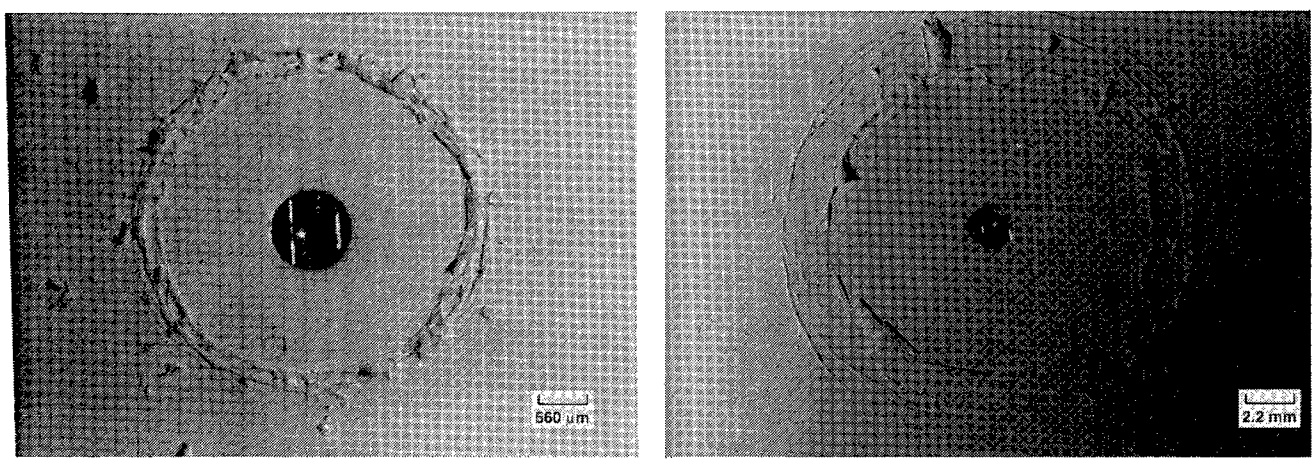
About 2400 impacts were recorded with damage zones of 0.001 in. (25 micron) or greater in an area of the panel measuring 15 by 42 cm. Subsequently, the remainder of the panel was surveyed by counting only those craters with diameters of 0.001 in. or greater. A total of 701 impacts were counted, which corresponds to 1795 impacts/m^2 for craters 0.001 in. or greater. Most of the craters were circular; however, 26 of these were oblong, possibly indicating that the impacting particles were highly oblique. The delaminated paint surrounding many of the craters was lifted in large flakes just above the aluminum substrate surface. Some craters appeared dark inside, possibly because they were deeper or contained residue, and, in some cases, a dark spot could be seen inside the crater. This may also be due to lighting artifacts. The largest impact was a 0.090 in. diameter hole through the aluminum panel with a 0.21 in. melt zone and a delamination area of about 1 in. In general, this panel was unique due to the absence of paint binder at the surface and revealed evidence of very small impacts, which were not detectable on other LDEF surfaces or samples.

B. D4 EPDS Sunshield

The EPDS Sunshield located on tray D4 was identical to the D8 sunshield prior to launch. Measurements of the paint of this surface indicated a thickness of about 60 microns (2.3 mils), a slightly thinner coating than the D8 sunshield. However, after exposure to the space environment, the Chemglaze A-276 paint darkened severely due to UV radiation.[2] Since the trailing edge of LDEF saw little atomic oxygen, there was no erosion of the paint's polyurethane binder. Thus, the surface of the sunshield consisted of a dark-brown glossy painted substrate. The response of this surface to debris/micrometeoroid impact was, therefore, quite different from the D8 sunshield. A total of 72 craters with diameters of 0.001 in. or greater was counted on the 43 by 93 cm panel, which translates to 184 craters/m^2. The largest crater was 0.020 in. in diameter. Although in many cases there was an area of bare metal around the crater, presumably due to melt, there was no area of delamination beyond the melt zone. In some cases, a loose flap of paint was still suspended over the area of bare metal surrounding the crater. Seven of the craters were oblong, indicating highly oblique impact. Some black spots were observed inside many of the craters and were possibly due to a primer coat. Brown primer residue was also observed around many of the crater



(a) (b)



(c) (d)

LANDSCAPE

Figure V-1. Representative impacts in the D8 EPDS sunshield.

rims. In addition to craters, there were many circular areas of various sizes with a yellowish-green stain. Figure V-2 illustrates representative craters from this panel.

C. D8 EECC Sunshield

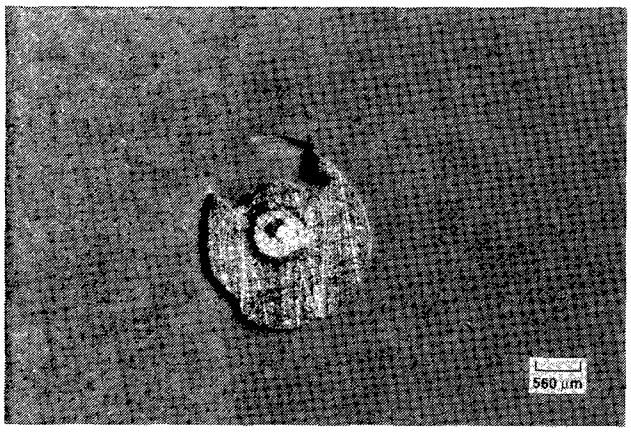
The D8 EECC sunshield was an aluminum sheet 0.16 cm (63 mil) thick measuring 41 by 45 cm mounted over the vacuum canister on the D8 tray. The surface was chromic acid anodized for thermal control purposes. After retrieval, the panel had a dull luster, presumably due to interaction with the leading edge atomic oxygen environment. Impacts appeared as craters with raised walls of aluminum. The diameters of the craters were measured to the inside of the raised walls. A total of 316 craters with diameters of 0.001 in. and greater were counted, corresponding to 1713 craters/m^2. The largest crater was 0.039 in. diameter. Some of the craters appeared to have dark interiors or dark spots within the crater. This may be due to lighting artifacts. Several oblong cavities were also observed, but these had no raised walls and were presumed to be flaws or gouges in the aluminum surface. Figure V-3 depicts typical damage due to impacts on this panel.

D. D4 EECC Sunshield

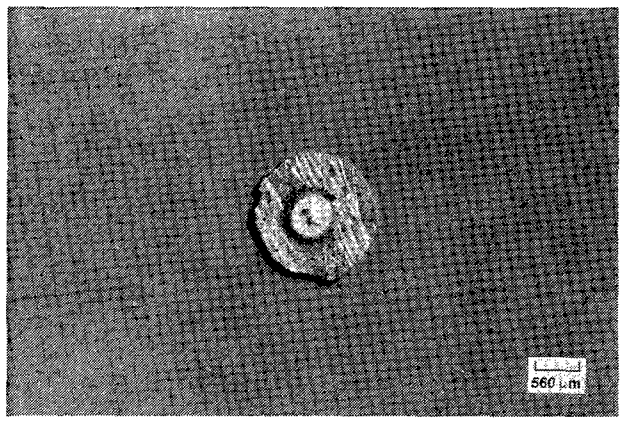
The D4 EECC sunshield was identical to that on D8 prior to launch; however, after LDEF retrieval, the surface of the aluminum panel was still shiny but had a reddish tinge due to staining from the ubiquitous contamination on LDEF.[2] There were also circular areas of brown residue of various sizes. The panel had the same flaws as the D8 sunshield. A count of 58 craters of 0.001 in. diameter and greater was made, or 314 craters/m^2. The largest crater was 0.015 in. in diameter. The phenomenology of the impacts on this surface was identical to that observed for the D8 panel. Figure V-4 shows representative impacts seen on this panel.

E. D8 Mod VI Panel

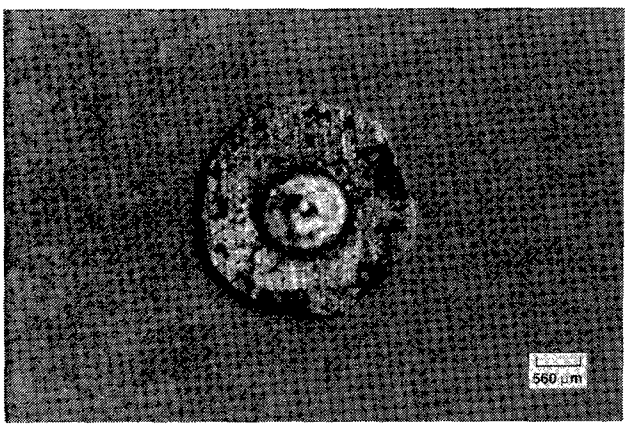
The D8 Module VI panel was a small companion panel to the D8 EECC sunshield panel mounted adjacent to it on the edge of the canister drawer. In construction, it was identical to the EECC sunshields, except it was smaller, measuring 14.1 by 37.5 cm. The appearance of the material after retrieval was similar to the D8 EECC sunshield as previously described. This panel had 134 craters larger than 0.001 in., and the largest measured 0.020 in. in diameter. The crater density for this panel is then 2534 craters/m^2. Impacts in this surface were identical to those seen on the D8 EECC sunshields, which are shown in Figure V-3.



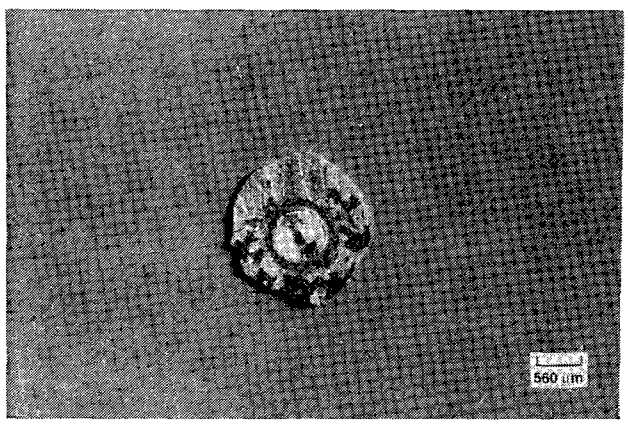
(a)



(b)



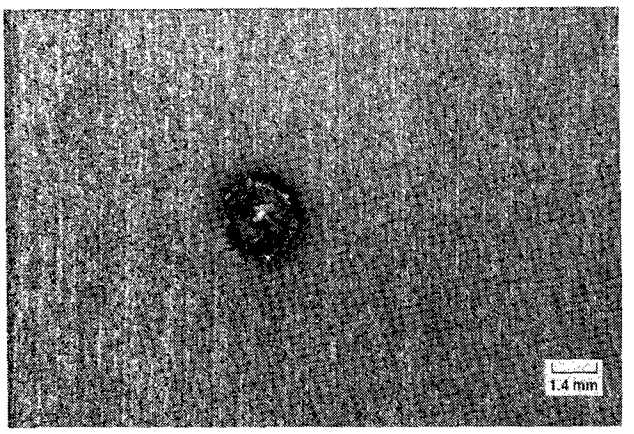
(c)



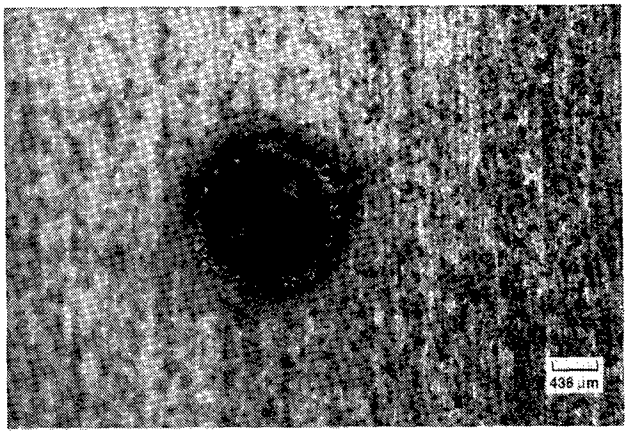
(d)

LANDSCAPE

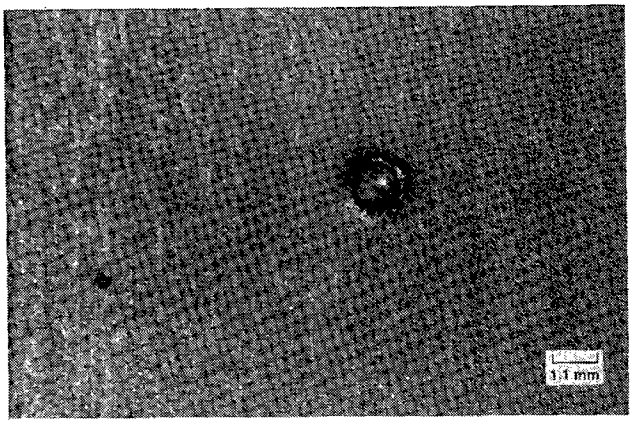
Figure V-2. Representative impacts in the D4 EPDS sunshield.



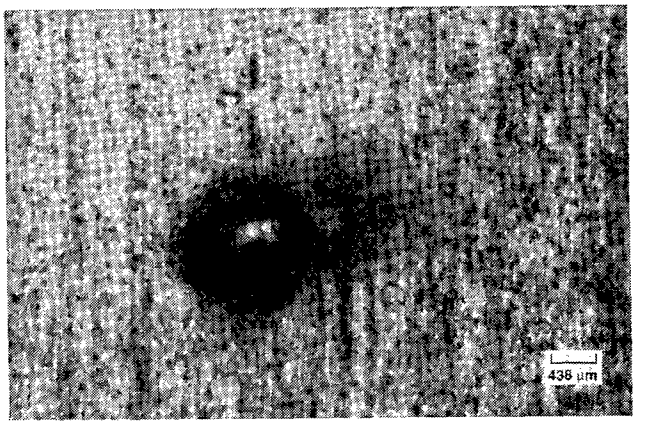
(a)



(b)



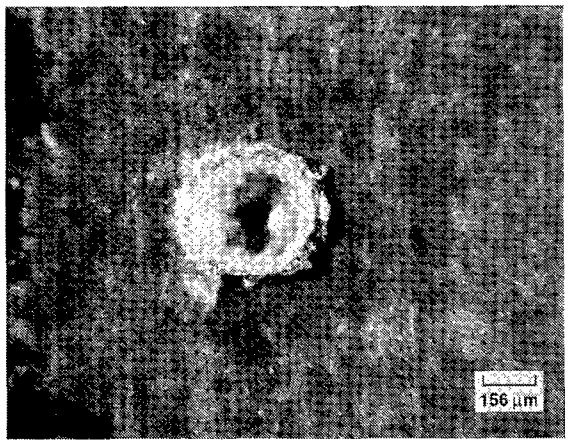
(c)



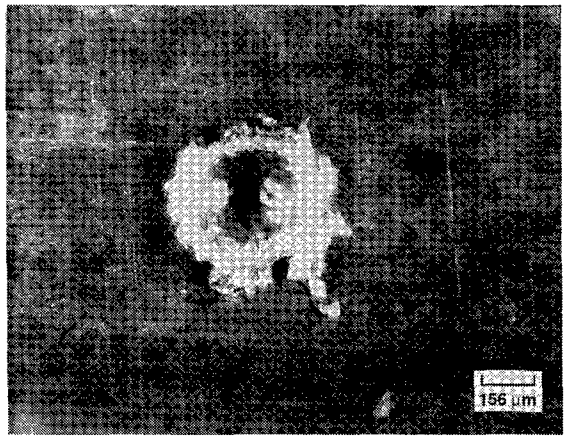
(d)

LANDSCAPE

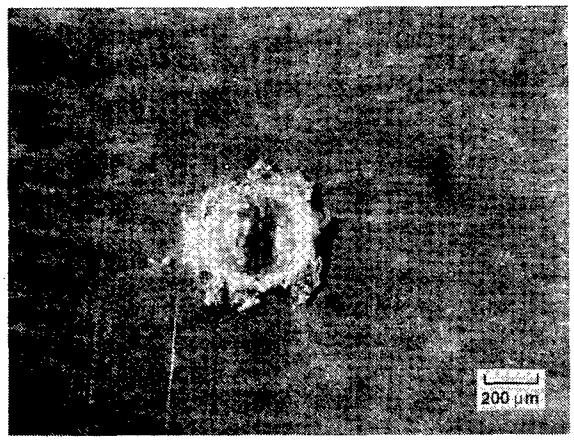
Figure V-3. Representative impacts in the D8 EECC sunshield.



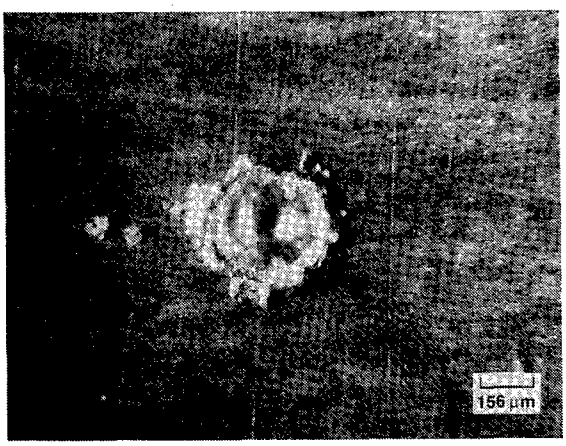
(a)



(b)



(c)



(d)

LANDSCAPE

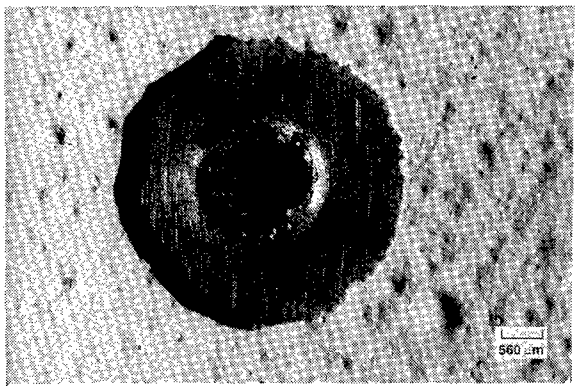
Figure V-4. Representative impacts in the D4 EECC sunshield.

F. D4 Mod VI panel

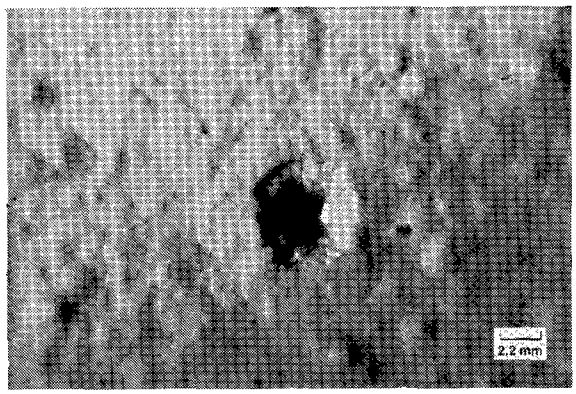
As with the panel previously described, this was a companion anodized aluminum panel that shielded the edge of the drawer of the EECC on the D4 tray. The appearance of this panel after LDEF recovery was similar to the D4 EECC cover in that it was shiny and had a thin contaminant film. Examination of this panel indicated 19 craters over 0.001 in. in diameter, the largest being 0.015 in. The crater density is 359 craters/m^2. As above, impacts in this surface were identical to those observed in the D4 EECC sunshields.

G. D8 SCU Cover

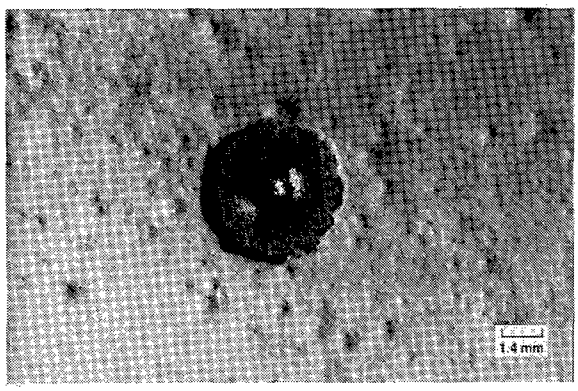
The D8 SCU cover was a box sunshield that fit over the signal conditioning unit on the D8 tray. It was constructed of aluminum sheet 0.086 cm (34 mils) thick and was double walled on the top surface, the surface scanned in this study. The aluminum was painted with a white thermal control paint, S13GLO, which is a zinc oxide pigment based paint that uses potassium silicate to encapsulate the pigment for UV stability. The binder for this paint is a methyl silicone material similar to GE RTV 602. The thickness of the paint was 230 microns (9 mils). This paint has significantly different mechanical properties than the Chemglaze A-276 paint used for the EPDS sunshields, primarily due to the elastomeric silicone binder, which imparts flexibility. The paint on the retrieved D8 SCU cover was crazed; however, it was still somewhat flexible and resilient, and the binder was still intact even after exposure to atomic oxygen. However, surface analysis using XPS indicated that a silicon dioxide coating had formed from the exposure. Moreover, the cover generally retained its white color in spite of the exposure to UV radiation. This was due to the interaction of atomic oxygen with the damaged material. The mechanism of this whitening process is still under investigation. The texture of the surface was quite rough as originally applied to the surface; the surface resembled, more than anything else, a stucco wall. This caused some difficulty in seeing and counting small impacts. In this material, the delaminated areas around the impacts were not folded back as on the D8 EPDS sunshield, but were simply eroded areas tapering down towards the craters. Bare metal between the crater and the delaminated area was observed on only three craters of the 59 that were counted in the diameter range of 0.001 in. and up giving a crater density of 434 craters/m^2. The largest crater was 0.075 in. in diameter with a 0.4 in. diameter area of bare metal surrounding the crater, with no apparent delamination of the paint beyond this melt zone. This impact would have punctured the aluminum if the surface had not been double thickness. The impact produced a deep crater in the material with a depth of 1.8 mm. This surface gave a lower crater density count than the other D8 panels, probably because the smaller impacts left no trace on the textured and resilient paint surface. Figure V-5 illustrates the response of this material to impacts.



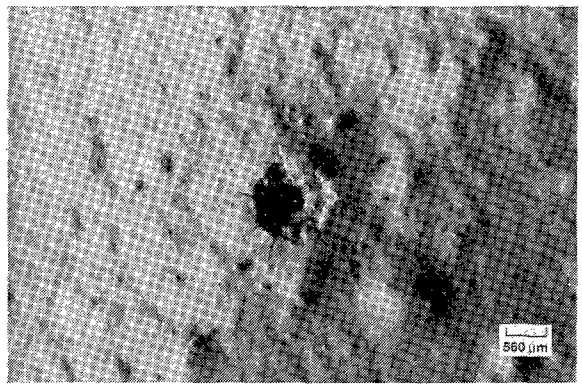
(a)



(b)



(c)



(d)

LANDSCAPE

Figure V-5. Representative impacts in the D8 SCU cover

H. D4 SCU Cover

The D4 SCU Cover was identical to the D8 cover prior to launch. The thickness of the base aluminum and the paint were essentially identical to the D8 SCU cover. However, exposure to the space environment produced a darkening of the paint due to UV radiation. Since this cover saw little or no atomic oxygen, there was no observed cleanup of the surface like that seen on the D8 cover. The surface was covered with a network of hairline cracks. Each crater also had hairline cracks spreading radially from the rim and extending for about 0.05 to 0.2 in. beyond. The cracks were easily observable because of their lighter color relative to the paint surface. A low count of 15 craters 0.001 in. in diameter and larger gave a crater density of 108 craters/m^2. The largest crater was 0.010 in. in diameter. Interesting photos of this surface are presented in Figure V-6.

I. Summary

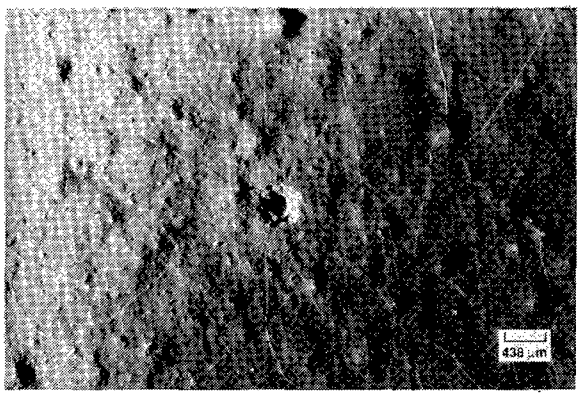
The raw counts for these various surfaces are presented in Table III, including the normalization to craters/m^2. Table IV gives the ratio of leading edge (D8) to trailing edge (D4) impacts for the surfaces.

Table III. Summary of Counts by Surface.

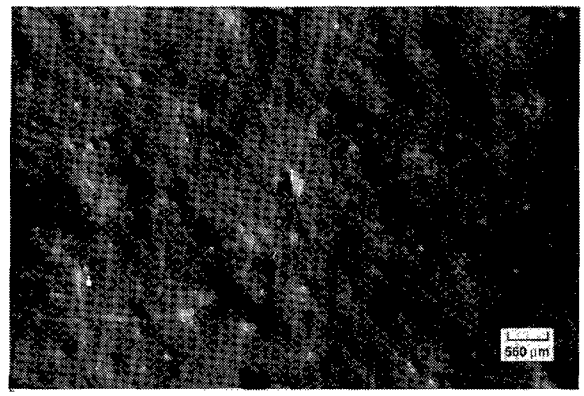
Surface	Area, cm^2	Raw Count	Counts/m^2
D8 EPDS Sunshield	3906	701	1795
D4 EPDS Sunshield	3906	72	184
D8 EECC Sunshield	1845	316	1713
D4 EECC Sunshield	1845	58	314
D8 Mod VI Panel	528.8	134	2534
D4 Mod VI Panel	528.8	19	359
D8 SCU Cover	1357.9	59	434
D4 SCU Cover	1394.9	15	108

Table IV. D8/D4 Impact Ratios for Various Surfaces.

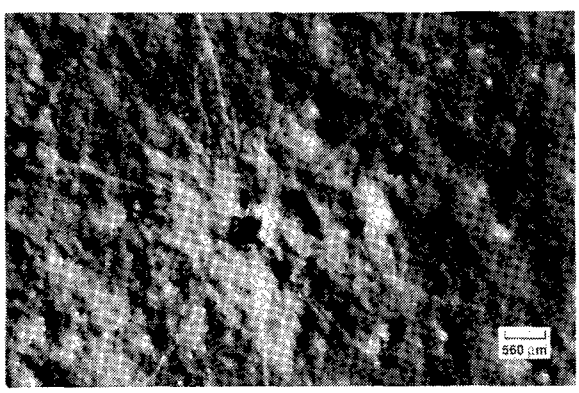
Surface	D8 Impacts/m^2	D4 Impacts/m^2	Ratio D8/D4
EPDS Sunshields	1795	184	9.76
EECC Sunshields	1713	314	5.46
Mod VI Panels	2534	359	7.06
SCU Covers	434	108	4.02



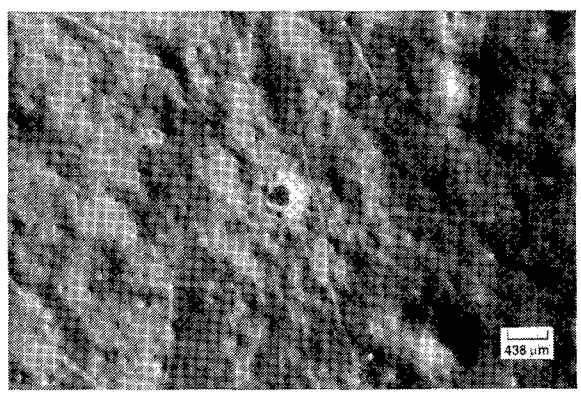
(a)



(b)



(c)



(d)

LANDSCAPE

Figure V-6. Representative impacts in the D4 SCU cover

This data is presented in the following graphs, which are of two types: dot plot and histograms. A plot of each type is included for each surface studied. To illustrate the size differences between the various surfaces, the dot plots have been scaled to actual relative sizes. The histograms have been plotted with both linear and logarithmic ordinates. This information is presented in Figures V-7 through V-15. It will be seen from these plots that the distributions are different for each surface. This might be expected statistically, and may have to do with the different material response of the different surfaces and/or surface roughnesses. The ratio of leading edge to trailing edge (D8/D4) impact craters in any particular size range can be discerned from these plots. This, too, is not very constant and varies from about 1:1 to 10:1.

Before comparing this data to a model, a statistical analysis of the data was performed to determine the effect of the different panel surface areas on the sampling accuracy. This becomes especially important for the larger craters where the number of impacts per area is very small. Since the positions of all craters were determined in the survey, it was easy to compute distances between various craters to determine the mean distances between impacts. The spatial distribution of 701 craters with diameters greater than 0.0025 cm (25 microns) on the D8 EPDS sunshield was examined mathematically for areas of localized crater clusters. This involved calculating the mean crater separation distance and the standard deviation of the mean. Groupings of clusters would tend to decrease the mean crater separation and increase the relative standard deviation of the mean compared to a random spatial distribution. Using these statistics, comparisons of the D8 EPDS sunshield to computer-generated, random and clustered models indicated a definite "random" character to the actual crater distribution. This suggests that over time a net random spatial distribution of craters would be expected on a ram facing LEO-exposed surface. Results on the D4 EPDS sunshield were also found to be consistent with a "random" spatial distribution; however, lower crater densities on the trailing edge created a larger statistical uncertainty.

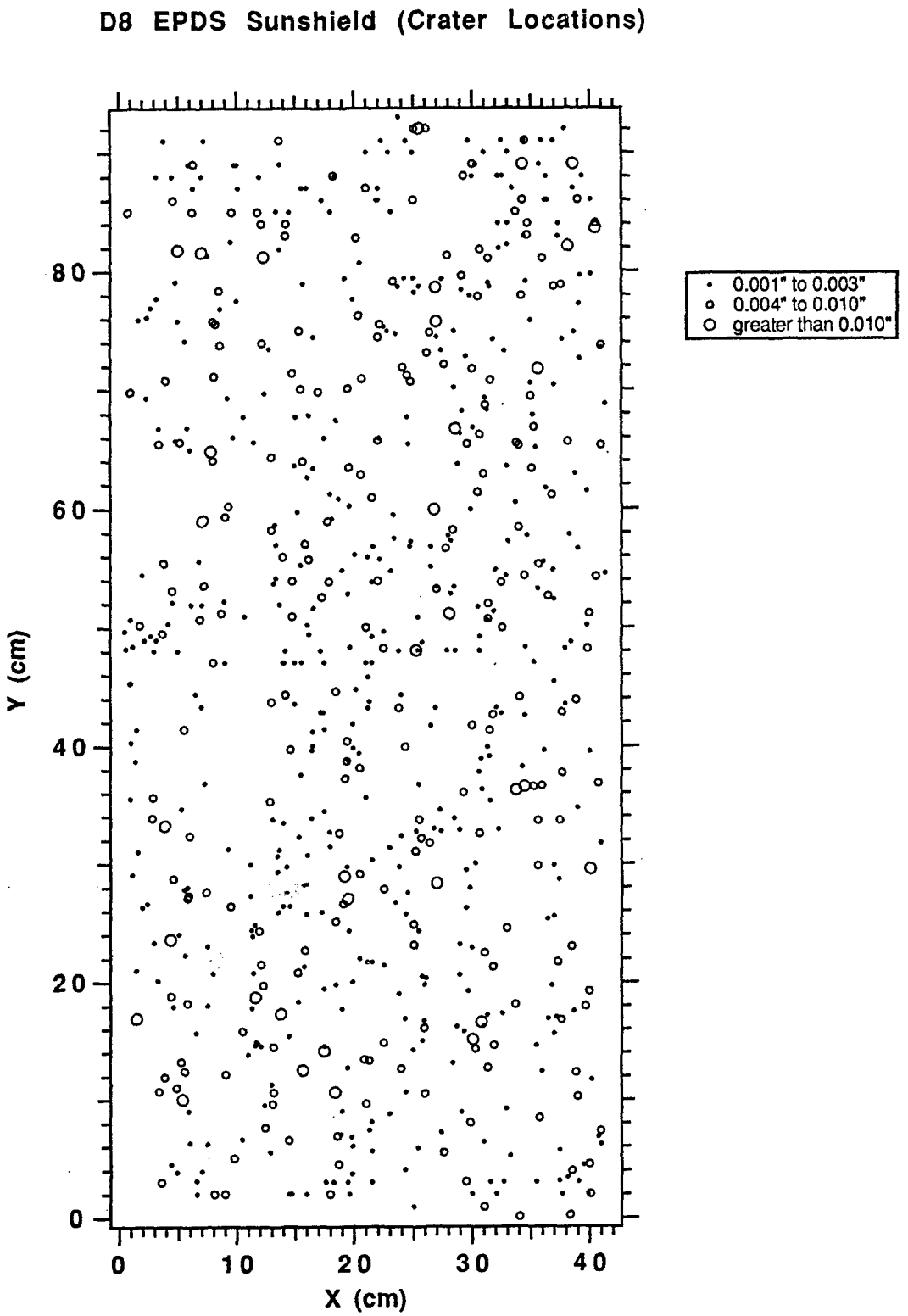


Figure V-7. Dot plot for D8 EPDS sunshield.

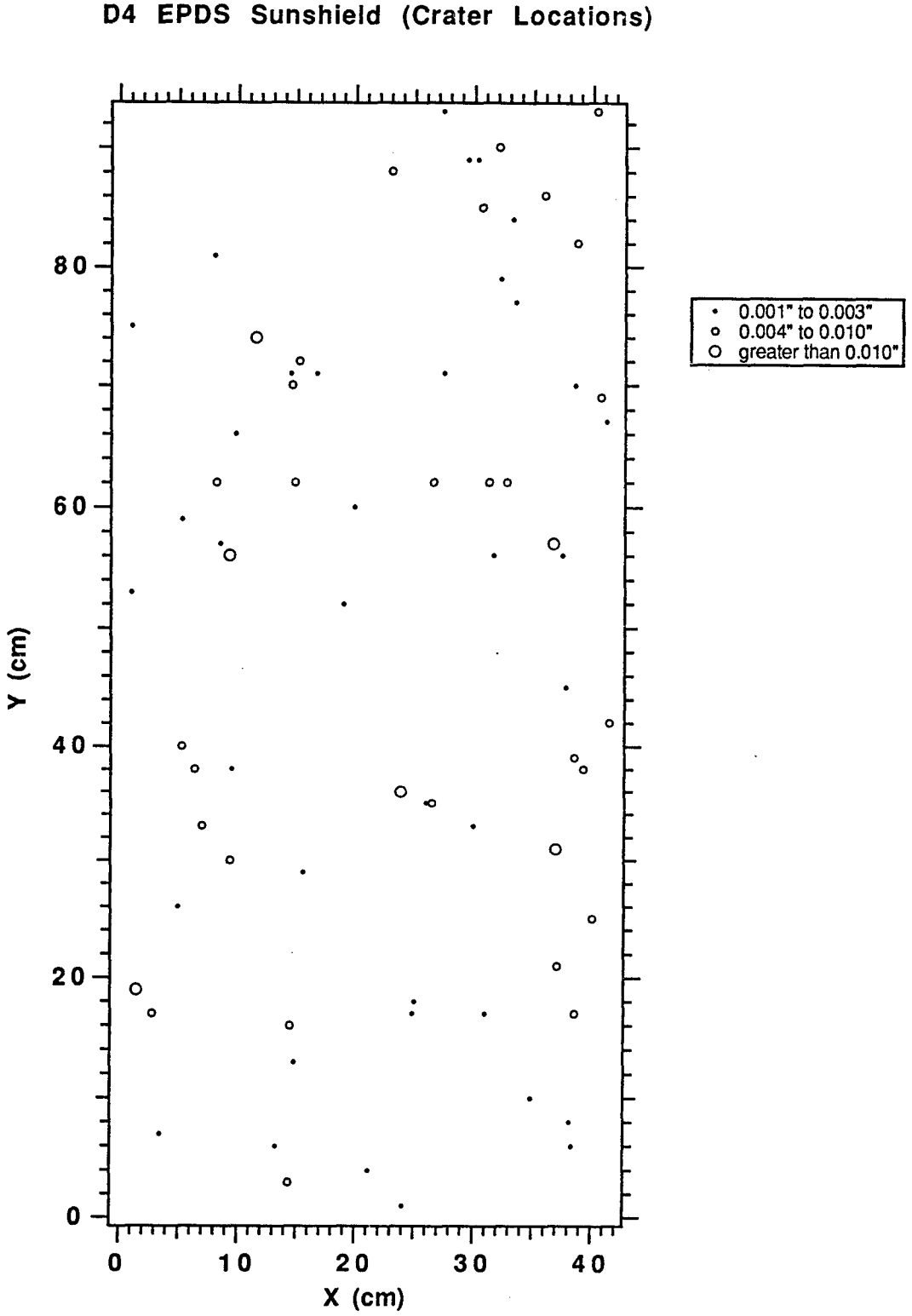
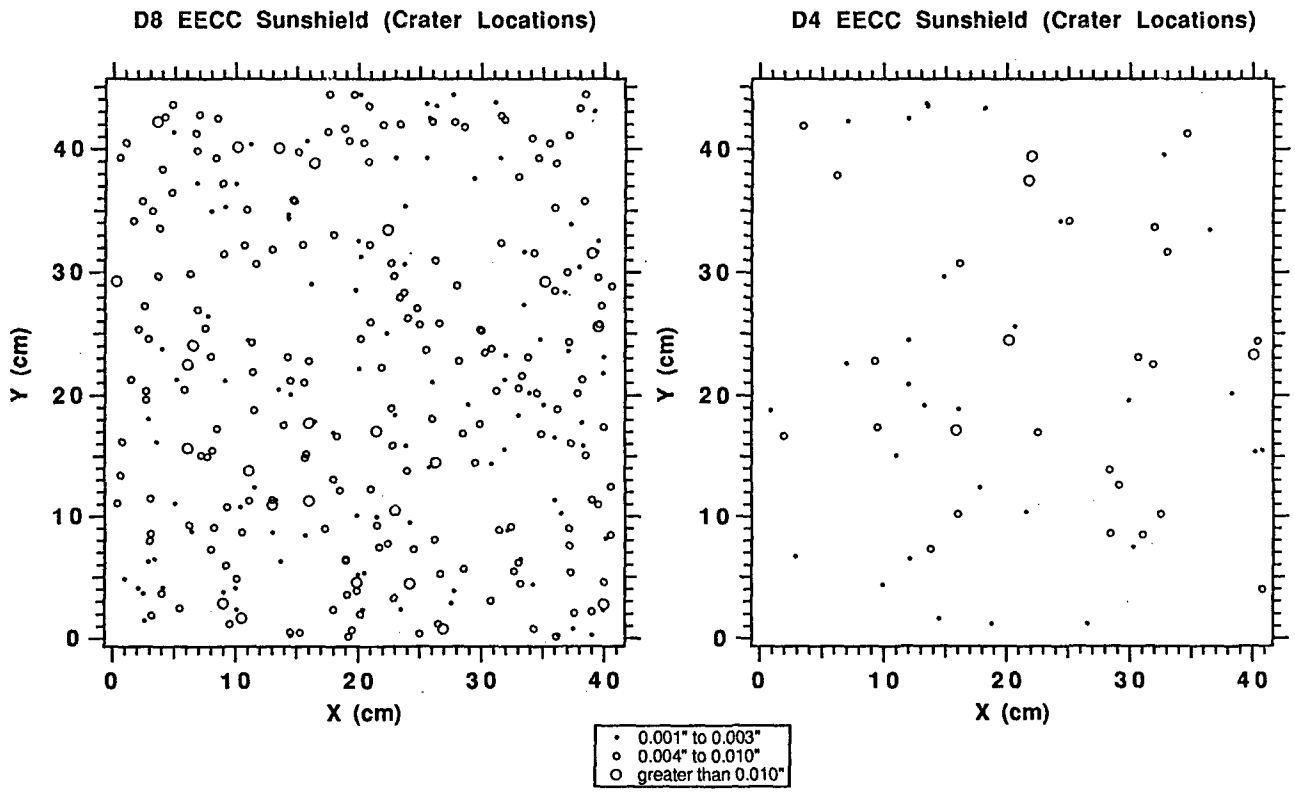
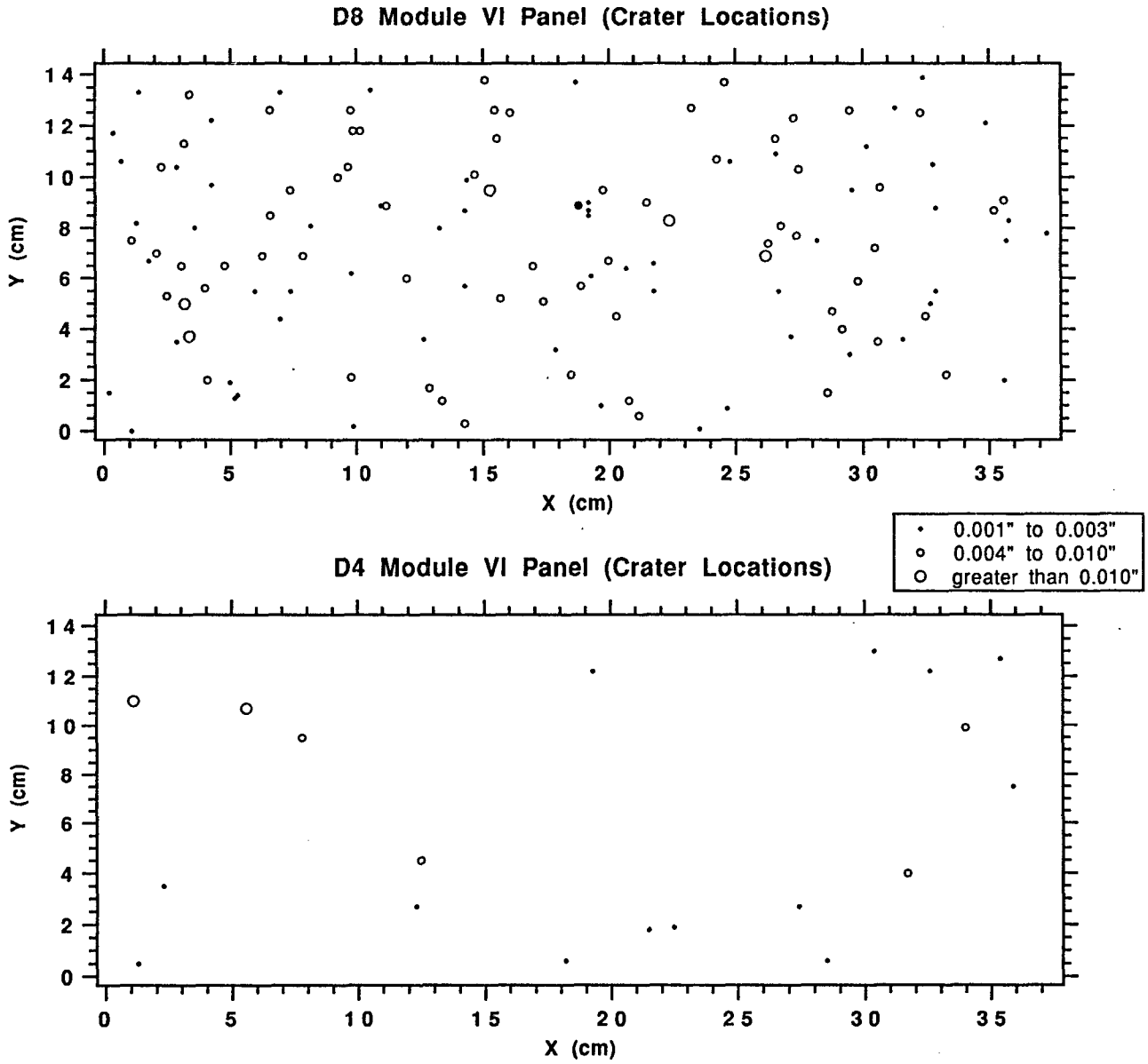


Figure V-8. Dot plot for D4 EPDS sunshield.



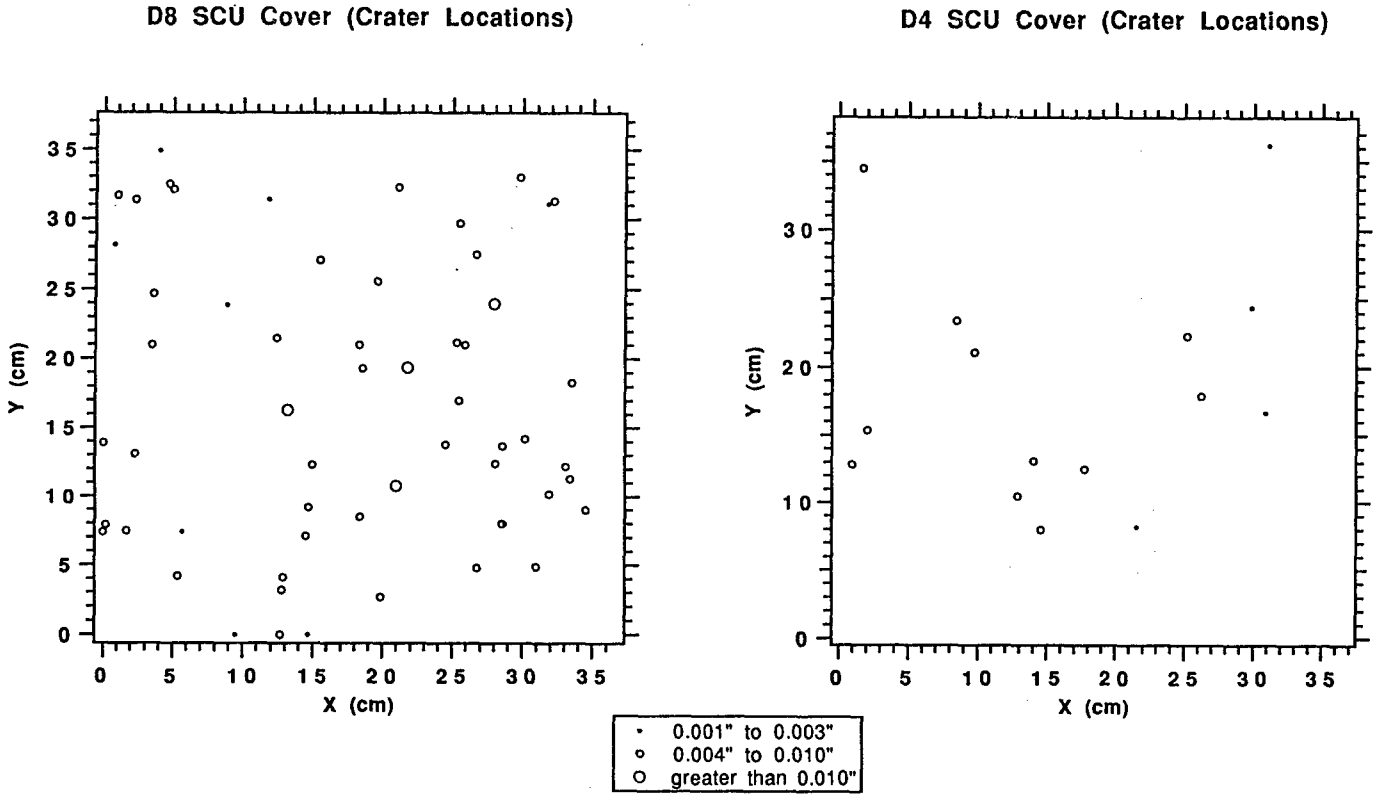
LANDSCAPE

Figure V-9 Dot plot for D8 and D4 EECC sunshields



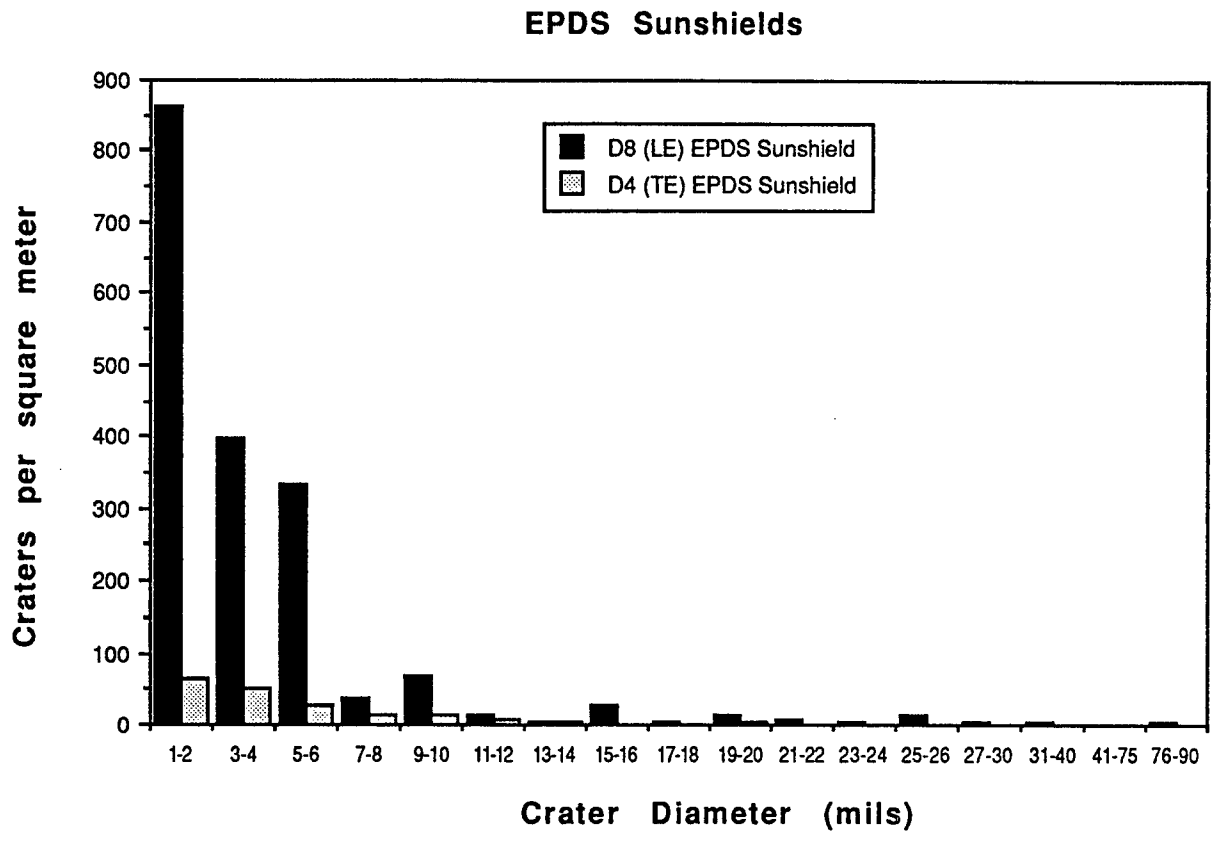
LANDSCAPE

Figure V-10 Dot plot for D8 and D4 Mod VI panels



LANDSCAPE

Figure V-11 Dot plot for D8 and D4 SCU covers.



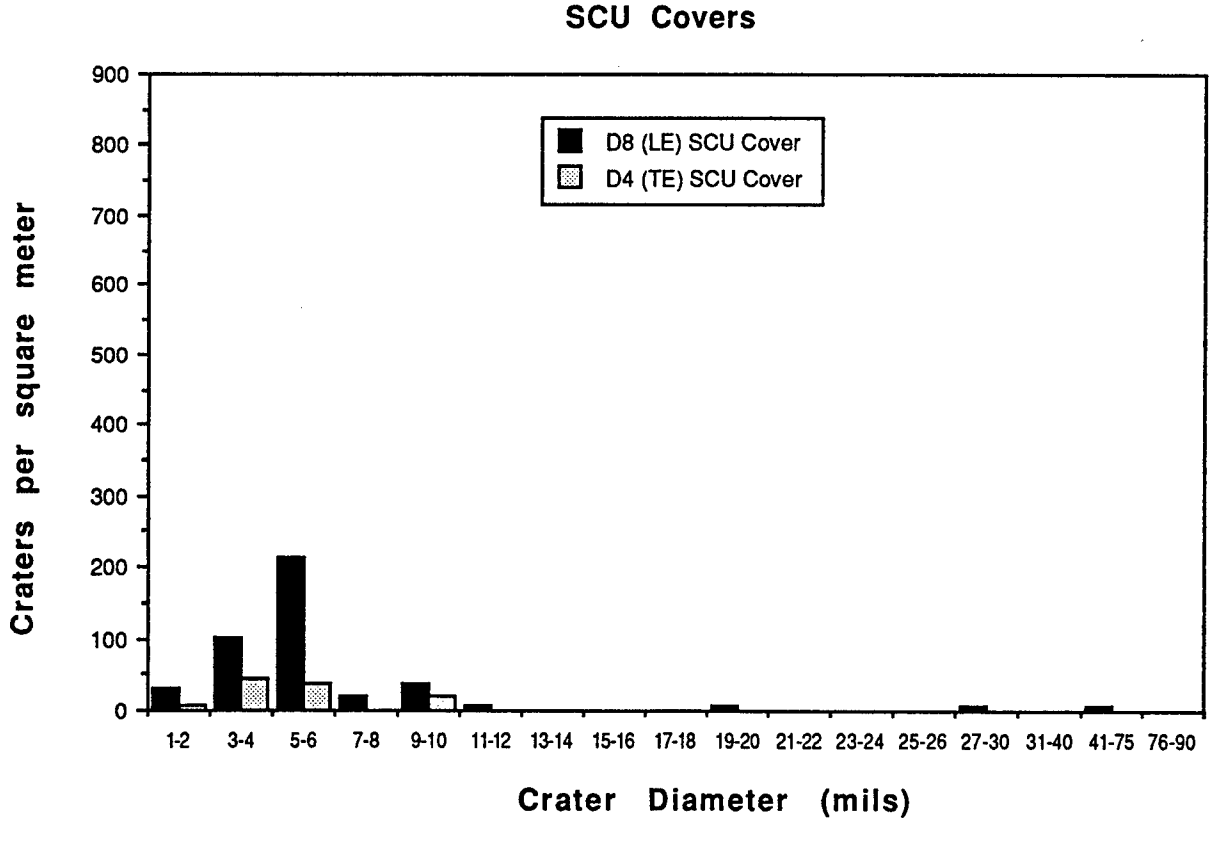


Figure V-12 Linear histograms for painted surfaces.

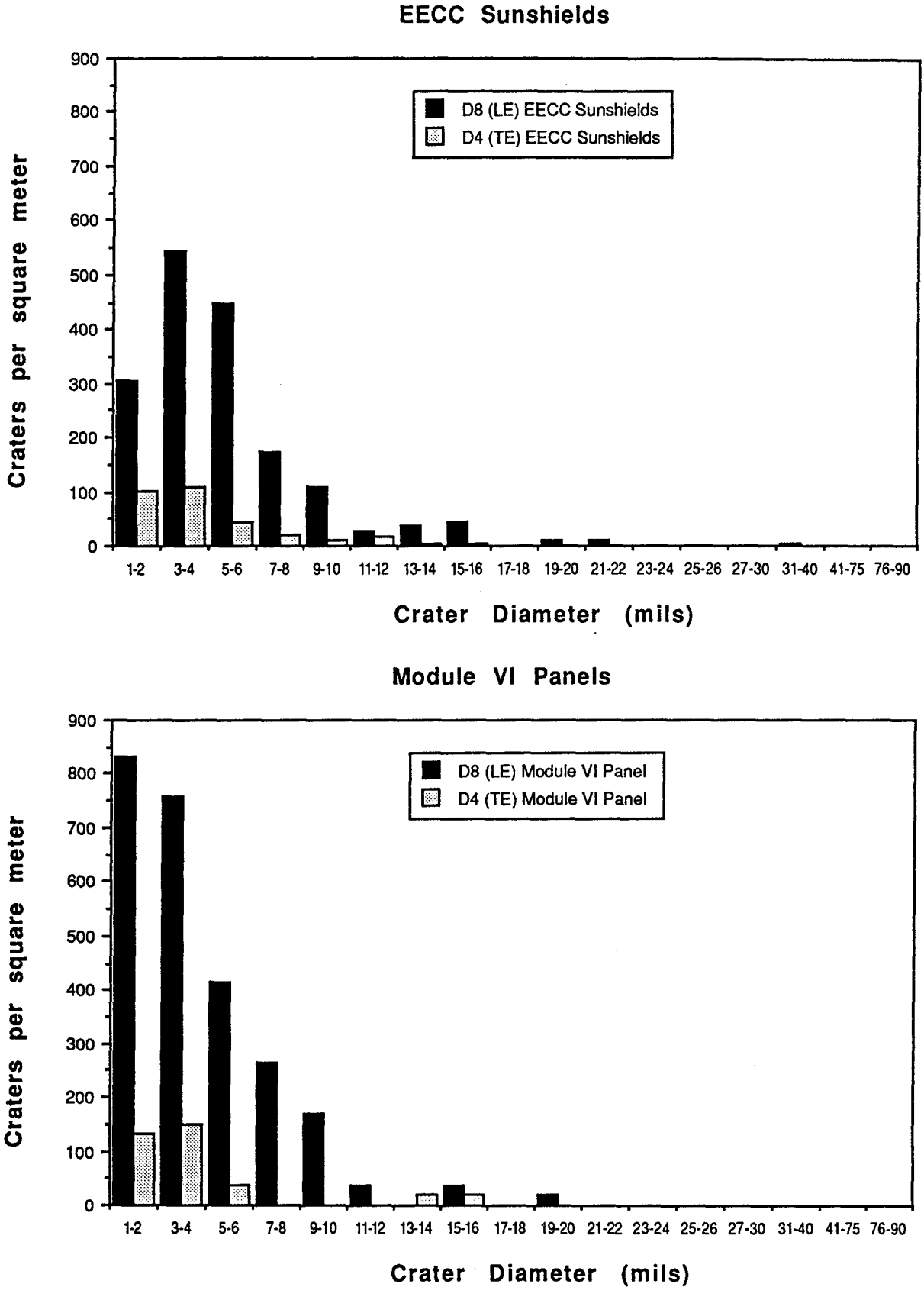


Figure V-13 Linear histograms for anodized surfaces.

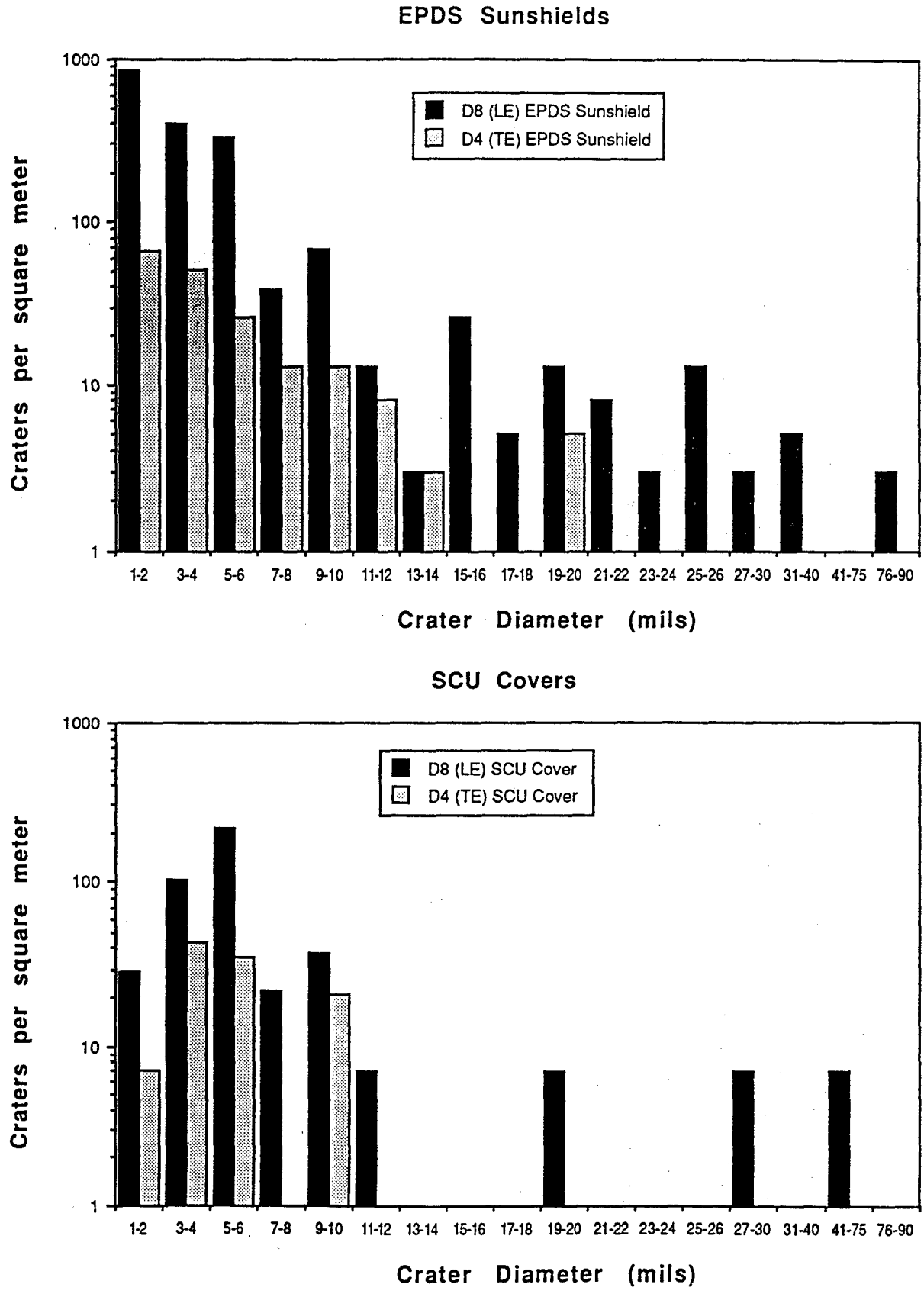


Figure V-14 Log histograms for painted surfaces.

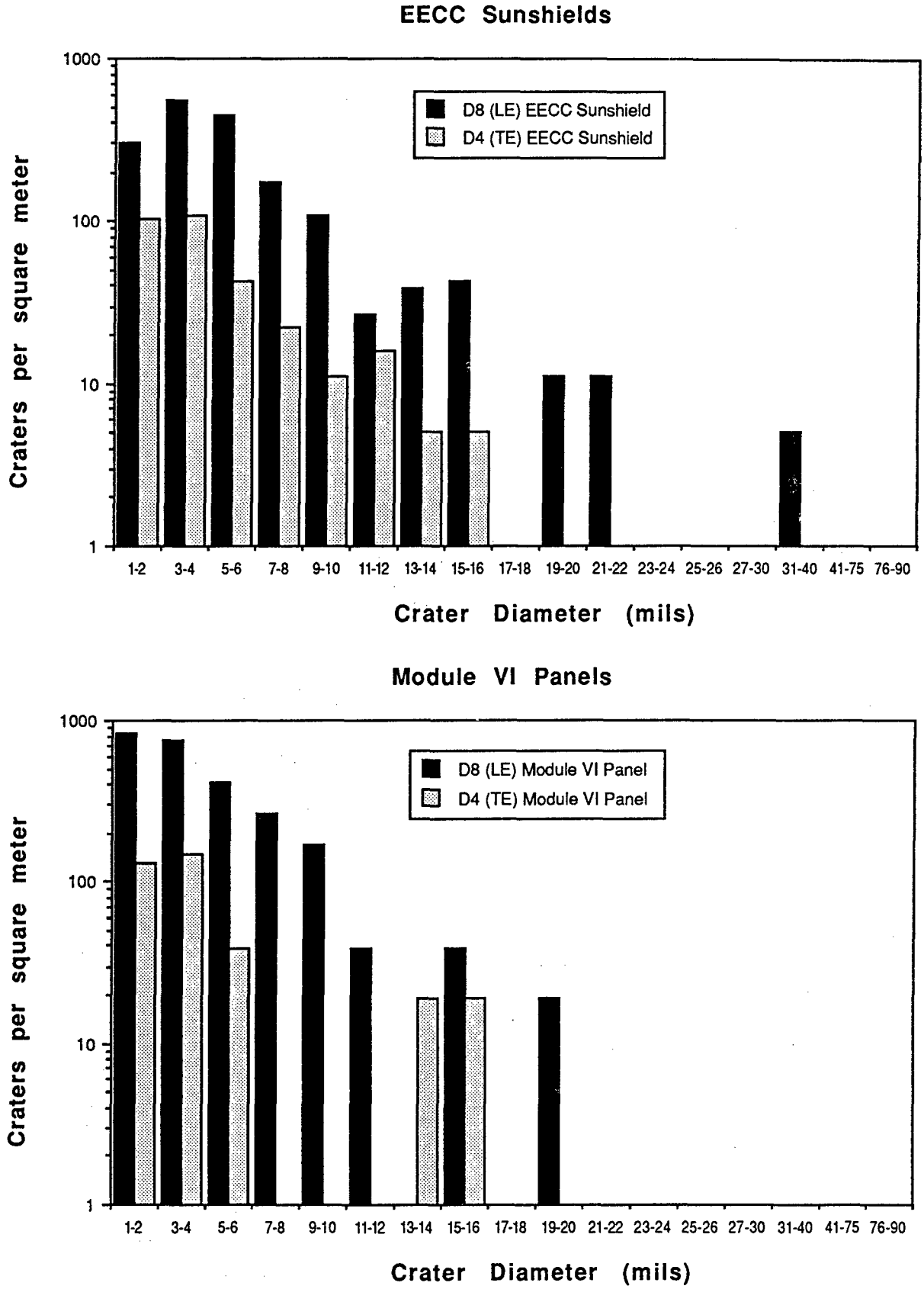


Figure V-15 Log histograms for anodized surfaces.

VI. RESULTS BY MATERIAL

A. Material Response to Hypervelocity Impacts

The material categories chosen for this discussion — metals, ceramics, glasses, composites, polymers and paints — parallel the categories used in the M0003 sample observation database.[18]

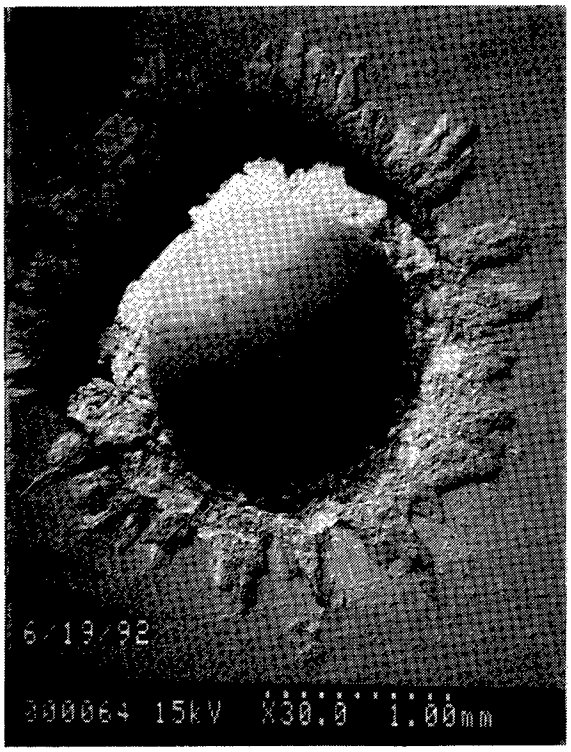
B. Metals

The general response of aluminum on LDEF to hypervelocity impacts has already been discussed for the chromic acid anodized aluminum EECC sunshields. Other examples of anodized aluminum and other metals are shown in Figures VI-1 through VI-14.

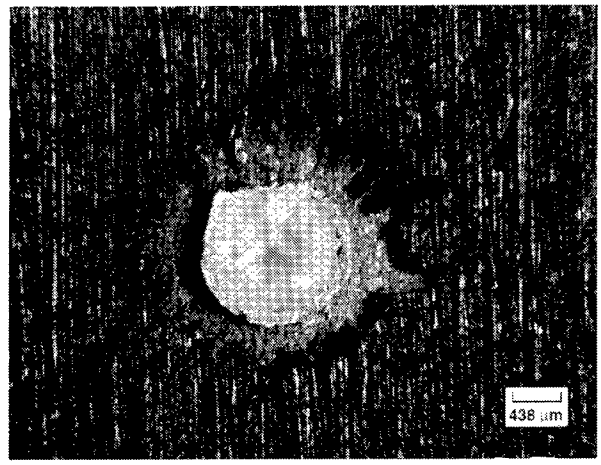
The response of the black anodized hardware is very similar to the sunshields. Impacts in the hardware are shown in Figure VI-1. In particular, this figure shows SEM photos of the entry and exit sides of a trailing edge (D3) perforation. All of these impacts display the classic raised lip structure, due largely to melt and hydrodynamic flow of the metal. The oxide layer has been shocked away.

Figure VI-2 shows representative impacts in metals. A typical impact crater in a copper mirror is shown in (a). There was no damage to this substrate beyond the area of the impact. In the nickel-coated copper mirror shown in (b), there are spatters of resolidified matter surrounding the craters; however, the damage is similar to that seen in the uncoated copper. While the samples did show some corrosion due to atomic oxygen exposure, this seemed to have no effect on the extent of damage. In (c), a typical crater in bare, polished molybdenum is shown. Only localized damage from the impact was seen in this material. The response of a rhodium foil on aluminum is illustrated in (d). This sample was from the trailing edge of LDEF (Row 3), as opposed to the three previous metals, which were leading-edge specimens. The foil has not been perforated, and there is a large amount of metal flow around the site. It may be that this impact resulted from a slow micrometeoroid.

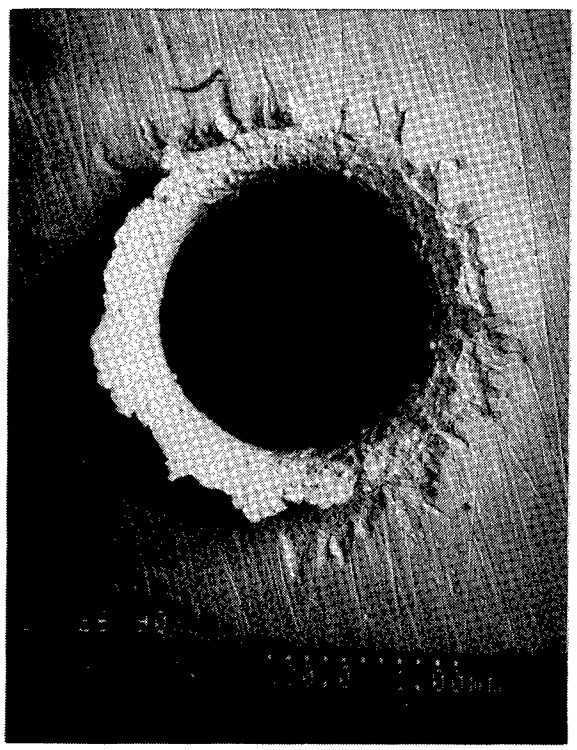
In contrast to the response of uncoated molybdenum substrates shown in Figure VI-2, the response of coated molybdenum can be quite different. Figure VI-3 graphically depicts the type of damage zone that can occur with hypervelocity impacts in some materials. In (a) we have a thorium fluoride-coated silver mirror on a molybdenum substrate with a 782-μm crater surrounded by a 1-cm blistered area. It would appear from the shape of the crater and the asymmetric damage zone that this impact occurred at a glancing angle. This type of damage was unusual (blistering without damage to the overlying layers), and its cause is not understood. Remarkably, the thorium fluoride coating was not cracked extensively, and no tarnishing of the silver layer was observed. There were other impacts in this sample, but they did not show the large damage zones observed around this impact. The cause of this difference is not known. It is hoped that further examination of these specimens will reveal more about material response and the effects of such impacts on performance. In (b), there is an impact in molybdenum coated with an aluminum oxide/silicon multilayer coating. Here, the brittle nature of the coating has caused it to crack and delaminate at the impact site. More damage to the sample could be anticipated as the coating flakes off. This sample was in the leading-edge



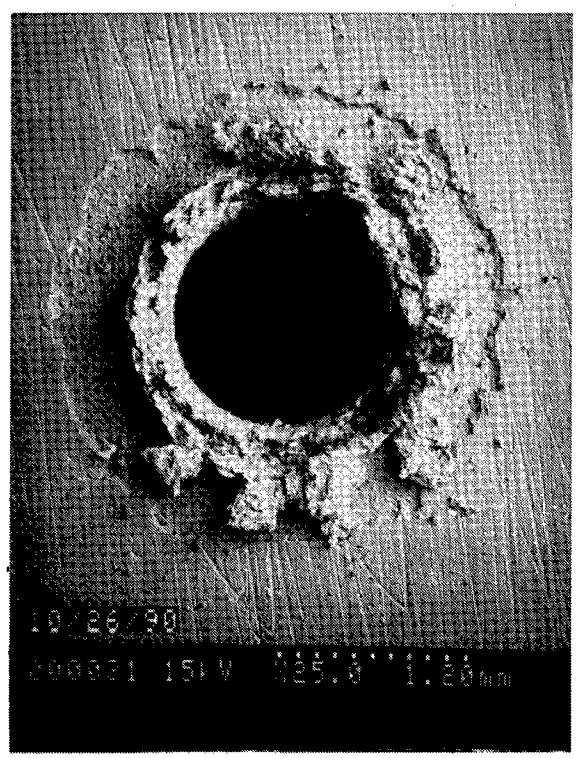
(a)



(b)



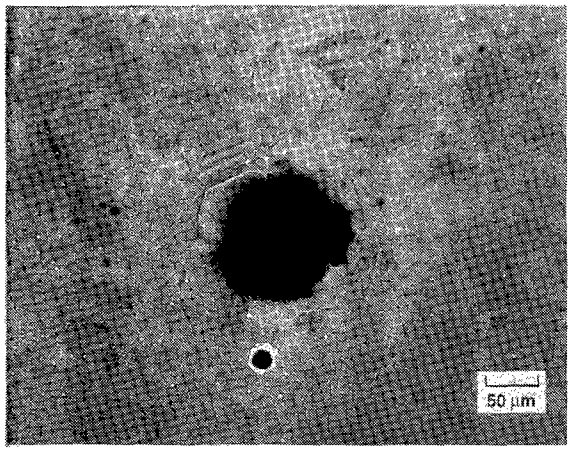
(c)



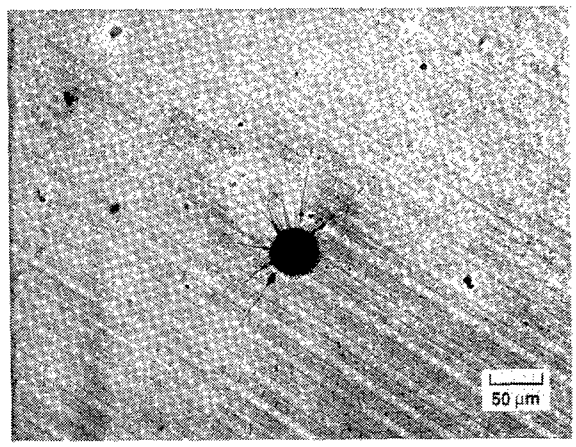
(d)

LANDSCAPE

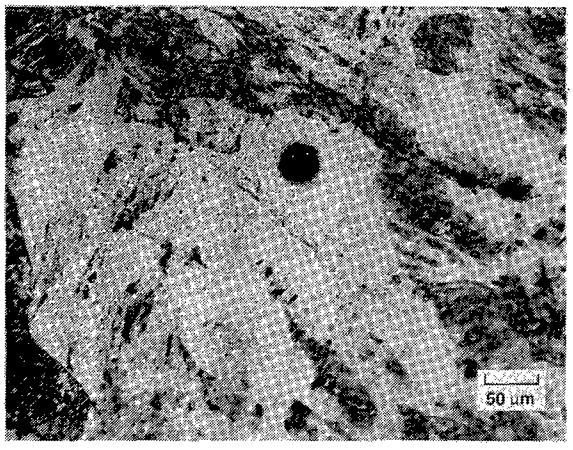
Figure VI-1. Typical impacts in the black anodized aluminum MOOO3 hardware.



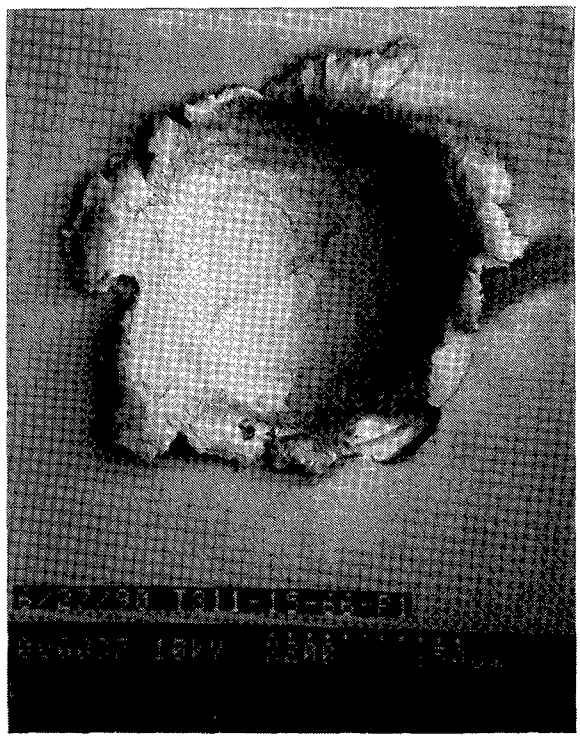
(a)



(b)



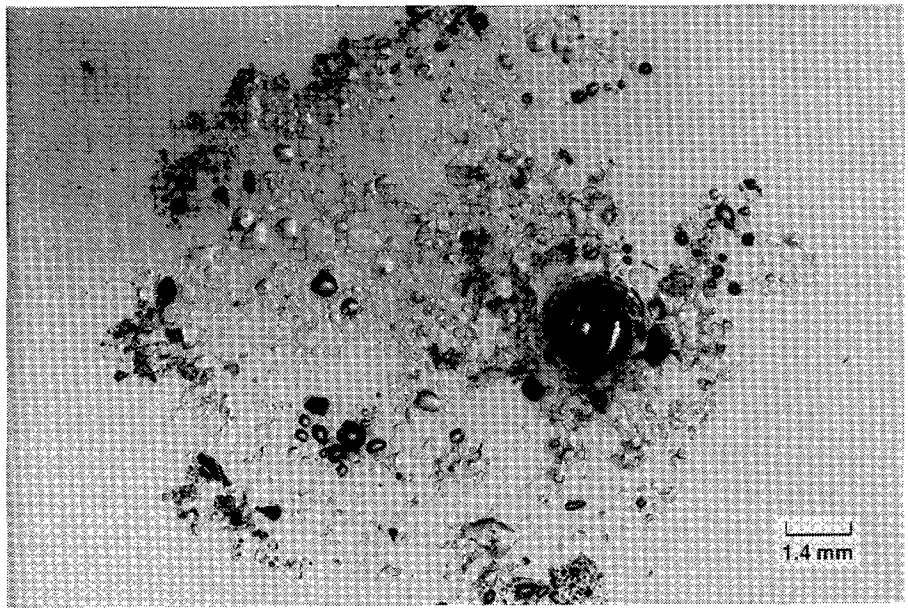
(c)



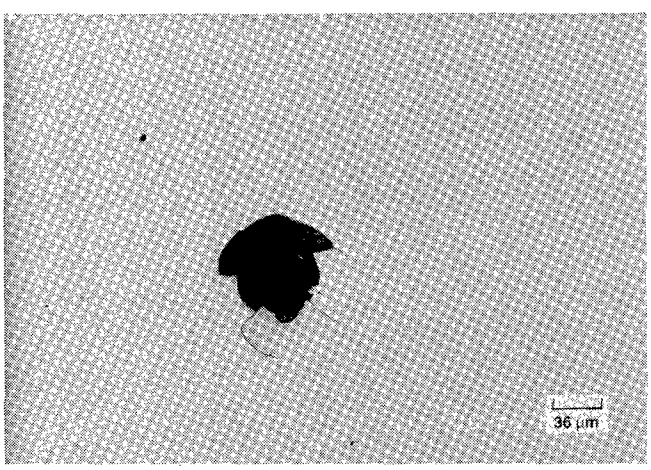
(d)

LANDSCAPE

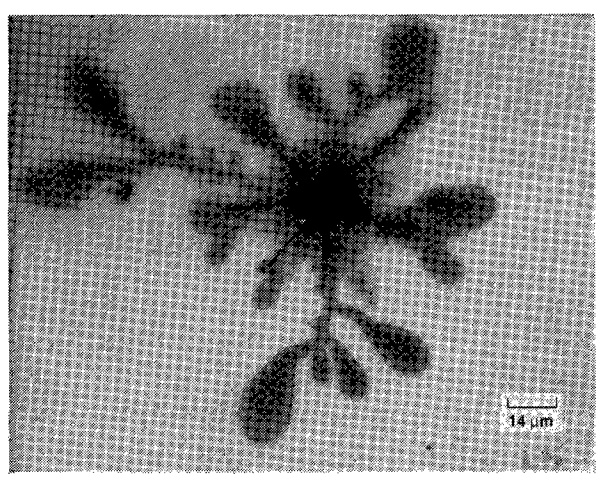
Figure VI-2. Impacts in metals: a) Copper mirror; b) Nickel-coated copper mirror; c) Molybdenum substrate; d) Rhodium foil on aluminum.



(a)



(b)



(c)

Figure VI-3. Impacts in coated molybdenum: (a) Thorium fluoride-coated silver mirror on molybdenum; (b) Alumina/Silicon multilayer coating on molybdenum; (c) ZnS/ThF_4 multilayer on molybdenum.

canister, and, therefore, only saw limited exposure to atomic oxygen. An interesting and unusual reaction zone around a ZnS/ThF_4 multilayer coating on molybdenum is shown in (c). The cause of this reaction zone is not known, but it is not due to a synergistic effect with atomic oxygen since this sample was mounted in the trailing edge canister.

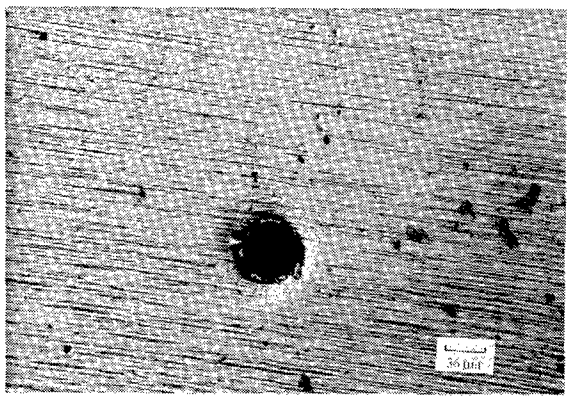
The response of unmounted molybdenum foils to impacts is shown in Figure VI-4. These are oxide-coated molybdenum foils approximately 2 mil thick. The sample shown in (a) has a SiO2 coating while (b) is coated with a proprietary coating, P-273. The radial cracking of the silica layer is evident in (a); however, no such effect is seen in (b). The exit view shown in (c) indicates considerable spall of the metal. The sample shown in (d) is also oxide coated. The coating has also been shocked away around the impact site.

Figure VI-5 illustrates an interesting impact in a piece of tray hardware, the D8 canister aperture plate; the impactor hit the anodized and Teflon-coated aluminum at an oblique angle, producing a large amount of aluminum spatter on the adjacent sample, a zinc selenide IR witness plate. The aluminum spatter on this sample is shown in (b) and (c). These photos clearly illustrate the type and amount of collateral damage that may occur from hypervelocity impacts, especially to optics.

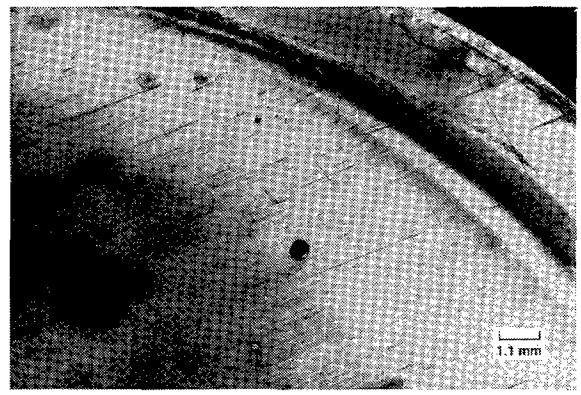
C. Ceramics and Glasses

Figure VI-6 illustrates the response of uncoated 7940 fused silica to hypervelocity impacts. In most cases, the damage is localized; however, radial cracking does occur to a limited extent. Contrary to expectations, the cracks did not propagate a great distance from the impact site. The effect of this damage on optical performance and its long-term effects are largely unknown. Coated fused silica as seen in Figure VI-7 often displays crazing or cracking of the coating in addition to chonchoidal substrate cracking; however, sometimes unusual and extensive propagation of cracks is observed, while infrequently there is only localized damage. In Figure VI-8, more impacts to coated fused silica are shown. For example, (a) depicts the damage to magnesium fluoride coatings on fused silica, consisting of chonchoidal cracking. The coating on all magnesium fluoride-coated fused silica samples was crazed, regardless of the location on LDEF. The laboratory control was crazed as well, indicating that this effect is not related to the space environment but may be due to aging, and/or to processing conditions. The crazing of the coatings did not result in an increase in damage area around the craters. Large damage sites surround two small impacts in another sample (b) composed of a sodium fluoride coating on fused silica. This is no doubt a synergistic effect since the coating has been damaged by exposure to UV and/or atomic oxygen, and it is this damaged layer that has been lost or removed around the impact site.

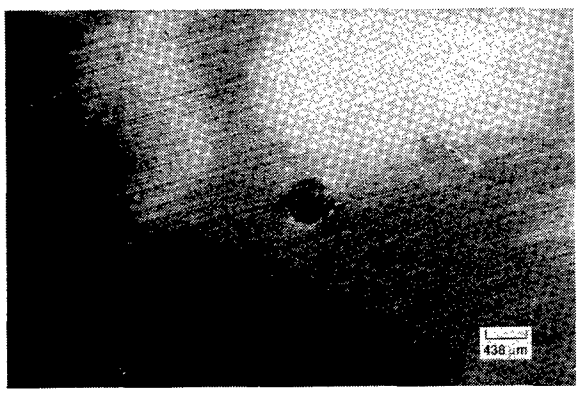
The effect of an impact on a silver-coated, fused-silica, second-surface mirror is shown in Figure VI-9 (a). The impactor produced small, localized damage and no delamination of the coating. Solar cell response to impact phenomena is typical of that shown in Figure VI-9 (b), which indicates some delamination at the impact site and chonchoidal cracking of the substrate. This particular impact is in a gallium arsenide cell. The response of bulk gallium arsenide to this type of impact is illustrated in (c). In this brittle material, the craters were typically small hemispheres surrounded by an irregular-shaped spall zone with many small radiating cracks. This type of damage was common to all electronic materials on the experiment of which the gallium arsenide was just one. None of the impactors perforated any of these materials. Figure VI-9 (d) shows an impact that penetrated a glassy carbon structure with a rhodium coating. The structure is webbed,



(a)



(b)



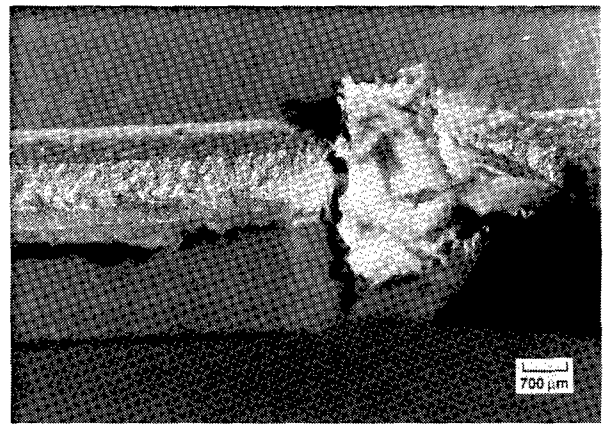
(c)



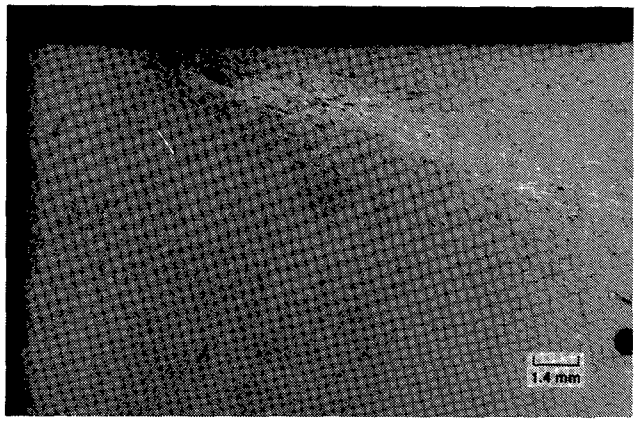
(d)

LANDSCAPE

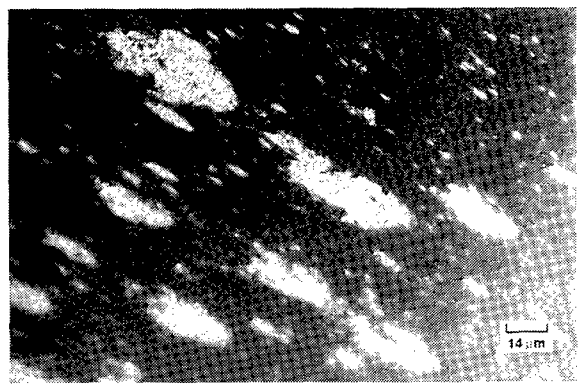
Figure VI-4. Impact perforations in coated molybdenum foils: a) Silica coated; b) P-238 coated; c) exit view of b); d) oxide coated Molybdenum.



(a)



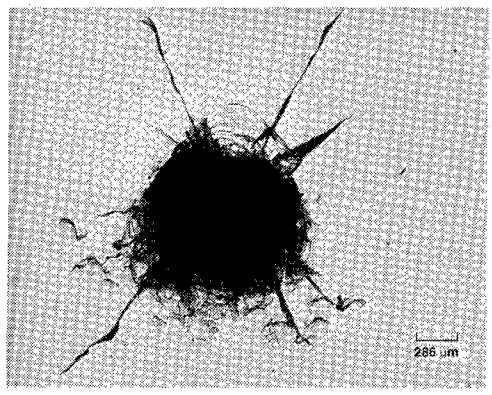
(b)



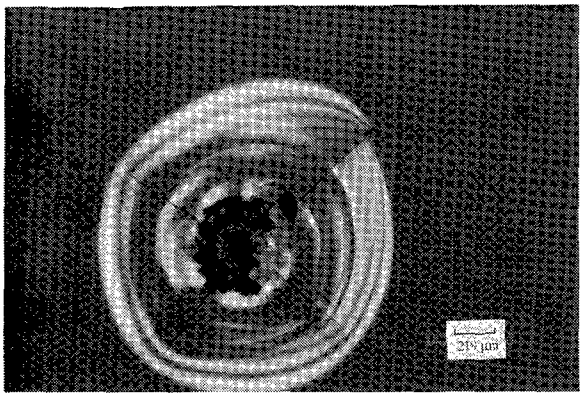
(c)

LANDSCAPE

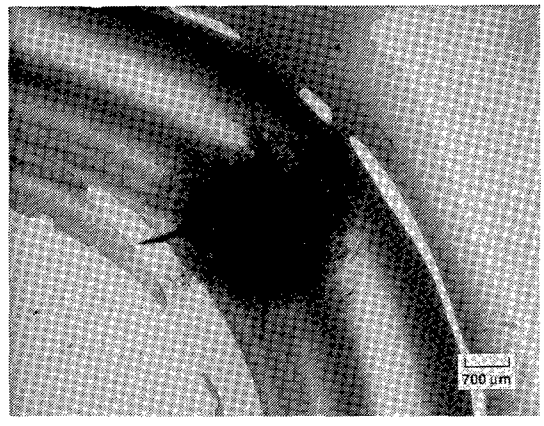
Figure VI-5. Impact damage causing collateral damage to optics



(a)



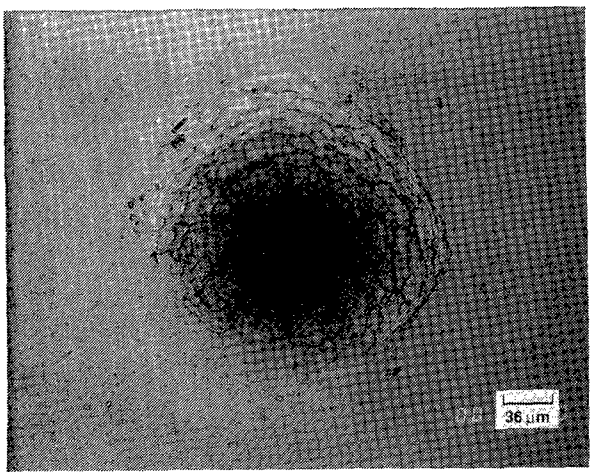
(b)



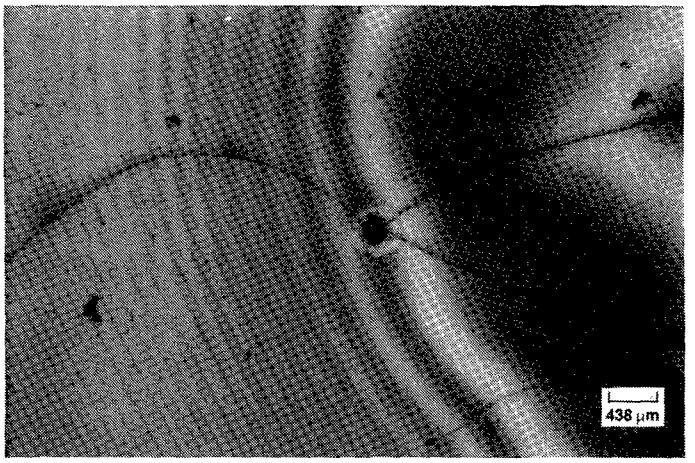
(c)

LANDSCAPE

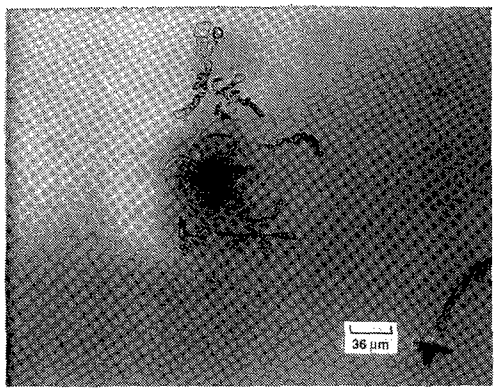
Figure VI-6. Representative impacts in 7940 fused silica substrates.



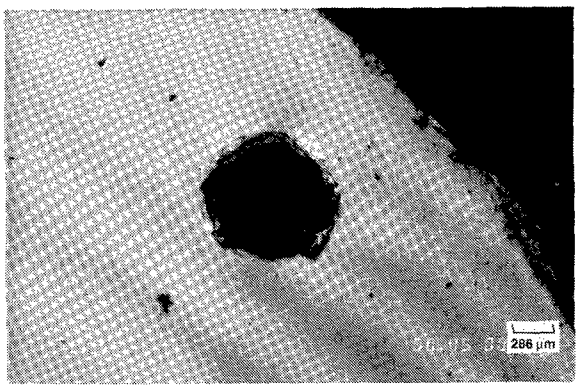
(a)



(b)



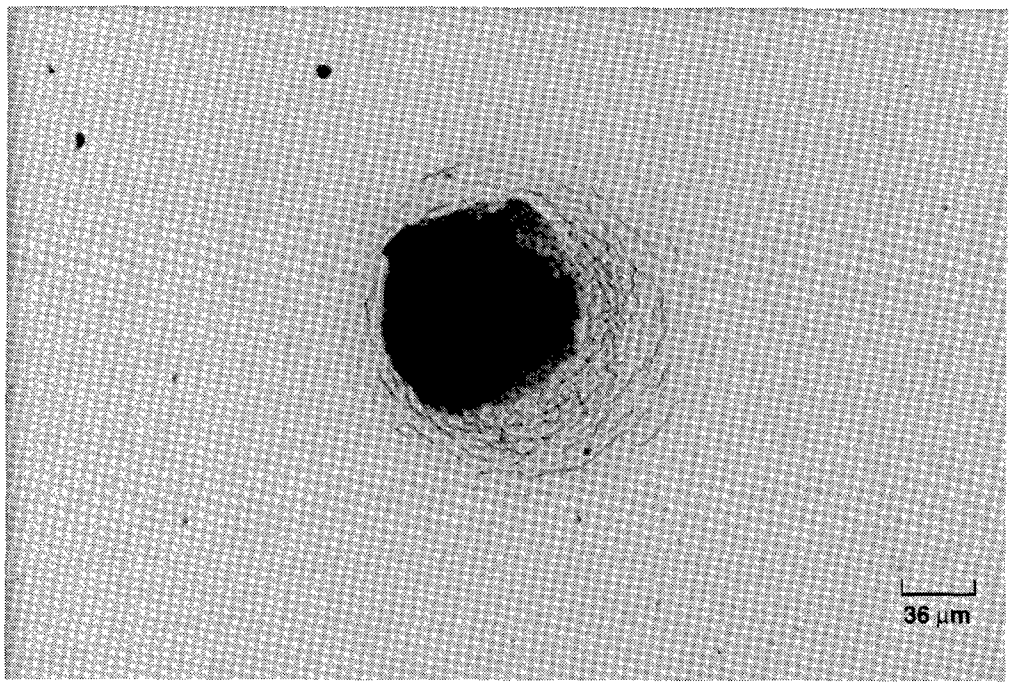
(c)



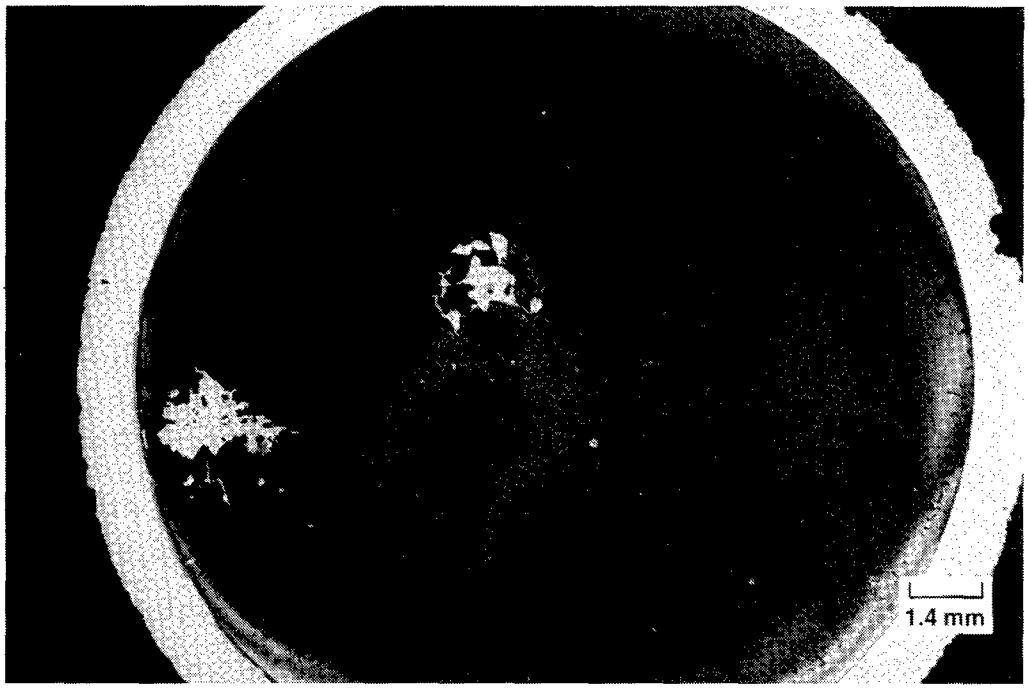
(d)

LANDSCAPE

Figure VI-7. Response of optical coatings on fused silica to hypervelocity impacts. All coatings are proprietary formulations from Optical Coating Laboratories, Inc.



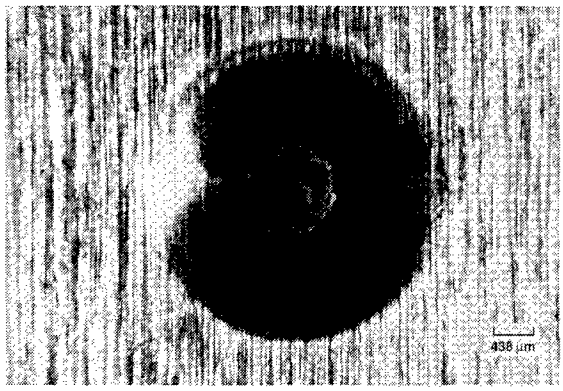
(a)



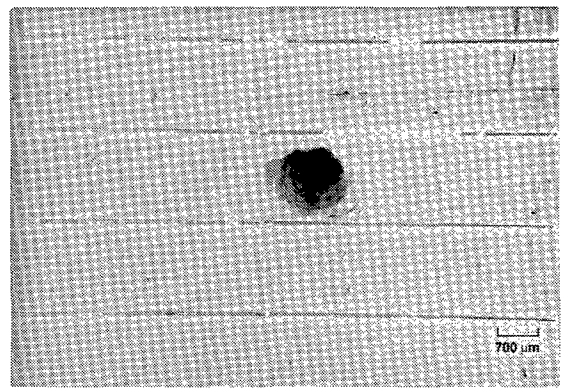
(b)

LANDSCAPE

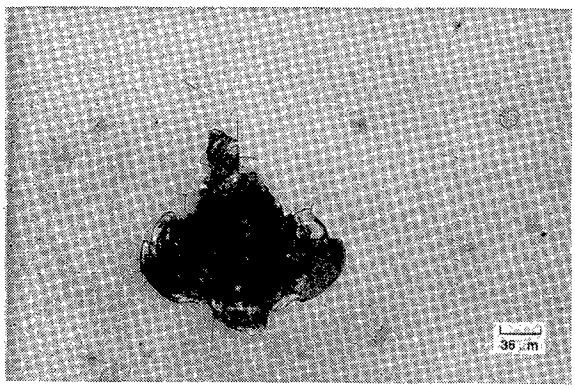
Figure VI-8. Impact damage to coated fused silica. (a) Magnesium fluoride coating; (b) Sodium fluoride coating.



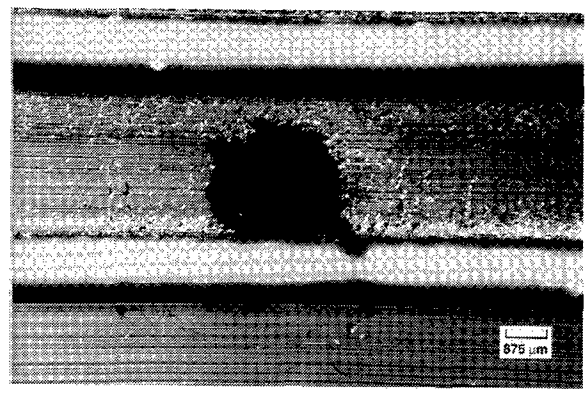
(a)



(b)



(c)



(d)

Figure VI-9. Impacts in ceramics and glasses. a) OCLI second surface mirror (Silver OSR); b) Gallium arsenide solar cell string; c) bulk Gallium arsenide; d) Rhodium coated glassy carbon.

and significant chonchoidal cracking is evident around the site and under the sidewalls (webbs). The glassy carbon is approximately 2 mm thick at the impact site.

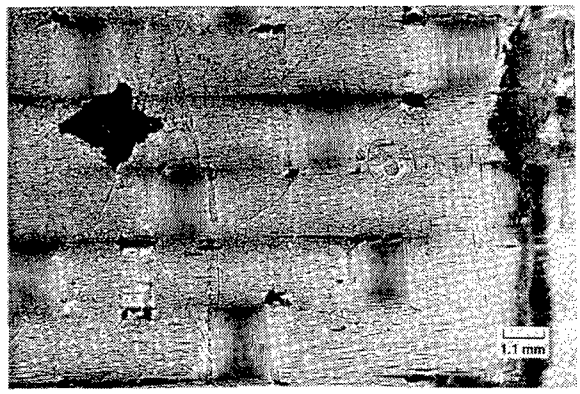
D. Composite Materials

The response of organic matrix composites, primarily graphite epoxy, to hypervelocity impacts is represented by Figure VI-10. The damage to such materials is generally localized, with some chipping of the matrix in the outer layers of the composite at the crater site. In all cases examined, no perforations were observed. This may be a result of chance or the result of many layers of the composite acting as bumpers to slow down and vaporize the impactor. Metal matrix composites, such as graphite/aluminum, respond differently than the organic matrix composites, and behave much the same as metals to impact phenomenology as shown in Figure VI-11.

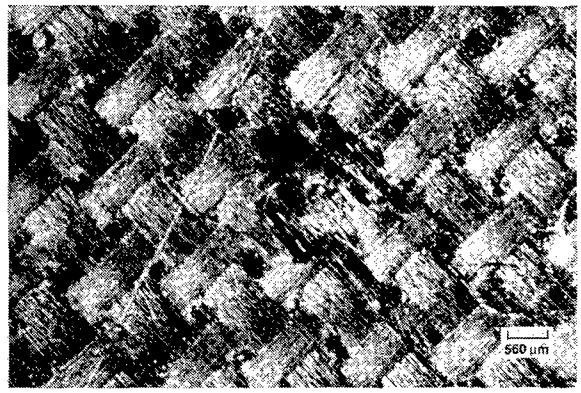
E. Polymers

Impacts in polymeric materials produced interesting synergistic phenomena primarily due to the exposure of the materials to atomic oxygen on the leading edge and UV on the trailing edge. Figure VI-12 (b) shows the damage around an impact crater in a sample of black RTV 602 located on the trailing edge. The embrittlement caused by UV exposure has produced a large degree of cracking in the material and at the impact site. In comparison, Figure VI-12 (a) shows that an identical sample of this material located on the leading edge displays similar cracking of the material, but, in addition, there is radial, star-type cracking at the impact site due to reaction of atomic oxygen with the surface of the silicone, which produced a glassy surface layer of SiO_2. The response of this surface layer to hypervelocity impacts is very similar to that observed with glasses such as silica. The larger degree of radial cracking in this sample relative to bulk fused silica may be due to the greater elastic response of the bulk RTV relative to the outer glassy layer due to the thin nature of this SiO_2 layer. Polymeric films that were not metallized did not exhibit unusual impact phenomenolgy or synergistic effects; rather they showed typical circular perforations that are assumed to be only slightly larger than the impactor. An impact site in a Tefzel strip is shown in (c). A plastic-metal laminate that received a perforating hit is shown in (d). This site displays the classic raised lip as a result of the melt and flow of the aluminum and vaporization of the polymer front surface.

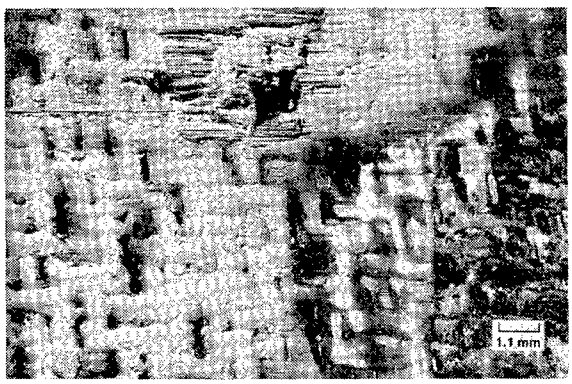
Metallized polymer films, however, did indicate some synergistic effects, the most significant being atomic oxygen oxidation of the backside reflective silver layer of silver-teflon. This effect produced a black spot resembling tarnish around the impact site. This is illustrated clearly in Figure VI-13(a). Note also the delamination of the Teflon from the silver layer at the impact site. This was also quite common to this material. Another perforation in (b) shows only small amounts of tarnish at the edges of the crater. Impacts in aluminized Kapton are shown from the backside of the Kapton strip in (c), one being a standard perforation and the other indicating melt and delamination of the aluminum around the impact site. An impact in a front surface aluminized Kapton sample is shown in (d).



(a)



(b)



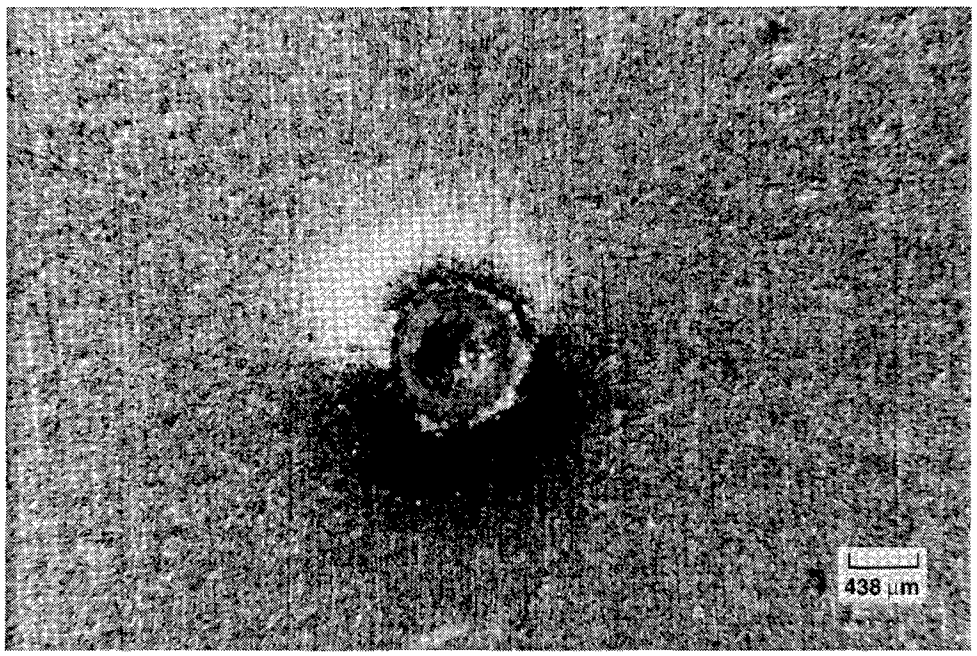
(c)



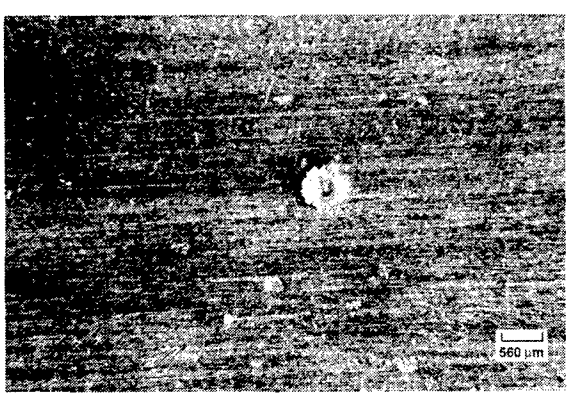
(d)

LANDSCAPE

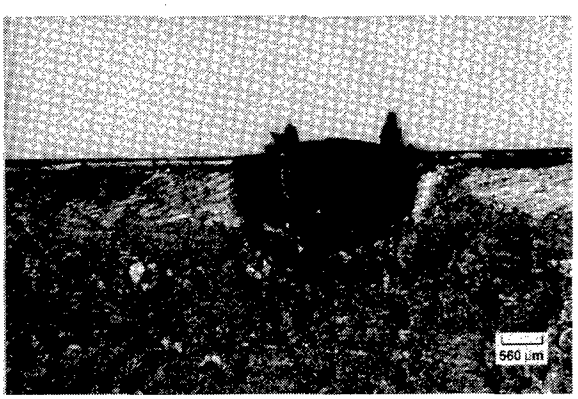
Figure VI-10. Representative impacts in organic matrix composites



(a)

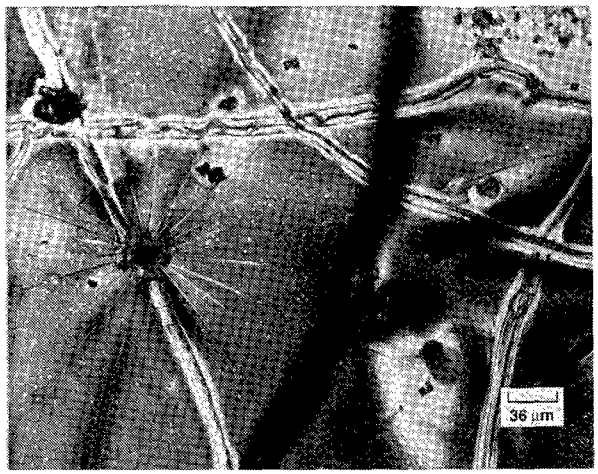


(b)

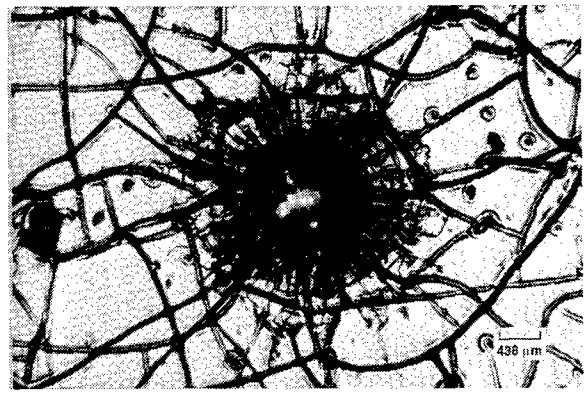


(c)

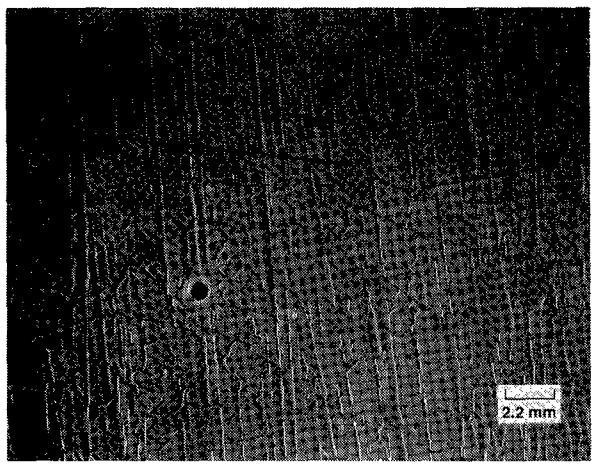
Figure VI-11. Representative impacts in metal matrix composites



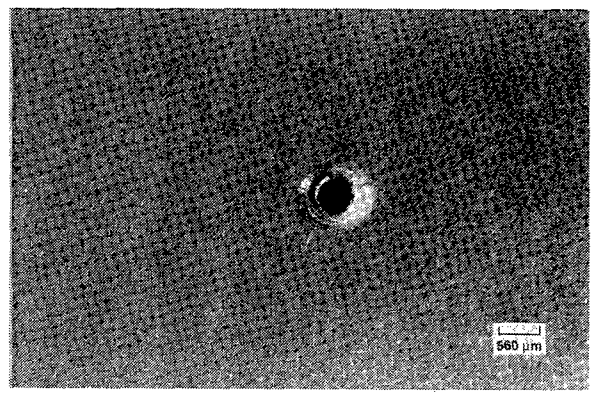
(a)



(b)

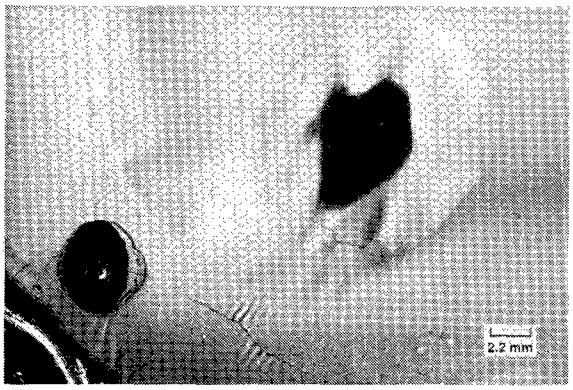


(c)

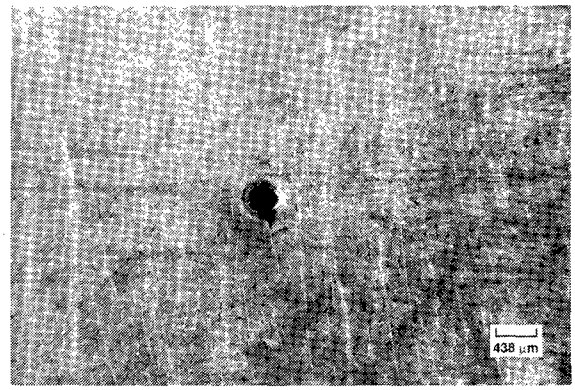


(d)

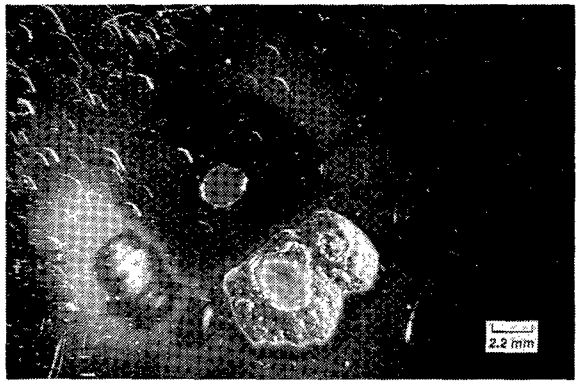
Figure VI-12. Impacts in polymeric materials. a) leading-edge black RTV 602; b) trailing-edge black RTV 602; c) Tefzel strip; d) plastic-metal laminate.



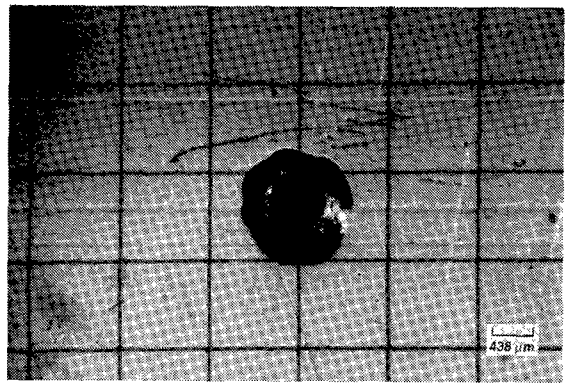
(a)



(b)



(c)



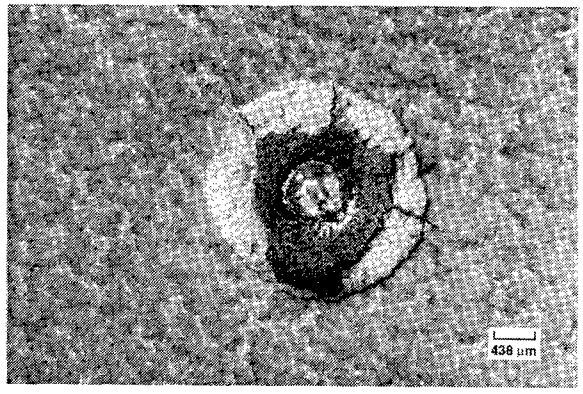
(d)

LANDSCAPE

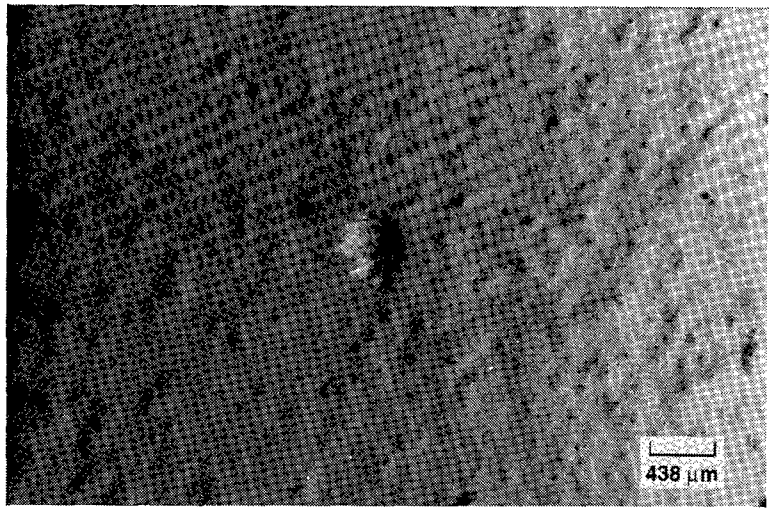
Figure VI-13. Impacts in metallized polymer films. a) and b) Silver-Teflon; c) and d) aluminized Kapton

In addition to the examples of impact phenomenology of white thermal control paints already presented in this report, Figure VI-14 presents three examples of hypervelocity hits in other thermal control paints. In (a), Sperex 101, a silicone-based paint, on aluminum indicates melt and flow of both the paint and the substrate, which, for unknown reasons, was generally not seen with the S13GLO. A silicate-based paint, Z-93, on aluminum shown in (b) indicates localized damage with no melt or flow of either paint or substrate. Lastly, in (c), Chemglaze Z-306, a black thermal-control paint, sprayed over a brown primer on graphite epoxy is shown indicating more the response of the substrate rather than the paint.

(a)



(b)



(c)

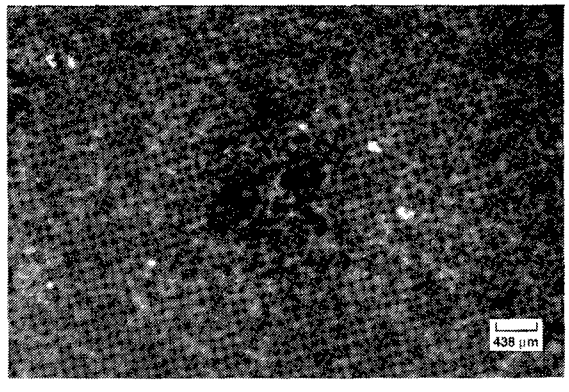


Figure VI-14. Impacts in miscellaneous paints: a) Sperex 101; b) IITRI Z-93; c) Chemglaze Z-306.

VII. COMPARISON TO CURRENT MODELS

The data from each surface was compared to currently accepted NASA models for space debris and micrometeoroids. The models used for the analysis are the Orbital Debris Environment for Spacecraft of Kessler[12] and the Meteoroid Environment Model of Cour-Palais[19]. For the D8 surfaces, these two models, as well as their sum, were used for a comparison to the data. The D4 surfaces are compared only to the meteoroid model since the debris model indicates several orders of magnitudes smaller fluxes relative to meteoroids for this surface of LDEF. The obvious rationale for this is that due to the three-axis stabilization of LDEF, the leading edge should see both meteoroids and space debris, while, simplistically, the trailing edge will only be hit by meteoroids. This is obviously an oversimplification since other LDEF data has indicated the importance of trailing edge impacts from space debris in elliptical orbits.[8,9]

The Kessler debris model[12] gives data on impactor hits per area versus impactor diameter. However, the data from this study, and LDEF in general, is in the form of impactor hits per area versus crater diameter. It therefore becomes necessary to relate impactor diameter to impactor crater diameter to translate these models so that this data can be compared to such predictions. One method of simple conversion is based on the fact that for a given impactor size, the greater the impactor speed and the greater the impactor density, the larger will be the impactor crater. Thus, a scaling law can be applied to relate the sizes of measured craters to the sizes of the impactors producing them. This simple scaling method, known as the energy rule, involves a cube-root law of density ratios of the impactor to the target surface, and uses a two-thirds power law for the collision velocity. The expression is normalized with a constant obtained from known terrestrial impact data of aluminum into aluminum. The aluminum/aluminum constant is fairly appropriate for this and other LDEF data since the vast majority of impacts were into aluminum or coated-aluminum substrates. The equation[20] is:

$$\frac{dc}{dp} = [k(P_p/P_t)^{1/3}]V^{2/3} ,$$

where P_p is the particle density, P_t is the target density, V is the collision speed, and k is a normalization constant for Al/Al impacts. Other scaling laws could be used and differ in the exponents for density and/or velocity. However, since all of these exponents are less than unity, the conversion of impactor diameters to crater diameters is relatively insensitive to changes in the scaling law.

For the Cour-Palais meteoroid model, a similar conversion must be made. This correction makes use of the NASA-recommended micrometeoroid density to arrive at the ratio of crater size to impactor size.[19] Both curves derived from these equations applied to these models were supplied by members of the LDEF Meteoroid and Debris Special Investigation Group.[21]

This data derived from the models is then plotted as crater density (in craters/cm^2) as a function of crater diameter (cm). The plots are log-log and are integral sums. That is, a point on the curve represents the number density of craters of a specific size and larger. Meteoroid and debris models have been run for every surface of LDEF.[20] However, we are only interested in the results for D4 and D8 in this study. The derived curves for these two locations on LDEF are shown in Figures VII-1 and VII-2. The data obtained in this study on crater counts are presented in Figures VII-3 through VII-11. Figure VII-3 is a plot of the data

for the largest area surface with the highest number of counts, the D8 EPDS sunshield. Recall that this was a friable surface and should show evidence of more impacts than other surfaces. This data is overlaid on the two models, and in Figure VII-4 it is overlaid on a line representing the sum of these models. Similar plots for all D8 surfaces and their comparison to the models and their sums are given in Figures VII-5 and VII-6, respectively. Similar graphs were made for the D4 surfaces as well. Figures VII-7 and VII-8 present this data. As is evident from Figure VII-2, the contribution due to debris on D4 is vanishingly small, so that no sum graphs were necessary.

Crater densities on the eight panels surveyed were reported in craters/cm^2. The standard deviation of these measurements was calculated using Poisson statistics. Error calculation in this manner was valid since the crater distribution on the panels satisfied the basic Bernoulli conditions: namely a large number of events (impacts) distributed randomly over a large surface area. The standard deviation in the crater density would follow as the square root of the actual crater count divided by the surface area. Error bars in the accompanying figures are $\pm$ one standard deviation.

For the D8 surfaces (leading edge), the general trend of the data is more in line with the meteoroid model as opposed to the debris model. While the sum of these models gives as good or better fit to the data in the intermediate range, the rollover of the crater population below roughly 100 microns is not predicted by the debris model. For the D4 surfaces (trailing edge), the correlation of the data to the meteoroid model prediction is better; however, the same rolloff of the crater number density at small diameters is observed to be more pronounced than predicted by the model. This may be a consequence of small particles impacting primarily in the anodic oxide layer, which is harder and more dense than the aluminum substrate. This would produce correspondingly smaller craters and cause a leftward shift to the data points.

Inspection of the curves for the D8 surfaces reveals some additional trends. The anodized aluminum panels on the leading edge give nearly identical fits to the model, with marked deviation from the prediction lines at diameters of 300 microns and smaller. This deviation amounts to a factor of about 2 for craters with diameters in the 100-micron range. In contrast, the two painted panels gave very different distributions, presumably due to the different materials used in the paints (silicone vs. urethane), as well as the high degree of surface roughness present in the S13GLO paint. Generally, the models give over predictions when compared to the data obtained for this surface. For the EPDS sunshield, the correlation appears very good, except below 50 microns. The disturbing point about the D8 surfaces is the slope of the curves relative to the model predictions at large diameters. While statistically the data does not indicate this with certainty, the trend is obvious and may indicate a divergence between theory and experimental data.

For the D4 surfaces, the correlation between theory and experiment is much better. Examples of excellent correlation are provided by the anodized aluminum panels. The painted surfaces, however, still have a more pronounced rollover below 100 microns.

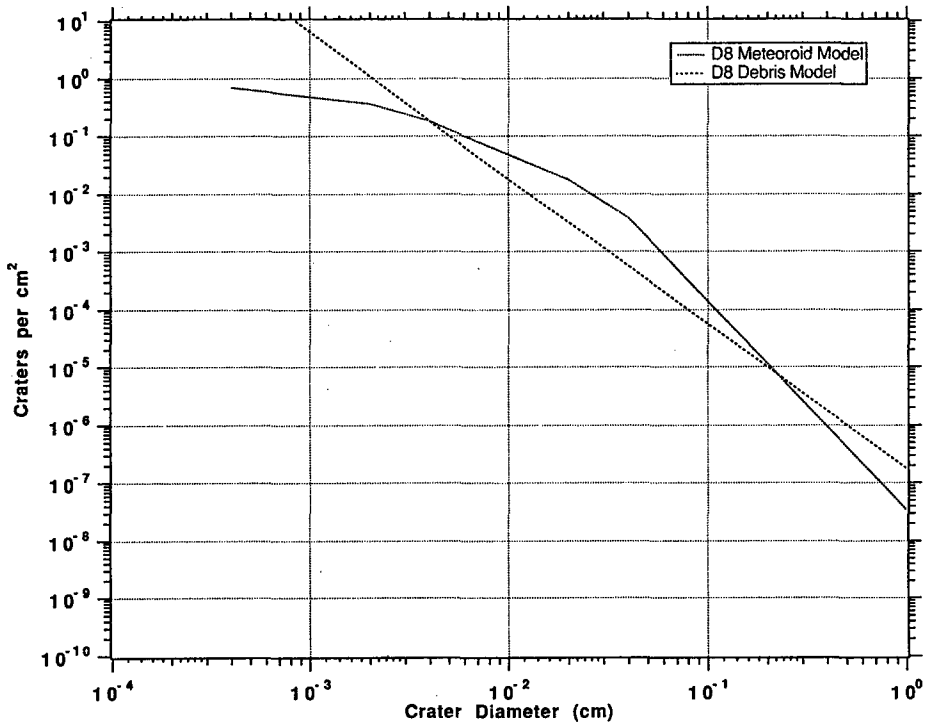


Figure VII-1. Meteoroid and Debris model predictions for LDEF row 8.*

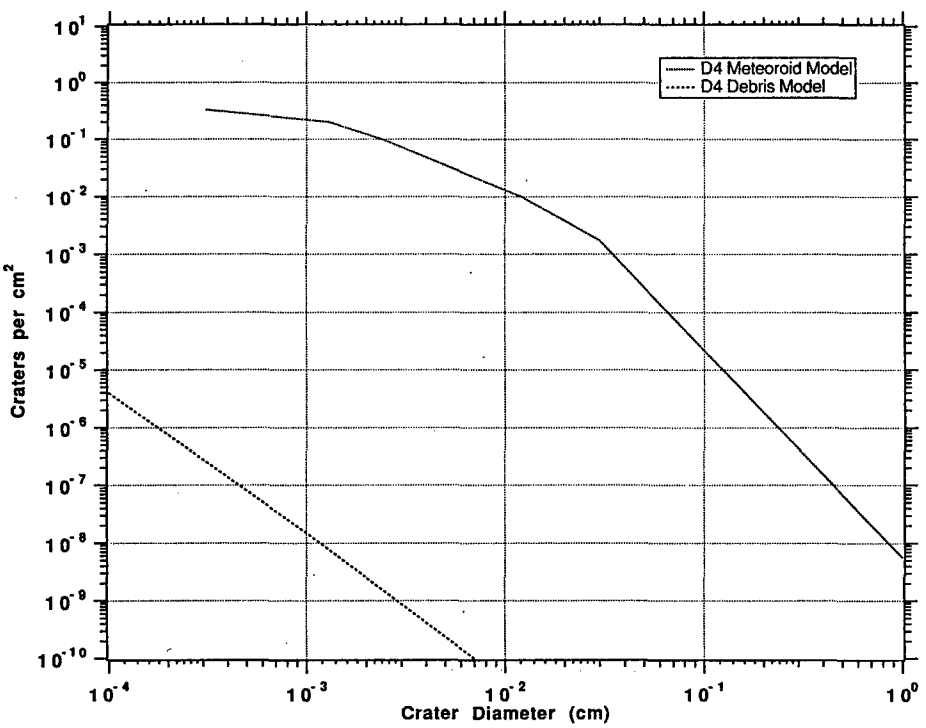


Figure VII-2. Meteoroid and Debris model predictions for LDEF row 4.*

*D. R. Atkinson, private communication.

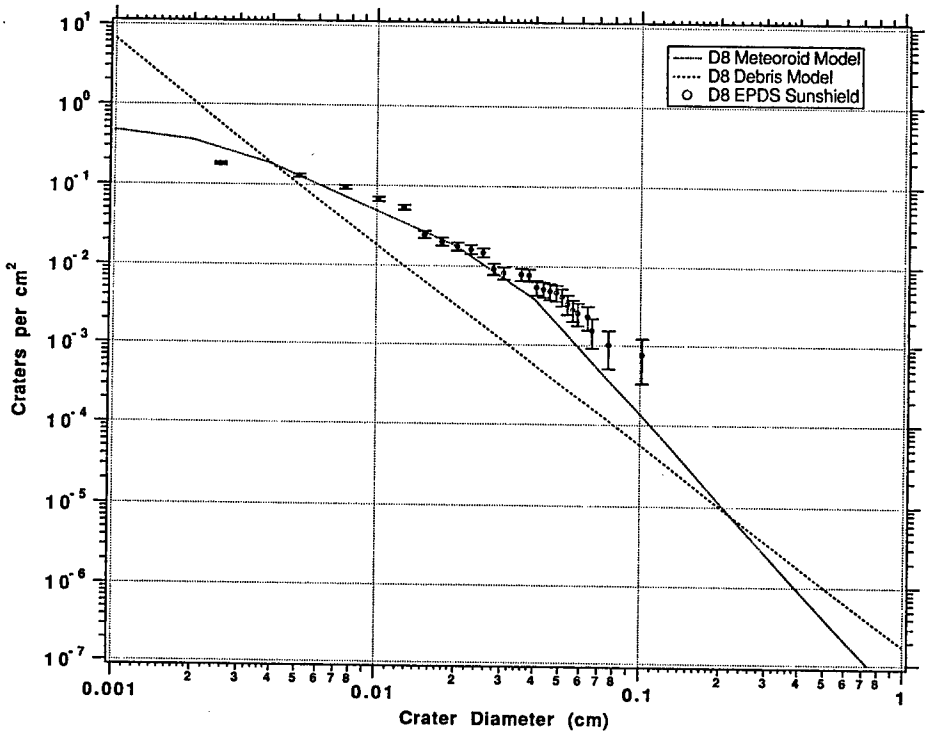


Figure VII-3. D8 EPDS sunshield data compared to meteoroid/debris models.

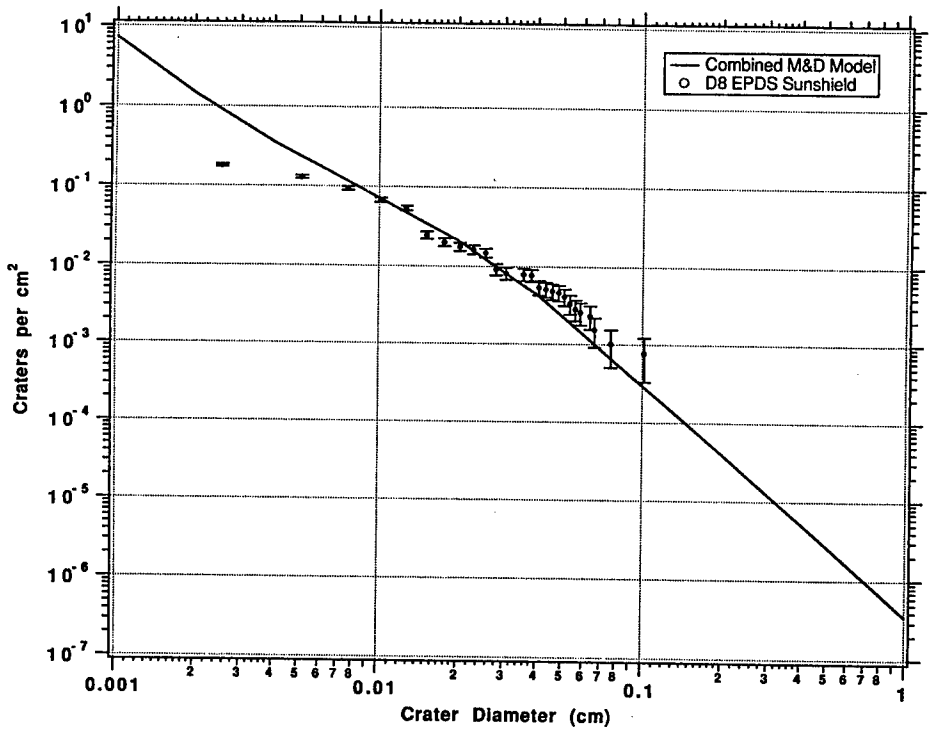


Figure VII-4. D8 EPDS sunshield data compared to the sum of meteoroid and debris models.

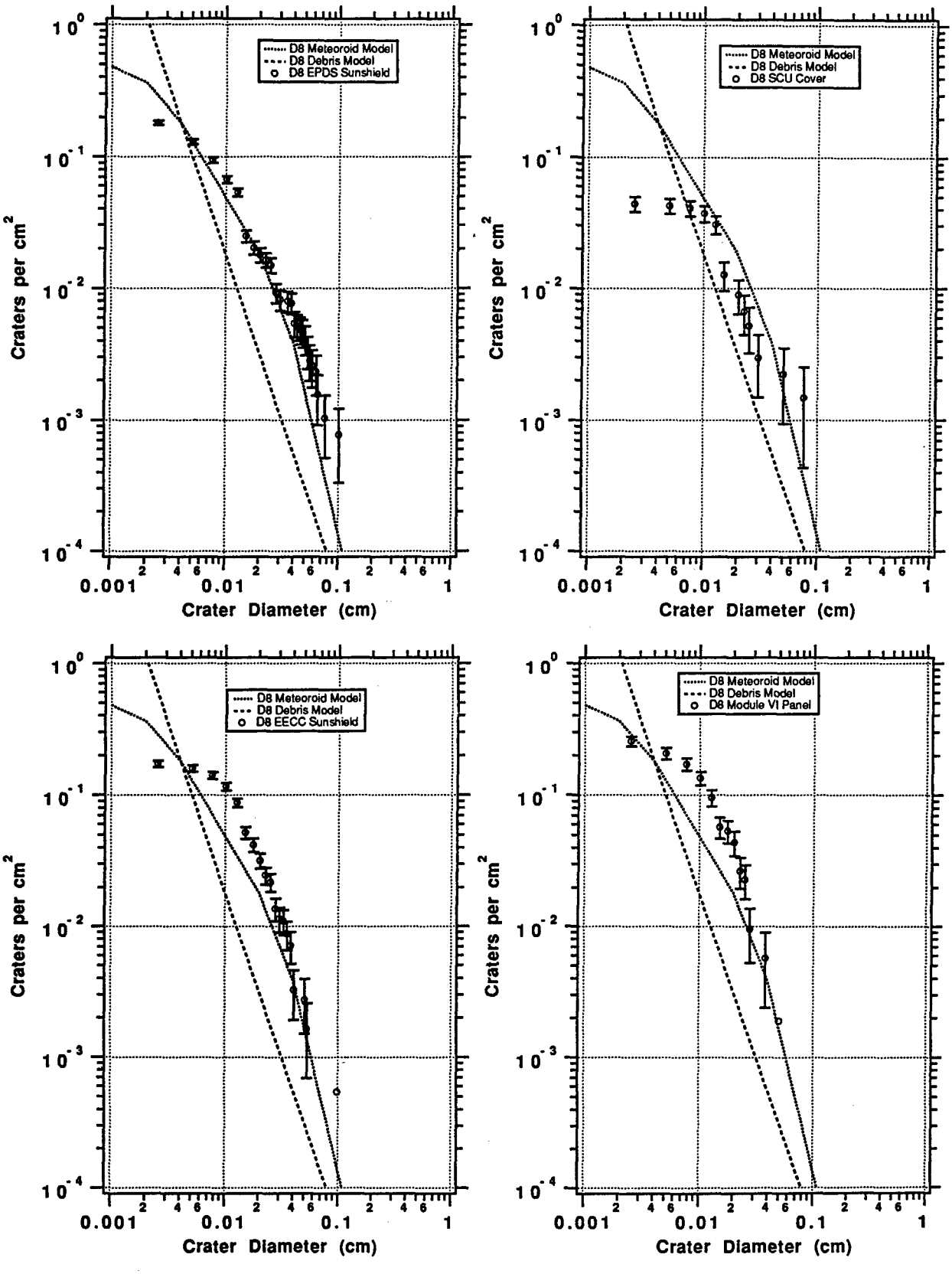


Figure VII-5. Graphs for each D8 surface compared to models.

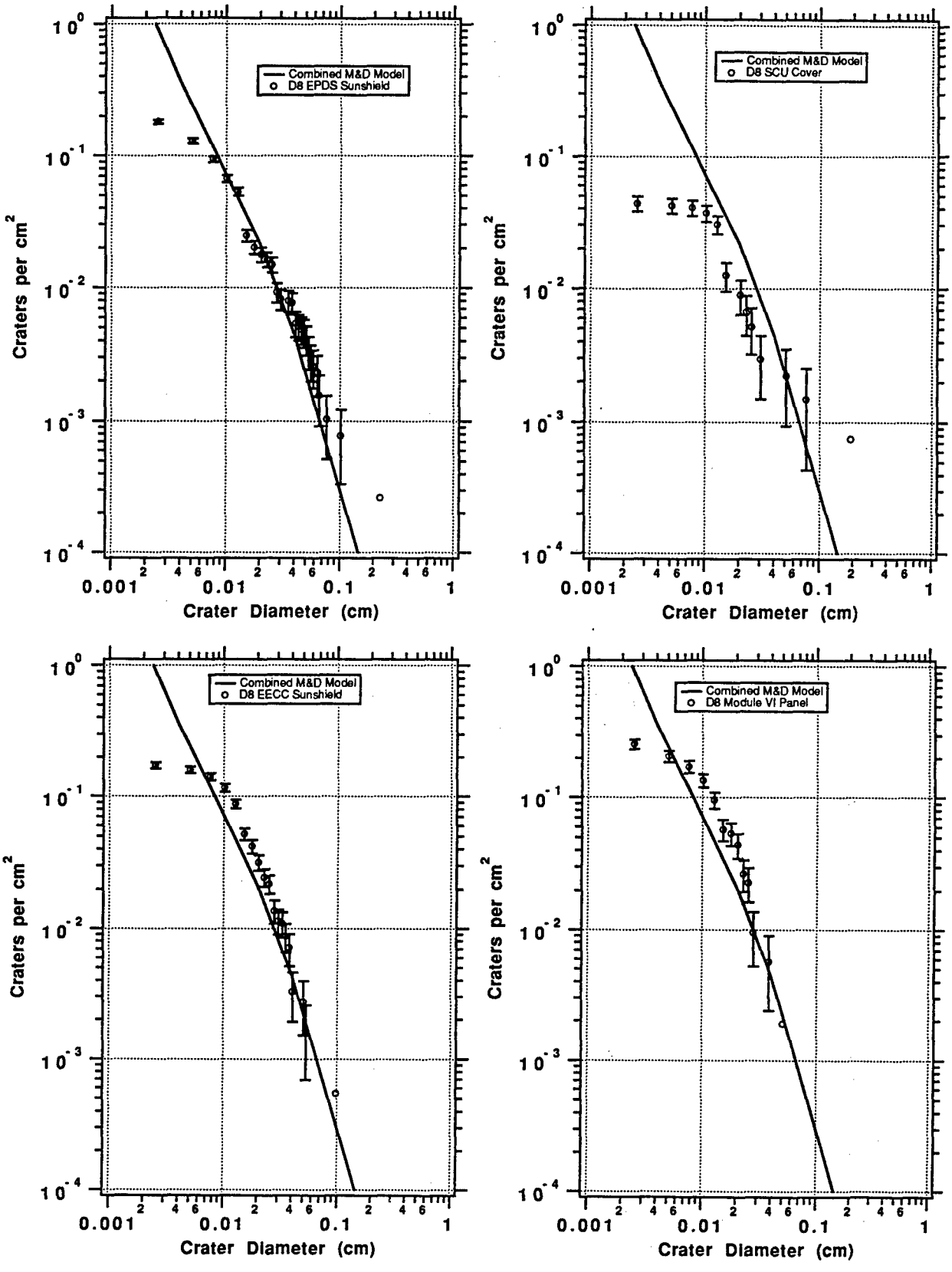
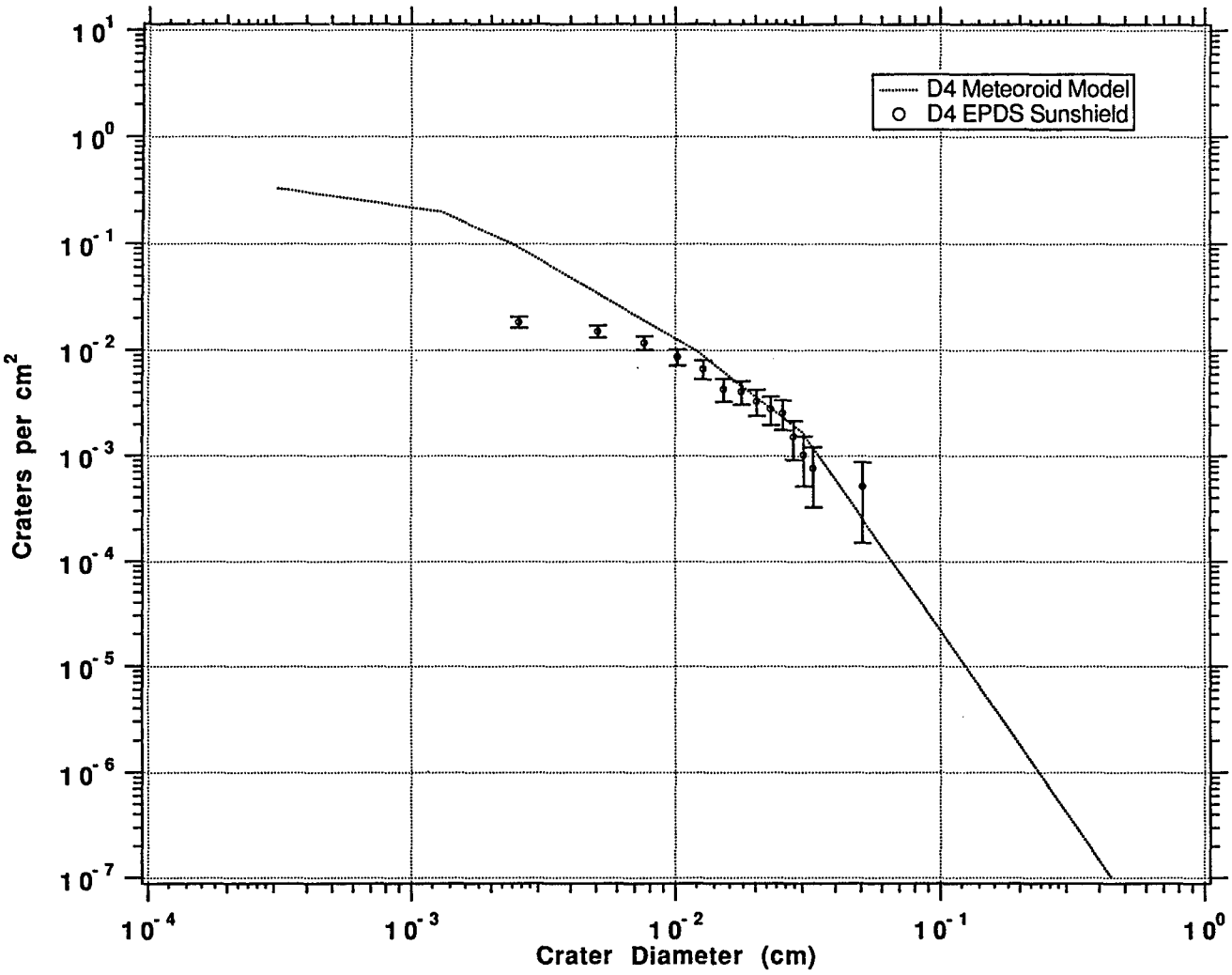


Figure VII-6. Graphs of each D8 surface compared to models' sums.



LANDSCAPE

Figure VII-7. D4 EPDS data compared to meteoroid model.

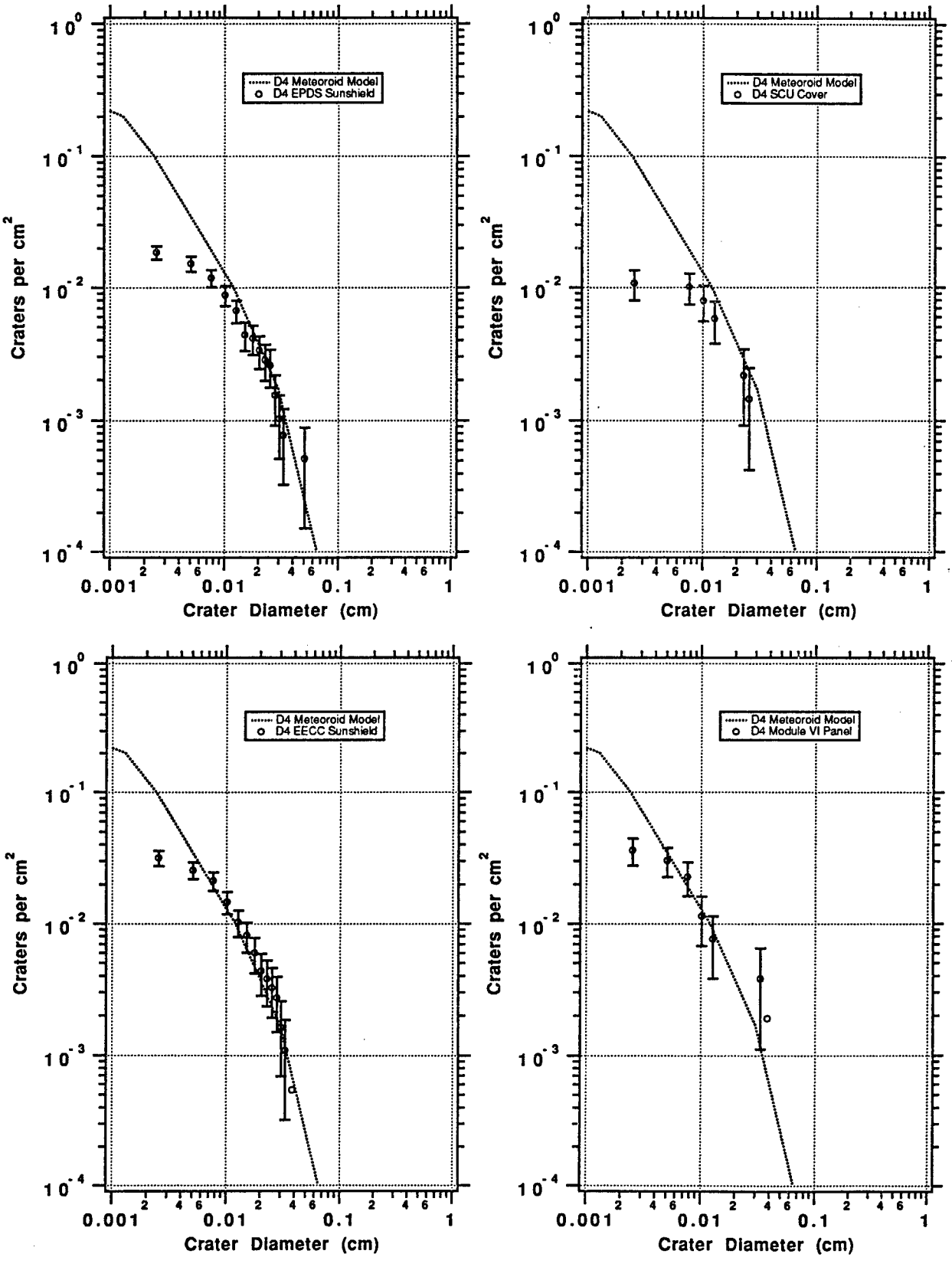


Figure VII-8. Graphs of each D4 surface compared to model.

VIII. CONCLUSIONS

From the information and analysis presented in this and other reports, it becomes obvious that space debris, and to a lesser extent micrometeoroids, are increasing concerns for space systems reliability. Models that describe these environments have been developed and appear to do an adequate job for general predictions. Ground simulation facilities have also been developed that allow research in the area of material response to hypervelocity impact phenomena. Our experimental observations of the general response to these impacts of various material types, such as brittle or ductile materials, compare well to other experimental data both from flight experiments and ground simulations. While the damage to materials from hypervelocity impact phenomena as observed and documented on this experiment is not catastrophic, the effects of these phenomena on mission performance, especially for optical systems, needs to be studied further to allow better quantification of their associated risks.

Unique to LDEF is the observation of synergistic phenomena associated with micrometeoroid and debris impacts, especially due to atomic oxygen exposure. Such phenomena are among the more interesting aspects of LDEF, and they are beginning to become understood; however, more work is needed to fully understand, model, and simulate these events.

From this work, it is concluded that current models for space debris and micrometeoroids have limited accuracy over wide ranges of impactor diameters. Whether or not this limited accuracy is good enough for predicting design lifetimes of 15 to 30 years is still a point of contention. Clearly, the data from this study correlates with predictions better for the D4 surfaces as opposed to the D8 surfaces, which indicates that there are difficulties associated with prediction of ram impactor densities from either separate or summed models. There is a marked tendency to over predict the impactor density with diameters smaller than 0.01 cm (100 microns). While this is not a serious problem from a spacecraft designer's perspective, it may indicate a basic problem with the current models.

From the data in this study, it would appear that the number density of small impactors levels off instead of increasing as predicted by the models. Higher populations of small-diameter impactors were observed on the Interplanetary Dust Experiment, but this may be due to non-steady-state fluxes seen during the first year of the mission since the active data indicates a higher impact count than that determined passively after LDEF recovery.[9] Except for the S13GLO painted surfaces, which were quite rough, the surface texture of the panels surveyed was smooth enough to allow accurate counts of the number density of impacts, and, therefore, we believe the leveling-off of impactor density is real and not an artifact. Clearly, the response of painted and coated aluminum substrates differs from that of uncoated aluminum, and this is not taken into account by current models. This contributes to the observed rollover at small diameters.

A potentially more serious discrepancy with accepted models occurs at larger diameter impacts where the slope of the curves for the experimental data and those for the models visibly diverges and thus indicates a tendency towards underprediction. In some cases, the number of craters is statistically quite small, and, therefore, this conclusion needs to be approached with caution. However, we believe that this points to a need to update these models in the light of the singularly enormous amount of data obtained from LDEF.

Acknowledgments

The authors wish to acknowledge the contributions of the following individuals: J. H. Rheinheimer, W. K. Stuckey, H. K. A. Kan, V. Chobotov, D. R. Atkinson, C. G. Simon, W. H. Kinard, T. H. See, L. Fishman, and R. A. Brose. We would also like to thank Col. M. Obal of the Strategic Defense Initiative Organization SDIO/TNI, Materials and Structures, and Lt. M. Jones, W. Ward and K. Davidson of Wright Laboratory, Materials Directorate for funding a portion of this work.

REFERENCES

1. T. H. See, M. A. Allbrooks, D. R. Atkinson, C. G. Simon and M. Zolensky, "Meteoroid and Debris Impact Features Documented on the Long Duration Exposure Facility, A Preliminary Report," *Planetary Science Branch Publication #84*, JSC #24608, August 1990.

2. For a description of LDEF and its experiments and environments see:

   R. L. O'Neal and E. B. Lightner, "Long Duration Exposure Facility-- A General Overview", LDEF-- 69 Months in Space First Post-Retrieval Symposium, NASA Conference Publication 3134 1992.

   W. H. Kinard and G. D. Martin, "Long Duration Exposure Facility (LDEF) Space Environments Overview", ibid.

3. D. H. Humes, "Large Craters on the Meteoroid and Space Debris Impact Experiment," ibid.

4. J. C. Mandeville and J. Borg, "Study of Dust Particles On Board LDEF, The Frecopa Experiments AO138-1 and AO138-2," ibid.

5. M. Finkenor, "Meteoroid and Debris Impacts on MSFC LDEF Experiments," ibid.

6. J. M. McDonnell and T. J. Stevenson, "Hypervelocity Impact Microfoil Perforations in the LEO Space Environment (LDEF, MAP AO023 Experiment)," ibid.

7. T. H. See, F. Horz, M. E. Zolensky, M. K. Allbrooks, D. R. Atkinson, and C. G. Simon, "Meteoroid and Debris Special Investigation Group Preliminary Results: Size Frequency Distribution and Spatial Density of Large Impact Features on LDEF," ibid.

8. F. Horz, R. P. Bernhard, J. Warren, T. H. See, D. E. Brownlee, M. R. Lawrence, S. Messenger and R. B. Peterson, "Preliminary Analysis of LDEF Experiment A0187-1: Chemistry of Micrometeoroids Experiment," ibid.

9. J. D. Mulholland, S. F. Singer, J. P. Oliver, J. L. Weinberg, W. J. Crooke, N. L. Montague, J. J. Wortman, P. L. Kassel and W. H. Kinard, "IDE Spatio-Temporal Impact Fluxes and High Time Resolution Studies of Multi-Impact Events and Long-Lived Debris Clouds," ibid.

10. C. G. Simon, J. L. Hunter, J. J. Wortman, and D. P. Griffis, "Ion Microprobe Elemental Analysis on Interplanetary Dust Experiment Sensor Surfaces," ibid.

11. H. A. Zook, "Deriving the Velocity Distribution of Meteoroids From the Measured Meteoroid Impact Directionality on the Various LDEF Surfaces," ibid.

12. D. J. Kessler, R. C. Reynolds, and P. D. Anz-Meador, "Orbital Debris Environment for Spacecraft Designed to Operate in Low Earth Orbit", *NASA -TM-100471*, September 1, 1988.

13. H. A. Zook, "Flux Versus Direction of Impacts on LDEF by Meteoroids and Orbital Debris," *Lunar and Planetary Science XXI*, 1990.

14. H. A. Zook, "The Velocity Distribution and Angular Directionality of Meteoroids that Impact on an Earth-Orbiting Satellite," *Lunar and Planetary Science Conference XVII Abstracts*, 1138-1139, 1987.

15. J. E. Erickson, "Velocity Distribution of Sporadic Photographic Meteors," *Journal of Geophysical Research, vol. 7, no. 12, 3721-3726, 1968.*

16. P. N. Peters and J. C. Gregory, "Pinhole Cameras as Sensors for Atomic Oxygen in Orbit; Application to Attitude Determination of LDEF", ibid.

17. M. J. Meshishnek, S. R. Gyetyay, and C. H. Jaggers, "Long Duration Exposure Facility Experiment M0003 Deintegration/ Findings and Impacts", *NASA Conference Publication 3134*, Part 2, 1073 1992.

18. S. R. Gyetvay, H. K. A. Kan, M. J. Meshishnek and J. M. Coggi, *M0003 Data Base Guide Book*, The Aerospace Corporation .

19. B. G. Cour-Palais et al., "Meteoroid Environment Model - 1969 (Near Earth to Lunar Surface)", *NASA SP-8013*, March 1969.

20. D. Atkinson, A Watts, and L. Crowell, "Spacecraft Microparticle Impact Flux Definition", UCRL-CR-108788, August 30, 1991.

DERIVATION OF PARTICULATE DIRECTIONAL INFORMATION FROM ANALYSIS OF ELLIPTICAL IMPACT CRATERS ON LDEF

P.J. Newman, N. Mackay, S.P. Deshpande, S.F. Green and J.A.M. McDonnell
Unit for Space Sciences
Physics Laboratory
University of Kent
Canterbury
Kent CT2 7NR, U.K.
Phone: [44] (227) 459616 Fax: [44] (227) 762616

SUMMARY

The Long Duration Exposure Facility provided a gravity gradient stabilised platform which allowed limited directional information to be derived from particle impact experiments. The morphology of impact craters on semi-infinite materials contains information which may be used to determine the direction of impact much more accurately. We demonstrate the applicability of this technique and present preliminary results of measurements from LDEF and modelling of interplanetary dust and space debris.

1 INTRODUCTION

The Long Duration Exposure Facility (LDEF) was retrieved in January 1990 after 69 months exposure to the Low Earth Orbit (LEO) space environment. In addition to the many experiments specifically designed to detect impacting dust particles of natural and terrestrial origin, any external surface of the spacecraft was exposed to potential damage from which particle properties may be determined.

LDEF was a gravity gradient stabilised, 12-sided cylinder with its long axis pointed approximately towards the Earth. One face (denoted East, Ram, or 9) was constantly pointed towards the spacecraft's orbital velocity vector (figure 1 illustrates the geometry). Definition of the exact orientation, deduced after recovery, incorporates tilt (rotation about the North-South axis - perpendicular to the Space-Earth axis) and an offset angle (rotation about the Space-Earth axis such that the true orbital velocity vector was offset to the North pointing direction). The distribution of impact data around the different faces of LDEF gives some information on the directionality of impacting particles. However resolution is limited since each face is accessible to impacts from a hemisphere and the normals to each peripheral face are only 30° apart. By deducing actual impact directions for individual impact sites from the shape of the crater, it is possible to determine the orbital direction causing such an impact. A number of well characterised solid surfaces are available for such a study, including the aluminium clamps supporting each experiment tray. Some of these clamps were available for examination at high magnification, yielding crater morphologies for further study (section 2). This paper describes how these data may be derived and compared with models of interplanetary and space debris particle orbit distributions.

2 IMPACT CRATER MORPHOLOGY

Several LDEF clamps have been examined using the Unit's Philips 525M scanning electron microscope to identify possible impact craters. Images of each of these sites were then taken from normal to the clamp surface and at $\pm 7.5°$ to the normal. The two off-axis images were examined using a stereo viewer, enabling positive identification of true hypervelocity impacts sites. The stereo

reconstructions of these impacts allowed the depth and the maximum and minimum diameter of each crater to be measured, using the plane of the clamp as a reference point. For "elliptical" craters, an estimate of the direction of impact could also be made using criteria obtained from experimental impact studies at oblique angles. Such impacts form elliptical craters with high raised lips on the side from which the impact occurred (the entrance side) and flattened lips on the exit side. The crater walls are steeper and sometimes undercut on the entrance side. The shape of the crater is not truly elliptical, but egg-shaped, being deeper and wider at the entrance side (Kinecke, 1960; Bryan, 1960) (see figures 2 and 3). "Ellipticity" used here is determined from the semi-major and semi-minor axes, a and b

$$e = (1 - b^2/a^2)^{1/2} \quad (1)$$

Craters on LDEF surfaces have been placed in three categories:

"Circular" - Irregularities in the surface and uncertainties in the exact crater edge result in ellipticities smaller than 0.3 being indistinguishable from circular.

"Elliptical" - Craters with morphology characteristic of oblique impacts. The direction of impact can be estimated with an accuracy of approximately 20 degrees.

"Undefined" - Craters with elliptical shapes but unusual morphology. It is not possible to determine which was the entrance or exit side or even if the crater was the result or an oblique impact.

Several examples of craters from LDEF clamps are illustrated in figure 2.

The relationship between eccentricity of an impact crater to the angle of impact has not yet been determined. Impact experiments into metals (eg Kinecke, 1960) indicate that craters are circular for impact angles up to a critical angle, above which they exhibit the properties described above (Bryan, 1960). As the particle velocity is increased, the critical angle increases (Culp, 1959). For material with no cohesive strength, the critical angle is large (>60° from the normal) and dependent on velocity and physical properties of the target and projectile (Gault and Wedekind, 1978). Impacts in solid non-metallic targets (Mandeville and Vedder, 1971) show central craters and spallation regions but the characteristic crater morphology for oblique impacts was easily distinguishable from craters produced by irregular particles. These experimental results apply to a range of materials and velocity and impact angle regimes but the relationship between crater ellipticity and such properties is not well quantified. It is theoretically possible to constrain this function using the relationship between the observed ellipticities of craters and the ratios of fluxes observed on different faces of LDEF (section 5). Much of the experimental data have been obtained in relatively low velocity regimes which favour non-circular crater production, whereas typical velocities in space are considerable larger. One might therefore expect most impact craters to be circular (as is the case for the Moon). However, a significant number of craters on LDEF are non-circular and therefore contain information on the direction of impact.

3 MODELLING OF MICROMETEOROID AND SPACE DEBRIS IMPACT DIRECTIONS ON LDEF

3.1 Impacts on LDEF

The impact model is based on input geocentric particulate velocity and flux or spatial density distributions, and a definition of the LDEF orbit and orientation. The resultant impact velocity on each face of LDEF is calculated for each geocentric particle velocity and direction. The results are then presented as $F(v,\eta,\psi)$ where v = impact speed in km s^{-1} and η,ψ are impact direction as defined in figure 1. v is specified in 1 km s^{-1} bins and η and ψ in 10° bins.

Parameters used in the model are

LDEF mean altitude = 460 km

LDEF orbital velocity = 7.64 km s^{-1}

Offset = 8°
Tilt = 1.1°
Earth radius = 6378 km
Effective atmospheric height = 150 km.

3.2 Interplanetary dust model

Interplanetary dust particles are assumed to have an isotropic geocentric flux distribution. The velocity distribution is assumed to be the same as found for photographic meteors (Erickson, 1968) corrected for the difference in escape velocity at LDEF's altitude (compared with typical meteor altitudes). Earth shielding removes particles from directions originating in a cone of semi-angle 73° from the Earth direction. If absolute numbers of impacts as a function of particle mass are required then the mass distribution for flux of interplanetary dust at a heliocentric distance of 1 A.U. (Grün et al, 1985) multiplied by a gravitational enhancement factor, $G = 1 + 0.76\ (r_e/r)$, is used.

3.3 Space debris model

The geocentric space debris velocities in a number of altitude and latitude cells are determined from the known orbital distribution of tracked debris to give a three dimensional model. The distributions of altitude, eccentricity and inclination are included, but the longitudes of nodes and lines of apsides are assumed to be random. Further details of the debris model are given by Green & McDonnell, ["A numerical model for characterisation of the orbital debris environment." Proc. of Workshop on "Hypervelocity Impacts in Space", Canterbury, Kent, UK, July 1991, in press].

4 INTERPRETATION OF RESULTS

4.1 Crater ellipticity

Elliptical craters measured on clamps can be presented in polar plots with angle = η and radial distance = e. The ellipticity, e, is a function of ψ (and other factors). Only a small number of clamps have so far been inspected to a resolution of 20μm with complete sampling. Craters as small as 4μm have been detected but sampling at this size is incomplete due to SEM resolution and clamp surface roughness. Table 1 provides a summary of LDEF surfaces for which analysis may be performed. Table 2 contains the data for the clamps measured so far, which are presented in figure 6 and discussed in section 4.4.

4.2 Interplanetary Dust

The Interplanetary dust model produces, for each face, $F_i(v,\eta,\psi)$, the flux in v, η, ψ bins, calculated assuming an isotropic interplanetary flux of 1 particle m^{-2} sr^{-1}. Results from the model are represented by polar plots with angle = η and radial distance = R_i where

$$R_i = K_i \sum_v \sum_\psi F_i(v,\eta,\psi) \sin\psi \qquad (2)$$

and K_i is a scaling constant (which can be used to incorporate the absolute flux of particles as a function of particle mass). The model plots therefore give an indication of the sum of the ellipticity of craters in a given direction. When the relationship between ψ and e is determined, a more direct comparison may be made.

Figure 4 shows the results for the East, West, North, South, Space and Earth faces for the interplanetary dust model. The same K_i value has been used for each face to illustrate the relative "fluxes" of elliptical craters on each face (see caption for relative plot scale).

On the East face the effect of the Earth shielding cone is immediately apparent. The angle corresponding to Earth shielding for a stationary spacecraft at this altitude is approximately 73° above the Earth direction. However, for a moving spacecraft the effective Earth shielding cone is rotated forward in the direction of motion (i.e. true East here). As a result, the 105° and 255° bins are much more significantly affected by Earth shielding than would be expected for a static spacecraft. The 8° offset causes the North side (and therefore the leading edge) to have a higher R_i value in general than the South side.

On the West face the R_i values are roughly a factor of 10 lower due to the spacecraft's velocity (requiring objects to "catch up" with the spacecraft). The effect of the spacecraft's motion on the Earth shielding region is again apparent, producing a decreased effective shielding angle so that the 105° and 255° bins are not affected. As before the 8° offset causes an increase in the values of R_i on the North side.

The North and South faces show the affect of the spacecraft's velocity as an enhancement of R_i in the East direction.

The Space face is the only one which is unaffected by Earth shielding. The maximum R_i value occurs offset by 8° from the East (Ram) direction.

Most of the impacts on the Earth face are blocked out by Earth shielding resulting in Ri values some 15-20 times lower than Space. The ratio of East-to-West Ri values is much less than for the Space face due to the spacecraft's tilt. The 1.1° tilt leans the Space face towards East and so increases the values on the East side and decreases those on the West. Conversely, the Earth face is tilted towards the West so producing a relative enhancement of the values on the West.

4.3 Space debris

The space debris model produces, for each face, $F_d(v,\eta,\psi)$, the flux in v, η, ψ bins, expressed as a fraction of the total debris population (with the constraints of the assumptions described in section 3.3). Results from the model are represented by polar plots with angle = η and radial distance = R_d where

$$R_d = K_d \sum_{v} \sum_{\psi} F_d(v,\eta,\psi) \sin\psi \qquad (3)$$

and K_d is a scaling constant (which can be used to incorporate the absolute flux of debris particles as a function of particle mass or size). Figure 5 illustrates the results for the entire debris population which can impact the East, West, North, South, Space and Earth faces in the same form as the interplanetary component. The same value of K_d has been adopted for each face (see caption for plot scales) but does not indicate the absolute numbers of debris particles.

The East face distribution indicates a high flux of elliptical craters (large R_d) from the North and South directions. This would be expected from the large proportion of debris in circular orbits (e=0) which would only intersect LDEF in a plane perpendicular to the LDEF orbit radius vector and

therefore along the North-South line. The values are not exactly on the North-South line as a result of the 1.1° tilt of the space face to the ram direction (causing a shift towards the space face direction) combined with the 10° quantisation of the data. The value of R in the South direction is greater than that of the North. This seems to contradict the known 8° offset towards the North face implying that the North face flux will be higher than that for the South. However, the R_d value is the impacting flux weighted by the sine of the impact angle to give a function representative of crater ellipticity (shallow impact angles producing higher ellipticity). Because of the "butterfly" distribution associated with space debris impact angles the 8° offset reduces the mean incidence angle y for the North lobe compared with the South and the sine ψ weighting therefore produces a higher R_d value in the South direction.

The West face experiences 500 times less elliptical impact craters than the East. The nominal West face should not receive impacts from debris in circular orbits, although debris in eccentric orbits can impact the West face if their mean altitudes are higher than that of LDEF. Due to the encounter geometry we would therefore expect impact directions to be symmetrical about the North-South line (impact before or after perigee) and the Earth-Space Line (impact from direction of higher or lower latitudes than LDEF). The 8° offset allows a tiny fraction of circular orbit particles to impact the West face from North and South directions at near grazing incidence with the 1.1° tilt shifting these directions slightly towards the Earth direction. The model angular distribution is highly sensitive to the small number of elliptical orbits with access to the West face.

The South and North faces have approximately the same number of elliptical craters as East, all originating from the East direction. The impact distribution on the South (North) face has a maximum R_d close to the East/West line with the 1.1° tilt causing a small shift towards the Space face.

The space face distribution shows the butterfly distribution associated with space debris towards the East face direction, albeit a factor of 100 less than the East face distribution. The 1.1° tilt is seen in the east bias of the distribution with a small number of impacts in the west direction from particles in highly eccentric orbits.

The Earth face distribution, at 1000 times less than the East face, is somewhat distorted by the quantisation effects of the model. The 1.1° tilt can be seen from the impacts in the West direction as this now becomes accessible to debris impacts with the addition of the 8° offset.

4.4 Impact Analysis

Figure 6 illustrates the data obtained so far for elliptical craters on clamps. The East face has very few impacts from the Earth direction due to Earth shielding. The results imply a mixture of the two sources with a distribution of impact directions from North through Space to South with rather more from the North/Space quadrant (natural) but with an excess lying on the North/South line (space debris).

On the North face the impacts have occurred predominantly from the East/Space quadrant with the impacts tending towards the East. This agrees with a combination of the natural and debris models which predict impacts from debris only from the East direction and for the natural particles predominantly from the forward facing direction. The single impact in the Space/West quadrant is probably a natural particle, as the model predicts a very low probability of debris impacts from that direction.

All of the impacts that have been measured on the South face come from the East/Space quadrant, again with a bias towards the ram direction. The two impacts which came directly from the East could be either space debris or natural particles, whereas the two other impacts 30 degrees from the ram direction should be of natural origin.

Impacts on the Space face would be expected predominantly from within 90° of the ram direction. However, of the two measured impacts one is from the West direction.

These preliminary results illustrate the potential power of the technique and the need for scanning of larger areas to improve the statistics, and for chemical analysis of as many sites as possible to determine their source independently.

5 CALIBRATION OF THE ELLIPTICITY FUNCTION

Currently, the crater morphology is only being used to determine impact angle (η). However, the precise angle from the normal (ψ) at which this occurs is unknown and the way in which the various aspects of the crater morphology (eccentricity, entrance and exit lip heights and crater wall slopes) vary with respect to the impact angle, velocity, material density and strength are not well defined. A series of non-normal impact experiments using the Unit's Van de Graaff particle accelerator and light gas gun have recently been initiated to investigate these relationships.

With a calibrated fit between the impact angle and crater morphology the impact ellipticities that have been measured may be converted to real particle directions. Since the mean impact velocity will vary with direction for any face this must be accompanied by use of dynamical models. The total fluxes on each face of LDEF provide a means of testing the validity of such a relationship, since the angular distribution predicted from the elliptical crater dimensions must be consistent with the relative numbers impacting each face. In theory it should be possible to derive this relationship from the flux data itself, but a combination of low angular resolution and the apparent nature of the relationship at small impact angles (shape almost independent of ψ for values less than ~55° has been derived for consistency of LDEF fluxes) mean that it is not well constrained.

6 CONCLUSIONS

The space debris and interplanetary particle models predict radically different impact angular distributions for each face of LDEF. The measured properties of elliptical craters provide a potentially powerful tool for determination of the relative contributions, at different particle sizes, of these two sources, which is complementary to chemical analysis. Further laboratory experiments on non-normal impacts are required to produce quantitative empirical relationships between crater morphology and impact direction, velocity, etc., which will allow the true three-dimensional distribution of debris velocities to be determined.

Acknowledgements

We acknowledge the financial support of the UK Science and Engineering Research Council, and F. Hörz for constructive criticism of the original manuscript.

References

Erickson, J. E.: (1968). "Velocity distribution of sporadic photographic meteors." J. Geophys. Res., **73** 3721-3726.

Bryan, G.M.: (1960). "A Model of Oblique Impact." Hypervelocity Impact, 4th Symposium, Air Proving Ground Center, Eglin Air Force Base, Florida, APGC-TR-60-39 (III), section 33.

Culp, F.L.: (1959). "Volume-Energy Relation for Craters Formed by High-Velocity Projectiles." Hypervelocity Impact, 3rd Symposium, Armour Research Foundation of Illinois Inst. of Technology, Chicago.

Gault, D.E. and Wedekind, J.A.: (1978). "Experimental Studies of Oblique Impact." Proc. 9th Lunar Planet Sci. Conf., 3843-3875.

Grün, E., Zook, H. A., Fechtig, H. and Giese, R.H.: (1985). "Collisional balance of the meteoritic complex", Icarus **62** 244-272.
Humes, D.H.: (1984). "Space Debris Impact Experiment", LDEF Mission 1 Experiments, (Eds. Clark, L.G., Kinard, W.H,., Carter, D.J. and Jones, J.L.) NASA SP-473 136-137.
Kineke, J.H. Jr.: (1960) "An Experimental Study of Crater Formation in Metallic Targets." Hypervelocity Impact, 4th Symposium, Air Proving Ground Center, Eglin Air Force Base Florida, APGC-TR-60-39 (I), section 4.
Mandeville, J.-C. and Vedder, J.F.: (1971). "Microcraters Formed in Glass by Low Density Projectiles." Earth and Planet. Sci. Lett. 11, 297-306.

Bibliography

See, T., Allbrooks, M., Atkinson, D., Simon, C. and Zolensky, M.: (1990). "Meteoroid and debris impact features documented on the Long Duration Exposure Facility, a preliminary report", Publication #84, JSC # 24608, 583 pp.

Table 1. Surfaces on LDEF available for crater ellipticity determination.

Surface	Material	Faces	Surface area	Crater size	Comments
Frames, Clamps, Flanges	Aluminium	All	~24m^2	a>2μm	Limit due to surface roughness. Restricted angular coverage
IDE experiment	Aluminium	Not E	~25m^2	a>0.1μm	(Humes 1984)
MAP Foils	Aluminium, Brass	E, W, N, S, Sp	~0.6m^2	0.1μm<a< (1.5-30μm)	Non-perforation required

Table 2. Ellipticity data for clamps measured to date.

Face	area, m^2	Clamps measured circular (e<0.3)	elliptical	undefined (see text)	Total clamp area available
East	5.7x10^{-3}	12	17	9	0.07 m^2
(a<20μm)	4.4x10^{-4}	23	6	6	
West	5.7x10^{-3}	0	0	0	0.07 m^2
North	5.7x10^{-3}	10	5	3	0.07 m^2
South	5.7x10^{-3}	14	4	0	0.07 m^2
Space	1.14x10^{-2}	14	2	0	0.49 m^2
Earth	-	-	-	-	0.42 m^2

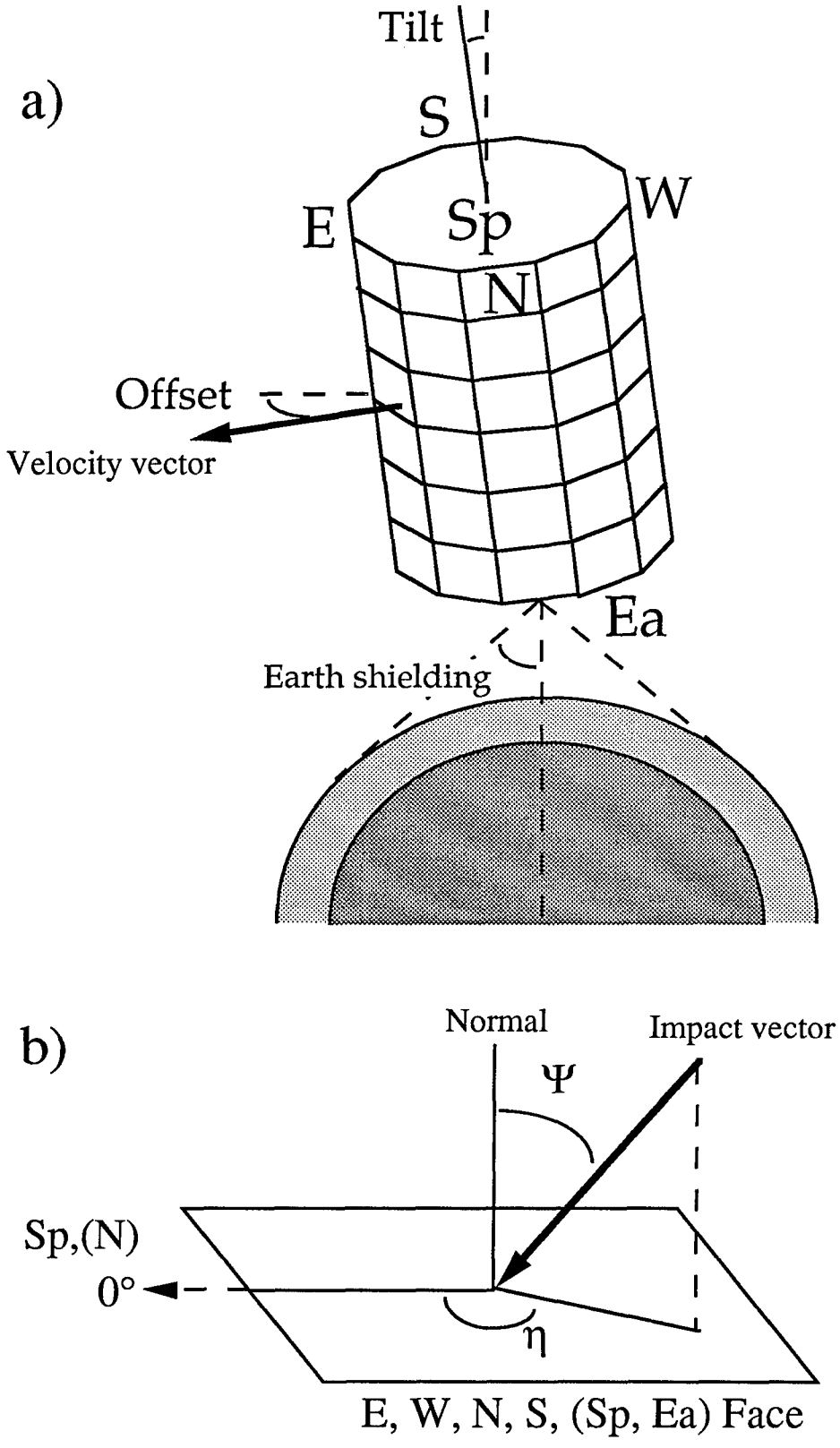
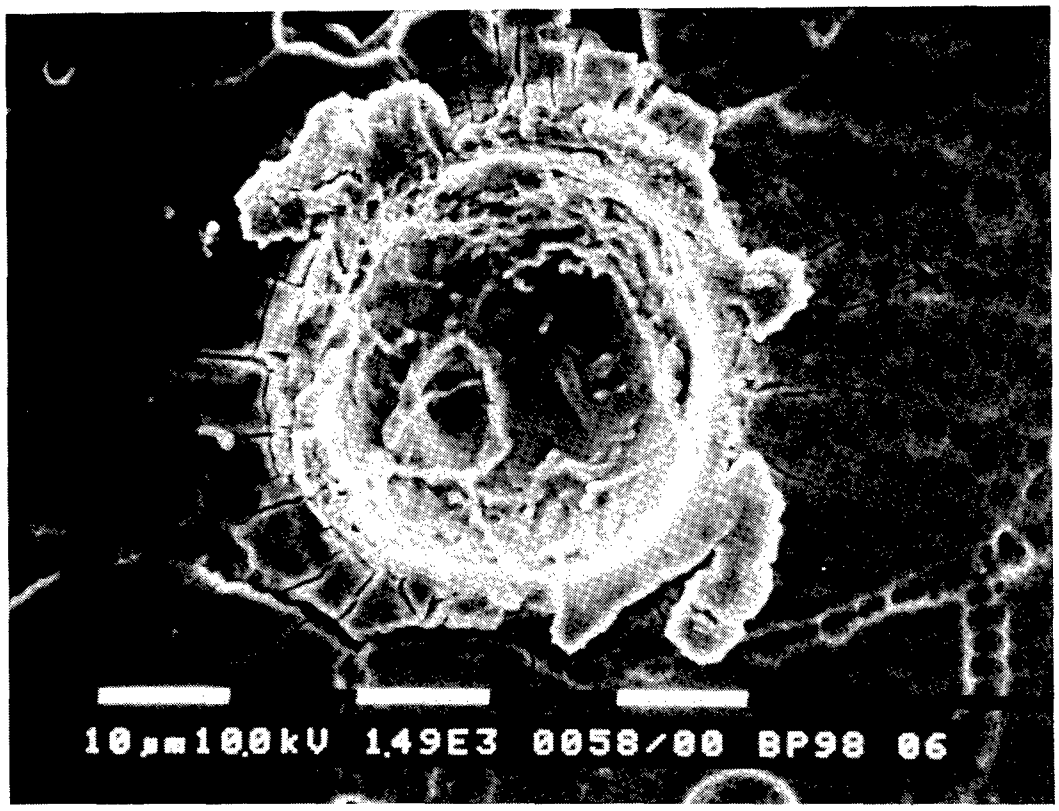


Figure 1. a) Orientation of LDEF in space showing tilt and offset angles.
b) Definition of impact angles on an individual face of LDEF.



a)



b)

Figure 2. Photomicrographs of typical impact craters on LDEF clamps.
a) circular: a = 34.8±0.9 µm, b = 34.8±0.9 µm, e < 0.3,
b) elliptical: a = 30.5±0.8 µm, b = 22.6±0.7 µm, e = 0.67±0.05,
c) undefined: a = 105±3 µm, b = 68±2 µm, nominal e = 0.77±0.03,

2c

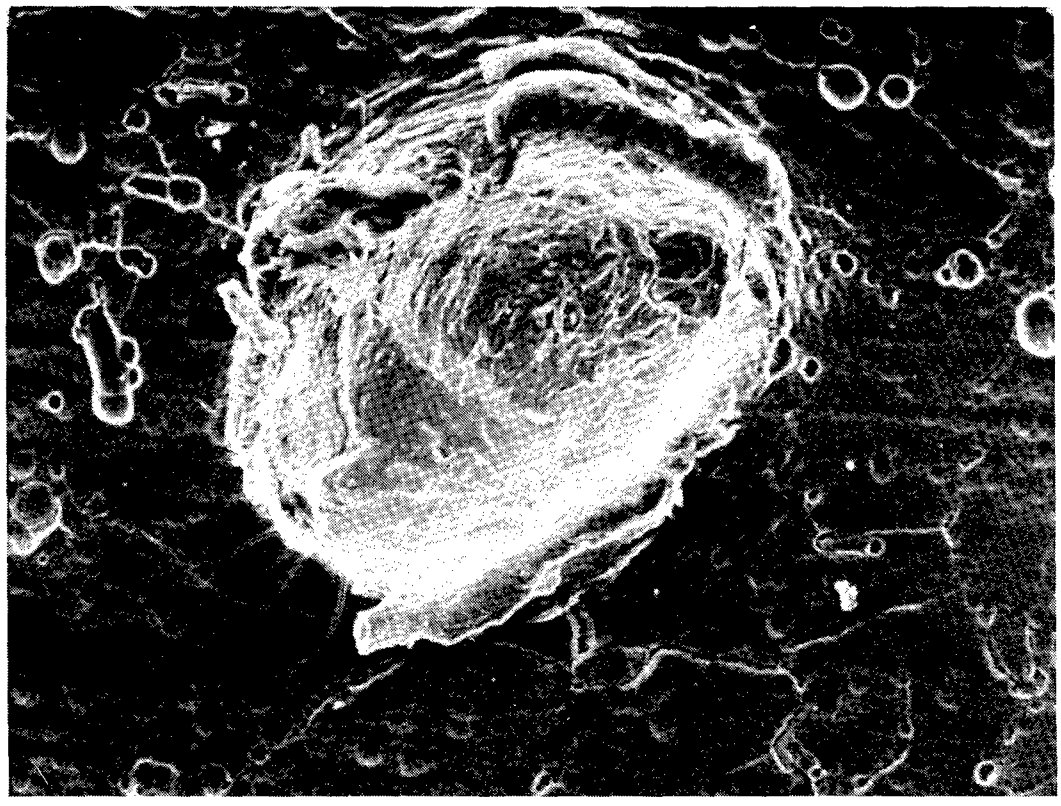


Figure 2. Concluded.

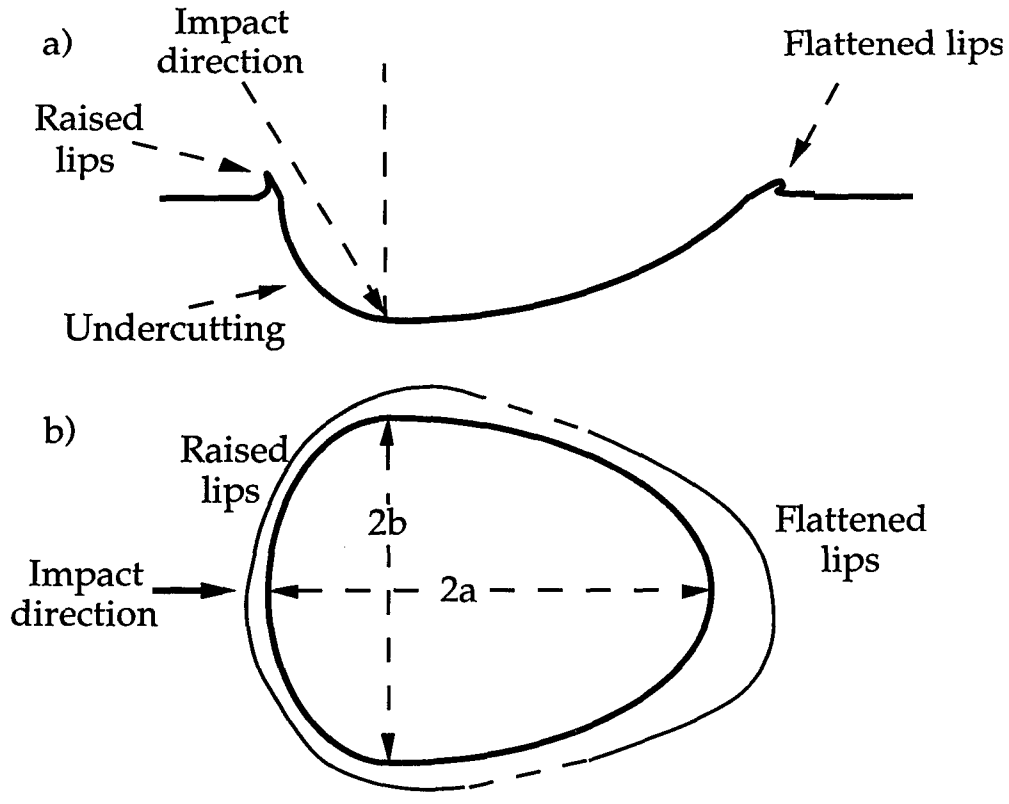


Figure 3. Schematic of crater shapes, a) profile, b) plan.

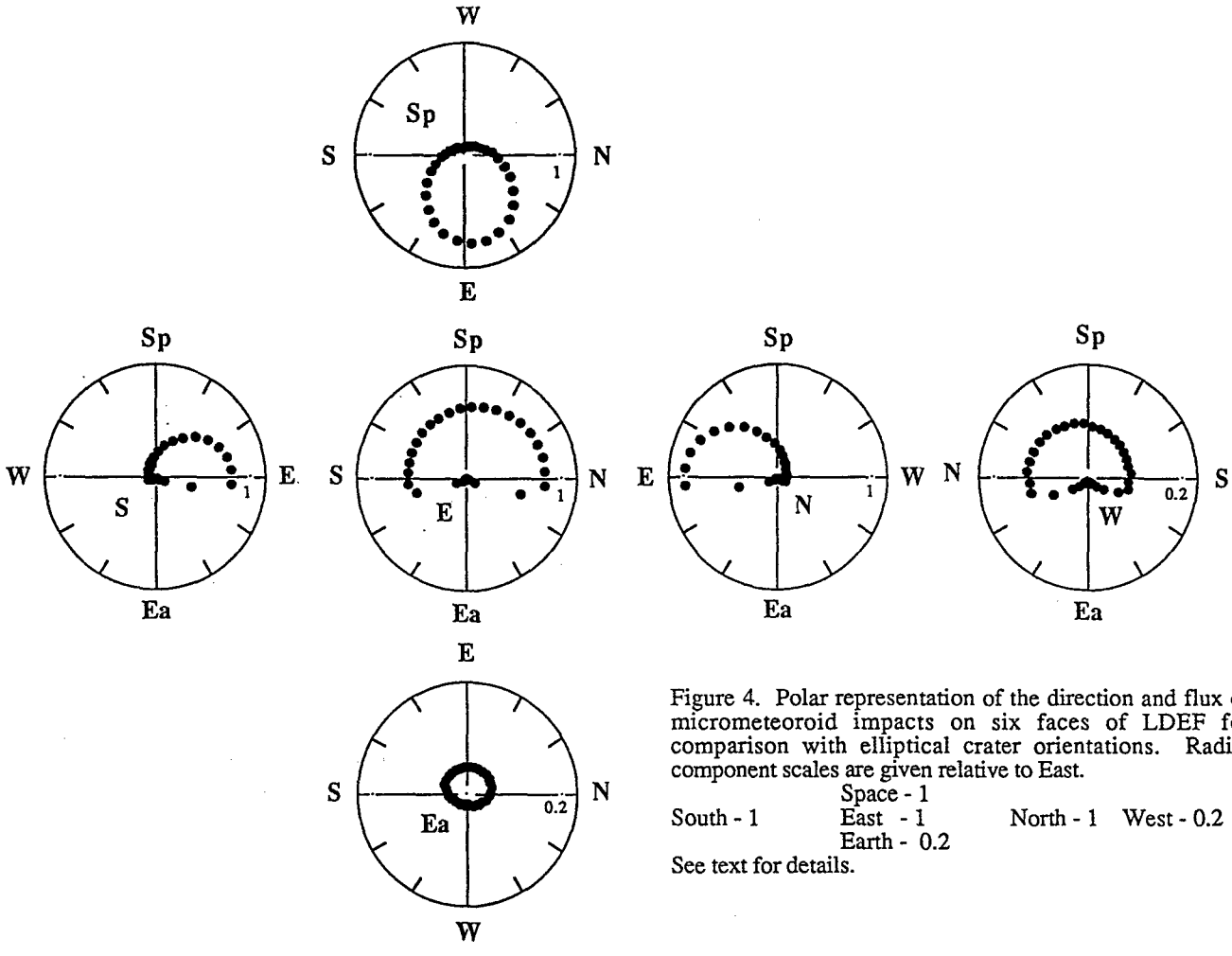


Figure 4. Polar representation of the direction and flux of micrometeoroid impacts on six faces of LDEF for comparison with elliptical crater orientations. Radial component scales are given relative to East.

Space - 1
South - 1 East - 1 North - 1 West - 0.2
Earth - 0.2

See text for details.

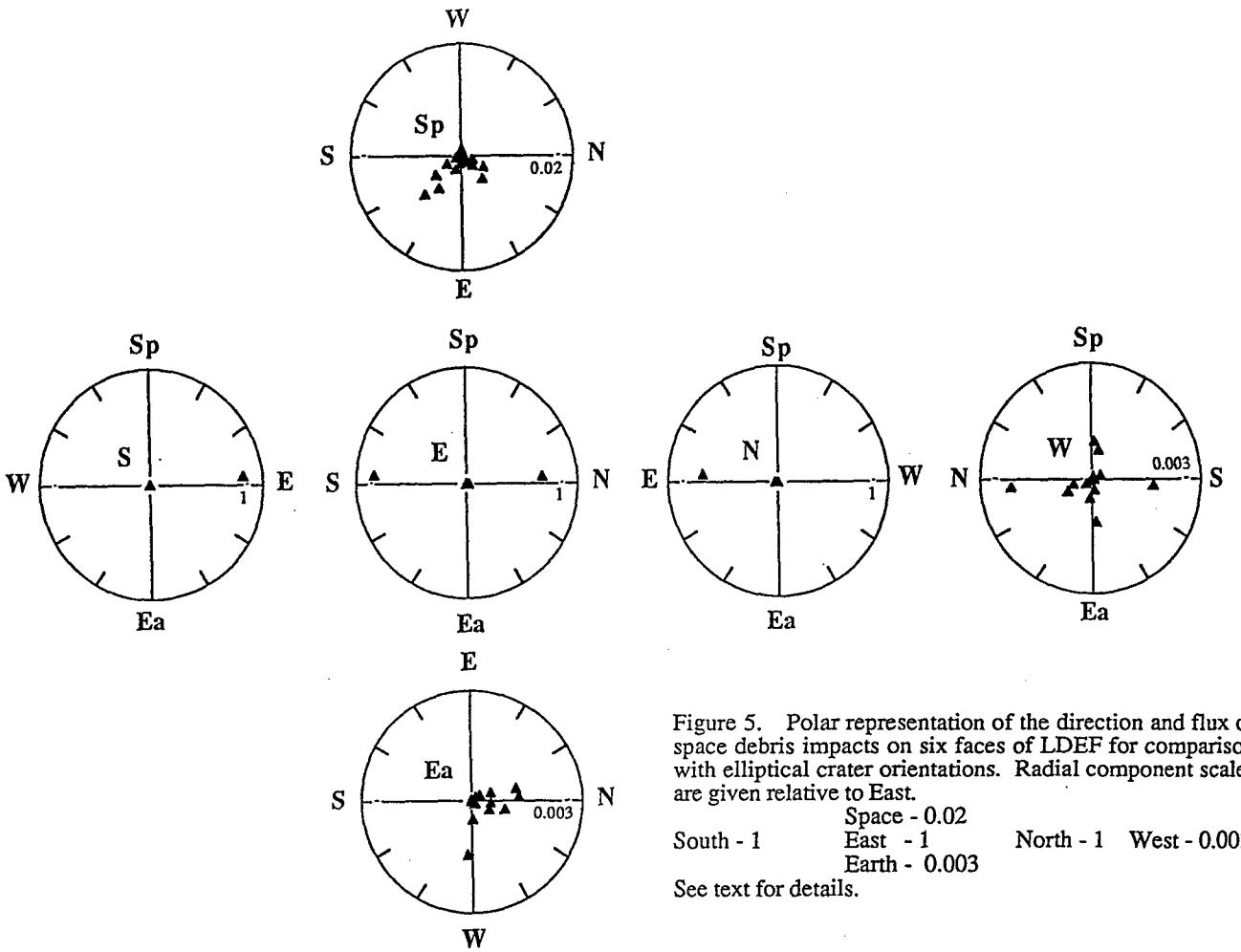


Figure 5. Polar representation of the direction and flux of space debris impacts on six faces of LDEF for comparison with elliptical crater orientations. Radial component scales are given relative to East.

Space - 0.02
South - 1 East - 1 North - 1 West - 0.003
Earth - 0.003

See text for details.

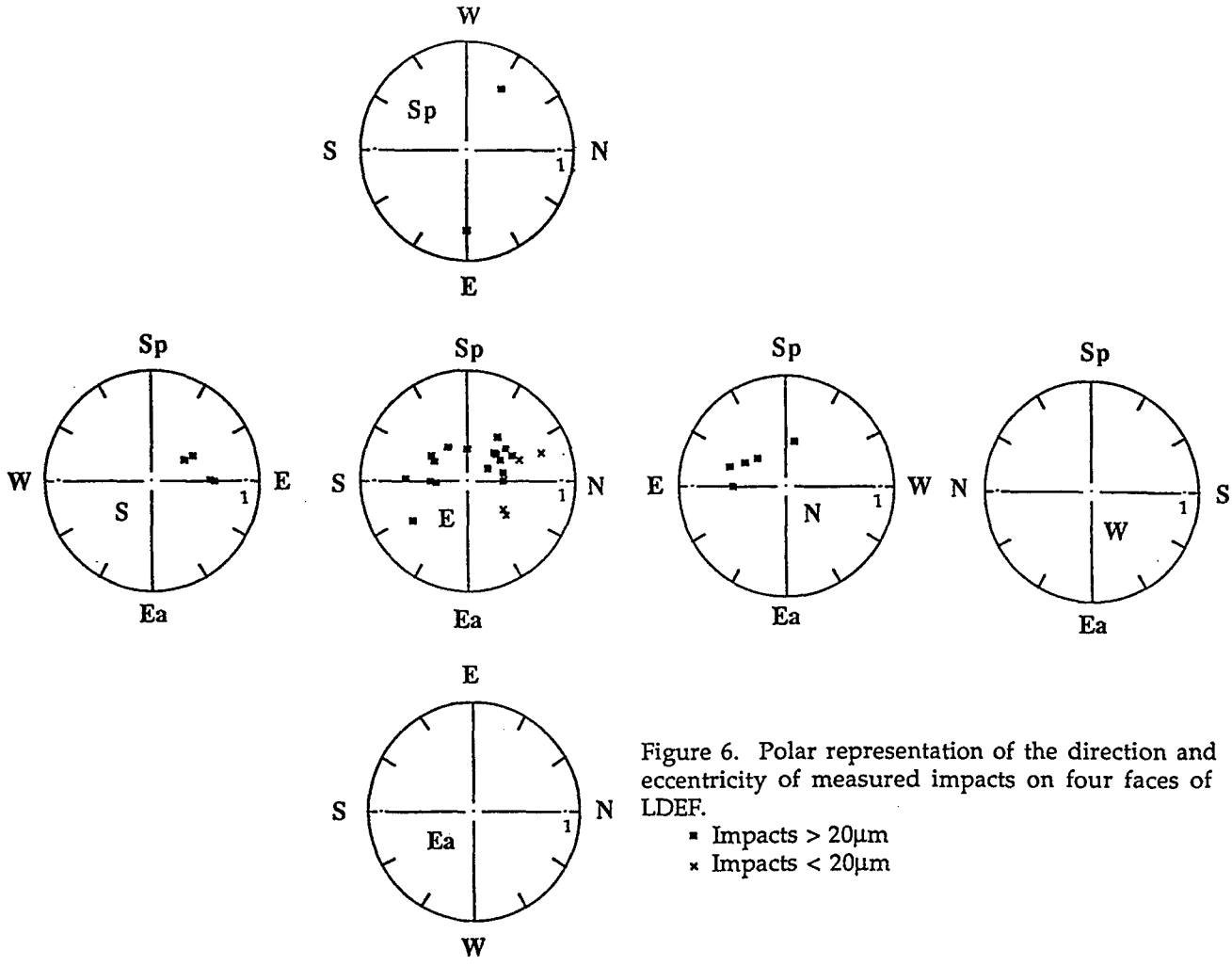


Figure 6. Polar representation of the direction and eccentricity of measured impacts on four faces of LDEF.

- ▪ Impacts > 20μm
- × Impacts < 20μm

CHARACTERISTICS OF HYPERVELOCITY IMPACT CRATERS ON LDEF EXPERIMENT S1003 AND IMPLICATIONS OF SMALL PARTICLE IMPACTS ON REFLECTIVE SURFACES

Michael J. Mirtich
Sharon K. Rutledge
Bruce A. Banks
NASA Lewis Research Center
Cleveland, Ohio

Christopher De Vries
Cornell University
Ithaca, New York

and

James E. Merrow
Cleveland State University
Cleveland, Ohio

SUMMARY

The Ion Beam Textured and Coated Surfaces Experiment (IBEX), designated S1003, was flown on LDEF at a location 98 degrees in a north facing direction relative to the ram direction. Thirty-six diverse materials were exposed to the micrometeoroid (and some debris) environment for 5.8 years. Optical property measurements indicated no changes for almost all of the materials except S-13G, Kapton, and Kapton-coated surfaces, and these changes can be explained by other environmental effects. From the predicted micrometeoroid flux of NASA SP-8013, no significant changes in optical properties of the surfaces due to micrometeoroids were expected. There were hypervelocity impacts on the various diverse materials flown on IBEX, and the characteristics of these craters were documented using scanning electron microscopy (SEM).

The S1003 alumigold-coated aluminum cover tray was sectioned into 2 cm x 2 cm pieces for crater documentation. The flux curve generated from this crater data fits well between the 1969 micrometeoroid model and the Kessler debris model for particles less than 10^{-9} gm which were corrected for the S1003 position (98° to ram). As the particle mass increases, the S1003 impact data is greater than that predicted by even the debris model. This, however, is consistent with data taken on intercostal F07 by the Micrometeoroid/Debris Special Investigating Group (M/D SIG).

The mirrored surface micrometeoroid detector flown on IBEX showed no change in solar reflectance and corroborated the S1003 flux curve, as well as results of this surface flown on SERT II and OSO III for as long as 21 years.

INTRODUCTION

The Ion Beam Textured and Coated Surfaces Experiment (IBEX) was designated S1003 on LDEF at a location 98 degrees relative to the ram direction in a north facing direction (ref. 1). Thirty-six diverse materials were exposed to the micrometeoroid and debris (M/D) environment for 5.8 years. Optical property measurements indicated no changes for almost all of the materials except S-13G (zinc oxide in a silicone binder), Kapton-H, and Kapton-H-coated surfaces, and these changes can be explained by other environmental effects. From the predicted micrometeoroid flux of NASA SP-8013, no changes in optical properties of the surfaces due to micrometeoroids were expected. However, there were hypervelocity impacts on the various diverse materials flown on IBEX. The characteristics of these craters were documented using SEM and are presented in the first section of this paper.

The S1003 tray cover was (alumigold coated, [chromic conversion process] Al type 6061 T6), 48 cm x 48 cm. An analysis using the micrometeoroid flux curve of Cour-Palais (ref. 2) and debris model of Kessler (ref. 3), indicated that there was sufficient area to generate a statistically meaningful M/D flux curve for particles of 10^{-6} cm or less. Because of the stabilized orientation of LDEF, a directional M/D flux curve could be obtained at 98° to the ram direction. With this in mind, the tray was sectioned into 690 pieces, 2 cm x 2 cm, for crater documentation. The flux curve thus generated could then be compared to both M/D fluxes of references 2 and 3, as well as other M/D data taken by other LDEF investigators. This is presented in the second part of the paper.

Interest in placing large solar concentrator/solar dynamic systems in space for power generation has brought up a concern for maintaining the integrity of the optical properties of highly specular reflecting surfaces in the near-Earth space environment. It has been shown that highly reflective polished metals and thin film coatings degrade when exposed to simulated micrometeoroids in the laboratory (ref. 4). At NASA Lewis Research Center, a shock tube was used to simulate the phenomenon of micrometeoroid impact by accelerating micron-sized particles to hypervelocities. Any changes in the optical properties of surfaces exposed to this impact were then evaluated. A calibrated sensor (2,000Å of Al/stainless steel) was developed to not only detect the small size micrometeoroid environment, but also to evaluate the degradation of the optical properties of thin aluminum films in space. This sensor (coated by G. Hass of Army Research and Development Center in 1963 of vapor-deposited Al) was flown on LDEF experiment S1003 and also on the OSO III and SERT II satellites that were launched in 1967 and 1970, respectively. The results of these experiments are also presented in this paper, and the relevance of the M/D fluxes on the optical properties of highly reflective surfaces is discussed.

RESULTS AND DISCUSSION

Characteristics of Craters in Various IBEX Surfaces

The largest crater found on the S1003 aluminum tray cover was 1478 micrometers (μm) as measured from outer lip edge to outer lip edge; the inner diameter was 984 μm. Figures 1a and 1b show the crater lip and the crater itself. EDAX of material in the crater indicates that it was caused by a debris particle.

Figures 2 through 4 show the characteristics of craters formed on ion beam textured metals (Cu, Ti, and S.S. type 304). The surfaces were textured to obtain high solar absorptance (α_s) or high thermal emittance (ϵ_{th}). Presented in each figure are the surface texture of the metal and two views of an impact crater. A hypervelocity particle impacting the surface removes the texture in the crater area, but has no effect on the texture beyond the impact crater itself. This is evident in the results of the measurement of the optical properties of the textured surfaces, for there were no measured changes (within the 2% accuracy of the instruments used for the measurements) in the values of α_s or ϵ_{th} of the textured surfaces after 5.8 years of exposure on LDEF.

Figures 5 and 6 show impact craters in black chrome and Grafoil. Again the impact crater affects only the cratered area and does not extend beyond the crater itself. So little of the area of the surface was impacted that the values of α_s and ϵ_{th} again remained unchanged.

Figures 7a-7e contain SEM photomicrographs of M/D impact sites observed on the coated Kapton samples (ref. 1, 5). The largest observed impact was on the 4% PTFE-96% SiO_2 sample (figure 7a). This appeared to be an impact by either a collection of particles or one large loosely distributed or extended particle. Another impact site on the same sample (figures 7b and 7c) is of a much smaller diameter. It appears that the type of damage is very dependent on particle size and probably particle velocity. Large impact areas appear to produce delamination, while smaller areas result in a region around the impact which is similar to the splash which is generated by a raindrop in a puddle (figure 7c). There is cracking around the splash region. Similar types of impacts were observed on the silicon dioxide and aluminum oxide coated Kapton samples (figures 7d and 7e). It appears that the impact site morphology is not dependent on the coating composition for these coatings and substrate materials since an area of delamination at an impact site on an aluminum oxide coated Kapton (ref. 5) sample flown on STS-8 looks similar to that on the 4% PTFE-96% SiO_2 coated Kapton. It appears that the area of crack damage or delamination is limited in extent for the impact crater sizes observed (ref. 5). In all cases the damage was contained within a diameter less than three times the impact crater diameter. This is very encouraging for the use of protective coatings in LEO since the damage that will result from an impact is small and thus not a significant cause for atomic oxygen attack of the underlying material.

S1003 Cumulative Flux Calculations

To evaluate the micrometeoroid and debris fluxes in lower earth orbit, the cover tray to experiment S1003 flown on the Long Duration Exposure Facility (LDEF) was cut into 690 samples, 2 cm x 2 cm, which were scanned randomly for craters. The total surface area of the cover tray is 0.17396 square meters. One hundred and eighty-five samples (0.044258 square meters) were scanned at 128 times magnification in order to find craters greater than or equal to 20 microns in diameter. Three hundred and twenty-three such craters were found. Two hundred and fifty-six samples (0.062543 square meters) were scanned at 80 times magnification in order to find craters greater than or equal to 38 microns in diameter. One hundred and thirty such craters were found. Then the remaining samples were scanned at 44 times magnification in order to find craters greater than or equal to 58 microns in diameter. One hundred and forty-eight craters greater than or equal to 58 microns in diameter have been found.

In order to plot the crater data as a cumulative flux curve as a function of particle mass, the following assumptions were made: the ratio of crater diameter to particle diameter is 5 to 1, which is the criteria used by the M/D SIG (ref. 6), and the particle density in low Earth orbit varies with respect to particle mass based on Kessler's meteoroid (ref. 6) and debris (ref. 3) models. These models assume that the particle density varies from a high of 2.5 gm/cc at 10^{-10} gm to 1.4 gm at 10^{-6} gm. Figure 8 shows a plot of the S1003 data for LDEF row 6 along with the standard deviation error range that is based on the S1003 cover tray area.

The results of the S1003 cover tray cumulative flux measurements can be compared to recent debris and meteoroid models corrected for LDEF row 6 as well as data from other parts of the LDEF.

The cumulative flux of debris in lower earth orbit is believed to follow the following equation (ref. 3):

$$F(d,h,i,t,S) = k \cdot \phi(h,S) \cdot \psi(i) \cdot [F_1(d) \cdot g_1(t) + F_2(d) \cdot g_2(t)] \qquad (1)$$

where

F = flux in impacts per square meter of surface per year
k = 1 for a randomly tumbling surface; must be calculated for a directional surface
d = orbital debris diameter in cm
t = time expressed in years
h = altitude in km (h < 2000 km)
S = 13-month smoothed 10.7 cm-wavelength solar flux expressed in 10^4 Jy (1 Jy = 10^{-26} Watts per square meter per hertz); retarded by 1 year from t
i = inclination in degrees

and

$$\phi(h,S) = \frac{\phi_1(h,S)}{\phi_1(h,S)+1}$$

$$\phi_1(h,S) = 10^{\frac{h}{200} - \frac{S}{140} - 1.5}$$

$$F_1(d) = 1.05 \times 10^{-5} \cdot d^{-2.5}$$

$$F_2(d) = 7.0 \times 10^{10} \cdot (d+700)^{-6}$$

$$g_1(t) = (1+2 \cdot p)^{(t-1985)}$$

$$g_2(t) = (1+p)^{(t-1985)}$$

p = the assumed annual growth rate of mass in orbit

The values for $\Psi(i)$, the flux enhancement factor, are given in Table 1 of reference 1 and depend on the inclination angle (i) of a surface.

The following assumptions were made for the LDEF:

h = 450 km (Rough average)

S = 115 (Rough average)

p = 10%

k = 1.24 (for LDEF row 6 on which experiment S1003 was flown. Row 6 was consistently 98° from ram direction.)

i = 28.5°

t = 1987 (Midpoint of LDEF mission)

With these assumptions, the debris model for row 6 is plotted in figure 8.

There are two meteoroid environment models which can be used to estimate the cumulative flux of meteoroids in low earth orbit. The first of these will be referred to as the 1969 model (ref. 2). The second will be referred to as the 1970 model (ref. 7). The 1969 model is designed to predict the meteoroid flux near the earth and moon, while the 1970 model is designed to cover the entire solar system. The 1969 model presents the following equation to determine cumulative flux.

$$\log_{10}N_t=-14.37-1.213\log_{10}m \qquad (2)$$

for

$$10^{-6}\leq m\leq 10^{0}$$

and

$$\log_{10}N_t=-14.399-1.584\log_{10}m-0.063(\log_{10}m)^2 \qquad (3)$$

for

$$10^{-12}\leq m\leq 10^{-6}$$

where

N_t = number of particles of mass m or greater per square meter per second

m = particle mass in grams

The cumulative 1969 micrometeoroid flux (N_t) was adjusted for the Earth's gravitational effect and the shielding of meteoroids by the Earth (ref. 2). The 1970 model presents a more complex way of finding cumulative flux curves in low Earth orbit as well as a different equation for calculating the effect of a planet's gravitation on the flux of meteoroids. The results of the calculations of both the 1969 model and the 1970 model for low Earth orbit are presented in figure 9. The 1969 and 1970 models are each presented before taking the effects of gravity and planetary shielding into account (the uncorrected curves), and the models are presented after taking the effects of gravity and planetary shielding into account (the corrected curves). The corrected 1969 model was chosen because it is easier to perform the required calculations to find the flux curve, and because it produces a curve practically indistinguishable from the corrected 1970 model.

Figure 8, therefore, shows a comparison of the S1003 data to the corrected debris and meteoroid models, for LDEF row 6. At low particle mass (10^{-9} gm), the S1003 impact data fits between the debris and micrometeoroid models. As the particle mass increases, the S1003 impact data is greater than that predicted by even the debris model.

However, comparisons between the S1003 cover tray and other parts of the LDEF indicate that there may have been a localized area where the particle flux was greater than usual. Figure 10 shows a comparison of the S1003 cover tray to Intercostals B06 and F07. S1003 does show a flux similar to that for intercostal F07 which was located on row 7, but closer to experiment S1003 than intercostal B06. Of course, the S1003 crater impact data is preliminary, and has not as yet been separated for debris or

micrometeoroid particles. This will be determined by the use of secondary ion mass spectrometry (SIMS), after which flux curves for debris and micrometeoroids for row 6 will be generated.

Implication of Micrometeoroid and Space Debris Models and Erosion of Surface Optical Properties

The micrometeoroid detector flown on IBEX was a 2000Å layer of Al vapor deposited on stainless steel. This surface has a long history in space and was ground calibrated in the 1960's when the majority of the micrometeoroid sensors (capacitor discharge or microplane sensors) had little or no such calibration (ref. 8).

A shock tube was used to accelerate (2-14)μ SiC particles to high enough speeds such that hypervelocity impact occurred in metals.[4] A series of polished metal discs composed of Al, stainless steel, and 1900Å Al on stainless steel substrates were chosen as potential materials for a space flight experiment. The discs, 4.45 cm^2, were progressively exposed to increasing amounts of simulated micrometeoroid exposure. Spectral reflectance measurements on all the discs were made before and after exposure to the simulated micrometeoroids. A typical reduction in spectral reflectance between 1.5 and 15.5 microns is shown in figure 11, for 1900Å Al on stainless steel after exposure to 0.22 J/cm^2 of 6 μ SiC particles travelling at 2.65 km/sec where the energy density is given as:

$$Energy\ Density = \sum \frac{\frac{1}{2} m_i v_i^2}{area} \qquad (4)$$

To obtain average reflectance values (for the sake of comparison), spectral reflectance data were weighted for the energy distribution corresponding to a 420 K blackbody. In figure 12, all of the average reflectance ratios for stainless steel, aluminum, and aluminum on stainless steel are plotted against the total energy of the impacting particles.

The data in figure 12 indicate that the reduction in the infrared reflectance ratio of aluminum is somewhat greater at any exposure than that of stainless steel. The reflectance of both, however, falls to less than 60% of the original value after only 7.5 J (1.65 J/cm^2) of laboratory exposure.

A space-environment-simulation facility was used to determine the equilibrium temperature of the surfaces presented in figure 12. In the working section of the inner "space" chamber, which was six feet in diameter and approximately ten feet high, four characteristics of the space environment were reproduced simultaneously and as accurately as possible. The four were: the low pressure of gases in space, estimated to be about 10^{-14} mm Hg., low background temperature (4°K), very nearly perfect absorption capability of space background for gases (blackened walls at LHe temperature), and sun radiation at proper intensity, uniformity, and collimation angle, as well as spectral distribution from .35 to 2.5 mm.

The "history" of the equilibrium temperature for discs composed of three different materials mounted on a simulated space vehicle and "flown" in the simulated space environment at 1.25 solar constant can be found in figure 13. These equilibrium temperatures are shown as they vary with exposure to the simulated micrometeoroid environment. The exposure is expressed in joules per square centimeter of energy of the impacting hypervelocity particles on the 2.38 cm diameter discs. The resulting variation in the equilibrium temperatures for all the discs is the result of reproducible changes in surface optical properties (α_s and ϵ_{th}) caused by calibrated exposure to high-speed, micron-sized particle impact. Perhaps the most important feature of these curves is that in spite of the large exposure to impacting particles, the resulting change in optical properties measured in the laboratory, and the efforts made to isolate the disc thermally from its support, the total variation in equilibrium temperature of the discs is small but measurable. For the aluminum disc, the measured change in equilibrium temperature is approximately 21 K or about 5% in absolute temperature level. For stainless steel, the temperature is almost constant, varying only about 0.1% in absolute temperature level. The largest variation occurred with the aluminum-coated stainless steel disc, which rose 50 K due to the exposure, or about 12% in absolute temperature level.

It was found in reference 8 that there was a similarity in the variation of reflectance with simulated micrometeoroid exposure as measured either by direct measurement of α_s or ϵ_{th} using optical spectrophotometers or by use of the equilibrium temperature method of a space simulation chamber (ref. 8). This suggested the possibility of making reflectance measurements in space without a reflectometer and using these reflectance measurements to determine the micrometeoroid flux.

This could be done by calibrating the change in temperature of a disc in a space-environment-simulation chamber with the measured (elsewhere) optical change of the surface caused by calibrated exposure of the disc to simulated micrometeoroid flux. Consequently, telemetering the temperature of the disc from a space experiment would give not only the change in reflectivity of the disc, but also, from correlation with the ground experiment, the micrometeoroid flux causing this reflectivity change. The surface chosen for space-flight experiments, because of its initial fast rise in equilibrium temperature and large changes initially in α_{sn} and ϵ_{th} when exposed to simulated micrometeoroids, (see fig. 13) was the 1900Å Al/stainless steel disc. Discs with 2000Å of Al/SS were placed thermally isolated from the spacecraft on OSO III and SERT II. Reference 9 describes the Reflection Erosion Experiment (REX) on the SERT II spacecraft in detail. The results of 21 years of exposure of the REX on SERT II, which was in a 1000 km polar orbit, will be highlighted here.

Figure 14 is a time plot of REX disc #2 temperature from launch of SERT II (February 1970) to July 1990. The shaded areas of figure 14 represent times when the spacecraft was intermittently shadowed by the earth. The disc temperatures in

figure 14, which were normalized to constant REX body temperature of 316 K and zero angle of sun incidence, show almost no long-term change or trend after 21 years in space.

Figure 15 is a plot of REX disc α_{sn} values calculated using actual values of REX disc and body temperatures, solar flux as a function of angle of incidence, day of the year, a heat transfer K of 14.8 x 10^{-12} J/sec-K^4 between disc and body, and a disc thermal emittance of 0.017 (ϵ_{th}) (ref. 8). The above-described parameters were combined in equation (B3) of reference 8 for each individual point taken, and a value of α_{sn} was calculated. The disc surface material (2000Å Al/SS) and temperature level were chosen to make the REX α_{sn} sensitive and not ϵ_{th} sensitive.

The initial launch value of α_{sn} was 0.111, as measured in ground testing. The initial value of α_{sn} measured in space was the same. The value of α_{sn} increased in the first two months in space to 0.128, and then levelled off at 0.134. As the sun angle of incidence increased in late 1970 and during 1971, the calculated α_{sn} value was reduced to about 0.120. The value of α_{sn} remained at 0.120 from 1979 to 1981. The scatter of α_{sn} values was probably caused by the spinning spacecraft and a $\pm 5^{\circ}$ uncertainty of the sun angle of incidence. At the next opportunity to obtain data, July, 1989, α_{sn} had increased to a value of about 0.130.

The changes in α_{sn} were quite small (0.11 to 0.13) over a 21-year period in space, compared to the change of 0.11 to 0.40 in 12 months predicted by the 1963 High Micrometeoroid Flux Model[10] was correct. The major result was that there has been no major change in disc temperature or α_{sn} over a 21-year period in space. This result indicates that the Micrometeoroid Flux Model of 1963 was considerably higher than the actual flux. The results are in better agreement with the 1969 Micrometeoroid Flux Model[10] and the 1987 Orbital Debris Model of Laurance and Brownlee.[11]

From the accuracy of the sensor, these results indicate that a reflector surface (a highly polished metal or thin metal film deposit) should lose less than 1% of its specular reflectance in near-Earth orbit over 21 years. This is an important factor in the design of space solar dynamic/concentrator systems. An extrapolation based on area damage derived from the 1969 Micrometeoroid Model and ground reduction in specular reflectance due to micrometeoroid simulation studies indicate that such a reduction of specular reflectance should not happen within the useful lifetime of currently conceived space systems.

CONCLUDING REMARKS

Thirty-six diverse materials were flown on S1003 at 98° (northward) relative to the ram direction. There were no changes in optical properties of the surfaces due to the micrometeoroid or debris environment. Characteristics of the hypervelocity craters formed in ion beam textured metals show that the hypervelocity particles impacting the surface removed the texture in the crater, but had no effect on the texture beyond the impact crater itself. This indicates that a surface textured to obtain select optical properties will retain those properties because the surface area impacted by micrometeoroids or debris particles is so small (area damaged = 10^{-4} x original area after 21 years in space).

A comparison of the S1003 cover tray hypervelocity flux data to the 1969 micrometeoroid and debris models corrected for LDEF row 6, show that for low particle mass (10^{-9} gm) the S1003 impact data fits between the debris and the micrometeoroid models. However, as the particle mass increases, the S1003 impact data is greater than that predicted by even the debris model. Comparisons between the S1003 cover tray and an intercostal on row 6 indicate that there may have been a localized area where the particle flux was greater than usual.

The mirrored surface (micrometeoroid detector) showed no change in solar reflectance and corroborated the results of this surface flown on OSO III and SERT II for as long as 21 years. This data does indicate that a reflector surface should lose less than 1% of its specular reflectance after 21 years in near-Earth orbit.

REFERENCES

1. Mirtich, M. J., Rutledge, S. K., Stevens, N., Olle, R., and Merrow, J., "Ion Beam Textured and Coated Surfaces Experiment (IBEX)," Proceedings of 1st LDEF Post-Retrieval Symposium, Kissimmee, FL, June 2-8, 1991, pp. 989-1004.

2. Cour-Palais, B. G., "Meteoroid Environment Model - 1969 [Near Earth to Lunar Surface]," NASA SP-8013, 1969.

3. Kessler, D. J., Reynolds, R. C., Anz-Meador, P. D., "Orbital Debris Environment for Spacecraft Designed to Operate in Low Earth Orbit," NASA TM 100471, 1989.

4. Mirtich, M. J., and Mark, H., "Feasibility of Accelerating Microns Size Particles in Shock Tube Flows for Hypervelocity Degradation of Reflective Surfaces," NASA TND-3187, January 1966.

5. Rutledge, S. K., and Olle, R. M., "Durability Evaluation of Photovoltaic Blanket Materials Exposed on LDEF Tray S1003," Proceedings of 1st LDEF Post-Retrieval Symposium, Kissimmee, FL, June 2-8, 1991.

6. Personal Communication by M/D SIG Members, M. Mirtich and M. Zolensky, at M/D SIG Meeting, Houston, TX, March 1992.

7. Kessler, D. J., "Meteoroid Environment Model - 1970 [Interplanetary and Planetary]," NASA SP-8038, 1970.

8. Mark, H., Summers, R. D., and Mirtich, M. J., "Effect on Surface Thermal Properties of Calibrated Exposure to Micrometeoroid Environment," AIAA Journal, 4 (10) (1966), 1811-1818.

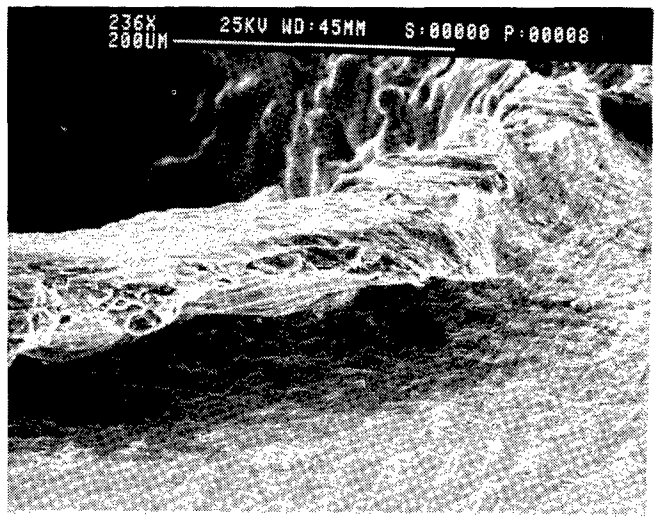
9. Mirtich, M. J., and Kerslake, W. R., "The Effect of the Near-Earth Space Environment on a Mirror Surface After 20 Years in Space," TMS Meeting, Los Angeles, CA, February 19-21, 1990, in "Materials Degradation in LEO," edited by Srinivasan and Banks, MMM Society, 1990, pp. 107-122.

10. Alexander, W. M., McCraken, C. W., Secretan, L., and Berg, O. E., "Review of Direct Measurements of Interplanetary Dust from Satellites and Probes," Proceedings of the Third International Space Sciences Symposium, edited by W. Priester (John Wiley and Sons, Inc., N.Y. 1963, Sec C2, Paper 1, 891-917).

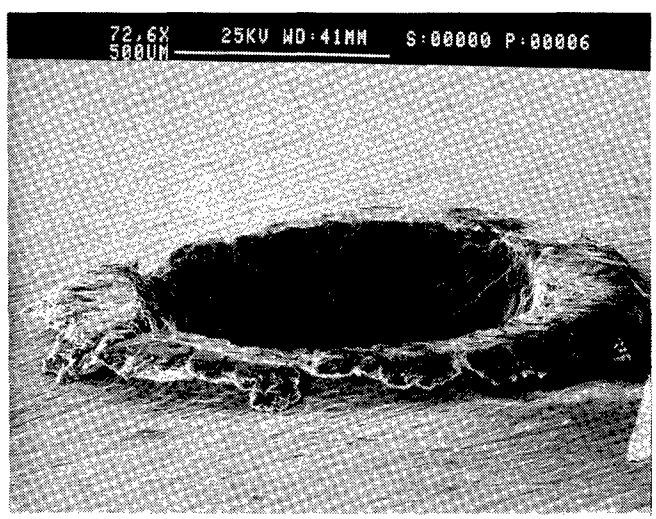
11. Cour-Palais, B. G., "Meteoroid Environment Model, Near-Earth to Lunar Surface," NASA SP 8013, 1969.

12. Laurance, M. R., and Brownlee, D. E., "The Flux of Meteoroids and Orbital Space Debris Striking Satellites in Low Earth Orbit," Nature, Vol. 323, 1986, pp. 136-138.

Micrometeoroid Impact
LDEF E06-S1003 Piece #278
Inner Diameter: 984 micrometers
Crater Edge to Edge: 1476 micrometers

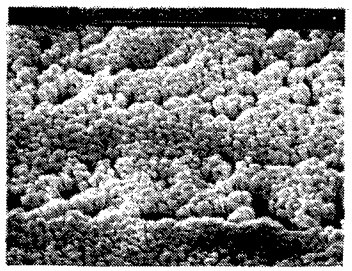


(a)

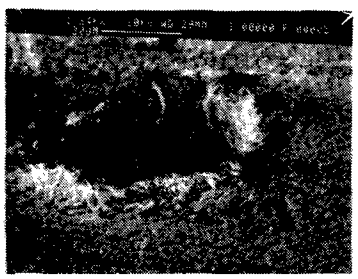


(b)

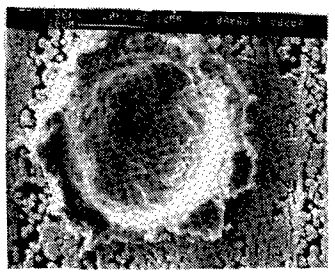
1. (a and b) Photomicrograph of largest crater found on S1003. Depicts the lip and crater itself.



Textured Cu Surface



Impact Crater



Impact Crater

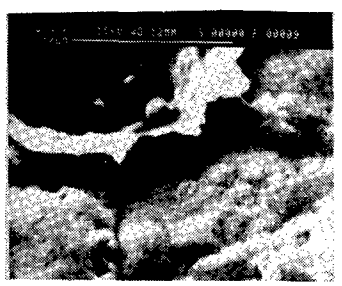
2. Photomicrograph showing textured copper and two different views of an impact crater.



Textured Ti Surface

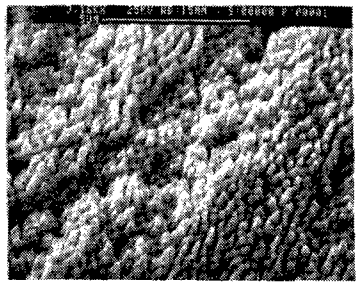


Impact Crater

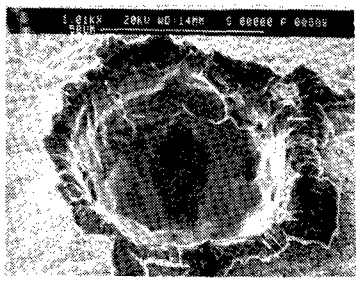


Impact Crater

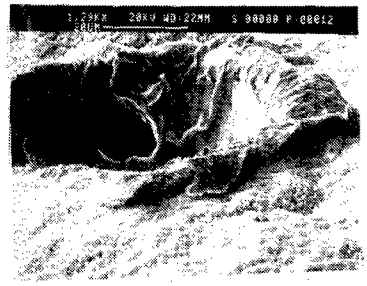
3. Photomicrograph showing textured titanium and two views of an impact crater.



Textured Stainless Steel Surface

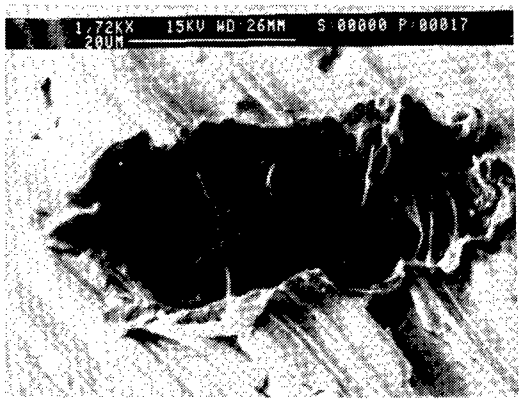


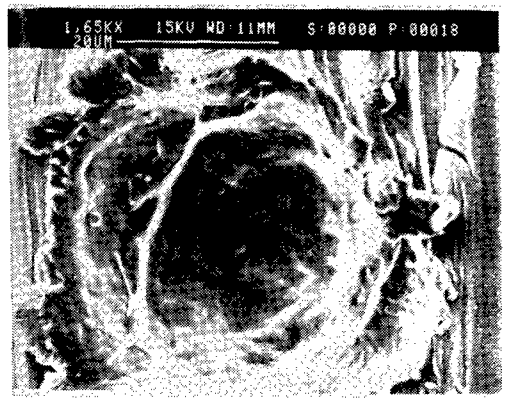
Impact Crater



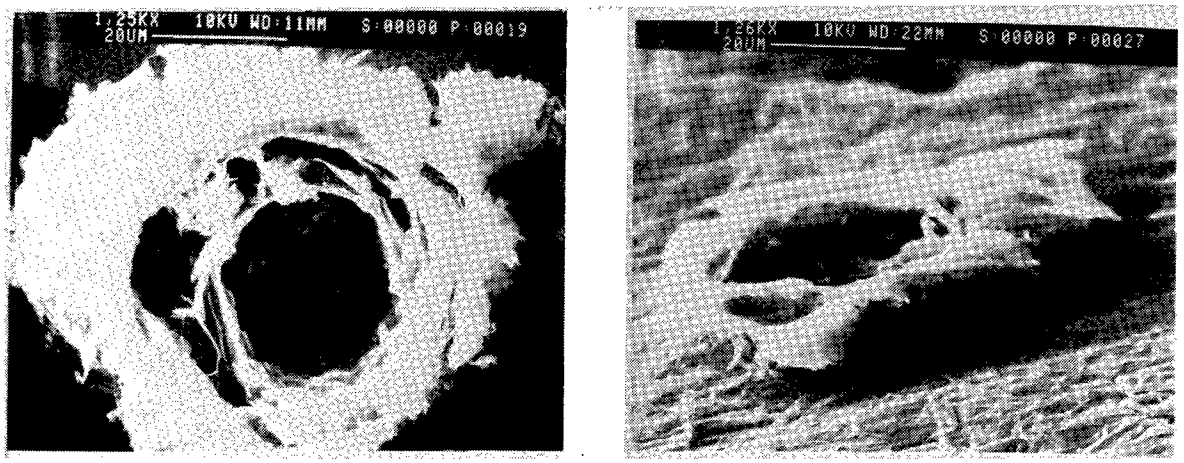
Impact Crater

4. Photomicrograph showing textured stainless steel type 304 and two views of an impact crater.

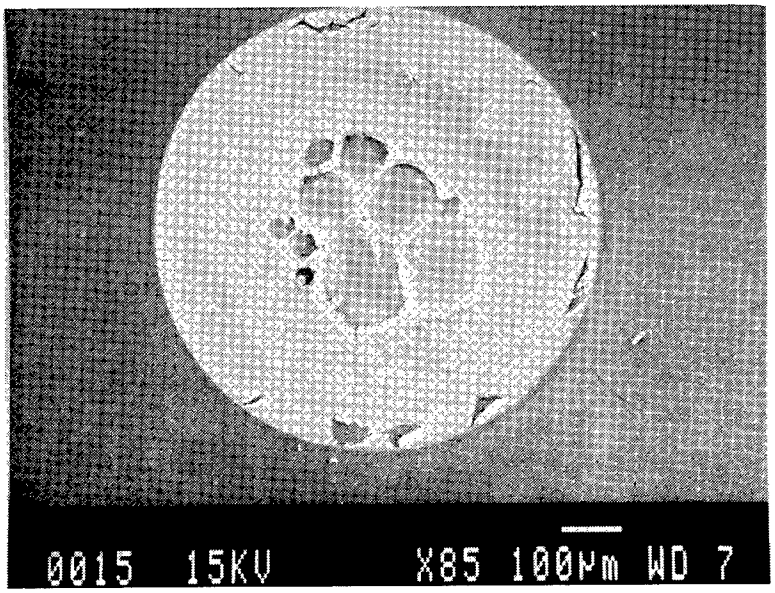




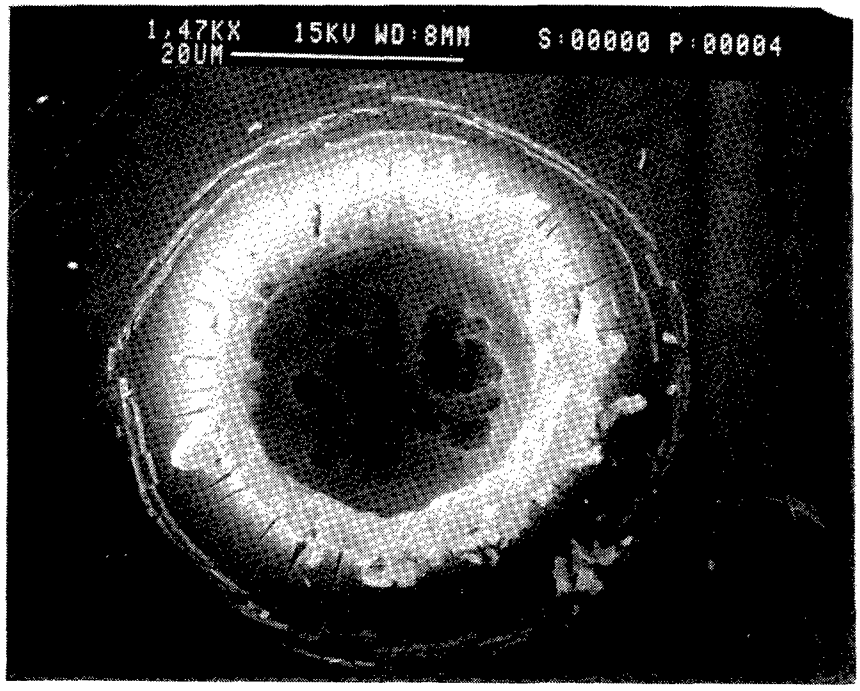
5. Photomicrograph of impact crater in black chrome.



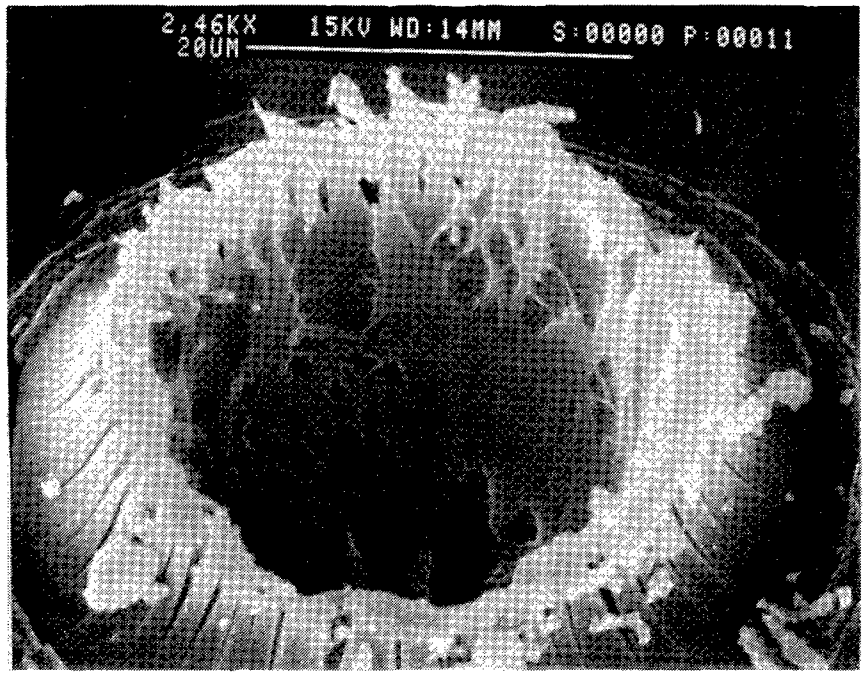
6. Impact craters in grafoil.



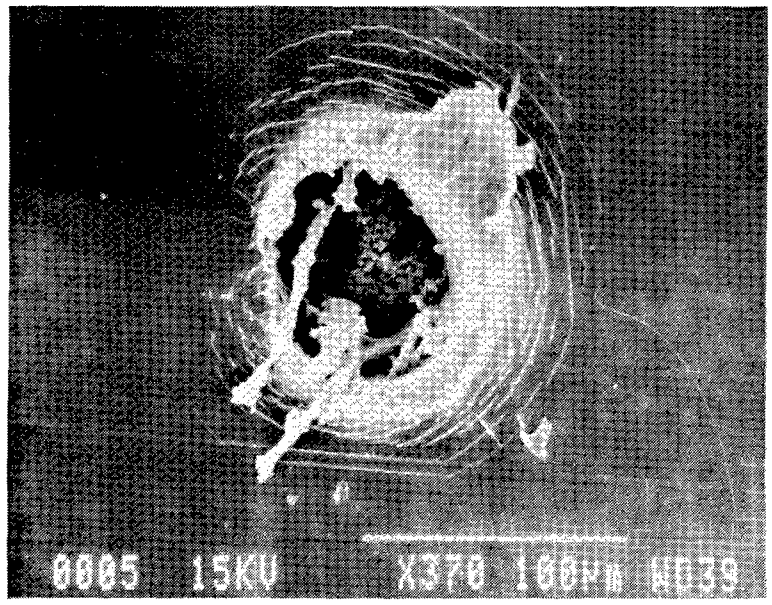
7. Scanning electron photomicrographs:
   (a) Conglomerate micrometeoroid or debris impact on 4% PTFE-96% SiO_2 coated Kapton.



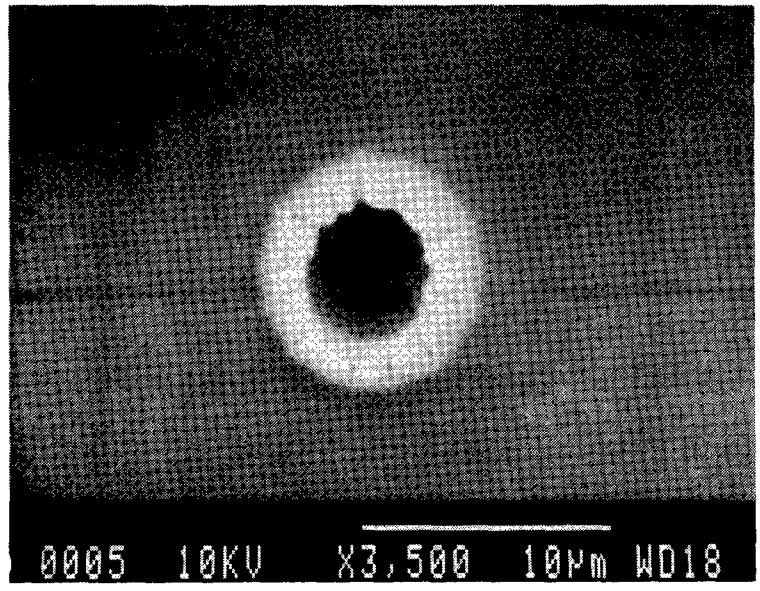
7(b) Micrometeoroid or debris impact on 4% PTFE-96% SiO_2 coated Kapton.



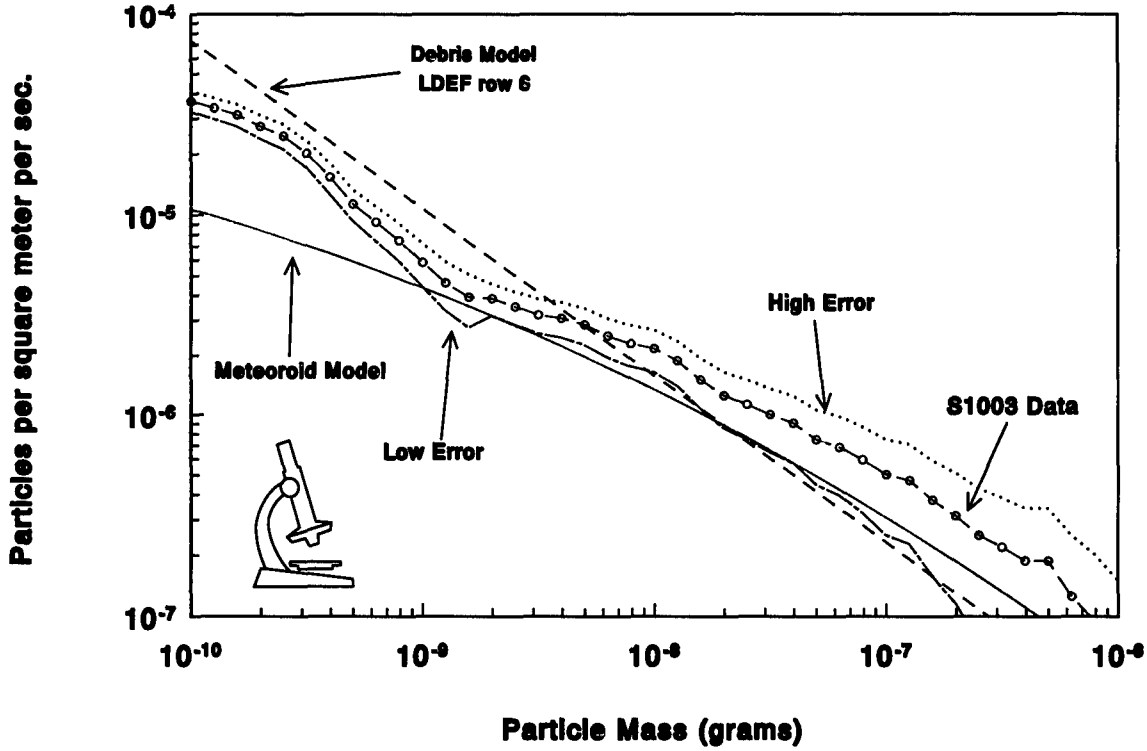
7(c) Micrometeoroid or debris impact on 4% PTFE-96% SiO_2 coated Kapton.



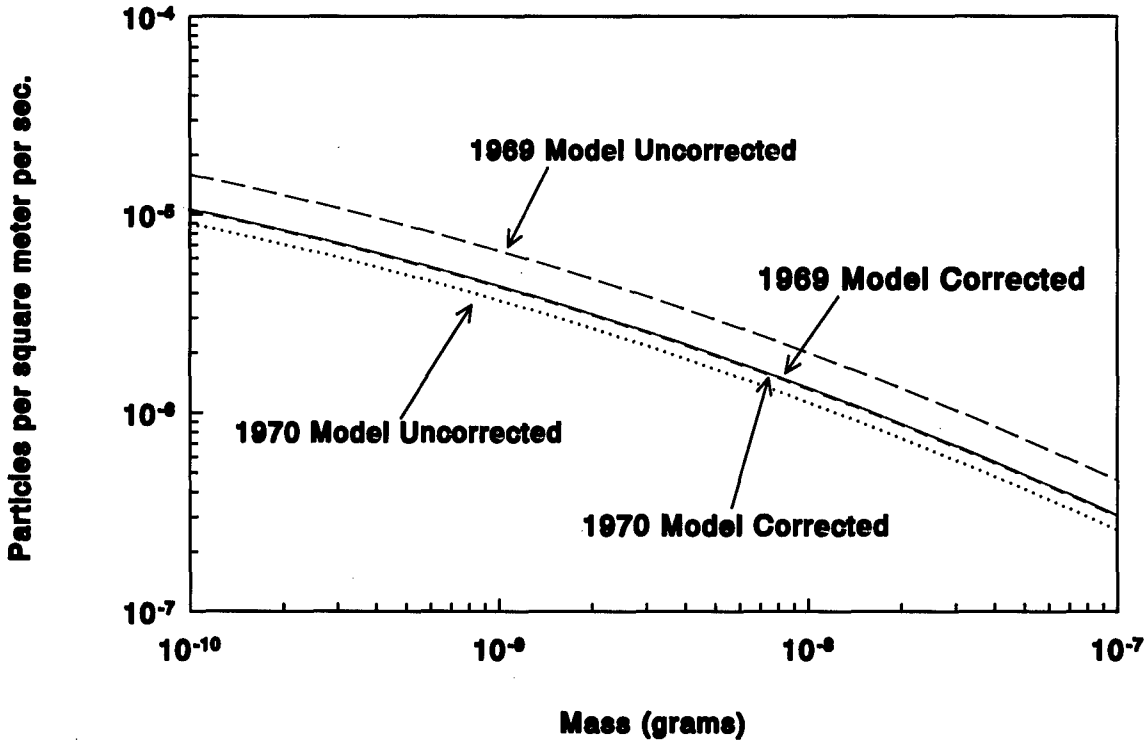
7(d) Micrometeoroid or debris impact on silicon dioxide coated Kapton.



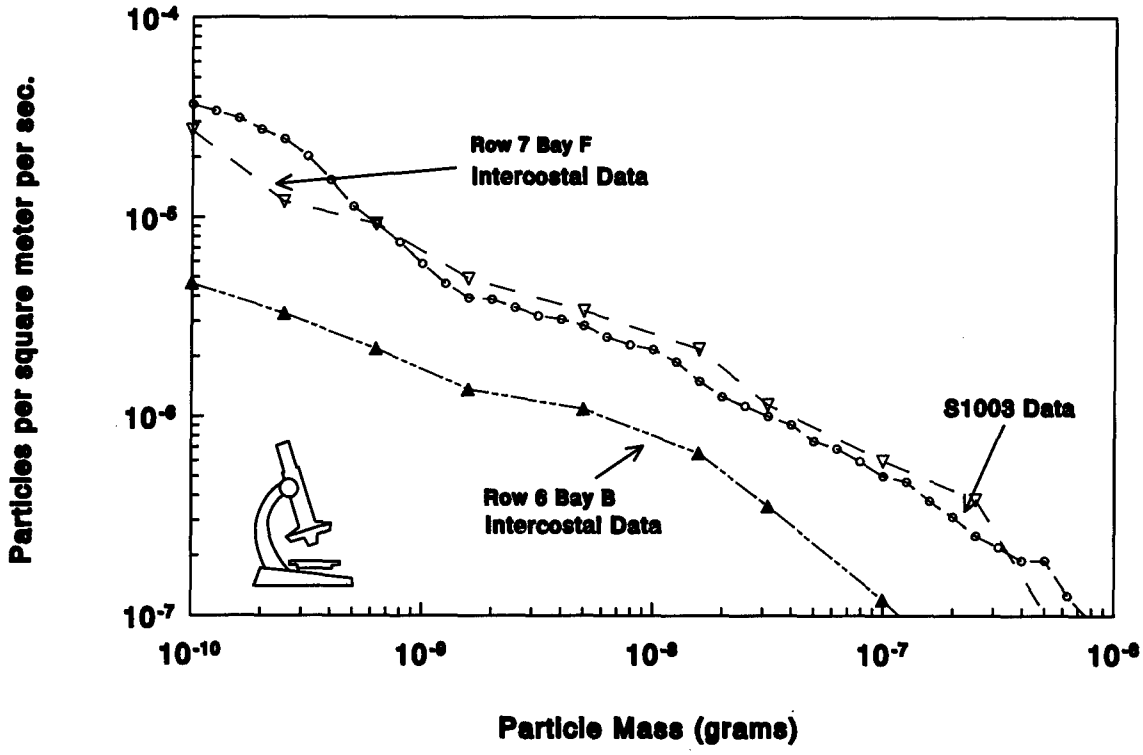
7(e) Micrometeoroid or debris impact on aluminum oxide coated Kapton.



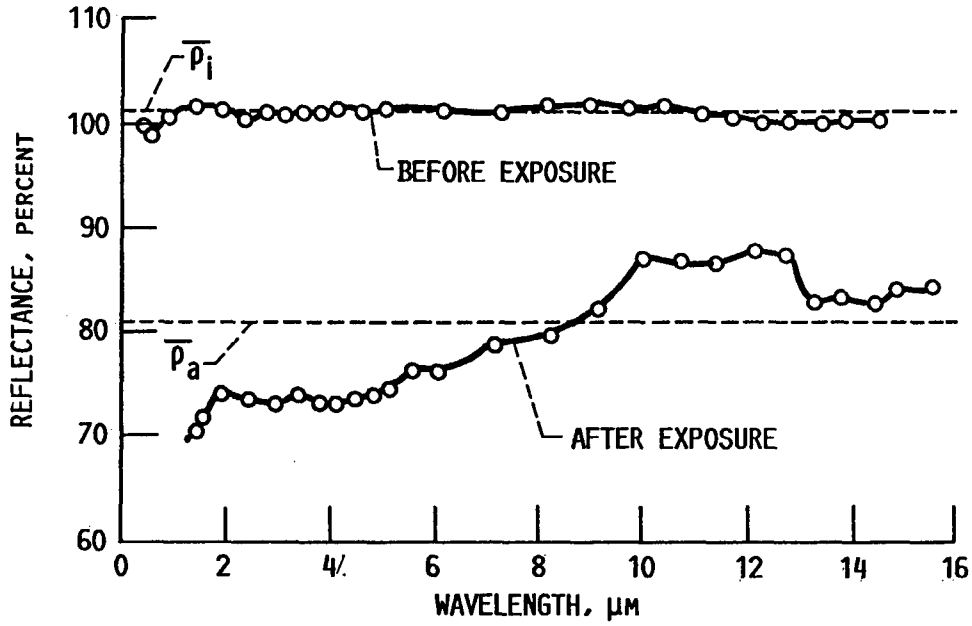
8. Comparison of S1003 crater data to the corrected debris and micrometeoroid models for LDEF row 6.



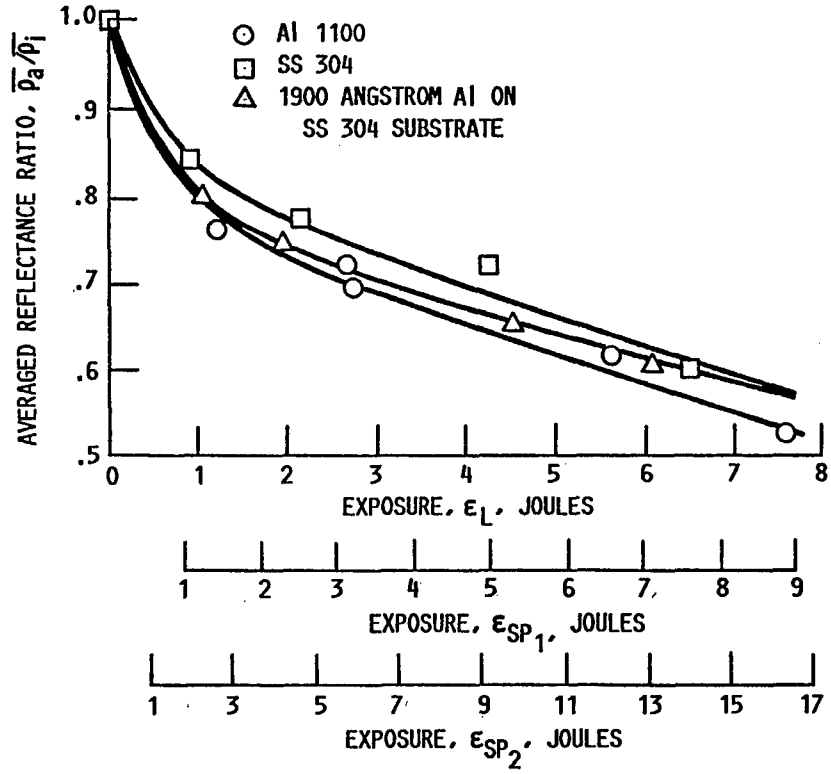
9. Comparison of 1969 and 1970 micrometeoroid models before and after correction for gravity and planetary shielding.



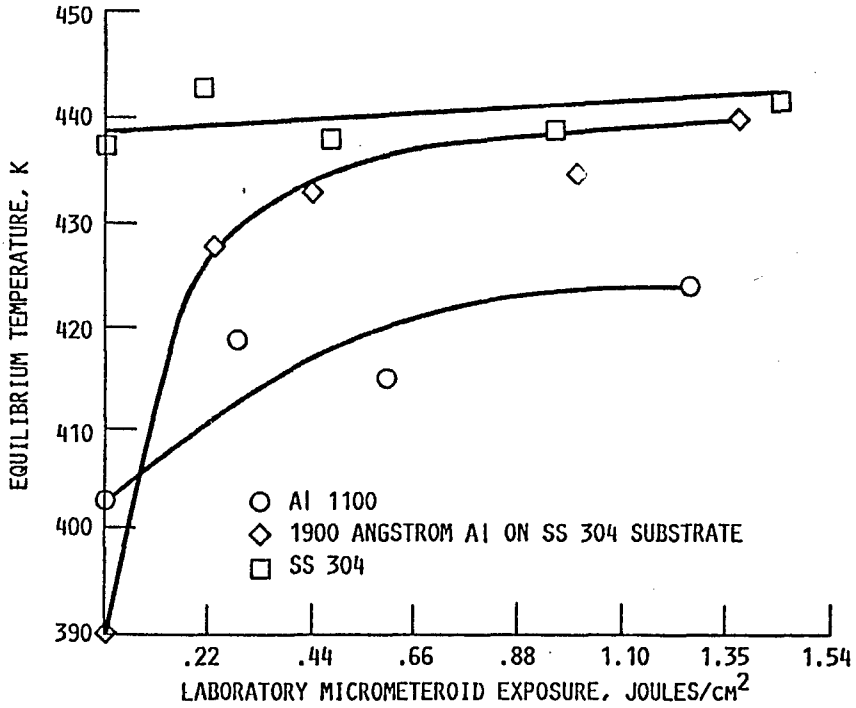
10. Comparison of S1003 data with intracoastal f07 (row 7) and intracoastal (row 6).



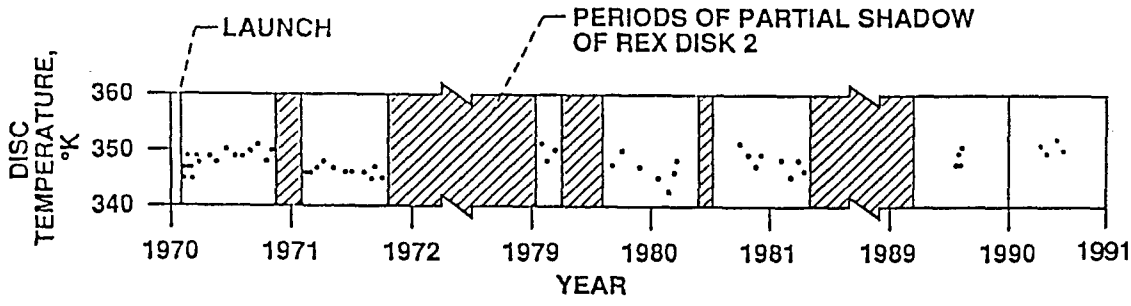
11. Spectral reflectance p_{H-A} for 1900Å aluminum on stainless steel substrate exposed to approximately 0.2 J/cm^2 of hypervelocity impaction.



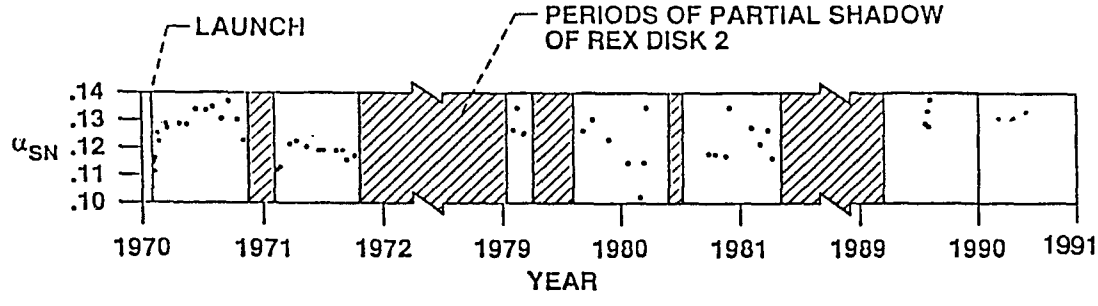
12. Degradation of average reflectance of various metal surfaces after exposure to impaction by 6-μm SiC particles traveling at 8500 ft/s in the laboratory. (Extra abscissas added to indicate exposure necessary for equal damage in space.)



13. Equilibrium temperature as a function of exposure to simulated micrometeoroids.



14. REX disk 2 temperature, normalized to constant body temperature (316°K) and zero-incident-sun angle.



15. Change of solar absorptance (α_{sn}) with time for Al/S.S. (SERT II) disk.

HYPERVELOCITY IMPACT SURVIVABILITY EXPERIMENTS FOR CARBONACEOUS IMPACTORS

T. E. Bunch
NASA Ames Research Center
Moffett Field, CA 94035-1000

Luann Becker and Jeffrey Bada
Scripps Institute of Oceanography
University of California at San Diego, La Jolla, CA 92093

John Macklin
Department of Chemistry
University of Washington, Seattle, WA 98195

Filippo Radicati di Brozolo and R. H. Fleming
Charles Evans and Associates
301 Chesapeake Drive, Redwood City, CA 94063

Jozef Erlichman
TMA/Norcal
2030 Wright Ave., Richmond, CA 94804

ABSTRACT

We performed a series of hypervelocity impact experiments using carbon-bearing impactors (diamond, graphite, fullerenes, phthalic acid crystals, and Murchison meteorite) into Al plate at velocities between 4.2 and 6.1 km sec^{-1}. These tests were made in order to (a) determine the survivability of carbon forms and organic molecules in low hypervelocity impact, (b) characterize carbonaceous impactor residues, and (c) determine whether or not fullerenes could form from carbonaceous impactors, under our experimental conditions, or survive as impactors.

An analytical protocol of field emission SEM imagery, SEM-EDX, laser Raman spectroscopy, single and 2-stage laser mass spectrometry, and laser induced fluorescence (LIF) found that : (1) diamonds did not survive impact at 4.8 km sec^{-1}, but were transformed into various forms of disordered graphite, (2) intact, well-ordered graphite impactors did survive impact at 5.9 km sec^{-1}, but were only found in the crater bottom centers; the degree of impact-induced disorder in the graphite increases outward (walls, rims, ejecta), (3) phthalic acid crystals were destroyed on impact (at 4.2 km sec^{-1}), although a large proportion of phthalic acid molecules did survive impact, (4) fullerenes did not form as products of carbonaceous impactors (5.9-6.1 km sec^{-1}); fullerene impactor molecules mostly survived impact at 5.9 km sec^{-1} and, (5) two Murchison meteorite samples (launched at 4.8 and 5.9 km sec^{-1}) show preservation of some higher mass polycyclic aromatic hydrocarbons (PAHs) compared with the non-impacted sample. Each impactor type shows unique impactor residue morphologies produced at a given impact velocity.

An expanded methodology is presented to announce relatively new analytical techniques together with innovative modifications to other methods that can be used to characterize small impact residues in LDEF craters, in addition to other acquired extraterrestrial samples.

INTRODUCTION

Observations of LDEF impact craters indicate that a small but unknown fraction of the craters contain dark residues, possibly carbon-bearing (e. g., refs. 1 and 2). Few detailed investigations of carbonaceous impactors have been made (e. g., ref. 3); however, the information contained within carbonaceous impactors is vital to understanding their origin and significance. Information on the behavior of carbonaceous materials on impact is virtually unknown, although Peterson *et al.*, 1991 (ref. 4) have performed shock experiments on amino acid survivability. Two of the three crystalline forms of carbon, diamond and graphite, are known to occur in meteorites (ref. 5) and diamond occurs in the interstellar medium (ISM) (ref. 6). Amorphous carbon and poorly crystallized graphite (PCG) in carbonaceous chondrites forms the bulk of their carbon inventories together with many organic compounds including polycyclic aromatic hydrocarbons (PAHs) which are also found in the ISM (ref. 7). These and other organic compounds may occur in comets (e. g., ref. 8). The possibility exists that LDEF sampled carbonaceous-bearing particles from all of these environments. In addition, fullerene, the third form of carbon, was recently found in an LDEF crater using single laser ionization mass spectrometry (ref. 9), although fullerenes have not yet been identified in meteorites or in the ISM.

In attempting to characterize and interpret LDEF carbonaceous residues, several first -order questions should be addressed: 1) Can carbon crystalline phases and organic compounds survive low velocity (< 6 km sec^{-1}) impact and if they do survive, what are their characteristics? 2) If they do not survive impact, what are their impact products? 3) Were the fullerenes made by impact from other carbonaceous materials or were they primary and survived impact? Light gas gun hypervelocity experiments were conducted in order to possibly constrain, within our experimental capabilities, these and other issues in addition to testing techniques and establishing characteristic impactor criteria.

In an attempt to achieve some of our stated goals, we used two relatively new analytical techniques that have exceptionally low detection limits for carbonaceous materials in very small particles. The survivability of PAHs and other carbonaceous materials in impacted Murchison meteorite was tested using laser desorption/laser ionization mass spectrometry techniques (2-stage laser mass spectrometry). At best, the detection limits for this technique are probably in the ppm to sub-ppm range. Although this sensitivity is adequate for the detection of PAHs, enhanced sensitivity may be necessary to determine whether or not other carbonaceous materials, e. g., fullerenes, are present in our test samples. By using laser induced fluorescence (LIF), 10^{-11}g or about 10^{-14} moles of C_{60} can be detected, which allows for the detection of C_{60} on the sub ppb level for a gram of sample (ref. 10).

We report here some of the preliminary results of morphological, compositional, and structural studies made on carbon and carbonaceous-bearing experimentally-formed impact residues.

SAMPLE SELECTION, EXPERIMENTAL AND ANALYTICAL TECHNIQUES

Sample Selection and Experimental Conditions

For the purposes of this study, the three forms of crystalline carbon (diamond, submicron graphite, coarse-grained graphite, fullerenes), Murchison carbonaceous chondrite and solid phthalic acid particles were chosen for impact experiments.The carbon forms were used to test the hypothesis that fullerenes may either form from graphite or diamond on impact, or that fullerenes are stable on impact at ≈ 6 km sec^{-1} and therefore preexisted before encountering LDEF (see ref. 9). Murchison was used to simulate carbonaceous meteorite impactors and solid phthalic acid was impacted to extend the impact survivability range initiated in an earlier study (ref. 3).

Submicron graphite, coarse-grained graphite, and fullerenes were accelerated into Al targets at 6.1, 5.92, and 5.89 km sec^{-1}, respectively; Murchison particles at 4.8 and 5.89 km sec^{-1} ;

diamond at 4.8 km sec^{-1}, and phthalic acid at 4.23 km sec^{-1}. The prelaunch impactor particle size for Murchison, coarse graphite, and phthalic acid was ≈ 0.2 mm (minimum diameter), diamond ≈ 0.3-0.4 mm, fullerenes ≈ 0.03-0.06 mm, and submicron graphite was < one micron but electrostatically attracted particle clumps as large as 0.1 mm were noted. For experiments of this type, the Ames light gas gun is limited to acceleration velocities of < 6.3 km sec^{-1}. Peak pressures and temperatures cannot be directly measured.

Experimental Methodology

Two-stage Light Gas Gun Experiments

Projectile grains were loaded into a small (3 mm cavity) Al carrier cup (Fig. 1a), capped with an Al plate and fitted into a sabot for launching (Fig. 1b). The two-stage light gas gun accelerates the sabot down a rifled barrel (1.2 m long; bore dia = 9 mm) to velocities of ≈ 2-6.5 km sec^{-1} depending on the amount of the powder charge (first stage), which in turn determines the speed of the deformable ram that compresses hydrogen gas (second stage). When the gas reaches a certain critical pressure, a diaphram ruptures and the gas propels the sabot down the barrel. At the end of the barrel, the sabot, carrier, and particles are separated in a "blast" chamber, particle velocities are electronically recorded, the in-flight particles are photographed, and the particles continue on to impact with the target plate (at 90°to the target) in an evacuated chamber (vacuum pressures nominally <1 mm of Hg). The impacted plate also serves as a witness plate (Fig. 1c) which has a 2.5 cm dia hole through which the carrier travels. This technique allows only particles to impact, the alignment of the launch can be measured, and the range in diameters of the launched particles at the impact point can be measured from the holes in the mylar covering which is attached beneath the hole (Fig. 1c). This cluster shot approach is necessary for projectiles < 1.0 mm in diameter as smaller grains cannot be individually launched.

Observational and Analytical

Observational

Samples were dry cut from the target plate. Craters and retained impactor debris were first observed by an optical light microscope, then by field emission scanning electron microscopy (FESEM). Samples were then submitted to the analytical protocol given below.

Analytical

Micro RAMAN Spectroscopy. Raman spectra were obtained by using the 488.0 nm line of a coherent radiation Innova 90 argon ion laser. The power of the laser radiation used here was between 20 and 40 mW and focused to a spot size of 5 microns. The scattered radiation was dispersed with a SPEX Industries 1477B Triplemate spectrometer equipped with a SPEX Micromate microsampling system that includes a modified Zeiss microscope and detected by a Reticon intensified diode array. The spectrometer slitwidth was kept at 300 microns. Integration times on the diode array ranged from 5 to 10 seconds and 10 or 20 acquisitions were averaged before data collection. Data acquisition and storage were accomplished by a PC computer system.

Single Stage Laser Ionization Mass Spectrometry (LIMS). Principles and applications of this methodology are described in Ref. (11). The fourth harmonic of a Nd:YAG laser (266nm; 1.0-1.5mJ/pulse; 50 to 10 nsec pulse width; 2.5 Hz repetition rate) is used to produce desorption and ionization of species at the sample surface. The strong selectivity in favor of low ionization

potential elemental signals (e. g., alkalis) or fullerenes, which have a strong absorption band in the UV at 264 nm (ref. 12), suggests that Resonance Enhanced Multiphoton Ionization (REMPI) is present under these conditions. The ions are mass separated in a reflector type time-of-flight (mass resolution = 450 at m/z 41), and detected with a 17 stage electron multiplier (Thorn-EMI). The data presented are the sum of typically 150 to 200 laser shots.

Laser Ionization Mass Spectrometry (L^2MS). The two-step laser methodology has been described elsewhere (ref. 13). In the first step, the pulsed output of a CO_2 laser (10.6 um; 20 mJ/pulse; 10 u-sec pulse width; 5-Hz repetition rate) is focused onto a small stainless steel disk (~1mm diameter) containing the meteorite sample. The infrared (IR) radiation is readily absorbed by the meteorite minerals and causes the ejection of intact neutral molecules from their surfaces in a rapid, laser-induced thermal desorption process. The fact that desorption dominates over decomposition in rapid laser heating processes is well documented (refs.13, 14). The sample can be rotated manually in order to expose fresh surface to the desorption laser. After an appropriate time delay (~130 usec), the fourth harmonic of a Nd:YAG laser (266 nm; 1.5-2.0 mJ/pulse; 10-nsec pulse width; 5-Hz repetition rate) is used to induce 1+1 resonance-enhanced multiphoton ionization (REMPI) of the desorbed molecules in an interaction region about 5mm from the surface. REMPI causes soft ionization so that the parent ions of the desorbed aromatic compounds almost exclusively dominate the spectrum. Total ionization efficiency is about a factor of 100 to 1000 greater than that of methods where ions are directly produced on a surface. One of the advantages to the L^2MS system is the spatial and temporal separation of the desorption and ionization which results in more control than in one-step desorption /ionization processes. The laser-generated ions are mass separated in a linear TOF system (mass resolution = 500) and detected with a microchannel plate array. Data for the meteorite samples were averaged over 100 laser shots, although a complete mass spectrum can be obtained from a single shot.

Samples were prepared using MALDI (matrix assisted laser desorption ionization). Previous reports have shown that laser desorption of neutral molecules can be improved by spraying a fine layer of sample on top of a matrix that absorbs at the wavelength of the laser (ref. 15). For our L^2MS system, the organic substrate sinapinic acid was used as the matrix. The matrix is sprayed directly onto the stainless steel disc (100 ng/mm^2) insuring that the substrate is evenly dispersed over the entire surface of the disc. The impacted meteorite sample (sonicated in toluene) is then sprayed on top of the sinapinic acid film. The sample disc is mounted on a 7-mm diameter teflon probe tip and is introduced to the TOF mass spectrometer through a separate antechamber pumped down to zero millitorr before introducing it to the high vacuum (10^{-7} torr) of the system. Sample introduction takes about 2 minutes and the spectrum can be recorded immediately thereafter.

Laser Induced Fluorescence (LIF). The development of LIF has provided a highly sensitive method for the detection of a variety of fluorescent molecules (ref. 16), especially those which exhibit weak fluorescence. The LIF system has been described elsewhere (ref. 17) and uses a 325 nm beam of a He-Cd laser focused into a 0.1 mm fused silica optic fiber which transports the excitation light into a 200 micron ID deactivated fused silica capillary column. The flow-through-cell, which was made by carefully removing about 0.5 cm of the polyimide coating on the fused silica column, has a volume of about 100 nl. The emission radiation is collected using two 0.6 mm fused silica optic fibers positioned at right angles to the excitation beam, passed through a 370 nm high pass cutoff filter, delivered to a monochromator set at 400 nm with a 10 nm exit slit, and detected with a photomultiplier. Toluene was used for column elution and was delivered to the capillary column by an HPLC pump. Samples containing various concentrations of Murchison meteorite in toluene were introduced into the capillary column with an injection valve fitted with a 100 microliter sample loop.

RESULTS

Crater and Impactor Residue Characteristics

Microscopic, FESEM, and Raman Characteristics

General. Figures 2 through 10 show microcsopic and FESEM images of the experimentally produced craters, in addition to one LIMS spectrum. Submicron graphite, graphite, and diamond craters show an increase in the presence of dark impactor crater liners from low amounts (Fig. 2a) to relatively high amounts of dark, thick liners (diamond: Fig. 5). Fullerene craters (Fig. 7) are similar to graphite craters (Fig. 4) in the amounts of visible, dark impactor residue, although the residue color is dark, purple-red which is the same as the unlaunched fullerenes. Phthalic acid craters are mostly clear with little visible dark residue; Murchison craters look very similar to graphite craters in terms of crater morphology and amount of impactor residue. Only the diamond craters show significant ejecta or particulate fall-out around the outside of the craters.

Crater diameters show considerable range for all experiments. For example, whereas diamond craters are mostly 1-1.3 mm in dia, some are as small as 0.01mm. Two factors are mostly responsible for the large variations in crater size: (1) break-down of a particle along zones of structural weaknesses during acceleration and/or (2) in-flight, mid-range collisions. In addition, observations of prelaunch submicron graphite projectiles indicate that they consisted of variable size lumps (microns to tens of microns) of electrostatically attracted submicron grains.

Graphite, diamond, fullerene, and Murchison craters tend to be round in shape with depth to diameter ratios (P/D_c) of between 0.55 and 0.8. Phthalic acid craters (Fig. 8) are irregular in shape and are shallower, on the average, than other craters ($P/D_c = 0.45$). The large oval submicron graphite crater in Fig. 2 has a P/D_c of only 0.4; all other submicron graphite craters are < 0.1 mm in dia and have a P/D_c of 0.45 - 0.55.

Submicron graphite Craters. Our original intent was to launch amorphous carbon as one of the impactors. However, Raman analysis of the commercially obtained prelaunched "amorphous" carbon shows that it is not amorphous and matches the characteristics of well-ordered graphite. Therefore, instead of having craters formed by graphite and amorphous carbon, we have craters formed by large graphite impactors ($\approx$ 0.2 mm) and impactors consisting of submicron grains of graphite aggregated by electrostatic attraction into various-sized lumps. Raman characteristics of both are given below under graphite craters.

Two distinct morphologies were observed: (1) a very thin liner with peculiar linear ridges in the large crater (Fig. 2a) and (2) liners that are lumpy and common to the small craters (Fig. 3). Figure 2b shows a series of subparallel ridges that traverse the entire crater and rim; the ridges do not appear to extend beyond the crater. FESEM images (Figs. 2c, d) show that these ridges consist of impact altered carbon and small amounts of Al. Carbon spheres (0.002-0.018 mm dia) are common on the upturned rims and Al melt splatter covered by carbon was found on the upper portions of the steep walls. The entire crater is thinly covered by a liner of smooth, vitreous-like carbon (Fig. 2c). The small crater liners are lumpy and are evenly distributed along the crater bottoms and walls, but are thin and discontinuous along the rims (Fig. 3). Melted Al droplets were not evident on the surface of the liners.

Graphite Craters. These craters also contain large areas of shiny, melt-like carbon, although crater liners are less lumpy compared to submicron graphite craters.(Fig. 3). The Raman spectrum of crystalline graphite consists of a single band (below 2000 cm^{-1}) at 1580 cm^{-1}. Raman spectra of poorly crystallized graphite (PCG) and glassy or vitreous carbon have additional bands in this spectral region at 1360 and 1620 cm^{-1}. The intensity of the band at 1360 cm^{-1}, relative to the band at 1580 cm^{-1} (height and width), is taken to indicate the degree of disorder in PCG and vitreous carbon.

The Raman spectrum of prelaunched graphite is shown in Fig.11a together with three typical spectra obtained from graphite impacted craters in Al. The spectrum shown in Fig. 11b is that of

mostly crystalline graphite with some disordered carbon. This measurement was obtained only from the centers of the craters. The spectrum shown in Fig. 11c was also obtained primarily from material inside the craters, although it is commonly observed when the incident beam is focused on the wall of the crater or between the crater wall and the area towards the crater center. This spectrum is similar to that obtained for typical vitreous carbon and carbon from the Allende meteorite (ref. 18). The Raman spectrum shown in Fig. 11c is also found for PCG when it is heated in argon beyond 1200°C for up to 0.5 hrs. The spectrum in Fig. 11d is most often obtained from areas on the raised rim of the craters and areas outside the craters just beyond the rims. The spectrum is indicative of even greater disorder in PCG material. It is comparable to the spectrum obtained from carbon in the Murchison meteorite (ref. 18). Upon heat treating such carbon at 1200-1500°C, the Raman spectrum becomes similar to that shown in Fig. 11c (ref. 18).

The variations observed in the Raman spectra are continuous among those shown in Fig. 11 and suggest mixtures of various types of carbon. Moreover, the spectra shown are those most commonly obtained from given regions of large (> 0.04 mm dia) craters. The above observations are based on ≈ 50 measurements obtained at various positions inside and outside the craters. More extensive correlations may show differences in distributions of carbon types and may also be crater-size dependent.

Diamond Craters. Regardless of their size, diamond craters contain much thicker, continuous liners compared to the other experimental carbon impactor craters (Fig. 5). Initial observations indicate several characteristic features of carbon residue. Figure 5c shows melt-like stringers and a large melt droplet on the crater wall. SEM-EDS analysis indicates a weak Al signal; thus, we conclude that the melt liner and the droplet are carbon. This melt liner is covered by a thin layer of dusty carbon. Raman analyses show that the layer is a mixture of amorphous carbon and highly disordered PCG. The crater bottom consists of submicron grains and tiny "melt" spheres (Fig. 6). The spheres may be the amorphous and vitreous carbon in the Raman analyses.

Raman spectrum of natural diamond consists of a broad band at 1330 cm^{-1}. Raman spectra of diamond impact craters in Al are the same as those obtained for PCG and vitreous carbons (Fig. 11c) and are similar to spectra given by carbon in the Allende meteorite. In some of the spectra, there is an indication of a shoulder at 1330 cm^{-1} which could be due to diamond; the vitreous band at 1360 cm^{-1} is intense and may obscure this portion of the diamond band.

There is apparently some difference in the various carbon distributions in the large craters (> 0.1 mm) and small craters (< 0.1 mm). Raman spectra of highly disordered (amorphous) carbon were obtained from the raised rim of small craters but not from the center of the crater, whereas no spectrum was obtained from the raised rim of the large craters, although measurements could be obtained from the crater interiors (bottoms).

Fullerene Craters. The bottoms and walls of these craters are characterized by a splatter-like texture that consists of spheres and branch-like structures of dark red fullerenes (Fig. 7). LIMS, (ref. 9) and Raman analyses confirm the presence of molecular C_{60} and C_{70} (fullerenes). Small amounts of red-brown dusty ejecta are present around many of the craters.

Raman spectra from prelaunched fullerenes (fullerenes have Raman bands at ≈ 1450 and 1560 cm^{-1}) and impact residues from inside and around fullerene craters are the same, indicating that fullerenes remained intact on impact (Fig.12).

Phthalic Acid Craters. Figure 8 shows that the irregular-shaped craters contain featureless impactor in crater bottoms with concentric ridges of impactor material on the walls. LIMS analyses indicate that the bulk of the impactor residuum is mostly intact phthalic acid molecule with lessor amounts of lower mass fragmented molecules and a few unidentified higher mass molecules (Fig. 9).

Murchison Meteorite Craters. These craters have considerable amounts of retained impactor, some apparently intact impactor, and impact alteration features that are unique among those described in this work (Fig. 10). Crater bottoms commonly have melt beads that grade into peculiar sponge-like structures at the lower portions of the wall (Figs. 10b and c). The upper walls and rims have large amounts of irregular-shaped melted to partially melted impactor.

Analytical Results

Murchison Meteorite Impactor Residues. For the purpose of comparison and proper identification of PAHs previously reported using conventional wet chemistry coupled with gas chromatography/mass spectrometry, a separate non-impacted sample of Murchison meteorite was analyzed (Figure 13). The dominant masses of 128, 178, 192, 206 and 220 correspond to naphthalene, phenanthrene/anthracene, methyl phenanthrene, fluoranthrene/pyrene, C_{16} - alkylphenanthrene/C_{16}- alkylanthracene and C_{17}-alkylphenanthrene/C_{17}-alkylanthracene respectively, which is consistent with the PAH analyses of Murchison reported by other groups (refs. 19, 20). The upper spectrum in Fig. 13 represents a single shot spectrum and the lower spectrum represents an average of 100 shots.

The two impacted samples were than analyzed and compared to the non-impacted Murchison samples (Figures 14 a and b). Figure 14a represents a 100 shot averaged spectrum for the sample impacted at 4.8 km sec^{-1}. The dominant masses of 142, 178, and 220 correspond to methylnaphthalene, phenanthrene/anthracene and C_{17}-alkylphenanthrene/C_{17}-alkylanthracene, respectively. Masses 128, 192, 202, and 206 present in the non-impacted Murchison sample are not seen in the impacted sample. Two different sample discs of the 4.8 km sec^{-1} sample were analyzed and show good reproducibility of the spectrum (Fig. 14b).

Figure 15a represents a 100 shot averaged spectrum for the sample impacted at 5.9 km sec^{-1}. Masses 184, 202, 206, 220, and 234 correspond to C_{14}- alkylnaphthalene, fluoranthrene/pyrene, C_{16}-alkylphenanthrene/C_{16}-alkylanthracene, C_{17}-alkylphenanthrene/C_{17}-alkylanathracene and C_{18}-alkylphenanthrene/C_{18}-alkylanthracene. In this sample the lower masses 128, 142, and 178 are no longer present but the higher masses 184, 202, 206, 220 are at least, in part, preserved. This is consistent with what one might expect to see since the lower molecular weight PAHs would likely be the first to decompose/evaporate with the temperatures incurred at impact. There also appears to be an increase in alkylation compared to the non-impacted Murchison (Fig. 13) which would indicate that some of these PAHs were derived from more extensively heated precursors (probably due to impact) since the high extent of alkylation of PAHs has been attributed ot the thermal cracking of the "organic polymer" (ref. 21). Two different sample discs (Fig. 15b) of the 5.9 km sec^{-1} were also analyzed and show good reproducibility of the spectrum.

All three samples were scanned for higher mass compounds both in the porphyrin and fullerene ranges, but no masses were observed.

Figure 16 shows the bulk fluorescence for the non-impacted sample (16a), the 4.8 km sec^{-1} impacted sample (16b), and the 5.9 km sec^{-1} impacted sample (16c). For these samples, we have not yet attempted to analyze for the individual species which will require a mating of the LIF to liquid chromatography. The fluorescence for both the non-impacted and the impacted meteorite bulk samples are intense and similar which suggests that at least PAHs identified by L^2MS can survive impacts. The LIF has been able to detect C_{60} standards in the 10^{-8} to $2x10^{-5}$ g range (ref. 20), although none were found in these analyses.

DISCUSSION

Examination of the experimental residues of graphite and diamond show diverse morphological features and impact-induced modifications, which were not unexpected in view of their differences in density, porosity, structural characteristics, bonding characteristics, bond energies, etc. On the other hand, phthalic acid, fullerenes, and Murchison PAHs show somewhat unanticipated molecular survivability on impact. The following discussion addresses these issues and first-order questions raised in the Introduction.

Diamond and Graphite

The apparent total destruction of diamond at an impact velocity < 5.0 km sec^{-1} is somewhat surprising. We can assume from our other experiments and theoretical considerations (refs. 22, 23) that residue material did not necessarily experience peak pressures and temperatures during impact, otherwise molecules such as PAHs would have been destroyed. By analogy, the carbon (PCG) in the diamond-formed craters probably formed from diamond at less than peak pressures and temperatures which occur only at the initial projectile/target interface. Any recovered material experienced less stress than the initial interface. We do not know what these P-T conditions were during impact, but from (ref. 22) we know that for impact of soda-lime glasses into Cu at ≈ 5 km sec^{-1}, peak pressures were > 65 GPa and temperatures ≈ 3000° K. Other clues come from the carbon phase diagram (Fig. 17) of Bundy (ref. 24). The presence of PCG (graphite) and melt carbon (liquid) and the absence of diamond suggest a position on the diagram near the triple point or in the range of 4000° K and < 14 GPa. This position on the diagram is near the region of "fast reaction" of diamond to graphite (ref. 25). Alternatively, our assumption that liquid carbon formed and is represented by the vitreous carbon droplets and balls in Fig. 6 may be incorrect and these graphitic objects may have formed as small, spherulitic graphite spheres from the decomposition of diamond at much lower temperatures. In either case, the evidence suggests that the pressures on the trailing side of the diamond impactor were insufficient to allow diamond to remain stable in a high temperature regime during impact.

The possibility that intact diamond is buried under the residue surface cannot be precluded. The analytical techniques that we have used are surface analyzers (tens of nanometers to micrometers deep); intact diamond may exist below the surface levels that we analyzed. Raman analysis of the residue does not show a well-defined peak for diamond at 1330 cm^{-1} (although it may be obscured by other carbon signals or weak signals from buried diamond below the surface). The band shape may indicate that diamond is just below the surface and out-of-range for a sharp signal or, conversely, that any diamond present at the surface is either highly disordered diamond or mixed phases of disordered diamond and graphite. In any case, the hope of seeing intact diamond from meteoritic or interstellar sources in LDEF craters is remote.

Raman spectra indicate that intact, well-ordered graphite did survive impact, together with partially disordered graphite in the crater bottom centers. The degree of disorder increases away from the crater centers. This suggests that material found in the centers probably represents material that experienced the least amount of shock-induced damage. Impactor material outside of the craters, which shows the highest degree of disorder, was probably ejected early in the crater formation stages and was exposed to higher pressures and temperatures, in addition to having cooled more rapidly. In fact, all residues cooled exceedingly fast as the entire crater forming event probably took no longer than nano- to microsecs (refs. 22, 23), although cooling continued after the pressures dropped to the ground state. The cooling rate is unknown, but sufficiently high to prevent annealing/ordering to occur. Thus, the graphite that was disordered by very high temperatures was not annealed. Rims and the upper walls captured some of the late-stage ejecta and melt splash before the crater cavity formation was completed; this residue material is intermediate in the degree of disorder between that of the centers and the outside ejecta.

Phthalic acid and Murchison Meteorite

The two impacted Murchison samples both show preservation and destruction of some PAHs compared with the non-impacted Murchison sample. The differences in PAH compositions between the two impacted samples may be attributed to the well-known inhomogeneous distribution of organics within the whole meteorite (ref. 26). The samples taken for these impacts may also represent different parts of the meteorite. However, the

consistent absence of the low mass PAHs in all cases of both impactor residues and the very good reproducibility of the analyses coupled with an average of 100 analyses for each impactor residue where the low mass PAHs are missing, strongly suggest that the missing lower mass PAHs, which have lower boiling points (T_b K), vaporized on impact. The T_b K values for the missing PAHs are < 500, whereas T_b K for the surviving PAHs are > 600 (ref. 27) which could imply an upper, effective evaporation temperature limit sustained during impact for the surviving PAHs. Thus, it appears that at least some of the higher mass PAHs common in meteorites like Murchison, can survive hypervelocity impact under the experimental conditions presented here.

From the above, we have shown that some organic molecules can survive low hypervelocity impact into Al targets (phthalic acid at 4.2 km sec^{-1} and Murchison meteorite higher molecular weight PAHs at least up to 5.9 km sec^{-1}). Kinetic parameters from shock tube experiments with simple, low molecular weight organic compounds show that they can withstand shock temperatures up to 1500° K for a duration of ≤ 1 sec.; heavier, more complex aromatics may also survive at these temperatures and reaction times (ref. 23). As we have indicated above, peak pressures and temperatures are unknown for our experiments; however, they would certainly be sufficient to destroy all Murchison organic compounds if all of the kinetic energy of the impactor were available for impactor melting. Actually, much of an impactor's kinetic energy is probably partitioned into target heating, target excavation, and target/impactor ejection (ref. 28). In addition, an uneven distribution of shock energy through the impactor would possibly allow some portion of the impactor to experience temperatures under which some organic compounds could survive. Thus, from these considerations and from the results of our experiments, we expect to be able to find some surviving organic species in LDEF carbonaceous impactor residues, if indeed, any were present in the preimpact IDPs.

Fullerene Formation/Destruction Conditions

Since no fullerenes were found in the ppm range in carbonaceous impactor craters, we can assume that conditions were inappropriate for their formation. Our failure to make fullerenes by impact could be due to any number of reasons, e. g., nucleation/growth kinetics, improper temperatures and pressures, accompaning compositional interference, etc. Shock compression ("flying plate") experiments made under known P-T conditions suggest that fullerenes are stable up to 17 GPa (ref. 29). However, these experiments recorded the stability of fullerenes under more evenly distributed shock loading compared to those that arise from crater forming events where pressures and temperatures fall rapidly as crater formation proceeds. Even though these experiments are not directly analogous to crater forming events, they do establish that fullerenes are remarkably incompressible and remain unchanged to moderately high shock pressures. Future experiments may be designed to further address the issues of fullerene stability or formation on hypervelocity impact. The questions as to whether fullerenes pre-existed before impact on LDEF or were formed by impact remain unanswered.

Laser ionization mass spectroscopy techniques have been able to detect PAHs in meteorites on the sub ppm level (ref. 20)and ppb range (ref. 30). Other analyses of PAHs in the Murchison meteorite by similar L^2MS techniques suggest that cosmic abundances of hydrogen in circumstellar or interstellar environments may have precluded the synthesis of fullerenes, but not the production of PAHs (ref. 30). Recently, a carbonaceous residue from an LDEF crater was analyzed by LIMS and Raman methods and the presence of fullerenes was confirmed (ref. 9). Very low concentration levels of fullerenes in other LDEF craters or in meteorites could be identified by using the LIF system which could help address the issues of fullerene formation in space environments.

CONCLUSIONS

Intact remnants of diamond impactors were not found. Diamond was converted during impact (4.8 km sec^{-1}) to various disordered forms of graphite (PCG). Diamond crater morphology is unique among carbon impactors in having thick residue liners. Graphite impactor residue, formed at impact velocities up to 5.9 km sec^{-1}, shows some intact, well-ordered graphite in the residue of crater bottom centers; the degree of disorder increases outward to the ejecta.

Fullerenes were not formed on impact from carbon-bearing precursors (diamond, graphite, phthalic acid, Murchison particles). Moreover, fullerene impactors mostly remained as fullerenes after impact at 5.9 km sec^{-1}.

Phthalic acid crystals were destroyed on impact, although much of the molecules remained intact at the impact velocity of 4.2 km sec^{-1}.

Murchison meteorite residues in the crater bottoms have an unusual, sponge-like morphology which may be the result of the precursor's abundance of water-bearing, layer-lattice silicates. This type of morphology may prove to be useful in distinguishing between hydrous and anhydrous particles that impacted at velocities ≤ 6 km sec^{-1}.

Some PAHs (mostly the higher mass species) in the impacted Murchison meteorite samples survived impact. From theoretical considerations and our experimental results, we expect to find some surviving carbonaceous impactor organic compounds in LDEF craters that formed up to ≈ 10 km sec^{-1} impact velocity.

LIF detection is not limited to bulk analyses such as those that we carried out, but can be used as an on-column detector for HPLC, microbore HPLC and open tubular liquid chromatography. The great mass sensitivity of LIF coupled with these systems should permit the analyses of trace quantities of organic compounds and help to differentiate among other carbonaceous materials such as fullerenes and thus determine whether fullerenes occur naturally in cometary and asteroidal (IDPs) samples.

REFERENCES

1. See, T.; Allbrooks M.; Atkinson D.; Simon C.; and Zolensky M.: Meteoroid and debris impact features documented on the Long Duration Exposure Facility a preliminary study. *Planet. Sci Branch Publ.* # **73** (JSC # **24608**), 1990.

2. Hörz, F.; Bernhard, R. P.; Warren, J.; See, T.; Brownlee, D. E.; Laurance M. R.; Messenger, S.; and Peterson, R. B.: Preliminary analysis of LDEF instrument A0187-1 "Chemistry of micrometeoroids experiment". *First LDEF Sym. NASA* **CP-3134,** 487-499, 1992.

3. Bunch, T. E.; Radicati di Brozolo, F.; Fleming, R. H.; Harris, D. W.; Brownlee, D. E.; and Reilly, T.: LDEF impact craters formed by carbon-rich impactors: A preliminary report. *First LDEF Sym. NASA* **CP-3134**, 549-564, 1992.

4. Peterson, E.; Hörz, F.; Haynes, G.; and See, T.: Modification of amino acids at shock pressures of 3 to 30 GPa. *Meteoritics* **26**, 384,1991.

5. Lewis, R. S.; Tang, M.; Wacker, J. F.; Anders, E.; and Steel. E.: Interstellar diamonds in meteorites. *Nature* **326**, 160-162, 1987.

6. Allamandola, L. J.; Sandford, S. A.; and Tielens, A. G. G. M.: Interstellar "diamonds" in dense molecular clouds. *Nature* 1992.

7. Allamandola, L. J.; Sanford, S. A.; and Wopenka, B.: Interstellar polycyclic aromatic hydrocarbons and carbon in interplanetary dust particles and meteorites. *Science* **237**, 56-59, 1987.

8. Langevin, Y.; Kissel, J.; Bertaux, J-L.; and Chassefiére E.: First statistical analysis of 5000 mass spectra of cometary grains obtained by PUMA 1 (Vega 1) and PIA (Giotto) impact ionization mass spectrometers in the compressed modes. *Astron. Astrophys.* **187**, 761-766, 1987.

9. Radicati di Brozolo, F.; Fleming, R. H.; and Bunch, T. E.: Observation of fullerenes in an LDEF impact crater. *Science* in press, 1992.

10. Chen, R.F.; Becker, L.; Bada, J.L.: Detection of C_{60} using Laser-Induced Fluorescence. *J. of Amer. Chem Soc.* 1992.

11. Odom, R. W.; and Schueler, B. W.: Laser microprobe mass spectrometry: Ion and neutral analysis. in *Lasers and Mass Spectrometry*, D. M. Lubman ed. Oxford University Press, 103, 1990.

12. Krätschmer, W.; Lamb, L.D.; Fostivopoulos, K.; and Huffman, D. R.: Solid C_{60}: A new form of carbon. *Nature*, **347**, 354, 1990.

13. Hahn, J.H.; Zennobi, R.; Zare, R.N.: Subfemtomole quantitation of molecular absorbates by two-step laser mass spectrometry. *J.Am, Chem.Soc.* **109**, 2842-2843, 1987.

14. Engelke, F.; Hahn, J.H.; Henke; W., Zare; R.N.: Determination of phenythiohydrandion-amino acids by two-step laser desorption/multiphoton ionization. *Anal. Chem.* **59**, 909-912, 1991.

15. Hillenkamp; F.; Karas, M.; Beavis; R.C.; Chait; B.T.: Matrix-assisted laser desorption/ionization mass spectrometry of biopolymolecules. *Anal. Chem.* **63**, 24-37, 1991.

16. Zare, R.N.: Laser chemical analysis. *Science* **226**, 298-303, 1984.

17. Chen, R.F.and Bada, J.L.: A laser-based fluorometry system for investigations of seawater and porewater fluorescence. *Mar. Chem.* **31**, 219-230, 1990.

18. Macklin, J.; Brownlee, D. E.; Chang. S.; and Bunch, T. E.: Micro-Raman spectroscopic measurement of carbon in meteorites and interplanetary dust particles. *Microbeam -87*, 211-212, 1987.

19. Oro, J. et al.: Amino acids, aliphatic and aromatic hydrocarbons in the Murchison meteorite. *Nature* **230**, 105-106, 1971.

20. Hahn; J.H.; Zenobi, R.; Bada; J.L., Zare; R.N.: Application of two-step laser mass spectrometry to cosmochemistry: Direct analysis of meteorites. *Science* **239**, 1523-1525, 1988.

21. See Tissot, B.P. and Welte, D.H.: *Petroleum Formation and Occurrence*. Springer-Verlag, Berlin, 1984 for a comprehensive review of pyrolysis of aromatic compounds.

22. Hörz, F.; Fechtig, H.; and Janicke, J.: Morphology and chemistry of projectile residue in small experimental impact craters. *Proc. 14th Lunar Planet. Sci. Conf. Part 1, J. Geophy. Res.* **88**, B353-B363, 1983

23. Chyba, C. F.; Thomas, P. J.; Brookshaw, L.; and Sagan, C.: Cometary delivery of organic molecules to the early Earth. *Science* **249**, 366-373, 1990.

24. Bundy, F. P.: *Physica* A**156**, 169-178. 1989.

25. Regueiro, M. N.; Monceau, P.; and Hodeau, J-L.: Crushing C60 to diamond at room temperature. *Nature* **355**, 237-239, 1992.

26. See Nagy, B., *Carbonaceous Meteorites*. Elsevier, Amsterdam, 1975 for a comprehensive review of this early research.

27. White. C. M.: Predictions of the boiling point, heat of vaporization, and vapor pressure at various temperatures for PAHs. *J. Chem. Eng. Data* **1986**, 31, 198-203, 1986.

28. O'Keefe, J. D. and Ahrens, T. J.: in *Geololgical Implications of Impacts of Large Asteroids and Comets on the Earth,* L.Silver and P. Schultz, eds. *Geol. Soc. Am.* **SP-190.** 103-120, 1982.

29. Yoo, C. S. and Nellis, W. J.: Phase transformations in carbon fullerenes at high shock pressures. *Science*, **254,** 1489-1491, 1991.

30. De Vries, M.S.; Wendt, H.R.; Hunziker, H.; Peterson, E.; and Chang, S.: Search for high molecular weight polycyclic aromatic hydrocarbons and fullerenes in carbonaceous meteorites. *Lunar and Planetary Sci. XXII*, 315-316 1991.

ACKNOWLEDGEMENTS

We thank B. Langedyk, W. Logsdon, and J. Vongrey for their assistance during the impact experiments and the NASA OSSA Exobiology 199-52-12 and OAST 506-48 Programs for partially supporting this work. F. R di B and RHF acknowledge support from NASA SBIR Contract NAS2-13178. We also thank Sherwood Chang and Fred Hörz for critical reviews and helpful suggestions.

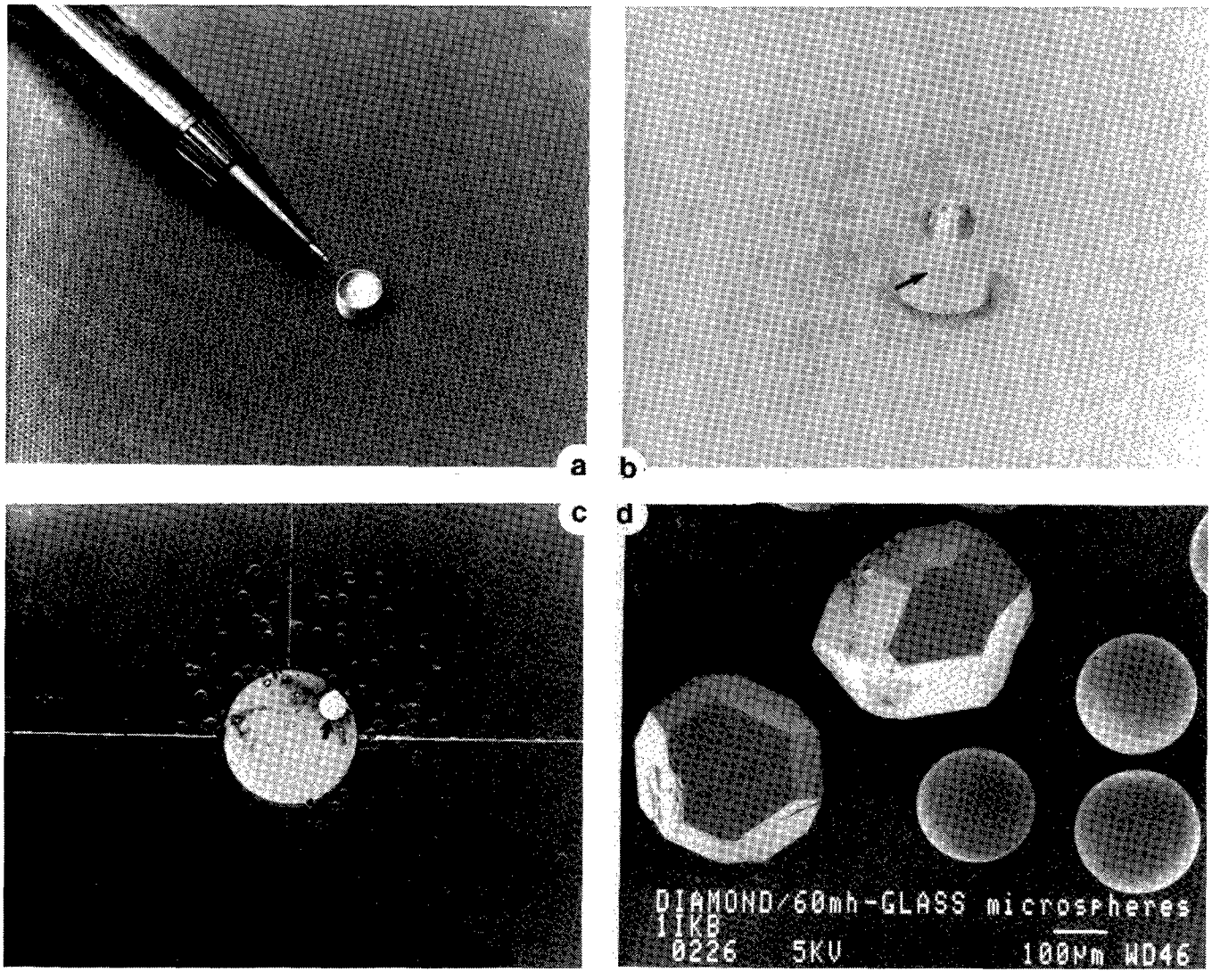


Figure 1. (a) Particle carrier for cluster launches. (b) Carrier with lid set in a plastic sabot. (c) Witness plate showing alignment test pattern of craters produced by boron nitride projectiles. Hole in the center (2.5 cm in dia; covered with mylar film) is the escape hole for the carrier which made the hole in the mylar covering (NE quadrant). Smaller holes in the film are from passage of projectiles. (d) Example of diamond projectiles.

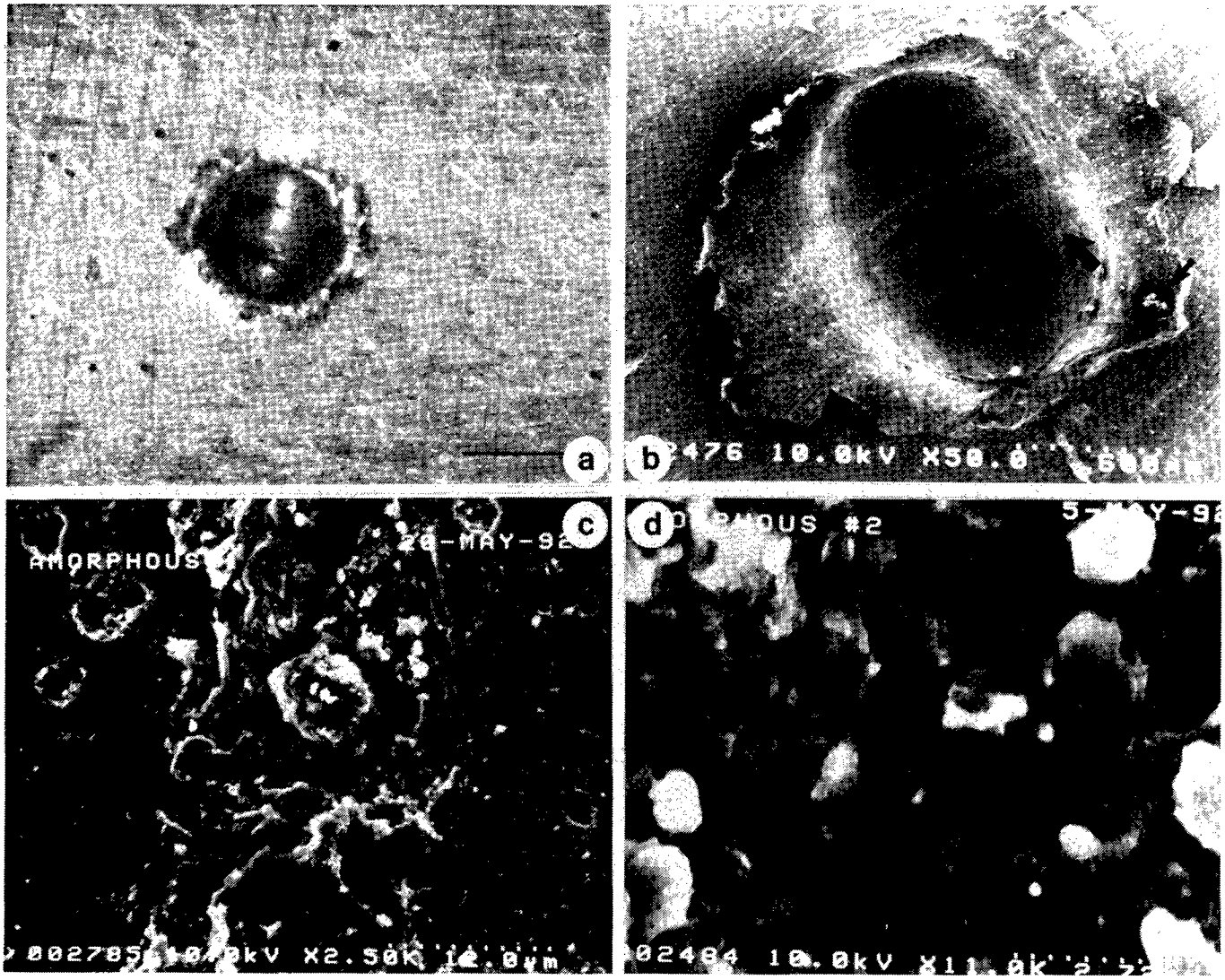


Figure 2. Large submicron graphite impactor craters. (a) Very large crater made from a statically clumped graphite impactor ball. Note the much smaller craters. Scale bar = 0.5 mm. (b) FESEM image of crater in a. Large arrow points to subparallel ejecta ridges. Small carbon melt spheres can be seen on the rim (small arrows). Scale for all FESEM images are given in the lower right hand corner. (c) Enlargement of ejecta ridge (center) on the carbon melt liner. (d) Enlarged view of the ejecta ridge material. Bright areas may be melted Al.

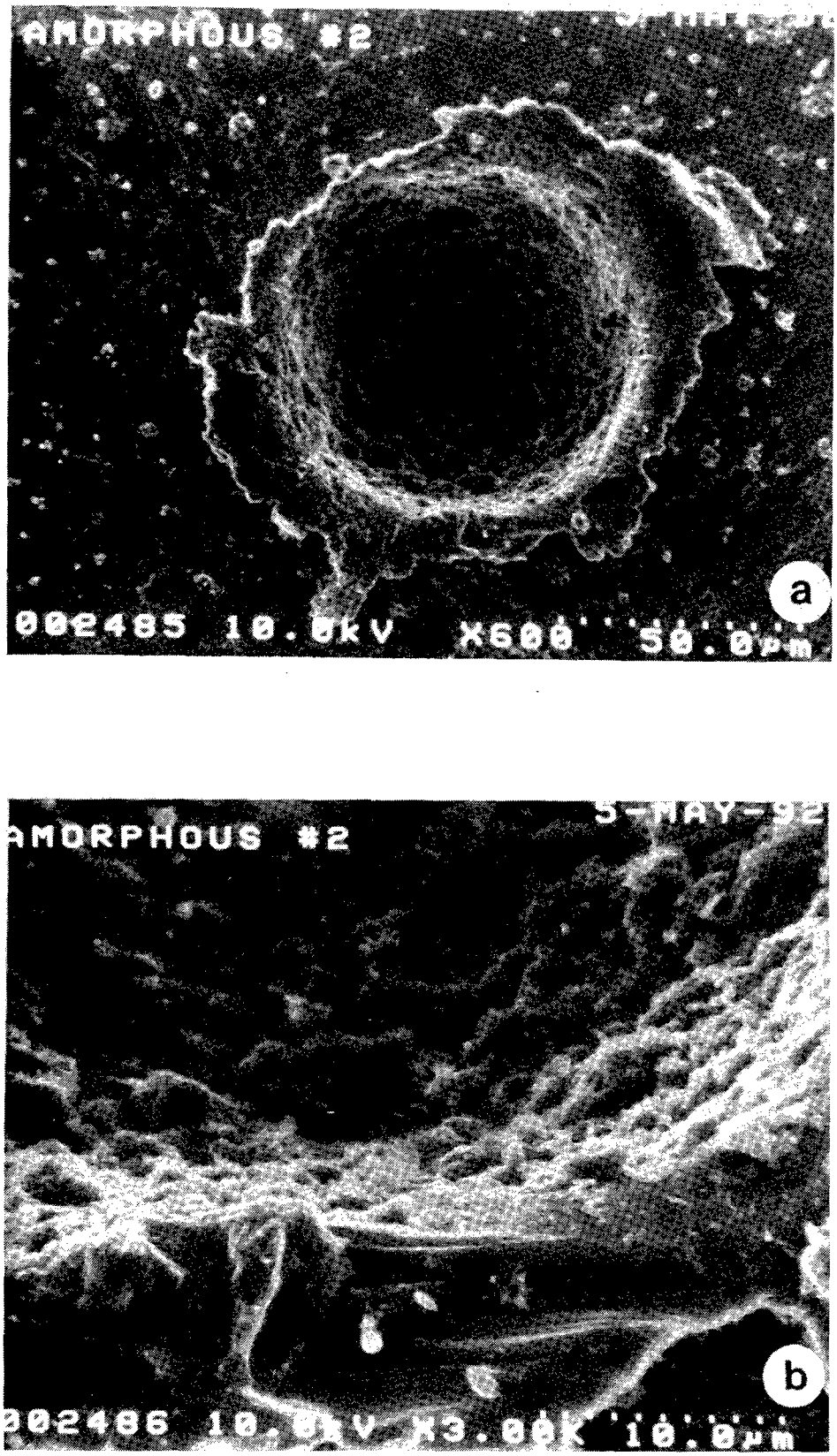


Figure 3. Small submicron graphite impactor craters. (a) Typical crater. (b) Image of impactor residue on the crater bottom (top), the wall (center), and rim (bottom).

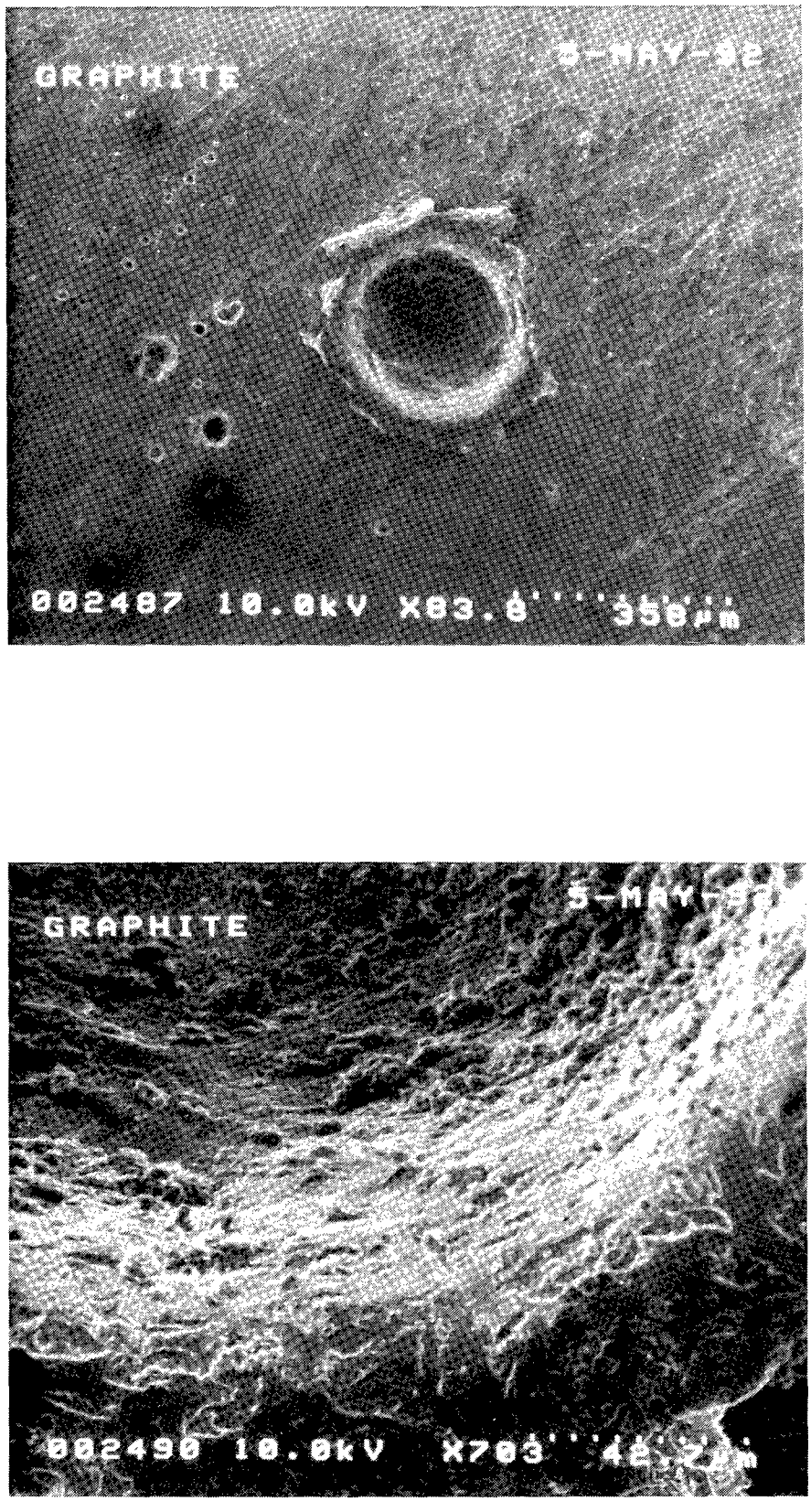


Figure 4. Coarse graphite impactor craters. (a) Typical crater. (b) Image of impactor residue on the bottom, wall, and rim.

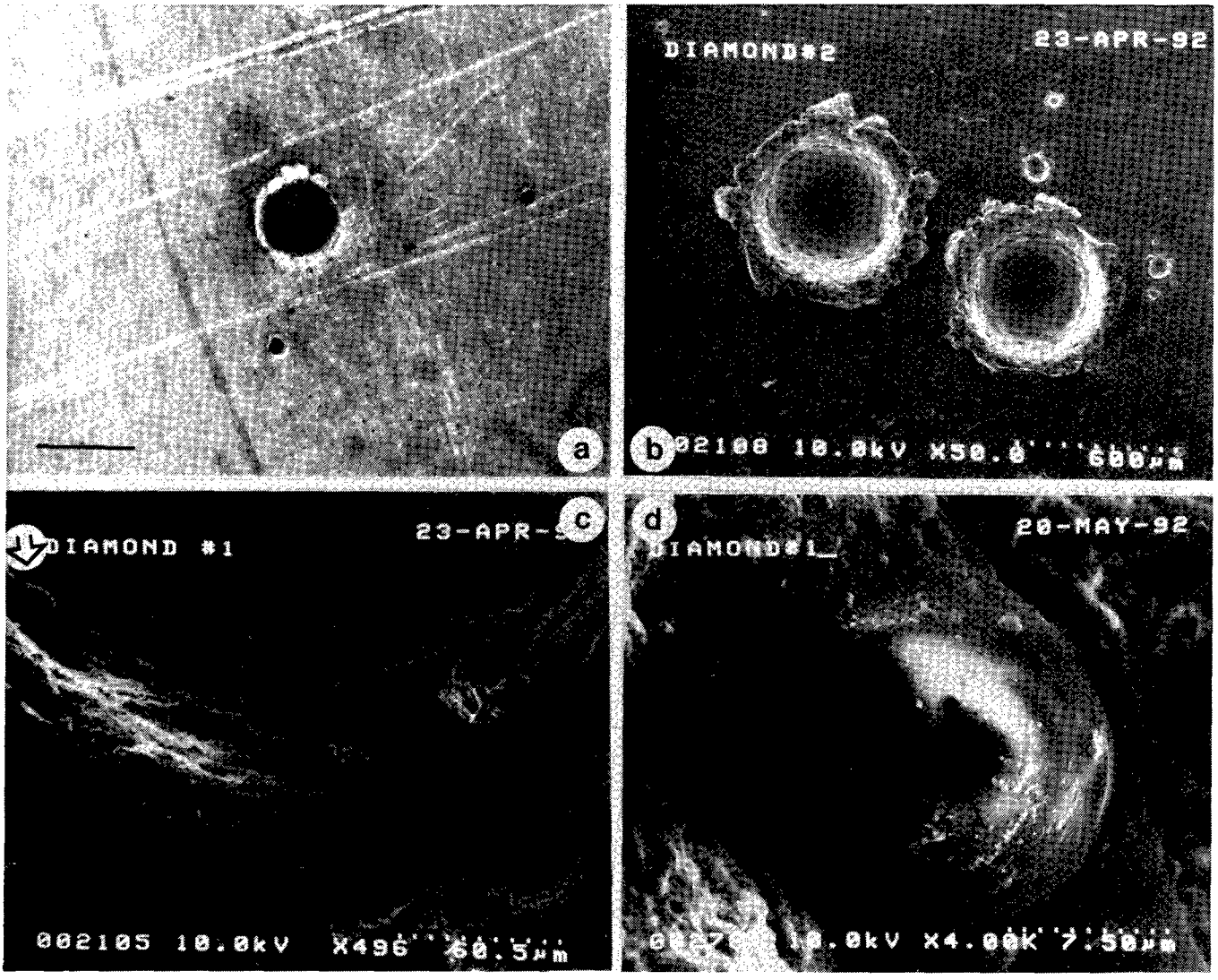


Figure 5. Diamond impactor craters. (a) Typical crater; note the black interiors. Scale = 0.5 mm. Oblique lighting, photomicrograph. (b) FESEM image; note darkened rims from carbon ejecta. (c) Image of impactor residue on bottom, wall, and rim. Note carbon melt droplet (arrow). (d) Close-up of droplet; arrow indicates a depression which may be due to shrinkage on cooling.

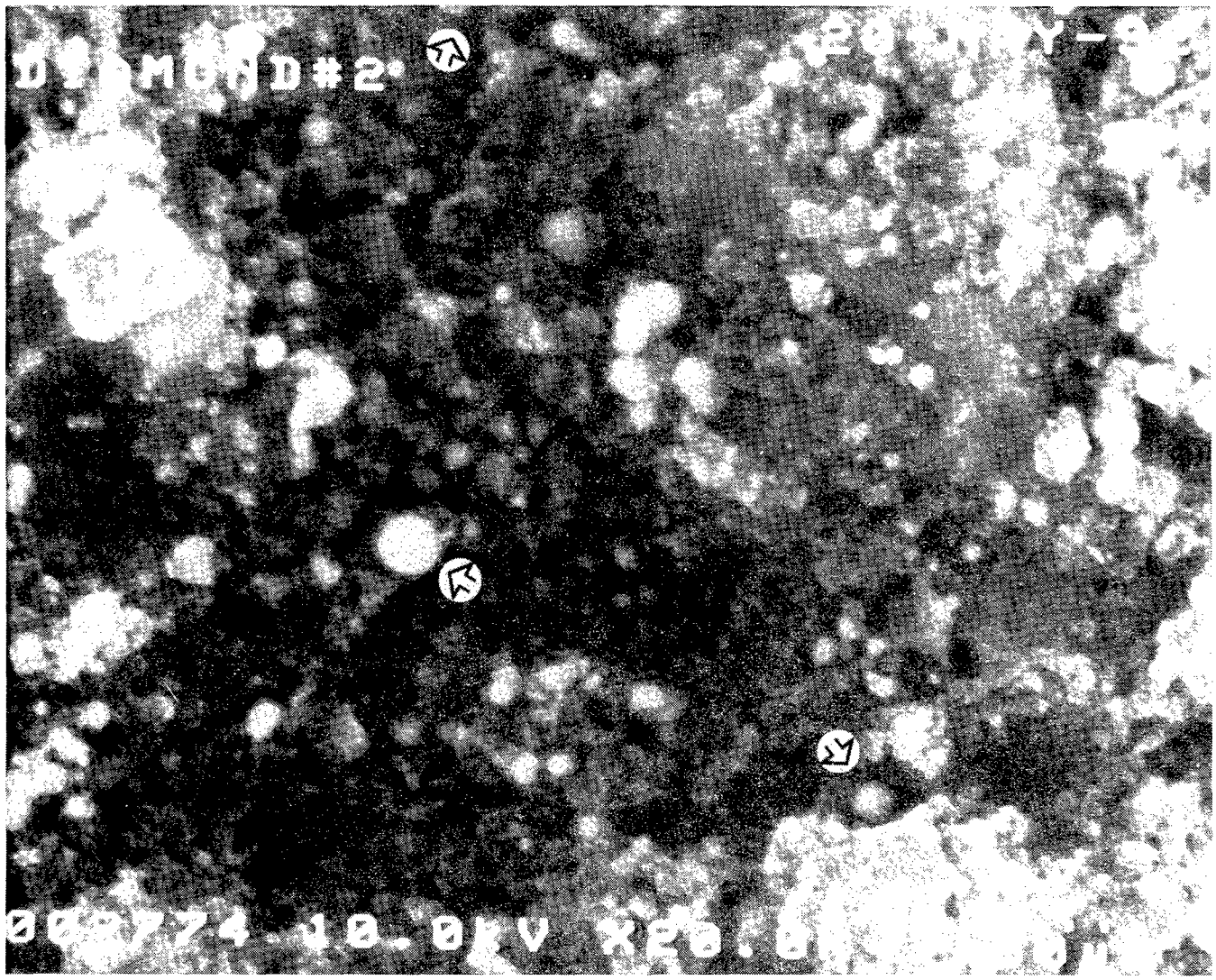


Figure 6. Enlarged image characteristics of diamond impactor residue. Arrows point to carbon melt balls (< 0.001 mm dia.) which, from Raman spectra, may be vitreous carbon; the other material is probably highly disordered graphite (PCG).

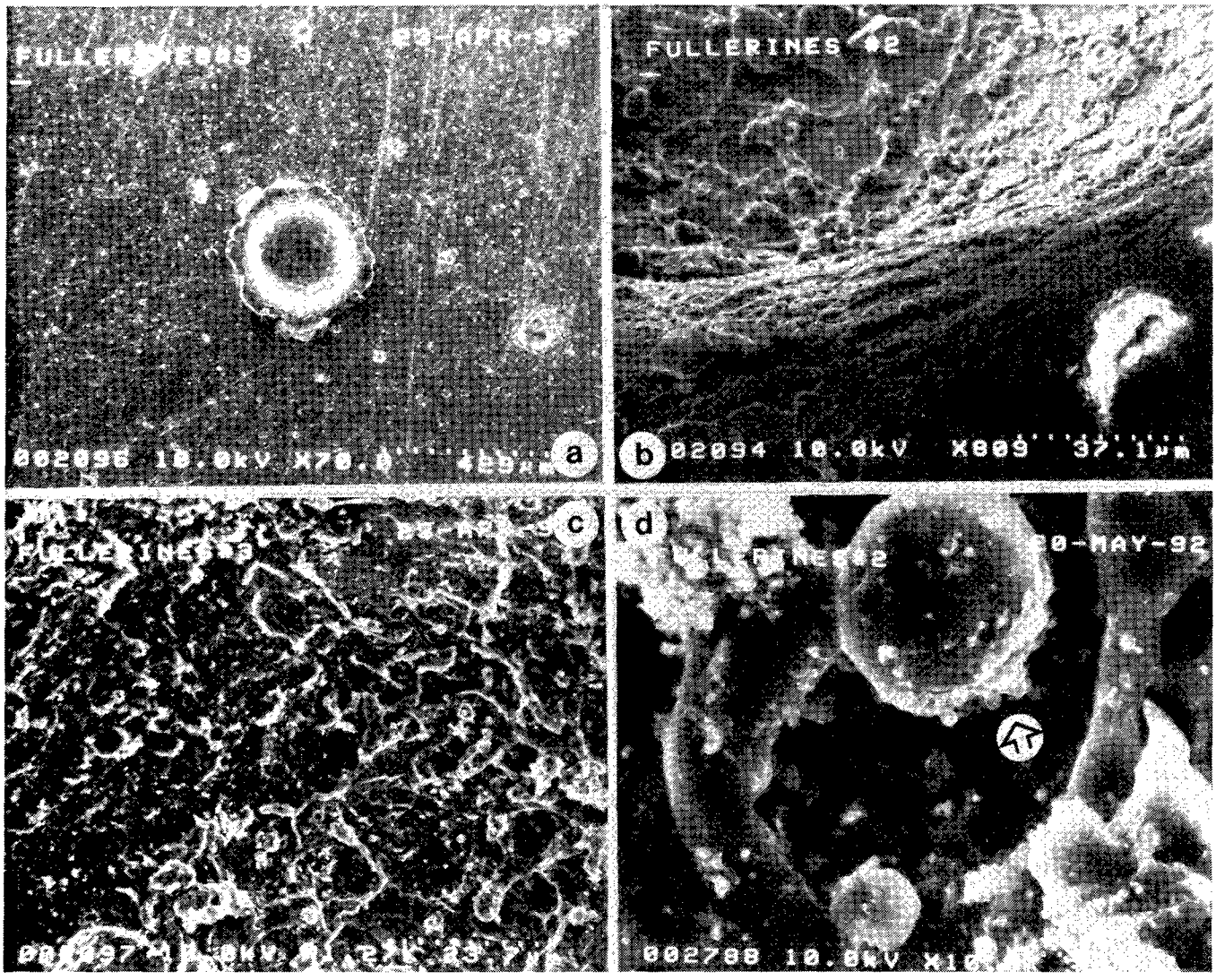


Figure 7. Fullerene impactor craters. (a) Typical crater. (b) Image of impactor residue on the bottom, wall, and rim. (c) Melt splatter features on the bottom and lower wall (turn image 180° to get a better perspective). (d) High resolution of material in c (arrow points to a 0.006 mm melt ball with attached rounded material (submicron).

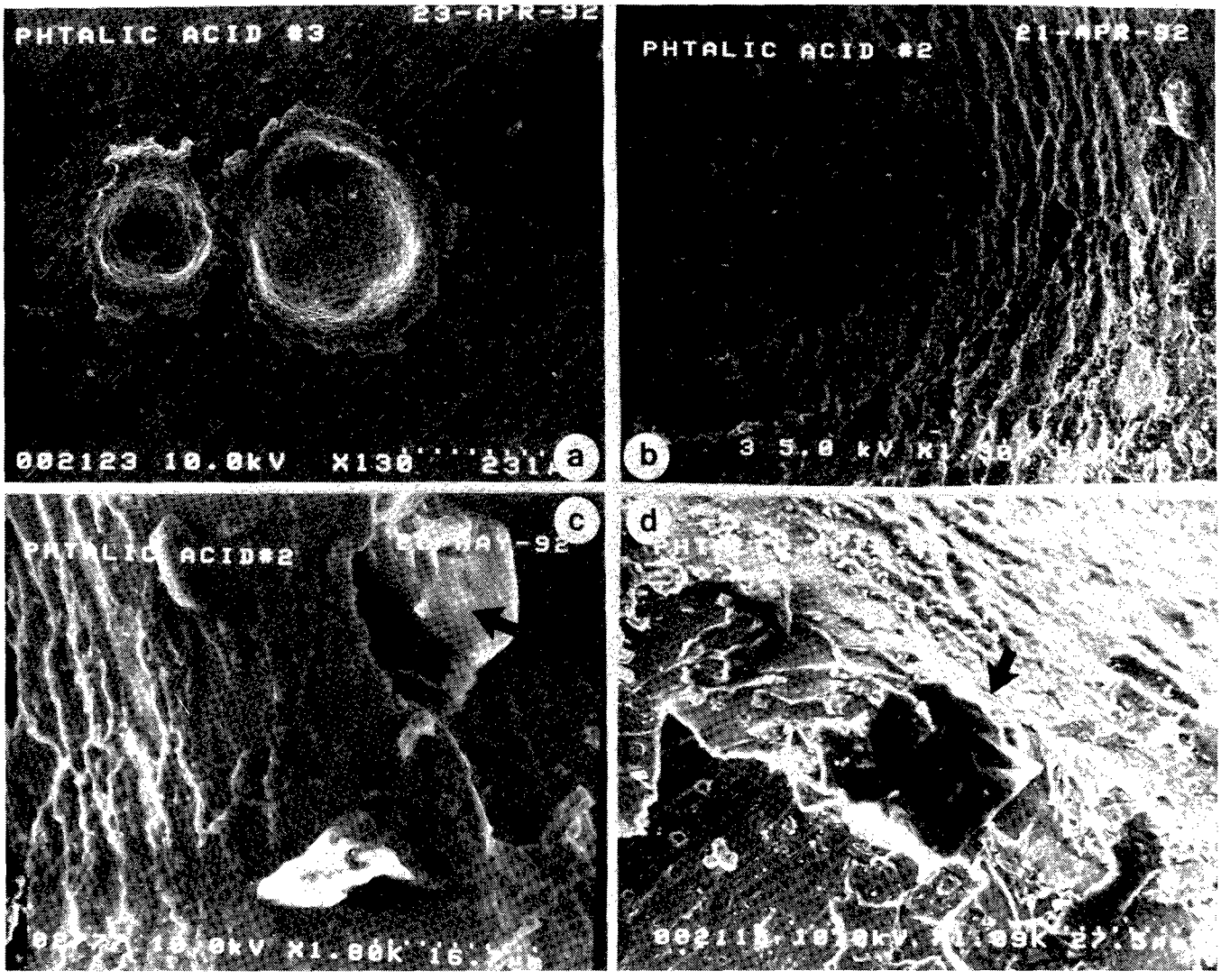


Figure 8. Phthalic acid impactor craters. (a) Typical craters showing irregular crater outlines. (b) Image of the residue on the bottom (left), lower wall (center), and upper wall (right). (c) Image showing top of rim and a partially melted impactor grain (arrow) that is outside of the crater and underneath the rim, possibly arising from ejection from a nearby crater. (d) Top of a rim; arrow points to a cluster of dipyramidal crystals of unknown composition.

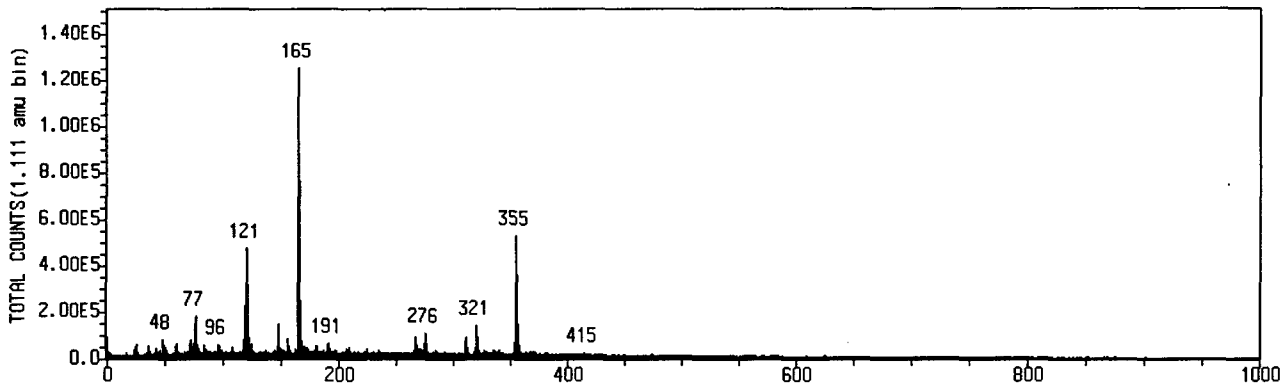


Figure 9. LIMS spectrum showing negative ion phthalic acid (mass 165), a phthalic acid molecular fragment (minus a carboxyl) at mass 121, and other unidentified masses.

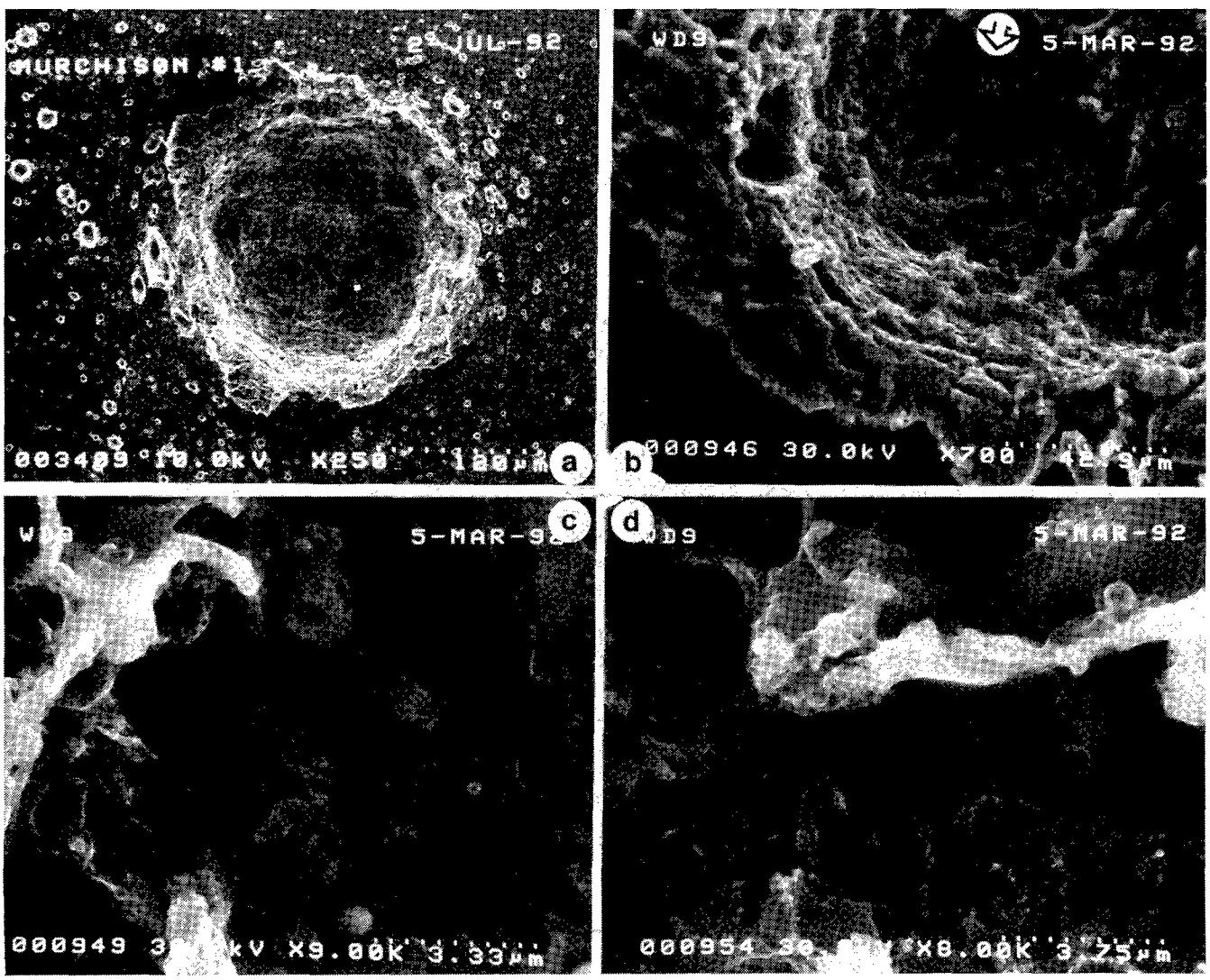


Figure 10. Murchison meteorite impactor craters. (a) Typical craters. (b) Image showing the residue on the bottom, wall, and rim (arrow refers to a melt blob in the bottom). (c, d) Close-up views of peculiar sponge-like melt features in the crater bottoms and walls.

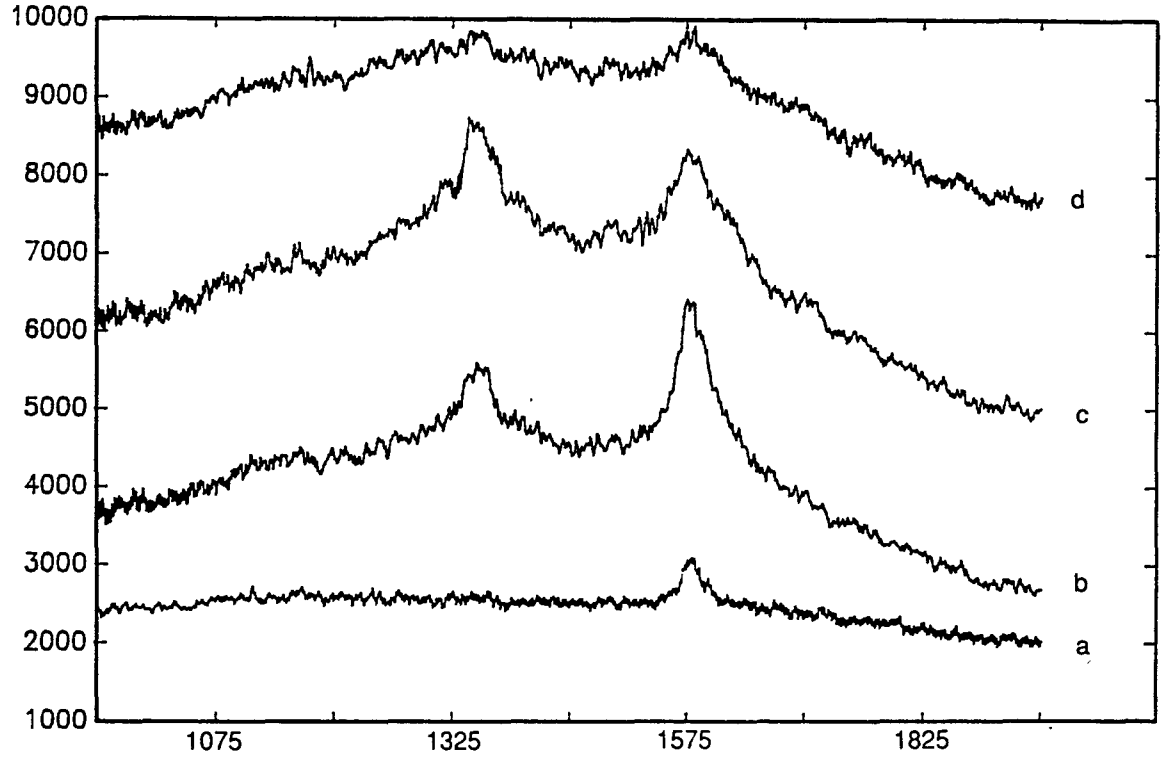


Figure 11. Typical Raman spectra of prelaunched graphite and impactor residues. (a) Precursor graphite. (b) Spectrum from crater centers. (c) Spectrum from crater walls to near the centers. (d) Spectrum from raised rim and outside ejecta.

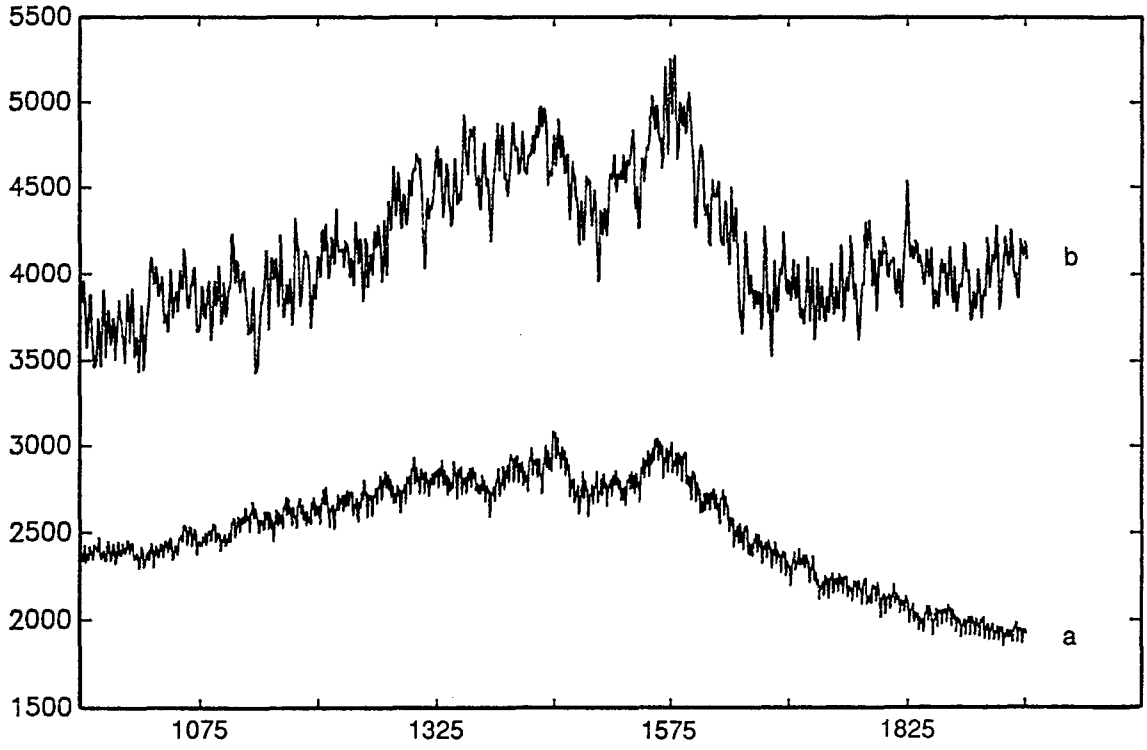


Figure 12. Typical Raman spectra of (a) precursor fullerenes and (b) fullerene impact crater residue.

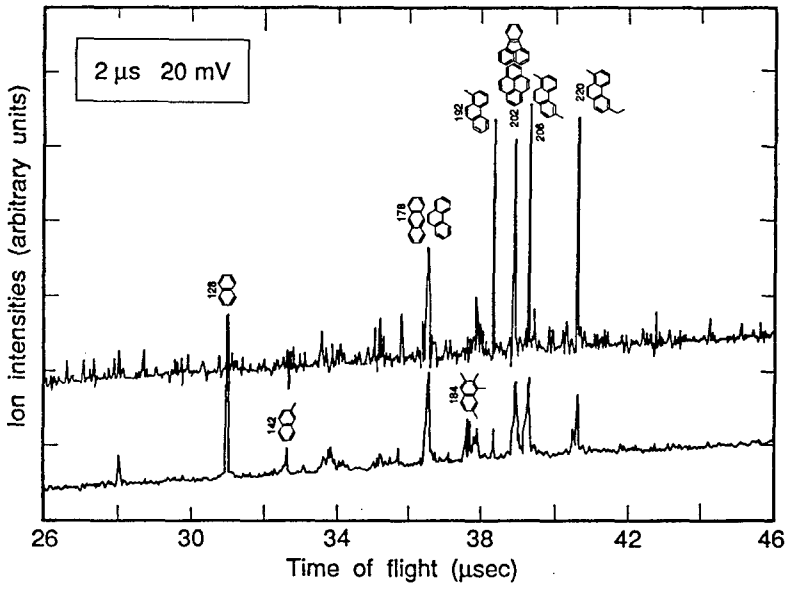


Figure 13. Laser desorption/multiphoton ionization TOF mass spectrum of non-impacted Murchison meteorite. Possible mass identification are: 128, naphthalene; 178, phenanthrene/anthracene; 192, methylphenanthrene; 202, fluoranthrene/pyrene; 206, C_{16}-alkylphenanthrene/C_{16}-alkylanthracene and 220,C_{17}-alkylphenanthrene/C_{17}-alkylanthracene. (a) Represents a single shot spectrum. (b) An average of 100 shots.

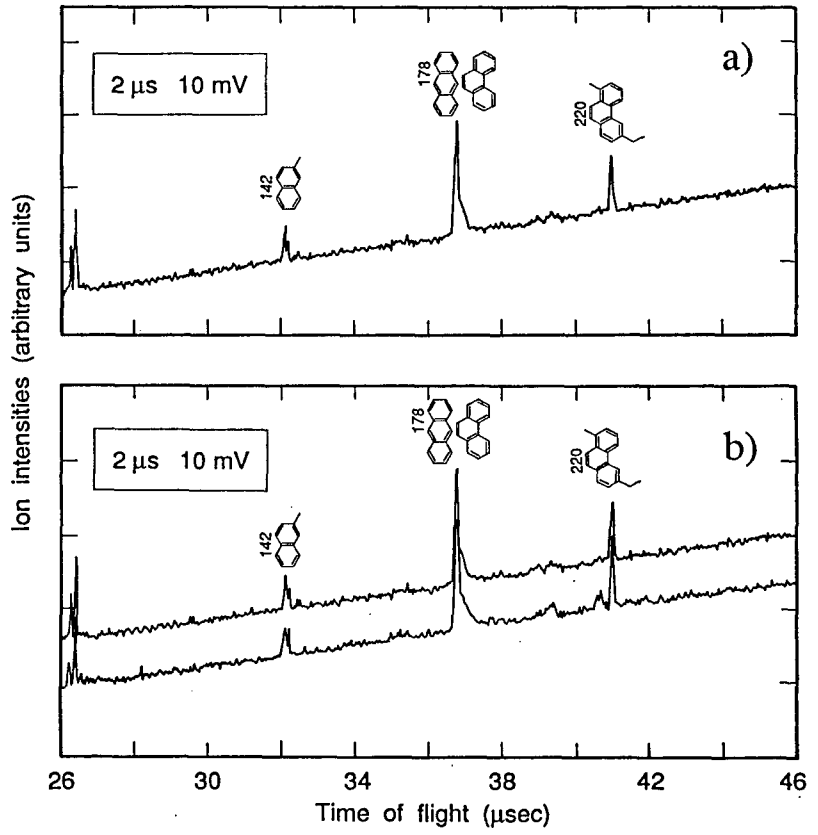


Figure 14. (a) 100 shot averaged spectrum for the sample impacted at 4.8 km sec^{-1}. Possible mass identification are: 142, methylnaphthalene; 178, phenanthrene/anthracene and 220, C_{17}-alkylphenanthrene/C_{17}-alkylanthracene. (b) Two different sample disks that show good reproducibility.

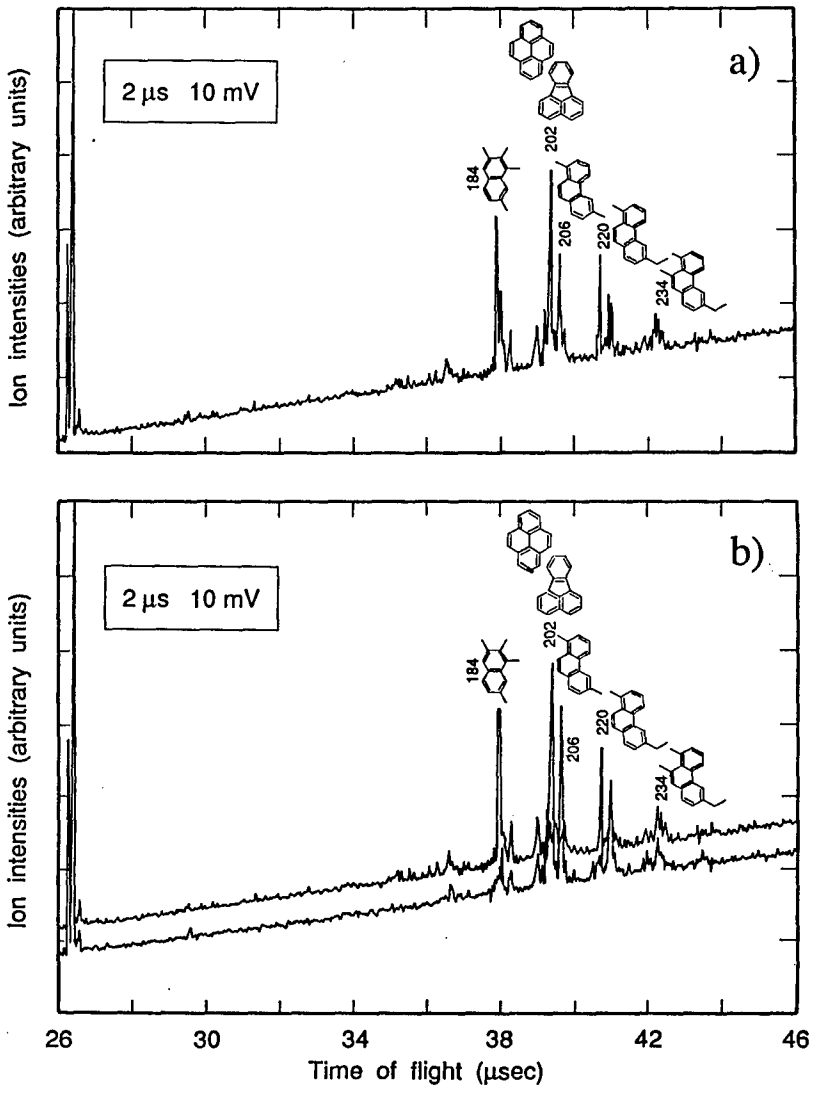


Figure 15. (a)100 shot averaged spectrum for the sample impacted at 5.9 km sec^{-1}. Possible mass identifications are: 184, C_{14}-alkylnaphthalene; 202, fluoranthene/pyrene; 206, C_{16}-alkylphenanthrene/C_{16}-alkylanthracene; 220, C_{17}- (b) Two different sample disks that show good reproducibility.

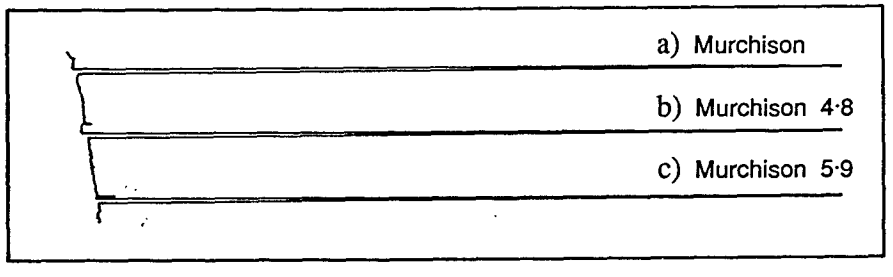


Figure 16. Bulk fluorescence using LIF for: (a) the non-impacted Murchison sample, (b) the 4.8 km sec^{-1} impacted sample, and (c) the 5.9 km sec^{-1} impacted sample.

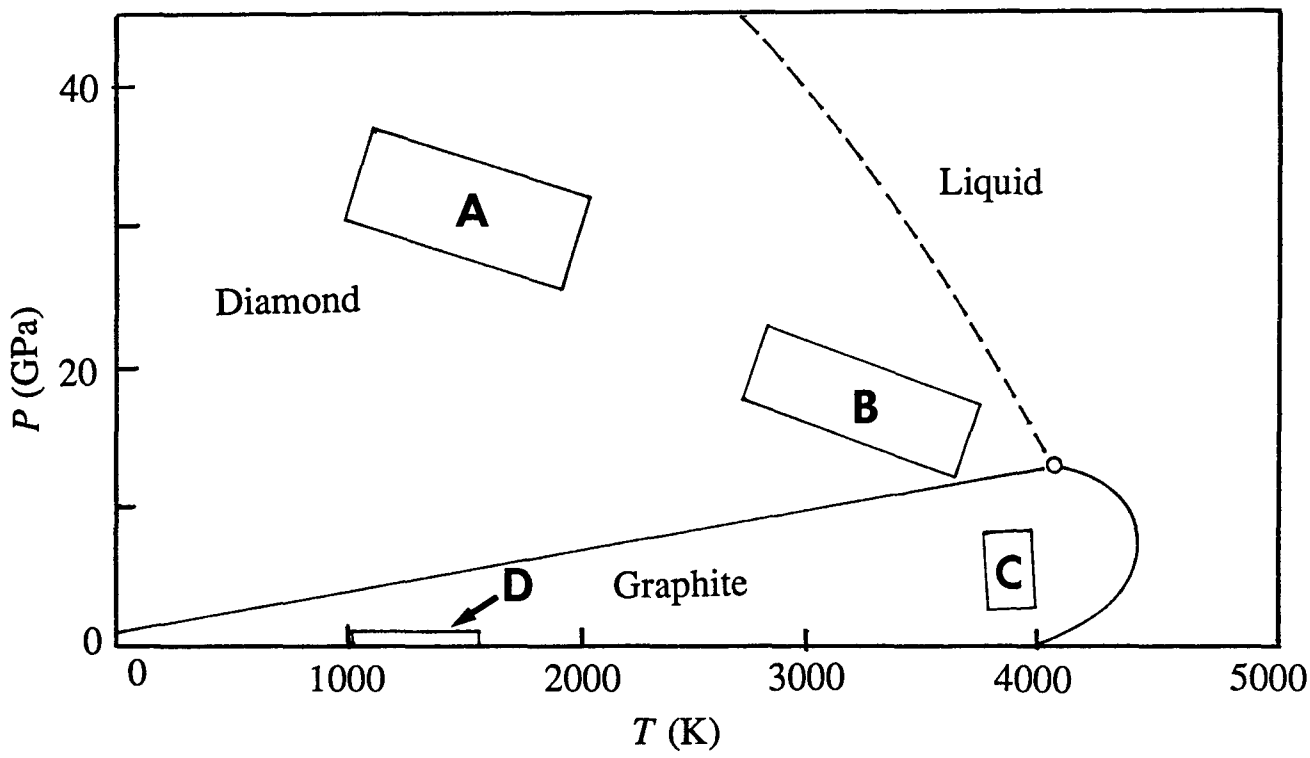


Figure 17. A portion of the carbon phase diagram (ref. 22). Field A is the region of shock conversion of graphite to diamond; field B is the region of "fast reaction", graphite to diamond; field C is the region of "fast reaction" diamond to graphite; field D is region of vapor deposited diamond films (ref. 25). The presence of both graphite and melt-droplet carbon (liquid carbon) and the absence of diamond in the diamond crater residue suggest that an area near the triple point in the diagram (liquid-diamond-graphite) was reached during impact for these products, but was below the diamond stability field, i. e., below a pressure of ≈ 14 GPa at 4000°K.

HYPERVELOCITY IMPACT FACILITY FOR SIMULATING MATERIALS EXPOSURE TO IMPACT BY SPACE DEBRIS

M. F. Rose,
S. Best, T. Chaloupka, B. Stephens, G. Crawford
Space Power Institute
Auburn University, AL

ABSTRACT

As a result of man's venturing into space, the local debris contributed by his presence exceeds, at some orbital altitudes, that of the natural component. Man's contribution ranges from fuel residue to large derelect satellites weighing many kilograms. Current debris models are able to predict the growth of the problem and suggest that spacecraft must employ armor or bumper shields for some orbital altitudes now and that the problem will become worse as a function of time. The practical upper limit to the velocity distribution is on the order of 40 km/sec and is associated with the natural environment. The maximum velocity of the man-made component is in the 14-16 km/sec range. The long duration exposure facility (LDEF) has verified that the "high probability of impact" particles are in the microgram to milligram range. These particles can have very significant effects on coatings, insulators, and thin metallic layers. The surface of thick materials becomes pitted and the local debris component is enhanced by ejecta from the impact events. In this paper, a facility is described which produces a reasonable simulation of the space debris spectrum in a controlled environment. The facility capability is discussed in terms of drive geometry, energetics, velocity distribution, diagnostics, and projectile/debris loading. The facility is currently being used to study impact phenomena on Space Station Freedom's solar array structure, other solar array materials, potential structural materials for use in the station, electrical breakdown in the space environment, and as a means of clarifying or duplicating the impact phenomena on the LDEF surfaces. The results of these experiments are described in terms of the mass/velocity distribution incident on selected samples, crater dynamics, and sample geometry.

INTRODUCTION

In addition to the natural space micrometeoroid environment, the constant injection by man of a non-natural component has led to additional concern. This "space pollution" has accelerated due to the steadily increasing frequency of launches by the industrialized countries even though there is a growing awareness that the debris problem must be addressed. As other countries become active in space and if space concepts such as those envisioned by the SDI are deployed, it is inevitable that future spacecraft will have to devote a substantial mass fraction to the armoring of critical components. Further, hypervelocity impact produced debris and plasma can trigger electrical breakdown and further reduce the effectiveness of insulators for space use. For the most favored low-to-medium earth orbits it is projected from some models [1] that significant design changes will be necessary by the year 2000. At geosynchronous orbits the problem would be a design driver not too many years thereafter.

The LDEF experiment clearly shows that over its limited time in space there were no structurally catastrophic hits. [2] There were, however, enormous numbers of impacts which could have effected solar arrays, transmission lines, optical and thermal coatings, and protective coatings used to shield against atomic oxygen and the effects of ultraviolet radiation. The analysis to date has shown that the damage produced is synergistic with other space environmental factors such as atomic oxygen and ultraviolet radiation. [3] By far, the preponderance of impacts are particles with masses in the microgram to milligram range over the entire velocity spectrum. Further, the analysis indicates both natural and abundant "man-made" sources of debris.

There are a number of options [4] for studying space impact phenomena. First, and perhaps most expensive is to place suitable materials in space for the requisite period of time. This is a "specialized long-term LDEF" approach and should be a part of any future LDEF experiment. The second quick-response approach is to use light gas gun technology to accelerate macro-projectiles in the gram range for impact studies. Due to the hydrodynamics of staged, compressed light gas guns, the velocity limit is about 10 km/sec and is unsuited to accelerating particles with the LDEF experimental profile. Further, unless judiciously designed, massive unwanted debris from the seals and sabots and the "large gas slug" also will impact the sample. As a result, it is difficult to do experiments on active systems or "mock ups" designed to simulate active spacecraft components. The third technique is to employ "electromagnetic accelerators" [5] to drive suitable projectiles in a vacuum chamber to more closely duplicate the space environment as well as inflict minimum additional damage to a sample.

EXPERIMENTAL DESCRIPTION

Figure 1 shows a block and schematic diagram of the electrical drives for an accelerator capable of driving small projectiles to hypervelocity.

The capacitor bank consists of a four segment bank with total capacitance of 53.6 microfarads storing some 67 kilojoules at a maximum charging potential of 50 kV. The desired experimental capacitor voltage is achieved by a high voltage power supply charging the capacitor bank through an appropriate charging resistor designed to limit the charging rate. In the event of a misfire, a suitable array of protective circuits and "dummy load resistors" are provided to discharge the bank. Once the desired voltage has been reached, the closing switch is triggered resulting in a current pulse of some 1 million to 1.5 million amperes flowing through the exploding foil driver. The current rise time is governed by external circuit inductance and is on the order of 200 ns.

The foil assembly rapidly explodes producing an extremely hot metallic plasma which is accelerated due to $\bar{J} \times \bar{B}$ forces and internal pressure from the explosion byproducts. The contacts to the assembly are constructed of stainless steel and, due to the enormous dynamic forces, are constrained by an insulating structure composed of high strength composite. The entire assembly is fastened to a high current feed-through plate.

Particulate suitable for impact studies can be generated by a number of techniques. The foil assembly itself is a source of ultra small particles and for this system these particles are aluminum. Secondly, the enormous currents generated by the discharge have a tendency to ablate particles from the stainless steel contacts and thirdly, an ablator plate, suitably loaded with fragments, can be designed to provide the vast majority of the fragments in a controlled way.

Figure 2 shows the design of an armature package typical of that used in this facility.

As the aluminum foil explodes, the hot plasma totally decomposes the plastic ablator plate into constituent gasses such as hydrogen and carbon at a temperature of several thousand degrees K. This plasma/gas slug/debris package is accelerated further down the drift tube both by $\bar{J} \times \bar{B}$ forces and due to the hydrostatic pressure generated by the hot gases. As a result, the microprojectiles are "dragged along" at a substantial fraction of the plasma velocity. The plasma/debris cloud velocity has been measured by high speed photography to be greater than 40 km/sec. Obviously, loading of the armature assembly with a selected particle size and mass determine the velocity distribution of the particles and, clearly, not all particles will have the same velocity.

Figure 3 shows the vacuum chambers and flight tube geometry for the facility. The first chamber holds the gun, high current feed-through and an experimental impact station. The chamber has four

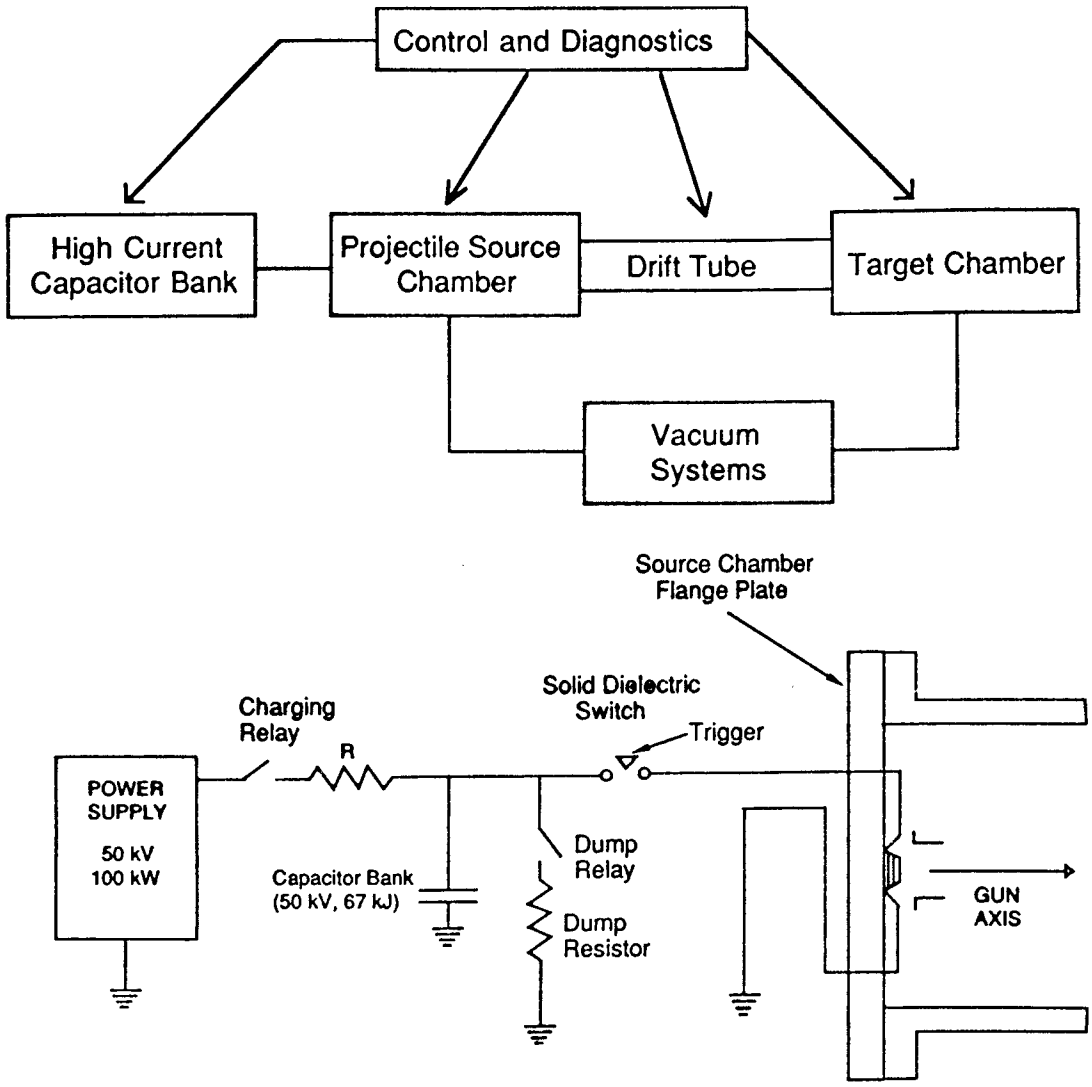


Figure 1. Block and schematic diagram of the facility and the gun drive circuits.

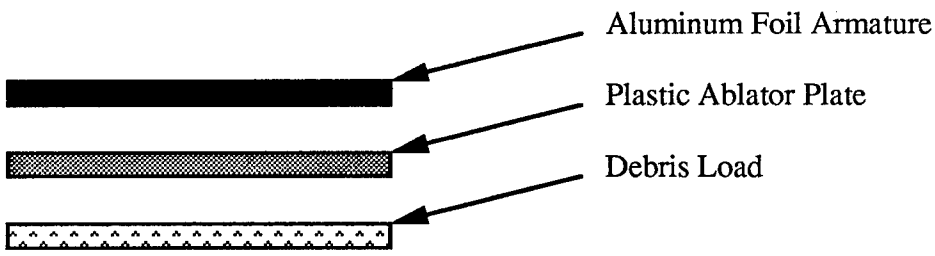


Figure 2. Projectile/debris assembly showing separate components.

viewing ports and several diagnostic feed-through flanges for use as needed. In addition, conical skimmers can be placed in this area to allow gas diversion and particle beam selection for propagation down the drift

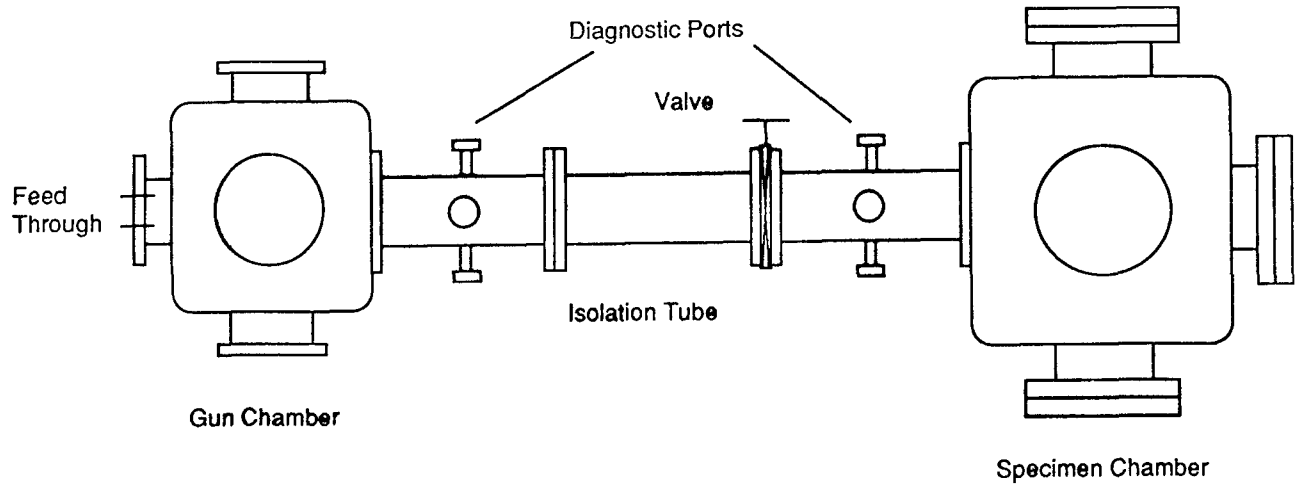


Figure 3. Vacuum chambers for hypervelocity facility.

tube. The chamber has its own pumping and diagnostic station. The maximum chamber diameter is 36 cm and along the flight axis allows about 1 meter of linear experimental space within the beam line.

The second chamber, the major impact/specimen chamber, is 1.45 meter in diameter and 2 meters long. It has numerous diagnostic ports, instrument feed-through stations, and specimen assembly racks. It too is separately pumped and has its own diagnostic station. Both chambers are made from stainless steel and can be pumped to 10^{-6} torr.

The chambers are separated by a 6.75 meter (variable) flight tube which effectively allows all electrical activity due to gun firing to subside before impact occurs in the main chamber. Further, the hot expanding gases have been allowed to cool, to be trapped, and almost all of the "unwanted" armature residue captured before striking the specimen located in the main chamber. To facilitate the diversion of unwanted gas and gun debris, additional skimmers are placed in the flight tube. The chambers are isolated by a suitable valve allowing the gun to be reworked without disturbing the experiment in the main chamber. In this mode, operational systems or semi-operational subsystems can be exposed repeatedly without returning to atmospheric pressure. The main chamber feedthroughs and Institute power capability allow for as much as 100 kW DC power to be supplied to the main chamber as needed.

It is extremely difficult to diagnose the velocity of a particulate stream moving at hypervelocity. The drift tube contains a six-port for diagnostic purposes. One set of ports are used to provide three "optical curtains" which can be produced by high intensity lights or by lasers. The "other set of ports" are fitted with sensitive photomultiplier tubes to look for scattered light from the passing particulate beam. The flight tube is segmented in a number of places allowing the six-port to be placed to minimize electromagnetic interference and residual illumination from the expanding drive products. The ability of this technique to resolve particulate matter is a function of the particle size, its velocity, the width of the optical curtains, particle scattering cross-section, optical intensity, and the sensitivity of the detector system. We have successfully resolved velocities on the order of 20 km/sec for particles of unknown size. In general, the diagnostic station is placed as far away from the drive section as possible to allow time of flight to produce an adequate particle separation for particles with nearly the same velocity, since it is impossible to resolve particles entering the light curtain simultaneously.

There are two other diagnostic techniques used to characterize the particle beam. For those samples sufficiently robust, high bandwidth piezo sensors can be mounted on the back of the specimen to record time of arrival, and hence velocity, over a wide range of particle velocities. As with the optical curtains, this technique does not allow unambiguous localization of a specific impact event with a specific velocity. It does extend the velocity region to greater than 40 km/sec. The best technique to employ is a high speed image converter camera utilized in the streak mode. The experimental set-up and an example of an "impact event" is shown in Figure 4.

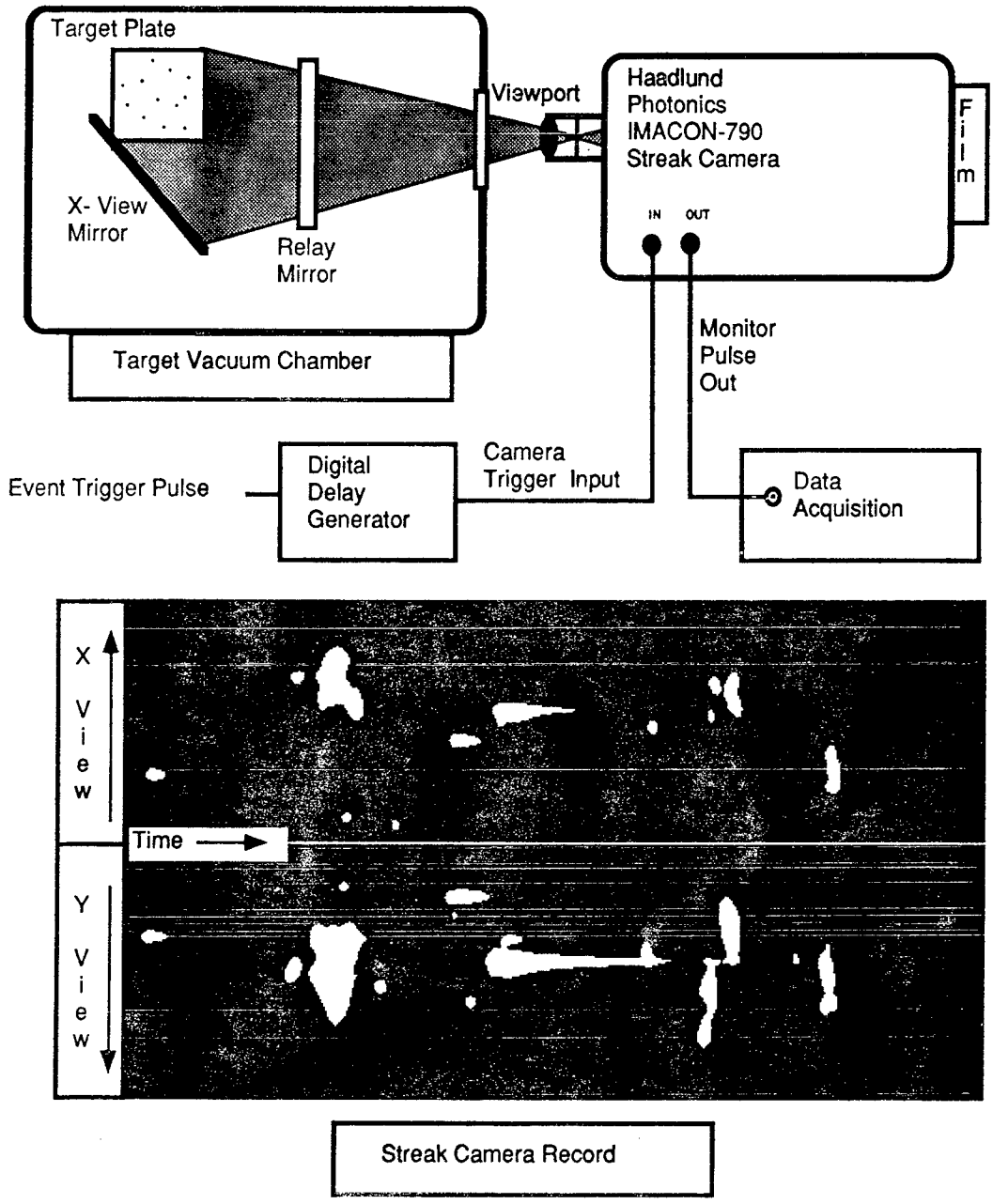


Figure 4. Streak camera diagnostic system schematic which allows both spatial location and velocity to be determined for each impact event.

Referring to Figure 4, a Haadlund high speed framing camera is used to monitor impact events due to the intense optical flash which occurs on impact. Using an optical lever the image slit is placed about 0.1 millimeters above the specimen plane in both directions. Both the x and y coordinate of any individual impact event can be directly measured from the streak record and the crater located precisely after applying an appropriate scale factor. Since the image is "streaked" across the film plane at a known rate, the position of the impact event on the film uniquely determines the velocity of the particle impacting the specimen. Modulated light emitting diodes are placed at the edges of the specimen to allow easy determination of the x-y coordinates and to facilitate in measuring the time of arrival. The camera is started after a suitable delay in order to improve resolution. This method is particularly suited to the measurement of particles which are moving at high velocities and produce highly luminous plasma clouds on impact. Within the limits of

sensitivity of the film, plasma lifetime can be measured within the field of view and correlated with particle size, species, and velocity.

The streak camera record also contains information related to the ejecta cone angle. If the slit viewing plane is set many particle diameters above the impact sample surface (a few hundred microns), the assumption that the impact is a point source of light is valid. Measurement of the width of the luminous spot on the film provides a measure of the cone ejecta diameter at the location of the slit. One single streak image now contains information on:

- x, y coordinates of each impact,
- number of impacting particles,
- velocity of each particle,
- duration of optical flash,
- approximate cone angle of the ejecta.

The only remaining piece of information necessary to uniquely characterize the impact event is to have a unique measure of the particle size. If the particle is moving at a sufficiently high velocity, on striking an extremely thin target, the particle will penetrate, suffering almost no damage and leave a "footprint" characteristic of its dimensions. [6] In general, the characteristic particle dimension should be many times the thickness of the film and the velocity greater than 5 km/s. In this facility ballistic films made of plastics 0.9 microns in thickness are supported on a wire grid and placed on a holder about 6 cm above the specimen. The film and specimen share a common fiducial mark allowing an impact crater to be uniquely identified with a "footprint" on the ballistic film. The technique is shown in Figure 5.

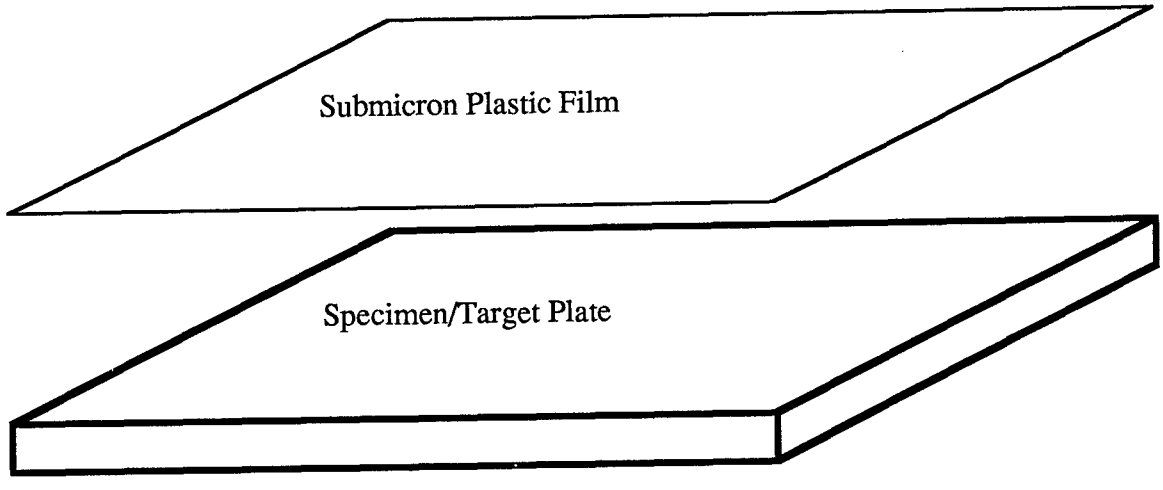
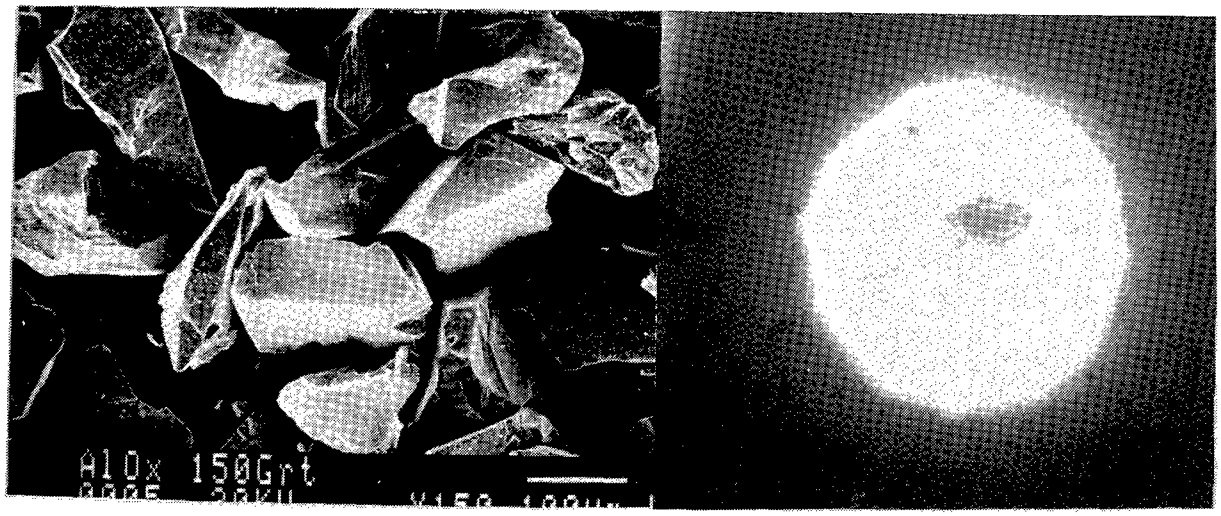


Figure 5. Ballistic film/specimen experimental arrangement.

In order to test the hypothesis that the ballistic film technique could be used to measure gun-induced breakup and particle size, the length (L) to width (W) ratio for nominal 100 micron aluminum oxide was measured. The average and deviation for 500 particles was 1.6 ± 0.5. Only 29 impact events were used to determine the L/W ratio for penetrations of the ballistic film. The L/W ratio was 1.98 ± 0.7. A correction factor for random orientation at penetration was also used. The lower limit in velocity for this experiment was on the order of 3 km/s which would leave a bigger footprint in the film. The absolute values in both L and W were comparable for the particles and the penetration "footprint." Additional data is being generated to improve the statistics and give more confidence in the technique. Our preliminary assessment is that there is little particle breakup during acceleration and that the ballistic film technique is valid to determine the approximate size for an impacting particle.

Figure 6 is a series of photographs to illustrate the total diagnostic technique. In the upper left hand corner is an electron micrograph of the nominal 100 micron aluminum oxide particles. The L/W ratio for



Particle Velocity: 12.1 Km/sec

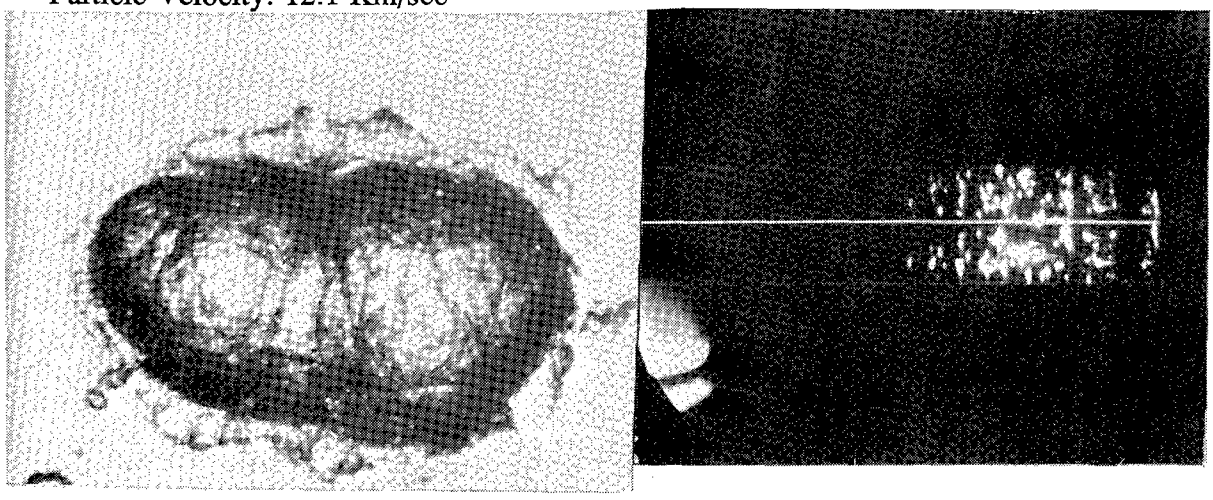


Figure 6. Collage of photographs illustrating the total diagnostic technique used in the hypervelocity facility.

some individual particles can be as big as 4. In the upper right hand corner, the "decorated footprint" made by one of the particles is shown. The photograph in the lower right hand corner is the impact crater formed in copper by the particle whose "footprint" is shown in the upper right hand corner of the figure. In the lower right hand corner is the streak record of all impact events in this experiment (3.0 km/s < V < 12.1 km/s). The impact event chosen for illustration was the fastest particle observed in the test and was moving at impact at a velocity of 12.1 km/s. There are some 55 particle impacts visible in this experiment. In general, it is hard to unambiguously resolve that many particles uniquely, especially near the center of the particle distribution.

Since the primary acceleration process is "plasma drag," there is always a gradient in the velocity of the particle stream. The maximum velocity obtainable and the velocity distribution are complex functions of the particle shape, particle density, absolute particle dimensions, and the gun parameters. Just as in space, there is always a wide range of particle velocities in a given experiment. From the point of view of simulation, this is desirable since it probably is a more accurate representation of the actual conditions in space. Figure 7 illustrates one of the many derived particle velocity distributions typical of the meteoroid flux in space.

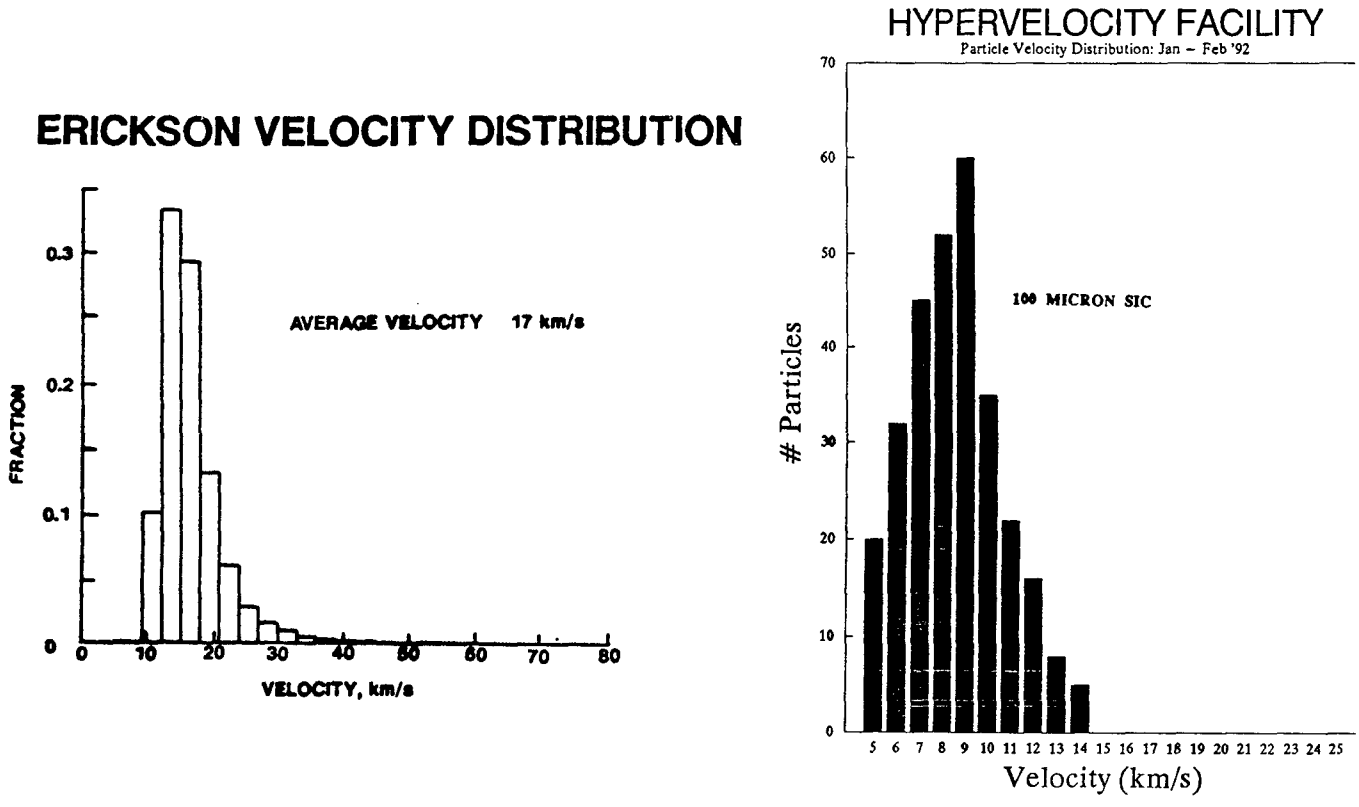


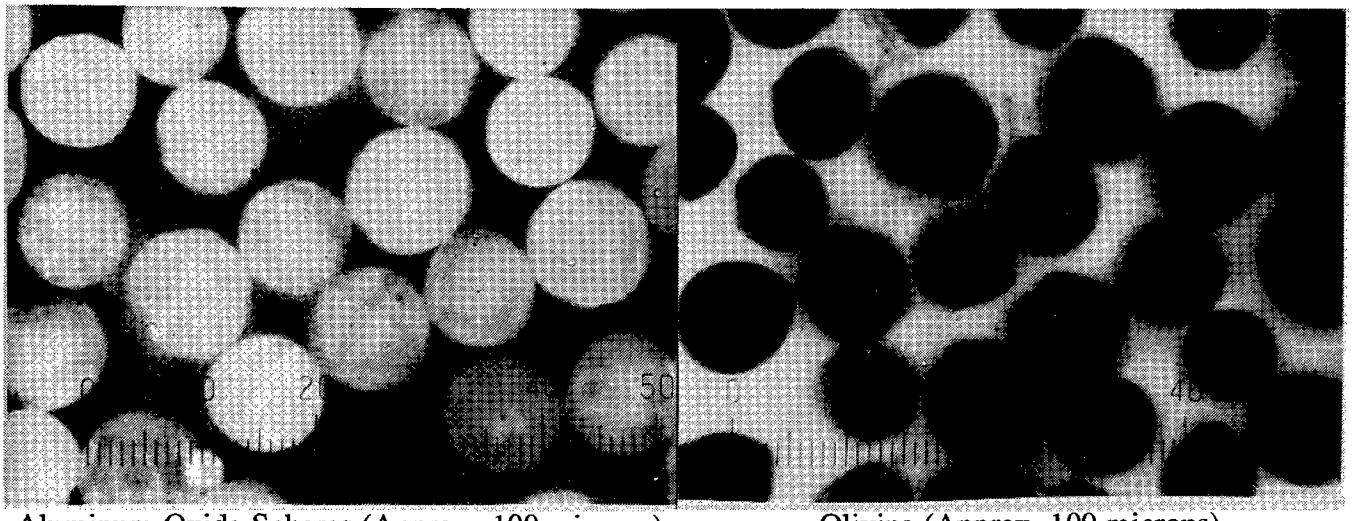
Figure 7. Velocity distribution postulated for meteoroids and the velocity distribution from the hypervelocity facility using nominal 100 micron silicon carbide particles.

Also shown in Figure 7 is an experimentally derived velocity distribution for nominal 100 micron silicon carbide particles. This distribution is based upon several experiments and while it does not duplicate the "Erickson distribution," it does overlap in the region of the distribution peak. Further, the particulate used in the facility is much larger than that typically seen on the LDEF experiments. We have collected experimental data on the velocity distribution for 400 micron and 100 micron aluminum oxide, and 100 micron olivines. The upper limit on the velocity distribution for 100 micron aluminum oxide is 11.5 km/s as compared to 14.5 km/s for the same size silicon carbide. This is to be expected since the density of aluminum oxide is roughly 1.2 times that of silicon carbide. At the moment, there is insufficient data to predict accurately the velocity distribution as a function of material and size.

In order to reduce the ambiguity in size, spheroidized olivine and aluminum oxide in a range of sizes from about 40 microns to greater than 100 microns have been fabricated. Figure 8 is an electron micrograph of the spheroidized particles. Unless requested otherwise, all future experiments in the facility will utilize these spheroidized particles for ease in determining gun performance from the ballistic film.

RESULTS AND DISCUSSION OF APPLICATIONS OF THE HYPERVELOCITY FACILITY

The facility is being used to study a variety of phenomena associated with hypervelocity impact. In the space plasma, dielectric coated surfaces can acquire a surface charge due to the electric currents in the spacecraft. [7] Without hypervelocity particle impact, the breakdown strength would be determined by the thickness of the coating and, in general, is several hundred volts. With hypervelocity particles destroying the dielectric layer, breakdown levels as low as -75 volts have been observed. The frequency of these events would depend on the meteoroid flux and the rate at which charge is trapped on the surface. Figure 9 illustrates impact events on dielectric/dielectric coated surfaces which produce craters many microns deep.



Aluminum Oxide Spheres (Approx. 100 microns) Olivine (Approx. 100 microns)

Figure 8. Spheroidized aluminum oxide and olivine particles for use in the hypervelocity accelerator.

The impact velocities were in the range of 8 - 12 km/sec and the particles consisted of nominal 100 micron silicon carbide. Figure 9a is an impact event on a thick painted aluminum surface. Note that the damage extends far beyond the central impact crater, a factor which must be taken into account when assessing the total effect of bombardment on surface properties. In addition, the area subject to atomic oxygen attack is several times the impact crater. In Figure 9b, a similar effect is seen in the impact area for kapton coated aluminum. Again, the damage due to film separation is several times the diameter of the impact crater. Figure 9c is an impact event which totally penetrated the woven thermal mat. The diameter of the hole is several times the particle dimension. The particle was totally destroyed on impact. Figure 9d is a typical impact on optical glass. The central impact zone is surrounded by a small damage zone several times the central region. The central region is highly fractured and shows some signs of melting. Evidence for extreme melting on optical materials was presented at this LDEF conference and it was judged that the particles were moving greater than 10 km/s on impact. For the event in Figure 9d, the particle velocity was about 8 km/s. These events are typical of the same phenomena witnessed on the LDEF surfaces and offer an excellent opportunity to duplicate and calibrate the data gathered from the various experiments on LDEF.

One of the more intriguing opportunities for analysis of the LDEF samples is to examine the crater sites for residue from the impacting particles. In space, there is ample opportunity for cross contamination due to debris from other impacts, outgassing from other materials on board, and due to terrestrial handling in a variety of modes. By studying these same phenomena in the hypervelocity facilities, tracer materials unique to the projectile can be used to study the residue as a function of impact velocity and location with respect to the impact site. Hypervelocity impact generates extremely high temperature which can totally vaporize the impacting particle in an explosive event with the resultant expulsion of almost all of the impacting particle mass. Using energy dispersive x-ray analysis, we have identified the contaminants which are produced as a result of the acceleration process. These are primarily aluminum, calcium, carbon, chlorine, iron, silicon, sulfur, and potassium. There are no measurable sources of magnesium in the materials used in the construction of the hypervelocity accelerator and the projectile assembly. As a result, the magnesium in the olivine projectile material can be used to trace the location of projectile debris in any impact event. Figure 10 is an electron micrograph of a crater formed by a nominal 100 micron olivine particle for an impact velocity of 8.9 km/s.

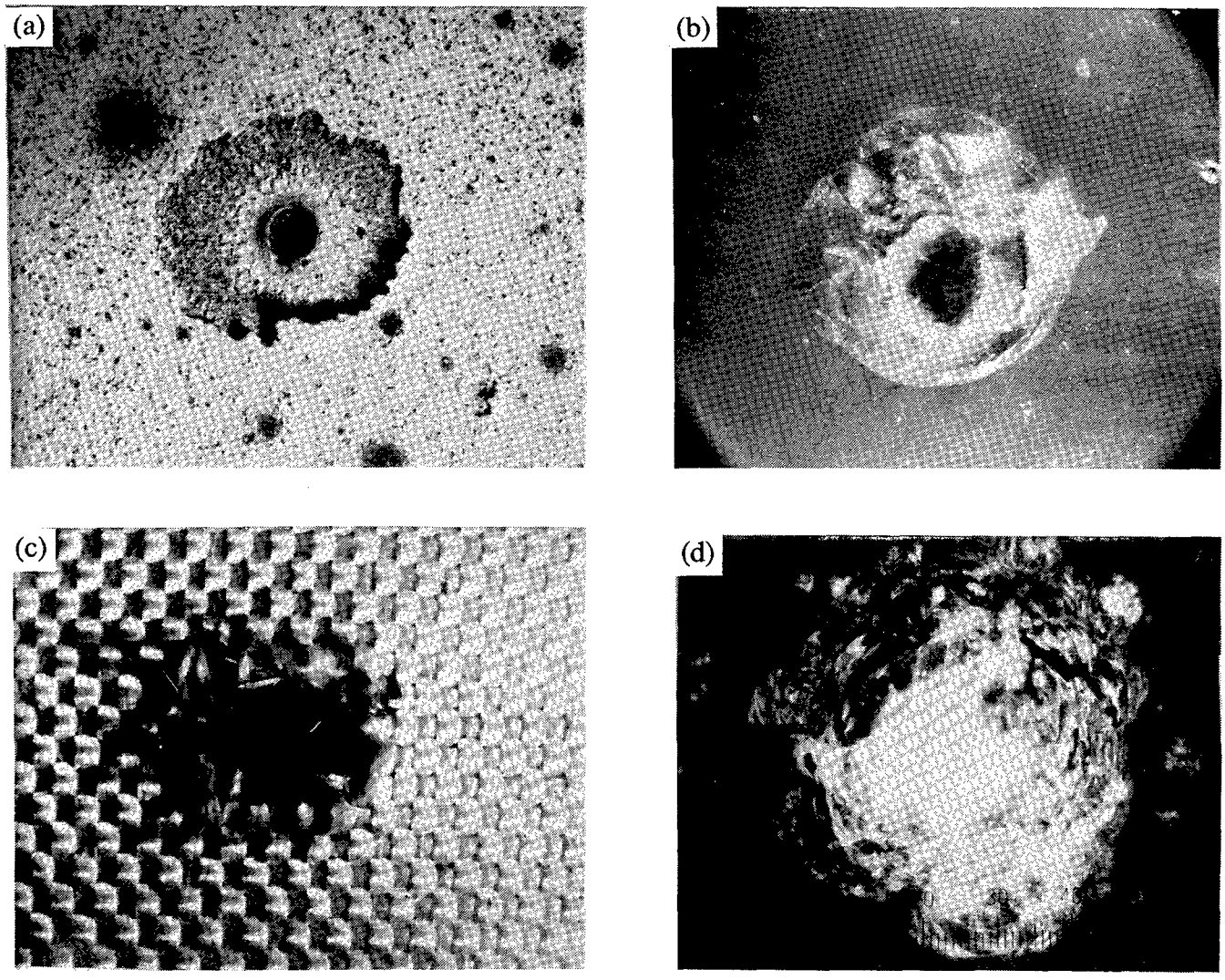


Figure 9. Impact phenomena generated in the hypervelocity facility typical of that seen on similar materials from LDEF. Photographs reproduced courtesy of J. Zweiner of the Marshall Space Flight Center.

The photo labeled 1 is an overall view of the impact site, which is some three hundred microns wide and five hundred microns in length. The x-ray scan below the crater image is typical of the area immediately adjacent to the crater. Note that the scan shows nothing but the copper of the specimen plate. The photo marked 2 is a high magnification image of the bottom of the crater. Immediately beneath it is the x-ray data which again shows no magnesium or gun contaminants within the sensitivity of our instrument. It appears that the site is at high temperature long enough to boil off any contaminants which might have come through the hole in the ballistic film routinely used in all of our experiments. Many sites within the crater were examined with the same result. Figure 11 is a closer analysis of the edges of the crater. All along the rim of the crater there are traces of the gun contaminants and the all important element, magnesium, which is indicative of olivine residue.

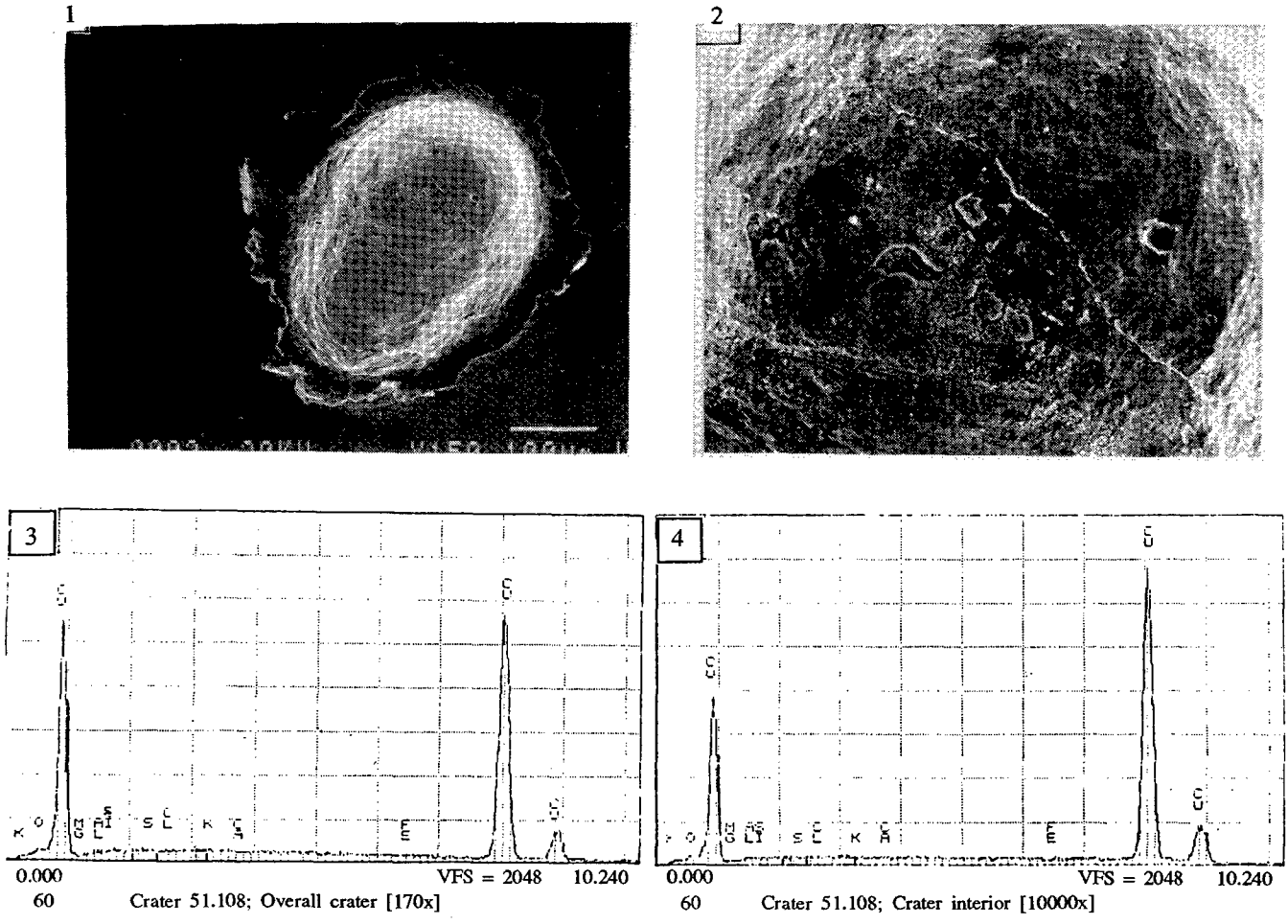


Figure 10. X- ray analysis of the residue external and internal to the impact crater for a velocity of 8.9 km/s. The impacting particle is olivine (magnesium iron silicate).

This same result has been obtained on other craters and is the subject of further research. To find ejecta from the crater containing material from the impacting particle on the rim of the crater is not inconsistent with the models for hypervelocity impact. A series of experiments are planned which will utilize the spheroidized olivine to produce many impacts over the range of 3 - 12 km/s. Selected craters will be examined for residual material, identifiable as being from the olivine, over the entire velocity range and as a function of location within the crater. The results of these experiments should clearly define the transition region where the result of impact is more akin to an explosion than to a penetration event where the materials remain largely intact and exhibit large plastic deformation rather than explosive vaporization.

Due to the large numbers of particles which can be accelerated simultaneously, the facility is useful to study accelerated aging phenomena associated with hypervelocity impact. In the 100 - 400 micron particle sizes, a single experiment is equivalent to many years in space. Figure 12 shows the impact distribution on solar cells produced from nominal 400 micron Al_2O_3 particles. A close-up of the individual craters is typical of that shown earlier on glassy materials. The maximum velocity for these particles is on the order of 8.5 km/s with the peak of the distribution on the order of 7 km/s. There have not been sufficient particles analyzed to accurately determine the velocity distribution.

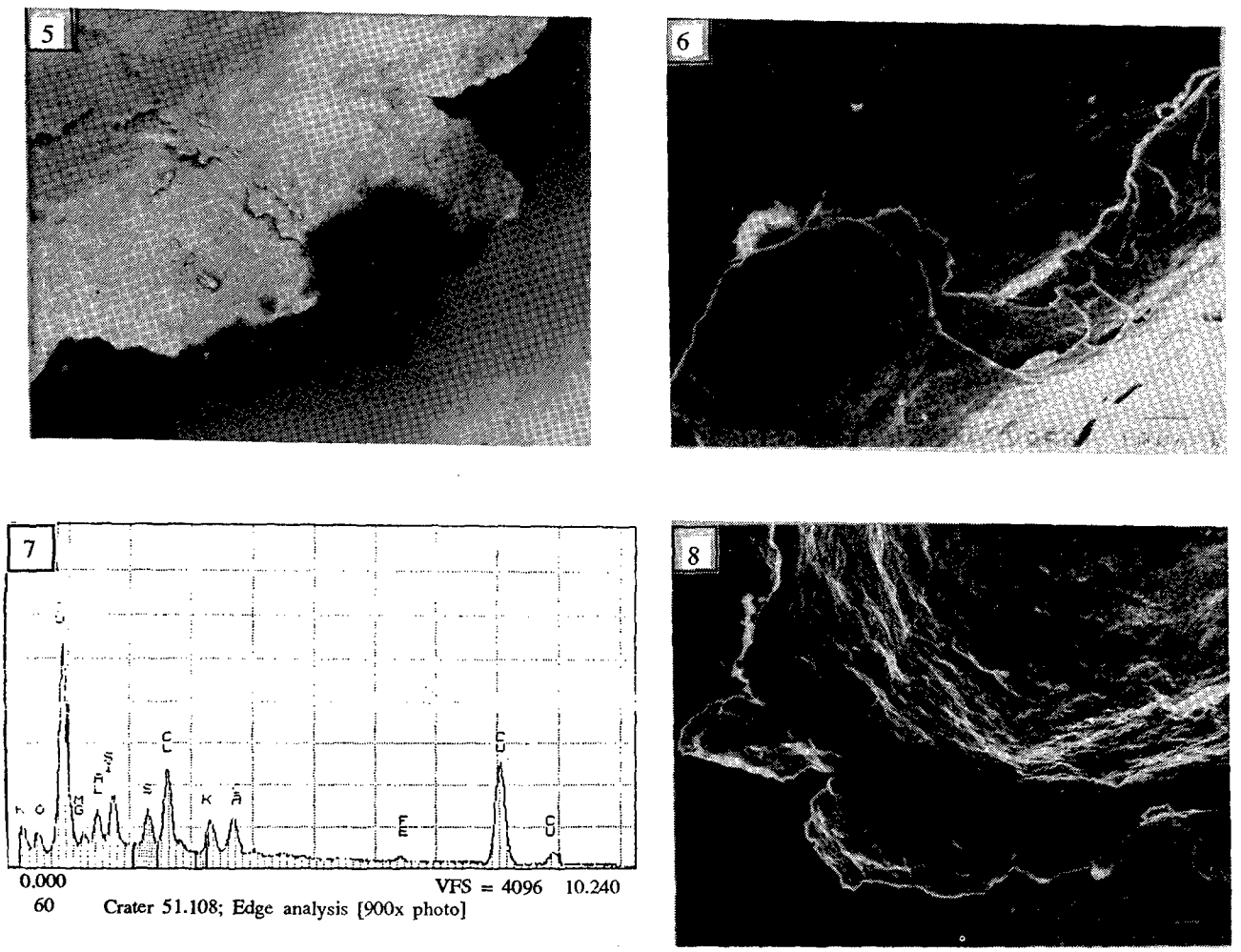


Figure 11. Electron micrograph of residue particles on the edge/rim of the crater in figure 10. X-ray dispersive analysis identifies gun contaminants and magnesium which is characteristic of the olivines used in the experiment.

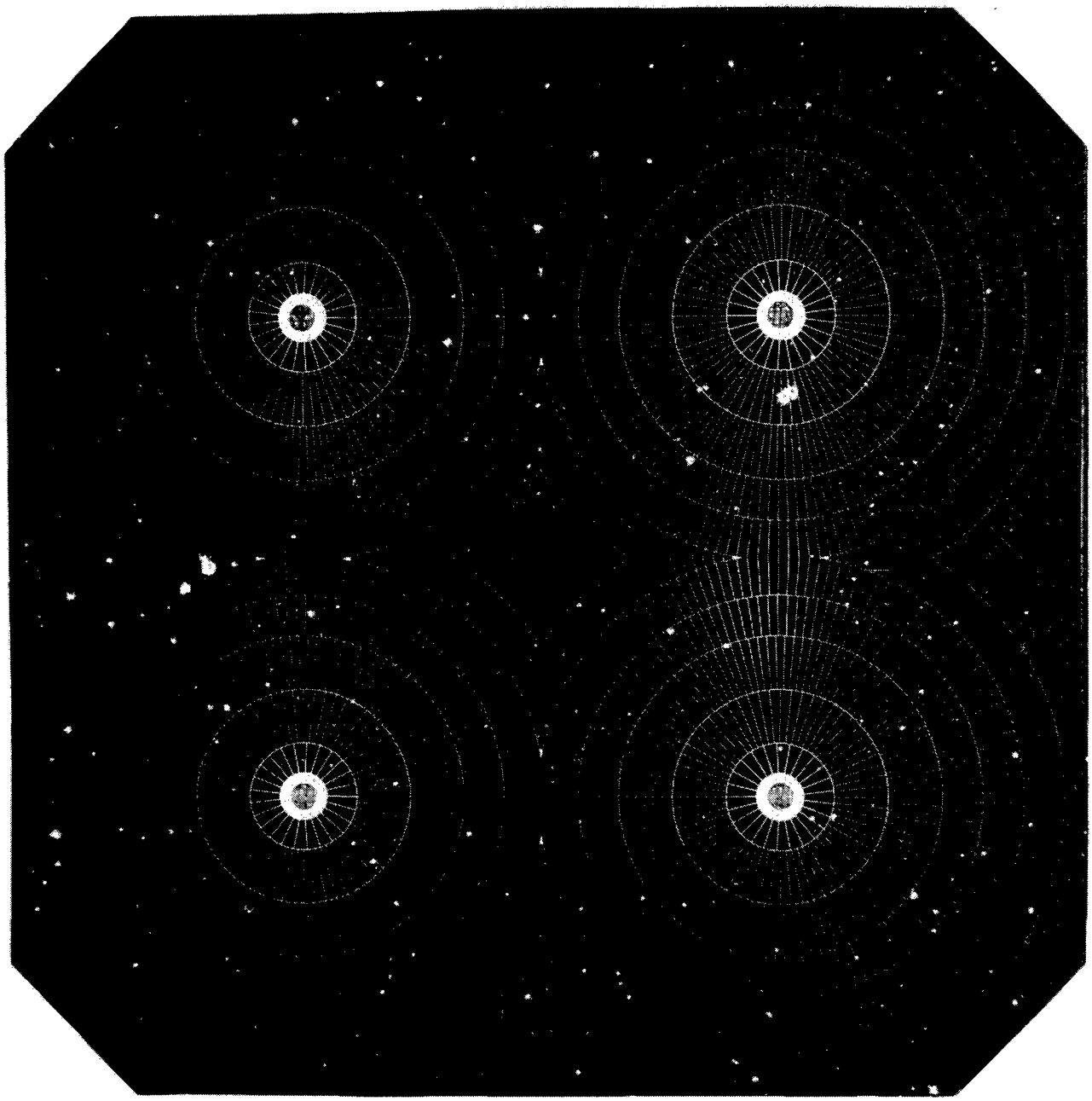


Figure 12. Impact distribution on solar cells typical of that planned for Space Station Freedom. Photograph reproduced with permission from R. Cristie of the Rocketdyne Division of Rockwell International.

SUMMARY

The hypervelocity impact facility located within the Space Power Institute at Auburn University is being used to study many phenomena associated with impacts on spacecraft and materials used in their construction. The facility has the following special attributes which make it unique and an outstanding tool to study impact and impact induced phenomena.

- Utilizes plasma drag phenomena to produce a particle stream with minimal breakup and a wide range of velocities in a single experiment.
- A wide range of materials can successfully be accelerated with the device.
- Capability to study accelerated aging effects by impacting target sample more than once without breaking vacuum.
- Advanced-unique diagnostic suite capable of tracking and completely characterizing up to 50 particles in a single experiment.
- Accelerator produced debris is minimal and identifiable resulting in a clean system.
- The facility is flexible enough to allow three experiments daily.
- The experiment chamber is large enough to accommodate large fully functioning spacecraft components or subsystems while under a variety of space stimuli such as ultraviolet radiation, micrometeoroids, space plasma, and atomic oxygen.
- There are up to 40 channels of electrical diagnostics available, some with bandwidth of 500 MHz.

ACKNOWLEDGEMENTS

This work was supported by a grant from the Marshall Space Flight Center, a grant from the NASA Langley Research Center, the Commercial Center for the Development of Space Power, and through internal funds at the Space Power Institute.

REFERENCES

[1] D.J. Kessler and Shin-Yi Su, Editors, Orbital Debris, Proceedings of a Workshop sponsored by the NASA Lyndon B. Johnson Space Center, NASA Conf. Publication 2360, 1985.

[2] Meteoroid and Debris Impact Features Documented on the Long Duration Exposure Facility, A preliminary report compiled by Members of the LDEF Meteoroid and Debris Special Investigation Group. JSC #24608, Aug. 1990.

[3] LDEF - 69 Months in Space, First Post-Retrieval Symposium, A.S. Levine, Ed., NASA Conf. Pub. 3134, parts 1,2,3, June 1991.

[4] J. A. Zucas, T. Nicholas, H. A. Swift, L. B. Greszczuk and D. R. Curran, Impact Dynamics, John Wiley & Sons, 1981.

[5] M.F. Rose, S. Best and T. Chaloupka, "Hypervelocity Impact Facility for Simulating the Effects of Space Debris Over a Wide Range of Conditions," Proc., 26th IECEC, Boston, Mass., 1991.

[6] W.C. Carey, J.A.M. McDonnell, and D.G. Dixon, "An empirical penetration equation for thin metallic films used in capture cell techniques," Proc. 85th Colloq. Int. Astron. Union Meeting, Paper B.5., 1984.

[7] M.F. Rose, "Insulation and Discharge Phenomena in the Space Environment," Proc. XVth ISDEIV, Darmstadt, Germany, Sept. 1992.

ANALYSIS OF LDEF MICROMETEOROID/DEBRIS DATA AND DAMAGE TO COMPOSITE MATERIALS

R. C. Tennyson and G. Manuelpillai
University of Toronto Institute for Aerospace Studies
4925 Dufferin Street
North York, Ontario, Canada
M3H 5T6
Phone: 416/667-7710, Fax: 416/667-7799

SUMMARY

This report presents published LDEF micrometeoroid/debris impact data in a nomogram format useful for estimating the total number of hits that could be expected on a space structure as a function of time in orbit, angular location relative to ram and exposed surface area. Correction factors accounting for different altitudes are given, normalized to the average LDEF altitude. Examples on how to use the nomogram are also included. In addition, impact data and damage areas observed on composite laminates (experiment AO 180) are discussed.

ANALYSIS OF LDEF MICROMETEOROID/DEBRIS IMPACT DATA

From the individual LDEF experiment trays, tables of micrometeoroid/debris impact feature sizes were compiled in Ref. 1. This data was then summarized for each longitudinal panel to yield an angular (θ) distribution of total impacts around LDEF after 5.75 years in low Earth orbit. Figure 1 presents two distributions based on the "total" reported hits, and those hits which were $\geq$0.5 mm in size. It should be noted that the data shown are strictly valid only at $\theta = 0°, \pm30°, \pm60°, 90°, \pm120°, \pm150°, 180°$, and the curves cannot be integrated to give a total number of impacts.

Based on the number distribution presented in Fig. 1, it is possible to construct a general purpose nomogram which permits a user to estimate the total number of impacts on a satellite or component (at the LDEF nominal altitude and inclination) for any value of time in orbit, angular location around the satellite or space structure (constrained by $\theta_n = n \times 30°$ where n = 0, 1, 2, ... 12, corresponding to a 12-sided polygon model of the satellite or component), and exposed area. For example, Figure 2 presents the nomogram for LDEF based on a longitudinal panel area of ~10 m^2, assuming a nominal impact fluence of 300 impacts/m^2. The example panel shown in Fig. 2 corresponds to $\theta = 30°$. Thus the intersection of $\theta = 30°$ and the LDEF time in orbit axis (~5.75 years) yields an impact fluence of ~300 impacts/m^2. Following up along this constant fluence curve until one intersects the desired panel area (10 m^2), one can then translate horizontally across the graph to the "Number of Impacts" ordinate. For this example, one obtains $N \cong 3100$ which agrees with the number plotted in Fig. 1.

Using the LDEF data from Fig. 1, knowing panel areas and total time in orbit, one can construct a general purpose nomogram for varying areas of exposure and impact fluence levels as shown in Fig. 3. Once again it must be stressed that these curves can only be used to estimate the total number of impacts at discrete angles defined by $\theta_n = n \times 30°$, n = 0, 1, ..., 12, and are strictly valid for an LDEF average altitude of ~463 km and inclination of 28.5°. Later it will be shown how to correct these numbers for different altitudes and orbital inclinations.

EXAMPLES OF NOMOGRAM APPLICATIONS

The following examples are presented to illustrate how one can estimate the number of impacts on satellite elements using the nomogram of Fig. 3.

(a) LDEF Impacts at RAM Location — Check Case

Use the nomogram to estimate the number of impacts at $\theta = 0°$ for LDEF after 5.75 years in orbit, using a panel area of 10 m^2. Compare result with data in Fig. 1.

Figure 4 presents the solution for $\theta = 0°$ which yields $N_0 \approx 3{,}100$ impacts. From Fig. 1, one also obtains $N_0 \approx 3{,}100$ impacts.

(b) Circular Cylindrical Space Structure

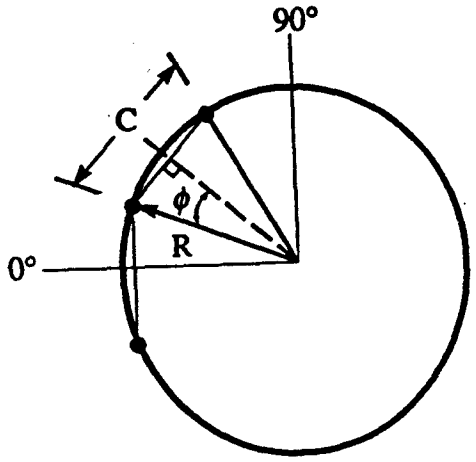
Demonstrate the application of the 12-sided polygon model to estimate the angular distribution of impacts for a circular cylinder, 0.5 m in diameter, 10 m long, after 30 years in orbit.

(i) Panel Area (A)

$c = 2R \sin \phi$

For the 12-sided polygon $\phi = 15°$

$\therefore c = 0.13$ m and $A \equiv 1.3\ m^2$



(ii) N_n Distribution from Fig. 3 (30 years)

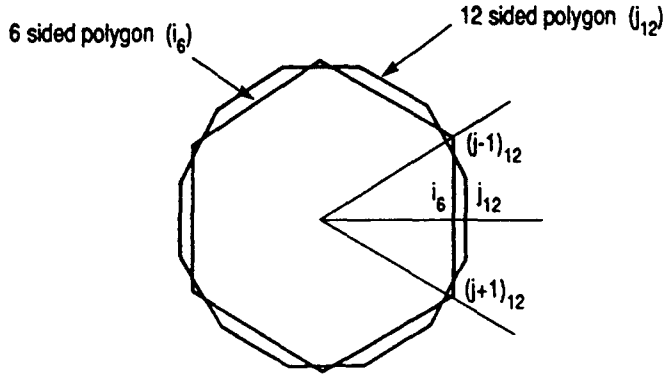
θ_n^o	N_n (est.)	D_n* (cms)
0	2070	2.5
30	2070	2.5
60	1680	2.8
90	1100	3.4
120	450	5.4
150	325	6.3
180	290	6.7

θ_n^o	N_n (est.)	D_n* (cms)
-30	2260	2.4
-60	1680	2.8
-90	615	4.6
-120	550	4.9
-150	225	7.6

*Average impact feature separation distance on panel, assuming uniform distribution.

(c) Interpolation Example

If one wishes to use fewer than 12 sides to model a space structure, interpolation of the nomogram data must be employed. To demonstrate, consider the previous cylinder example. Let us replace the 12-sided polygon representation of the circular cross-section with the 6-sided model shown below.



If one examines any panel i_6, for example, it is comprised of one facing j_{12} and half of each of the adjoining panels, denoted by $(j-1)_{12}$, $(j+1)_{12}$. Thus the number of impacts on this i_6 panel is given by,

$$N_{i_6} = \frac{1}{2}\left(N_{j-1_{12}} + 2N_{j_{12}} + N_{j+1_{12}}\right)$$

For example, the panel (i=4) corresponding to $\theta = 180°$ on the reduced element model would sustain a number of impacts given by

$$N_{46} = \frac{1}{2}(325 + 2 \times 290 + 225)$$
$$= 565$$

A comparison of the impact number distribution is given below. Note that both "totals" must be equal.

θ_n	$N_{j_{12}}$	N_{i_6}
0°	2070	4235
30°	2070	—
60°	1680	3265
90°	1100	—
120°	450	1162.5
150°	325	—
180°	290	565
-150°	225	—
-120°	550	970
-90°	615	—
-60°	1680	3117.5
-30°	2260	—
Totals:	13315 =	13315

$$-\left(\frac{1}{2}N_{-30°} + N_{0°} + \frac{1}{2}N_{30°}\right)$$

$$-\left(\frac{1}{2}N_{30°} + N_{60°} + \frac{1}{2}N_{90°}\right)$$

$i_6 = 1, 2, ..., 6$

$j_{12} = 1, 2, ..., 12$

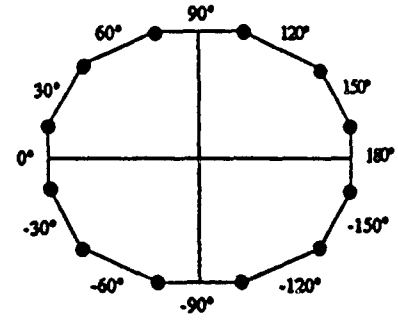
MODIFICATIONS OF NOMOGRAM DATA

(a) Micrometeoroid/Debris Impacts > 0.5 mm Diameter

For design purposes, it may be useful to know the number of impacts >0.5 mm in diameter and their angular distribution around a satellite. The figure shown below is based on the LDEF distribution plotted in Fig. 1 and provides a % allocation of the total number of hits attributable to this larger size category.

θ_n	% N_n
0	9
30	8
60	13
90	10
120	17
150	6
180	9
-150	9
-120	5
-90	9
-60	8
-30	9

% distribution on each panel of micrometeoroid/debris impacts >0.5 mm based on LDEF data



(b) Variation in Number of Hits with Altitude — Natural Micrometeoroid Environment

From Ref. 2, the flux of micrometeoroids in Earth orbit is given by

$$\phi = SF \cdot GE \cdot F^{ip}$$

where F^{ip} is the interplanetary flux,

SF is a shielding factor due to Earth's atmosphere,

GE is a factor which accounts for focussing by the Earth's gravity.

Again, Ref. 2 gives these factors as

$$SF = \frac{1 + \cos \eta}{2} \quad \text{where} \quad \sin \eta = \frac{R_e}{R_e + H} \quad \text{and} \quad GE = 1 + \frac{R_e}{r}$$

R_e represents the radius of Earth plus 100 km of atmosphere (= 6478 km), H the height above Earth's atmosphere, and r the orbit radius. Due to the considerable uncertainty in the physical properties of micrometeoroids, there is a 0.1 to 10 factor of uncertainty in the flux relationship.

However, one can determine the altitude dependence from

$$\frac{\phi}{F^{ip}} = \frac{1}{2}\left\{1 + \left[1 - \left(\frac{1}{1 + H/R_e}\right)^2\right]^{1/2}\right\}\left(1 + \frac{1}{1 + H/R_e}\right)$$

Assuming an average altitude for LDEF of ~463 km, then one can apply a correction factor to the nomogram data to account for flux changes with altitude. This factor is plotted in Fig. 5. Note that this correction must be applied to only the natural micrometeoroid component of the total number of hits recorded for LDEF.

(c) Variation in Number of Space Debris Hits with Altitude

From Ref. 2, the orbital debris model proposed is based on the assumption that the accumulation of objects in low Earth orbit is constant. One can derive a normalized debris flux ($\bar{\phi}_{OD}$) as a function of altitude (for $h \leq 2000$ km) having the form

$$\bar{\phi}_{OD} = \frac{\psi_i \phi(h, S)}{\phi(h, S) + 1}$$

where S represents a solar activity factor,
ψ_i is an inclination-dependent function = 0.91 for 28.5° (see Ref. 2 for table of ψ_i values),
and $\phi(h, S) = 10^{(h/200 - S/140 - 1.5)}$.

For particles with $d < 1$ cm, one can estimate an altitude correction factor that can be applied to the nomogram data, as shown in Fig. 5. Inclination correction factors can be found in Ref. 2.

It should be noted that at this point in time, the impact data for LDEF cannot be separated into "natural" or "debris" populations. Thus the individual correction factors shown in Fig. 5 cannot be applied. However, it is evident that for altitudes <400 km, one could use the debris correction factor, whereas at ≥400 km the micrometeoroid correction factor can be applied to all of the LDEF data derived from the nomogram to obtain conservative estimates.

MICROMETEOROID/DEBRIS IMPACTS ON EXPERIMENT AO180

Experiment AO180 consisted of various graphite, aramid and boron fiber-reinforced epoxy materials mounted at station D-12, about 82° from the LDEF velocity vector. The exposed surface area was ~0.6 m^2 and was subjected to a total of 84 hits (Fig. 6). The predicted number of impacts for this area after 5.75 years is ~80, based on the nomogram in Fig. 3 (assuming $\theta = 90°$). This agreement is particularly noteworthy since it demonstrates that after sufficient exposure time in orbit, one can predict the number of impacts likely to occur in relatively small areas.

From a detailed inspection of the composite samples (both tubes and flat plates), only 10 of the 84 hits were found on these materials, the balance located on end fixtures and the aluminum base plates.

MICROMETEOROID IMPACT ON ALUMINUM SUPPORT STRUCTURE

The largest impact (~1 mm diameter) found on experiment AO180 occurred on an aluminum base plate, with an ejecta splash observed on an adjacent flange structure (Fig. 7). SEM/EDX spectra of the crater rim material composition (Fig. 8) exhibited a strong Fe peak along with the Al substrate. Based on chemical composition evidence it is assumed that the crater resulted from debris impact. Figure 9 contains SEM photographs of the surface ejecta splash patterns on the flange structure. An aluminum ejecta particle, visible in Fig. 9, is enlarged in Fig.10. Figure 10 presents two different forms of aluminum ejecta particles and their associated splash patterns. The lower photograph shows the remnants of a molten particle while the upper photograph shows the full spherical form of an aluminum particle.

IMPACT DAMAGE ON COMPOSITE LAMINATES

Micrometeoroid/debris impacts on polymer matrix composites do not produce the typical hemispherical craters found on metallic structures. Rather, because of the brittle nature of the resin matrix, one generally finds penetration holes with adjacent surface damage, some internal ply delamination and local fiber fractures. For brittle fibers such as graphite, the impact and exit holes exhibit brittle fiber fractures as shown in Fig. 11, as well as rear surface spallation [5208/T300; $(\pm 45^\circ)_S$]. Note that the spallation damage-to-hole size ratio is about 5:1. On the other hand, tough non-brittle fibers such as aramid fail in a "brush or broom" mode surrounding the impact damage region. Figure 12 presents four impacts on a single Kevlar®/epoxy tube [SP-328, $(\pm 45)_{4S}$]. It can be seen that three penetrations occurred with one grazing (or low energy) impact that produced only local surface damage. Note the fiber failure mode in photo 4. From the enlargements, it was possible to scan the images to calculate the surface damage area and impact hole size. These images were digitized using a Houston Instruments "Hipad" digitizer to obtain an accurate reproduction of the impact site (~200 data points on average). The X-Y coordinates of the digitized photograph were then analysed using spreadsheet/graphics programs (Supercalc 5.0™ and Grapher™). A trapezoidal model was used to numerically integrate the digitized image to obtain damage area and crater size (assuming a circular hole). Figures 13, 14 and 15 present a summary of the images obtained for nine impact sites. At this point in time, only 10 impact sites (out of 84) have been found on the composite samples, a summary of which is given in Table 1 with estimates of surface damage area, hole size and penetration depth. Such data will be useful for estimating total damage on composite structures that arises from micrometeoroids/debris. Note that the penetration depth was based on the image enhanced backlighting technique, which is useful for translucent materials.

Using only the Kevlar®/epoxy impact data, one can construct a plot of surface damage area vs. major axis length, as shown in Fig. 16. It would appear that an elliptical model can be used to describe the damage area.

Figure 17 shows an SEM photomicrograph of the base of a crater (~0.076 mm^2 in area) in a Kevlar®/epoxy laminate (2T16) after the uppermost plies have been peeled off. An enlargement of a particle believed to have caused this crater is also shown (~10 μ in diameter). An SEM-EDX spectra is given in Fig. 18 where it can be seen that the debris particle is composed of Cr-Mn-Fe. Note that Al, Cu and Au come from the support fixtures holding the sample in the SEM.

REFERENCES

1. "Micrometeoroid and Orbital Debris Impact Features Documented on the Long Duration Exposure Facility — A Preliminary Report", LDEF SIG, NASA JSC, 1990.

2. Sisson, J: "Update of the Meteoroid and Orbital Debris Environment Definition," Space Station Level-II Change Request, CR #BB000883A.

Table 1. Summary of Impact Features on Composite Specimens (Experiment AO180)

Material Type	Sample Type	Number of Plies	Sample No.	Surface Damage Area (mm^2)	Hole Area (mm^2)	Nominal Hole Diameter (mm)	Particle Penetration Depth (Number of plies)
Graphite/Epoxy (T300/5208)	Plate	4		0.222	0.222		>4
Graphite/Epoxy (SP 288/T300)	Tube	4	1T10	1.064	0.083	0.325	>4
Aramid* Fiber/Epoxy (SP 328)	Tube	4	2T2	1.162	0.036	0.215	1~2
"	Tube	4	2T4	0.498	0.015	0.139	~1
"	Tube	4	2T11	0.423	0.018	0.152	~1
"	Tube	4	2T16	1.253	0.076	0.312	2~3
"	Tube	4	2T17(1)	0.223	—	—	1~2
			2T17(2)	1.445	0.033	0.204	2~3
			2T17(3)	0.370	—	—	~1
			2T17(4)	0.881	0.020	0.159	2~3

*Kevlar

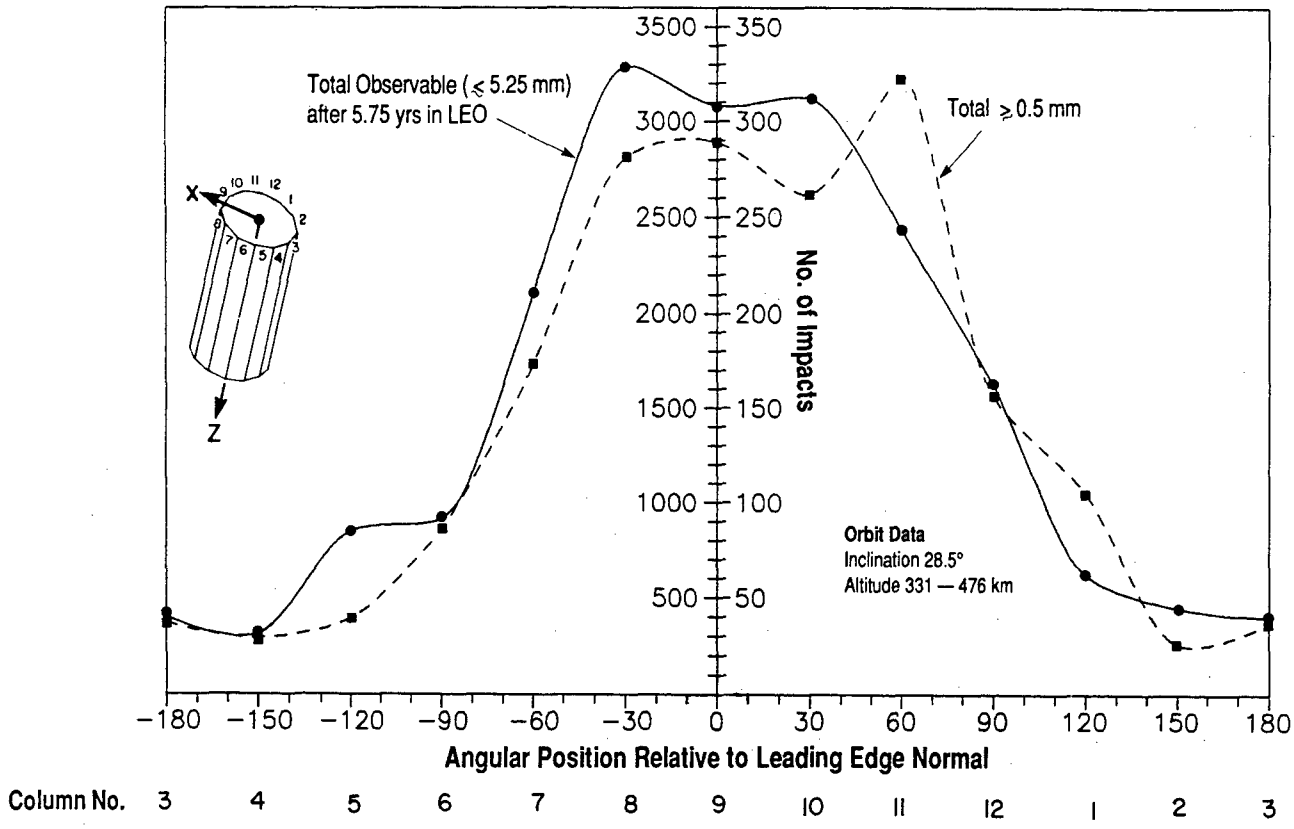


Figure 1. Circumferential distribution of micrometeoroid/debris impacts on LDEF (NASA M&D/SIG Report; Aug. 1990)

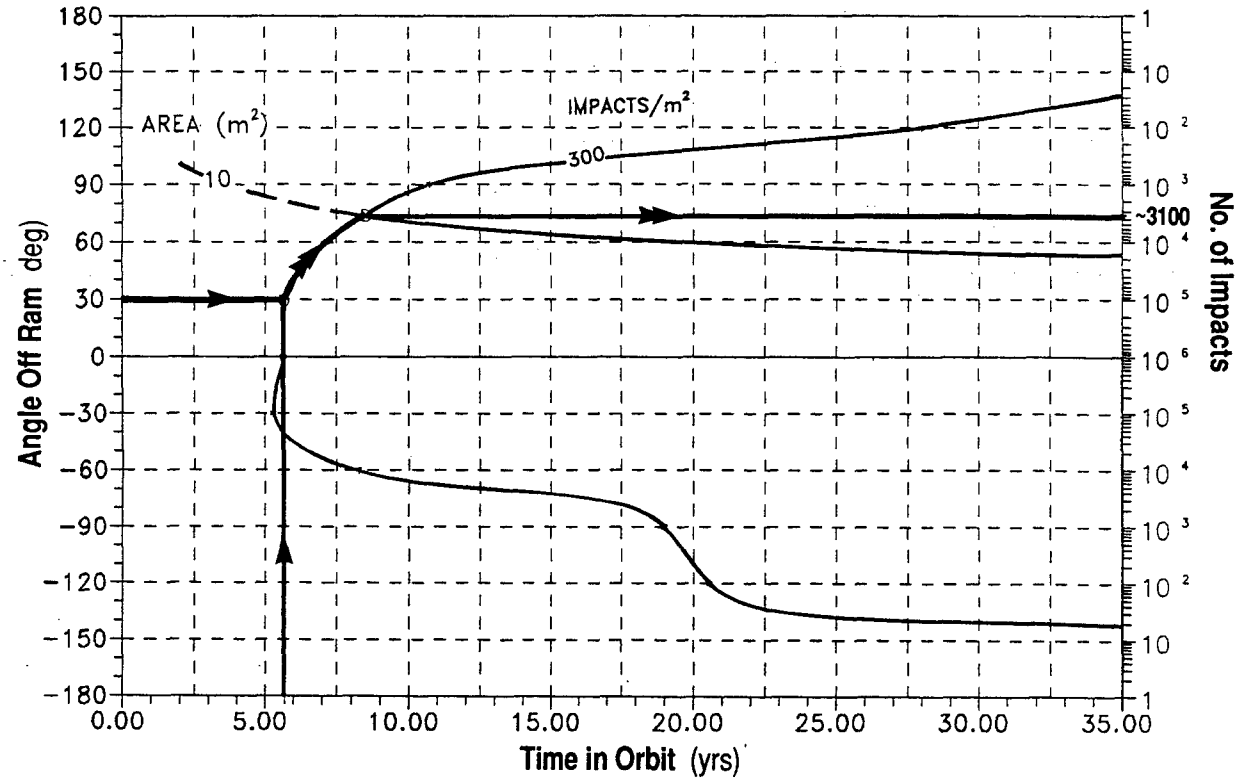


Figure 2. Nomogram for LDEF

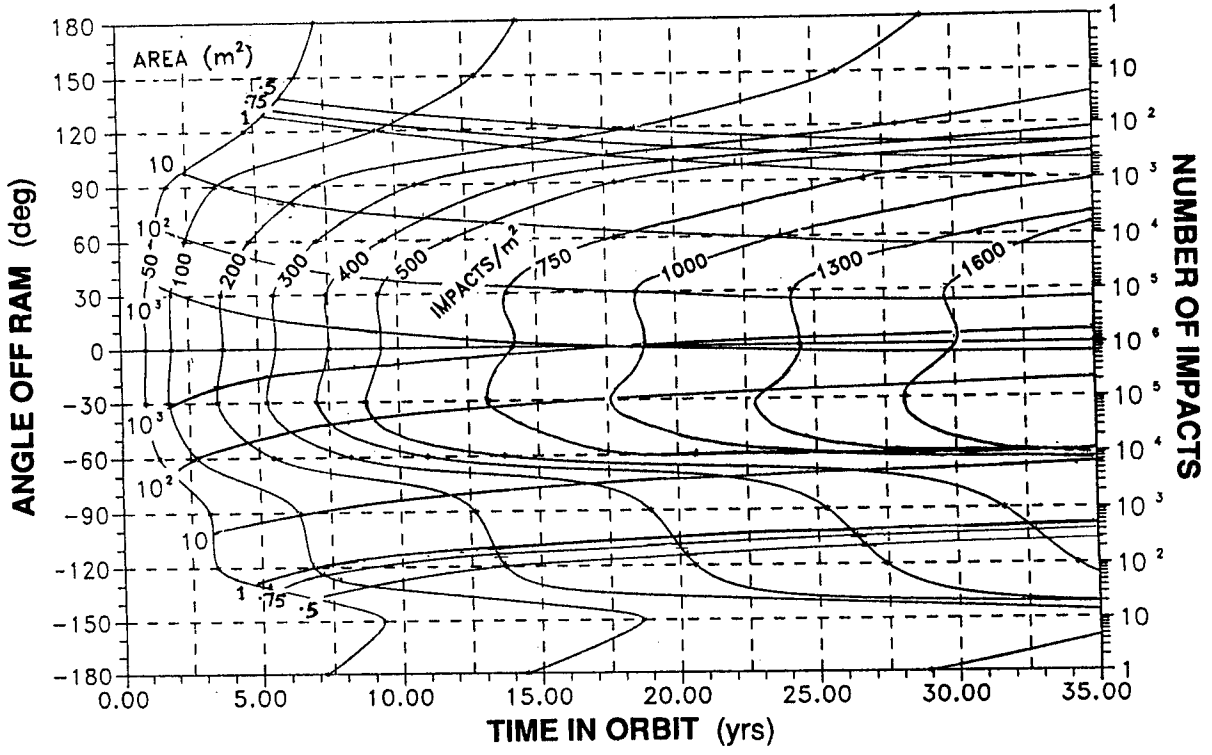


Figure 3. Nomogram for estimating total number of micrometeoroid/debris impacts for arbitrary exposed surface areas as a function of angle off ram and time in orbit

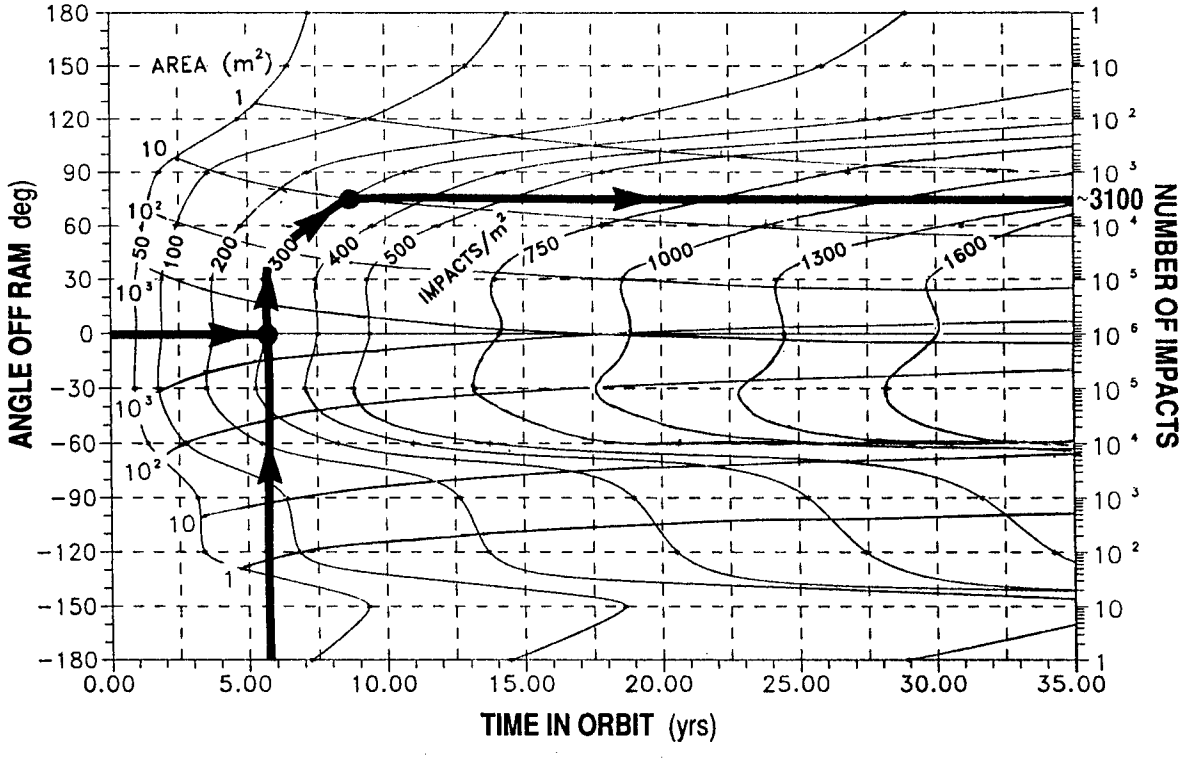


Figure 4.

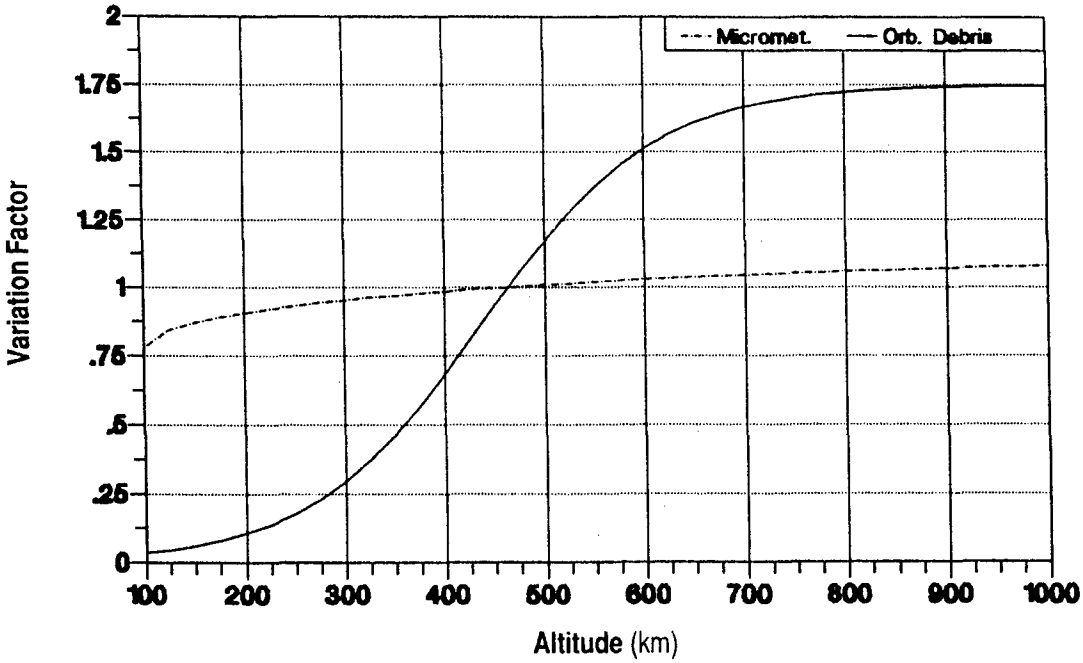


Figure 5. Normalized altitude variation factors (normalized to 464 km)
Note: orbital debris factors are for 1995 (projected)

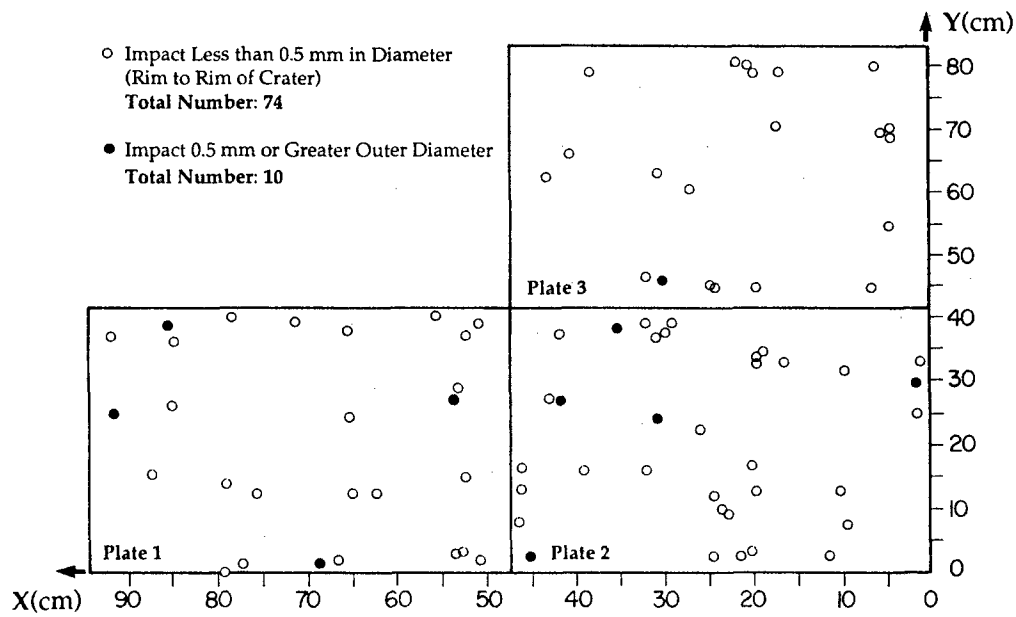


Figure 6. Micrometeoroid/debris impacts on UTIAS composite materials LDEF experiment (AO180, location D-12)

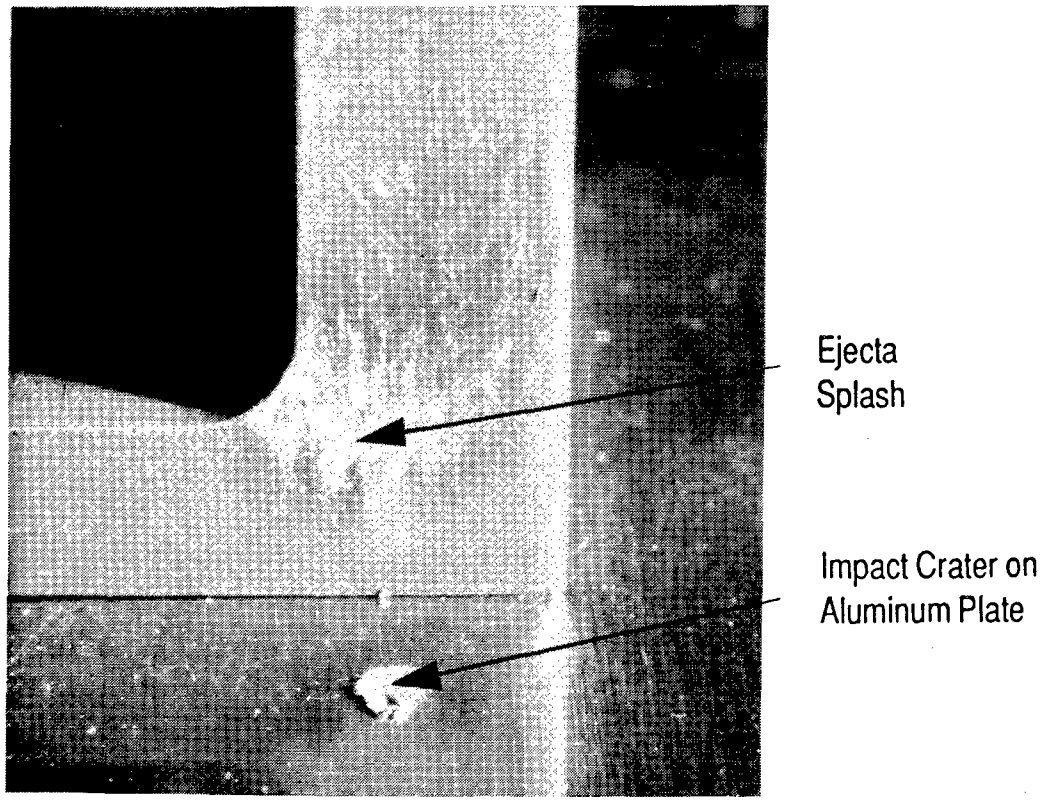


Figure 7. View of micrometeoroid impact crater and ejecta splash pattern on adjacent vertical flange structure

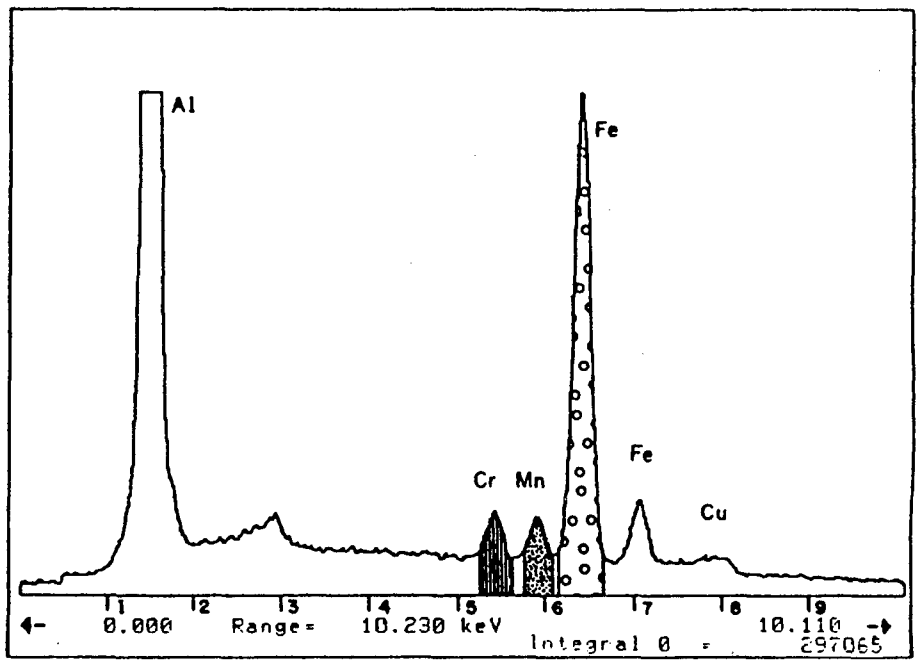


Figure 8. Crater ejecta and elemental composition (EDS spectra)

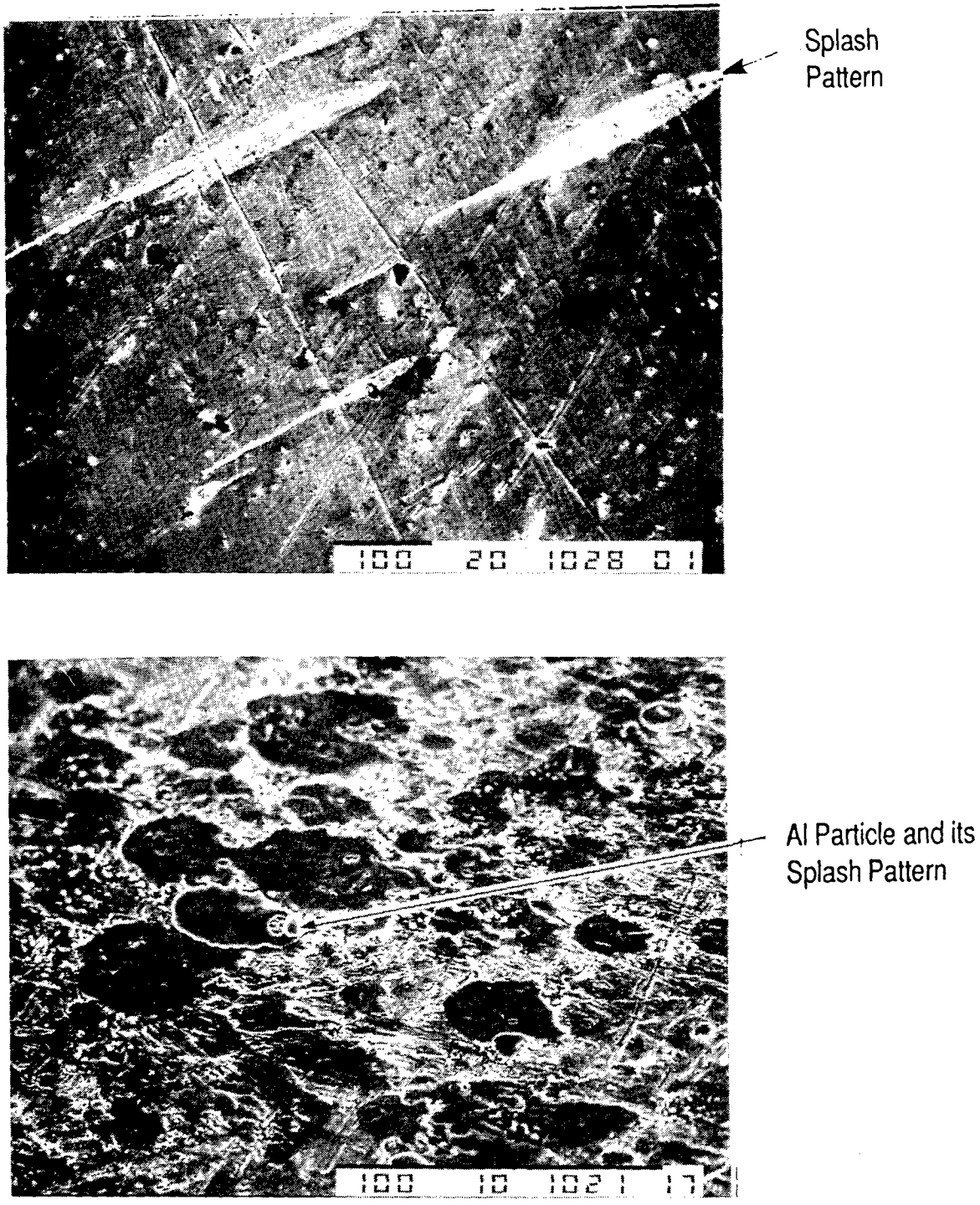


Figure 9. Different splash patterns formed by ejecta from micrometeoroid impact

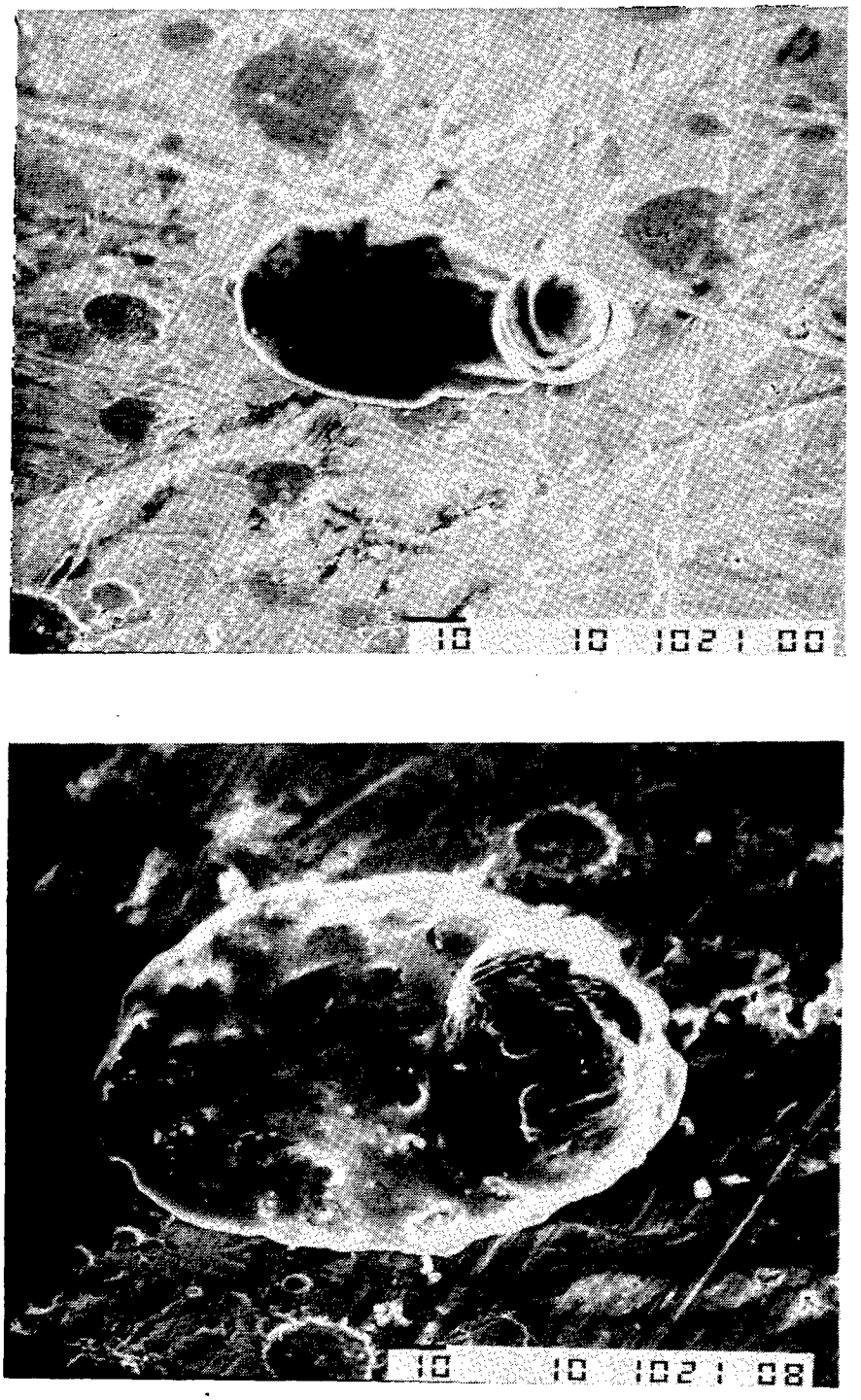
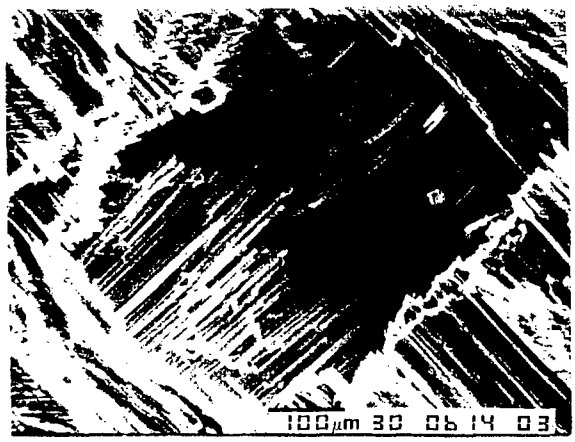
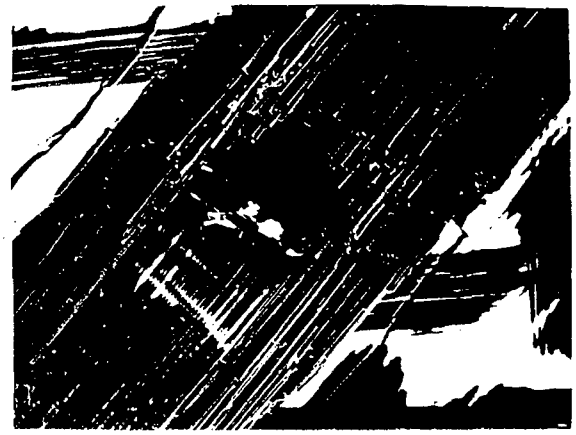


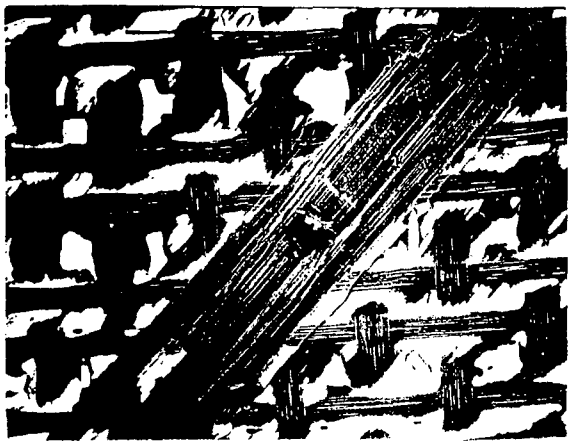
Figure 10. Aluminum ejecta particles with associated splash patterns



View of front face
impact hole (x100)



View of back face
exit hole (x100)



View of exit face damage
to composite laminate (x35)

Figure 11. SEM photographs of micrometeoroid/debris impact damage to graphite/epoxy laminate $(\pm 45°)_4$

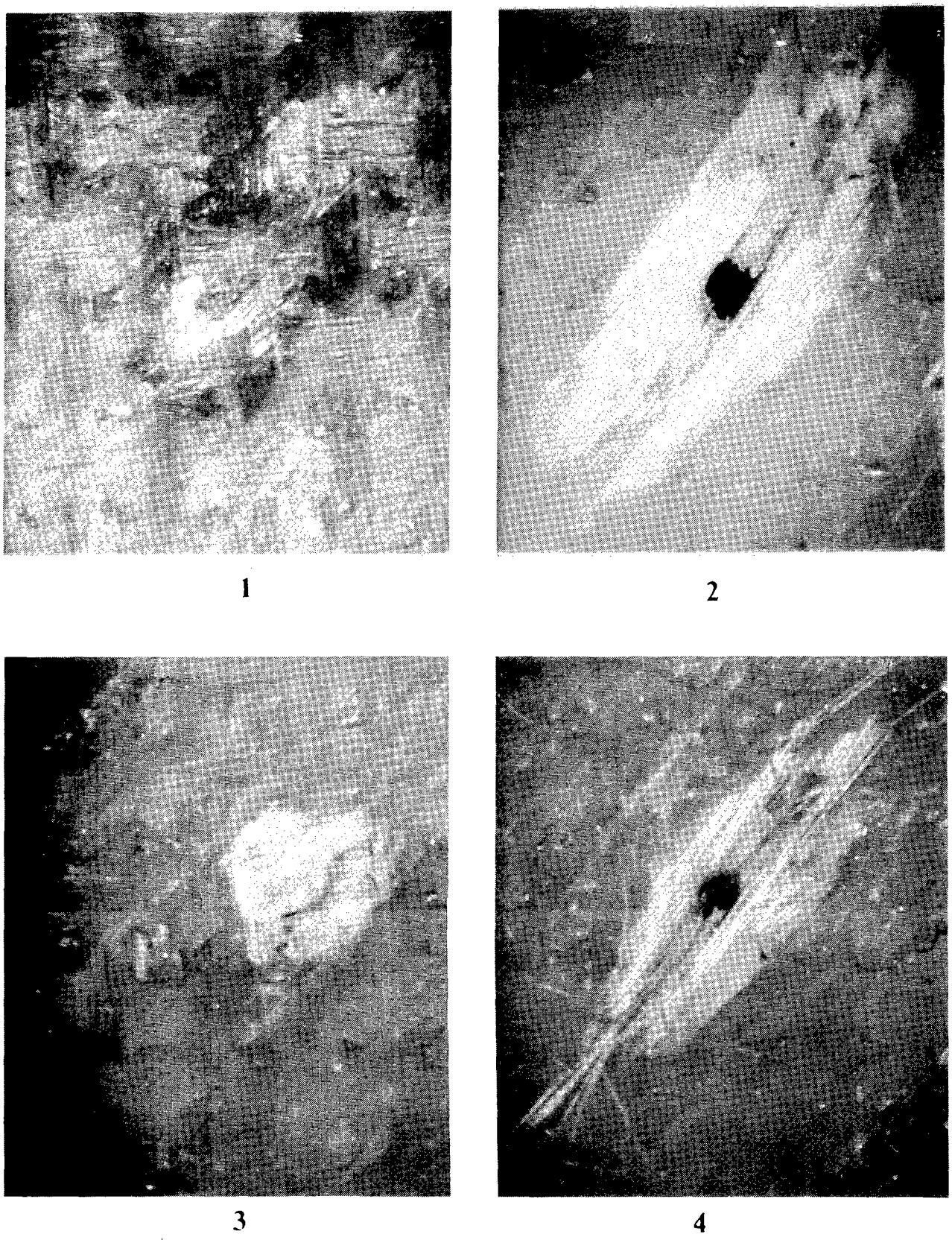


Figure 12. Micrometeoroid/debris impact damage (×100) on Kevlar®/epoxy tube [SP-328, $(\pm 45°)_{4S}$]

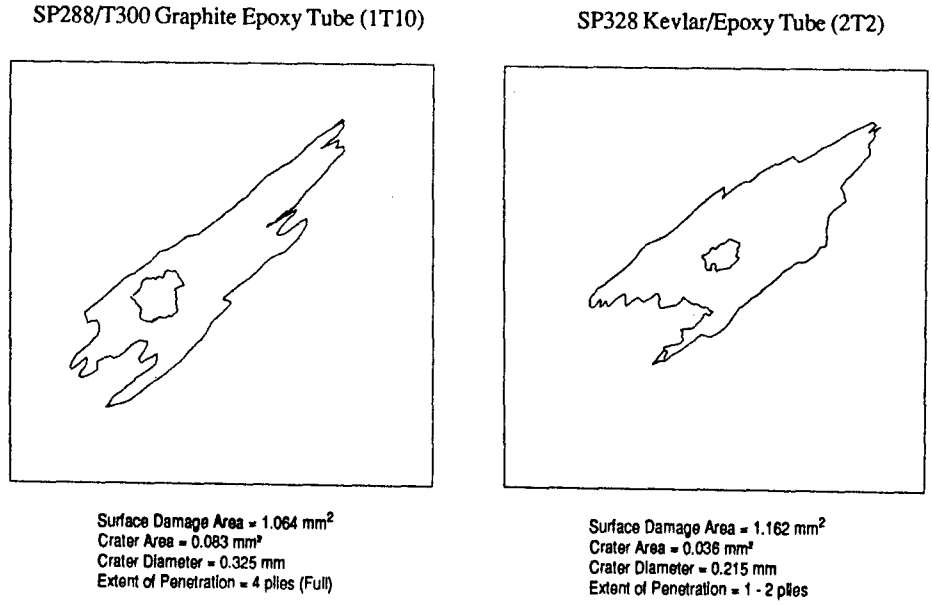


Figure 13. Micrometeoroid/debris impact damage

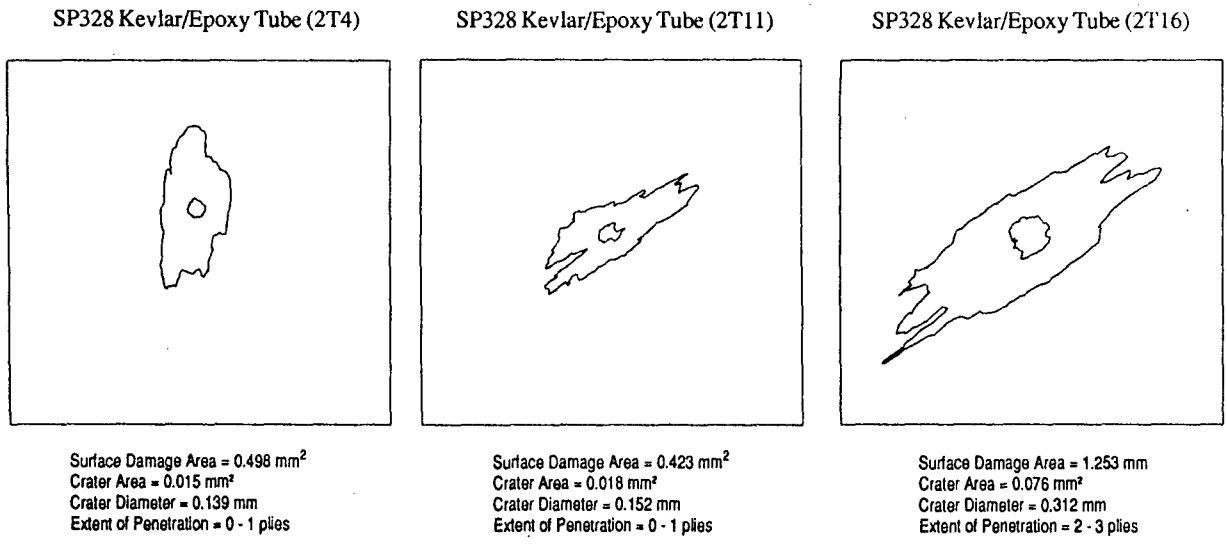


Figure 14. Micrometeoroid/debris impact damage

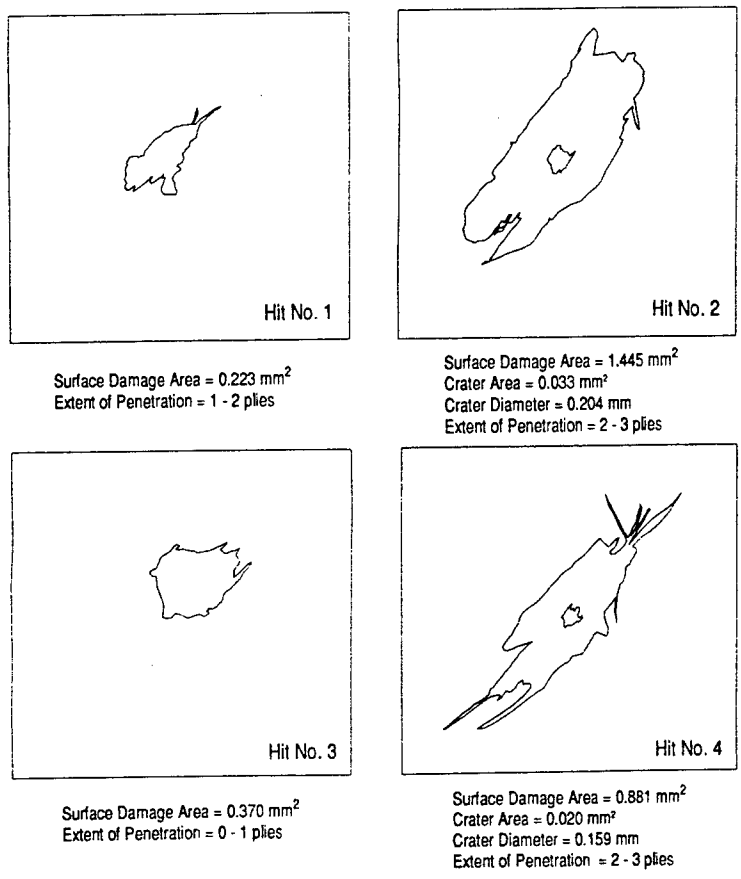


Figure 15. Micrometeoroid/debris impact damage, SP328 Kevlar®/epoxy tube (2T17)

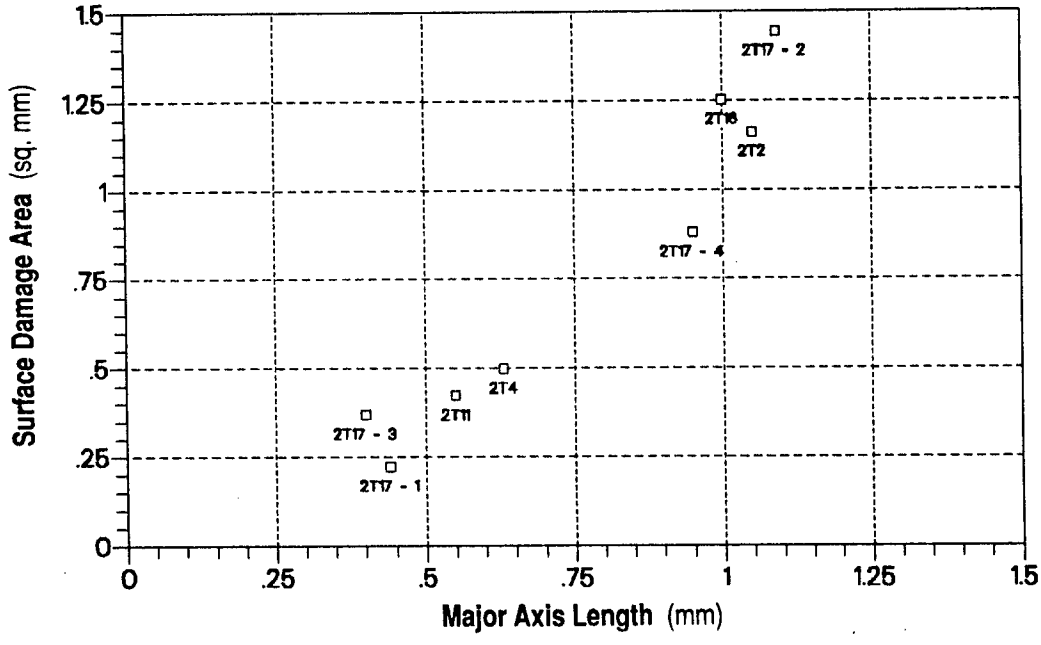
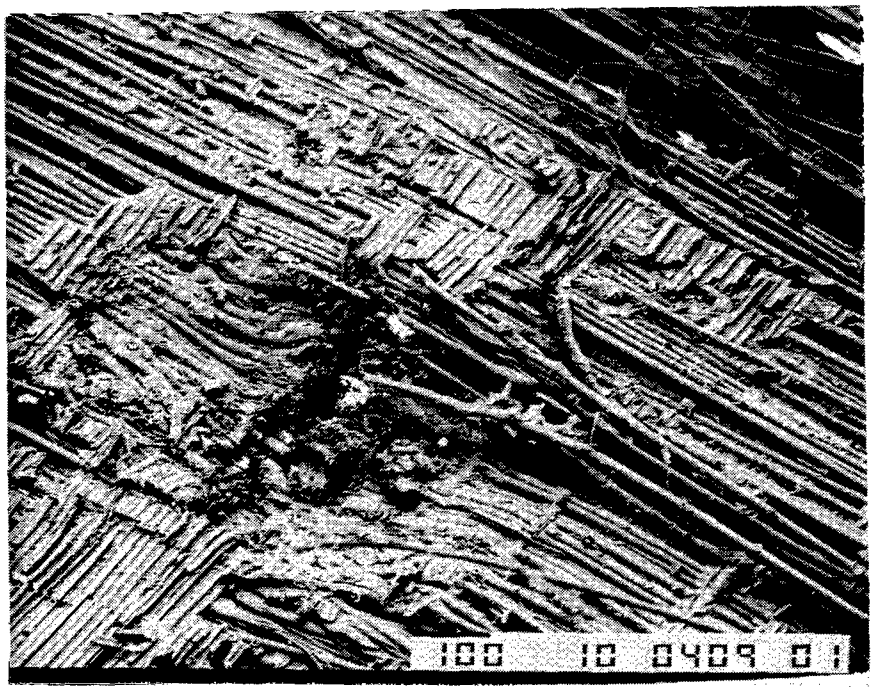
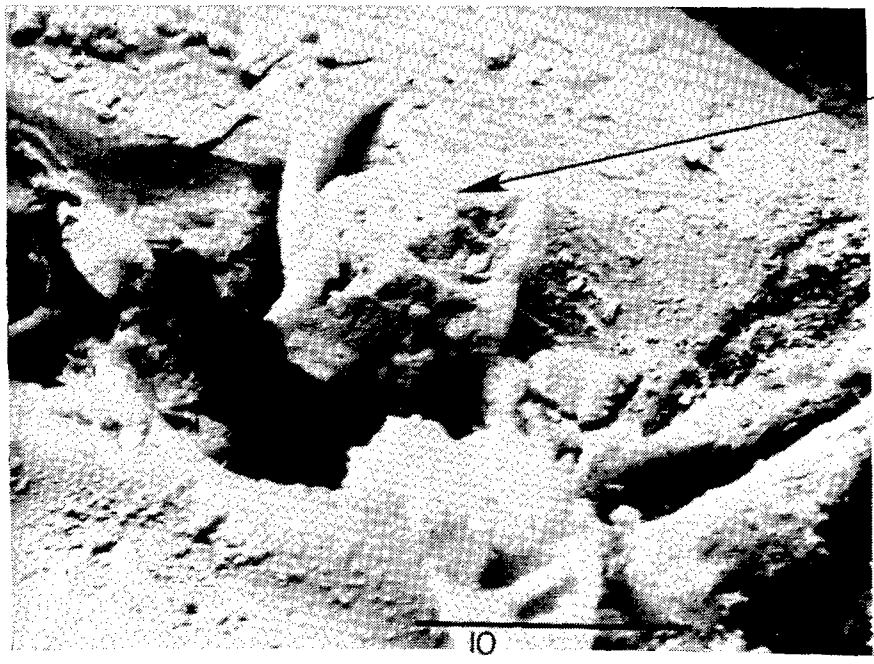


Figure 16



(a) Base of Impact Crater at 3rd Ply Interface



(b) Foreign Particulate in Crater

Figure 17. SEM photomicrographs of (a) impact crater base, and (b) particulate in crater for Kevlar®/epoxy tube (2T16)

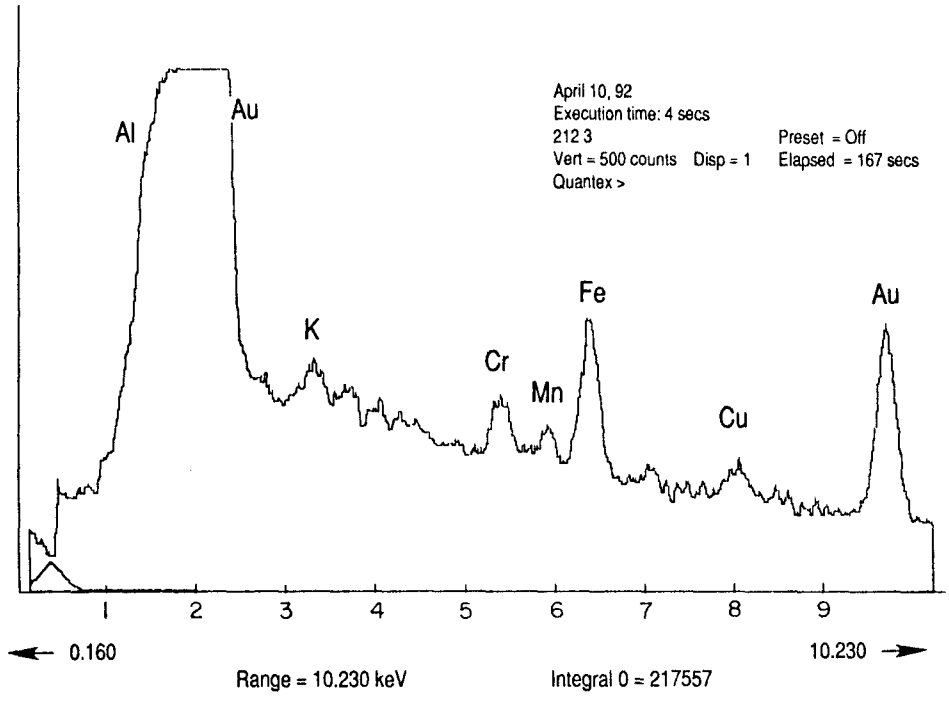


Figure 18. SEM-EDX spectra of particle in impact crater

SIMS CHEMICAL ANALYSIS OF EXTENDED IMPACTS ON THE LEADING AND TRAILING EDGES OF LDEF EXPERIMENT AO187-2

S. Amari, J. Foote, P. Swan, R. M. Walker, E. Zinner
McDonnell Center for the Space Sciences and Physics Department
Washington University
One Brookings Drive
St. Louis, MO 63130-4899
Phone: 314/935-6257, Fax: 314/935-6219

G. Lange
Max-Planck-Institut für Kernphysik
Postfach 103980
D-6900 Heidelberg, Germany
Phone: 6221 516 247, Fax: 6221 516 540

SUMMARY

Numerous "extended impacts" found in both leading and trailing edge capture cells have been successfully analyzed for the chemical composition of projectile residues by secondary ion mass spectrometry (SIMS). Most data have been obtained from the trailing edge cells where 45 of 58 impacts have been classified as "probably natural" and the remainder as "possibly man-made debris." This is in striking contrast to leading edge cells where 9 of 11 impacts so far measured are definitely classified as orbital debris. Although all the leading edge cells had lost their plastic entrance foils during flight, the rate of foil failure was similar to that of the trailing edge cells, 10% of which were recovered intact. Ultra-violet embrittlement is suspected as the major cause of failure on both leading and trailing edges. The major impediment to the accurate determination of projectile chemistry is the fractionation of volatile and refractory elements in the hypervelocity impact and redeposition processes. This effect had been noticed in a simulation experiment but is more pronounced in the LDEF capture cells, probably due to the higher average velocities of the space impacts. Surface contamination of the pure Ge surfaces with a substance rich in Si but also containing Mg and Al provides an additional problem for the accurate determination of impactor chemistry. The effect is variable, being much larger on surfaces that were exposed to space than in those cells that remained intact. Future work will concentrate on the analyses of more leading edge impacts and the development of new SIMS techniques for the measurement of elemental abundances in extended impacts.

INTRODUCTION

LDEF experiment A0187-2 consisted of 228 Ge-mylar cells for the capture of interplanetary dust material. The principle of the experiment and a more detailed description of the capture cells is given by Amari et al. (ref. 1). One full tray of capture cells was exposed on the leading edge and an area equivalent to a full tray in two locations on the trailing edge.

All cells on the leading edge and 90% of the cells on the trailing edge had lost their plastic covers (bare cells) during exposure in space. However, Ge plates from both leading and trailing edge bare cells contain extended impact features that must have been produced by high velocity projectiles while the mylar foils were still intact. Moreover, these extended impact features contain projectile material that could be measured by secondary ion mass spectrometry (SIMS), an extremely sensitive surface analysis technique.

Last year we reported results of the optical scanning of 100 bare cells from the trailing edge as well as the first results of SIMS analysis of 24 extended impacts on Ge from these cells (ref. 1). In the present paper we extend the SIMS analysis to 16 additional impacts from bare trailing edge cells and 18 impacts from the 12 trailing edge cells that had retained their plastic covers. We also optically scanned the Ge plates of 106 capture cells from the leading edge for single craters and extended impacts and analyzed 11 of the latter by SIMS.

OPTICAL SCANNING FOR SINGLE CRATERS AND EXTENDED IMPACTS

All cells were optically scanned under oblique illumination at a magnification of 240× as previously described by Amari *et al.* (ref. 1). The results are given in Table 1. There is a clear distinction between "extended impact features" and "single craters." The former consist of complex patterns of debris and ejecta, and must have been produced while the plastic cover foils were in place. In contrast, "single craters" show no evidence of associated debris deposits and represent direct hits on the Ge plates after the foils had failed in flight. The distinction between "extended impacts A and B" is subjective with the former generally being larger than the latter and being visible with the unaided eye. Although we have chosen to analyze the type A impacts first, we consider it likely that also many of the type B impacts contain sufficient material for chemical and isotopic analysis.

Table 1. Analysis of Cells on AO187-2

	Cells scanned	Single Craters	Extended Impacts A	Extended Impacts B	Measured by SIMS	
					Ge	Foil
Trailing Edge Bare	100	203	53	155	40	
Trailing Edge Covered	12	-	20	26	18	5
Leading Edge	106	5121	403	298	11	

There are several differences between the impacts on the two sides of the spacecraft. Figure 1 shows histograms of the sizes of extended impacts on the leading and trailing edge cells. As can be seen, the trailing edge impacts have, on average, much larger diameters than those on the leading edge. This is undoubtedly a reflection of the lower projectile velocities and shallower impact directions (ref. 2) for the trailing edge. An additional reason could be differences in the chemical compositions and physical properties of the projectiles, since a large fraction of leading edge impacts appear to be caused by man-made debris (see below), while those on the trailing edge are predominately produced by cosmic dust particles.

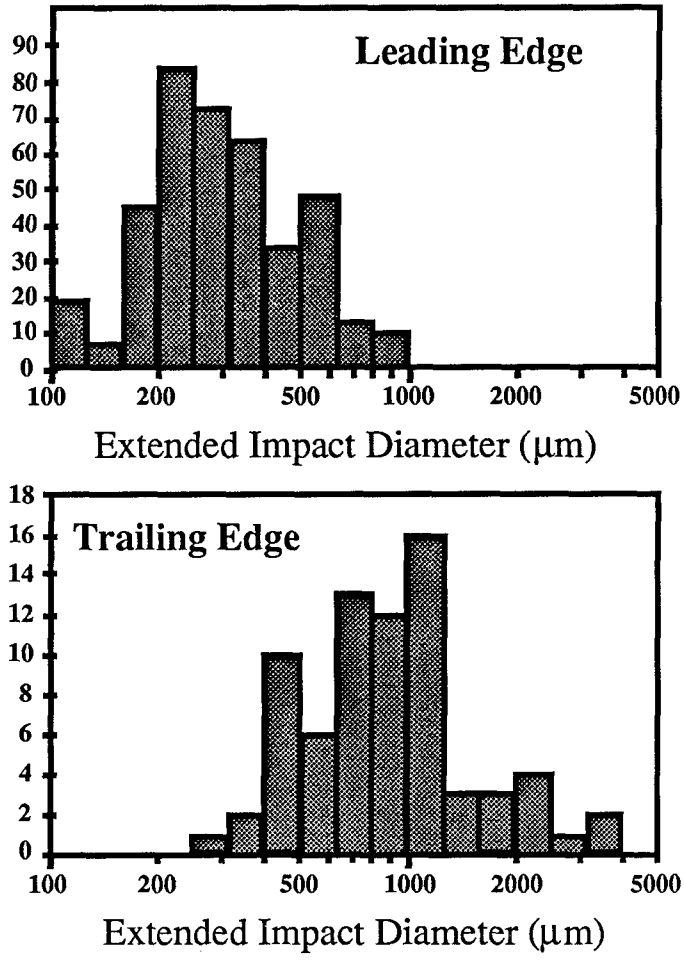


Fig. 1. Distribution of the sizes of extended impacts on Ge plates for both leading and trailing edge capture cells.

LIFETIMES OF ENTRANCE FOILS - FRONT AND BACK

All of the plastic cover foils on the leading edge failed during flight while ~ 10% on those of the trailing edge survived. At first glance it thus appears that there may have been a qualitative difference in the foil destruction processes between front and back. However, as we will show below, this is a somewhat misleading impression. While it is true that the foil loss occurred at a higher rate on the leading edge, foils on this edge lasted for long periods of time in space. The difference in foil survival between front and back is thus more quantitative than qualitative.

Although some corners and edges of many cells contained small pieces of intact or rolled up foil material, when different foils ruptured they appear to have done so suddenly, exposing a major part of the area of any given cell to free space. Since direct hits producing single craters are possible only after the foil has been removed, the density of single craters in a given cell is proportional to the time it was exposed without a foil provided, of course, that the flux of impacting particles is constant in time.

Consider first the results from the leading edge cells. Although none of the plastic foils survived for the entire exposure, it is clear that many remained in place for a considerable period of time. In Fig. 2, we show a histogram of the number of single craters per cell. The width of the distribution far exceeds that expected for a single exposure time for all cells and indicates, in itself, a distribution of survival times. The locations of individual impacts were plotted for the two cells with the largest density of single craters. No clustering was seen, consistent with the assumption that single craters represent a random population of impinging particles.

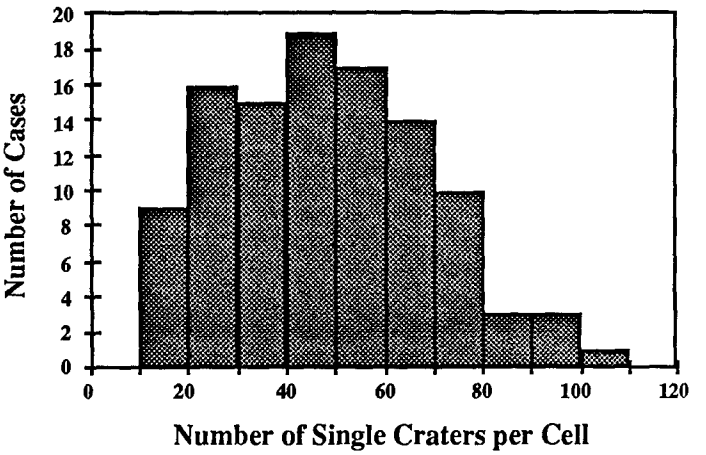


Fig. 2. Distribution of the number of single craters per cell for leading edge capture cells. Such craters are produced only after the entrance foils have ruptered and their numbers are a measure of the time different Ge surfaces were exposed to space. The width of this distribution indicates a considerable spread in foil lifetimes.

The maximum number of single craters per cell is 101. If we assume that the foil on this cell failed immediately after launch, the distribution of craters in Fig. 2 would indicate that more than 50% of the foils survived at least to the half way mark and that some foils lasted through almost 90% of the total exposure time before rupturing.

In contrast to single craters, the density of extended impacts is a measure of the time the foils remained in place. However, only a small fraction of the particles that produce single craters produce extended impacts that are visible under the same scanning conditions. Thus the statistics on extended impacts are less favorable than those for single craters. Figure 3 is a scatter diagram showing the relation between extended impacts (A plus B) and single craters. This figure also shows the same data after binning into groups of 20 single craters and averaging the number of extended impacts in each bin. The data show the expected inverse relationship between number of extended impacts and number of single craters (Fig. 3). Furthermore, the best-fit line through these binned averages intercepts the abscissa at 111 craters per cell, not very different from the maximum number of 101

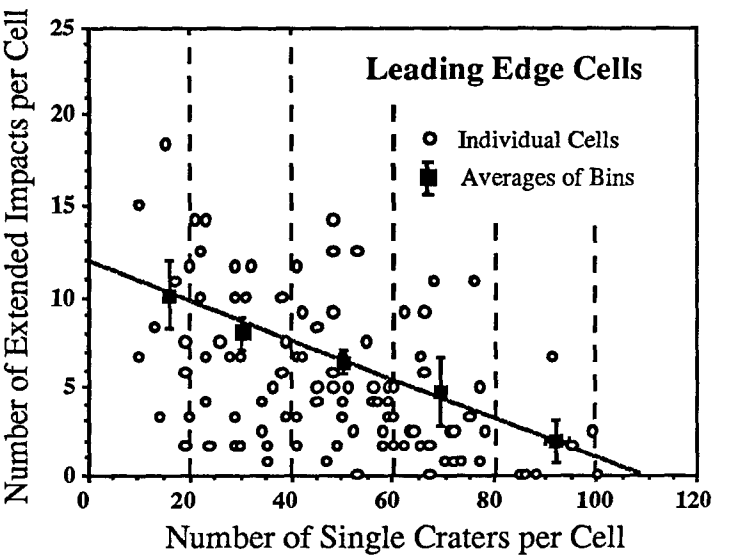


Fig. 3. Extended impacts and single craters for leading edge capture cells. The solid squares show averages for the number of extended impacts versus single crater counts binned in groups of 20. Since extended impacts are produced only when the entrance foils are intact and single impacts only after they have ruptured, there is an inverse correlation between the two densities.

we assumed to be the number of craters on a cell whose foil was removed right after the launch of LDEF. Thus the two indicators of foil lifetimes yield consistent results and a sizable fraction of the foils on the leading edge survived a considerable fraction of the total time of LDEF in orbit.

Consider next the data on the trailing edge cells. The 12 cells which remained covered during the entire period have a total of 46 extended impacts of types A and B for an average of 3.8 impacts/cell. The bare cells have an average of 2.1 extended impacts/cell, suggesting that the foils lasted, on average, about half of the total time. This is similar to the result inferred for the leading edge cells from consideration of the single impact crater data. The first order conclusion is thus that the foil failure rates are similar for both the leading and trailing edge cells.

While we do not know in detail what caused the foils to fail, certain general aspects of the problem seem clear. Firstly, since the rates at which the foils failed were approximately the same for both the leading and trailing edges, the same causative factors must be present. Thus neither atomic oxygen erosion nor enhanced impact fluxes, which are characteristic of the front side only, appears to be the principal cause of failure. However, both effects could have contributed to an enhanced failure rate of the leading edge cells.

Some contribution of atomic oxygen erosion indeed seems likely since we have evidence that most impacts alone do not destroy foils. This conclusion is based on the presence of peculiar elliptical features that accompany approximately half of the extended impacts on the leading edge. Fig. 4 shows two such features that are associated with extended impacts. The fact that these elliptical features occur only on the leading edge Ge plates and only in connection with extended impacts indicates that they must have been caused by the interaction of the residual atmosphere, mostly atomic oxygen, with the penetration hole left by the high velocity impact. At present we do not have any detailed understanding of this process.

Foil failure probably results from repeated stressing of the foils due to cyclical temperature changes, coupled with degradation of the mechanical properties of the foils in the space environment. In spite of the fact that the plastic was metal-coated, we consider UV

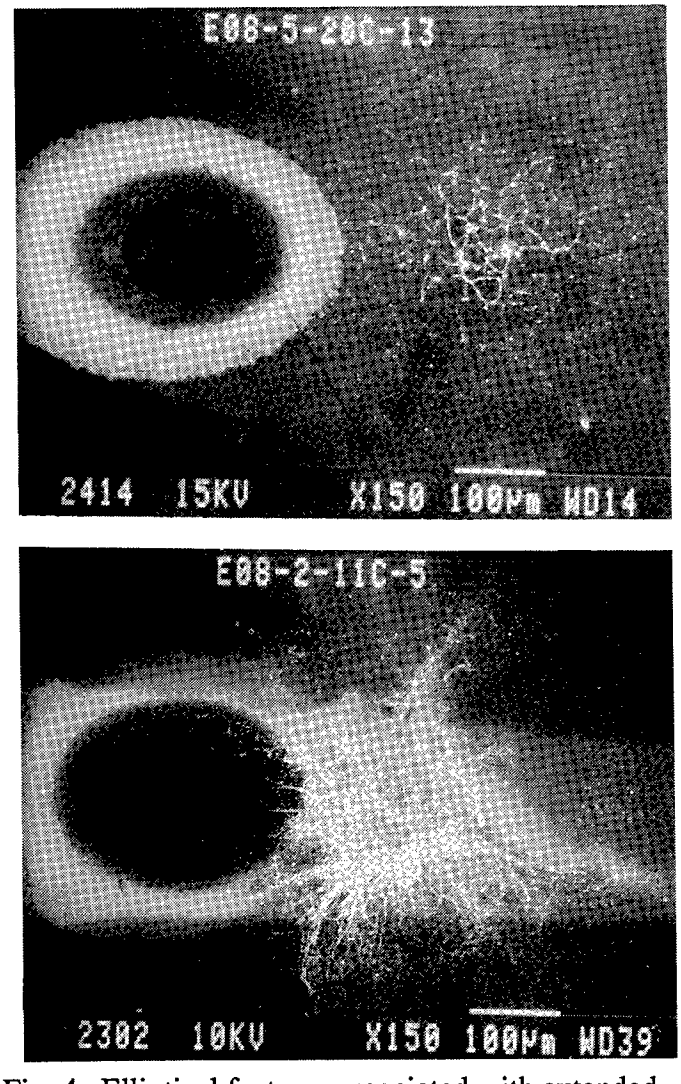


Fig. 4. Elliptical features associated with extended impacts. These multi-ringed concentric features are seen in about half of the extended impacts found in the leading edge cells. Their presence indicates that the entrance foils did not rupture immediately upon impact.

embrittlement to be a likely source of this degradation.

We plan to continue to address the question of foil lifetimes by determining the density of small craters (down to ≤1 μm diameter) that can be seen by scanning at 1000× in an SEM. A possible difficulty with this approach, however, is the observation of temporal changes of the flux of very small particles impinging on the leading edge capture cells (ref. 3).

SIMS CHEMICAL ANALYSIS OF EXTENDED IMPACTS

The procedures for the SIMS chemical analysis of projectile deposits in extended impacts have been described previously (ref.1). To summarize briefly: lateral multielement profiles across extended impacts are obtained by integrating secondary ion intensity depth profiles measured in areas 40 μm apart. From the ion signals we obtain elemental ratios by applying sensitivity factors determined from measurements on standards. Previous measurements have shown that different elements can be distributed differently in a given impact, apparently reflecting compositional heterogeneity of the projectile. While we plan to use a newly acquired secondary ion digital imaging system to determine the spatial distribution of various elements over the entire impact area, for the time being we have adopted a compromise – elemental ratio determinations from lateral profile data are estimated by taking ion intensities measured at the maximum of the $^{24}Mg^+$ signal.

During SIMS measurements of extended impacts on the Ge plates it became clear that the sensitivity of the analysis technique is not one of the limiting factors (interestingly, SEM-EDS studies of the same impacts gave no signals of projectile material, even at low voltages). The major

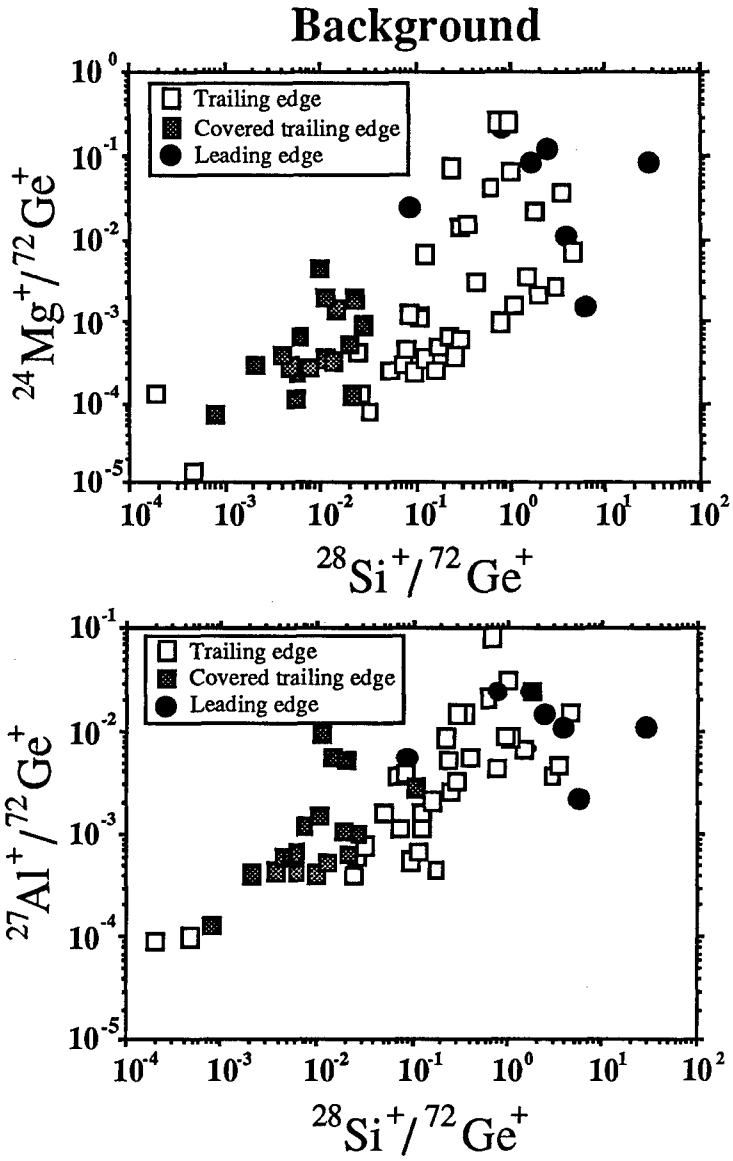


Fig. 5. Surface contamination on Ge target plates in regions well removed from impact debris.

limitation on the SIMS data is rather the high level of contamination encountered on the surface of the Ge plates. While contamination with Si is worst, high background levels are found also for other elements. Fig. 5 shows ion signals measured outside of the impact areas normalized to the $^{72}Ge^{+}$ signal. Background levels of Mg and Al are correlated with those of Si. The plots furthermore clearly show that the contamination levels are related to the exposure of the cells during flight: on average, the backgrounds are lowest on the plates from capture cells that retained their plastic foils and highest on the plates exposed on the leading edge. While we originally thought that outgassing of the RTV that was used to bond the Ge plates to the Al substrate was the main source for the Si contamination, the fact that other elements correlate with the Si demonstrates that there must be other sources of contamination. The fact that the leading edge plates have the highest background levels may be an important clue suggesting, for example, that redeposition of atomic oxygen induced erosion products may be significant.

Analysis of Impacts on the Leading Edge

To date we have performed SIMS analyses on 11 extended impacts from the leading edge. In 8 of these impacts enhancements were seen only for Al. Fig. 6 shows one of the impacts and the corresponding lateral ion intensity profiles. One additional impact showed enhancements mostly in Ti with minor Al. Its SEM micrograph and lateral ion intensity profiles are presented in Fig. 7. The remaining two impacts have hardly any elemental enhancements that can be attributed to projectile material in the region that exhibits damage features in the SEM. It has already been mentioned that the leading edge Ge plates suffer from extremely high levels of contamination (Fig. 5), and this may be the reason that no projectile material above background could be detected in these two impacts.

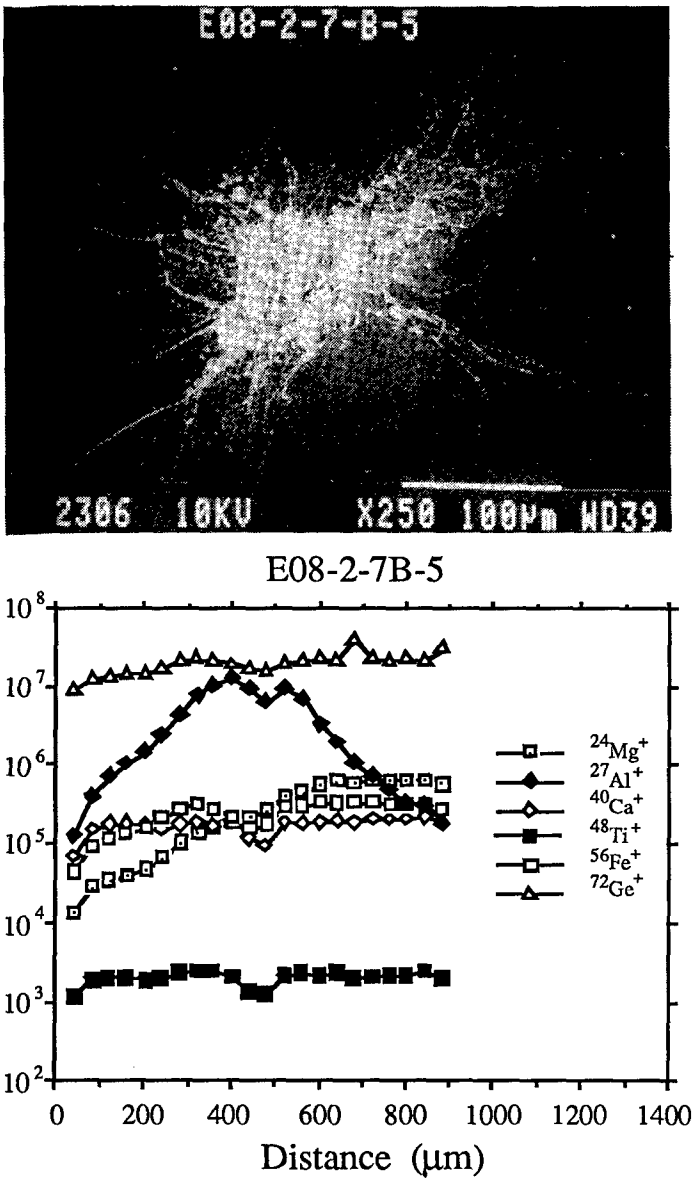
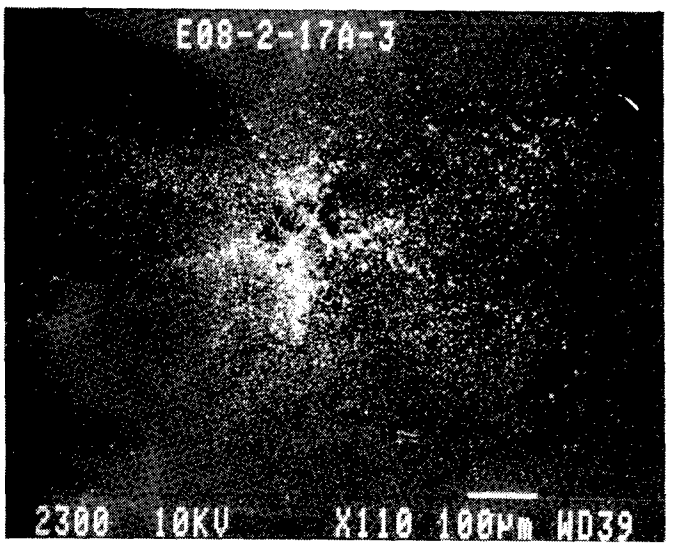


Fig. 6. Signature of an orbital debris impact found in a leading edge cell. The ion microprobe scan across impact E08-2-7B-5 shows Al as the only element that is present at enhanced levels.

The extended impacts from the leading edge capture cells thus differ significantly from those from the trailing edge capture cells in the chemical composition of their deposits. No impacts with only Al or Ti deposits such as those depicted in Figs. 6 and 7 have been seen on the trailing edge Ge plates. We can thus, with reasonable certainty, assign the 9 leading edge impacts that contain only Al or Ti to man-made debris. The first are most likely Al-oxide particles produced by solid-fuel rocket engines, the latter (mostly Ti) either is a chip of paint or a fragment of spacecraft hardware. Although the number of investigated leading edge impacts is still extremely limited, their chemical analysis shows that they are dominated by man-made debris.



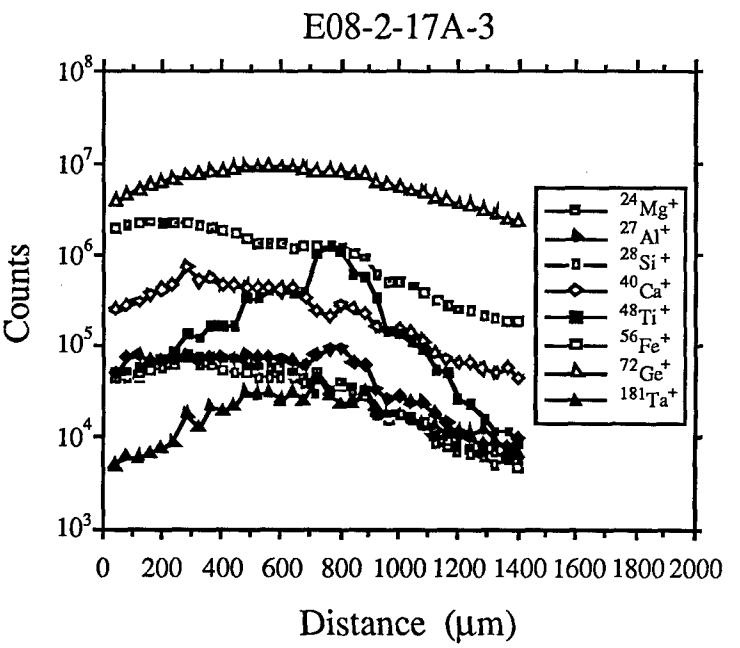


Fig. 7. Another probable orbital debris impact in a leading edge cell. The ion microprobe traverse across extended impact E08-2-17A-3 shows enhancements of both Ti and Al.

Analysis of Impacts on the Trailing Edge

In the present work, we analyzed another 16 extended impacts from the bare trailing edge capture cells (increasing the total number of impacts from these cells analyzed by SIMS to 40) and 18 extended impacts from the 12 trailing edge cells that had retained their foils. Histograms of computed elemental ratios for all impacts with clear maxima of the plotted elements in the lateral intensity profiles (32 of the bare cell impacts and 16 of the covered cell impacts) are shown in Fig. 8. They are compared with elemental ratios measured by SIMS in interplanetary dust particles collected in the stratosphere (ref. 4,5). Chondritic ratios are indicated for reference.

For the Ca/Mg, Ti/Mg and Fe/Mg ratios there appears to be no systematic difference between the impacts from the bare and covered capture cells. The Al/Mg ratios, however, are on average smaller in impacts from the covered cells than in those from the uncovered cells. A possible explanation for this discrepancy is the higher level of contamination on the exposed Ge plates (Fig. 5).

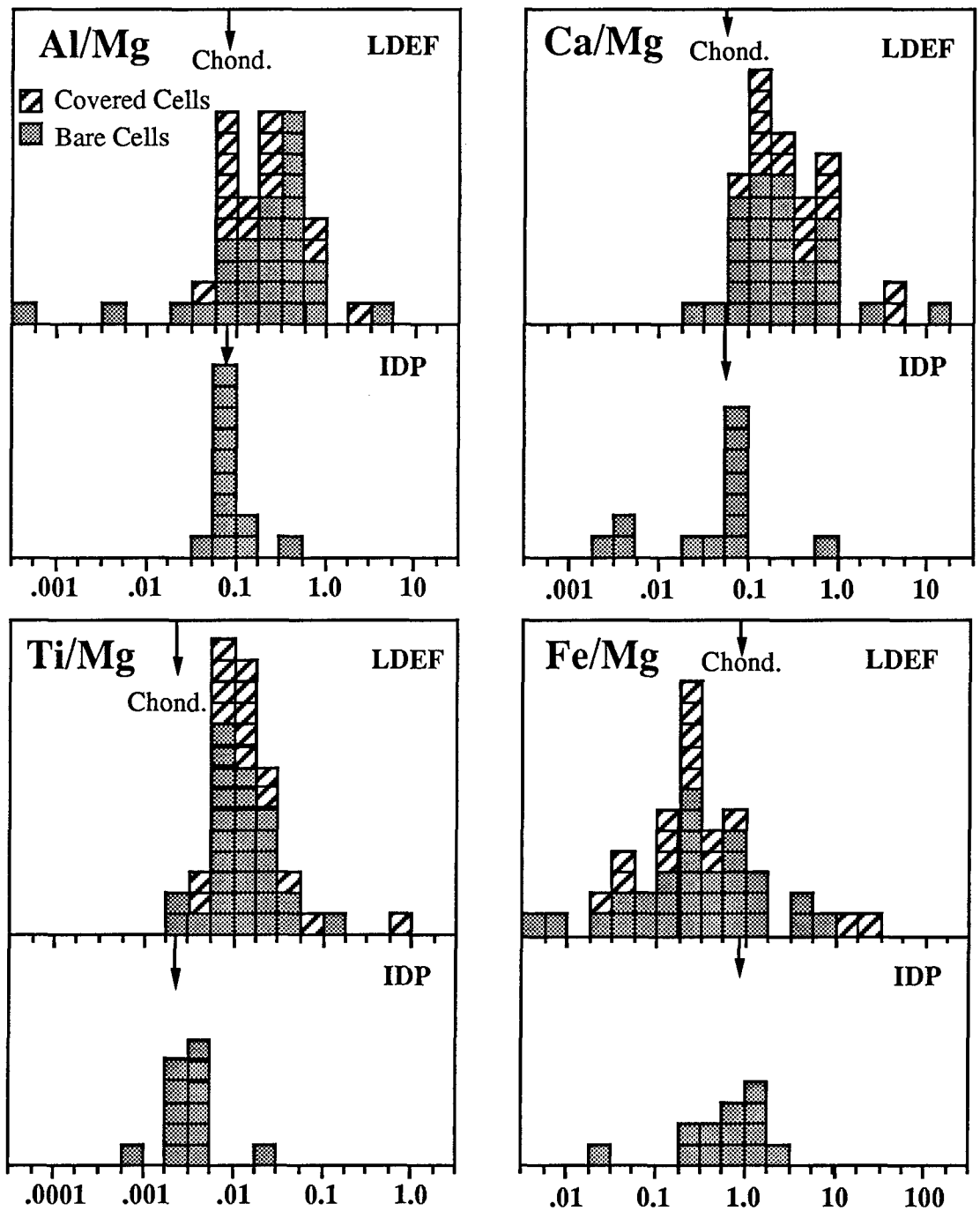


Fig. 8. Histograms of elemental ratios measured in LDEF extended impacts compared to previous measurements of a set of interplanetary dust particles (IDPs) collected in the stratosphere. Average chondritic values are indicated by the arrows.

The systematic shift of the elemental ratios measured for extended impact residues compared to IDPs and chondritic ratios has previously been noted and discussed by us (ref. 1). We pointed out that laboratory simulation experiments indicated that projectile residue material on the Ge plates is

fractionated in its elemental composition relative to the original projectile with refractory elements being enhanced in the deposits relative to less refractory elements (ref. 6). These simulation experiments on foil/Ge cells identical to those flown on LDEF also showed that the elemental fractionations are larger for material on the Ge plates than for material deposited on the backside of the entrance foil (Fig. 9).

The impacts in the covered trailing edge cell provided us with the opportunity to test this elemental fractionation effect for projectiles captured on LDEF. So far we have attempted the analysis of foil deposits from 5 impacts in the covered cells. Unfortunately, the SIMS measurements of the foils are very difficult, mostly due to extreme embrittlement of the samples and their failure to stay stretched and smooth when mounted for ion probe analysis. We obtained a good SIMS analysis on only one foil deposit of the five tried. Data for this impact are discussed next.

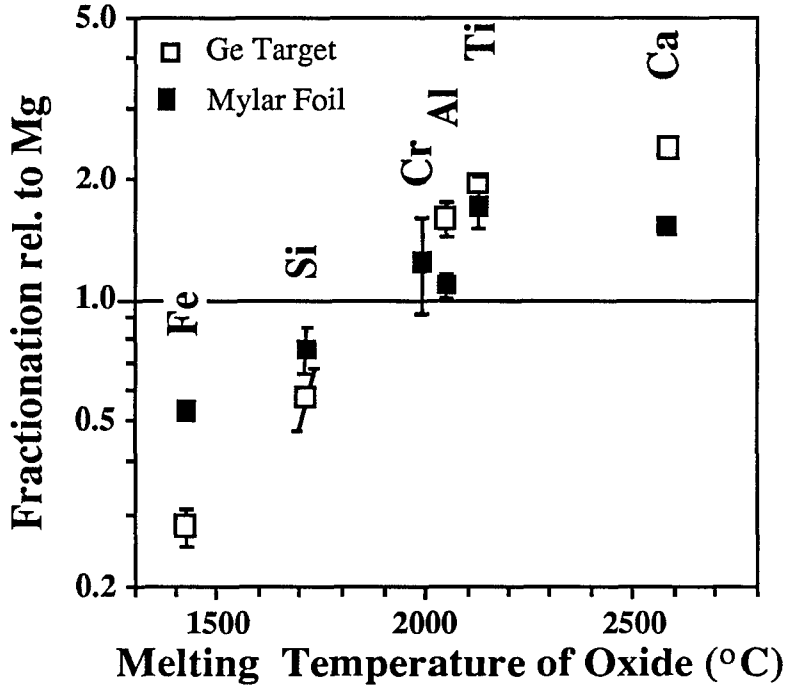


Fig. 9. Element fractionation trends measured in laboratory impact experiments. The data are from the thesis of G. Lange Heidleberg, 1986 and were obtained with the W.U. ion microprobe. The ordinate shows measurements of the relative abundance of different elements in the impact debris compared to the abundance of those same elements in the glass projectiles used in the impact experiments. The abscissa orders the elements by a volatility index.

The extended impact on Ge and the backside of the foil featuring the penetration hole and signs of secondary ejecta are shown in Fig. 10 together with lateral profiles across the Ge impact and the deposits on the foil. The elemental ratios obtained from these profiles are plotted in Fig. 11 and compared to the fractionation of a projectile of chondritic composition expected from laboratory experiments. As expected, the material from impact EO3-2-11A-3 deposited on the Ge plate is more fractionated than the material found on the backside of the mylar foil. The relative fractionation for the LDEF impact is larger than the average obtained from the simulation experiments. This is probably a reflection of a difference in the impact velocities but could also reflect differences in chemical composition and physical properties (density, shape) of the projectile.

Although additional measurements on foil deposits are needed, the presence of elemental fractionations between Ge and foil deposits in one LDEF impact makes it likely that the dominant cause for the large differences between elemental ratios measured in extended impacts from the trailing edge and those measured in IDPs is elemental fractionation during the high velocity impact process. Intrinsic, large differences in chemical compositions between these two populations is less likely, although still possible.

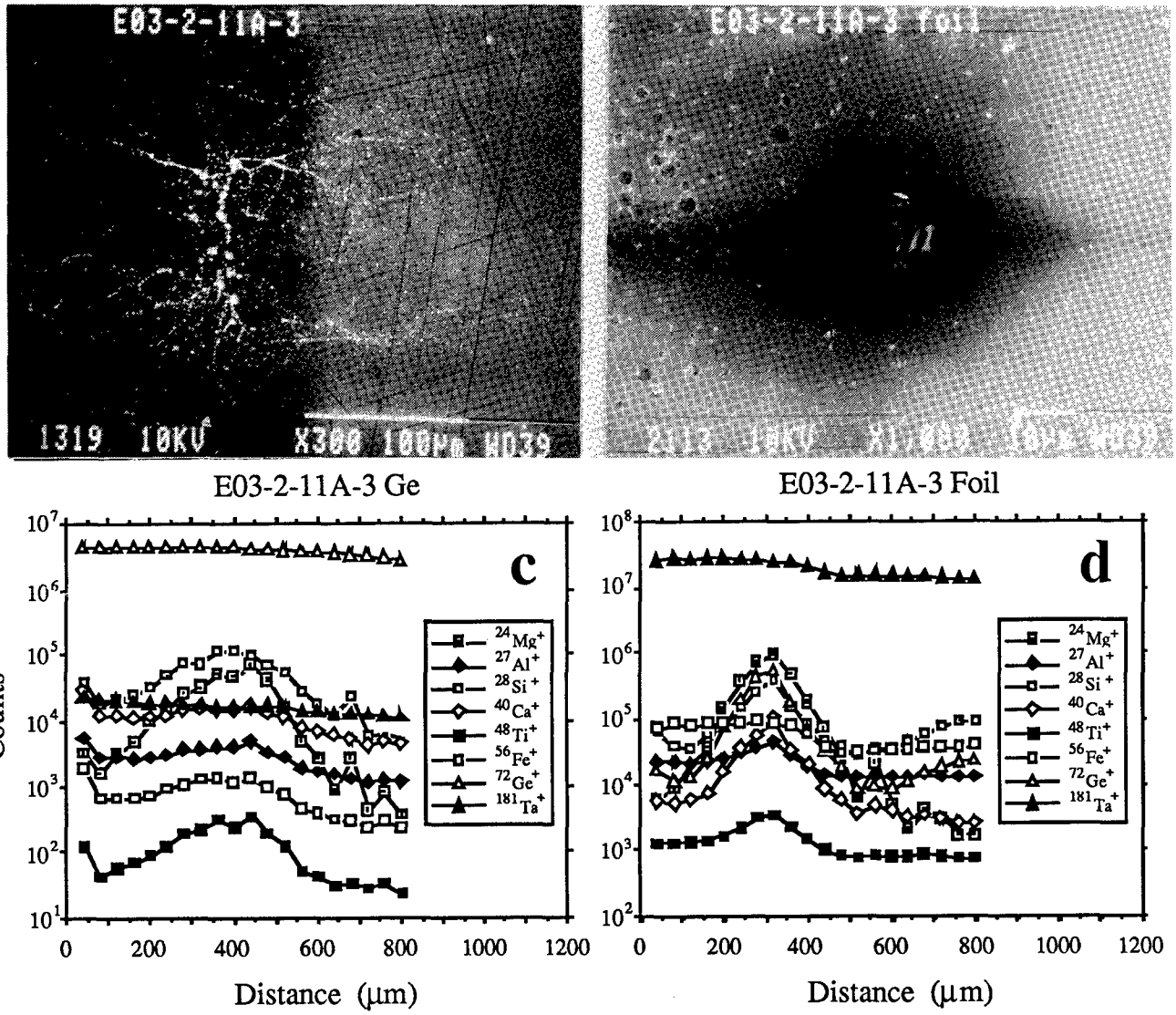


Fig. 10. Ion microprobe profiles on both the Ge target plate and the underside of the entrance foil for impact E03-2-11A-3. Most of the capture cells lost their entrance foils during flight and those that survived are extremely brittle and difficult to mount. The data shown are for the only cell for which it has been proven possible to study impacts in the way that we had originally intended. As expected from simulation experiments the projectile signals are much higher for the debris on the foil than for the debris on the Ge target plate.

The presence of elemental fractionations in the impact deposits is the single largest impediment to accurate determination of projectile chemistry. In principle, all of the projectile material, except the small fraction that escapes back through the impact hole in the entrance foil, is deposited in the capture cell, i.e. in our design either on the Ge plate or the backside of the foil. However, more volatile elements are apparently deposited over a wider area of the Ge plate and foil and, when the surface concentration becomes too low, can no longer be detected. It is therefore important to measure the surface deposits over as wide an area as possible. Measuring the radial dependence of the abundances of different elements may allow the development of normalization procedures that could correct for fractionation

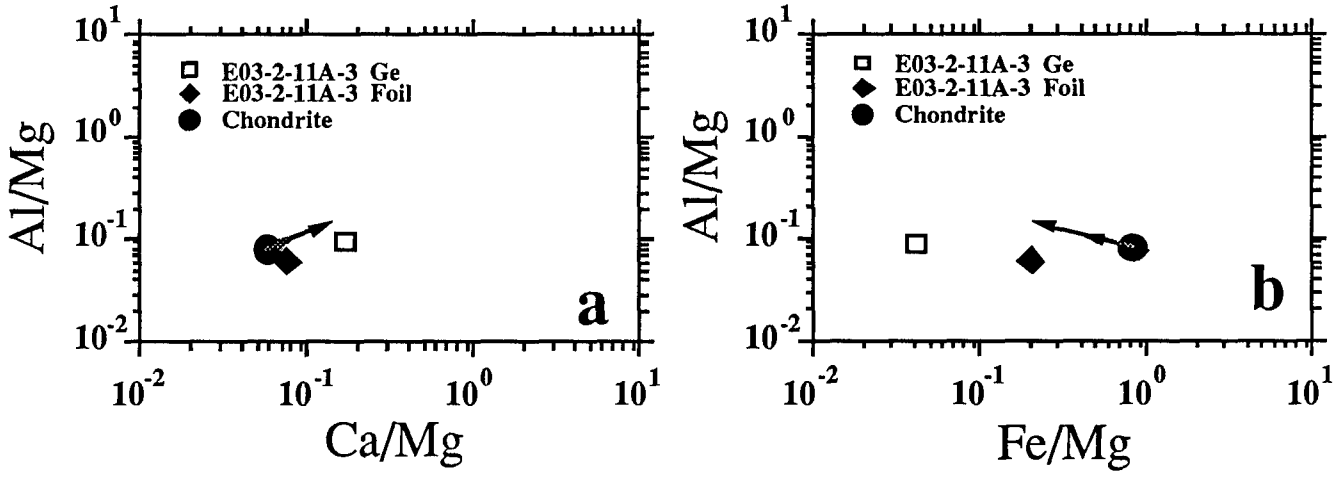


Fig. 11. Fractionation trends from the data on the intact cell shown in Fig. 10. The arrows indicate the fractionation trends previously obtained from laboratory simulation experiments of the type shown in Fig. 9. As expected from the prior work, the projectile material on the Ge plate is fractionated relative to that on the foil.

effects. In future space experiments, it would be desirable to have partitioned capture cells which would limit the area on which material from a given impact was deposited. It is not obvious, however, how to construct such a device while keeping all surfaces accessible to SIMS analysis.

IDENTIFICATION OF THE ORIGIN OF PROJECTILE MATERIAL

In spite of the problems caused by elemental fractionation the abundance data can be used to decide which LDEF impacts were caused by micrometeoroids and which ones by man-made debris. The situation is fairly simple for the extended impacts from the leading edge. Eight of these impacts show only Al enhancements and one shows Ti with minor Al and all can therefore be attributed to man-made debris with high confidence. Two impacts do not contain any clear enhancements and are thus unidentified.

The identification of the origin of trailing edge impacts is more difficult. One of them does not show any noticeable element enhancements and its origin is unidentified. Two impacts have enhancements in Fe only without any accompanying enhancements in Cr and Ni. They therefore cannot be caused by stainless steel debris particles. It is not unlikely that the projectiles are FeS particles. Such particles have been found in the stratospheric dust collection (ref. 7) and unmelted FeS fragments have been identified in LDEF craters (ref. 8). Since S is much more sensitive when measured as a negative secondary ion we do not have any S analysis yet on these two impacts but for the time being tentatively classify them as being of cosmic origin.

There are another four trailing edge impacts for which Fe is the dominant element (always discounting Si for which, as already discussed, no reliable measurements are possible because of its

extremely high contamination level). In one case the Fe is associated with Al, which makes man-made debris the most likely source for this particular impact. Although in the other three impacts Fe is very high, Mg enhancements are also clearly present. The Fe/Mg ratios are 24.8, 25.7, and 45.2, respectively. With some elemental fractionation during impact, the true Fe/Mg ratios of the projectiles are probably even higher. Although all three particles could have consisted mostly of FeS with some chondritic material attached, we cannot exclude a debris origin (Cr is low, however). The same is true for another two trailing edge impacts in which Al and Ca are dominated by contamination on the Ge plate and in which Fe/Mg is high.

The remaining 49 trailing edge impacts have their elemental ratios Al/Mg, Ca/Mg, Ti/Mg and Fe/Mg plotted in Fig. 12. Also plotted are the same ratios for interplanetary dust particles collected in the stratosphere and for chondrites. The arrows indicate the directions of elemental mass fractionation during hypervelocity

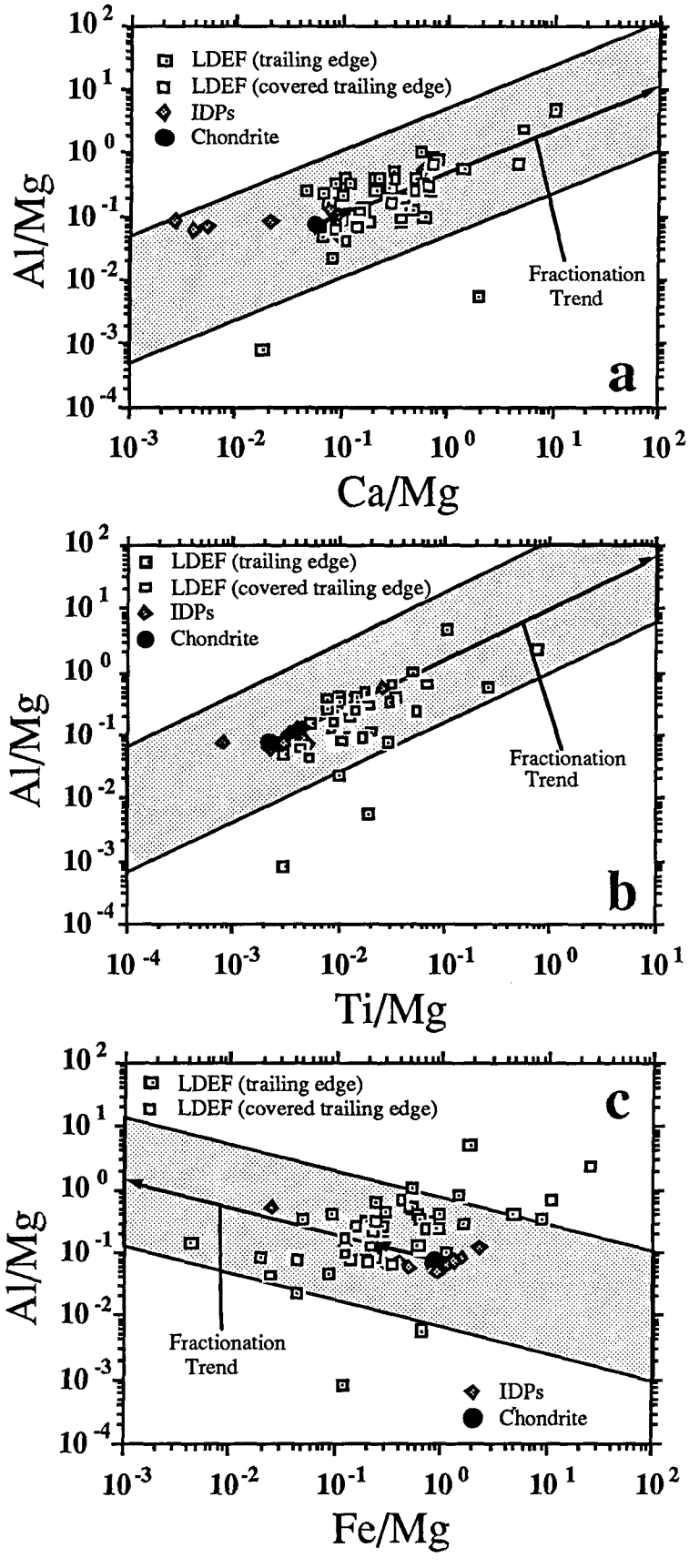


Fig. 12. Elemental ratios measured in the ion microprobe for trailing edge extended impacts. The arrows indicate elemental fractionation trends determined from laboratory simulation experiments. As discussed in the text, impacts whose compositions lie in the shaded regions are classified as "probably natural" and those outside as "possibly orbital debris." In striking contrast to the results for the leading edge cells, it appears that the majority of trailing edge impacts are produced by cosmic dust particles.

impacts determined in laboratory simulation experiments. The Al/Mg, Ca/Mg and Ti/Mg ratios of most trailing edge impacts actually deviate from the chondritic composition in the expected directions but, as already mentioned, the deviations are much larger than the fractionation seen in the laboratory experiments. We consider such large fractionations to be the likely result of the higher velocities of the LDEF impacts. As a working criterion for distinguishing between cosmic dust and man-made debris, we classify impacts that plot inside a region bounded by lines a factor of 10 above and below the fractionation trend extrapolated from laboratory experiments as being of likely interplanetary dust origin. Impacts that plot outside this region are classified as being of possibly man-made debris origin. In Figs. 12a and 12b all impacts except two plot inside of the region while in Fig. 12c, 7 plot outside.

A tentative classification of all impacts analyzed by SIMS is thus as follows (Table 2): nine of 11 leading edge impacts are of man-made origin, the origin of two impacts without projectile material cannot be identified. In contrast, 45 of 58 impacts on the trailing edge are of probably natural origin, two of them probably from FeS particles, 43 from particles with compositions similar to those of chondrites, whereas 12 impacts are possibly caused by man-made debris. It should be pointed out, however, that the identification of man-made debris is much more certain for the leading edge impacts than those from the trailing edge. The former have compositions (only Al, Ti) that are expected for debris while the debris classification for the trailing edge is mostly by default; only one impact (mostly Fe and Al) can reasonably be associated with an expected terrestrial composition and there are no impacts with Al only on the trailing edge. Thus, most of those classified as possibly man-made debris may, in fact, be cosmic particles.

Table 2. Identification of Projectile Material

	Leading edge			Trailing edge		
	Micro-meteoroids	Debris	Unid.	Micro-meteoroids	Debris	Unid.
No enhancements	-	-	2	-	-	1
Enhancement in single element	-	8 (Al)	-	2 (Fe)	-	-
Enhancement in several elements	-	1 (Ti)	-	43	12 (poss.)	-
Total	0	9	2	45	12 (poss.)	1

SUMMARY AND CONCLUSIONS

1. The basic capture cell design worked successfully. As long as the entrance foils stayed in place projectile particles produced "extended impacts" that could be successfully analyzed by ion probe mass spectrometry.

2. All of the entrance foils on the leading edge and 90% of those on the trailing edge failed during flight. However, the statistics of single craters and extended impacts show that many foils on both edges lasted for a considerable period. Thus, analysis of "extended impacts" on both the leading and trailing edges was possible.

3. Analysis of leading edge impacts shows that at least 9 of 11 impacts studied are produced by man-made debris (the remaining two did not yield any elemental enhancements due to projectile material).

4. In contrast, the analysis of the impacts on the trailing edge area shows that 45 out of 58 are of probably natural origin. The identification of the remainder is uncertain but they are possibly due to orbital debris. However, no unambiguous example of a space debris impact was found on the trailing edge.

5. Most extended impacts have compositions that differ markedly from those measured for IDPs collected in the stratosphere. The differences are consistent with volatile/refractory element fractionation affecting particles with cosmic compositions. This effect had previously been seen by us in simulation experiments of hypervelocity impacts, but is more pronounced in the LDEF data, probably due to the high velocities of the impactors. Elemental fractionation in the impact process itself represents the largest single impediment to accurate measurements of projectile chemistry.

6. Contamination of initially clean Ge surfaces during exposure in space was also found to be a significant effect limiting the ability to make accurate measurements of projectile chemistry. The source of the Si seems to be outgassing from RTV, but other sources, contributing elements such as Mg and Al, are still unknown.

7. Because leading and trailing edge entrance foils failed at comparable rates, the major causative failure factors must be similar. While atomic oxygen erosion contributed to a somewhat higher failure rate on leading edge cells, it cannot be the major cause of failure. We suspect that UV embrittlement coupled with thermal cycling is responsible for most of the foil degradation.

8. Future work will concentrate on the analysis of more leading edge impacts and the development of new techniques for measuring elemental abundances in extended impacts.

REFERENCES

1. Amari, S.; Foote, J.; Simon, C.; Swan, P.; Walker, R.; Zinner, E.; Jessberger, E. K.; Lange, G.; and Stadermann, F. J.: SIMS chemical analysis of extended impact features from the trailing edge portion of LDEF experiment AO187-2. LDEF - 69 Months in Space, NASA CP-3134, part 1; 1991, pp. 503-516.

2. Zook, H. A.: Asteroidal versus cometary meteoroid impacts on the Long Duration Exposure Facility (LDEF). Second LDEF Post-Retrieval Symposium, NASA CP-3194, 1993.

3. Mulholland, J. D.; Simon, C. G.; Cooke, W. J.; Oliver, J. P.; and Misra, V.: Long-term particle flux variability indicated by comparison of interplanetary dust experiment (IDE) timed impacts for LDEF's first year in orbit with impact data for the entire 5.75-year orbital lifetime. Second LDEF Post-Retrieval Symposium, NASA CP-3194, 1993.

4. Stadermann, F.: Rare earth and trace element abundances in individual IDPs. Lunar Planet. Sci. XXII, 1991, pp. 1311-1312.

5. Stadermann, F.: Messung von Isotopen- und Elementhäufigkeiten in einzelnen interplanetaren Staubteilchen mittels Sekundärionen-Massenspektrometrie. Ph.D. Thesis, University of Heidelberg, Germany, 1990.

6. Lange, G.: Quantitative Multielementanalyse von Einschlagsrückständen auf LDEF-Staubdetektoren. Ph.D. Thesis, University of Heidelberg, Germany, 1986.

7. Brownlee, D. E.; Tomandl, D. A.; and Olszewski, E.: Interplanetary dust; a new source of extraterrestrial material for laboratory studies. Proc. 13th Lunar Planet. Sci. Conf., 1977, pp. 149-160.

8. Brownlee, D. E.; Hörz, F.; and Bradley, J.: Interplanetary meteoroid debris in LDEF metal craters. Second LDEF Post-Retrieval Symposium, NASA CP-3194, 1993.

CRATERING IN GLASSES IMPACTED BY DEBRIS OR MICROMETEORITES

David E. Wiedlocher and Donald L. Kinser
Department of Materials Science and Engineering
Vanderbilt University
Nashville, TN 37235

ABSTRACT

Mechanical strength measurements on five glasses and one glass-ceramic exposed on LDEF revealed no damage exceeding experimental limits of error. The measurement technique subjected less than 5% of the sample surface area to stresses above 90% of the failure strength. Seven micrometeorite or space debris impacts occurred at locations which were not in that portion of the sample subjected to greater than 90% of the applied stress. In consequence of this the impact events on the sample were not detected in the mechanical strength measurements. The physical form and structure of the impact sites has been carefully examined to determine the influence of those events upon stress concentration associated with the impact and the resulting mechanical strength. The size of the impact site insofar as it determines flaw size for fracture purposes was examined. Surface topography of the impacts reveals that six of the seven sites display impact melting. The classical melt crater structure is surrounded by a zone of fractured glass. Residual stresses arising from shock compression and from cooling of the fused zone cannot be included in fracture mechanics analyses based on simple flaw size measurements. Strategies for refining estimates of mechanical strength degradation by impact events are presented.

INTRODUCTION

Damage of glass in space systems by space debris and micrometeorites is of interest due to the susceptibility of glass to catastrophic fracture under impact load. The Gemini window impact[1] and simulated meteoroid[2] impact failures in orbiter windows indicate possible catastrophic effects of impact events in space. Lunar soil samples[3] collected during the Apollo 11 mission reveal micrometeorite impacts in glass spheres formed from the ejecta of larger meteorite impacts. Impacts in such glasses exhibit central melt regions surrounded by fracture zones and spall areas. These features are characteristic of many of the impacts observed on LDEF glasses. The influence of debris or micrometeorite impacts on mechanical properties of glass determine, in part, their sensitivity to the space environment.

Physical properties of six LDEF glass types listed in Table 1 were found to be unchanged by the 5.8 year exposure to low Earth-orbit[4]. The strength of exposed glasses is statistically indistinguishable from control samples as shown in Table 1. Mechanical damage to these samples included 7 impacts in the glass and glass-ceramic. The impacts had no effect on the strength reported by Wiedlocher et al[4] due to the mechanical testing technique.

Clearly damage from the impact event will reduce the stress to induce fracture but the testing conducted did not characterize the resulting strength loss. Fracture mechanics provides a qualitative estimate of the damage induced by micrometeorite and space debris impacts.

EXPERIMENTAL PROCEDURE

The shape and size of micrometeorite and space debris damaged areas were characterized using scanning electron microscopy and stereo techniques. Fragments from the mechanical testing[4] which contained micrometeorite or space debris impacts were gold coated and examined in an Hitachi X-650 scanning electron microscope (SEM) with ultimate resolution of approximately 5.0 nm. Stereomicrographs of each crater were taken at several magnifications and examined in stereo.

Mechanical testing of glasses impacted by micrometeorites was performed using a diametral flexure test (ASTM 394-74T) as described in reference 4. The test subjects a centrally loaded disk, supported at three points, to dynamic loading in a controlled environment. This method of testing eliminates effects of flaws on the periphery of the sample.

RESULTS

Four impacts occurred in glass samples and three occurred in glass-ceramic samples located on the trailing-edge of the satellite. Scanning electron microscopy revealed 6 of the 7 impacts contained a central crater lined with melted glass as illustrated by one of the three impacts in Zerodur shown in Figure 1. The central pit is surrounded by a zone of fragmented material with numerous radial cracks extending into the sample. The annular region adjacent to the melt zone is missing numerous fragments which spalled and were generally lost. Remnants of debris, presumed to originate from the fragmented area, were captured in the melt zone in this sample and several others. The region away from the impact site also displays damage from grit blasting with silicon carbide which was part of the sample preparation previously described[4].

Damage surrounding the impacts extends to a radius about 5 times the central pit radius as seen in the micrograph of an impact site in Pyrex shown in Figure 2. Pre-flight sample preparation damage, not due to micrometeorite or space debris impact, is also apparent in this micrograph. Bubbles escaping the melt region of a BK-7[a] sample shown in Figure 3 indicate temperatures and pressures at impact reached those needed for vaporization of the micrometeorite and/or glass. Evidence of vaporization was observed in BK-7 and soda-lime-

[a]The BK-7 glass and Zerodur glass ceramic manufactured by Schott Glass Company are identified only for reference purposes and no product endorsement is intended.

silica[b] glasses which contain volatile components. Impact features in fused silica include glass fibers which extend from the melt crater as a consequence of molten glass jetting as shown in Figure 4. Fibers as long as 100 μm were observed projecting from the fused zone. One of the three impacts observed in Zerodur[a] shows no evidence of melting as shown in Figure 5. Careful study of this sample at higher magnifications reveals fragmentation down to dimensions of the order of 0.5 μm. The damage associated with this impact is similar to that of impacts displaying melting except in the central fusion zone. Radially unsymmetric splash in the ejecta field of the Pyrex[c] sample visible in Figure 6 indicates the micrometeorite may have impacted at an oblique angle. The crater appears to be nearly circular; however, the splash produced by the impact is strongly directional.

Mechanical stresses imposed on the tensile surface of the sample during mechanical testing are symmetric with respect to the loading points of the fixture as shown in Figure 7. Impacts not occurring in the geometrical center of the sample are subjected to stresses less than the maximum applied stress. No micrometeorite or space debris impacts occurred in the geometrical center of the samples and no fracture was observed to initiate from surface flaws associated with micrometeorite or space debris impacts. Strengths of the samples given in Table 1 include the percentage of maximum stress at the impact site determined from its location in the stress field.

DISCUSSION

One of the important questions of this work was the mass and velocity of the particles which produced the impact damage. The lower limit of velocity of particles impacting samples located on the trailing edge must be the 8 km/s orbital velocity of the satellite. The *relative* velocity required to produce the fusion zones observed in 6 of 7 cases must have been of the order of 10 km/sec based upon hyper-velocity impact tests[5] which suggest a lower limit exists at which melting occurs in glass. Particle impacts resulting in melting generally require speeds on the order of 10 km/s although melted material has been reported at velocities as low as 6 km/s[6]. The mean impact velocities of micrometeorites and space debris impacting LDEF on row 2 has been calculated by Zook to be approximately 13 km/s[7]. We thus argue that melting in impacted glasses on the trailing edge indicates the impacts occurred with particle velocities on the order of 10 km/sec or greater. The remaining impact occurred from a particle with a velocity less than 10 km/s.

During impact ejecta with the highest velocity are generated closest to the central pit. According to the model after Melosh[5] a particle impacting at a velocity of 13 km/s produces ejecta with velocities up to 5 km/s. Presuming fibers were produced by the highest velocity

---

[b]The soda-lime-silica glass manufactured by American Saint Gobain is identified only for reference purposes and no product endorsement is intended.

[c]The Pyrex glass manufactured by Corning Glass Works is identified only for reference purposes and no product endorsement is intended.

ejecta, the time to pull fibers 100 microns in length was about 2 X 10^{-8} seconds.

The bubbles observed in surfaces of BK-7 and soda-lime-silica glasses clearly indicate that these samples suffered pressure/temperature conditions in which boiling occurred. These phenomena may be a consequence of the energy delivery to these samples being higher than other samples or may be a consequence of the relative volatility of these two glasses. These two glasses are clearly the most volatile of those glasses examined in that they include relatively low boiling components unlike the Pyrex or fused silica glasses which did not display evidence of bubble evolution.

The highest stress at an impact site was 50% of the stress to produce failure, thus we argue that the effect of micrometeorite or space debris impacts reduced the glass strength by less than 50% for the impacts experienced in these experiments. Apart from the crater visible on the surface, damage to glass extends beneath the flaw a distance depending on propagation of the radial cracks. Though a micrometeorite impact may not penetrate the glass, the resulting defect lowers the maximum stress the glass is capable of sustaining before fracture. Stress concentration developed by the presence of a surface impact degrades the strength with a square root dependence on flaw size. Fracture mechanics[8] permit calculation of strength from flaw size and fracture toughness parameters:

$$K_{IC} = 1.12\sigma\sqrt{\pi\alpha}$$

where 1.12 is the free surface correction factor, σ is failure strength, and α is the flaw size. K_{IC} for Zerodur is .9 $MPam^{1/2}$.[9] Using a strength of 129 MPa from Table 1, the mean flaw size at the initiation site for the glass-ceramic is of the order of 10 μm. Assuming the damage field from a micrometeorite or space debris impact is hemispherical, the influence of impact damage penetrating to a depth of 100 μm (2α = D) decreases the strength to 35% of the measured value. Based on these arguments failure of the Zerodur sample should have initiated at the impact site with an applied load at the geometric center of the sample of less than 100 MPa. This suggests the extent of damage below the impact is actually no greater than 1/4 the radius of the crater observed on the surface, thus a hemispherical damage zone surrounding the impact site is improbable. This agrees with geological cratering observations which have determined the penetration depth to diameter ratio of meteorite impacts in the Earth's strata to be about 1/3 to 1/4. Deviations of the depth/diameter ratio from 1/3 arise from changing physical properties of the projectile and target.

Cratering mechanics[5] indicate that typical projectile diameters are 1/3 the central pit diameter which gives a projectile size between 15 μm and 30 μm for most impacts observed here. Some ambiguity in crater dimension measurement occurs with our measurements. The literature often discusses impacts in soils or metals and the diameter measured at the lip of the uplifted zone is commonly used. In our case the central melt crater whose dimensions are easily characterized and the extrema of the radial cracks could easily be measured but no uplifted zone has been identified, hence the use of the term "crater diameter" is potentially ambiguous when applied to our work.

Crater shape is relatively independent[5] of impact angle for impacts at angles greater than

10° from the surface plane of the target. Projectile shape largely determines crater shape, even for normal impact. Impact features believed to arise from meteorites incident at angles between 20° and 45° have been observed in lunar craters[5]. The unsymmetric glass ejecta or debris field associated with the impact in the Pyrex sample is evidence that impact occurred at an oblique angle. As previously discussed, the formation of frozen strands of glass develops in the early stages of impact. This would account for the extension of filaments in the direction of impact before excavation of the crater was complete. Also, radial cracks extending from the impact extrapolate to an origin off center of the excavation in the direction of the splash. These observations indicate the projectile velocity had a large component in the direction of the debris field.

CONCLUSIONS

1. Six of the seven impact events on glass and glass ceramic samples exposed on LDEF produced melting or vaporization in craters which are similar to those produced by laboratory impacts at velocities above 10 km/s.

2. Glass fibers produced during impact by jetting of molten material have been observed with lengths up to approximately 100 μm. Presuming that these fibers were produced from ejecta with maximum velocity, the fibers were produced in about 2×10^{-8} second.

3. The impact observed in Pyrex may have occurred at an oblique angle.

4. The damage field associated with the 7 impact features cannot be treated as hemispherical. Flaw size determined from the depth of penetration scales similar to geological depth to diameter ratios. This depth is on the order of 1/5 the crater diameter. Based on this flaw size the mechanical strength after the impact event is approximately 1/2 of the original.

ACKNOWLEDGEMENTS

The authors gratefully acknowledge financial support of NASA through grants NAS-8-156 and NAS-8-32695 and contract L-17761D.

Table 1
Mechanical Strength and Impact Site Damage Size

Sample	Strength (MPa)	Standard Deviation (MPa)	Strength Control (MPa)	Standard Deviation (MPa)	Stress Contour (% Max)	Central Melt Pit Diameter μm	Crater Diameter μm	Spall Surface Diameter μm
BK-7	126	8	124	8	10	40	100	200
Fused Silica	97	4	97	4	38	50	120	250
Soda-lime-silica	104	4	100	9	35	80	175	475
Pyrex	105	7	111	4	10	85	200	400
Vycor	101	5	103	4	NI[d]	NI	NI	NI
Zerodur (I)[e]	129	8	128	5	30	NM[f]	100	275
Zerodur (II)	129	8	128	5	50	75	200	400
Zerodur (III)	129	8	128	5	25	50	150	300

[d]NI indicates no impact on this type sample.

[e]The mechanical strength reported is the average of a group of 9 samples while impacts were measured on three individual samples.

[f]No melt zone observed.

REFERENCES

1. J. B. Singletary and J. B. Rittenhouse, "Spacecraft Materials Experience," *Space Materials Handbook*, 3rd ed., NASA SP-3051, 1969.

2. J. W. Gehring, Jr., "Engineering Considerations in Hyper-velocity Impact," Chapter IX in *High-Velocity Impact Phenomena*, edited by R. Kinslow Academic Press, NY, 1970.

3. C. Frondel, C. Klein, J. Ito and J. C. Drake, "Mineralogical and Chemical Studies of Apollo 11 Lunar Fines and Selected Rocks," *Proceedings of the Apollo 11 Lunar Science Conference*, Vol. 1, Pergamon Press, New York, 445-474, 1970.

4. D. E. Wiedlocher, D. L. Kinser, D. S. Tucker and R. Nichols, "Low Earth-Orbit Effects on Strength of Glasses," *J. Am. Cer. Soc.*, Vol. 75, Nov. 1992.

5. H. J. Melosh, *Impact Cratering: A Geological Process*, Oxford Monographs on Geology and Geophysics No. 11, Oxford University Press, New York, 1989.

6. D. E. Gault, cited by H. J. Melosh, ibid.

7. H. A. Zook, "Meteoroid Directionality on LDEF and Asteroidal versus Cometary Sources," *Lunar Planet. Sci. XXII*, 1577-1578, 1991.

8. S. W. Freiman, "Fracture Mechanics of Glass," *Glass: Science and Technology*, Vol. 5, *Elasticity and Strength in Glasses*, ed. by D. R. Uhlmann and N. J. Kreidl, Academic Press, New York, 1980.

9. M. J. Viens, "Fracture Toughness and Crack Growth of Zerodur," NASA Technical Memorandum 4185, NASA Scientific and Technical Information Division, 1990.

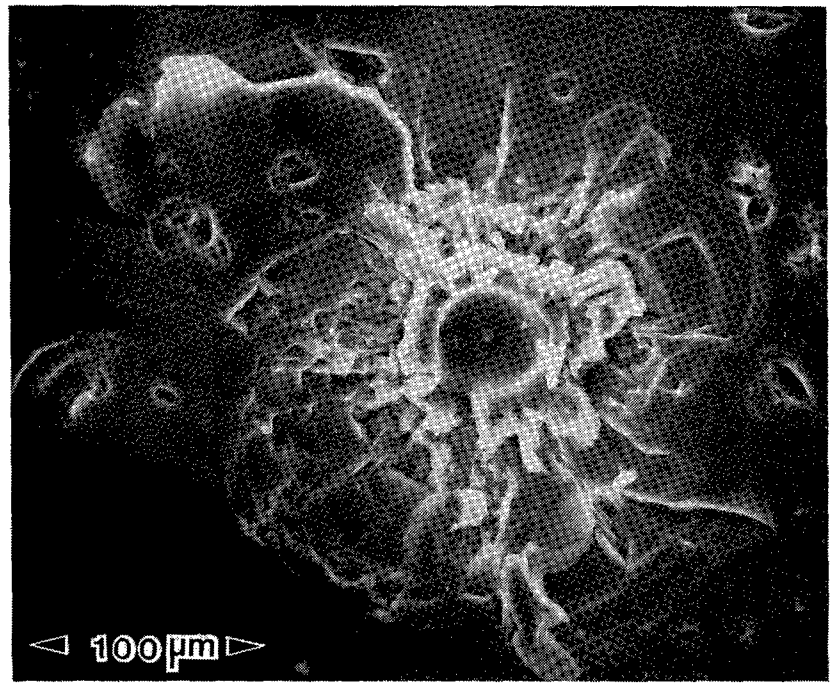


Figure 1: Scanning electron micrograph of impact in Zerodur displaying melt crater formation.

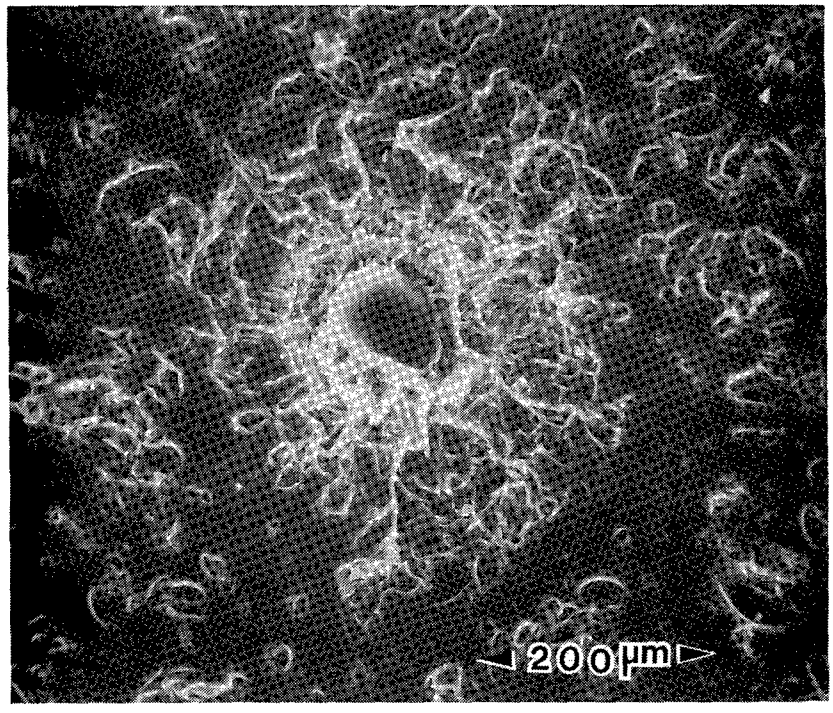


Figure 2: Scanning electron micrograph of impact crater in Pyrex displaying impact melting.

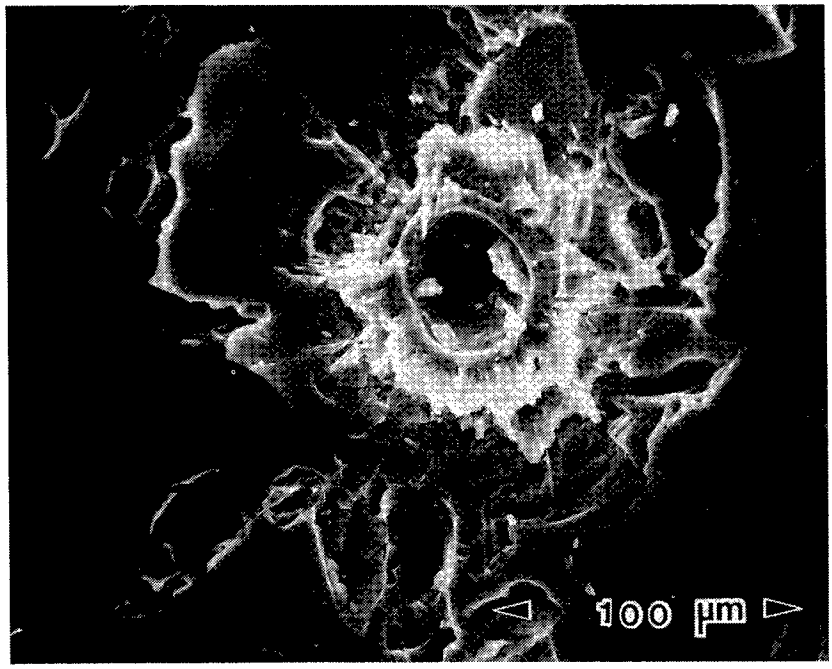


Figure 3: Scanning electron micrograph of impact crater in BK-7 glass displaying melt zone and trapped bubbles.

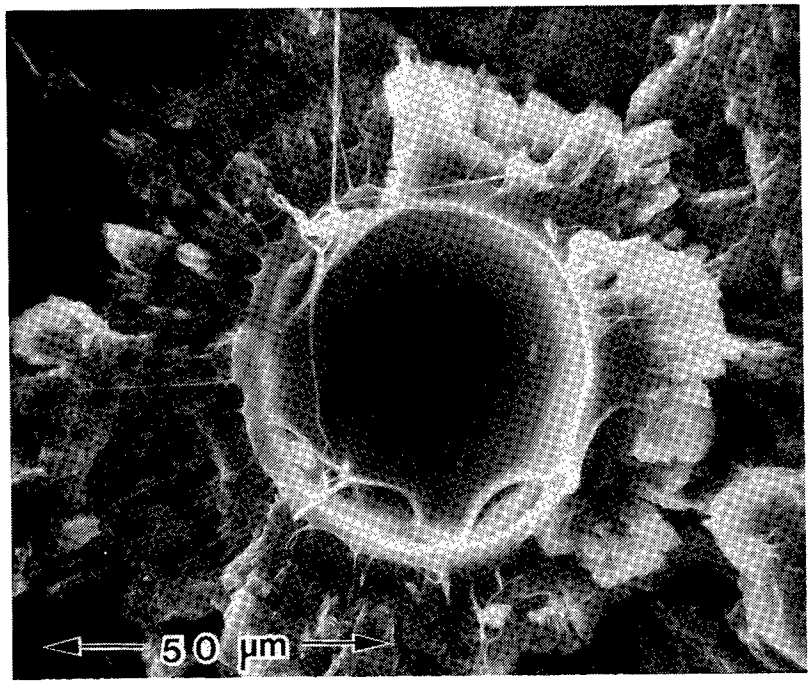


Figure 4: Scanning electron micrograph of impact crater in fused silica glass displaying jetting of molten glass and resulting glass fibers extending from melt crater.

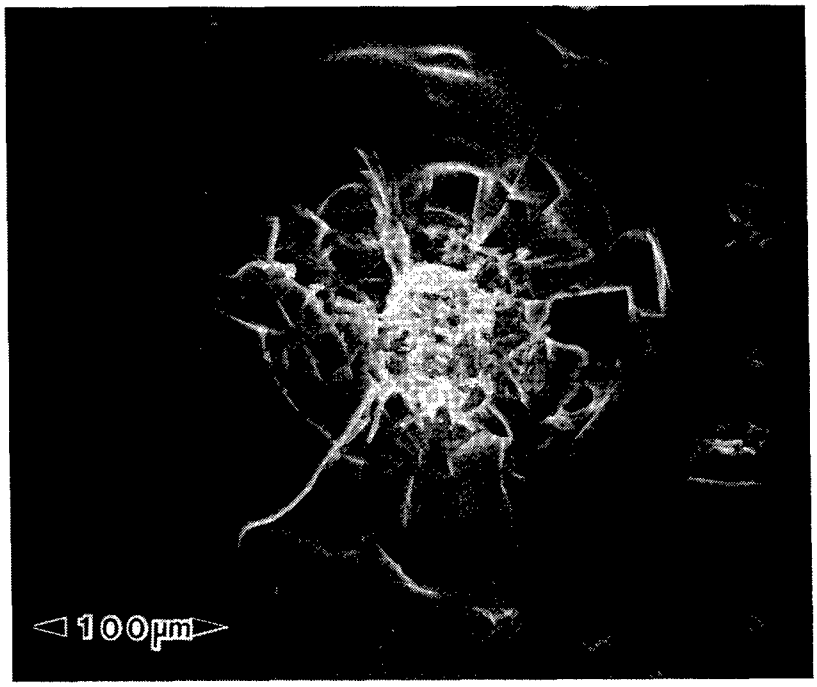


Figure 5: Scanning electron micrograph of impact site in Zerodur which displays no evidence of impact fusion.

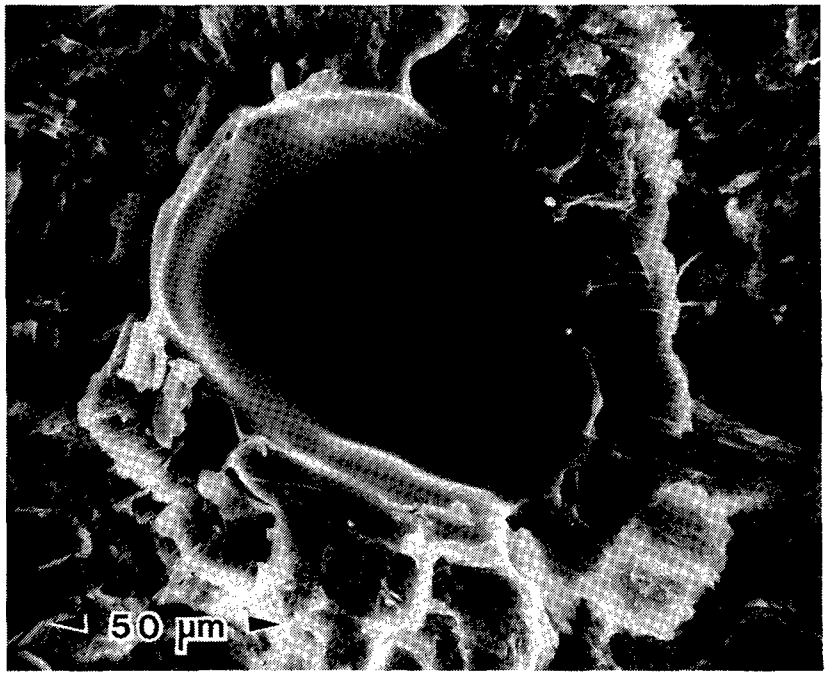


Figure 6: Scanning electron micrograph of impact crater in Pyrex displaying unsymmetric splash of ejecta possibly arising from oblique impact.

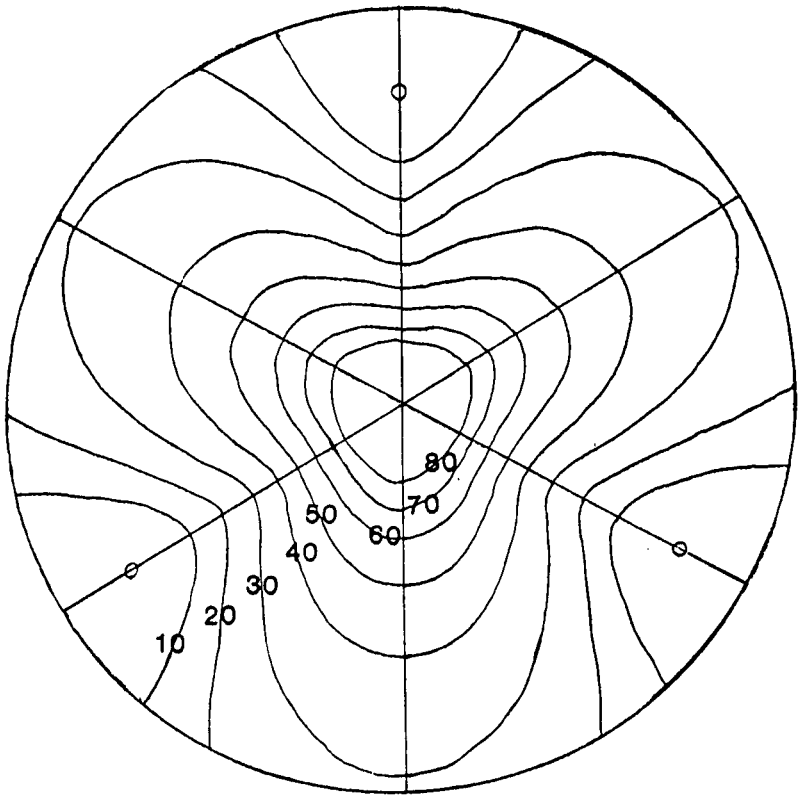


Figure 7: Stress contour diagram for mechanical testing employing three point support with central load.

SCANNING ELECTRON MICROSCOPE/ENERGY DISPERSIVE X-RAY ANALYSIS OF IMPACT RESIDUES IN LDEF TRAY CLAMPS

Ronald P. Bernhard
Lockheed ESC
NASA/JSC
Houston, TX 77058

Christian Durin
CNES - Toulouse FRANCE
Fax n 33.61.27.47.32

Michael E. Zolensky
SN2, NASA Johnson Space Center
Houston, TX 77058

SUMMARY

Detailed optical scanning of tray clamps is being conducted in the Facility for the Optical Inspection of Large Surfaces at the Johnson Space Center to locate and document impacts as small as 40 microns in diameter. Residues from selected impacts are then being characterized by Scanning Electron Microscopy/Energy Dispersive X-ray Analysis at CNES. Results from this analysis will be the initial step to classifying projectile residues into specific sources.

INTRODUCTION

To better understand the nature of particulates in low-Earth orbit (LEO), and their effects on spacecraft hardware, we are analyzing residues found in impact features on Long Duration Exposure Facility (LDEF) tray clamps. Detailed optical scanning of the tray clamps provided to the Meteoroid and Debris Special Investigation Group (M&D SIG) is being conducted in the Facility for the Optical Inspection of Large Surfaces (FOILS) at the Johnson Space Center (JSC) to locate and document impacts as small as 40 microns in diameter, starting with Bay A and working toward Bay H. To date, scanning of the Bay A clamps has been completed.

These impacts are then inspected by Scanning Electron Microscopy/Energy Dispersive X-ray analysis (SEM/EDX) to select those features which contain appreciable impact residue material. Based upon the composition of projectile remnants, and using criteria developed at JSC (ref 1), we have made a preliminary discrimination between micrometeoroid and space debris residue-containing impact features. Based upon these

analyses, we forwarded 13 impact features containing significant amounts of unmelted and semi-melted micrometeoritic residues to Centre National d'Etudes Spatiales (CNES) in France. At the CNES facilities the upgraded impacts were analyzed using a JEOL T330A SEM equipped with a NORAN Instruments, Voyager X-ray Analyzer. Results from these analyses will be the critical step in classifying projectile residues into specific source groups. This information is critical to construction of flux models for natural vs. man-made particulates in LEO.

LDEF TRAY CLAMPS

LDEF experiment trays were held in place by a series of chromic-anodized aluminum (6061-T6) clamps; eight clamps were used to attach the experiment trays on each of the 12 sides of LDEF, while experiment trays on the Earth and space ends were held in place by 12 clamps. Each clamp was fastened to the spacecraft frame using three stainless steel hex bolts. Clamps exposed an area of approximately $58cm^2$ each (4.8cm X 12.7cm X .45cm, minus the bolt coverage). All 774 clamps were surveyed for impacts greater than 0.5 mm during spacecraft deintegration at the Kennedy Space Center. Some 337 out of 774 LDEF tray clamps have been archived by the M&D SIG in the Curatorial Facility at JSC and are available for scientific examination through the Meteoroid & Debris Special Investigation Group (M&D SIG).

A numbering scheme was devised by the M&D SIG for the clamps which would provide hardware location information with respect to its position within a particular bay (Fig. 1). From the labeling scheme, it can be seen that a clamp occupying position 1 of Bay A02 would be identified by the label A02C01, with A02 indicating the experiment location of Bay "A" and Row "02", and C01 interpreted as "C" for clamp and "01" being the clamp number. Each clamp uses a Cartesian coordinate system to reference impact locations on exposed surfaces. The X and Y coordinates were measured in millimeters in a grid system (positive or negative) from a standard origin assigned by the M&D SIG at the lower-left corner (fig. 1).

RESULTS

Table 1 lists preliminary results for our clamp analyses. For each entry clamp number, impact feature numbers and SEM/EDX determined impact residue constituents are listed.

Table 1 Results of Clamp Analyses

CLAMP NUMBER	IMPACT NUMBER	IMPACT DIAMETER	RESIDUE COMPONENTS
A01 CO1	001	200	Mg, Si, Ca Fe
A01 CO1	002	100	Trace
A01 CO1	003	100	Unknown
A01 CO3	001	120	Contamination
A01 CO3	002	230	Mg, Si, Ca Fe
A01 CO4	001	100	Paint Patch
A01 CO4	002	180	Trace
A01 CO8	001	370	Unknown
A03 CO1	001	150	Mg, Si, Ca Fe
A03 CO3	001	220	Unknown
A04 CO3	001	260	Unknown
A04 CO5	001	210	Contamination
A04 CO5	002	120	Fe, Ni, Cr
A04 CO8	001	160	Unknown
A04 CO8	002	400	Unknown
A05 CO3	001	180	Unknown
A05 CO6	001	250	Si, Ca S, K, Fe
A05 CO6	002	70	Unknown
A05 CO6	003	140	Trace
A05 CO6	004	50	Unknown
A05 CO6	005	90	Unknown
A05 CO7	001	400	Unknown
A05 CO7	002	100	Unknown
A05 CO8	001	180	Contamination
A06 CO6	001	320	Unknown
A07 CO1	001	210	Unknown
A07 CO1	002	120	Si, Ca, Fe
A07 CO1	003	110	Si, Ca, S, Fe
A07 CO1	004	210	Unknown
A07 CO1	005	130	Trace
A07 CO3	001	380	Unknown
A07 CO3	002	260	Contamination
A07 CO3	003	N/A	No Impact
A07 CO3	004	40	Unknown
A07 CO3	005	180	Paint
A07 CO3	006	400	Unknown
A07 CO3	007	40	Contamination
A07 CO6	001	100	Unknown
A07 CO6	002	220	Unknown
A07 CO6	003	200	Si, Ca, Na, Mg, Fe
A07 CO6	004	240	Unknown
A07 CO6	005	100	Fe, Ni, Cr
A07 CO6	006	150	Unknown
A07 CO6	007	300	Trace

CLAMP NUMBER	IMPACT NUMBER	IMPACT DIAMETER	RESIDUE COMPONENTS
A07 CO6	008	150	Unknown
A07 CO8	001	200	Unknown
A07 CO8	002	220	Trace
A07 CO8	003	300	Unknown
A07 CO8	005	260	Si, Ca, K, Fe, S, Mg
A07 CO8	006	140	Si, Mg, Ca, Fe
A08 CO1	001	900	Unknown
A08 CO1	002	130	Si, Mg, Ca, Fe
A08 CO1	003	250	Trace ?
A08 CO1	004	140	Unknown
A08 CO1	005	200	Si, Mg, K
A08 CO1	006	80	Si, Mg, Fe, Ca
A08 CO1	007	100	Unknown
A08 CO1	008	110	Unknown
A08 CO3	001	400	Unknown
A08 CO3	002	140	Paint
A08 CO3	003	80	Unknown
A08 CO3	004	200	Unknown
A08 CO3	005	160	Unknown
A08 CO3	006	150	Unknown
A08 CO3	007	380	Unknown
A08 CO7	001	360	Paint Patch
A08 CO7	002	350	Unknown
A08 CO7	003	270	Paint
A08 CO7	004	470	Unknown
A08 CO7	005	130	Si, Mg, Ca, Fe
A08 CO7	006	60	Unknown
A08 CO7	007	160	Contamination
A08 CO7	008	60	Paint Patch
A08 CO7	009	130	Unknown
A08 CO7	010	170	Unknown
A08 CO7	011	140	Paint Patch
A08 CO7	012	230	Paint Patch
A08 CO7	013	40	Paint Patch
A08 CO7	014	100	Paint Patch
A08 CO8	001	700	Unknown
A08 CO8	002	500	Unknown
A08 CO8	003	500	Trace ?
A08 CO8	004	150	Unknown
A08 CO8	005	200	Unknown
A08 CO8	006	120	Si, Mg, Ca, Fe
A08 CO8	007	190	Unknown
A08 CO8	008	90	Unknown
A08 CO8	009	110	Unknown
A08 CO8	010	100	Paint
A08 CO8	011	400	Unknown
A08 CO8	012	350	Unknown

CLAMP NUMBER	IMPACT NUMBER	IMPACT DIAMETER	RESIDUE COMPONENTS
A08 CO8	013	120	Si, Mg, Ca
A08 C10	001	250	Unknown
A08 C10	002	100	Unknown
A08 C10	003	120	Unknown
E09 C05	001	180	Trace
E09 C05	002	250	Unknown
E09 C05	003	160	Unknown
E09 C05	004	170	Paint
E09 C05	005	280	Unknown
E09 C05	006	330	Unknown
E09 C05	007	240	Unknown
E09 C07	001	75	Fe
E09 C07	002	150	Unknown
E09 C07	003	200	Unknown
E09 C07	004	140	Fe, Ni, Cr, Mn
E09 C07	005	160	Unknown
E09 C07	006	300	Unknown
E09 C07	007	130	Si, Mg, K, Fe S
E09 C07	008	220	Si, Mg, Fe
E09 C07	009	150	Unknown
E10 C01	001	1200	Si, Mg, Fe
E10 C01	002	120	Unknown
E10 C01	003	180	Trace
E10 C01	004	120	Trace ?
E10 C01	005	180	Unknown
F09 C05	001	120	Unknown
F09 C05	002	270	Unknown
F09 C05	003	70	Paint
F09 C05	004	380	Unknown
F09 C05	005	240	Unknown
F09 C05	006	190	Unknown
F09 C07	001	280	Unknown
F09 C07	002	280	Unknown
F09 C07	003	200	Unknown
F09 C07	004	150	Trace
F09 C07	005	100	Unknown
F09 C07	006	70	Unknown
F09 C07	007	210	Contamination
F09 C07	008	120	Unknown
F10 C05	001	100	Unknown
F10 C05	002	140	Paint
F10 C05	003	270	Unknown
F10 C05	004	90	Unknown
F10 C05	005	460	Unknown
F10 C05	006	100	Unknown
F10 C05	007	90	Unknown
F10 C05	008	100	Unknown

Because the initial intent of this survey was to identify only those impacts which contained large amounts of micrometeoritic residue, a minimal amount of time was spent analyzing for small or not obvious projectile remnants. The spectra are qualitative and can establish a basic classification of either "natural" or "man-made", although many of the impacts are classified as having no detected origin. We believe that further, more detailed, analyses would undoubtedly uncover evidence of impactor residues in many of the latter craters. A factor hindering our analyses is the fact that the clamps have all been anodized, which deposited a surface layer of Si, Mg, and S, all of which are important elements. This contamination has been properly considered as background, but in many instances its presence makes characterization of the residues extremely difficult. A breakdown of analyzed clamp-impact residues into categories of "natural", "man made", "unknown" and "contaminated" is illustrated in Fig.2. These data are only preliminary, and await confirmation by the more detailed EDX analyses being performed at CNES; these latter results will be reported at a later date.

Documentation of these clamps will be presented in catalog form at a later date. In these catalogs each clamp impact feature will be documented with scanning electron micrographs and EDX spectra, as shown in Figs. 3-6.

REFERENCE

1 Zolensky M.E., Zook H., Atkinson D., Coombs C., Dardano C., See T., Simon C. and Kinard W. (1992) Interim report of the Meteoroid and Debris Special Investigation Group. This volume.

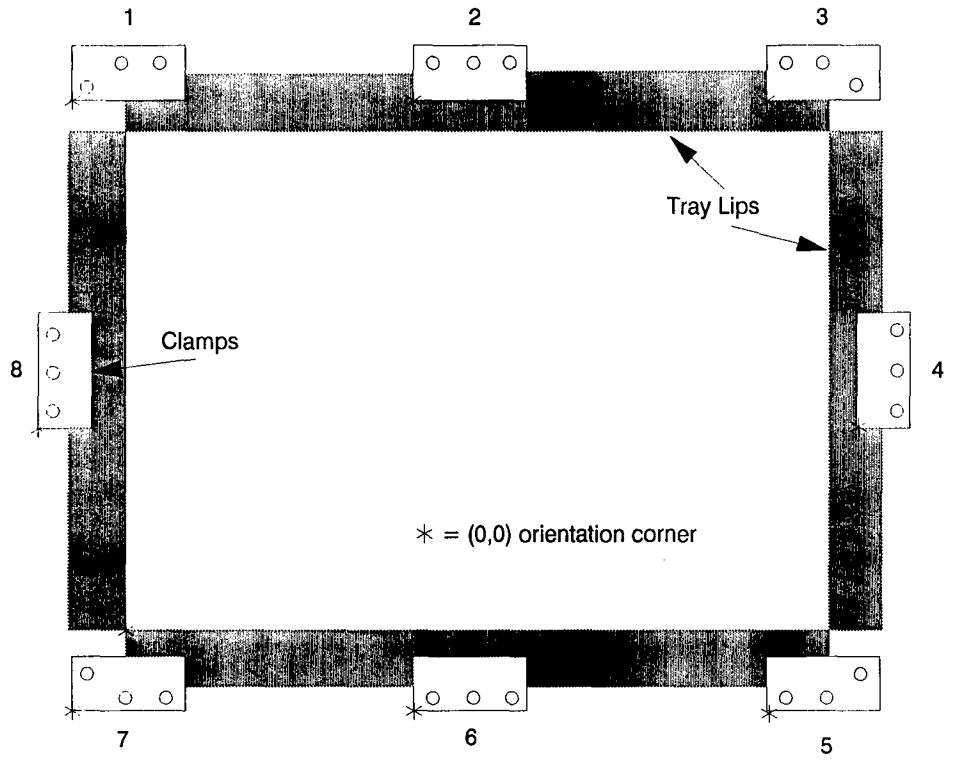


Figure 1. Disposition of tray clamps around experiment trays in Bays A-F. Circles indicate bolt holes; asterisks indicate the registration origin point for each clamp.

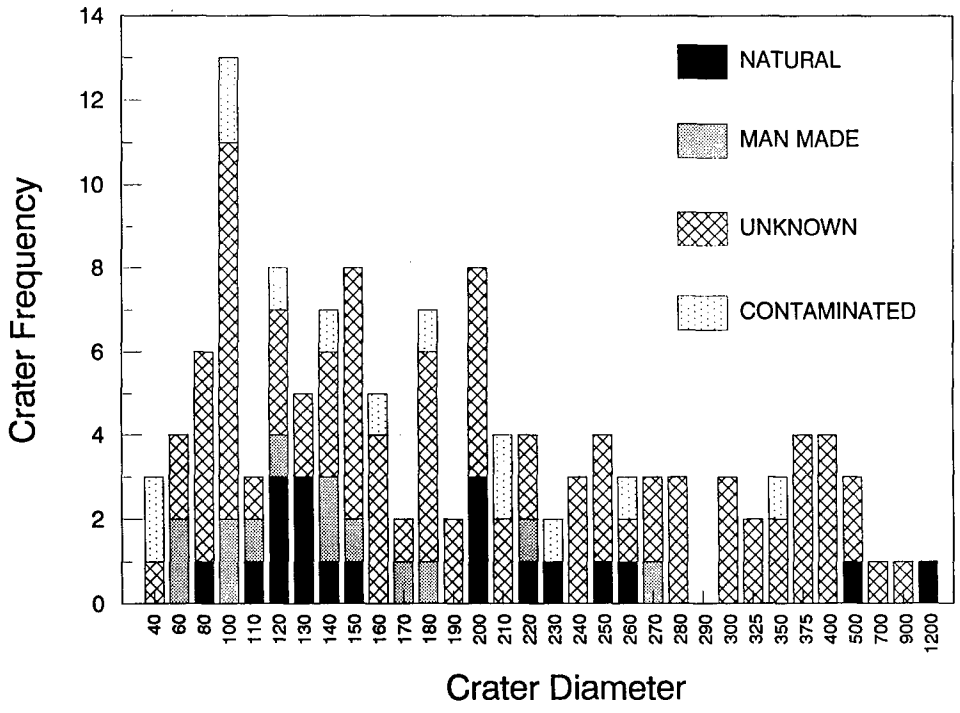


Figure 2. A breakdown of analyzed clamp-impact residues into categories of "natural," "man made," "unknown" and "contaminated."

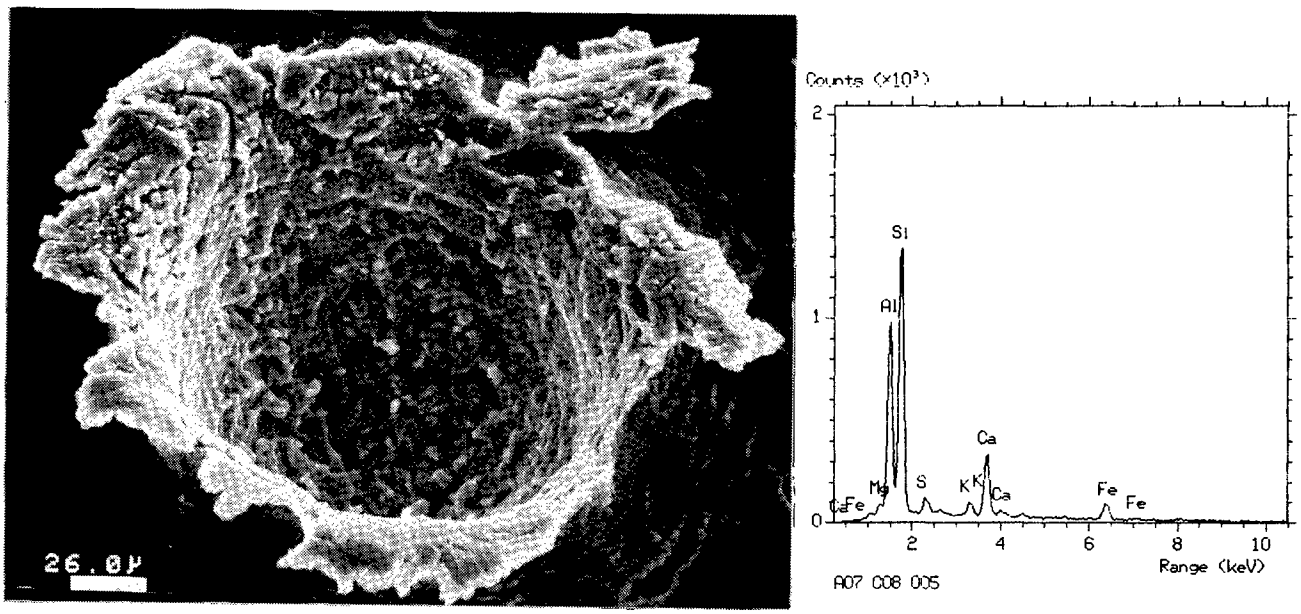


Figure 3. Impact crater into clamp number eight of Bay A07. The large amounts of micrometeoritic residue in the bottom and on the walls of the crater are rare for most features found on LDEF surfaces. The X-ray spectra displays a micrometeoritic composition associated with this projectile residue.

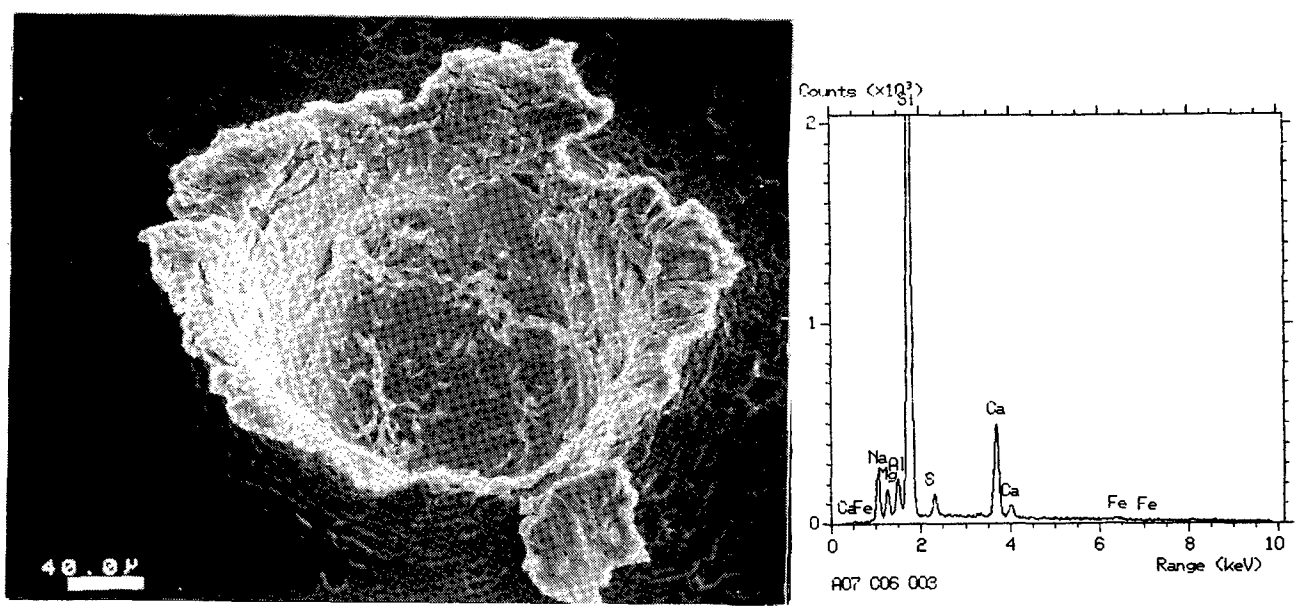


Figure 4. The morphology of the interior of this impact shows a lining of projectile residues present. Although the crater has typical depth to diameter ratios the amount of projectile preserved after shock is relatively high. A general X-ray spectra taken from a small grain within the crater illustrates the components which exist.

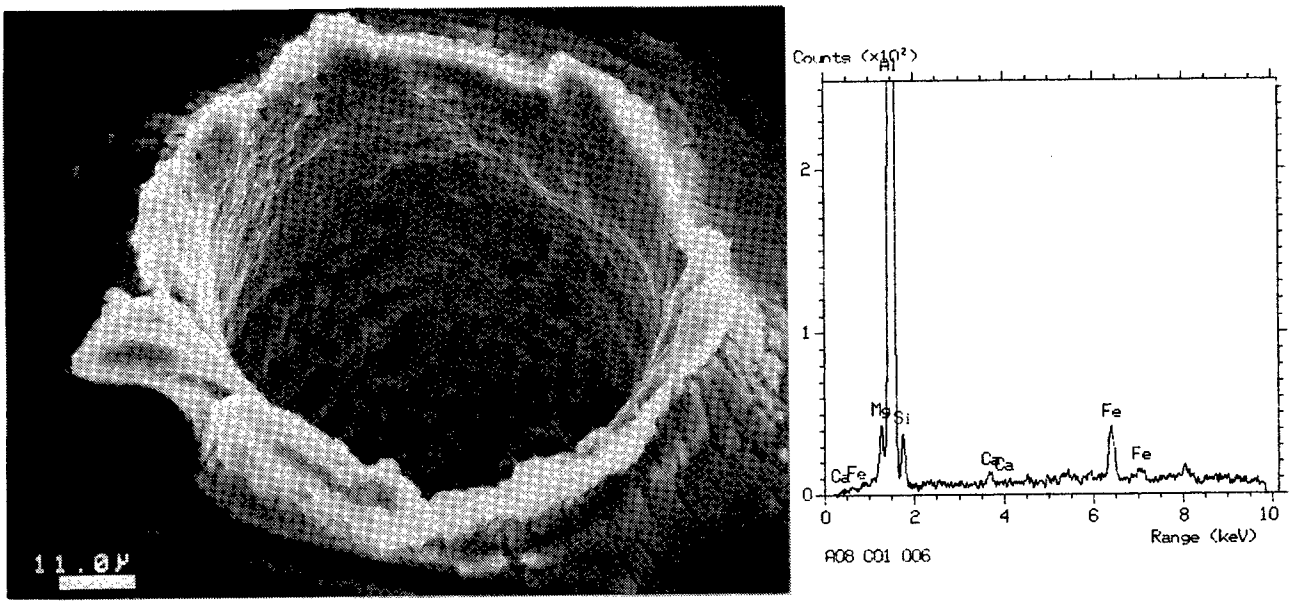


Figure 5. Closer to the leading edge of LDEF, clamp number one of tray A08 has an unusually deep morphology as seen in this oblique view. The walls and bottom to the impact feature are completely coated with micrometeoritic residues. The X-ray spectra retains large amounts of the clamp target material. The anodized layer of the aluminum clamp is very evident when shown as radial cracking around the parameter of the crater.

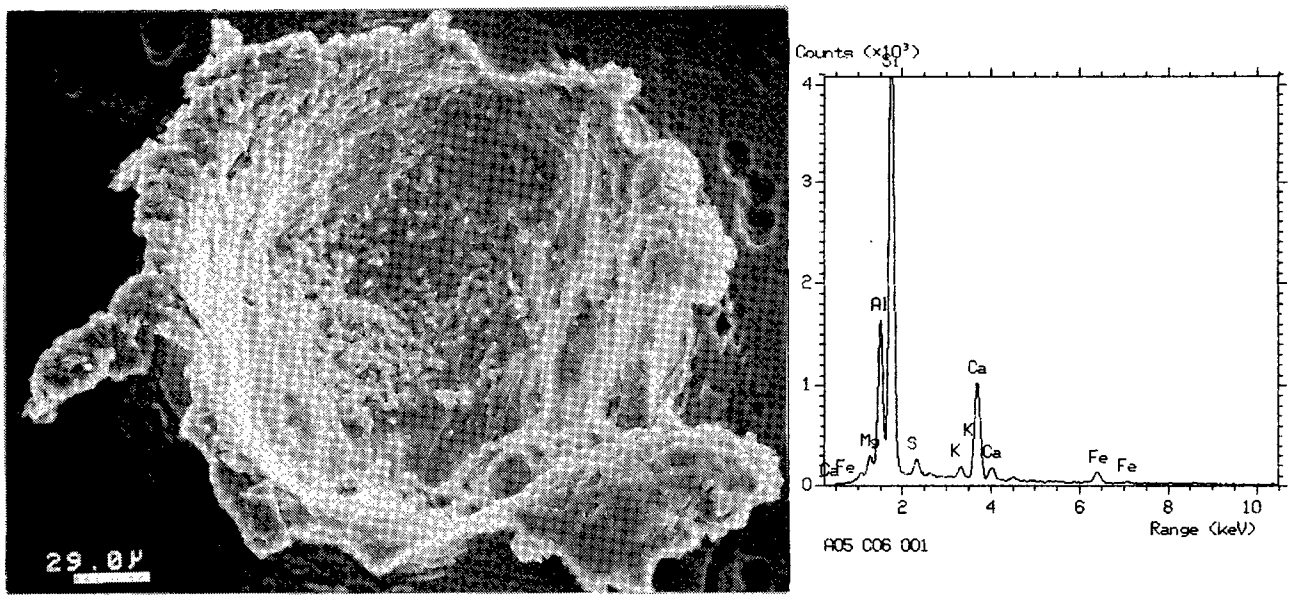


Figure 6. In some cases the projectile collides with the exposed surface at large oblique angles or the projectile contains large voids of porosity, in these cases the impact crater may be asymmetrical. Impact feature number 001, on clamp six, from tray A05 contains grains which appear to be relatively unaffected by collision. Energy dispersive X-ray analysis reveals a typical micrometeoritic spectra.

PROJECTILE COMPOSITIONS AND MODAL FREQUENCIES ON THE "CHEMISTRY OF MICROMETEOROIDS" LDEF EXPERIMENT

Ronald P. Bernhard, Thomas H. See
Lockheed Engineering & Science Company
Houston, Texas 77058
(713) 483-5018/5027 / FAX (713) 483-5347

and

Friedrich Hörz
NASA / Johnson Space Center
Houston, Texas 77058
(713) 483-5042 / FAX (713) 483-5347

SUMMARY

The Chemistry of Micrometeoroids Experiment (LDEF instrument A0187-1) exposed witness plates of high-purity gold (>99.99% Au) and commercial aluminum (>99% Al) with the objective of analyzing the residues of cosmic-dust and orbital-debris particles associated with hypervelocity impact craters. The gold substrates were located ~8^0 off LDEF's trailing edge (Bay A03), while the aluminum surfaces resided in Bay A11, ~52^0 from LDEF's leading edge.

SEM-EDX techniques were employed to analyze the residues associated with 199 impacts on the gold and 415 impacts on the aluminum surfaces. The residues that could be analyzed represent natural or man-made materials. The natural particles dominate at all particle sizes >5 μm. It is possible to subdivide both particle populations into subclasses. Chondritic compositions dominate the natural impactors (71%), followed by monomineralic, mafic-silicate compositions (26%), and by Fe-Ni rich sulfides (~3%). Approximately 30% of all craters on the gold collectors were caused by man-made debris such as aluminum, paint flakes, and other disintegrated, structural and electronic components. Equations-of-state and associated calculations of shock stresses for typical LDEF impacts into the gold and aluminum substrates suggest that substantial vaporization may have occurred during many of the impacts, and is the reason why ~50% of all craters did not contain sufficient residue to permit analysis by the SEM-EDX technique.

After converting the crater diameters into projectile sizes using encounter speeds typical for the trailing-edge and forward-facing (Row 11) directions, and accounting for normalized exposure conditions of the CME collectors, we derived the absolute and relative fluxes of specific projectile classes. The natural impactors encounter all LDEF pointing directions with comparable, modal frequencies suggesting compositional (and dynamic) homogeneity of the interplanetary-dust environment in near-Earth orbit.

INTRODUCTION

The Chemistry of Micrometeoroids Experiment (CME) exposed two substantially different instruments, one active, the other passive (ref. 1). The active experiment consisted of clamshell-type devices that could be opened and closed such that the collectors were protected against contamination during all ground handling and LDEF deployment. This experiment exposed ~0.82 m^2 of high-purity gold (>99.99%) on LDEF's trailing-edge (*i.e.,* Bay A03). The actual collectors consisted of seven individual panels (~20 x 57 cm each) ~0.5 mm thick. The Au collectors exhibited relatively low crater densities because (1) of the specific pointing direction (*i.e.,* trailing edge) which inherently yields the smallest particle flux (ref. 2), and (2) the collectors were only exposed for a total of 3.4 years (refs. 1 and 3). In contrast, the passive experiment (Bay A11) continuously exposed ~1.1 m^2 of aluminum (commercial series 1100, annealed; >99% Al) for the entire 5.7 years in which LDEF was in low-Earth orbit (LEO). Six individual panels (~41 x 46 cm, each) ~3.2 mm thick made up the exposed collector surface for this forward-facing experiment. We previously reported on the detailed optical examinations of these surfaces to determine projectile size-frequency distributions and spatial densities; this earlier report also included some preliminary assessment of the compositional nature of a small set of impactors (ref. 1).

The present report focuses on our subsequent efforts to produce statistically meaningful assessments of the compositional variability of hypervelocity particles in LEO. We have now surveyed all craters >30 μm in diameter on the Au-collectors, as well as a randomly selected suite of smaller impacts, ~10-30 μm in size, resulting in a total of 199 craters. Therefore, the results are complete for all "large" craters on the trailing-edge instrument. To date, we have completed chemical analysis of all 415 craters >75 μm in diameter on two of the six aluminum panels. This latter suite is believed to be representative of the "large" crater population on the forward-facing aluminum collectors.

In general, we followed the analytical procedures and compositional particle classifications developed during the analysis of interplanetary dust recovered from the stratosphere (refs. 4 and 5), or of space retrieved surfaces such as Solar Maximum Mission replacement parts (refs. 6 and 7), or the Palapa satellite (ref. 8). The present effort specifically adds to previous work by analyzing a much larger number of events and by being able to place them into a dynamic dust environment, since LDEF was gravity-gradient stabilized, while all previously analyzed surfaces originated from spin-stabilized spacecraft. Unlike spin-stabilized satellites, LDEF offers the potential to yield substantial directional information (*e.g.,* refs. 2, 9, 10, 11, and 12).

ANALYTICAL METHOD AND GENERAL OBSERVATIONS

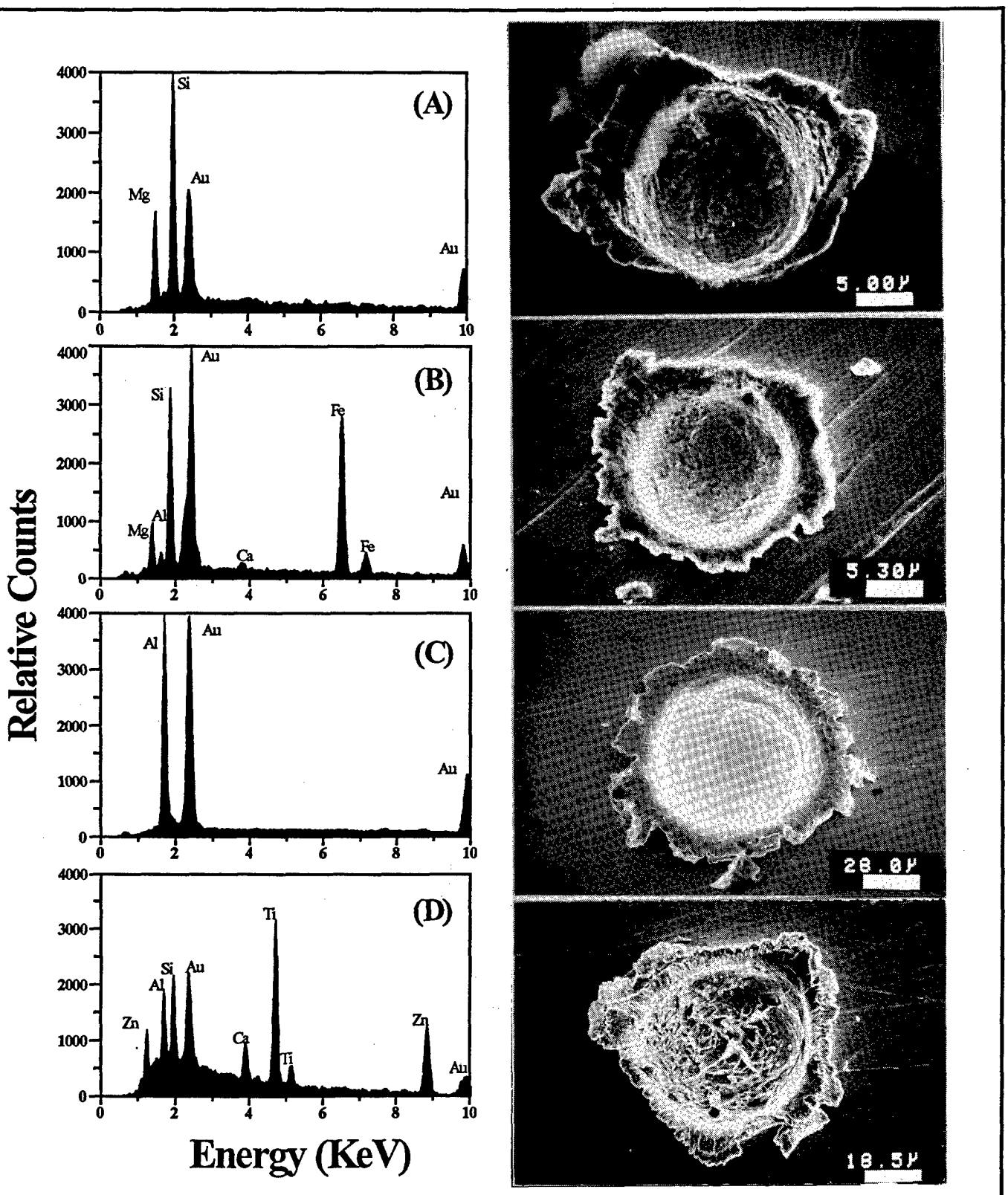
An ISI-SR50 Scanning Electron Microscope (SEM) was employed to collect energy dispersive X-Ray (EDX) spectra using a Si(Li) detector on a LINK eXL analyzer with the detector arranged at 90° to the beam path. Although we characterize our analyses as qualitative

and of a survey-type nature, we spent considerable efforts in optimizing the signal to noise ratio of the X-Ray spectra. Initially it was found that an uncomfortably large fraction of craters yield spectra that contained no detectable signal above that of the background. Therefore, we used a number of craters to investigate a range of electron-beam geometries (diameter and take-off angle), low- and high-beam voltage, and widely variable count times (minutes to hours). From these efforts it was determined that a relatively high-beam voltage (25-20 KeV) and long count times (500-1000 seconds) with the specimen tilted at 30° yielded the best results. It is our belief that high-beam voltages are best because the surface relief of the crater interiors tends to be uneven permitting excitation of more near-surface specimen volume compared to less penetrative, low-energy electrons. Count times in excess of 1000 seconds do not appreciably improve signal to noise ratios and do not warrant the additional expenditure of resources.

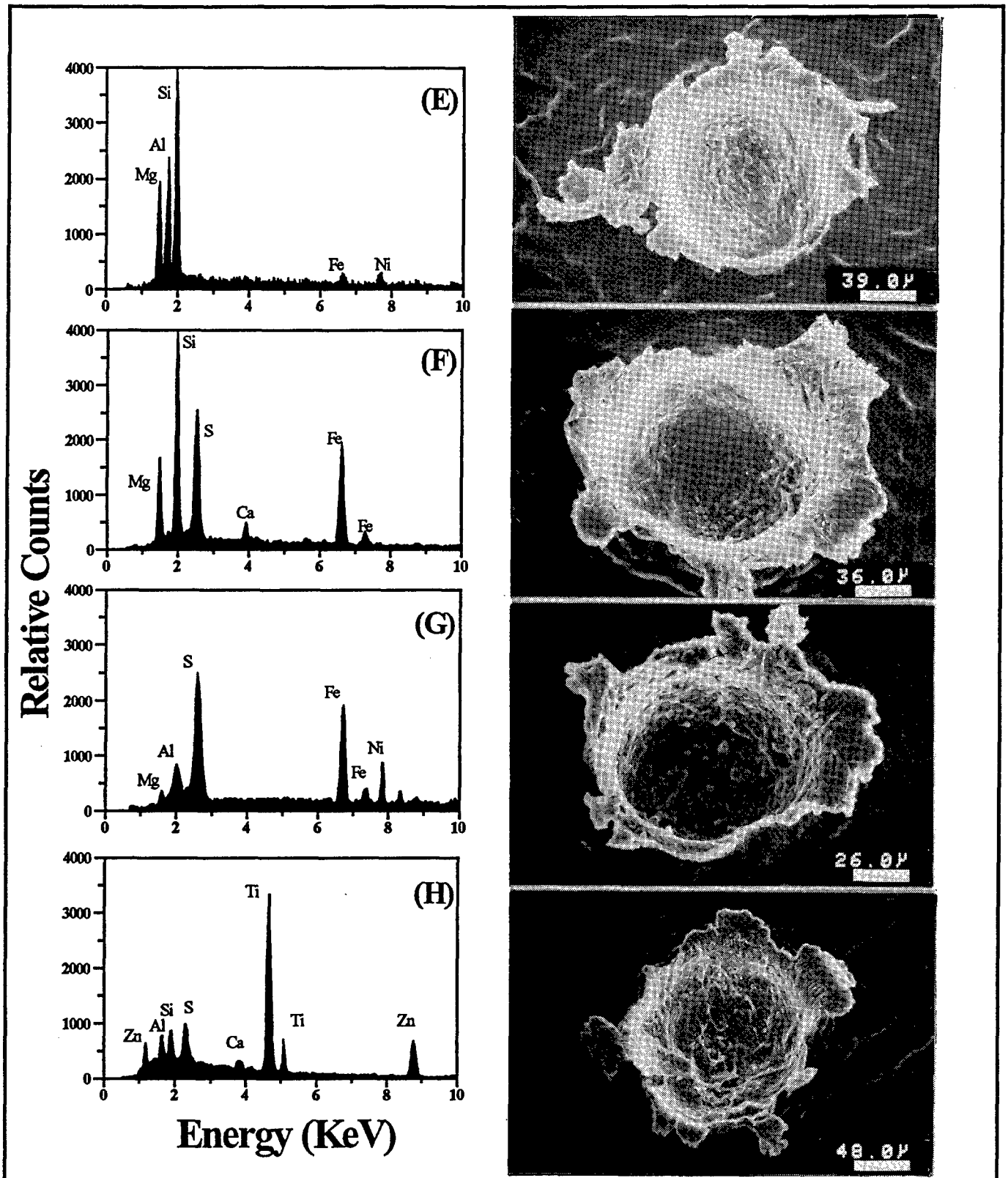
Generally, contamination of our surfaces was not a problem because the composition of such contamination tends to differ dramatically from that of the projectile residues. Nevertheless, we have observed Si-Ca rich deposits, presumably outgassed RTV (ref. 13) in some crater interiors. Interestingly, such deposits can have distinctly asymmetric distributions in some craters, substantiating the macroscopic LDEF observations of highly directional flow of gaseous contaminants and their condensates. We also observe some intrinsic, heterogeneously distributed contaminants, the result of manufacturing procedures in our collector materials, most notably As in the gold and Si in the aluminum. There is no question that contamination can be a nuisance, but we do not think that it affects the recognition of discrete compositional groupings of projectile types, the major objective of this work.

For many individual craters one may obtain different spectra, especially for those craters that possess mixtures of molten material and unmelted fragments. The latter yield spectra consistent with component minerals of dust grains (*e.g.*, olivines or pyroxenes) that differ distinctly from the melted bulk-residue. However, variability within the pure melts was observed with the largest variations occurring in those craters that contained unmelted residues, suggesting the presence of incompletely mixed mineral melts (refs. 14 and 15). Generally, this melt variability relates to subtly different elemental ratios among different spectra obtained from the same specimen. Nevertheless, this specimen heterogeneity does not affect our classification into natural and man-made particle sources, nor the assignment to a specific compositional subclass.

Our observations for the Au collectors have been summarized in a catalog that contains an SEM image of each crater, its diameter, a typical EDX-spectrum, and our tentative assignment of particle origin and subclass (ref. 16). A less polished compilation is being maintained for the aluminum surfaces that contains ~400 entries which are summarized here. However, it should be noted that aluminum impactors cannot be detected on a substrate composed of aluminum, like that used on the forward-facing A11 collectors.



FIGURES 1A - 1D. Representative morphologies of hypervelocity impact craters and associated X-Ray spectra for natural and man-made projectile residues. Figures on this page portray observations from the trailing-edge gold collectors (LDEF Bay A03). For detailed descriptions and comments see text.



FIGURES 1E - 1H. Representative morphologies of hypervelocity impact craters and associated X-Ray spectra for natural and man-made projectile residues. Figures on this page portray observations made on the forward-facing aluminum plates (LDEF Bay A11). For detailed descriptions and comments see text.

SUGGESTED PARTICLE CLASSIFICATION

Several typical craters and their associated spectra are displayed in Figure 1 to illustrate the large compositional variability, as well as the substantial differences in crater morphology caused by the wide range of initial impact conditions. This variety in compositional and dynamic particle properties cannot be over emphasized; each crater seems different.

The crater in Figure 1a possesses a largely forsterite-olivine rich residue, while the residue associated with the crater in Figure 1b exhibits a typical chondritic particle composition. Note the relatively rough surfaces of the residue melts. Note also that these examples have unusually large volumes of preserved residue. The crater visible in Figure 1c is substantially smoother than either of the previous features and is draped with a thin melt layer containing aluminum only. This clearly indicates an aluminum particle impacting on the trailing-edge surface, with the gold peaks reflecting the collector-material background. Finally, the crater depicted in Figure 1d possesses residue that is rich in Ti and Zn, which is typical for thermal protective paints used in the manufacture of spacecraft. Again note that this is an impact on the trailing-edge gold surfaces, the Al and Ca being components of the paint. Also note the relatively shallow crater depression, combined with large volumes of residue, suggesting modest impact speeds. Figures 1e-h illustrate craters from the forward-facing, aluminum collectors. The spectrum associated with Figure 1e again reflects a monomineralic, forsteritic-olivine projectile. The crater is modestly elliptical suggesting a somewhat oblique impact. Figure 1f is typical of many craters that contain residues of essentially chondritic compositions, yet the spectrum displays substantial quantities of sulfur as well suggesting the presence of sulfides. Figure 1g represents one of the rare impacts that is dominated by Fe-Ni rich sulfides, but also could have included some Mg-rich phase such as forsterite or enstatite. Lastly, Figure 1h depicts a crater in the aluminum collectors caused by a paint flake; note how shallow this structure is. These examples illustrate that a wide variety of impactor compositions exist in LEO, and that specific compositional subclasses can be differentiated.

Based on the analyses of approximately 600 craters, we propose three major classes of natural impactors and two major classes for man-made debris particles. Those craters that possessed insufficient residue mass to permit characterization by SEM-EDX methods are classified as "unknown" or "indeterminate" projectiles.

Natural Particles

Chondritic

Residues falling within this subclass typically contain little, if any clastic materials. On the other hand they frequently exhibit fairly homogeneous composition suggesting that they are derived from particles that are largely made up of relatively well-mixed and homogenized, fine-grained matrices. Nevertheless, this mixture can be variable, as evidenced by somewhat variable

elemental ratios of the major and minor elements among different craters. Future work, employing multi-variate mixing models and size-frequency distribution of major phases obtained from the analysis of stratospheric dust particles, will be needed to determine whether the observed variability may warrant the establishment of specific particle subclasses within the current chondritic group. Such a proposal would also require that many spectra be taken from a single crater to obtain reliable average compositions. Some of the variability currently observed may merely reflect variable modal proportions of component minerals, rather than systematic differences of potential genetic significance. As we alluded to in the descriptions of Figure 1, we would already be in a position to discriminate between S-rich and S-deficient chondritic particles.

Monomineralic Silicates

Residues typical of this class are characterized by high concentrations of Si, Mg, and Fe to the exclusion of other elements. They are frequently recognizable fragments of initially larger mineral grains such as olivine or pyroxene (Ol/Px). However, we also observed texturally homogeneous melts of this composition indicating that the projectile was completely melted. Olivine- or pyroxene-dominated melts also abound in those craters where unmelted residues occur, thereby attesting to large particles predominantly made up of single crystals. Conversely, the latter craters also can contain chondritic melts, albeit rarely, suggestive of crystalline materials in a largely chondritic matrix. Consequently, we believe that chondritic and monomineralic residues may be genetically related with the significant difference referring to the texture and grain size only, rather than to fundamentally different astrophysical sources and formative processes. Interestingly, many craters that do contain unmelted mineral fragments are relatively shallow, suggesting modest encounter speeds.

Fe-Ni Sulfides

Without exception the craters possessing Fe-Ni rich residues are melt-lined and contain no fragmental particles. Nevertheless, they also suggest largely monomineralic projectiles composed of Fe-Ni sulfides (*i.e.,* major mineral phases) such as troilite, a common component of meteorites, and especially of carbonaceous chondrites.

Orbital Debris

Aluminum

The pure gold substrates afforded the opportunity to detect pure aluminum particles. They are, without exception, characterized by a single aluminum peak in the EDX spectrum, even for count times approaching an hour. There simply is no natural compound of sufficient abundance which contains only aluminum, notwithstanding Al_2O_3 (*i.e.,* corundum and its gemstone forms of ruby and sapphire). Particles in LEO that only contain aluminum must be considered man-made; they can occur either as metallic or oxidized particles. The former should largely be due to

disintegrated structural aluminum spacecraft components, yet metallic aluminum is also used in solid-rocket fuels which yield large numbers of spherical aluminum-oxide particles upon firing (ref. 17). In principle, it is possible to detect oxygen via SEM-EDX methods and therefore, to distinguish between metallic and oxidized species. However, we have not yet conducted such specialized investigations. Resolution of the question whether the aluminum impactors are largely metallic or oxidized seems significant, as collisional fragmentation products could possibly be distinguished from solid-rocket fuel exhaust products.

Miscellaneous

Consistent with previous analyses of space-retrieved surfaces, we have identified a wide variety of impactors derived from man-made spacecraft structures; these include Fe-Ni-Cr-rich particles representing stainless steel, Zn-Ti-Al rich residues suggestive of thermal protective paints, or Ag- and Cu-rich compositions associated with components employed in the manufacture of electronic components. We have grouped all such particles into a single "miscellaneous" category because they could have all resulted from collisionally or explosively disintegrated spacecraft, and thus, from a single, generic source. Note that this category includes a wide diversity of materials and compositions.

Craters Due To Unknown Projectiles

Despite diligent efforts, a large number of craters did not yield spectra that contained measurable signals above that of the collector background. As our experience and analytical methods matured to extract signals from previously marginal cases, a large number of events simply continued to resist analyses. Efforts are underway to explore the utility of more sensitive analysis methods such as SIMS (ref. 18) to hopefully characterize the impactor residues associated with such craters.

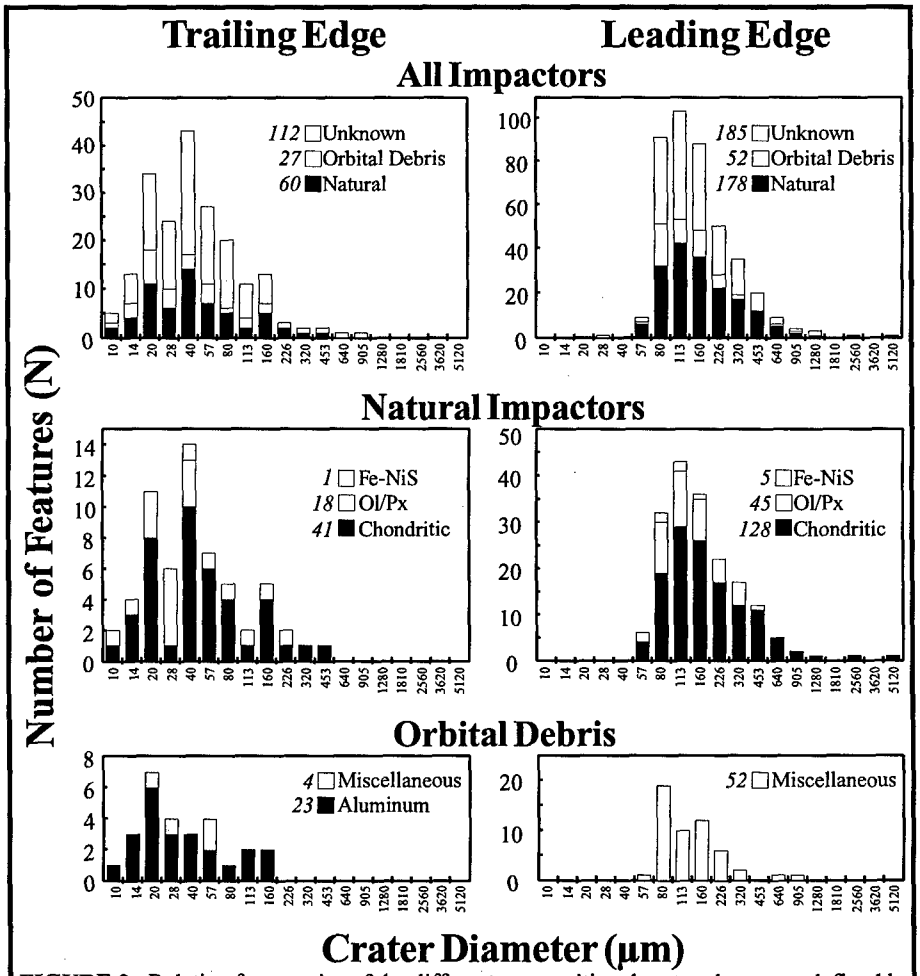


FIGURE 2. Relative frequencies of the different compositional crater classes, as defined by this study, of ~600 impactors that encountered the trailing- and leading-edge CME surfaces.

Also, under the assumption that the principal projectile loss-mechanism is due to excessive, and possibly complete vaporization of the projectile, the relative frequency of such "unknown" impactors on the whole should be a measure of the high-velocity component of natural or man-made impactors that apparently encountered LDEF above some threshold velocity (see Discussion section, below). In any case, these events constitute approximately 50% of all CME impacts.

OBSERVED FREQUENCY OF PARTICLE TYPES

Figure 2 summarizes all analyses to date and is a plot of the number/frequency of recognized projectile types versus the crater size for the trailing-edge (gold) and leading-edge (aluminum) surfaces. The intent is to illustrate the relative frequencies of the major particle types and of the specific subclasses. Again, we emphasize when discussing these frequencies that aluminum impactors cannot be detected on the aluminum collectors; this constitutes an important limitation and qualifier for some of the interpretations offered. We conclude the following from Figure 2:

(a) The craters that do not possess identifiable residue, via the EDX methods employed, compose ~56% of all caters in the gold surfaces and ~45% of those examined on the aluminum collectors. Consequently, approximately half of all projectiles that encountered CME remain unidentified, at present.

(b) The majority of events that contain identifiable residues were caused by natural, cosmic-dust particles accounting for ~68% on the gold and 77% on the aluminum collectors.

(c) Most exceptionally large craters on both collectors which possessed analyzable residues seem to have resulted from natural impactors, yet the statistics are insufficient to permit a more definitive statement. Nevertheless, of all 47 craters >320 μm in diameter, 23 were derived from natural sources and only 2 appear to have resulted from man-made impactors. Some of the indeterminate events on the A11 aluminum surfaces could be the result of aluminum impactors.

(d) Among interplanetary dust particles the chondritic subgroup is by far the most populous composing ~72% of all impactors on the aluminum and ~68% of all impactors on the gold surfaces.

(e) The largest craters observed on both surfaces reflect chondritic impactors, implying that the relative frequency of the natural subclasses may be size-depended. This seems natural if one were to interpret the largely monomineralic silicates and sulfides as coarse-grained components dislodged from a largely chondritic, fine-grained matrix.

(f) The man-made sources are dominated by aluminum particles on the trailing-edge gold surfaces (*i.e.,* 23 of the 27 craters). Note, however, that the forward-facing aluminum

collectors permit recognition only of miscellaneous debris particles and that the frequency of aluminum projectiles is unknown on the A11 surfaces.

(g) Although not illustrated, paint flakes are the most dominant debris species in the miscellaneous category on the forward-facing side (~50%).

Other investigators (refs. 18, 19, 20, and 21) have analyzed projectile residues associated with LDEF craters from various surfaces and their results are consistent with those observed on the CME collectors. In general, however, the impact features and associated projectiles investigated by these other groups are smaller than the CME events summarized in Figure 2. Thus, caution is necessary when comparing the CME findings with the results currently available from other LDEF instruments. On LDEF, small and large impactors may not have the same modal frequency, because specific sources may produce particles of variable size-frequency distributions. In addition, Refs. 18, 20 and 21 employed the more sensitive SIMS methods for analysis. Therefore, some of the events that are indeterminate by our SEM-EDX techniques, would be part of the SIMS data sets; the point here is that different analytical sensitivities may introduce some (unknown) bias. Furthermore, the number of events analyzed by Refs. 18, 19, 20, and 21 for a given viewing direction was small (typically N<20), compared to our CME data. Nevertheless, the major findings of the CME data set are corroborated by other investigators. There is substantial particle variety, natural and man-made impactors can be differentiated, and man-made impactors were encountered on other trailing-edge surfaces of LDEF.

PRODUCTION RATE OF CRATERS BY SPECIFIC PROJECTILES

Figure 2 illustrates the observed raw frequency data. While they do correctly represent the relative particle frequencies for each of the two viewing directions, they are unsuitable to directly compare the trailing-edge surface with the forward-facing direction, because different total surface areas were analyzed and the host surfaces had different cumulative exposure histories. Therefore, we normalized the raw frequencies to some unit surface area (m^2) and exposure time (5.7 years; total LDEF mission) and plot these normalized data in Figure 3, in cumulative form, for each of the recognized crater/residue types. The purpose of Figure 3 is to reconstruct the absolute and relative crater-production rates due to specific projectile types for the A03 and A11 locations on LDEF. We can extract the following conclusions from Figure 3, yet we must note that the large fraction of unknown projectiles constitutes a strong qualifier for many of these conclusions:

(a) The above normalization of exposure conditions results in different absolute frequencies of specific residues compared to those of Figure 2.

(b) The crater production rate for natural impactors, at 100 μm crater diameter, is approximately a factor of 12 smaller for the trailing edge when compared to the A11 location, a result that is consistent with the dynamic model for natural impactors (ref. 2).

(c) The relative frequency of the subclasses of natural impactors is invariant per viewing direction, with all of the A03 curves being offset by a comparable factor (approximately an order of magnitude) from the cor-responding A11 curves. These similar relative frequencies indicate that the natural dust environment is fairly homogenized with regard to specific particle species or, conversely, that there is no compositionally distinct astrophysical source that dominates a specific LDEF direction. This should not be too surprising since LDEF's orbital motion and precession tends to average large fractions of the sky (ref. 2).

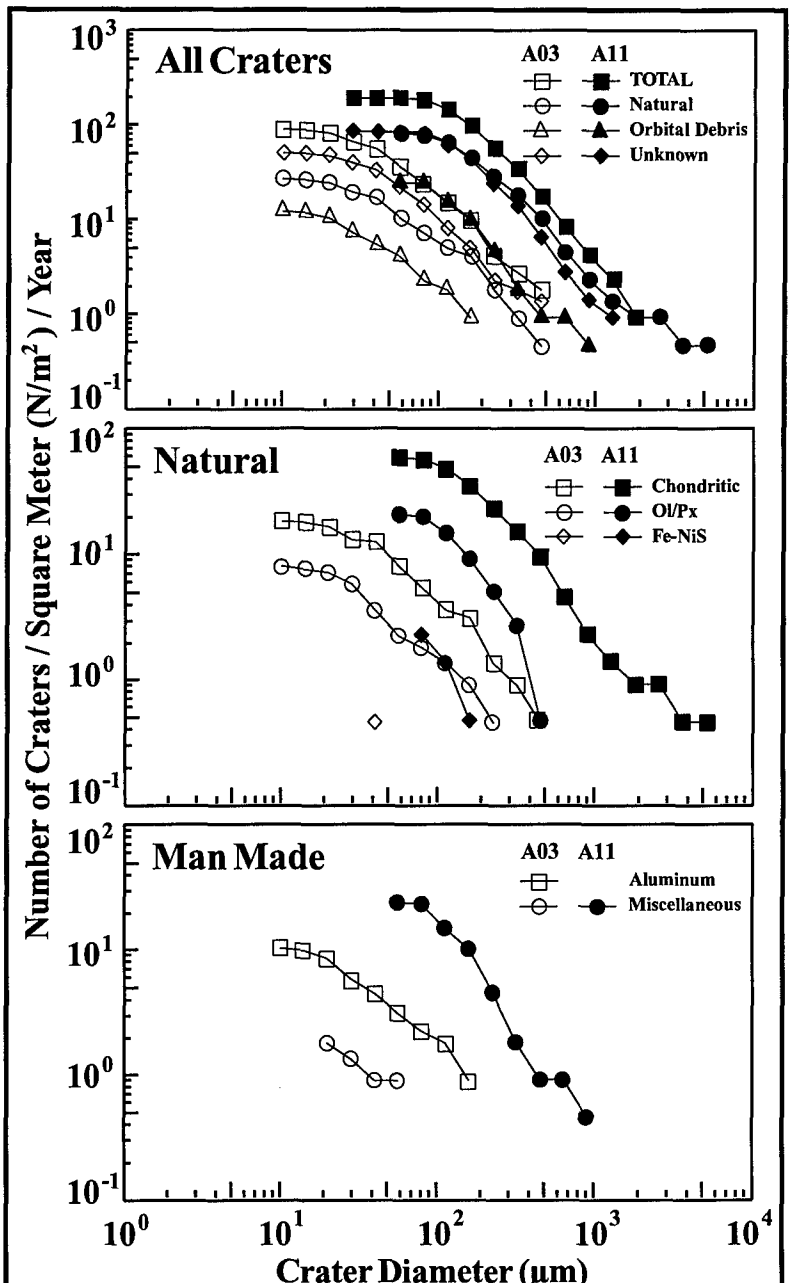


Figure 3. The crater-production rates of specific projectile types, both natural and man-made.

(d) Crater production rates for orbital debris are only available for the "miscellaneous" category. These differ by a factor of 40-50 between the leading and trailing edges at a 100 μm crater diameter, which is grossly consistent with predictions (ref. 20).

(e) Unfortunately, crater production rates for aluminum debris, the most prominent species on the trailing edge, cannot be extracted from the leading-edge CME surfaces. On the other hand, if the same modal ratio for aluminum and miscellaneous craters observed for the trailing-edge gold (~6:1) were applied to the forward-facing direction, the total number of craters calculated for debris only would approach the number of all craters actually observed.

CUMULATIVE FLUXES ON A PARTICLE DIAMETER BASIS

While the crater production rates illustrated in Figure 3 resemble an improved portrayal of relative frequencies compared to Figure 2, the ultimate objective is to produce such frequencies on a projectile-size, if not projectile-mass basis. The latter is the primary information needed (1) to permit reconstruction of potential astrophysical sources (refs. 22 and 23), (2) to assess production mechanisms, particle dynamic properties and associated collisional hazards of the debris environment (refs. 24 and 25), and (3) to predict possible yields in future particle-collection efforts (ref. 26).

To derive such information one must consult cratering mechanics and associated scaling laws that predict the size or mass of the impactors responsible for any given crater. The wide range in possible encounter speeds, angles of impact, and physical properties of the prospective projectiles (none of which is amenable to direct measurement during post-mortem investigation of individual craters, much less of substantial crater populations) mandates a statistical approach that uses reasonable average conditions, as well as some assumptions. Conversion of crater size into projectile size is not, therefore, without risk, even more so if uncertainties in the velocity scaling (substantially beyond current laboratory data) of crater dimensions are considered. Nevertheless, we extracted projectile sizes from our present set of crater diameters using the assumptions and average conditions described below.

First, we assume a common density (*i.e.*, 2.7 g/cm^3) for all particles, which strictly applies to aluminum, and possibly to a fair number of natural particles as well. This density is also characteristic of the typical projectiles utilized in the laboratory calibration experiments discussed below. We also assume a normal angle of incidence (*i.e.*, 90°) for all craters, a permissible assumption because the average velocities used in our conversions refer only to the normal velocity component. These assumptions are then combined with dynamic models predicting average encounter speeds for each of the forward and trailing-edge viewing directions. For the A03 and A11 pointing directions we utilized velocities of ~12 and 23 km/s, respectively (refs. 1 and 2), for natural particles. On the other hand, Kessler (ref. 25) modeled the orbital debris environment and derived mean encounter velocities of ~1.75 and 7.85 km/s for the A03 and A11 sites, respectively, (Kessler, personal communication).

Table 1. Model assumptions and conversion factors for crater diameters (D_c) into projectile diameters (D_p). Mean impact velocities for natural particles are from Ref. 2, while those associated with man-made particles are from Kessler (personal communication).

LOCATION	TARGET	MEAN IMPACT VELOCITY NATURAL	MEAN IMPACT VELOCITY MAN-MADE	CRATER CALIBRATION	CONVERSION FACTOR (D_c/D_p)
A03	Gold	12 km/s		(ref. 1)	5.7
A03	Gold		1.75 km/s	(ref. 1)	1.5
A11	Aluminum	23 km/s		(ref. 27)	10.4
A11	Aluminum		7.85	(ref. 27)	6.0

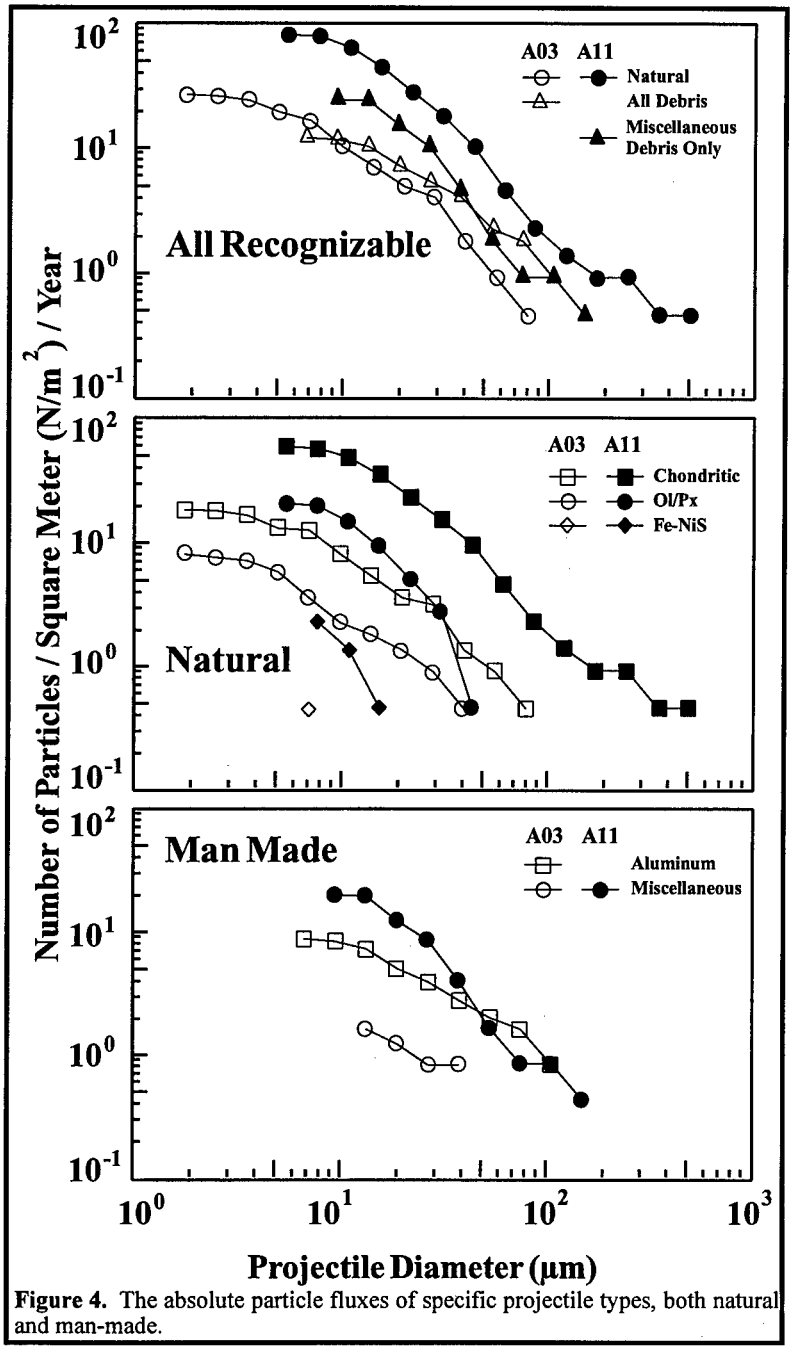


Figure 4. The absolute particle fluxes of specific projectile types, both natural and man-made.

Table 1 summarizes these assumptions, as well as the resulting relationships between crater diameter (D_c) and projectile diameter (D_p) determined via laboratory cratering experiments into aluminum (ref. 23) and gold targets (ref. 1).

The resulting projectile-size frequencies and associated fluxes are illustrated in Figure 4. Note, that we only calculated associated projectile diameter for craters of known origin. This results in fewer curves in Figure 4 compared to Figure 3. Not surprisingly, substantial shifts in the relative frequency of the various particle types resulted because the crater-diameter curves were horizontally shifted by (unequal) factors corresponding to D_c/D_p. These shifts are most pronounced for the orbital-debris impactors, owing to their low encounter velocities and the resulting small D_c/D_p ratios, relative to the natural particles. Figure 4, therefore, carries the important message that extreme care is necessary when discussing relative frequencies on the number-of-analysis basis (Figure 2), on the crater-diameter basis (Figure 3), or on the projectiles-size basis (Figure 4). Sub-stantially different frequencies and interpretations may result de-pending on the actual data being considered. From the projectile-size frequencies (generally re-ferring to impactors >24 μm in diameter; Figure 4) and comparisons with Figures 2 and 3 we conclude:

(a) The relative flux of natural impactors differs by a factor of ~6 between the trailing and leading edges, whereas the crater production rates suggested factors of 10-12.

(b) The number of chondritic particles impinging on the A03 surfaces approaches the flux of Ol/Px particles for the A11 collectors, while their crater production ratios differed by a

noticeably larger factor. Other relative shifts among the natural impactors could be pointed out, all caused by a constant, horizontal shift by a factor of ~2 for the curves depicted in Figure 3 (see Table 1; 10.4/5.7).

(c) Because the specific subclasses of natural craters were all converted with a constant D_p/D_c ratio per viewing direction, their modal frequencies remained constant for a given orientation.

(d) The particle size-frequency distribution is fairly similar among the natural subclasses.

(e) Orbital debris impactors at D_p=24 μm in diameter tend to be more populous on the trailing-edge surfaces than all recognized natural particles combined. This substantially reverses the trends of Figure 3, which suggested ~3 natural craters for every debris impact.

(f) A qualitatively similar trend applies to the A11 surfaces. Natural impactors >24 μm in diameter are only a factor of 3 more abundant than the miscellaneous debris category only (remember, no aluminum projectiles could be detected on A11), whereas the crater production ratios differed by a factor of 7 to 8.

(g) The size-frequency distribution of aluminum and miscellaneous debris particles seem different. Figure 4 suggests that the miscellaneous population may have a steeper size index than the aluminum particles.

(h) The statement made earlier during the discussions of Figure 2 that craters >250 μm are predominantly caused by natural impactors is a valid observation, but it does not necessarily follow that all large impactors on LDEF are from natural sources. Note, in Figure 4, that particles >100 μm occur among both natural and man-made populations and that the data do not suggest a systematic decline of large orbital-debris particle sizes.

These examples and interpretations from Figure 4 suffice to emphasize that crater-size frequencies and associated projectile-size frequencies must be rigorously distinguished between when addressing the particle environment in LEO. Conclusions based on crater-size frequency alone may not necessarily be identical to those based on projectile size, and vice versa. It should be noted as well that the observed crater and penetration features on LDEF *cannot* be interpreted properly by applying "global" average impact conditions (*e.g.,* ref. 1 and many others) to any given set of impact features. The differences in the velocity regimes between natural and man-made particles are so substantial that they must be treated separately. At a minimum, LDEF investigators need a single, internally consistent, dynamic model that combines natural (*e.g.,* ref. 2 and others) and orbital-debris particles (*e.g.,* ref. 25 and others), and that estimates the absolute fluxes and mean velocities of these two populations such that appropriate weighting factors may be applied to any specific set of impact features for a non-spinning platform in LEO.

DISCUSSION

Loss Of Projectile Due To Vaporization

A large number of craters, ~50% of all impact events, on both the forward-facing and trailing-edge surfaces did not yield analyzable projectile residues via the SEM-EDX techniques employed. We consider vaporization of the projectile during impact to be the major loss process, ultimately resulting in insufficient mass within the crater to yield significant X-Ray counts. The number of such events is of comparable frequency on both collectors, although mean encounter speeds of natural and man-made particles differ substantially for the A03 and A11 directions (see Table 1). Because of the higher velocities associated with the forward-facing A11 location, one would intuitively expect the higher shock-stresses and more vaporization on the forward-facing surfaces which, however, is not observed. Therefore, we utilized equation-of-state data to calculate shock stresses and to explore the degree with which the density differences of the gold and aluminum targets may compensate for these velocity differences. The results are illustrated in Figure 5.

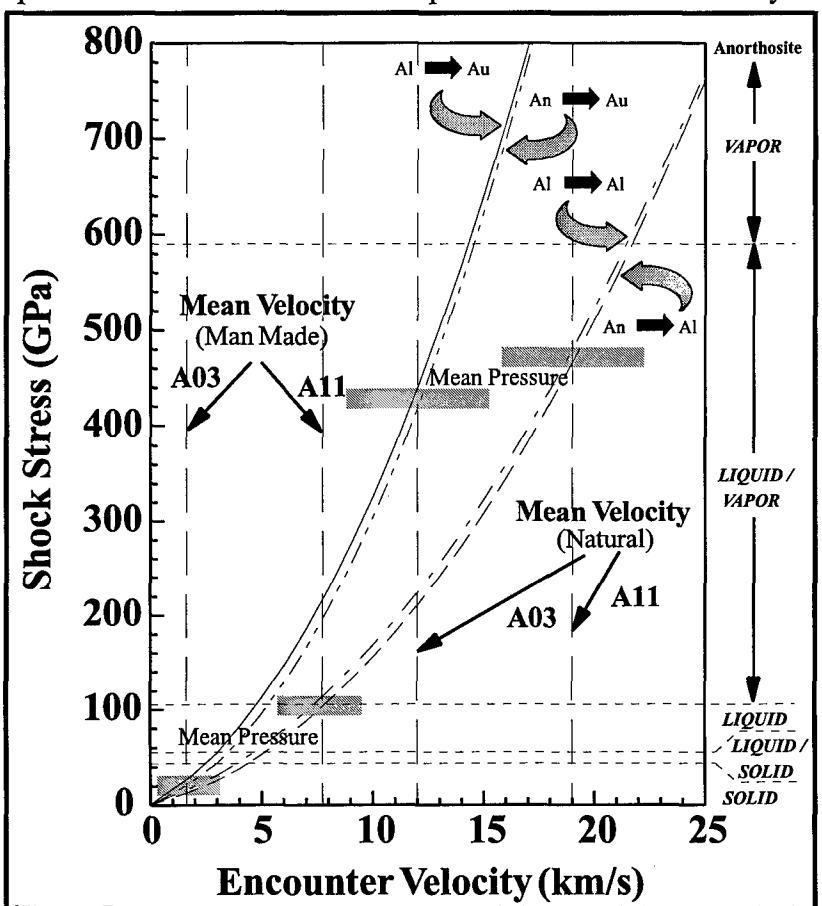


Figure 5. Shock pressures (refs. 28 and 29) of aluminum (Al) and anorthosite (An) projectiles impacting gold and aluminum targets at velocities up to 25 km/s. Also illustrated are the phase transitions of anorthosite upon release from a specific shock stress (ref. 30). Note the dramatically different stress regimes characterizing typical debris and cosmic-dust impacts. Also note that the typical cosmic-dust impact resides substantially into the vaporization regime for both aluminum and gold targets.

Figure 5 is based on the equation-of-state for aluminum 6061 (Al), gold (Au), and anorthosite (An; a dense feldspar-rich rock, ref. 28), and the thermodynamic model of Cintala (ref. 29) that solves for the peak stress generated by aluminum and anorthosite impactors colliding with the CME collectors at velocities up to 25 km/s. In addition, the calculations of Ahrens and O'Keefe (ref. 30) that address the thermodynamic states and phase transitions of anorthosite upon pressure release are included. Principally, all calculations employ two-dimensional shock geometries and apply specifically to the peak pressure at the target/projectile interface only, rather than to the bulk impactor. Because

both CME collectors were thick enough to act as infinite-halfspace targets, substantial volume fractions of the impactors should have experienced pressures comparable to, yet modestly smaller than those extracted from Figure 5.

First, looking at natural particles, that have encounter velocities of 12 and 23 km/s for the A03 and A11 locations, respectively, one obtains rather similar peak stresses for both collector materials. Therefore, it is not surprising to find a comparable number of craters which resisted SEM-EDX analysis for both CME orientations. This statement may be extended to particles of widely variable physical properties, such as low-density, high-porosity particles that should be common among interplanetary dust, unlike the dense (2.9 g/cm^3) anorthosite used in Figure 5. As long as standard particles, even of widely variable physical properties, impact gold and aluminum at 12 and 23 km/s, respectively, grossly similar peak stresses will result. However, the absolute magnitude of stress depends strongly on the impactor itself, predominantly on its density. Absolute peak stress may be lower for low-density, porous dust particles than is portrayed in Figure 5, yet consider that low-density particles also require lower stresses for the onset of melting and vaporization (refs. 31, 32 and others).

Based on thermodynamic calculations (ref. 30), substantial fractions of dense-silicate impactors are vaporized at conditions typical for LDEF encounters. Amari *et al.* (refs. 18 and 20) observed many vapor deposits in their LDEF particle capture cells. Based on Figure 5, anorthosite particles impacting at velocities greater than ~14 and 25 km/s may be completely vaporized on CME's gold and aluminum targets, respectively. Therefore, the large fraction of indeterminate crater residues seems understandable.

As for orbital-debris particles, the very low encounter velocities on the trailing edge result in peak pressures of ~50 GPa, which would not be high enough to vaporize most orbital-debris materials. Due to the substantially different velocities, peak stresses of ~100 GPa will be achieved on the forward-facing aluminum target. Such pressures would be sufficient to melt a wide variety of materials, yet complete vaporization of the projectile should be rare.

Overly specific conclusions from Figure 5 are not warranted because each individual impact may have unique initial conditions. Figure 5 is largely illustrative and merely shows that the number of craters with indeterminate natural projectiles should be similar for both the aluminum and gold collectors, and that even the large fraction of indeterminate projectiles (~50%) seems readily explained. Our preferred inference is that the indeterminate craters represent a velocity-biased set. This must not necessarily be the case, because a strictly compositional bias may also apply (*i.e.*, impactors enriched in relatively volatile components). Indeed, differences in the physical properties of the impactors, specifically of porosity, may result in significant differences in the onset of vaporization at otherwise identical initial conditions. Furthermore, it is possible that substantial fractions of impactor melts escaped the crater cavity at high impact velocities (ref. 33). Any of the above suggestions may combine to produce craters with little or no apparent residues.

Furthermore, one may safely conclude from Figure 5 that most man-made impactors should result in analyzable residues for impacts occurring on the trailing edge, leading to the suggestion that all (!) debris particles were accounted for on the gold collectors. Conversely, this would make all indeterminate craters on the trailing edge the result of natural cosmic-dust impacts. Unfortunately, the situation for the forward-facing aluminum collectors is not as clear cut. The indeterminate fraction of craters at the A11 location must include all aluminum impactors, no matter what the encounter velocity, as well as a significant number of substantially vaporized cosmic-dust impacts, judging by their frequency on the trailing edge. The fraction of natural versus debris impacts responsible for the indeterminate residues on the aluminum surfaces remains basically unknown.

Aluminum Particles On LDEF's Trailing Edge

This discussion takes off from the above suggestion that all orbital-debris projectiles are basically accounted for on the trailing edge. Based on projectile-size considerations (Figure 4), the flux of aluminum projectiles at 24 μm projectile diameter is approximately a factor of five higher on the trailing edge than that of "miscellaneous" debris. Assuming that this relative frequency also applies to the forward-facing A11 location, one could multiply the observed A11 miscellaneous-debris population >24 μm ($N=15/m^2/y$; Figure 4) by a factor of 5 to obtain the prospective number of (non-analyzable) aluminum impactors for the A11 tray. This results in a total of ~75 aluminum particles >24 $\mu m/m^2/y$ on the A11 surfaces. Note that Amari *et al.,* (ref. 20) found the small (<10 μm) particles on LDEF's leading edge to be dominated by aluminum impactors. Including the hypothetical (75) aluminum impactors, the total flux of particles >24 $\mu m/m^2$/year on the A11 CME surface is 124 (*i.e.,* 15 miscellaneous debris, 38 natural and 75 aluminum debris). This value essentially corresponds to the total number of craters observed on the A11 aluminum collectors and does not permit for any significant contribution by natural impactors to the indeterminate crater population. We concluded earlier that most of the indeterminate craters on the A03 gold surfaces should be due to natural impactors. These natural impactors should also be prominent on the A11 surface, if current models of particle dynamics in LEO (*e.g.,* refs. 2, 24 and 25).are applied. Relative to these models we are faced with the dilemma that the fluxes of specific particle classes, as deduced from the A03 gold surfaces, apparently do *not* produce enough craters on the A11 surface.

This previous statement is entirely based on current models which predict the relative fluxes of natural (ref. 2) and man-made (refs. 24 and 25) particles as a function of LDEF location, specifically the trailing- and leading-edge extrema. Our relative particle fluxes for the A03 gold surfaces do not seem to extrapolate within the context of these models to those observed on the A11 experiment. Without question, our inability to extract projectile compositions from ~50% of all CME craters substantially contributes to some of the apparent inconsistencies between our observations and the models. For this reason, none of the above statements should be construed as being overly critical of ongoing theoretical efforts. In contrast, we appreciate and totally subscribe to the iterative nature and approach in transforming the LDEF observations into a

generalized, theoretical understanding and framework. This is a difficult task and the observational database is presently incomplete.

The craters known to have resulted from orbital-debris particles that impacted the trailing-edge gold collectors did not possess the morphologies that would be expected from predominantly oblique (<45°), low-velocity (<2 km/s) impacts; such conditions should dominate for orbital-debris particle encountering the trailing edge (ref. 25). Such conditions should lead to relatively shallow, substantially elongated, elliptical craters for orbital-debris particles (refs. 34 and 35), which should differ systematically from those associated with natural impactors. However, this was not observed on the A03 gold surfaces. Those craters in which man-made residues were detected did not differ morphologically from those that were caused by natural impactors. Certainly not in systematic fashion that would reflect the dominantly oblique, low-velocity trajectories of man-made particles. Again, the observational (and experimental) database is presently insufficient to mandate revision of dynamic models, yet indications are that current observations and models appear at odds regarding the morphology of craters resulting from orbital-debris particle on LDEF's trailing edge.

Kessler (ref. 25) alludes to the principal difficulties and constraints in producing any debris hits on the trailing edge of a non-spinning spacecraft. The only reasonable sources must be in highly elliptical orbits of low to medium inclinations, typical for transfer vehicles of payloads to geosynchronous orbit. Such transfer vehicles are propelled by solid-fuel rocket motors, which is a know source of aluminum particles in LEO (refs. 17 and 36). The vast majority of Al_2O_3 spheres produced during test firings of solid-rocket motors of these vehicles are <5 μm in size, and even the largest particles do not exceed 10 μm in diameter (refs. 17 and 36). The aluminum is loaded into the fuel mixture as granular material, typically tens of microns in diameter, with 60-80 μm particles very common (Anderson, 2392, personal communications). Generally, rocket-exhaust products seem reasonable candidates for the smallest aluminum craters, yet not for those requiring projectiles >>10 μm in diameter, which is necessary to produce ~40% of all aluminum events on the gold surfaces. The latter may be associated with unburned fuels left after premature shut-down of IUS motors, or failure to ignite in the first place. If this unburned fuel were exposed to space, differential erosion could readily produce free-flying metallic aluminum particles.

While we cannot be sure that this suggestion is valid, our point here is that the aluminum projectiles experienced by LDEF's trailing edge are not necessarily the result of collisionally or explosively fragmented structural components; solid-rocket fuels are possibly a substantial source of aluminum particles. Improved understanding of production mechanisms for orbital debris is needed to evaluate the relative roles of catastrophic comminution versus other processes so that improved calculations of the number of parent satellites responsible for the current debris environment in high-eccentricity orbits are possible (ref. 25). In addition, many paint flakes may not necessarily be derived from catastrophically destroyed satellites, but could be the spall products of numerous micro-impacts, even more so if radiation, thermal and atomic oxygen effects combine to render structurally weakened and degraded paint layers. The nature and potential role of mechanisms other than collisional and explosive fragmentation seem important in reconstructing the possible number of part satellites involved (ref. 25).

SUMMARY

We analyzed ~600 individual craters in aluminum and gold plates exposed on LDEF's forward-facing and trailing edges for traces of projectile residues. Approximately 50% of these craters did not yield analyzable residue because shock stresses approached, or exceeded vaporization thresholds, and because aluminum projectiles cannot be detected on the aluminum collectors. Of those craters possessing analyzable residues, ~70% resulted from natural impactors, among which chondritic compositions dominate, followed by mafic silicates and Fe-Ni rich sulfides. The modal proportions of the various natural dust-grain subclasses are approximately the same for the trailing-edge and leading-edge directions, which in turn suggests that the natural dust environment is compositionally homogeneous.

Metallic or oxidized aluminum particles impinged on the trailing edge of the non-spinning LDEF with unexpected frequency (ref. 24), a finding that precipitated detailed examination of high-eccentricity/low-inclination transfer vehicles to geosynchronous orbits (ref. 25). We suggest additional investigations of these aluminum-containing craters to determine whether oxidized or metallic impactors were involved, thus refining our understanding of the source mechanisms of this aluminum.

We also demonstrated that extreme care is necessary when addressing the relative frequency of natural versus man-made particles, or any of their compositional subgroups. It is important to rigorously differentiate between crater-production rates and actual particle fluxes (*i.e.,* between crater size and projectile size). The latter relate to each other, in large measure, by impact velocities, which differ substantially between natural and orbital-debris populations such that seemingly contradicting conclusions can be drawn, depending whether one refers to crater or projectile size.

Clearly, additional craters will have to be analyzed from the remaining aluminum collectors to improve the compositional-frequency statistics for the forward-facing collectors. In addition, more sensitive methods (*i.e.,* SIMS) will have to be applied to the currently indeterminate residues to obtain a more complete inventory of all particles. While we interpreted the unknown craters to be a velocity biased set, other biasing mechanisms may contribute as well. Recent calculations regarding the astrophysical source objects for interplanetary dust in near-Earth space suggest that cometary sources may have systematically higher encounter velocities than asteroidal sources (refs. 22 and 23). Attempts at extracting compositional information from a set of craters, presumably characterized by high encounter velocities, may be particularly rewarding as they could be residues of cometary particles.

ACKNOWLEDGMENTS

We appreciate many useful discussions with D. Brownlee, D. McKay, C. Simon, R. Peterson, M. Zolensky, and H. Zook, and the skillful contributions to sample preparation by W.

Davidson, K. Mack and J. Warren. We are grateful to M. Cintala and D. Kessler for making some of their computational results available to this study, and to H. Zook, E. Zinner and C. Simon for constructive reviews of this manuscript.

REFERENCES

1) Hörz, F., Bernhard, R.P., Warren, J., See, T.H., Brownlee, D.E., Laurance, M.R., Messenger, R., and Peterson, R.P. (2391) Preliminary Analysis of LDEF Instrument A0-231-1 Chemistry of Micrometeoroids Experiment", *LDEF - 69 Months in Space, First Post-Retrieval Symposium, NASA CP-2434*, p. 487-501.

2) Zook, H. A. (2391) Deriving the Velocity Distribution of Meteoroids from The Measured Meteoroid Impact Directionality on the Various LDEF Surfaces, *LDEF - 69 Months in Space, First Post-Retrieval Symposium, NASA CP-2434,* p. 569-579.

3) Dursch, H. (2391) Personal Communication and formal memorandum detailing the Findings Of The LDEF Systems SIG Regarding the On-Orbit Performance of the Active CME Instrument.

4) Zolensky, M.E. ed. (2390), Particles from Collection Flag L2405, *Cosmic Dust Catalog, 11, 1, JSC # 24461-SN-83,* pp. 170.

5) Brownlee, D.E. (2385) Cosmic Dust: Collection and Research, *Ann. Rev. Earth. Planet. Sci., 13,* p.134-150.

6) Warren, J.L. and 10 co-authors, (2389) The Detection and Observation of Meteoroid and Space Debris Impact Features on the Solar Max Satellite, *Proc. Lunar Planet. Sci. Conf., 23th*, p. 641-657.

7) Rietmeijer, F.J.M., Schramm, L. Barrett, R.A., McKay, D.S., and Zook, H.A. (2386) An Inadvertent Capture Cell for the Orbital Debris and Micrometeoroids; the Main Electronic Box Thermal Blanket of the Solar Maximum Satellite, *Adv. Space Res., 6,* p. 145-149.

8) Bernhard, R.P. (2390) *Impact Features on Returned Palapa Hardware*, Internal NASA Report.

9) Mullholland, J.D. and 8 co-authors (2391) IDE Spatio-Temporal Fluxes and High Time-Resolution Studies of Multi-Impact Events and Long-Lived Debris Clouds, *LDEF - 69 Months in Space, First Post-Retrieval Symposium, NASA CP-2434,* p. 517-532.

10) McDonnell, J.A.M. and Sullivan, K. (2391) Dynamic (Computer) Modeling of the Particulate Environment: Transformations from the LDEF Reference Frame to Decode Geocentric and Interplanetary Populations, *LDEF - 69 Months in Space, First Post-Retrieval Symposium, NASA CP-2434,* p. 565-566.

11) Humes, D.H. (2391) Large Craters on the Meteoroid and Space Debris Impact Experiment, *LDEF - 69 Months in Space, First Post-Retrieval Symposium, NASA CP-2434,* p. 399-422.

12) See, T.H., Allbrooks, M., Atkinson, D., Simon, C. and Zolensky, M. (2390) *Meteoroid and Debris Impact Features Documented on the Long Duration Exposure Facility: A Preliminary Report*, NASA - Johnson Space Center Publication # 24608, pp. 583.

13) Crutcher, E.R., Nishimura, L.S., Warber, K.J., and Wascher, W.W. (2391) Migration and Generation of Contaminants from Launch Through Recovery: LDEF Case History, *LDEF - 69 Months in Space, First Post-Retrieval Symposium, NASA CP-2434,* p.125-140.

14) Schaal, R.B., Hörz, F., Thompson, T.D. and Bauer, J.F. (2379) Shock Metamorphism of Granulated Lunar Basalt, *Proc. Lunar Planet. Sci. Conf., 10th*, p. 2547-2571.

15) Stöffler, D. (2372) Deformation and Transformation of Rock-Forming Minerals by Natural and Experimental Shock Processes; Behavior of Minerals under Shock Compression, *Fortschr. Mineral., 49*, p. 50-113.

16) Bernhard, R.P. and Hörz, F. (2392) Compositional Analysis and Classification of Projectile Residues in LDEF Impact Craters, *NASA TM, 104750,* pp. 250.

17) Girata, P.T., W.K.McGregor, and Quinn, R. (2381), *Arnold Air Force Station, Tennessee, Report AEDC-TMR-E55, 2381,* pp. 25.

18) Amari, S., Foote, J., Simon, C., Swan, P., Walker, R.M. , Zinner, E., Jessberger, E.K., Lange, G. and Stadermann, F. (2391) SIMS Chemical Analysis of Extended Impact Features from the Trailing Edge Portion of Experiment A0231-2, *LDEF - 69 Months in Space, First Post-Retrieval Symposium, NASA CP-2434,* p. 503-516.

19) Mandeville, J.C. and Borg, J. (1991) Study of Dust Particles On-Board LDEF: The FRECOPA Experiments A0138-1 and A0138-2, *LDEF 69 Months in Space, First Post - Retrieval Symposium, NASA CP, 2434,* p. 423-434.

20) Amari, S., Foote, J. Swan, P., Walker, R.M., Zinner, E., and Lange, G. (1993) SIMS Chemical Analysis of Extended Impacts in the Leading and Trailing Edges of LDEF Experiment A0231-2, *LDEF - 69 Months in Space, Second Post-Retrieval Symposium, NASA CP-*3194, 1993.

21) Simon, C.G., Hunter, J.L., Griffis, D.P., Misra, V., Ricks, D.A., Wortmann, J.J., and Brownlee, D.E. (1993) Elemental Analyses of Hypervelocity Microparticle Impact Sites on Interplanetary Dust Experiment Sensor Surfaces, *LDEF - 69 Months in Space, Second Post-Retrieval Symposium, NASA CP-*3194, 1993.

22) Dermott, S.F., Gomes, R.S., Durda, D.D., Gustafson, B.A.S., Jayaraman, S., Xu, Y.L., and Nicholson, P.D. (1992) Dynamics of the Zodiacal Cloud, in *Chaos, Resonance, and Collective Dynamical Phenomena in the Solar System*, S.Ferraz-Mello, ed., Kluwer Academic Publishers, Dordrecht, p. 333-347.

23) Jackson, A.A. and Zook, H.A. (1992) Orbital Evolution of Dust Particles from Comets and Asteroids, *Icarus, 97,* p.70-84.

24) Kessler, D.J, Reynolds, RC. and Anz-Meador, P.D. (2388) *Orbital Debris Environment for Spacecraft Designed to Operate in Low Earth Orbit, NASA TM-100-471*, April 2388.

25) Kessler, D. J. (1992) Origin of Orbital Debris Impacts on Long Duration Exposure Facility's (LDEF) Trailing Surfaces (abstract), *Second LDEF Post-Retrieval Symposium Abstracts*, p. 53.

26) F. Hörz (editor) (1990) *Cosmic Dust Collection Facility: Scientific Objectives and Programmatic Relations*, NASA Technical Memorandum #102560, p. 23.

27) Cour-Palais, B.G. (2387) Hypervelocity Impacts into Metals, Glass, and Composites, *Int. J. Imp. Eng., 5*, p. 225-237.

28) Marsh, S.P., ed. (2380) LASL Shock Hugoniot Data, University of California Press, pp. 658.

29) Cintala, M. J. (1992) Impact-Induced Thermal Effects in the Lunar and Mercurian Regoliths, *J. Geophys. Res., 97,* p. 947-973.

30) Ahrens, T.J. and O'Keefe, J.D.(2376) , Equations of State and Impact-Induced Shock Wave Attenuation on the Moon, in *Impact and Explosion Cratering,* Roddy *et al.*, eds., Pergamon Press, New York, p. 639-656.

31) Kieffer, S.W.(2371) Shock Metamorphism of the Coconino Sandstone at Meteor Crater, Arizona, *J. Geophys. Res., 76,* p. 5449-5473.

32) Ahrens, T.J. and Cole, D.M. (2374) Shock Compression and Adiabatic Release of Lunar Fines from Apollo 17, *Proc. Lunar Sci. Conf., 5th,* p. 2333-2345.

33) Coombs, C., Watts, A., Wagner, J., and Atkinson, D. (1993) LDEF Data: Comparison with Existing Models, *LDEF - 69 Months in Space, Second Post-Retrieval Symposium, NASA CP-* 3194, 1993.

34) Gault, D. E. (2373) Displaced Mass, Depth, Diameter and Effects of Oblique Trajectories for Impact Craters Formed in Dense Crystalline Rock , *The Moon , 6*, p. 25-44.

35) Herrmann, W. and Wilbeck, J.S. (2387) Review of Hypervelocity Penetration Theories, *Int. J. Impact Engn, 5*. p. 237-252.

36) VerPloeg, K.L. and McKay, D.S. (2389) Impacts on Shuttle Orbiter Caused by the Firing of a PAM D2 Solid Rocket: Results of the STS61B Plume Witness Plate Experiment. NASA Report on Orbital Debris.

ASTEROIDAL VERSUS COMETARY METEOROID IMPACTS ON THE LONG DURATION EXPOSURE FACILITY (LDEF)

Herbert A. Zook
NASA Johnson Space Center
Houston, TX 77058
Phone: 713/483-5058; Fax: 713/483-5276

ABSTRACT

Meteoroids that enter the Earth's atmosphere at low velocities will tend to impact the apex side (that surface facing the spacecraft direction of motion) of a spacecraft at a very high rate compared to the rate with which they will impact an antapex-facing surface. This ratio--apex to antapex impact rates--will become less as meteoroid entry velocities increase. The measured ration, apex to antapex, for 500 micron diameter impact craters in 6061-T6 aluminum on LDEF seems to be about 20 from the work of the meteoroid SIG group and from the work of Humes that was presented at the first LDEF symposium. Such a ratio is more consistent with the meteoroid velocity distributions derived by Erickson and by Kessler, than it is with others that have been tested. These meteoroid velocity distributions have mean entry velocities into the Earth's atmosphere of 16.5 to 16.9 km/s.

Jackson and Zook (in a paper submitted to Icarus) have numerically simulated the orbital evolution of small dust grains emitted from asteroids and comets. For those asteroidal grains small enough (below about 100 microns diameter) to drift from the asteroid belt to the orbit of the Earth, under P-R and solar wind drag, without suffering collisional destruction, the following results are found: as their ascending or descending nodes cross the Earth's orbit (and when they might collide with the Earth), their orbital eccentricities and inclinations are quite low ($e < 0.3$, $i < 20^\circ$), and their mean velocity with respect to the Earth is about 5 or 6 km/s. When gravitational acceleration of the Earth is taken into account, the corresponding mean velocities relative to the top of the Earth's atmosphere are 12 to 13 km/s. This means that, at best, these small asteroidal particles cannot comprise more than 50% of the particles entering the Earth's atmosphere. And when gravitational focusing is considered, they cannot comprise more than a few percent of those in heliocentric orbit at 1 AU. The rest are presumably of cometary origin.

INTERPLANETARY METEOROID DEBRIS IN LDEF METAL CRATERS

D.E. Brownlee
Dept. of Astronomy
University of Washington
Seattle, WA 98195
Phone: 206/543-8575, FAX: 685-0403

D. Joswiak
Dept. of Astronomy
University of Washington
Seattle, WA 98195
Phone: 206/543-8575, FAX: 685-0403

J. Bradley
MVA. Inc.
5500 Oakbrook Parkway No. 200
Norcross, GA 30093
Phone 404/6628532, FAX 662-8509

F. Horz
NASA Johnson Space Center
Houston, TX 77058
Phone: 713/483-5042, FAX 483-5347

SUMMARY

We have examined craters in Al and Au LDEF surfaces to determine the nature of meteoroid residue in the rare cases where projectile material is abundantly preserved in the crater floor. Typical craters contain only small amounts of residue and we find that less than 10% of the craters in Al have retained abundant residue consistent with survival of a significant fraction (>20%) of the projectile mass. The residue-rich craters can usually be distinguished optically because their interiors are darker than ones with little or no apparent projectile debris. The character of the meteoroid debris in these craters ranges from thin glass liners, to thick vesicular glass containing unmelted mineral fragments, to debris dominated by unmelted mineral fragments. In the best cases of meteoroid survival, unmelted mineral fragments preserve both information on projectile mineralogy as well as other properties such as nuclear tracks caused by solar flare irradiation. The wide range of the observed abundance and alteration state of projectile residue is most probably due to differences in impact velocity. The crater liners are being studied to determine the composition of meteoroids reaching the Earth. The compositional types most commonly seen in the craters are: A) chondritic (Mg,Si,S,Fe in approximately solar proportions), B) Mg silicate and C) iron sulfide. These are also the most common compositional types for extraterrestrial particle types collected in the stratosphere. The correlation between these compositions indicates that

vapor fractionation was not a major process influencing residue composition in these craters. Although the biases involved with finding analyzable meteoroid debris in metal craters differ from those for extraterrestrial particles collected in and below the atmosphere, there is a common bias favoring particles with low entry velocity. For craters this is very strong and probably all of the metal craters with abundant residue were caused by asteroidal dust impacting at minimum velocities.

INTRODUCTION

The systematic study by Bernhard et al., 1993 has demonstrated that approximately half of the craters in pure Al and Au contain detectable projectile residue. In our SEM study of >200 craters in pure Al we have found that in the majority of cases the residue consists of small patchy deposits representing at most only a few percent of the projectile mass. In the majority of cases the projectile is either almost entirely vaporized or ejected from the crater. In rare craters however, large amounts of residue survive in the crater. These craters are easily identified in the SEM and in most cases they can be identified optically because their interiors are darker than the typical craters that have smooth walls and are nearly devoid of residual projectile. In this study we have concentrated on the craters with abundant residue because they can be studied in detail to provide information on composition, mineralogy and other projectile properties. Because a significant fraction of the projectile remains in the crater it is expected that the surviving residue is a reasonably representative projectile sample. In the more common case where only trace amounts of the projectile survive, the residue may not be representative. Laboratory studies of collected interplanetary dust samples have shown them to be highly heterogeneous at the micron scale. The sparse distribution of residue in typical craters also complicates the general analysis problem due to the combined effects of crater geometry and dilution of the small signal from the residue with the substrate material.

RESIDUE TYPES

The extraterrestrial meteoroid residue found lining craters in LDEF aluminum is highly variable in both quantity and type. We observed the following sequence of natural meteoroid residue types that in broad terms represents decreasing modification of original projectile properties. The frequency of occurrence of the types decreases downwards in the list but the relative amount of residue retained in a crater tends to increase.

- No residue
- Thin glass
- Thicker glass sometimes vesicular with metal beads
- Vesicular glass with some unmelted mineral fragments
- Unmelted mineral fragments on crater bottom

The most common craters are smooth bottomed and contain either no or only trace amounts of residue detectable by SEM-EDX techniques. Figure 1 shows a SEM photo of a 150 μm crater in Al that contains moderate to trace amounts of chondritic composition projectile material. In approximately 10% of the craters, residue occurs that is both common on the crater floor or wall and thick enough (>0.5μm) to give reasonably strong EDX spectra. Usually this material is a mixture of glass and either Fe metal or sulfide

beads. In some cases the glass is highly vesicular but there is a complete range in porosity. The degree of vesicularity is presumably determined by heating and the abundance of volatile compounds in the projectiles.

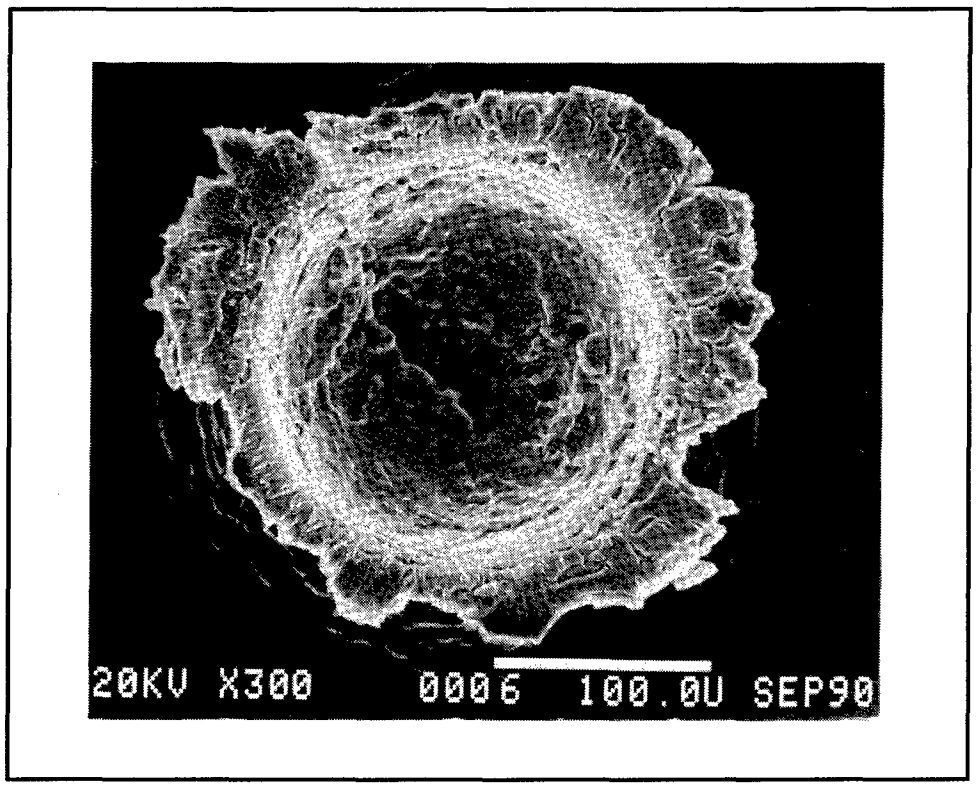


Figure 1 SEM photo of a 150μm crater that contains a moderate to trace amount of melted chondritic meteoroid lining the crater floor.

By direct SEM analysis of a crater it is usually not possible to quantitatively determine the amount or composition of the residue. Major complications with quantitative EDX analysis are the unknown thickness of the residue and its relationship with the substrate metal. Correction for absorption and other effects to quantify the x-ray spectra requires knowledge of the geometry and mixing of the projectile and target. For several craters we have made 0.1 μm microtome sections through the glass/metal interface and in these cases the sample geometry does allow accurate analysis but only for the regions within the section. EDX analysis of the sections in the transmission electron microscope can give excellent analyses using standard thin film correction techniques. This works well for some craters but for those where the liner is inhomogenous and sparsely distributed, a truly representative analysis is not practical even with microtome sections. A representative analysis would require an impractically large number of sections.

Metallic spherules. In the glass-bearing craters that were sectioned, the projectile melt was a discrete liner composed of a mixture of silicate projectile melt and substrate aluminum. (Figures 2 and 3). These crater liners are dominated by a Mg,Fe silicate glass that contains high but variable amounts of Al from the substrate. For Al to enter the silicate glass it must oxidize and it is apparent that redox reactions occur during the impacts in-spite of the short time scales involved. Metallic Fe and FeNi beads are commonly seen in the glass (Figure 2) and it is likely that some of these were formed by reduction. FeS beads are observed in some craters. Analogous to thermite reactions it appears that some of the aluminum target oxidized during the impact while some of the FeO in the projectile was reduced to form metal beads

ranging in size from 10 nm to 1 μm . There are two populations of metal beads, one that has meteoritic Ni levels and one that appears to be Ni free. The Ni-bearing metal may be original metal melted and shock dispersed while the pure Fe droplets may be formed by in-situ reduction. The FeNi metal beads are amorphous presumably to very rapid quenching rates.



Figure 2 SEM photo of vesicular silicate glass liner that contains numerous FeNi and FeS beads.

Unmelted Meteoroid Fragments. In rare cases we observed large amounts of unmelted mineral grains in the crater floors (Figures 4 and 5). Although our data set on these craters is not large it appears that an abnormally high fraction of these craters were produced by projectiles dominated by forsterite (Mg_2SiO_4) and enstatite ($MgSiO_3$). These phases have melting points of 1890 C and 1557 C, respectively, and it is likely that their high melting points played a role in their preservation. High melting point is not an exclusive requirement for survival of unmelted mineral fragments because relatively large iron sulfide grains are seen in some craters (Figure 4). It is extraordinary that unmelted mineral grains survive in some of the hypervelocity impacts into solid Al and Au targets. Although fragmented to micron size during the impact, they contain many of their original properties. Solar flare tracks have been seen in fragments in some of the craters (Figure 6). These linear defects caused by Fe group cosmic rays provide information on the cosmic ray lifetimes of the projectiles and also provide insight into shock and thermal modification during cratering. Tracks usually anneal and are erased when samples are heated to temperatures above 600 C. The survival of tracks suggests that noble gasses are probably also retained in the fragments.

THE ORIGIN OF METEOROIDS PRODUCING RESIDUE-RICH CRATERS

The survival of unmelted mineral fragments and the general retention of significant amounts of residual projectile material are most probably the results of low velocity impact. Calculations by Bernhard et al., 1993 indicate that plausibly low impact velocities on LDEF can limit shock heating effects to the pressure regime where some solid mineral grains can survive intact. The craters with abundant natural meteoroid residue and particularly those with unmelted mineral grains are a highly selected subset of meteoroids that approach the Earth at minimal velocity and with favorable orbital parameters to minimize impact velocity. Because asteroidal particles approach the Earth with relatively low velocity (Flynn, 1990) it is likely that all of the craters with abundant residue are exclusively asteroidal in origin.

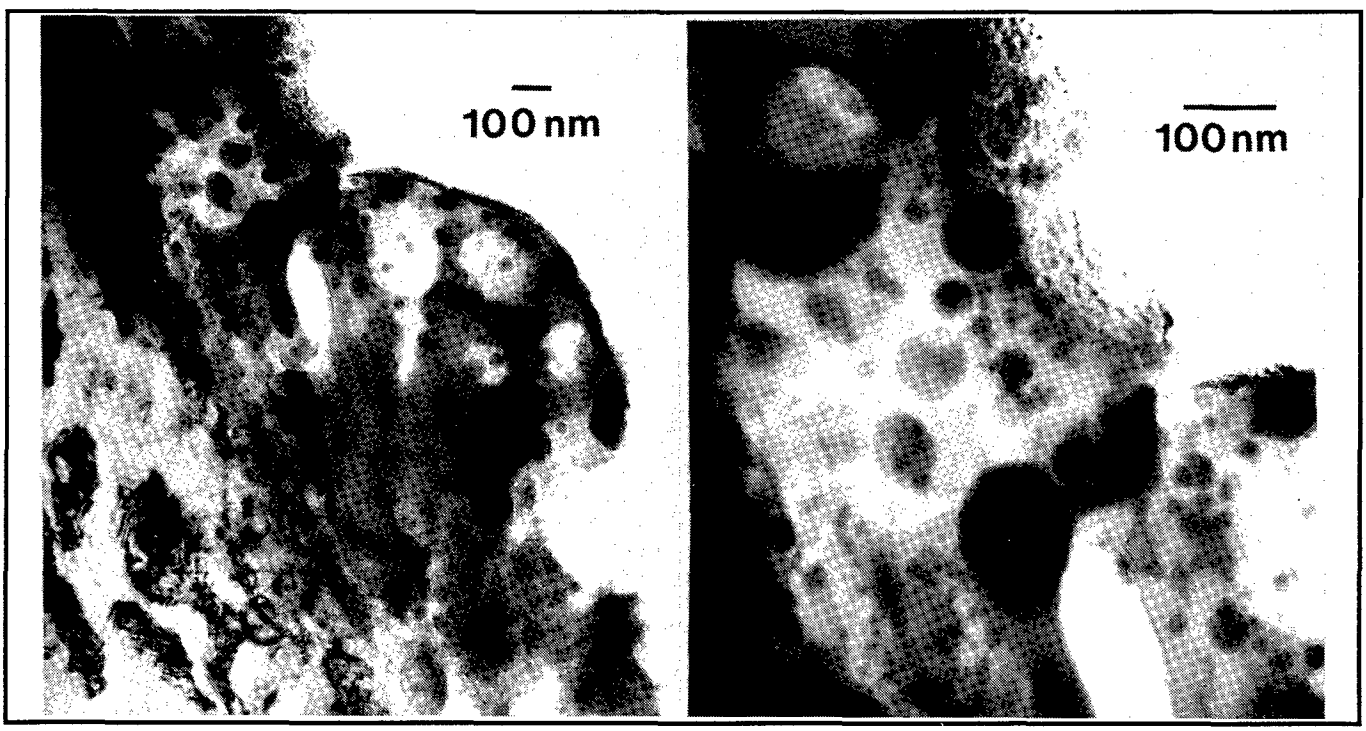


Figure 3 Transmission image of 0.1μm microtome section of chondritic meteoroid residue on pure aluminum from experiment A0187-1. The lower magnification image on the left shows the vesicular silicate glass with imbedded FeNi spherules. The contact between the glass and the underlying aluminum is only 0.1μm thick and is seen as a diagonal line from the upper left to the bottom center of the image. The higher magnification image on the right shows details of the 5nm to 100nm amorphous metal beads inside the glass projectile residue.

CONCLUSIONS

Rare craters in pure aluminum and gold on LDEF contain substantial amounts of projectile material occurring as melted and unmelted debris. These samples provide excellent material for determining the nature of the natural meteoroids impacting LDEF. If residue retention is strongly dependent on impact velocity, then these residue-rich craters were made by a highly selected subset of meteoroids whose orbital parameters yielded low encounter velocities with LDEF probably in the 5-10 km s^{-1} range. Even though the collection is selective, the LDEF metal craters show that it is possible to collect natural meteoroids from Earth orbiting platforms. Only a small fraction of the LDEF metal craters contain abundant residue but the results are highly suggestive that other materials specifically designed to reduce the shock pressure during impact could provide effective capture over a broad velocity range. Silica aerogel and other such low density capture media may provide extraordinary capabilities for future direct capture of hypervelocity meteoroids.

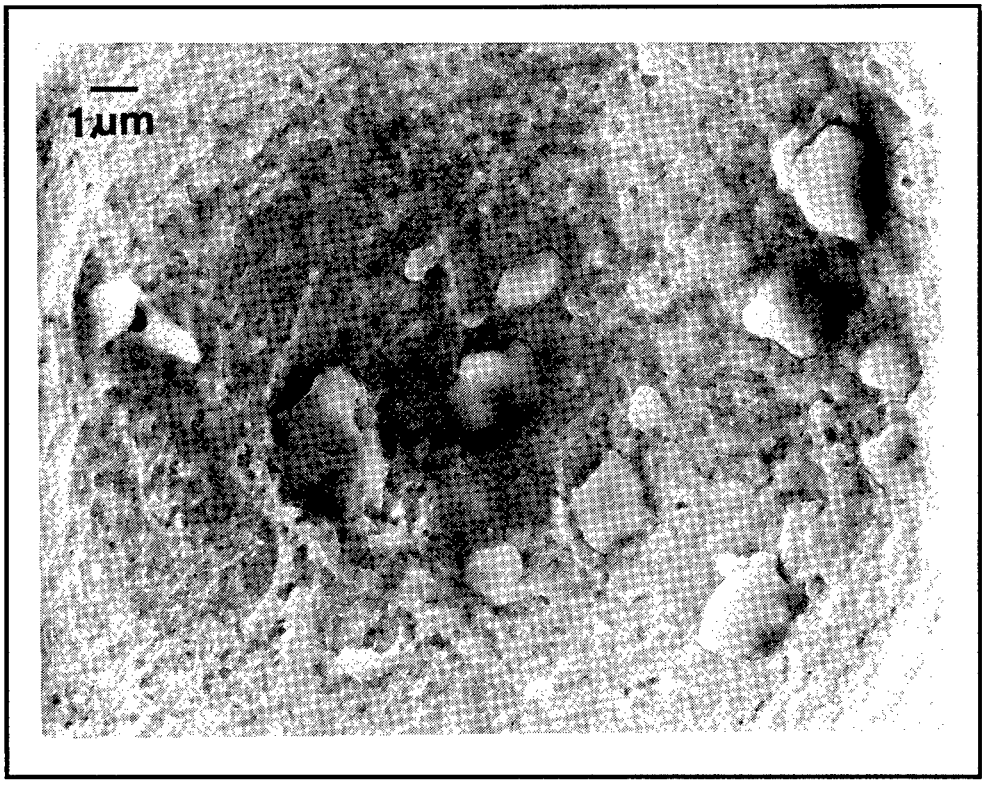


Figure 4 Glass and micron-sized unmelted FeS grains lining the base of a crater in pure Au.

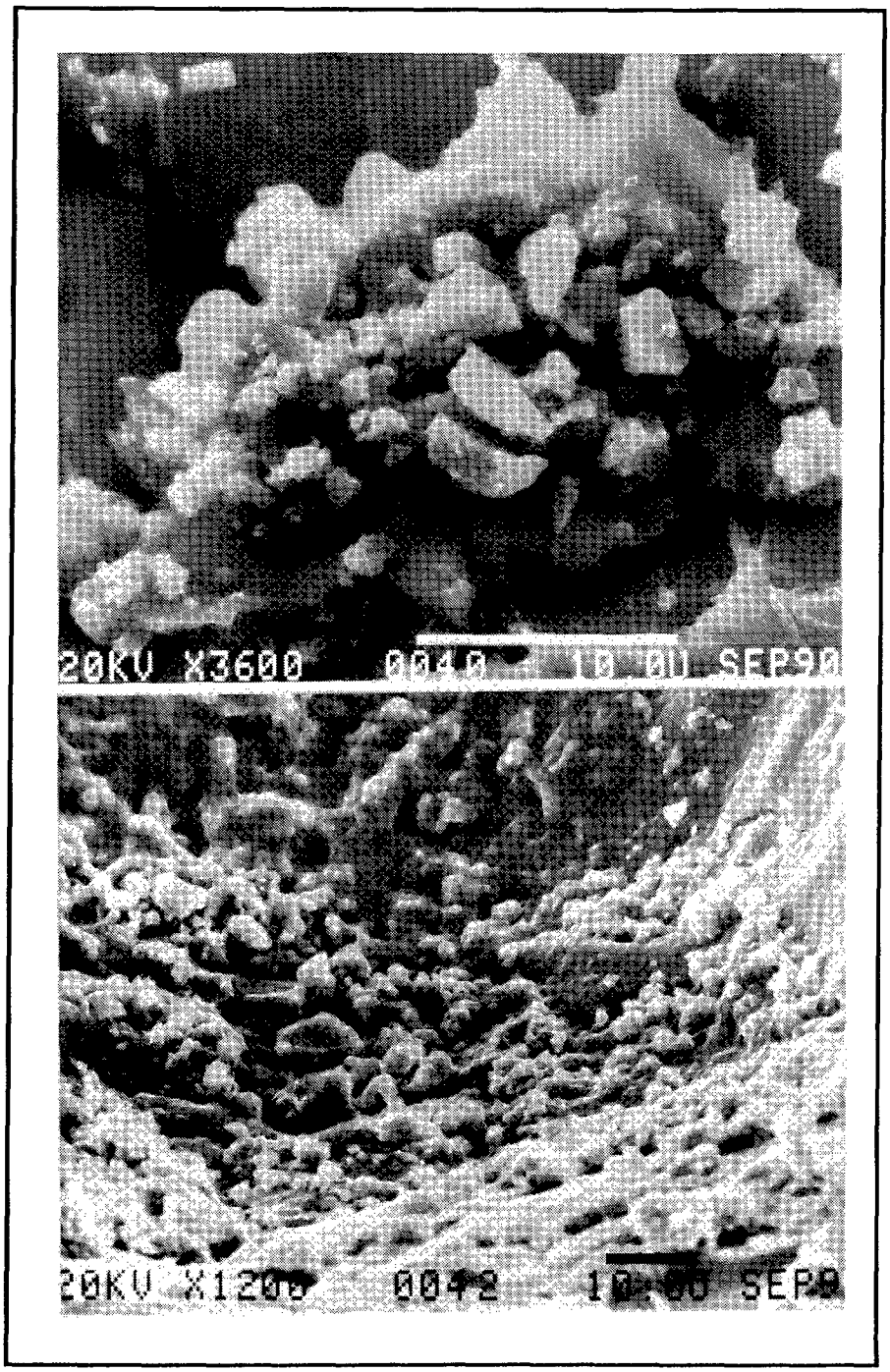


Figure 5 Micron-sized fragments of $MgSiO_3$ and Mg_2SiO_4 lining the walls of crater .in pure LDEF aluminum (Exp A0187-1). Some glass, sulfides and other materials exist in these craters.

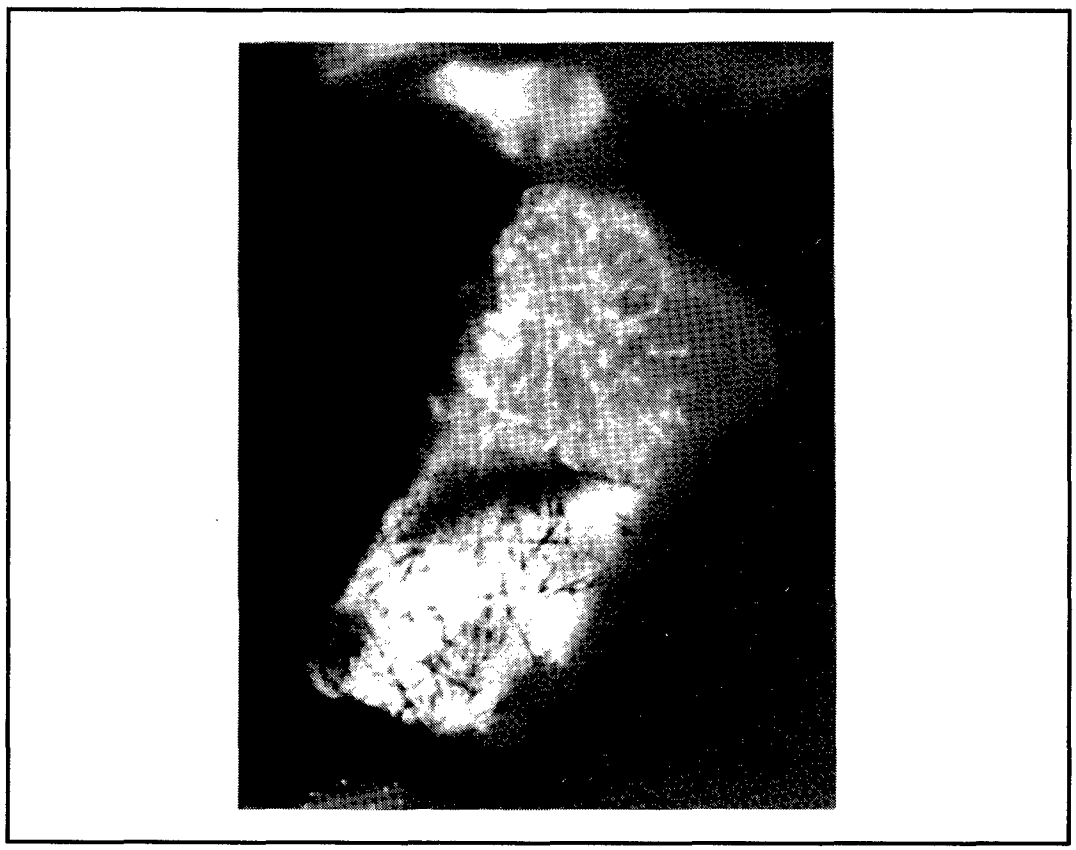


Figure 6 Solar flare tracks in a 0.3μm long anorthite grain extracted from the bottom crater in Figure 5. The tracks are imaged in both darkfield and bright field conditions in the transmission electron microscope. Many of the grains extracted from this crater are track-rich indicating an unshielded exposure to solar cosmic rays for >10,000 years. The preservation of tracks implies only moderate alteration during the cratering event with peak heating not significantly above the track erasure temperature of 600 C.

Acknowledgments: We gratefully acknowledge the skill and efforts of Anna Teetsov of McCrone Associates in extracting unmelted meteoroid residue from LDEF craters.

REFERENCES

Bernhard, R.P., See, T.H., and Horz, F., Projectile chemistry and modal frequency on "CME" LDEF experiment, Second LDEF Post-Retrieval Symposium, NASA CP-3194, 1993.

Flynn, G. The Near-Earth enhancement of asteroidal over cometary dust, Proc. of the 20th Lunar and Planet. Sci. Conf. 363-371, Lunar Planetary Institute, Houston, 1990.

ORIGIN OF ORBITAL DEBRIS IMPACTS ON LDEF'S TRAILING SURFACES

Donald J. Kessler
NASA Johnson Space Center
Houston, TX 77058
Phone: 713/483-5313, Fax 713/483-5276

SUMMARY

A model was developed to determine the origin of orbital debris impacts measured on the trailing surfaces of LDEF. The model calculates the expected debris impact crater distribution around LDEF as a function of debris orbital parameters. The results show that only highly elliptical, low inclination orbits could be responsible for these impacts. The most common objects left in this type of orbit are orbital transfer stages used by the U.S. and ESA to place payloads into geosynchronous orbit. Objects in this type of orbit are difficult to catalogue by the US Space Command; consequently there are independent reasons to believe that the catalogue does not adequately represent this population. This analysis concludes that the relative number of catalogued objects with highly elliptical, low inclination orbits must be increased by a factor of 20 to be consistent with the LDEF data.

INTRODUCTION

Most of the man-made objects in low Earth orbit that are tracked and catalogued by the US Space Command are in near circular orbits. The number of objects in elliptical orbits are so few that models which describe the directional properties of orbital debris generally assume that all orbits are circular. Such an assumption leads to the conclusion that orbital debris will not impact the trailing surfaces of other spacecraft in circular orbits (ref. 1).

However, objects in elliptical orbits, especially those with low inclinations, are more difficult to detect and catalogue than objects in circular orbit. This is because elliptical orbits spend a smaller fraction of their time at low altitudes where ground based sensors can detect them, and there are fewer ground based sensors located to detect low inclination orbits. Consequently, the US Space Command catalogue is not likely to be representative of the various orbit classes of large objects. This lack of representation of elliptical orbits by the catalogue is likely to increase with decreasing orbital debris size. The orbital lifetime of small debris in circular orbits at low altitudes is much shorter than elliptical orbits. Calculations of collision probabilities integrated over these lifetimes lead to a prediction that orbital debris in elliptical orbits could be important to impacts on spacecraft at low altitudes (ref. 2).

The "Chemistry of Micrometeoroids Experiment" located on LDEF bay A03 has found a significant fraction of the impacts on a trailing surface to be of orbital debris origin (ref. 3). The

purpose of this paper is to determine in more detail the types and relative contributions of orbits responsible for these impacts, and the implications to impacts on other LDEF surfaces. This will be accomplished by using collision probability theory to calculate the expected impact crater distribution around LDEF for various types of orbital debris orbits. This expected impact crater distribution is then compared with that observed on LDEF.

FUNDAMENTAL LDEF DATA AND ASSUMPTIONS

Parts of two sets of LDEF data will be used here: The results of chemical analysis of the Chemistry of Micrometeoroids Experiment (CME) given in references 3 and 4, and the flux as a function of direction around LDEF as measured by the Space Debris Impact Experiment and reported in reference 5. The following is a brief summary of that data and the assumptions used in this paper concerning that data.

In analysis completed on the CME, 15% of the impacts on the experiment's rear located gold surface (location A03) was determined to be man-made, 29% was determined to be meteoroid, and 56% had no residue, so their source is unknown. The planned rear locations were actually facing 172 degrees from the spacecraft orbital velocity vector. For the purpose of this paper, all of the impacts into gold which had no residue will be assumed to be the results of meteoroid impacts. This would seem to be a valid assumption because all debris impacts on the rear surface would be at a much lower velocity than most meteoroid impacts. High velocity impacts into a dense material like gold are more likely to cause vaporization, leaving no residue in the surface. About 80% of the man-made impacts contained only aluminum. The remaining 20% of non-aluminum impacts represents a small sample of 5, and although it may not be statistically significant, only one of those 5 was paint.

Analysis of the CME aluminum surface (location A11) has concluded that 17% of the impacts are non-aluminum man-made, 39% was determined to be meteoroids, and 44% had no residue or the residue was aluminum. The lower density of the aluminum surface would suggest that vaporization is less likely to occur on these surfaces than the gold surface. Consequently, meteoroid impacts are more likely to be identified than impacts on the gold surface. This would suggest that the residue was aluminum in some fraction of the pits where no residue could be identified. As will be shown, any orbiting source which impacts the gold surface has an even greater chance of impacting the aluminum surface. So, some of the unidentified impacts into aluminum should be expected to be aluminum. If one assumes the same ratio of aluminum to non-aluminum impacts on the aluminum surfaces as was measured on the gold surfaces, one would expect more than the 44% of the unidentified pits to be man-made aluminum impacts.

However, the orbital debris impacts on the aluminum surface appear to have a different character than on the impacts on the gold surface: 57% of the orbital debris impacts on the aluminum surface are paint. This could suggest different types of orbits for orbiting paint flecks. In addition, the limiting threshold size on the gold surfaces is smaller than on the aluminum surfaces, and a larger fraction of the smaller pits are aluminum. This may also represent a different source of small aluminum pits, aluminum oxide dust from solid rocket motors. If only pits that are 30 microns and

larger are counted, the orbital debris flux is reduced to 11% of the total number of impacts on the gold surface. In addition, if paint is subtracted out from both the gold and aluminum surfaces, and only pits that are 30 microns and larger are used, then the ratio of aluminum to non-aluminum, non-paint on the gold surfaces is about 4. If this same ratio is expected on the aluminum surfaces, then 29% of the impacts on the aluminum surface could be expected to be aluminum. This would mean that about 66% of the pits where no residue could be found were aluminum impacts into aluminum, and that the number of orbital debris impacts on this surface was 46% of the total number of impacts. An orbital debris flux which is 46% of the total flux on the CME aluminum surface will be adopted in this paper.

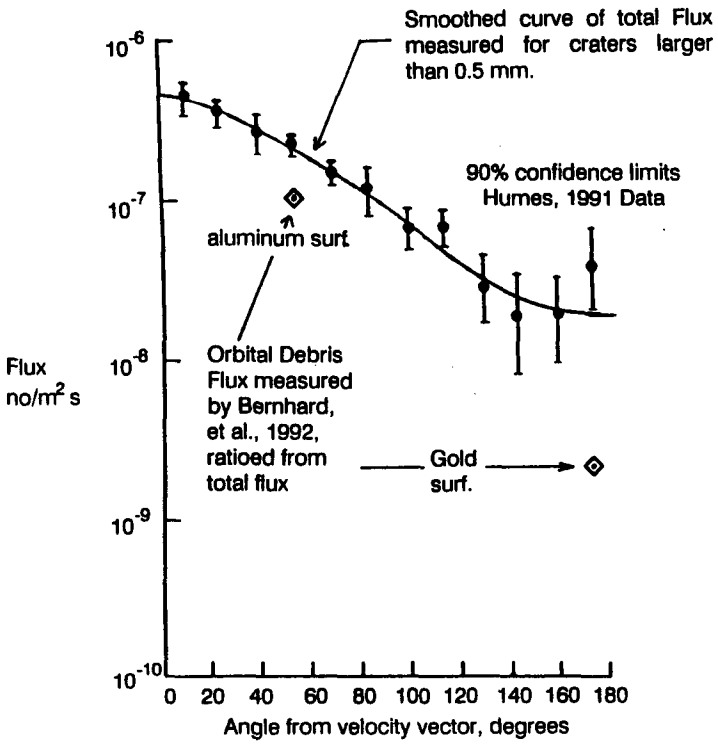


Figure 1. LDEF data used.

The total measured flux on LDEF of impacts craters larger than 0.5 mm as a function of the surface direction (i.e., the angle between the surface normal vector and the orbital velocity vector) is shown in figure 1 (ref. 5). The assumption is made that the smoothed curve also shown is representative of the actual distribution, and that departures from the curve are statistical fluctuations in the data. This assumption seems justified given the error bars, the smoothing effect of similar data in reference 6, and the fact that there is no theoretical reason for a large change in flux on both adjacent surfaces.

Also shown in figure 1 are the CME data points obtained by taking 11% of the total measured flux on the LDEF row 03 (surface direction of 172 degrees), and 46% of the total measured flux on row 11 (surface direction of 52 degrees). By taking these percentages, the assumption is made that the chemistry and frequency of orbital debris in the smaller size range of 0.03 mm craters and larger into gold is also characteristic of 0.5 mm craters and larger into aluminum. A sufficiently large data base containing the chemistry of impact craters larger than 0.5 mm does not yet exist to test this assumption. However, it is apparent that for craters smaller than 0.03 mm, both the chemistry and

frequency of orbital debris do change. Although the statistics are still poor, the CME shows increased aluminum impacts for these smaller sizes. In addition, both the Microabrasion Foil Experiment (ref. 7) and the Interplanetary Dust Experiment (ref. 8) have shown an Earth orbiting population which dominates the meteoroid flux for particle sizes of the order of 1 micron and smaller. Ground observations by the Goldstone (ref. 9) and Haystack (ref. 10) radar measure an orbital debris environment larger than 2 mm which exceeds the meteoroid environment; consequently, there is sufficient data to know that the assumption is not valid over larger size ranges. How inappropriate the assumption is for figure 1 will have to await further data.

The problem is then to determine the distribution of orbital debris orbits that will produce an orbital debris flux that passes through the CME points on figure 1. Collision probability theory is used to determine this distribution.

COLLISION PROBABILITY

Theory and Assumptions

The probability that an orbital debris object will collide with LDEF (or any other spacecraft) at a particular point in orbit is a function of the orbital debris' perigee, apogee, and inclination, as well as the relative velocity between the two objects and their collision cross-sectional area. Equations expressing this probability are given in reference 11, as well as equations for the relative velocity (both magnitude and direction). These equations are used to calculate the relative number of impacts, or flux, on each LDEF surface for various orbital debris orbits.

However, the observed data are in terms of a limiting impact crater diameter. Crater diameter is a function of impact speed and direction, as well as debris size; consequently, impact speed and direction are also calculated for each LDEF surface. The assumption is made that crater diameter is proportional to debris diameter raised to the first power and the normal component of velocity raised to the 2/3 power. The assumption is also made that the flux of orbital debris varies as the orbital debris diameter raised to the -2.5 power. This later assumption is consistent with previous orbital debris models (ref. 1) and recent measurements (refs. 9 and 10). These two assumptions are required to convert flux to a limiting particle diameter to flux as a function of limiting impact crater diameter. This conversion is then accomplished by weighting the flux to a limiting size by the normal component of velocity raised to the 2.5 times 2/3 divided by 1.0 power, or 1.67 power (ref. 12).

Results

The orbit sets contained in the US Space Command catalogue for December, 1989 were used to provide a set of orbits to predict the distribution of craters around LDEF. The resulting calculations were normalized to pass through the aluminum surface CME data point. The results are shown in

figure 2, assuming an LDEF altitude of 400 km. As can be seen, based on the US Space Command catalogue, a very small fraction of the craters would be predicted to be on LDEF's rear surface. Past approximations obtained this same result, and lead to the conclusion that orbital debris directionality can be approximated by assuming circular orbits. The CME gold surface data point would suggest that the past assumptions are not valid, and that elliptical orbits are important to orbital debris directionality. Figure 2 suggests that the relative number of catalogued objects in certain types of elliptical orbits must be increased by at least an order of magnitude. The amount of increase is a function of the assumed LDEF altitude. An assumed altitude of 500 km for LDEF would have underpredicted rear impacts on LDEF even more than shown in figure 2, while an assumed altitude of 300 km would have underpredicted less than shown in figure 2. This implies that the relative number of orbital debris impacts on LDEF's rear surfaces should increase with decreasing altitude of LDEF. This introduces some uncertainty in the correct "average" altitude; however, the consequences of this uncertainty is small compared to the greater than an order of magnitude underprediction shown in figure 2 for an LDEF altitude of 400 km.

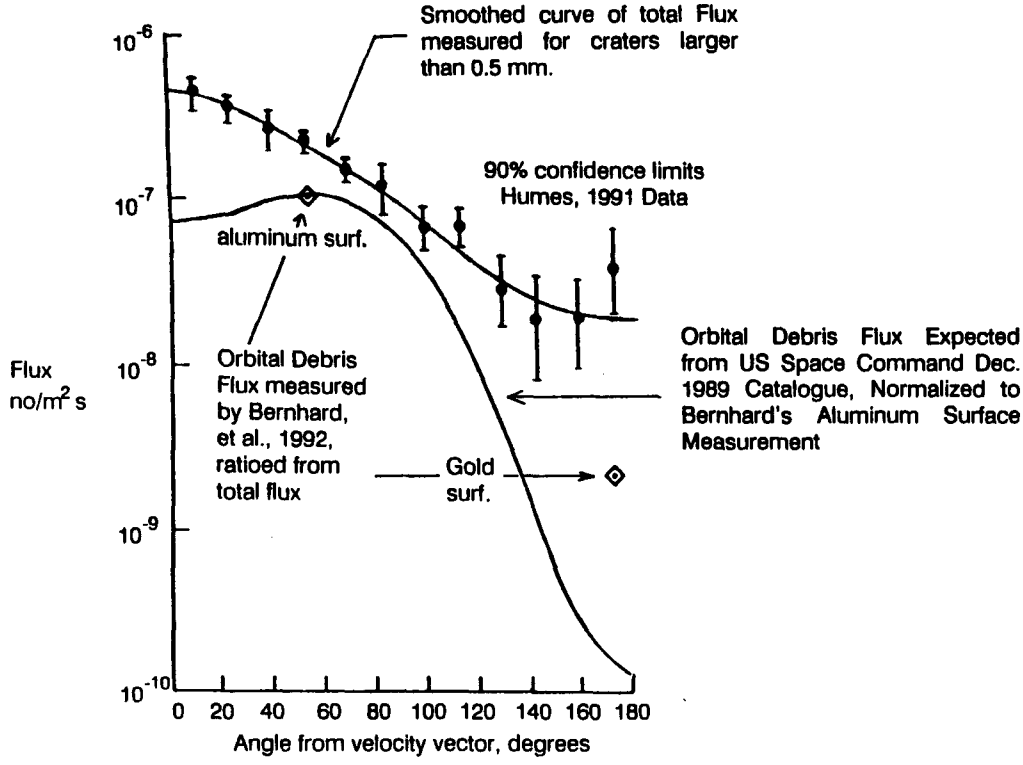


Figure 2. LDEF crater distribution expected form orbits in US Space Command catalogue.

In order to determine which types of elliptical orbits are contributing to impacts on the rear surface, the contribution from individual orbits was also calculated. The results of this calculation are shown in figure 3 for selected orbital debris orbits. The selected orbits fall into three groups: 1. Near circular orbits. 2. Highly elliptical orbits. 3. Moderately elliptical orbits. The results show that for a given number of objects in Earth orbit at LDEF's altitude, circular orbits can be expected to produce about 100 times more craters on LDEF than highly elliptical orbits. Most of the craters from circular orbits would be on LDEF's leading and side surfaces. Lower inclinations would produce fewer

craters on the leading surfaces; no craters would be expected on the trailing surfaces from circular orbits.

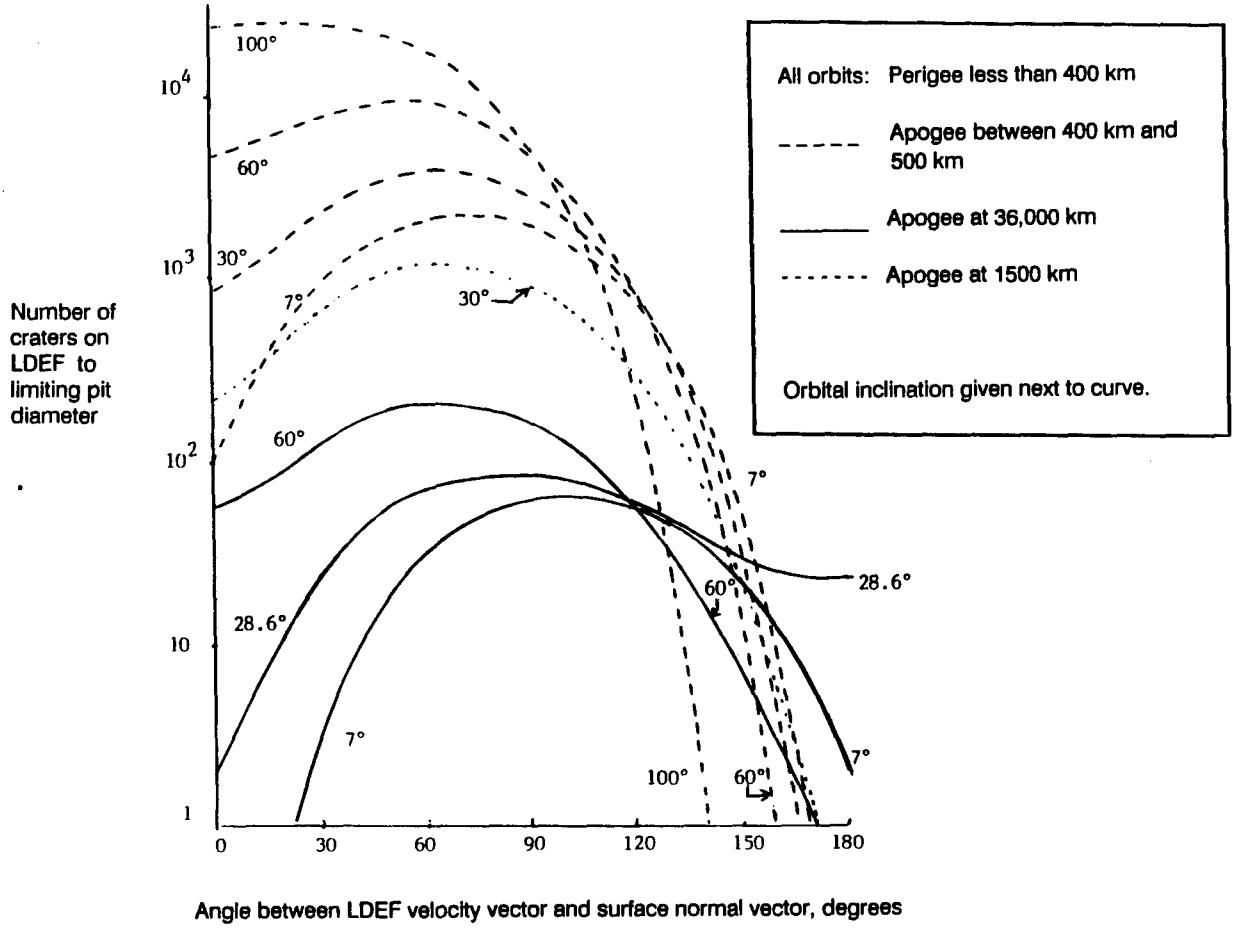


Figure 3. Predicted distribution of craters around LDEF due to various types of orbits.

The highly elliptical orbits have perigees below LDEF's altitude and apogees near geosynchronous orbit. This group of orbits is characteristic of orbital transfer stages from low Earth orbit to geosynchronous orbit. When an object is placed into geosynchronous orbit, an upper stage rocket is usually left in this type of orbit. The results show that these types of orbits are expected to produce craters on LDEF's rear surface only if the inclination is low. Highly elliptical orbits with inclinations larger than about 50 degrees are not capable of producing a significant number of impact craters on LDEF's rear surface without also producing a larger number of craters on the CME aluminum surface than was measured. The orbits most capable of producing a large number of pits on LDEF's rear surfaces are highly elliptical orbits with inclinations close to the inclination of LDEF, or 28.5 degrees. Orbital debris impacts on the CME gold surface from this type of orbit will also produce about 3 times as many orbital debris impacts on the CME aluminum surface. However, figure 1 gives a measured orbital debris flux on the CME aluminum surfaces which is 40 times larger than the flux on the gold surface. Therefore, other inclinations must be responsible for most of the orbital debris impacts on the aluminum surface.

Inclinations as low as 7 degrees can also produce a significant orbital debris flux on the rear surfaces. From figure 3, orbital debris impacts on the CME gold surface from highly elliptical 7 degree inclination orbits will also produce about 10 times as many orbital debris impacts on the CME aluminum surface. This ratio is also less than was determined by the CME, so other sources of orbital debris are required.

Moderately elliptical orbits to circular orbits are required to account for the total number of orbital debris impacts on the CME aluminum surface. A moderately elliptical orbit is one with its apogee near 1500 km and perigee below LDEF altitude. This type of orbit might be expected as a result of explosions at altitudes between 1000 and 2000 km, where nearly all explosions have occurred which produced long orbital lifetime orbits. As can be seen from figure 3, a moderately elliptical orbit with an inclination as close as 30 degrees to the LDEF inclination is not capable of producing a significant crater population on LDEF's rear surface without also producing a much larger crater population on the side surfaces. Consequently, while this type of orbit, along with near circular orbits, may be responsible for impacts on the leading and side surfaces of LDEF, moderately elliptical orbits are not responsible for a significant number of impacts on LDEF's rear surface.

Therefore, the only types of orbits capable of providing the necessary number of impacts on LDEF's rear surface are highly elliptical, low inclination orbits. This is the type of orbit which is most difficult to catalogue and maintain by the US Space Command. The US is mostly responsible for leaving orbital transfer stages in highly elliptical orbits with inclinations near 28.5 degrees, and the European Space Agency (ESA) is responsible for leaving orbital transfer stages with highly elliptical orbits with inclinations usually near 7 degrees. At least 2 of ESA's upper stages in this type of orbit are believed to have exploded (ref. 13); a total of 3 fragments were catalogued from these 2 events. When the same upper stage exploded in a circular low Earth orbit with a high inclination, 488 fragments were catalogued. Consequently, it is not unreasonable to expect that the catalogue does not adequately represent this low inclination population.

The December, 1989 US Space Command catalogue was again used to predict the distribution of craters around LDEF; however, this time all orbits with both apogee greater than 10,000 km and inclination less than 50 degrees were weighted by a factor of 20. All other orbits were unweighted. Again the resulting calculations were normalized to pass through the aluminum surface CME data point. The results are shown in figure 4. As can be seen, the results go through both CME data points.

There have been 17 satellite breakups (mostly upper stage explosions) in highly elliptical orbits with inclinations over 50 degrees; an average of less than 4 fragments per breakup were catalogued (ref. 13). A valid assumption might be that this population is equally not represented by the catalogue. Such as assumption would require a weighting factor larger than 20 because the higher inclination orbits do not contribute to impacts on the trailing surface...only to impacts on the leading and side surfaces. If all orbits with an apogee greater than 10,000 (regardless of their inclination) are weighted by a factor of 30, the results are almost identical to that shown in figure 4 for the lower inclination orbits. Because the directional properties of highly elliptical, high inclination orbits are so close to the directional properties of circular orbits, there is no way to discriminate between weighting factors of 20 or 30 for these two respective possibilities.

Consequently, the ratio in the amount of small debris in these highly elliptical, low inclination orbits to the amount of small debris in other types of orbits must be at least 20 times the same ratio for larger, catalogued objects in order to be consistent with the CME LDEF data. If all elliptical orbits are equally not represented by the catalogue, then the ratio for small debris must be 30 times the ratio for catalogued objects.

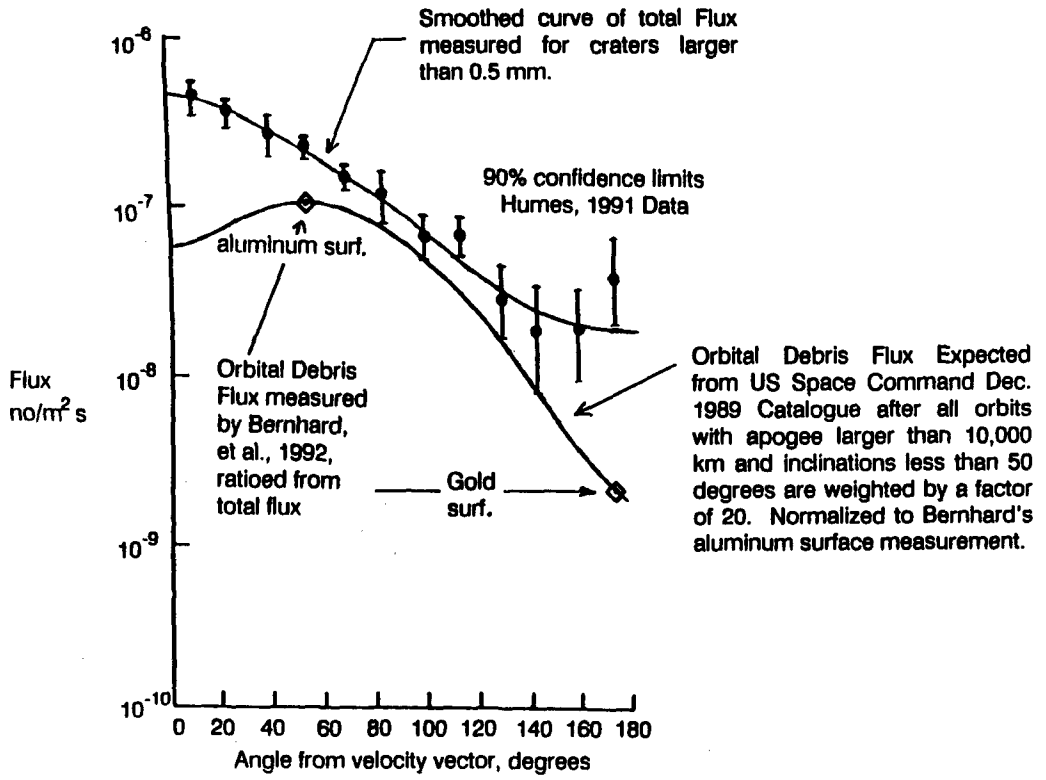


Figure 4. LDEF crater distribution expected from weighted highly elliptical, low inclination orbits in US Space Command catalogue.

CONCLUSIONS

Orbital debris impacts on LDEF's rear surface can only be caused by debris in highly elliptical, low inclination orbits. The US Space Command catalogue underpredicts the relative contribution of orbital debris impacts on LDEF from this type of orbit by at least a factor of 20. The reasons for this underprediction are the result of a combination of difficulty in cataloguing objects in these orbits, and that small debris in highly elliptical orbits is a larger fraction of the flux at low altitudes than is larger, catalogued debris.

ACKNOWLEDGMENTS

The author gratefully acknowledges helpful discussions with Fred Hörz and Ron Bernhard concerning the interpretation of both of their published and unpublished CME data.

REFERENCES

1. Kessler, D.J.; Reynolds, R.C.; and Anz-Meador, P.D.: Orbital Debris Environment for Spacecraft Designed to Operate in Low Earth Orbit. NASA TM-100-471, April, 1989.

2. Kessler, D.J.: Collision Probability at Low Altitudes Resulting from Elliptical Orbits. Adv. Space Research, Vol.10, No. 3-4, pp. 393-396, 1990.

3. Bernhard, R.; and Hörz, F.: Compositional Analysis of Projectile Residues on LDEF Instrument A0187-1. Second LDEF Post-Retrieval Symposium, NASA CP-3194, 1993.

4. Hörz, F.; and Bernhard, R. P.: Compositional Analysis and Classification of Projectile Residues in LDEF Impact Craters. NASA TM 104750, June 1992.

5. Humes, D.H.: Large Craters on the Meteoroid and Space Debris Impact Experiment. First LDEF Post-Retrieval Symposium, NASA CP-3134, pp. 399-418, 1991.

6. See, T.H.; Hörz, F.; Zolensky, M.E.; Allbrooks, M.K.; Atkinson, D.R.; and Simon, C.G.: Meteoroid and Debris Special Investigation Group Preliminary Results: Size-Frequency Distribution and Spatial Density of Large Impact Features on LDEF. First LDEF Post-Retrieval Symposium, NASA CP-3134, pp. 477-486, 1991.

7. McDonnell, J.A.M.; and Stevenson, T.J.: Hypervelocity Impact Microfoil Perforations in the LEO Space Environment (LDEF, MAP AO 023 Experiment). First LDEF Post-Retrieval Symposium, NASA CP-3134, pp. 443-458; 1991.

8. Mulholland, J.D.; Singer, S.F.; Oliver, J.P.; Weinbeg, J.L.; Cooke, W.J.; Montague, N.L.; Wortman, J.J.; Kassel, P.C.; and Kinard, W.H.: IDE Spatio-Temporal Impact Fluxes. First LDEF Post-Retrieval Symposium, NASA CP-3134, pp. 517-527, 1991.

9. Goldstein, R.; and Randolph, L.: Rings of Earth Detected by Orbital Debris Radar. JPL Progress Report 42-101, May 15, 1990.

10. Stansbery, E.G.; Bohannon, G.; Pitts, C.C.; Tracy, T.; and Stanley, J.F.: Characterization of the Orbital Debris Environment Using the Haystack Radar. JSC-32213, April 24, 1992.

11. Kessler, D.J.: Derivation of the Collision Probability Between Orbiting Objects: The Lifetimes of Jupiter's Outer Moons. Icarus, Vol. 48, pp. 39-48, 1981.

12. Kessler, D.J.: A Guide to Using Meteoroid-Environment Models for Experiment and Spacecraft Design Applications. NASA TN D-6596, March, 1972.

13. Johnson, N.L.; and Nauer, D.J.: History of On-Orbit Satellite Fragmentations. TBE Technical Report CS91-TR-JSC-008, July, 1991.

Damage Areas on Selected LDEF Aluminum Surfaces*

Cassandra R. Coombs, Dale R. Atkinson, Martha K. Allbrooks,
Alan J. Watts, Corey J. Hennessy and John D. Wagner
POD Associates, Inc.
2309 Renard Place, SE
Suite 201
Albuquerque, NM 87106

ABSTRACT

With the U.S. about to embark on a new space age, the effects of the space environment on a spacecraft during its mission lifetime become more relevant. Included among these potential effects are degradation and erosion due to micrometeoroid and debris impacts, atomic oxygen and ultraviolet light exposure as well as material alteration from thermal cycling, and electron and proton exposure. This paper focuses on the effects caused by micrometeoroid and debris impacts on several LDEF aluminum plates from four different bay locations: C-12, C-10, C-01, and E-09. Each plate was coated with either a white, black or gray thermal paint. Since the plates were located at different orientations on the satellite, their responses to the hypervelocity impacts varied. Crater morphologies range from a series of craters, spall zones, domes, spaces, and rings to simple craters with little or no spall zones. In addition, each of these crater morphologies is associated with varying damage areas, which appear to be related to their respective bay locations and thus exposure angles. More than 5% of the exposed surface area examined was damaged by impact cratering and its coincident effects (*i.e.*, spallation, delamination and blow-off). Thus, results from this analysis may be significant for mission and spacecraft planners and designers.

INTRODUCTION

There is an increasing concern over the consequences of micrometeoroid and debris (M&D) impacts on space vehicles particularly due to an increasing debris population. However,

* This work was performed under subcontract to W.J. Schafer Associates, Inc., under prime contract to SDIO, contract no. SC-89W-26-11, SDIO-89-C-0034. POD Internal Project No.: 019202.

the current approach used by most satellite designers in assessing this environment produces great uncertainties in the damage estimates for certain material classes such as coated thermal control surfaces, multilayer coatings, and glasses. As the debris population grows, these uncertainties will also increase leading to more erroneous damage estimates.

The recent LDEF flight provides a unique opportunity to characterize the natural and man-made particle populations in Low-Earth Orbit (LEO) and more accurately quantify the damage areas created on a satellite which was in orbit for nearly six years. LDEF exposed 130m^2 of surface area to the space environment at altitudes between ~475 km (launch) - 326 km (recovery) on its 12-sided closed cylinder frame. During its tenure in space, LDEF was gravity-gradient stabilized with one end constantly facing the Earth (EARTH-end) and the opposite end constantly facing space (SPACE-end). Row 9 was constantly oriented 8° from the normal to the velocity or ram direction (RAM). This constant orientation provided a superb experimental and control platform for monitoring the effects of exposure to the LEO environment.

In this study we concentrated on the collection and evaluation of damage areas created by impact craters into thermal painted aluminum surfaces located about LDEF. These data are intended to: (1) aid in the characterization of the effects of the LEO M&D environment on satellite systems and materials, (2) update the current theoretical models for LEO, (3) help assess the survivability of spacecraft and satellites which must travel through or reside in LEO, and (4) help define future spacecraft material components.

BACKGROUND

Two major components currently exist within the dynamic LEO environment, namely natural micrometeoroids from the solar system and man-made debris dating back to the onset of space exploration in 1957. While the micrometeoroids arrive at the Earth from almost all directions, the debris is in both near-circular and elliptical orbits around the Earth. Although both types of particles exist all the way out to geosynchronous (GEO) orbits, the major populations of debris are within the altitude range of 350 - 2000 km.

Micrometeoroids arrive at the Earth with differential speeds of from below 12 km/s to 72 km/s. However, when the spacecraft orbital speed is included, the resulting impact speeds range from below 5 km/s to 79 km/s, yielding an overall average collisional speed of 20 km/s (Zook[1]). The flux (number of impacts per area per time) of particles is approximately isotropic in free space as seen from the Earth, but the effect of Earth shielding causes an asymmetry as seen by an orbiting spacecraft in LEO, resulting in a minimum number of impacts for Earth-facing satellite surfaces. As a result, either the RAM surface or the SPACE-facing surfaces (depending upon altitude) receive the highest number of impacts (Atkinson, *et al.*[2]).

Debris population distribution is largely a function of launch frequencies and sites with subsequent perturbations caused by accidental (and/or deliberate) explosions, collisions, fragmentations, surface erosion, and manned or unmanned mission-related debris (*e.g.* ejected lens covers, explosive bolts). Currently, the greatest concentration of debris occurs at inclinations toward the pole, with peaks at 60°, 80°, and 100° (Kessler [3]). Once created, differential precessions will cause the initial "clouds" of space debris to form a toroid, or belt, around the Earth with holes near the pole. Consequently, the flux of particle impacts on a spacecraft is a function of the latter's inclination and also altitude, and the resulting impact speeds can range from zero to about 16 km/s for near-circular orbits (or to about 19 km/s for highly elliptical debris orbits such as Hohman transfer orbits out to GEO).

For both micrometeoroids and debris, the particles can range in size from sub-microns to many centimeters. However, both components display a power law of number versus size, with the smaller particles being far more numerous than the larger ones. While particles greater than 1 mm can penetrate typical satellite skins and cause catastrophic damage, the smaller particles mostly cause a gradual degradation of a satellite's surfaces, including thermal control paints, thermal blankets, coatings to provide protection against atomic oxygen (AO) or ultraviolet light (UV), solar cells and optics. Many satellite surfaces employ coatings which range from sub-micron (*e.g.*, optics) to mils (*e.g.*, thermal control, AO and UV protection, and solar cell covers). At impact speeds of 5 - 20 km/s particles can penetrate materials (either punching holes or causing craters with associated radial (star) cracks for brittle materials), and can cause damage

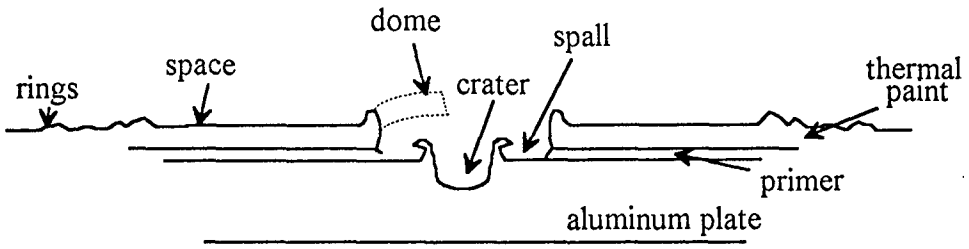
regions which are considerably larger than the incoming particle. Consequently, the thermal paint coatings can be locally disrupted even by particles as small as 1 to 100 μm, and the areal number density (hits per square meter) can easily exceed 1000/m^2 for a multi-year mission.

When a hypervelocity particle impacts a surface it either creates a crater or perforates the surface (also referred to as the target). In addition to crater formation, surrounding areas can experience spallation, cracking or delamination of an attached layer as depicted in Figures 1a and 1b. These damage effects can lead to reduced structural strength, thermal and optical property degradation and erosion of underlying materials. The physical response of any target to an M&D impact depends on the material, induced stress level, material temperature, number of projectiles and the system configuration. These phenomena may be enhanced by subsequent exposure of underlying layers to the UV, atomic oxygen, charged particles, and thermal cycling. This subsequent exposure can modify a material and thus enhance cracking and delamination regions. Also, material embrittlement, erosion and other property degradation can occur to either the surface or exposed underlying material. For example, AO can creep under locally delaminated regions causing greater damage, or previously protected materials may become exposed to UV through small cracks or fissures. In short, the synergistic environment can lead to accelerated damage rates and a significant increase in the damage zone.

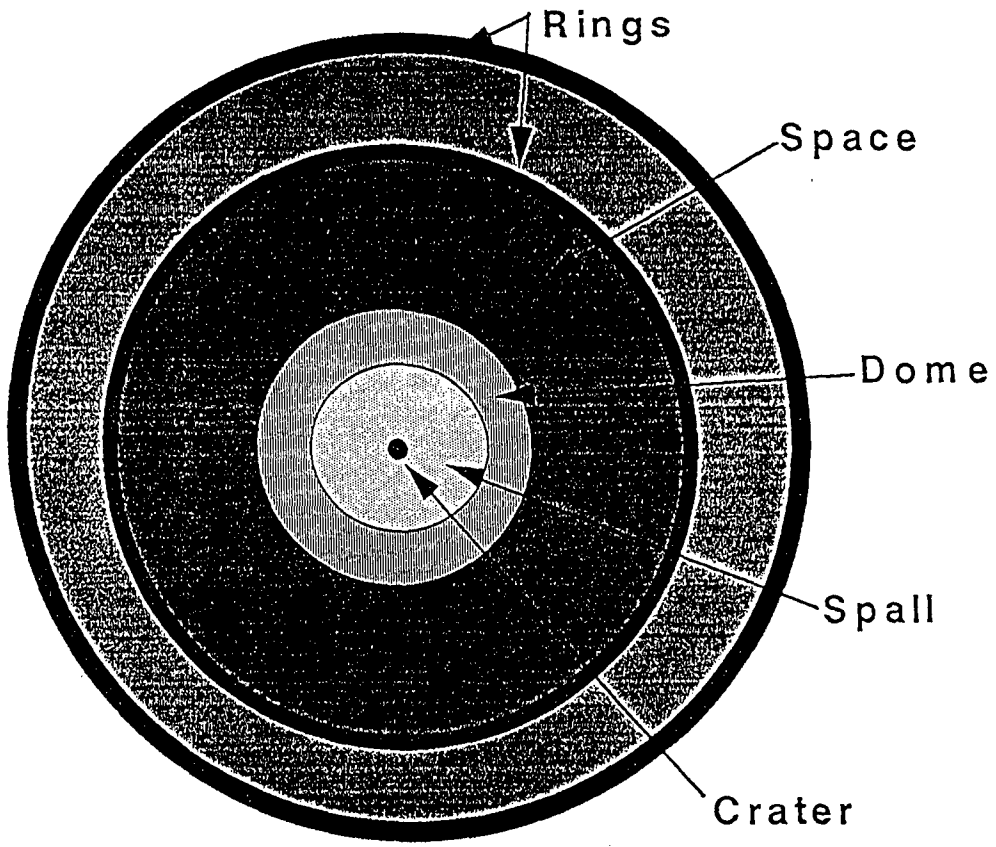
DATA COLLECTION

Impact craters were analyzed on three leading edge components (C-10 EOOB, Active Grapple; C-12 EOOA, Experiment S0109; and E-09 E00A, E00B, E00C, and E00D, Experiment S0014) and one trailing edge component (C-01 EOOB, Inactive Grapple). These materials were composed of anodized aluminum and coated with either black or white Chemglaze thermal control paints. Each plate is discussed more completely below.

The crater measurements were taken at the NASA Johnson Space Center Facility for Optical Investigation of Large Surfaces (FOILS) Laboratory. This facility is a Class 100 clean room designed specifically for analyzing space hardware. The scanning apparatus consists of a



(a)



(b)

Figures 1a and 1b: (1a) Schematic cross-section of a "typical" impact into a thermal painted aluminum plate on LDEF. (1b) Plan view of a "typical" crater on LDEF, corresponding to the cross-section in 1a.

binocular microscope attached to a scanning table along with computer operated data collection and monitoring system. Once measured, each crater was catalogued and became part of the Meteoroid and Debris Special Investigation Group (M&D SIG) database.

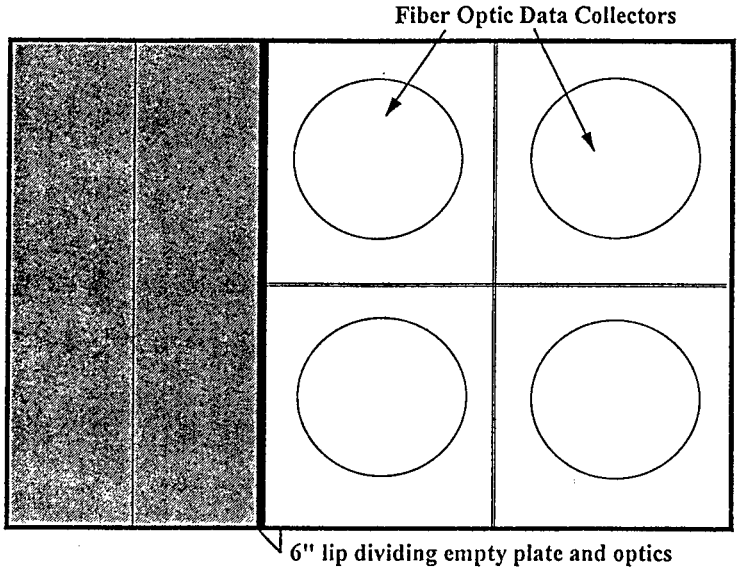
Before crater measurement began on the LDEF hardware, a cursory analysis was made of the surface of the component and a decision was made to only measure those craters larger than 75 microns as these could be consistently identified. All craters smaller than this that could be discerned were counted and recorded. For measurement and logistic purposes, individual impact zones were divided, or categorized, into five different morphologic features (Figures 1a and 1b). These include: crater, spall, dome, space, and ring. Individual measurements, in microns, were made of crater, spall, dome and ring radii at the four "clock" positions, 3, 6, 9 and 12.

Virtually all features which measured greater than 0.2 mm in size possessed a spall zone in which all of the paint was removed from the aluminum surface immediately adjacent to the crater. These spall zones varied in size from approximately 2 - 5 crater diameters. The actual craters in the aluminum substrate varied from central pits without raised rims, to morphologies more typical of craters formed in aluminum under hypervelocity laboratory conditions. Most features also possessed what is referred to as a "shock zone"[1] as well. These zones varied in size from approximately 1 - 20 crater diameters. In most cases, only the outer-most layer of paint was affected by this impact related phenomenon. Several impacts exhibited ridge-like structures ringing the area in which this outer-most paint layer was removed. There was only one noticeable perforation and associated backside spallation feature, which was on component E-09 E00D. All other trays showed no evidence of such phenomena.

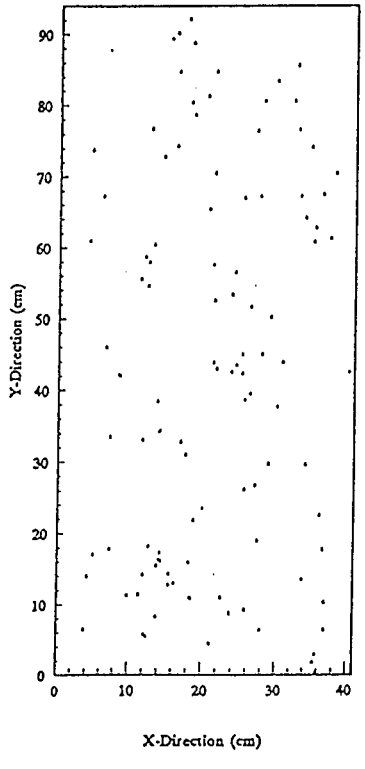
LDEF Components Measured

Bay C-12

The C-12 plate examined was a Chemglaze A278 white-painted aluminum electronics coverplate that occupied the left third of the C-12 experiment tray (Figure 2a). Bay C-12 was located approximately 82° from RAM. Figure 2b shows the distribution of impacts on this painted aluminum plate.



(a)



(b)

Figure 2a and 2b: (2a) Schematic diagram of the relationship between the C-12 aluminum plate and the S0109 experiment. (2b) Schematic diagram of LDEF aluminum plate from Bay C-12.Small dots represent locations of impacts measured on this plate.

Bays C-10 and C-O1

Bay C-10 was occupied by one of two grapple fixtures aboard the spacecraft. This particular grapple fixture was the active grapple located toward the leading edge, approximately 22° from RAM, and was used to give the initiate signal through the LDEF initiation system to the Experiment Power and Data Systems (EPDS). The grapple fixture was attached via a base (abutment) plate to a 3.2 mm thick 6061-T6 anodized aluminum plate which resided in the bottom of the tray. Next to the grapple fixture was a small array of light emitting diodes (LEDs), which were used to show the active status of the LDEF spacecraft. These were mounted in a black painted aluminum plate which was mounted flush with the bottom of the grapple tray. Each grapple fixture consisted of an aluminum grapple pin, three brushed aluminum spindles to which the Shuttle Remote Manipulator System (RMS) could attach itself, and an alignment target for the RMS operator to use when grappling the spacecraft.[4] A small (approx. 1" dia.) Teflon button was located at the end of each grapple pin. During deintegration of the satellite, the grapple fixtures were dismantled completely. Thus, during this study, only the abutment plate sections of these grapple fixtures were examined. Figure 3 shows the distribution of impacts on the C-10 abutment plate. The C-01 grapple fixture was totally passive and was used exclusively for the deployment and retrieval of the LDEF spacecraft. This grapple fixture was located toward the trailing edge of LDEF, at 112° from RAM. Figure 4 shows the distribution of impacts on the C-01 abutment plate.

Bay E-09

Housed in Bay E-09 was an active experiment tray (Figure 5a) which contained experiment S0014, the Advanced Photovoltaic Experiment.[5] This tray was oriented approximately 8° from RAM. Specific objectives of this experiment were to provide information on the performance and endurance of advanced and conventional solar cells, to improve reference standards for photovoltaic measurements, and to measure the energy distribution in the extraterrestrial solar spectrum.

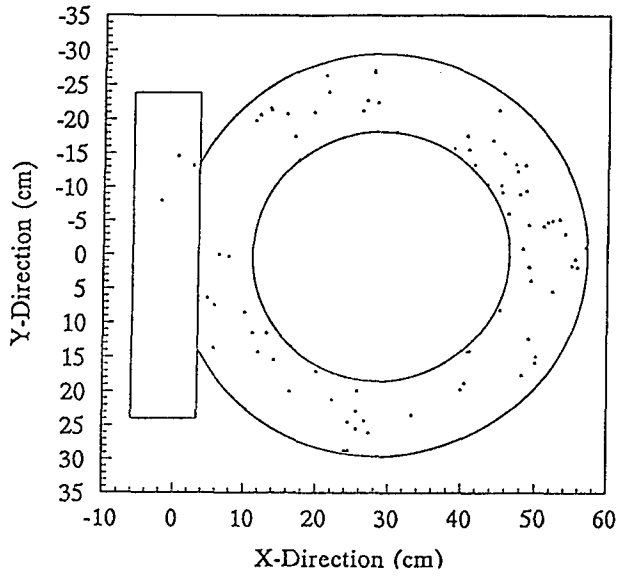


Figure 3: Schematic diagram of the active grapple abutment plate from Bay C-10. The small dots represent the locations of the craters measured in this study.

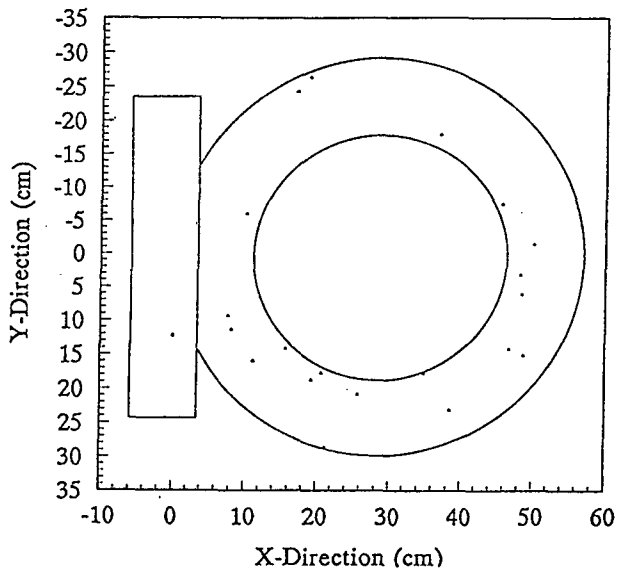
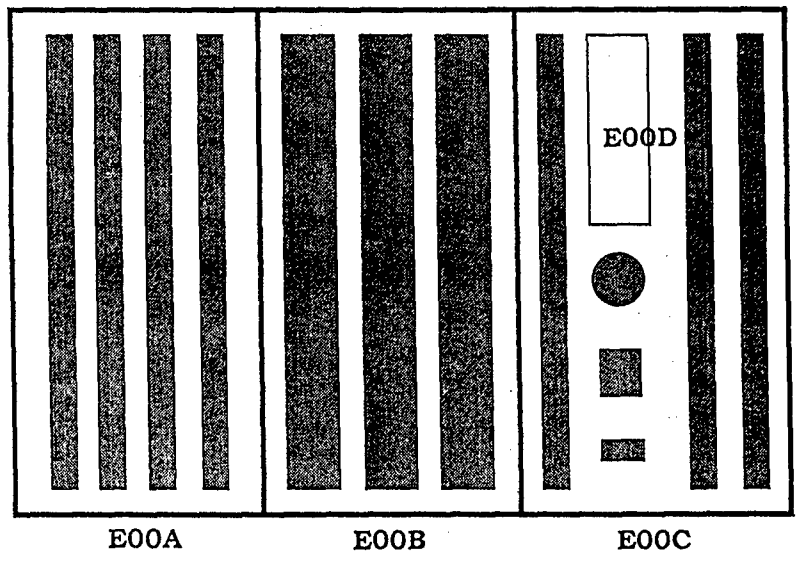
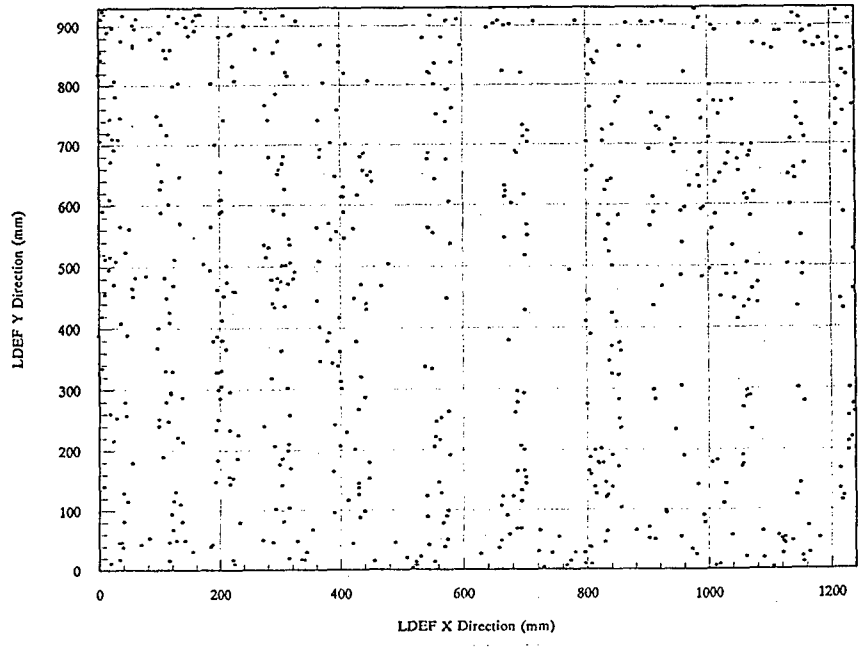


Figure 4: Schematic diagram of the inactive grapple plate from Bay C-01. The small dots indicate the locations of the craters measured in this study.



(a)



(b)

Figures 5a and 5b: (5a) Schematic diagram of the aluminum plates measured from Bay E-09. (5b) Schematic diagram of the distribution of impact craters on these plates. The small dots indicate the locations of the craters measured in this study.

The 12 inch-deep experiment tray used two $LiSO_2$ batteries to run the Experiment Power and Data System Collection. The hardware onboard consisted of numerous silicon and gallium arsenide solar cells, solar cell covers, and solar cell modules and assemblies. The experiment also contained a series of optical bandpass filters with multiple layers of materials such as aluminum, magnesium fluoride, silicon dioxide, silver, thorium fluoride, zinc sulfide, lead fluoride, and cryolite. Optical materials and substrates were composed of a variety of fused silica, Corning, and Schott glasses. Each of the experiment samples was mounted under a slotted, Chemglaze Z306 black thermal control painted 6061-T6 aluminum frame. The ~1.6 inch thick aluminum plates were intended to limit the field of view of the solar cells and other hardware. Figure 5b shows the distribution of impacts on these aluminum plates.

RESULTS

Results from the crater measurements taken in this study are summarized in Table I and discussed below.

Bay C-12

There were more than 250 impact features measured on this tray with an average damage area of 1.1×10^8 μm^2. The largest crater was 0.95 mm in size, and the total average damage area for this leading edge plate was 3.14%.

As described above, a paint spall zone was commonly found in association with the central pit or crater in most of the impacts examined from this tray. Around this spall zone was a smooth area (*e.g.*, "space", Figure 1) varying in size from five to 10 crater diameters. One or more rings were typically found outside this smooth region. Several of the more notable rings appear as "fold-over" flaps (or wrinkles) in the paint, while the remainder of the rings appear as powdery ripples (*e.g.*, powdered remnants) as seen in Figures 6, 7, 8 and 9.

Table 1: LDEF Damage Area Data on Selected Aluminum Panels

LDEF Aluminum Plate	Number Impacts Observed	Total Damage Area	Average Damage Area (μm^2)	Mean Crater Diameter (μm)	Mean Spall Diameter (μm)	Number Impacts per cm^2
C-12	253	3.14 %	1.09×10^8	322.5	658.9	0.07
C-10	94	2.09 %	4.36×10^7	299	696.0	0.05
C-01	30	0.26 %	1.88×10^7	316.5	877.1	0.01
E-09	521	0.32 %	3.034×10^5	185	208.5	0.11

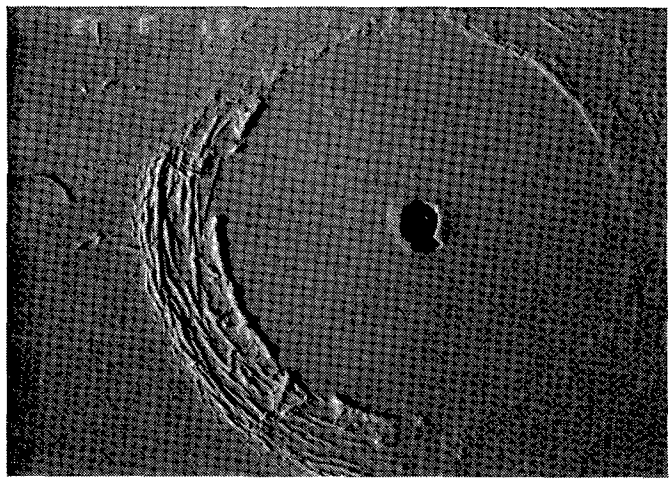


Figure 6: Impact crater from Bay C-12 showing crater, spall, dome, space, and rings. This crater is considered "young" as described in the text. Crater diameter ~200 μm, outer ring diameter ~ 11 mm; magnified 12x.

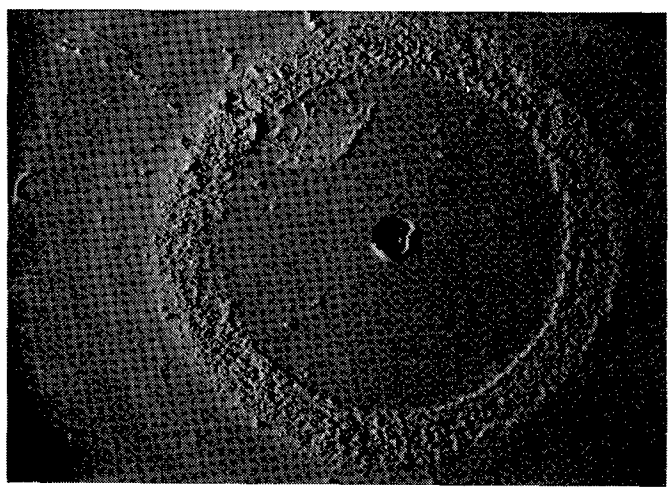


Figure 7: "Middle" age impact crater from Bay C-12 as discussed in text. "Blob" at eleven o'clock center is ejecta from central crater. Crater diameter ~350 μm, outer ring diameter ~ 15 mm; magnified 8x.

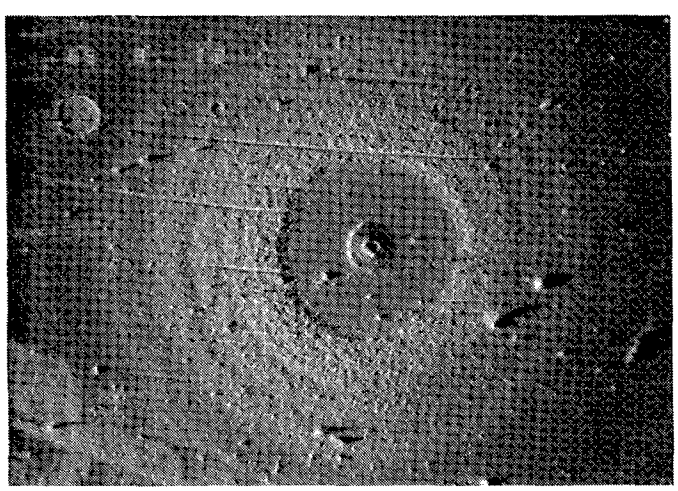


Figure 8: "Old" impact crater from Bay C-12 as discussed in text. Crater diameter ~90 μm, outer ring diameter ~4.5 mm; magnified 18x.

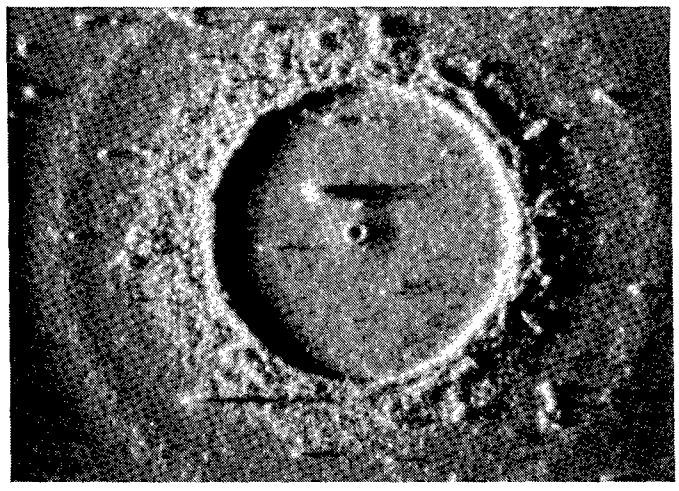


Figure 9: Impact crater from Bay C-12 showing fine powderiness of ring structure and paint surface. Crater diameter is 35 μm, total ring diameter is ~1.6 mm; magnified 40x.

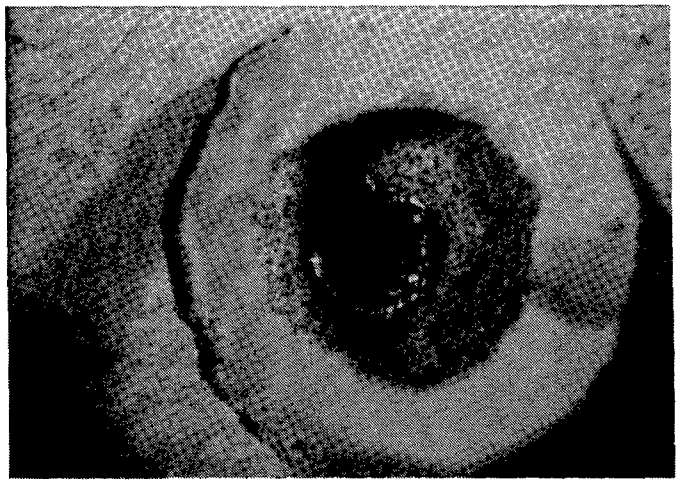


Figure 10: Typical impact crater from Bay C-10 showing crater, spall and domed regions. Crater diameter is ~85 μm; magnified 50x.

Bays C-10 and C-01

We documented a total of 94 craters on C-10, and 30 on C-01. This corresponds to approximately one impact crater per 19 cm^2 for C-10, and one impact crater per 72 cm^2 for C-01. The craters ranged in size from 0.45 mm to 1.53 mm with an average damage area of 5×10^7 μm^2 for C-10 and 2.1×10^7 μm^2 for C-01. These craters are typical of craters produced in aluminum during laboratory hypervelocity impact tests. Impacts into the painted surfaces of the grapple fixture caused front surface spallation, and the craters were sometimes surrounded by minor spall zones, small domes, and rings (Figure 10).

Bay E-09

More than 520 craters were measured on the four components of E-09, yielding approximately one impact per 94 cm^2. The average damage area for these craters was 3.4×10^5 μm^2, with a mean crater diameter of 185 μm.

These craters typically did not exhibit multiple ring structures, nor were large "spaces" observed. For the most part, the morphologies of these craters consisted of a central impact crater with minor spall and/or doming. This data from Bay E-09 is difficult to assess since the black thermal control paint had been almost entirely eroded, leaving behind only the primer coat. Space weathering and erosion probably removed all vestiges of the rings, as well as many of the other impact features.

Statistical Analyses

Crater diameter was compared to spall diameter, dome diameter, ring diameter, space diameter, and total damage zone using statistical techniques to attempt to find simple math models which would correlate damage effects per impact. The statistical analysis tools in the commercial software packages *Superbase*[6], *GrafTool*[7], and *Matlab*[8] were employed in this effort.

The models developed in this analysis are acceptable first-order models of the damage effects on these components *within the bounds of the actual data*. It is always hazardous to extrapolate best-fit curves beyond the bounds of the data, and particularly so if the leading

coefficient is negative. This is because the negative leading coefficient implies a decreasing (for example) spall diameter for large crater diameters, which will eventually yield a zero spall diameter for large crater diameters, and a negative spall diameter for some very large crater diameter. The idea of a negative spall diameter is clearly nonsense, so these, like all simple models, should be regarded as valid only within the bounds specified.

In conducting this analysis, we assumed that all data fit a Poissonian distribution which collapses into a Gaussian distribution for large numbers and applied the tools that would be appropriate for such a distribution. While not strictly correct, the errors introduced by this particular approximation are probably not large. Further, the data sets analyzed were of such small size that all results should be regarded as indicators of trends, and not as absolute answers. It is generally accepted that Gaussian statistics only begin to be valid at sample populations of 30 or more, and that populations on the order of 1000 or more are required to establish an answer with any confidence. Few of our data sets had 30 or more samples, and none had anywhere near 1000. Limited data sets are an inherent problem in field collection of random-event phenomena, and, as a result, one is forced to live with a less-than-perfect analysis.

The first effect examined was spall formation as a function of crater diameter. The best-fit curve for the data in all cases was a second order polynomial, yielding an equation of the form

$$y = ax^2 + bx + c \qquad (1)$$

where y is the variable (*i.e.*, spall, dome, space, ring or damage zone) diameter and x is the crater diameter and a, b, and c are constants. The second effect analyzed was dome formation as a function of crater diameter, followed by the relationship between ring and crater diameters, space and crater diameters, and lastly the total damage zone versus crater diameter. Regression coefficients for each curve were calculated, along with their squares, also sometimes referred to as the "goodness-of-fit" parameter. Math models are generally considered acceptable if the square of the correlation coefficient is 0.50 or greater. These condensed data are shown in Table 2.

Table 2: Statistical Data from Selected LDEF Aluminum Panels

LDEF Bay Location	Component ID	Spall vs. Crater		Dome vs. Crater		Space Vs. Crater		Ring vs. Crater		Total Damage Area vs. Crater	
		r*	r^2*	r	r^2	r	r^2	r	r^2	r	r^2
C-12	E00A	0.92	0.85	0.53	0.29	0.6	0.36	0.65	0.42	0.69	0.49
C-10	E00B	0.88	0.77	0.58	0.33	0.65	0.43	0.91	0.83	0.67	0.45
C-01	E00B	0.91	0.82	0.93	0.87	NA	NA	NA	NA	0.91	0.82
E-09	E00D	0.88	0.78	0.5	0.25	NA	NA	0.77	0.59	0.76	0.58

*r = correlation coefficient from best fit curve

r^2 = square of correlation coefficient; number > 0.5 indicates a good math fit

The best fits were found for the spall and dome comparisons. This might be expected, since both spallation and dome formation happen immediately upon impact,and are localized to the impact point. The space and ring phenomena are probably sensitive to such factors as local thickness of paint and the degree of embrittlement or erosion or changes in mechanical properties (*e.g.*, modulus or strength). Thus these other effects of interest yielded much less satisfactory correlations.

The four plots shown in Figures 11a through 11d include comparisons of average crater diameters to average spall, dome, space, and ring diameters in the 3-9 and 6-12 clock positions. These figures also illustrate the variation in regression curves for the LDEF aluminum plates measured. These fits are reasonable but not great.

SUMMARY AND DISCUSSION

The three leading edge sections, C-12, C-10 and E-09, have undergone a considerable amount of atomic oxygen erosion as they were facing in the RAM (velocity) direction. As such, the paint surfaces have been etched and pitted. The rough texture is produced as a result of the organic binder in the paint being sputtered away upon contact with the atomic oxygen while the paint pigment particles are left behind. A distinct difference in degree of space weathering was noticed between the grapple plates (C-10 and C-01) which, as mentioned above, faced opposite directions. Both were painted with a gray colored thermal control paint prior to launch. While the initial gray paint surface on the leading edge plate (C-10) was weathered to a rough grayish-white color, the trailing edge plate (C-01) turned a darker grayish-brown due to UV darkening of the organic paint binder. In addition, the impacts into the C-10 plate produced larger damage areas relative to crater size as compared to those in C-01.

Three "types" of ringed impact features were identified and loosely characterized as "young", "middle", or "old". This is an indication of their possible relative sequence of formation (Figures 6, 7, and 8 respectively). Preliminary analyses suggest that the different characteristics may signify a difference in relative ages between the three types of impact features. Type one, or

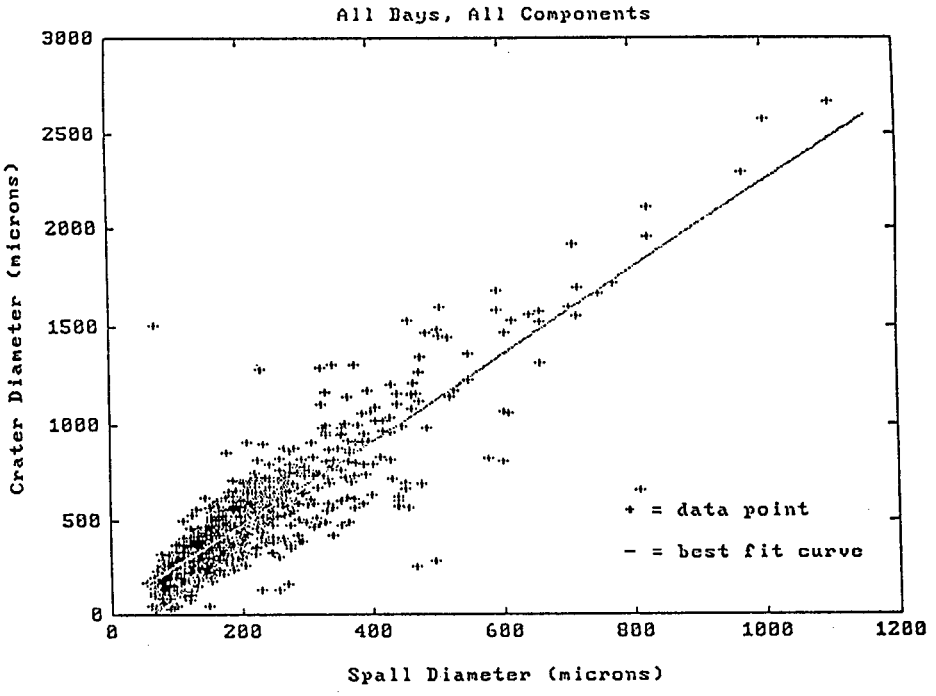


Figure 11a: Comparison plot of crater diameter versus spall diameter for all four components measured in this study.

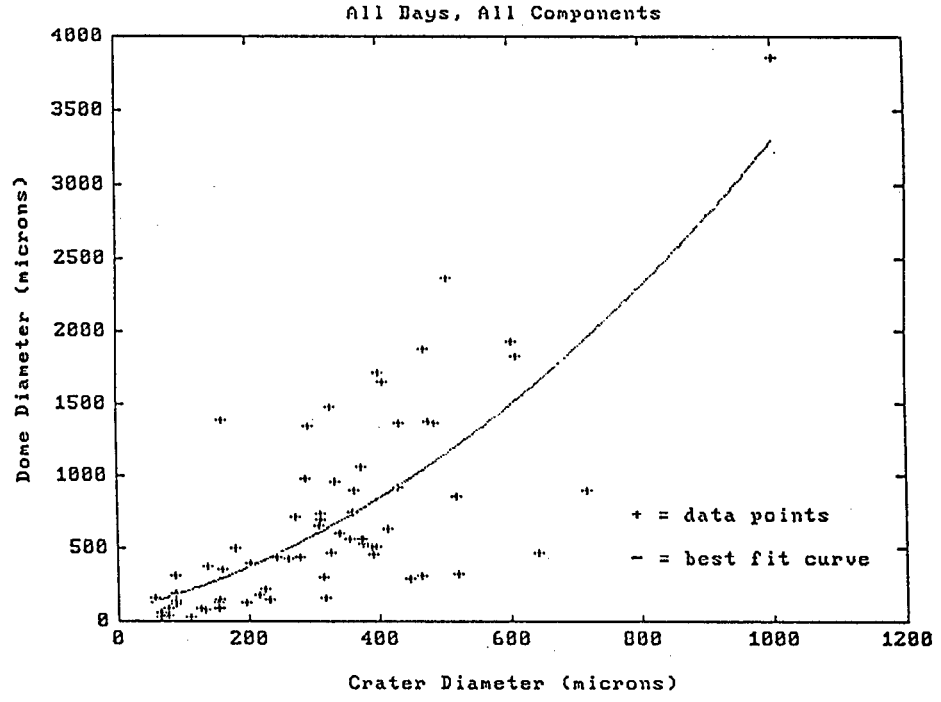


Figure 11b: Comparison plot of crater diameter versus dome diameter for all four components measured in this study.

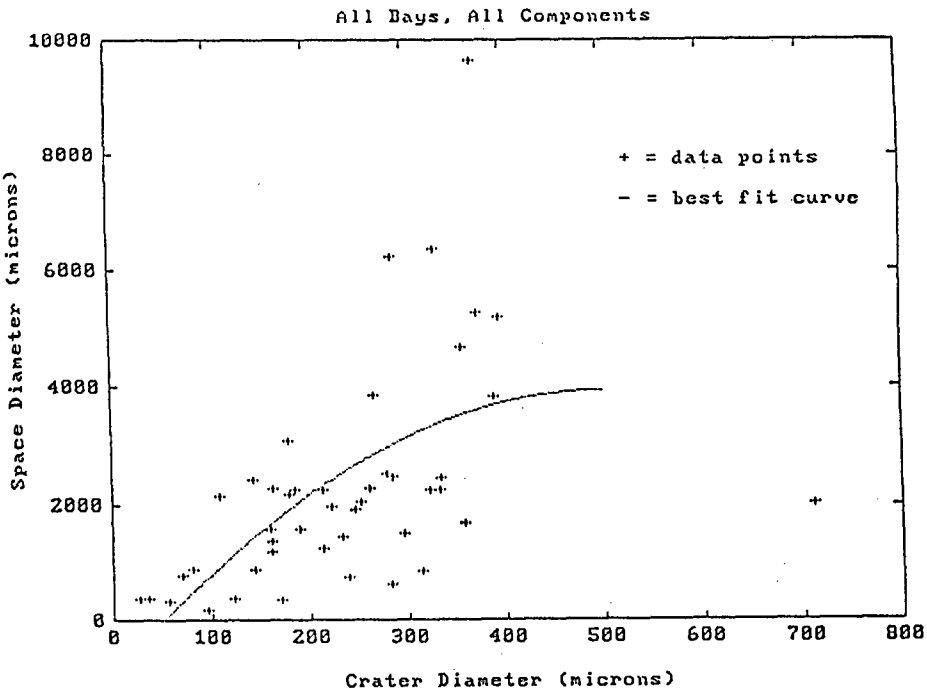


Figure 11c: Comparison plot of crater diameter versus space diameter for all four components measured in this study.

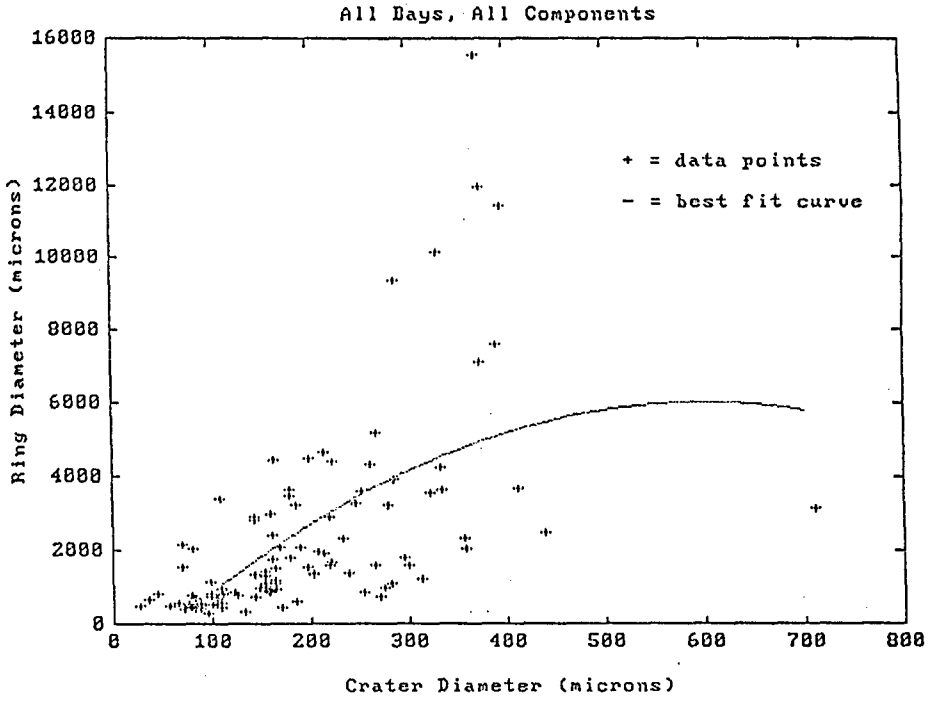


Figure 11d: Comparison plot of crater diameter versus ring diameter for all four components measured in this study.

the "young" group are characterized by very distinct crater lips, and excavation cavity rims where distinct, visible "flaps" or folds compose the ring zone (Figure 6). In these impact features, it appears as if the shock from the impact separated a layer or two of paint from the substrate and caused it to curl and fold back on itself, much as if one were scraping old paint from a wall. The impact feature as a whole is very clean and fresh. The second, or "middle" stage, appears slightly degraded. The ring edges are still distinct and some trace of the folded over layers may still be seen. In general, however, the impact feature is less obvious, and the rings appear to be rougher (Figure 7). In the third, or "old" stage, the impact feature is noticeably eroded. Little or no trace of the foldover flaps are visible and the rings have degraded into masses of rubble that appear as if they were deposited on the surface. No indications of layer fold-back are present (Figure 8).

Following discussions with Dr. Bruce Banks[9] of NASA Lewis Research Center, we conclude that these effects are predominantly due to AO weathering along with some synergistic effects from the rest of the space environment (*e.g.*, UV embrittlement, thermal cycling). While we had initially thought that the rough, worn-down edges of these rings were due to AO weathering of the paint following impact, we now believe that the surface has been AO weathered considerably prior to impact and thus created the "powdery" effect. The spaces and rings associated with some of the craters are most likely created by Rayleigh wave propagation through the loosely adhered pigment particles on the surface, combined with interference shock waves reflecting from the front and rear surfaces of the paint and aluminum. The greater the powderiness, the more AO weathering the surface experienced prior to impact. We still cannot, however, predict the ages of these craters and features, only the relative time frame in which they occurred: *i.e.*, the more pronounced rings occurred early in LDEF's exposure, while the most powdery rings occurred much later in LDEF's exposure history, after the AO had degraded the thermal paint surface. Therefore, "age" refers to the status of the target surface *prior* to impact.

Damage Area vs. Impact size

Estimation of damage areas and combined effects degradation can produce dramatically different results than simply predicting crater size or surface degradation due to the M&D

environment alone. Typical effects found in targets impacted by space debris include surface spallation, fracture zones and delamination from the interface layer as presented and discussed above. Once cracks or openings form they provide stress concentration centers for thermal induced lateral stresses as well as entry points for AO, UV, electrons, protons and so on. Depending on the intensity and timing of this loading it is likely that continued crack propagation and/or delamination will continue into the subsurface material(s). The level of degradation and increased damage will depend on the length of impact generated cracks or delaminations and the amount of exposure to the external elements.

Data from LDEF indicates that damage areas associated with an individual impact are much larger than the initial crater or penetration area. This is illustrated by the data in Table 3. Here, degradation data from C-10 (a gray thermal painted aluminum plate), C-12 (a white thermal control coated aluminum plate), and E-09 (a black thermal control coated aluminum plate) were combined and averaged over all satellite locations. For example, for the white thermal control paint, the ring diameter ratios ranged from 5 to a maximum of 40 with an average ring diameter ratio of 17.4.

Table 3. Damage Area Ratios on LDEF

Damage Region Description	Mean Diameter Ratio (Total Damage Diameter /Crater Diameter)	Mean Area Ratio
Spall	3	5
Dome	5	7
Space	8	78
Ring	13	279

Caution is advised, however, when estimating total damage areas for a spacecraft in a given scenario. Although this LDEF example illustrates the potential severity of the problem, the LDEF orbit was relatively benign with respect to impacts. Also, virtually no data exists on the damage areas for the different materials being used by satellite designers. Due to this lack of data,

estimates of degradation from the M&D environment may be erroneously small as shown in this discussion. Therefore, while a first estimate may be based on the assumption that a small particle will merely penetrate the coating surface and the resulting damage area will also be small, the combined effects may show the damaged area to be substantial. Also, the total number of impacts will increase with mission length, and should be considered a non-linear function due to the steady escalation of the man-made debris population. Hence, future satellites could suffer greater areas of damage due to M&D induced degradation or perforation.

Recommended Approach for Assessing Damage Zones

The following outlines an approach to obtaining the needed data for estimating damage zones for spacecraft materials. This information will essentially supply the missing data and theoretical developments to the "Meteoroid Damage Assessment" report written by V.C. Frost (1970).[10]

1) Identify different material classes and any thin coatings for estimating damage zones. Material classes would include metals, composites, ceramics (*i.e.*, glasses, paints and structures), refractories, inorganic and organic plastics. Single layer materials should be considered separately from multi-layered ones.
2) Obtain multiple samples of each type for inclusion in test program.
3) Select facility(ies) which produce particles with a range of mass and velocities for micrometeoroid and debris in a controlled, accurate and reliable fashion.
4) Pre- and post-characterize all samples for relevant performance properties (*i.e.*, optical, thermal, and mechanical).
5) Identify samples and facilities for testing combined environmental effects. For example, damage areas for an alumina coated silver mirror sample will change upon exposure to an M&D environment, which may make the underlying silver layer susceptible to atomic oxygen erosion.
6) Develop empirical fits to data as a function of material class, environment(s), and configuration (*i.e.*, layers).
7) Develop damage models as a function of the same variables in (6) which can be imported into existing hydrodynamic codes in order to predict response.

8) Benchmark hydrodynamic code(s) against experimental data.

These data will allow theoretical and empirical formulations to be developed to predict damage zones which will better quantify expected damage and degradation suffered during a mission due to the synergistic space environment.

REFERENCES

(1) Zook H.A. : Meteoroid Directionality on LDEF and Asteroidal Cometary Surfaces (abstract). *In Lunar and Planet. Sci. Conf. XXII,* Lunar and Planetary Institute, Houston, TX, pp. 1385-1386, 1990.

(2) Atkinson D.A.; Watts A.J.; Crowell L.: *Final Report: Spacecraft Microparticle Impact Flux Definition.* Prepared for: LLNL, Univ. of Calif. by POD Associates, Inc., 1991.

(3) Kessler D.J.; Reynolds R.C.; Anz-Meador P.D.: Orbital Debris Environment for Spacecraft Designed to Operate in Low Earth Orbit. *NASA TM-100471,* 1988. See also D.J. Kessler, Orbital Technical Interchange Meeting, Phillips Laboratory presentation, 2-3 April, 1991.

(4) See T.H.; Allbrooks M.K.; Atkinson D.R.; Simon C.; and Zolensky M.: Meteoroid and Debris Impact Features on the Long Duration Exposure Facility: A Preliminary Report. *NASA JSC #24608,* 1990.

(5) Clark L.G.; Kinard W.H.; Carter D.J. Jr.; Jones J.L. Jr., *eds.*: The Long Duration Exposure Facility (LDEF): Mission 1 Experiments, *NASA SP-473,* 1990.

(6) *Superbase,* Precision Inc., Irving, TX, 1990.

(7) *GrafTool,* 3-D Visions Corporation, Redondo Beach, CA, 1990.

(8) *Matlab,* The Math Works Corporation, Worchester, MA, 1989.

(9) Banks, B.: Personal Communication, 1991.

(10) Frost V.C.: Meteoroid Damage Assessment. *NASA SP-8042,* 1970.

LDEF DATA: COMPARISONS WITH EXISTING MODELS

Cassandra Coombs, Alan Watts, John Wagner and Dale Atkinson
POD Associates, Inc.
2309 Renard Pl, SE
Suite 201
Albuquerque, NM 87106

ABSTRACT

The relationship between the observed cratering impact damage on the Long Duration Exposure Facility (LDEF) versus the existing models for both the natural environment of micrometeoroids[1] and the man-made debris[2] was investigated. Experimental data was provided by several LDEF Principal Investigators, Meteoroid and Debris Special Investigation Group (M&D SIG) members, and by the Kennedy Space Center Analysis Team (KSC A-Team) members. These data were collected from various aluminum materials around the LDEF satellite. A PC (personal computer) computer program, SPENV, was written which incorporates the existing models of the Low Earth Orbit (LEO) environment. This program calculates the expected number of impacts per unit area as functions of altitude, orbital inclination, time in orbit and direction of the spacecraft surface relative to the velocity vector, for both micrometeoroids and man-made debris. Since both particle models are couched in terms of impact fluxes versus impactor particle size, and much of the LDEF data is in the form of crater production rates, scaling laws have been used to relate the two. Also many hydrodynamic impact computer simulations were conducted, using CTH[3], of various impact events, that identified certain modes of response, including simple metallic target cratering, perforations and delamination effects of coatings.

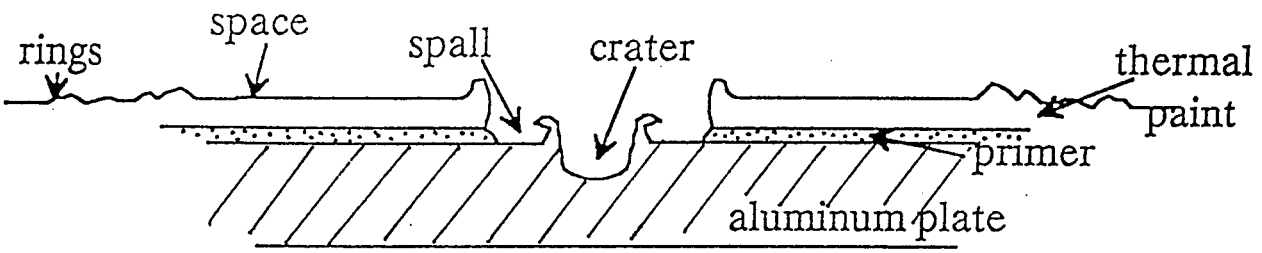
Work performed under contract to Lockheed ESC/NASA Johnson Space Center; Contract No.: 960-12-171, SC 02N0165768. POD Contract No.: 019201

INTRODUCTION

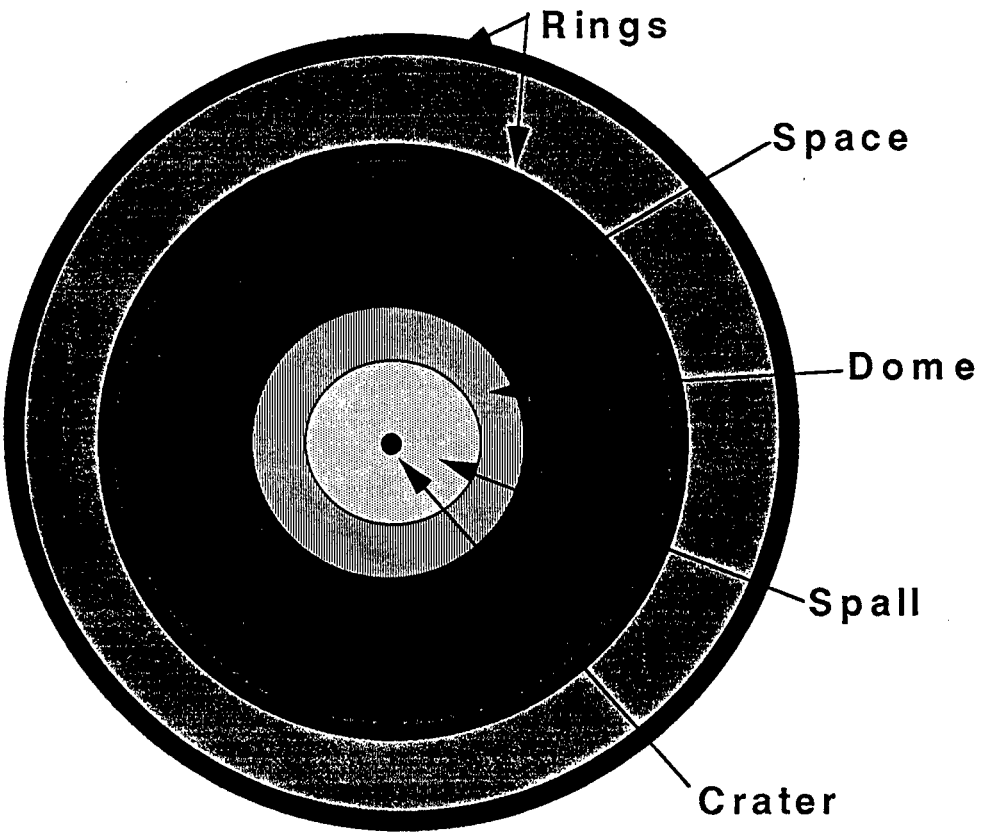
Since the return of LDEF there has been a continuous gleaning of impact data, from both the activities of the M&D SIG and from individual PI's. A large number of impact craters have been studied for almost all possible surface orientations relative to the velocity vector (*i.e.*, the direction of orbital motion, RAM direction), and cover a wide size range from below 10 μm to 5.3 mm. The target materials range from Al 6061-T6 frame components (studied in this report) to various painted surfaces and glasses. The individual craters have been carefully documented with regard to exact position on the various plates, and frame components (longerons and intercostals) of LDEF, and each specific impact event has been studied with regard to crater size, lip dimensions and any associated cracking or delamination (Figures 1a and 1b). The data have been reduced to the form of impact fluences (hits per unit area, or the integral of the crater production rates) versus crater diameter for various surface orientations. These data are then compared with the predictions of the two existing "standard" models for micrometeoroids and debris fluxes for Low Earth Orbit (LEO).

MODELLING THE PARTICLE ENVIRONMENT

POD has written a PC-based computer code SPENV (**SP**ace **ENV**ironment) which incorporates the Cour-Palais[1] model of near-Earth micrometeoroids and the Kessler[2] model of debris in LEO. The code predicts the "impact fluences" (note: we define this term to mean the time-integrated areal density of impacts) as functions of altitude, orbital inclination, specific time period in orbit, and orientation of the LDEF surfaces relative to the velocity vector: *e.g.*, RAM, SPACE, EARTH, SIDES and TRAIL (Figure 2). In the LDEF terminology of some these surfaces are EAST, SPACE, EARTH, NORTH & SOUTH, and WEST, respectively. Since both the micrometeoroid and debris models presently assume symmetry about the velocity vector the two SIDE predictions are normally identical. However, a small misallignment of the RAM surface of 8 degrees introduces a small asymmetry to the data. Details of the SPENV code and its use of the models are given in Atkinson *et al.*[4]



(1a)



(1b)

Figures 1a and 1b: (a) Schematic cross-section of an impact into painted aluminum. (b) Schematic plan view of a "typical" crater in painted material measured on LDEF. A slight asymmetry is typical for most craters. Note: diagrams are not to scale.

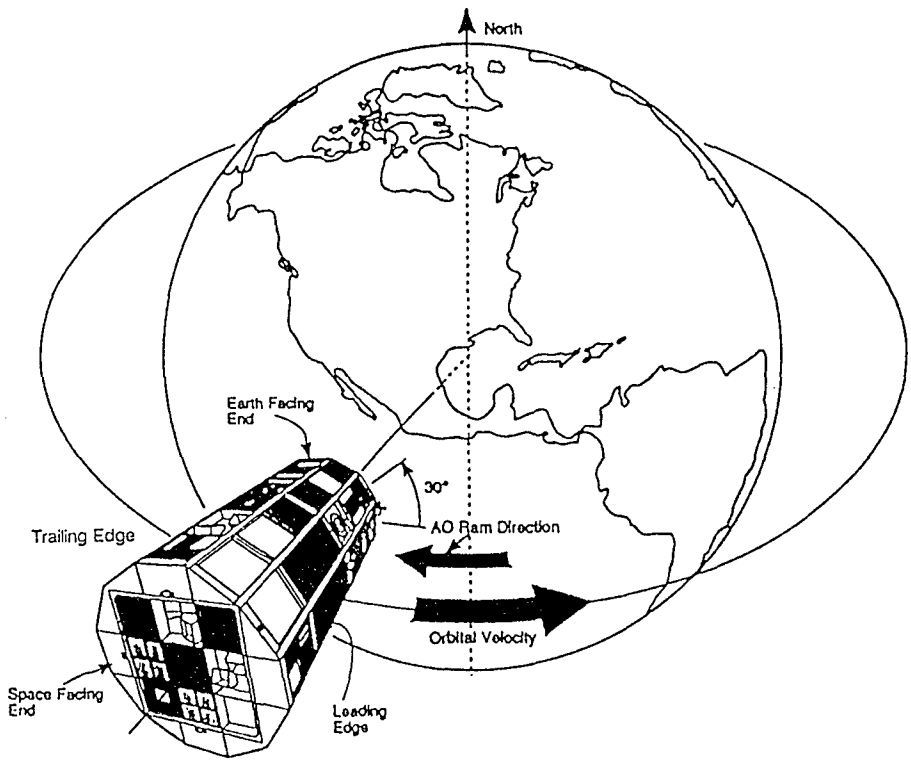


Figure 2: Illustration of LDEF's orientation while in gravity-gradient stabilized Earth orbit. Note RAM, SIDES (top and bottom on figure),TRAIL, EARTH, and SPACE faces.

The micrometeoroid model takes into account the shielding subtended by the Earth as seen by LDEF, and thus is a function of altitude. For cratering predictions the mean density of micrometeoroids has been set at 0.5 gm/cm^3 as suggested by Cour-Palais[1]. (In reality, the true density of micrometeoroids is uncertain. *Captured* particles have had densities of up to 3.5 gm/cm^3. However, the recommended flux model of Cour-Palais is itself based on the lower density and would need revising if the density were changed). The micrometeoroid model assumes that the particles arrive at the Earth uniformly from all directions (*i.e.*, appear geocentric). This is not strictly true, but is a reasonable approximation for the 5.75 year exposure time period of LDEF, since during this time the LDEF orbit underwent about 38 complete cycles of precession and thus "sampled" a large region of the 4π solid angle of space.

The debris model assumes a density of aluminum (2.8 gm/cm^3) for particles about 1 cm diameter, which decreases for larger pieces (since large pieces are not chunky bodies but rather pseudo-porous items such as bits of plates, antennas, and so on), and increases for smaller sizes to about 4.0 gm/cm^3, which is representative of alumina propellent particles and flakes of paint pigment.

The debris model presently assumes pseudo-circular orbits, which immediately prevents collisions on the TRAIL surface of LDEF. The LDEF data, based on impact fluence and both scanning electron microscopy (SEM)[5] and secondary ion mass spectrometry (SIMS)[6] analysis, is revealing that debris particles **did** impact on the TRAIL surfaces. The obvious explanation is that some of the debris are in elliptical orbits. Kessler has been aware of the limitations of his original model, but until recently had little data with which to update it. With the new LDEF data Kessler now concludes that there are significant amounts of debris (*i.e.*, about 20-30 times that tracked by Space Command) in GPS transfer-type orbits at low inclination.[7] This debris should mainly be aluminum oxide effluent from orbital transfer rocket firings.

POD has also independently used an ephemeris code to identify the possible orbit of the particle causing the **largest** crater observed on LDEF. This crater (5.3 mm) occurred on an

aluminum Z-frame on the SPACE end of LDEF, but on a surface facing into the RAM and slightly depressed below the outer envelope of LDEF. In order for the impactor to reach the impact point it must have "come over" the leading edge of the tray, which implies it arrived from the RAM direction but with a SPACE-component angle of at least 15 degrees. The ephemeris code gives a potential solution for a particle in an orbit typical of a GPS transfer stage or for a retrograde launch from Vandenburg. This is in basic agreement with the present conclusions of Kessler.[7] Detailed studies of impacts using the CTH hydrodynamic code (see CTH discussion below) indicate that the most probable source was a piece of aluminum debris. This conclusion is based on determination of perforation limits for either debris or the lower density micrometeoroids.[8] Only a high density particle fits the scenario, ruling out the likelihood of a lower-density micrometeoroid, but allowing the more common high density ones. The inferred particle size is about 1 mm, and for this size the present models predict a higher impact fluence for debris than for micrometeoroids, again suggesting that the impactor was debris. Recent chemical analysis of this impact feature (M. Zolensky, private communication) reveals the presence of no non-Al material (a *null* result) which is still consistent with almost any kind of impactor.

MODEL SCALING LAWS

Whereas the environment models are given in terms of particle diameters, all of the data from LDEF is in the form of impact feature diameters. In order to relate the two for craters it is necessary to invoke a scaling law to give crater sizes versus impactor sizes. The SPENV code presently invokes the simplest of the known cratering laws, namely the "energy" law. This law equates the incoming kinetic energy of the impactor with the energy necessary to "carve out" a hemispherical crater. The result is:

$$D_c/D_p = \text{constant } (\rho_p/\rho_t)^{0.333}\, u^{0.666} \qquad (1)$$

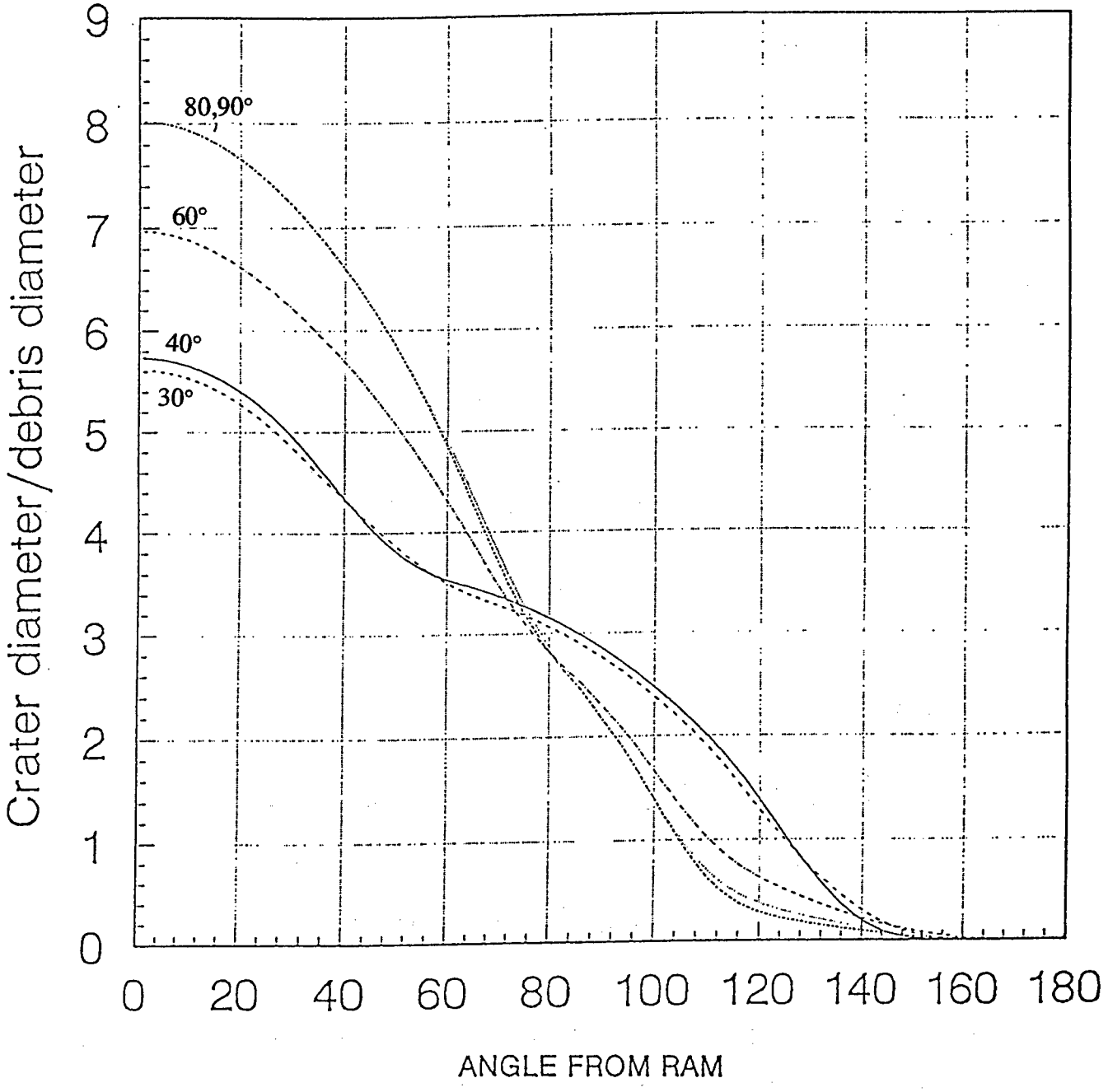


Figure 3: Plot of Dc/Dp versus angle from RAM for debris, in the plane parallel to the Earth. The numbers adjacent to the curves indicate the orbital inclination for that particular curve.

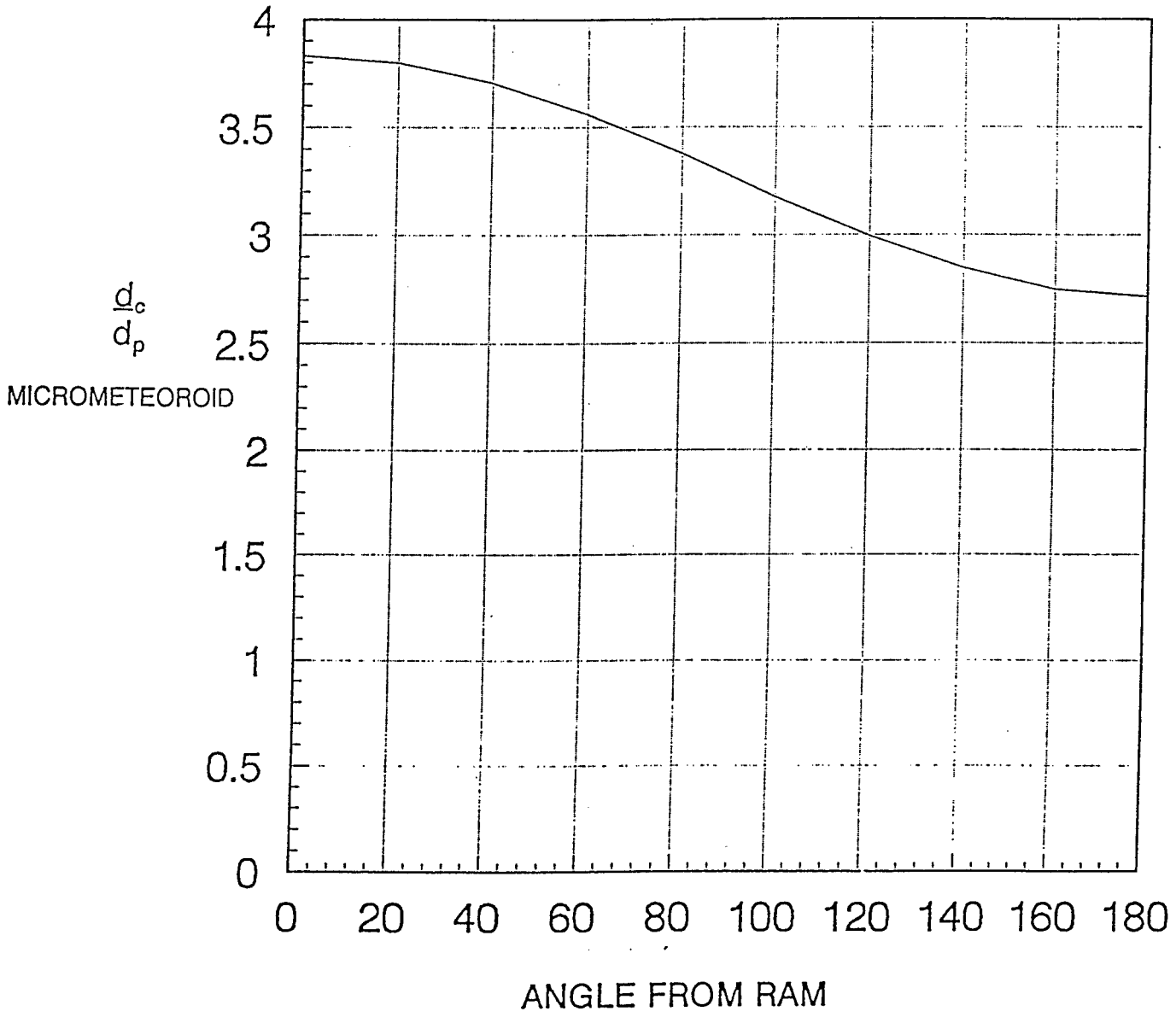


Figure 4: Plot of Dc/Dp versus angle from RAM (velocity vector) for micrometeoroids, assuming a density of 0.5 gm/cm^3, in the plane parallel to the Earth.

where D_c is the crater diameter, D_p is the particle diameter, ρ_p and ρ_t are the impactor and target densities, u is the impactor speed normal to the target surface, and the constant is determined by laboratory experiments.[8] This equation is sensitive to the normal component of impact velocity, and the existing particulate models predict that practically **none** of the impacts are normal. Further, the impact velocities are themselves functions of arrival direction and thus of the orientation of a specific surface relative to the RAM. Consequently, the value of D_c/D_p is a function of surface orientation which is also a function of orbital inclination, and, in principle, of altitude. Figures 3 and 4 illustrate this dependence for debris and micrometeoroids, respectively.

Figure 5 shows the distribution of relative debris impacts in the form of a polar plot versus the RAM direction ("butterfly plot") based on the Kessler model. These impacts are in the plane parallel to the surface of the Earth. The corresponding impact speeds are given by the relation $v = 15.4 \cos A$ km/s, where A is the angle between the RAM direction (zero degrees) and the apparent approach direction of the debris. The component of the impact velocity along the normal to a surface is given by $v = 15.4 \cos A \cos (B-A)$ km/s, where B is the angle between the surface normal and the RAM direction. For the RAM surface itself this reduces to the value $v = 15.4 \cos^2 A$ km/s. If the angle (B-A) exceeds 180^0 then impacts cannot occur on that surface. The data in Figure 3 is obtained by integrating over all the possible angles of approach for a specified surface, based on the relative weighting given by the Kessler model (this weighting explains the butterfly shape).

Figure 6 shows the distribution of **average** impact speeds versus approach direction for the micrometeoroids (RAM direction equals zero degrees). This polar plot represents a body of revolution symmetric about the RAM axis. The effect of Earth-shielding is to remove a section of the solid angle for this figure, which results in a modification of the impact fluxes for all surfaces except that facing towards SPACE. The source of data for this plot is that due to Erickson[9] which describes the relative number of micrometeoroids versus speed as seen from the Earth (so-called "stationary satellite" data). This data is transformed into the reference

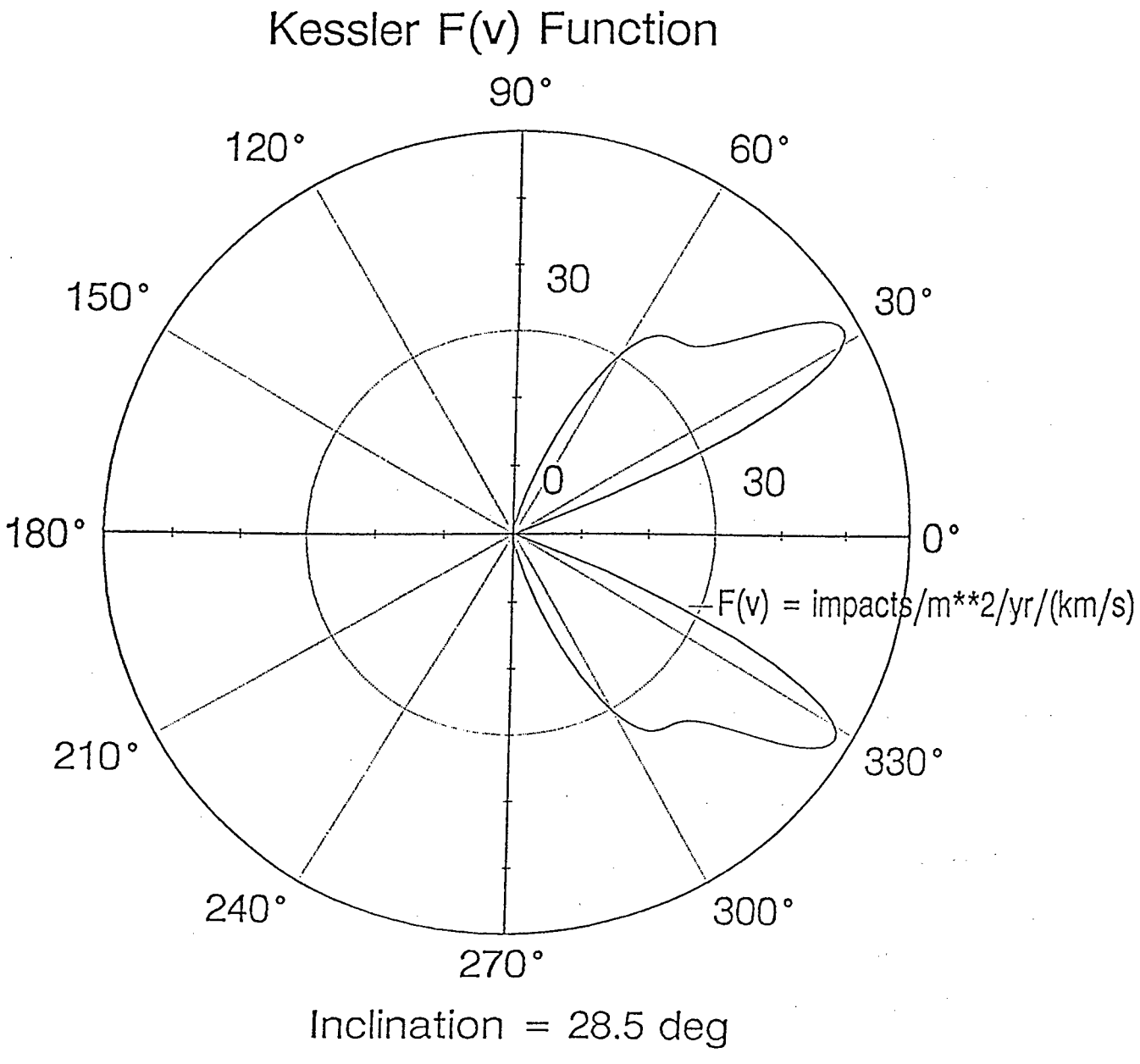


Figure 5: Plot of polar distribution versus angle from RAM (velocity vector) for debris, in the plane parallel to the Earth, for LDEF.

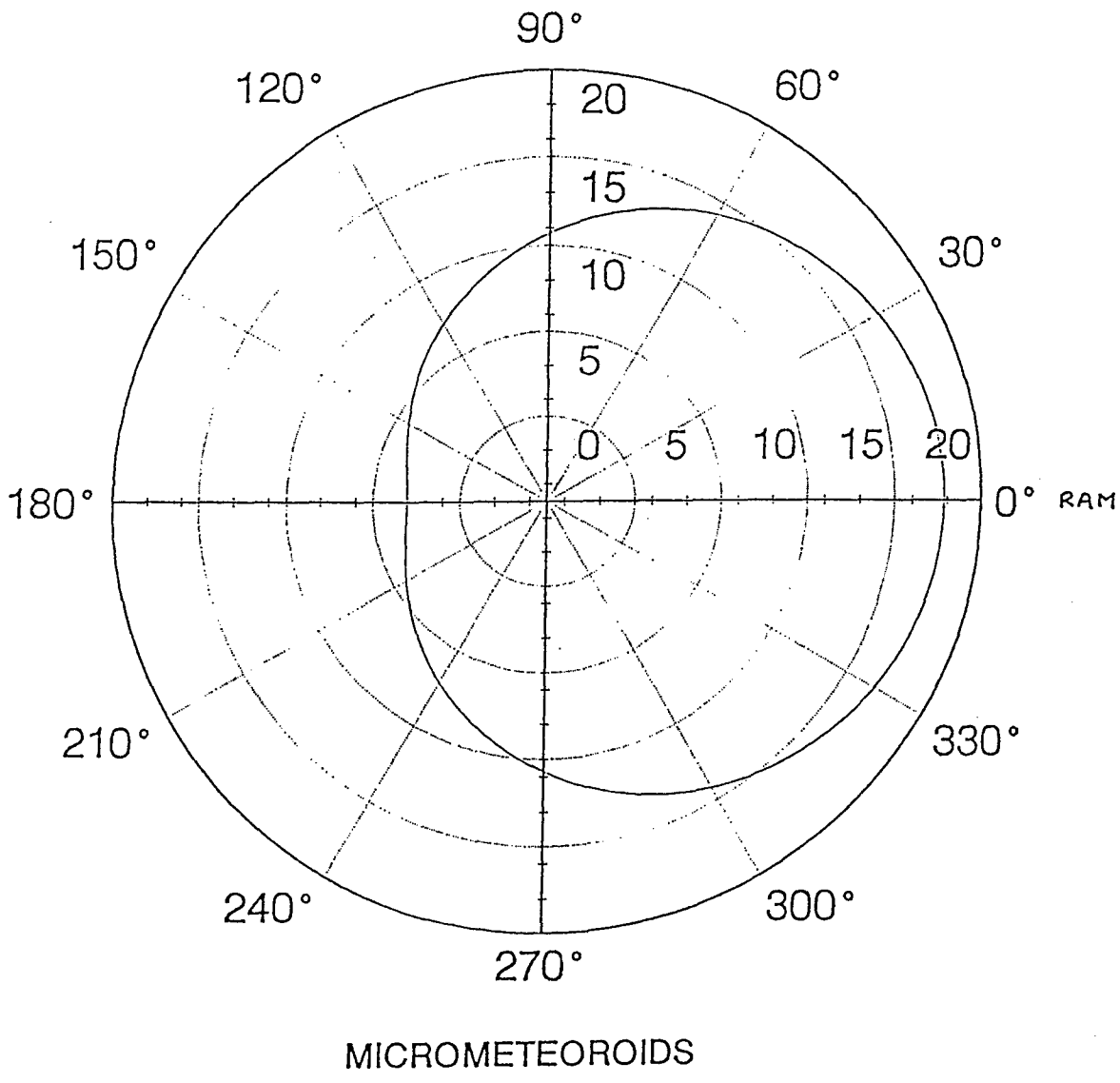


Figure 6: Plot of polar distribution of impact velocity versus angle from RAM (velocity vector) for micrometeoroids. This figure is axisymmetric about the RAM axis, and ignores Earth shielding.

frame of the orbiting satellite to produce Figure 6. As with debris the effects of micrometeoroid impacts are obtained by integrating over all particles taking into account the components of velocity along the normal to the specific surface.

There are several other proposed crater scaling laws (*e.g.*, Cour-Palais[1,10] and Christiansen[11]). In general, the differences in these laws are variations in the power indices for densities (and/or masses) and velocity. Since the indices are less than unity, the effect is a relatively small shift in the values of D_c/D_p. The data are presented in the form of cumulative fluences, or rather, impacts per area for craters greater than or equal to a specified size, versus crater size. The effect of changes in scaling law is primarily a horizontal shift in the plots. For example, changing the power index for density from 0.333 to 0.5 moves the curves by only a factor of 1.34 even for the extreme case of a tantalum impactor (density 16.6 gm/cm^3) into aluminum (density 2.8 gm/cm^3), and clearly has no effect for symmetric impacts such as aluminum into aluminum. Likewise, a change in the assumed density of a micrometeoroid (*e.g.*, from 0.5 gm/cm^3 to 3.0 gm/cm^3) produces a factor of 1.82 or 2.45 for power indices of 0.333 and 0.5, respectively.

CTH HYDROCODE CALCULATIONS

The CTH computer code[3] from Sandia Laboratory, Albuquerque, has been used to simulate several classes of impacts. In order to benchmark the code, specific calculations were done to replicate laboratory-generated ballistic penetration (*i.e.*, perforation) cases for aluminum. These data were provided by Fred Hörz of NASA JSC. Material parameters were adjusted in the CTH runs until good replications were obtained. The agreements involved standard, acceptable Equation of State (EOS) and constitutive data for the impactors and targets, and in particular, identified the aluminum targets as Al 1100 with temper H16 (Hörz could not specify the exact temper of his samples, but the suggested solution is very credible being a reasonably common alloy). Details of these comparisons are given in the Appendix.

The CTH results were then plotted as functions of perforation limits for various aluminum sphere diameters versus normal impact velocities, and for various aluminum wall thicknesses, and the data were fitted analytically by least-squares techniques. The result was a fit very similar to the perforation-limit conditions predicted by the McDonnell equation.[12] Within the accuracy of determination of the "best-fit" equation for the CTH data, the results essentially agreed with the predictions of McDonnell, except for about a 20% decrease in the prediction of wall thickness. Based **only** on this fact, we presently recommend use of the McDonnell equation for perforation predictions, at least for symmetric Al/Al conditions (*Note*, we have **not** yet validated the "strength" term in the McDonnell equation). This equation is:

$$T = 1.023\ d_p^{1.056}\ (\rho_p/\rho_t)^{0.476}\ (\sigma_{Al}/\sigma_t)^{0.134}\ u^{0.664} \qquad (2)$$

where T is the wall thickness, d_p is the particle diameter, densities (ρ) refer to particle or target, respectively, σ values are the yield strengths of Al or the target, and u is the normal impact speed. For a symmetric aluminum into aluminum (Al/Al) impact this becomes:

$$T = 1.023\ d_p^{1.056}\ u^{0.664} \qquad (3)$$

The corresponding "best-fit" from CTH for Al/Al impacts was:

$$T = 0.81\ (+/-\ 0.20)\ d_p^{0.9375\ (+/-0.105)}\ u^{0.625\ (+/-0.09)}\ \text{(ref.8)} \qquad (4)$$

CTH has been used to simulate impacts on coated materials in order to understand such effects as the "ring" and "dome" structures seen on painted aluminum, together with localized delamination effects. To date, the CTH runs have been able to simulate the formation of "domes" and demonstrate the development of delaminations. However, while the runs have predicted transient "ring" motions (*i.e.*, Rayleigh wave ripples propagating away from the impact site), we have not yet identified the parameters necessary to cause a "freezing" of these waves to yield permanent rings. It appears that the behavior is very sensitive to the amplitude

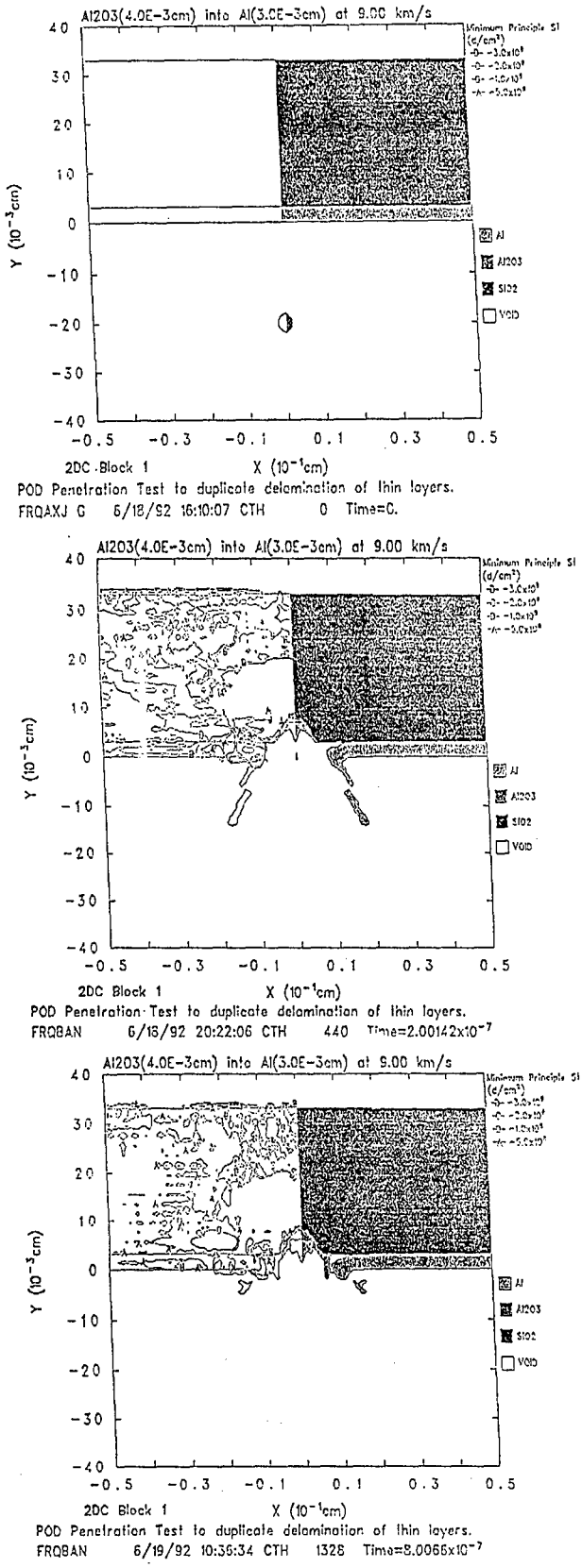


Figure 7: Example results from a CTH run where an alumina projectile impacted a 2-layer target at 9.0 km/s. Time is in sec. Note the factor of 100 vertical exaggeration.

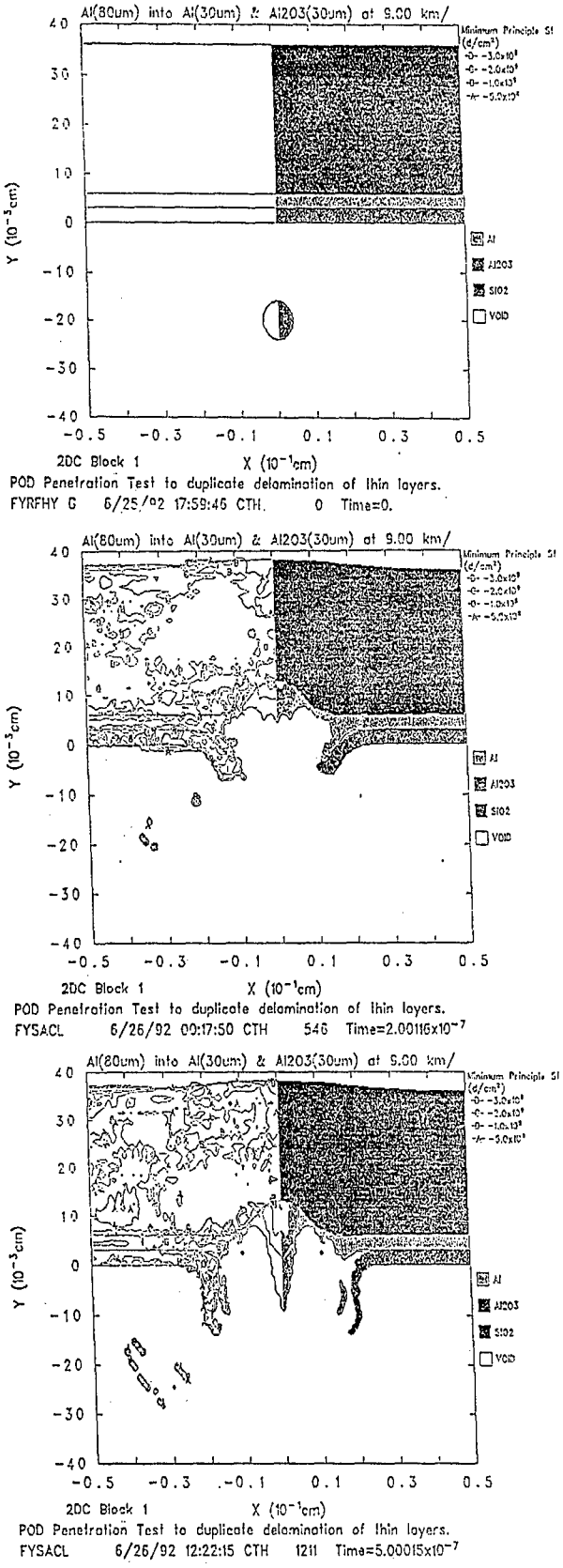


Figure 8: Example results from a CTH run where an aluminum projectile impacted a 3-layer target at 9.0 km/s. The bottom figure shows the impactor jetting back out of the crater.

of the induced wave structure and the yield strength of the materials, since the CTH calculations either gave rapidly dampened waves or else indicated material loss due to localized jetting around the impact site. We do **not** presently understand this since basically **all** of the painted surfaces exhibited "rings" and the impact conditions cannot have been identical. Figures 7 and 8 show some typical CTH results. These example problems include an aluminum coating on a silica substrate (Figure 7) and a two-layer alumina/aluminum coating on silica (Figure 8). In both cases the impactors have been alumina or aluminum. Parameter options investigated include impact speed and interlayer adhesion strength. In each figure, the sequence progresses from the top to bottom, with the top image at 0 time. Projectile velocity was 9.0 km/s for both examples.

The effect of interlayer (bond) strength is interesting. For zero strength the layer locally "peels back" by a small amount around the impact hole in the layer and the layer debonds rapidly in a radial manner away from the hole, such that the entire layer essentially jumps off the substrate. The silica substrate develops a typical crater. As the bond strength is increased so the debonding becomes limited to a region around the impact site, but at the expense of greater localized peel back at the hole edge. Depending on details, the local peel back can resemble the standard lips for a metal target impact, or can spall off and cause secondary ejecta. If the coating is a brittle one (alumina) with high compressive yield strength but low fracture strength, the tendency is to crack off the lips. Conversely, for the soft metal (Al) coating the tendency is to develop considerable plastic/molten flow, and droplets peel off.

In all high speed (>9 km/s) impacts modelled to date, the impacting particle (whether brittle alumina or soft aluminum) has always been forged into a self-forming jet structure which expels itself back out of the hole. This occurs because the impact pressures are sufficiently high to cause gross plastic flow at elevated (shock induced) temperatures, and the geometry causes convergence effects, thus producing the jet. The result is that only small portions of the impactor remain within the crater. We cannot presently identify the exact amount of material remaining, since this involves "late-time behavior" and requires long computer run times. This

behavior is consistent with many LDEF observations, where frequently the impactor is either difficult or impossible to identify due to limited or zero remnants. In particular, the calculations indicate that the impactor does **not** need to completely vaporize in order to explain negligible remnants. For the two-layer coating problem both layers peel back and delaminate from each other and the substrate. Figure 8 shows such a case, and indicates the complicated morphology around the impact site.

Of relevant interest to this discussion is some data provided by Maxwell Laboratory, San Diego.[13] Workers there used the flash X-ray machine, *Blackjack 5*, to throw debris particles at single crystal silicon. The latter target was simultaneously surface heated by the associated X-ray plasma. The result was the development of ring structures very similar to those seen on LDEF. The pictures resemble a frozen version of the "stone in a pond" effect! The postulated explanation is that the hot surface (almost molten) of the silicon was forced to undergo plastic yielding due to the Rayleigh waves, and that hysteresis "locked in" the ripples.

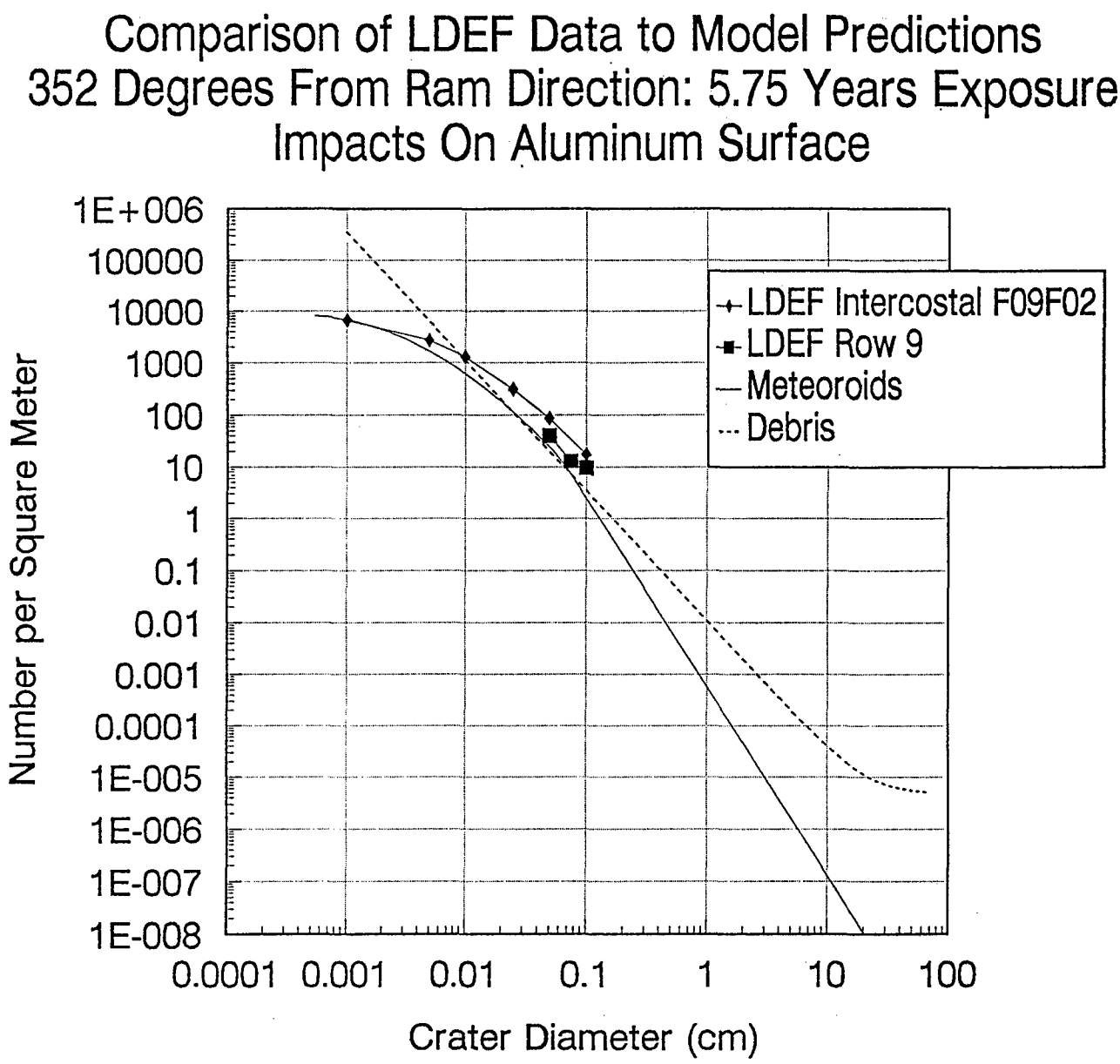
LDEF EXPERIMENTAL RESULTS

Data utilized in this portion of the study originated from three sources: (1) For craters larger than 0.05 cm diameter, measurements were taken by the LDEF Meteoroid and Debris Special Investigation Group's (M&D SIG) Kennedy Space Center Analysis Team on the entire LDEF aluminum structure,[14] and (2) for craters larger than 0.01 cm diameter, measurements were taken by the authors from specific aluminum experiment tray covers and sun shields, and (3) for craters larger than 0.001 cm diameter, measurements were taken by See *et al.*[15] on LDEF intercostals. Separate environment models were utilized to make predictions for the meteoroids and debris and computed using the SPENV model. For meteoroids, the Cour-Palais *et al.*[1] model was used with the Kessler-Erickson velocity distribution as described by Zook.[9] For debris, the Kessler model[2] was used. Our SPENV program models both the micrometeoroid and debris environments that may be encountered by a spacecraft in an orbit

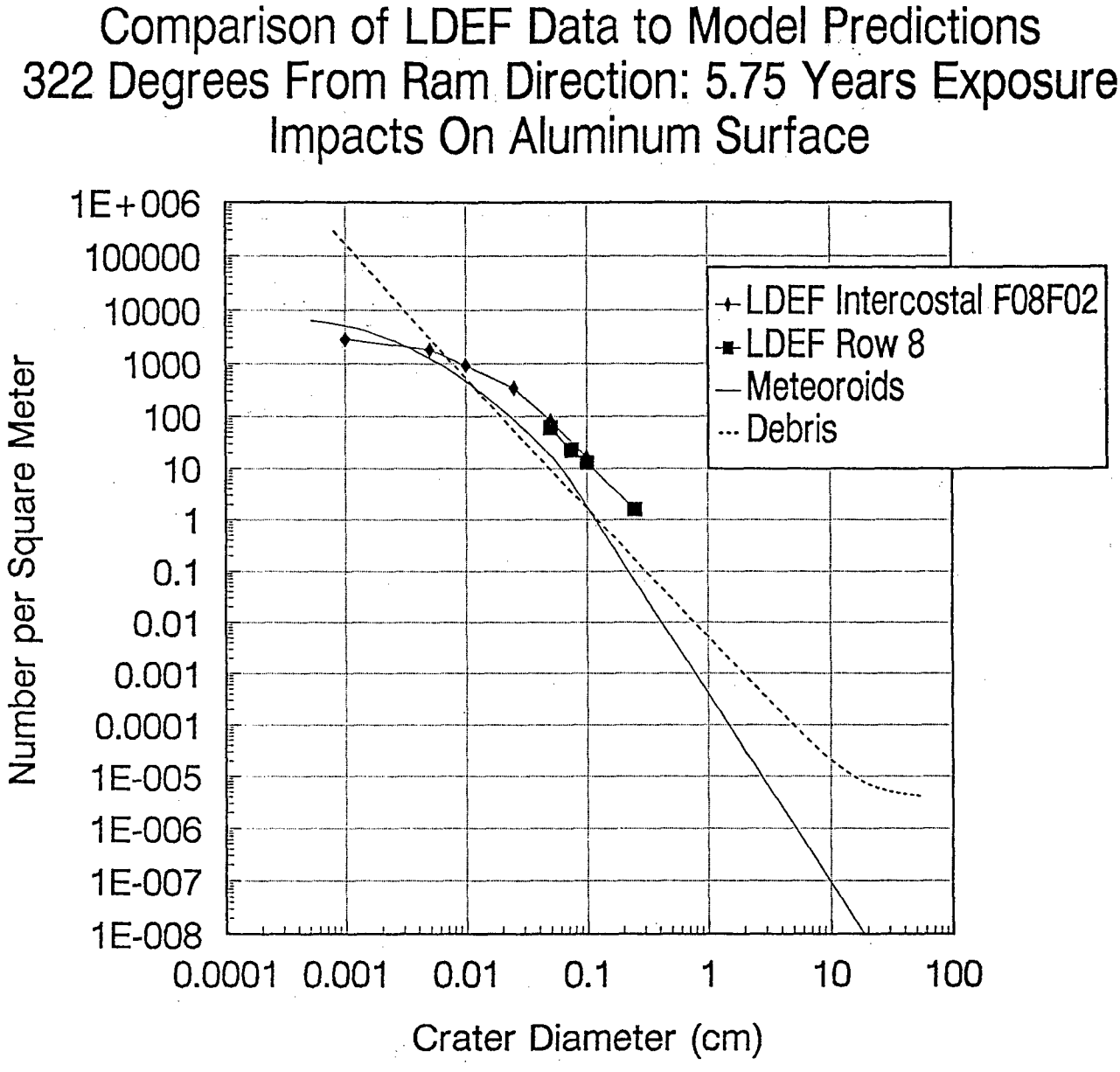
between 200 and 2000 km. As both the Kessler and Cour-Palais models[1,2] predict particle diameters, the scaling law presented previously was applied to these data, thus reducing them to the form of cumulative impact fluences (hits per square meter) for craters greater than or equal to specified diameters.

LDEF was a gravity-gradient stabilized satellite, intended to always have one surface facing EARTH, and one side (row 9) always facing into the RAM. In actuality, LDEF was slightly rotated about its long axis such that row 9 was about 8 degrees off of the true RAM (towards the SOUTH). This fact explains the angular quotes for the intercostals and rows, given below.

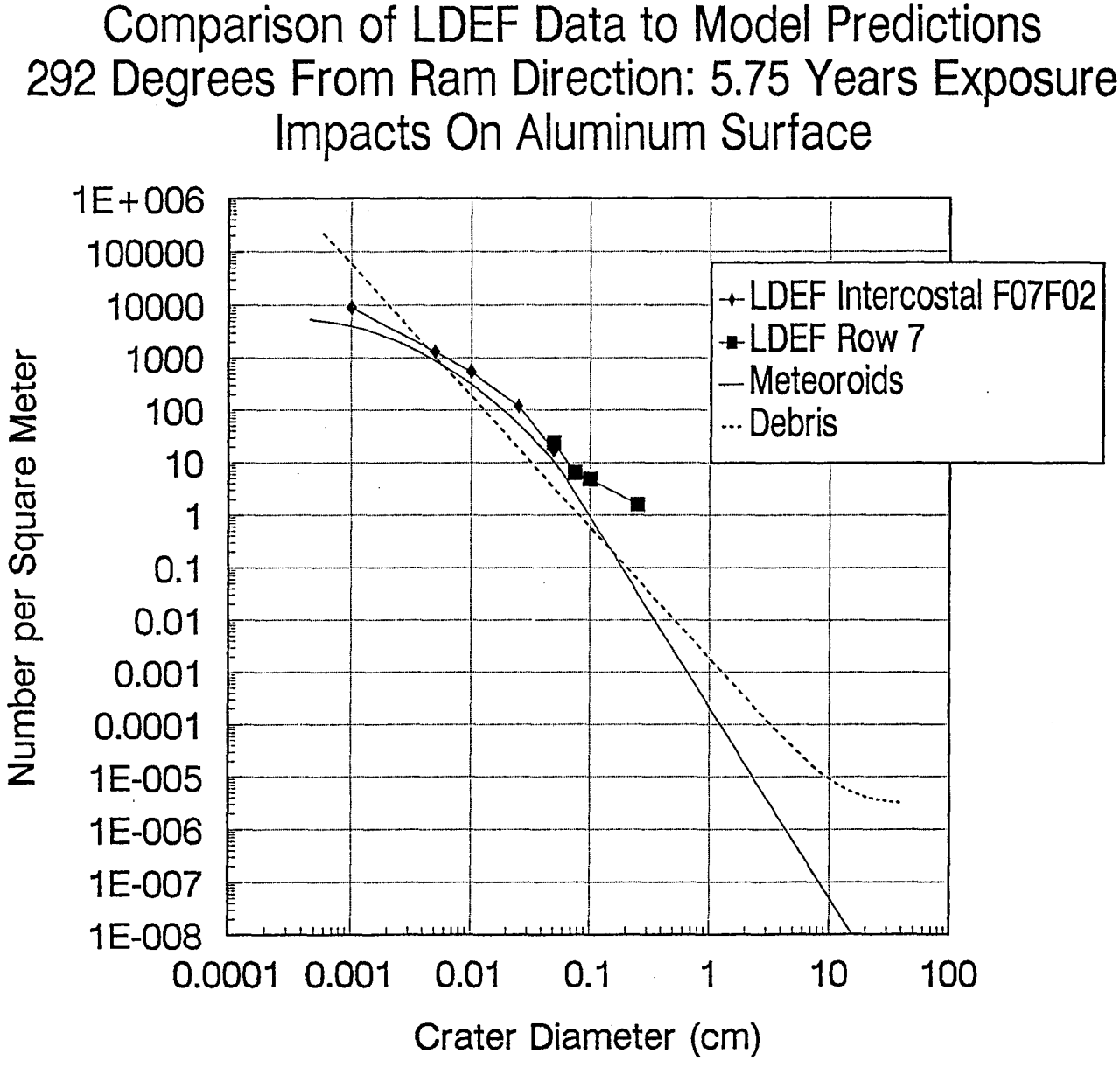
Figures 9a-l and 10a-e illustrate the data, together with comparisons of the existing micrometeoroid and debris model predictions. Each of the plots in Figure 9 compares measured crater diameters to the number of craters per square meter (fluence) for different locations on LDEF: RAM (row 9, 352 degrees) through 22 degrees (row 10) (anticlockwise, as viewed from the Earth). For directional reference and location purposes, the plots refer to various intercostals (aluminum frame pieces which run "around" the LDEF central axis), and the corresponding rows (*i.e.*, faces), from LDEF. Each plot shows the data collected from the intercostal and other components in that same row as compared to the meteoroid and debris models. For example, data for craters larger than (say) 500 μm originated from the intercostal which was scanned for that row, and the fluence was derived by dividing by the area of the specific intercostal. A similar process was done for all craters larger than 500 μm on other surfaces as well. Figures 10a-e illustrate the comparison between the LDEF data to the M&D model predictions as a function of row or intercostal location on the satellite (degrees from RAM) vs. fluence. These plots represent the number of craters with diameters greater than or equal to 50 μm, 100 μm, 250 μm, and 500 μm, respectively. **In general**, the sum of the model predictions agrees within a factor of two to three for surfaces toward the RAM. However, toward the TRAIL the agreement is worse by a factor of four or more.



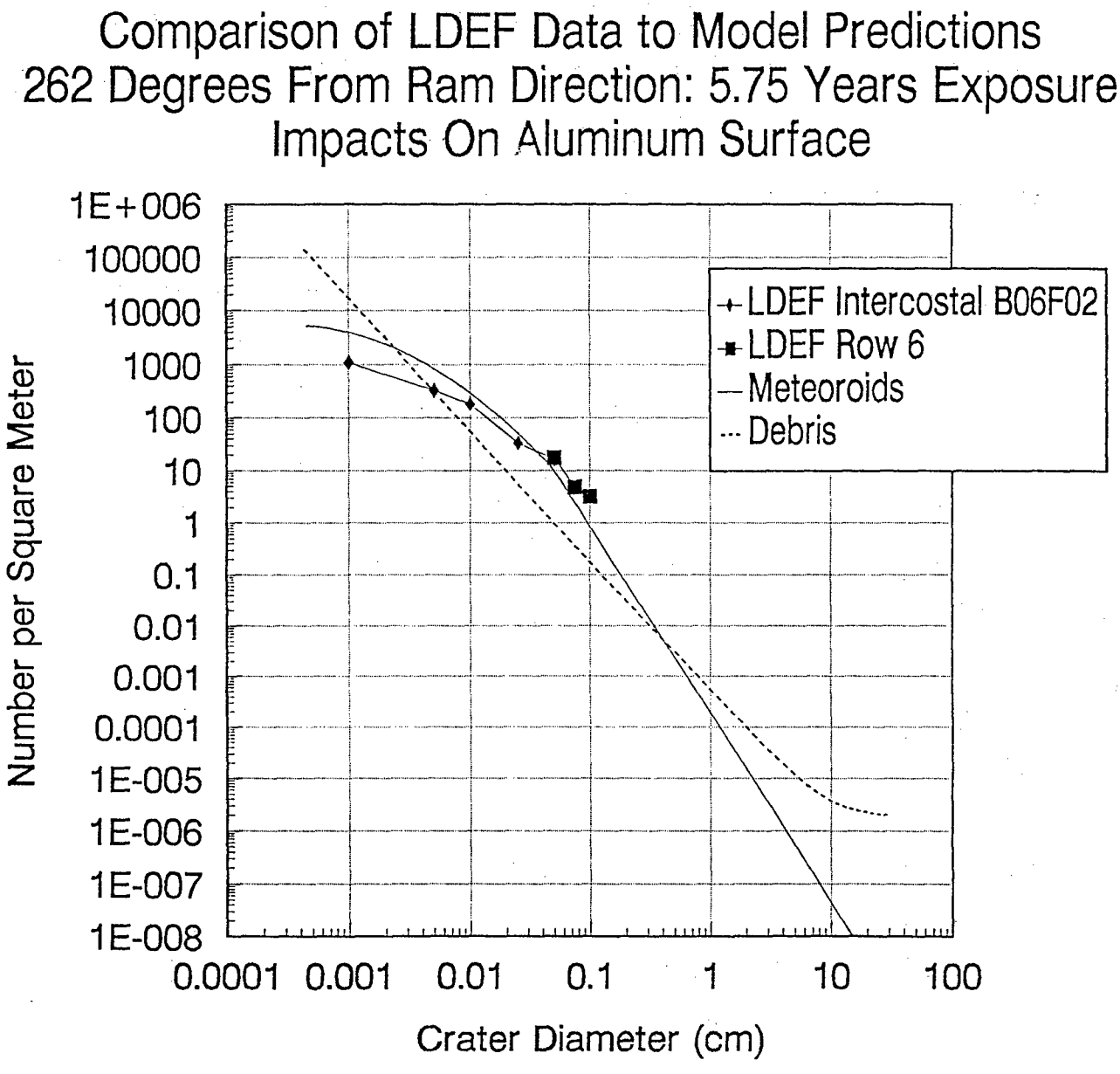
Figures 9a: Comparison of crater diameters to number of craters per square meter. Data collected from the LDEF intercostals and rows.



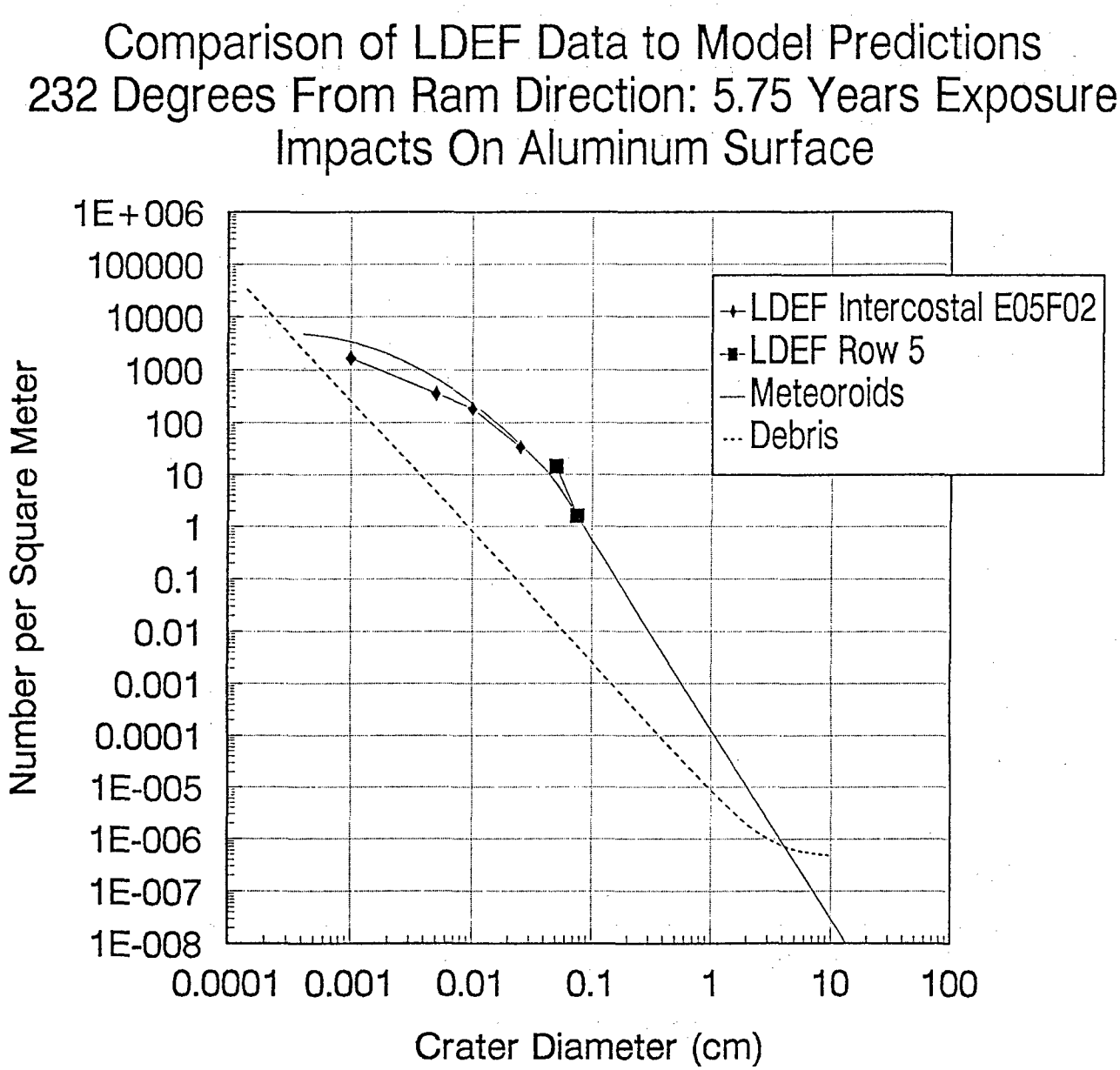
Figures 9b: Comparison of crater diameters to number of craters per square meter. Data collected from the LDEF intercostals and rows.



Figures 9c: Comparison of crater diameters to number of craters per square meter. Data collected from the LDEF intercostals and rows.



Figures 9d: Comparison of crater diameters to number of craters per square meter. Data collected from the LDEF intercostals and rows.



Figures 9e: Comparison of crater diameters to number of craters per square meter. Data collected from the LDEF intercostals and rows.

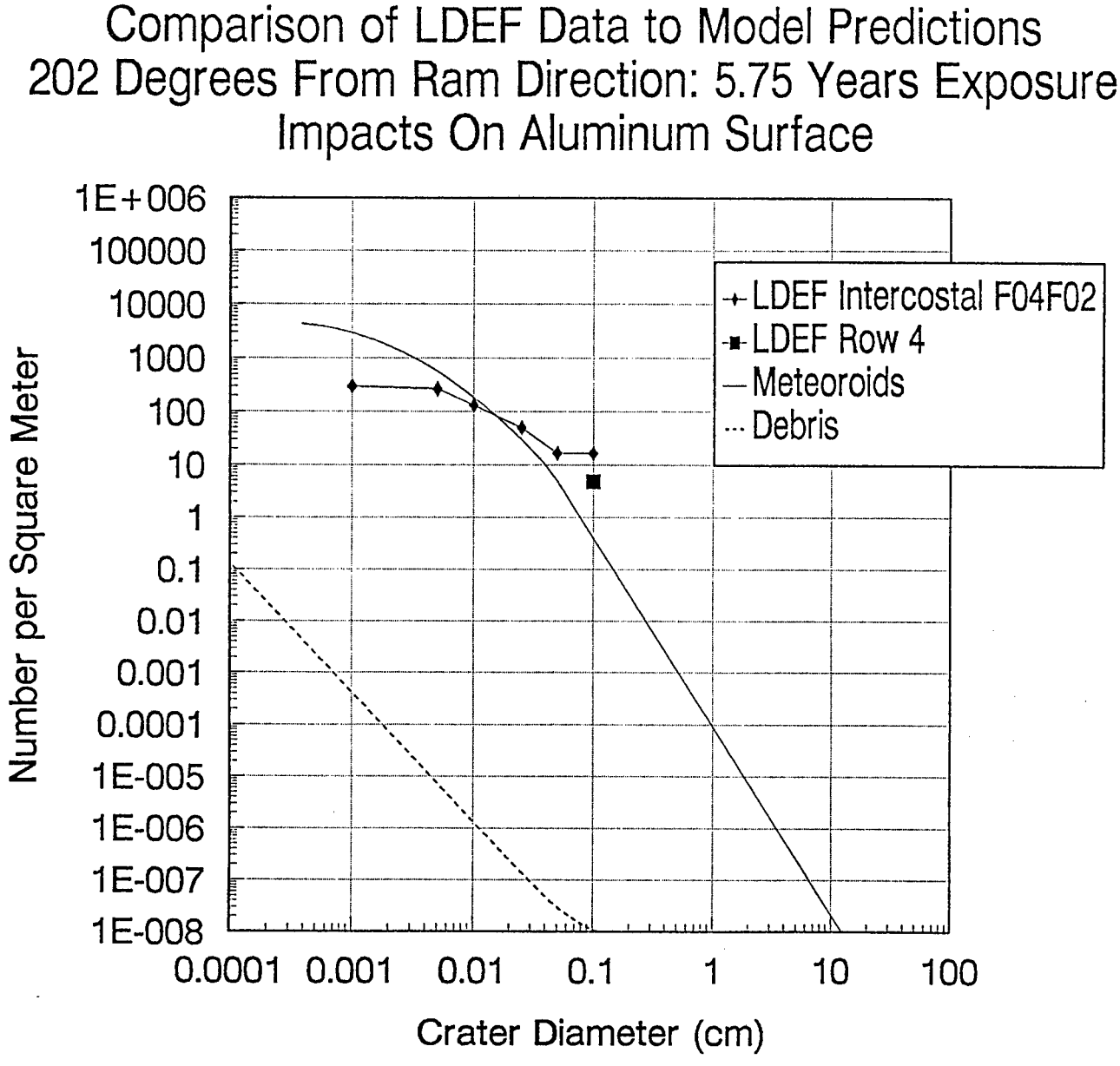
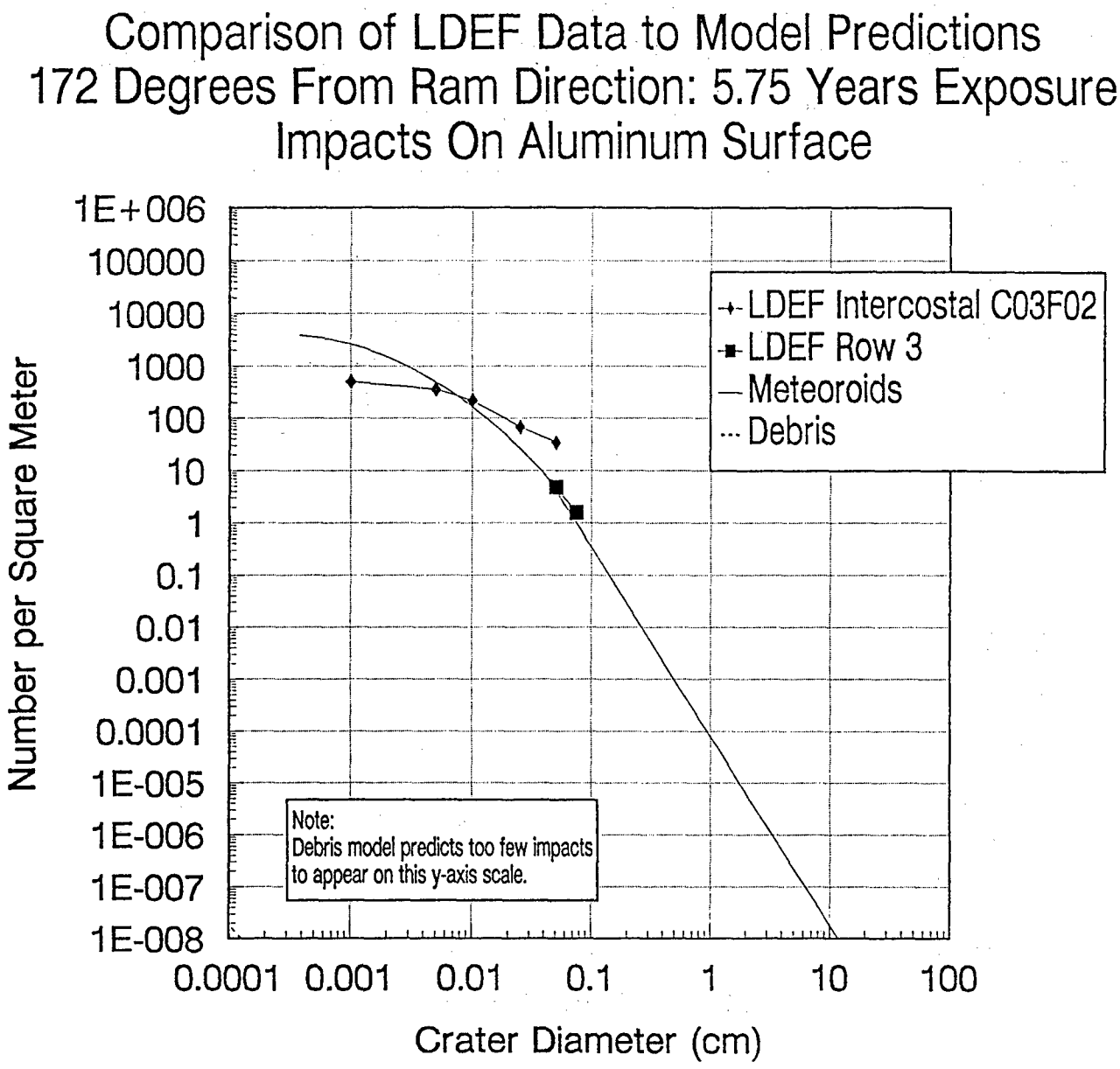
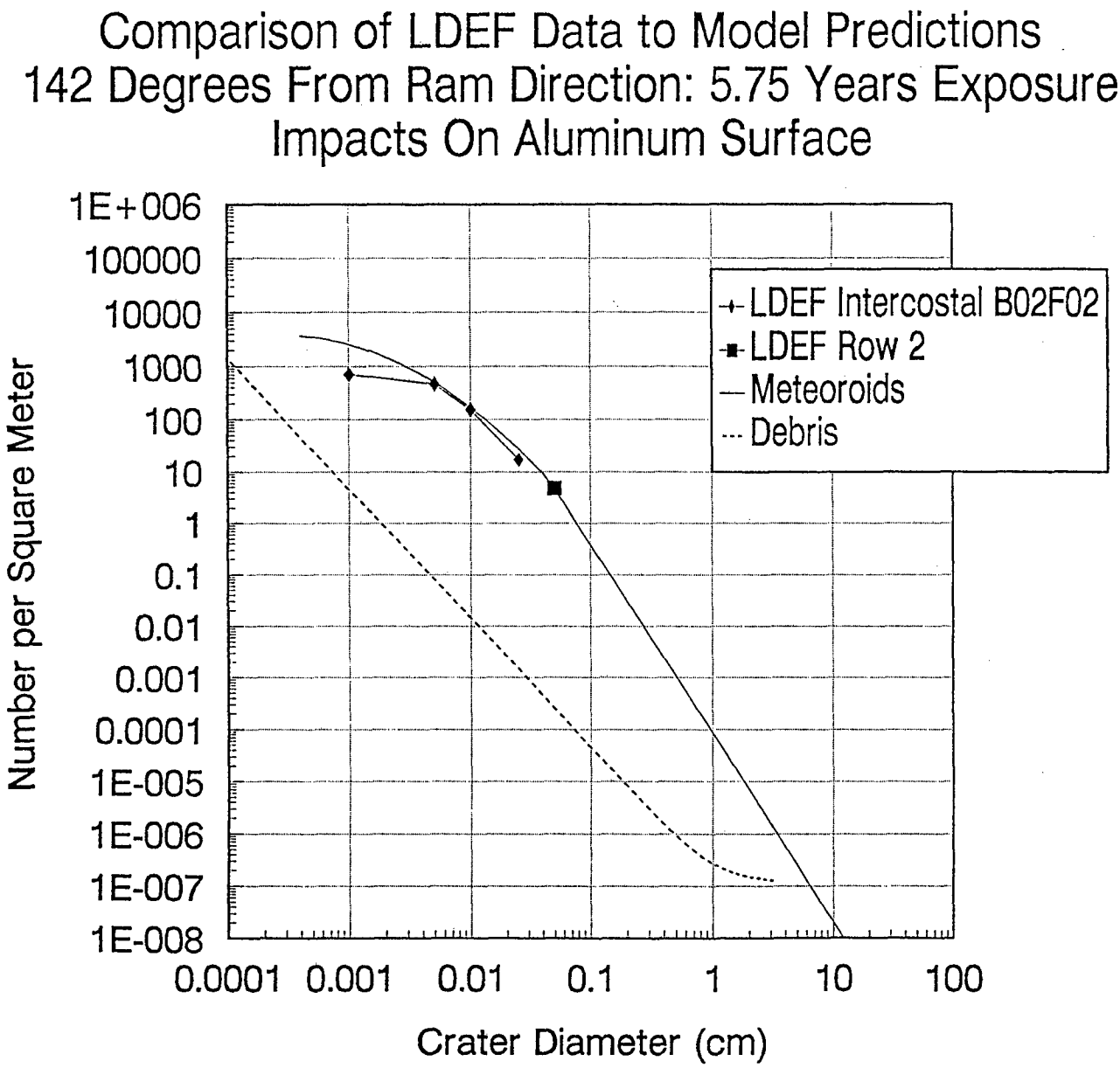


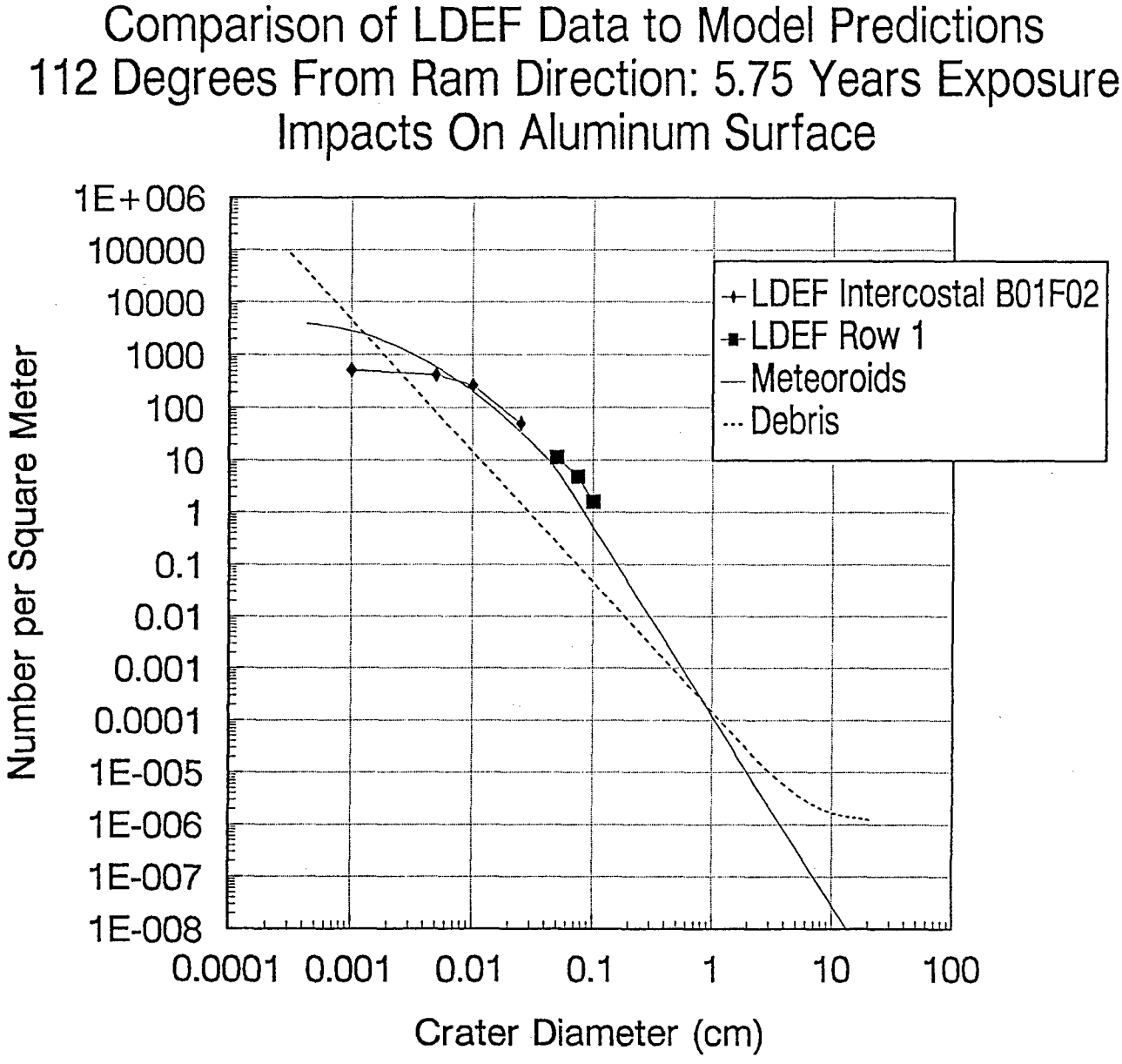
Figure 9f: Comparison of crater diameters to number of craters per square meter. Data collected from the LDEF intercostals and rows.



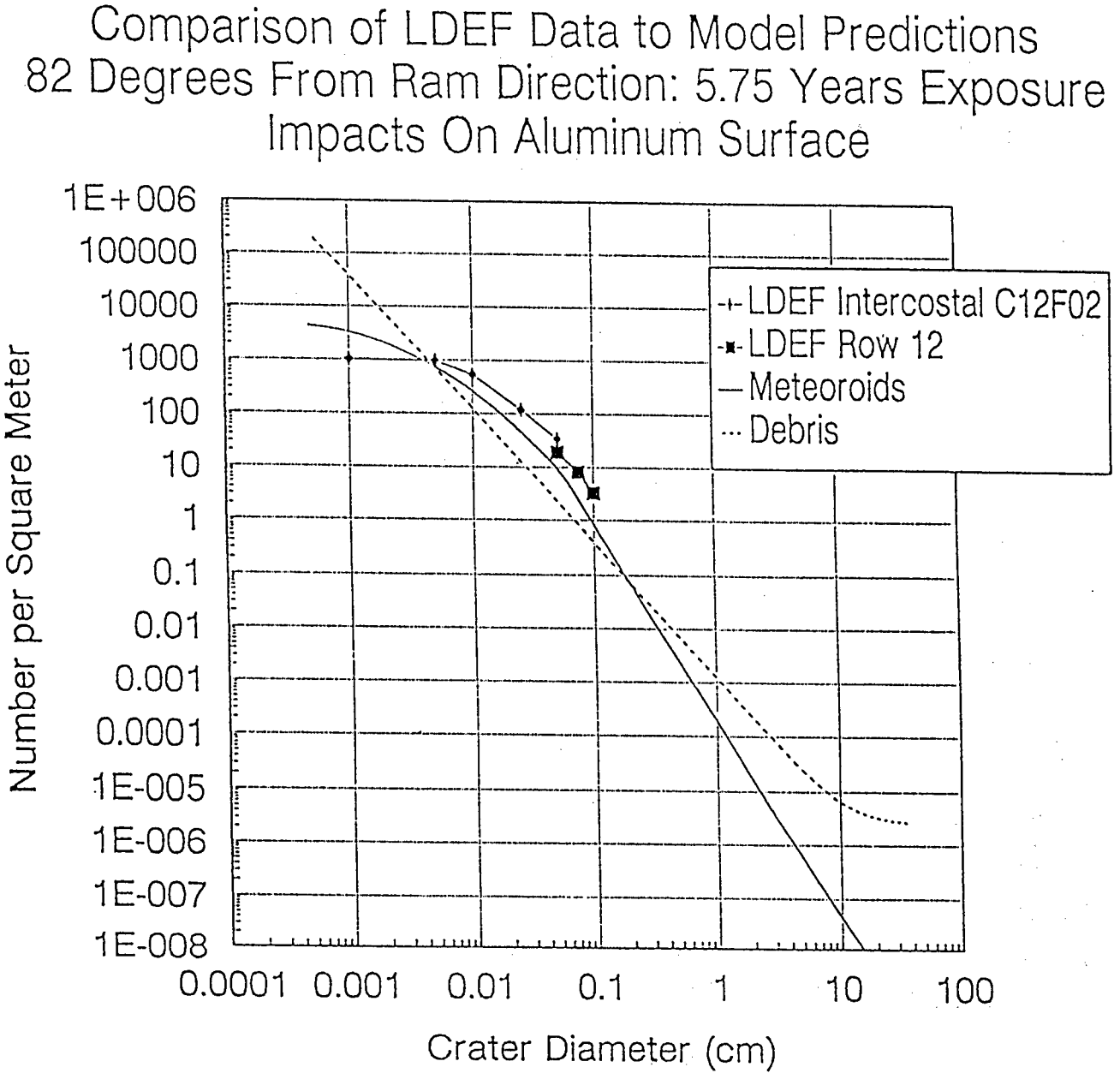
Figures 9g: Comparison of crater diameters to number of craters per square meter. Data collected from the LDEF intercostals and rows.



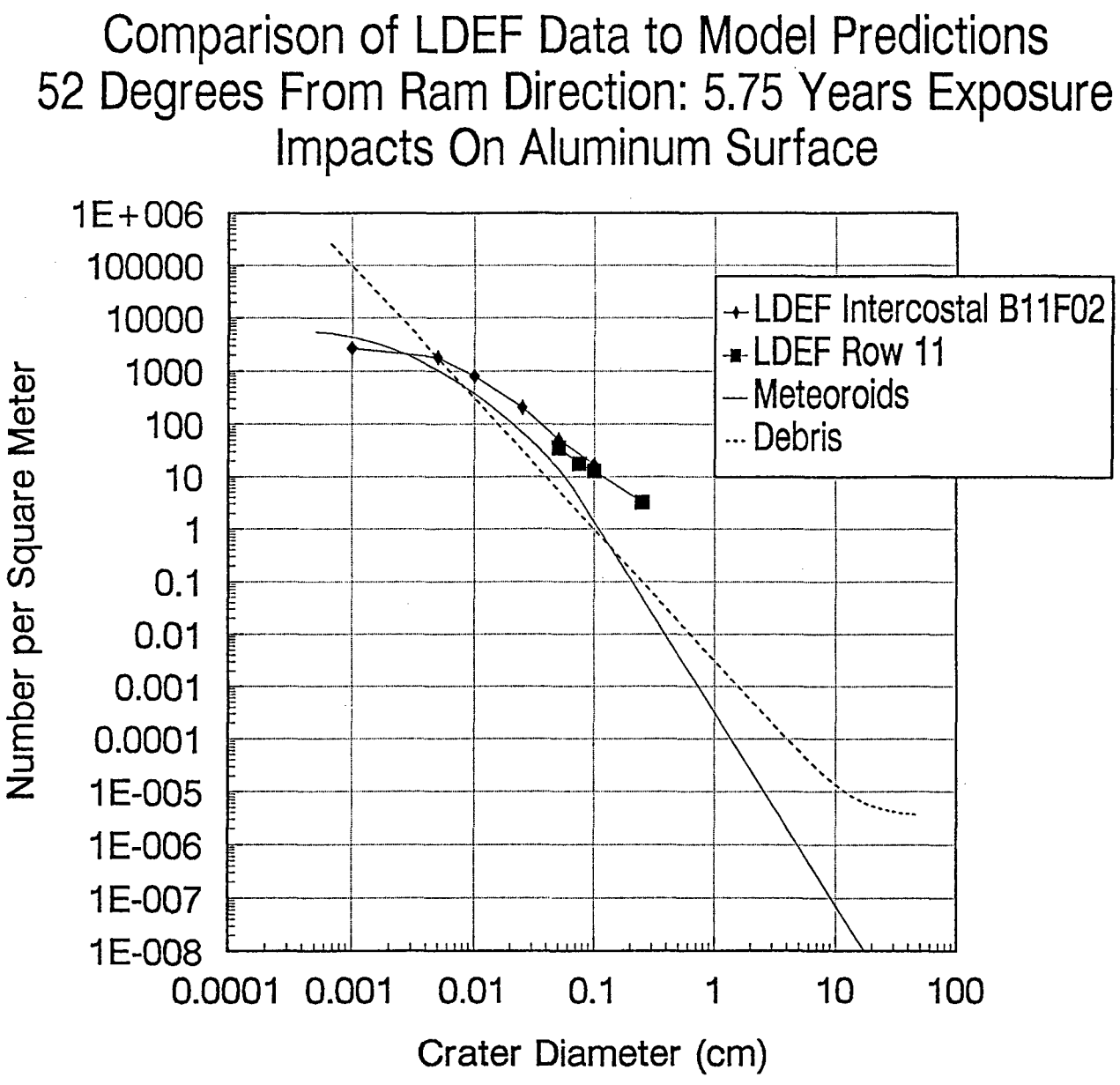
Figures 9h: Comparison of crater diameters to number of craters per square meter. Data collected from the LDEF intercostals and rows.



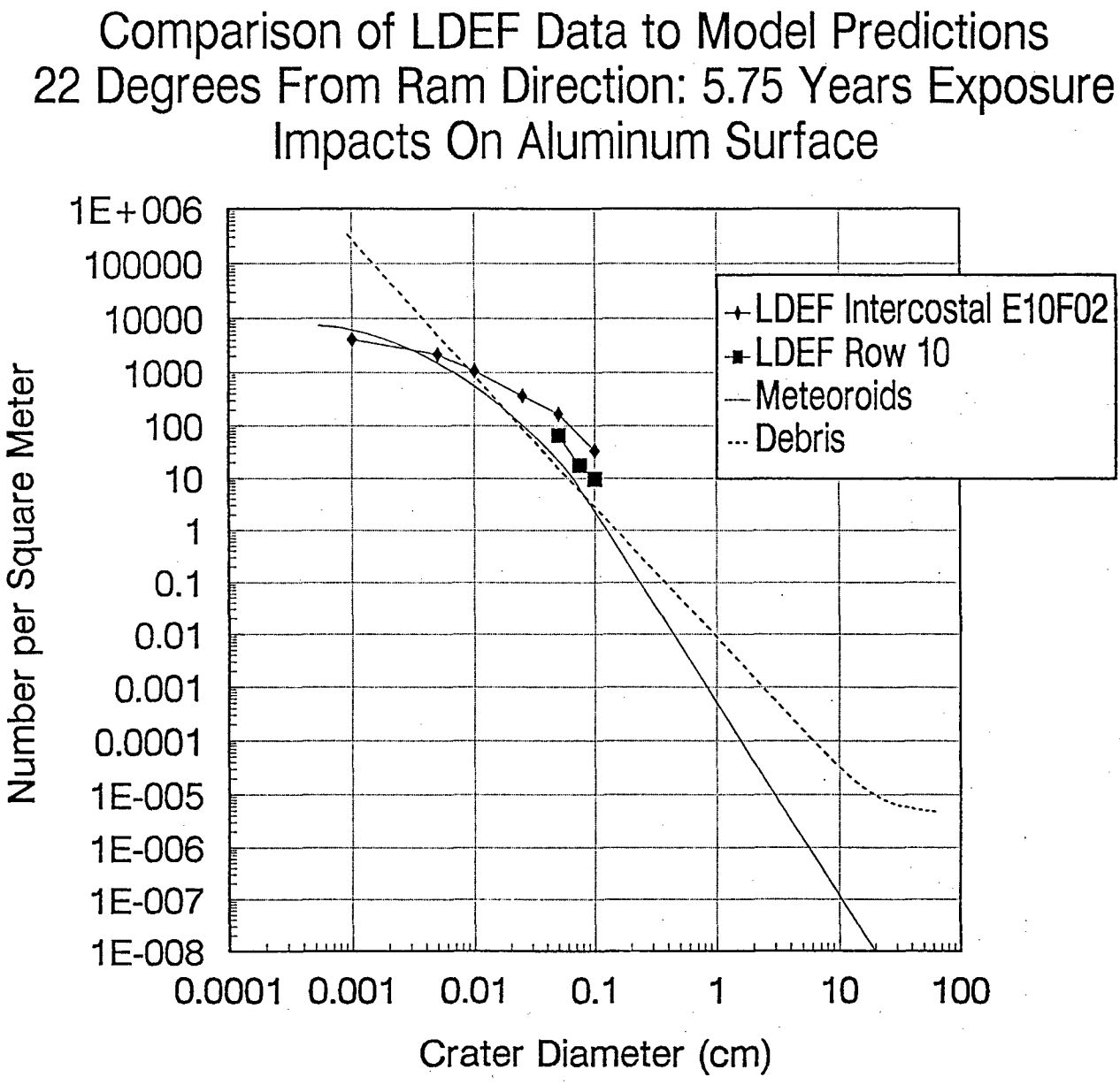
Figures 9i: Comparison of crater diameters to number of craters per square meter. Data collected from the LDEF intercostals and rows.



Figures 9j: Comparison of crater diameters to number of craters per square meter. Data collected from the LDEF intercostals and rows.



Figures 9k: Comparison of crater diameters to number of craters per square meter. Data collected from the LDEF intercostals and rows.

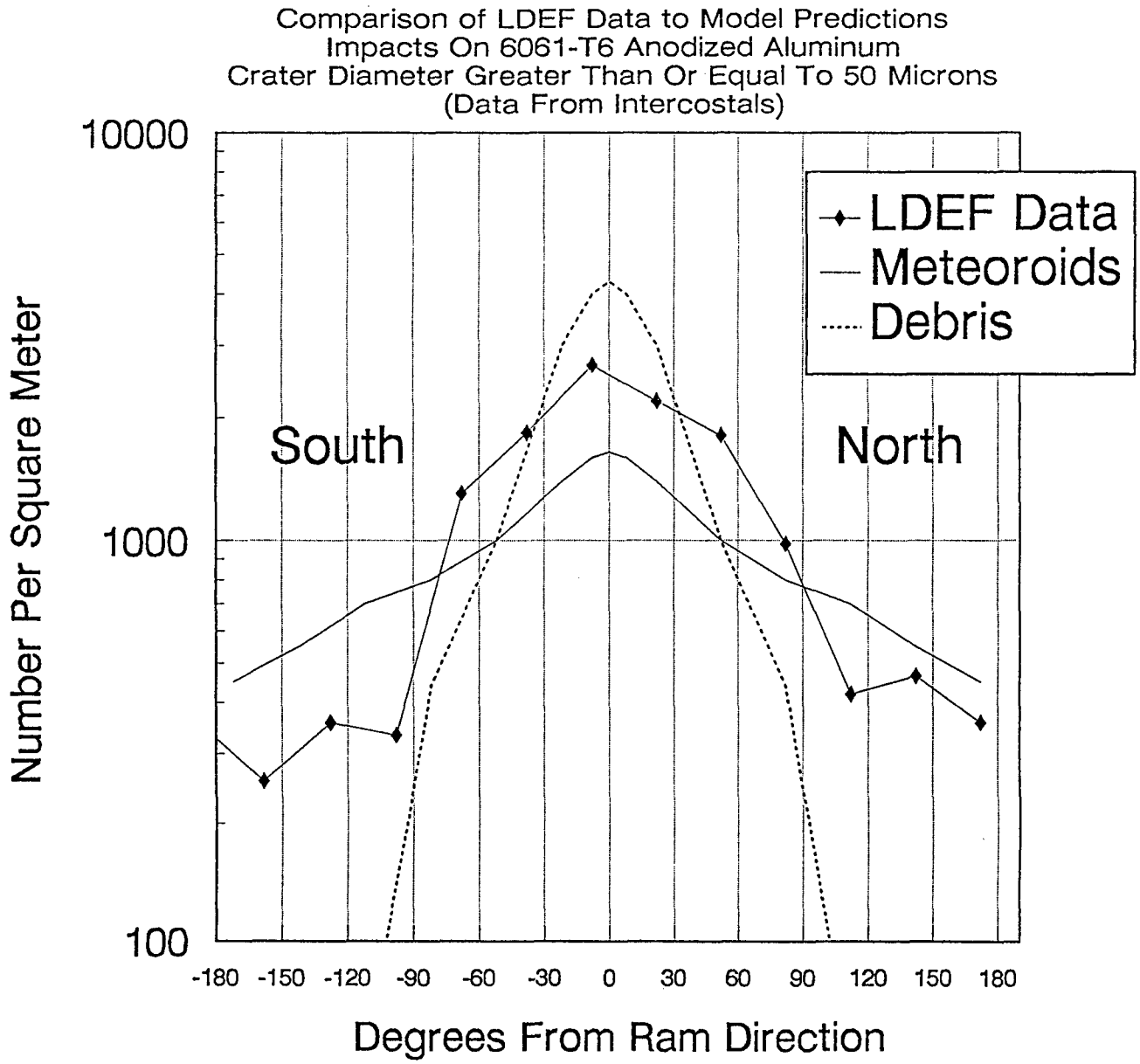


Figures 9l: Comparison of crater diameters to number of craters per square meter. Data collected from the LDEF intercostals and rows.

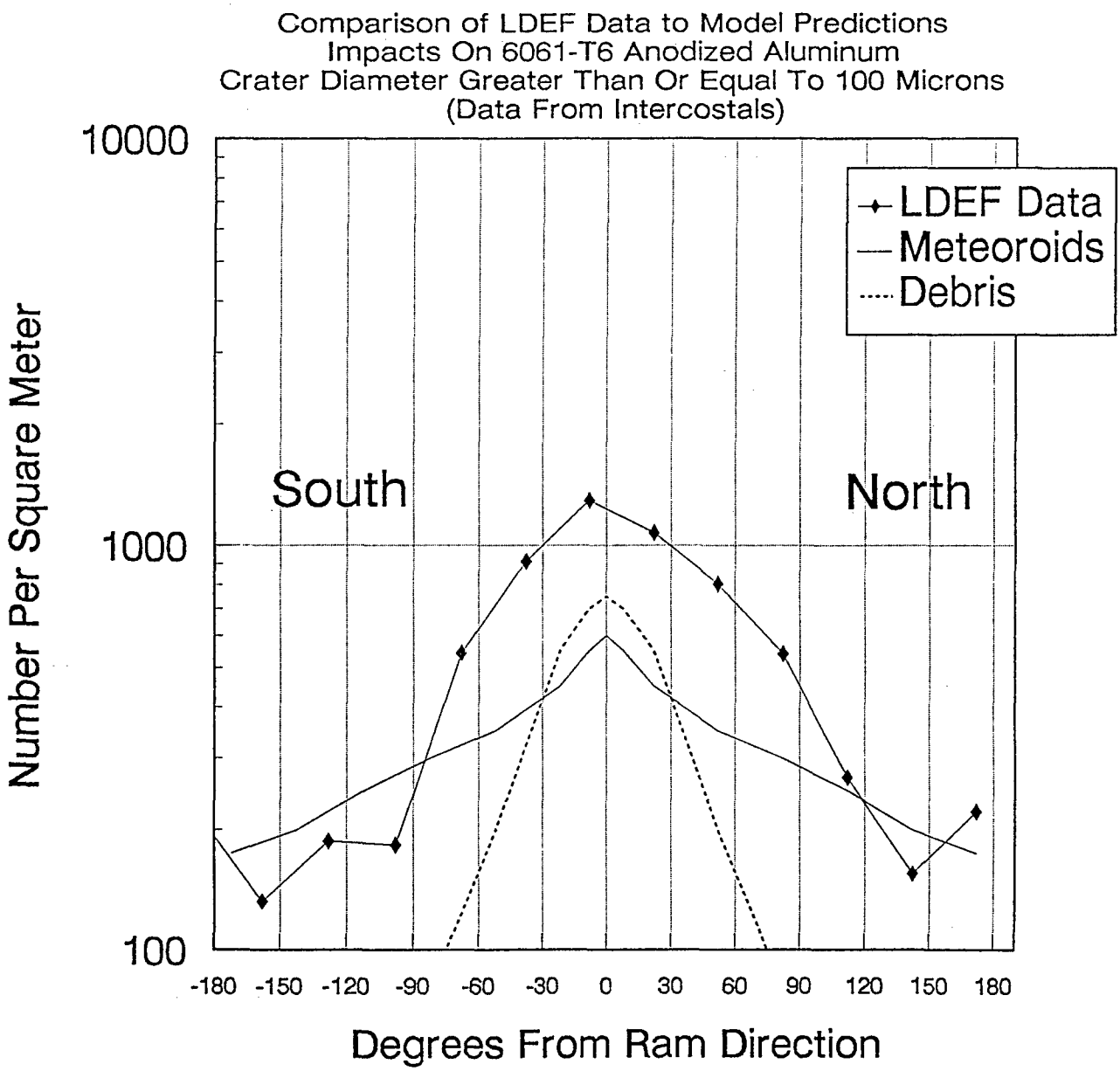
Overall, the measured data tends to oscillate around the predictions for the micrometeoroids. More specifically, the Kessler debris model[2] overpredicts the mean flux of small craters (~0.005 cm diameter), while the Cour-Palais micrometeoroid model[1] slightly underpredicts the mean flux for these small craters, for the RAM (row 9) surface. A similar divergence has been noted for the EARTH- and SPACE-facing ends (not covered in this report). This divergence may be indicative of either elliptical orbital particles from natural or man-made sources, of β-meteoroid fluxes, or a combination of the two. The Interplanetary Dust Experiment[16] data has positively identified a β-meteoroid component of the natural environment, which is not currently accounted for in the Cour-Palais model[1] we used. Grün *et al.*[17] did, however, take the β-meteoroids into account when they updated Cour-Palais' model in 1985. This version of the model is currently being analyzed and incorporated into our in-house SPENV model.

Other observed trends, most clearly seen in Figures 10a-e, include an asymmetry wherein the impact fluence tends to be greater than the predictions (for the crater sizes measured) towards the NORTH surface (angles in the range 0 to 180 degrees), and lower than predictions for the SOUTH surface (180 to 360 degrees, *i.e.* -180 to -0 degrees on Figures 8a-e). Scrutiny of Figures 9a-l also reveals a tendency for the data to exceed the predictions for the larger of the measured craters. Care must be exercised in the interpretation of Figures 10a-e. The "true" RAM direction is 0 degrees, and the micrometeoroid and debris models assume symmetry about this direction (the occasional "kinks" in these curves are due only to the interpolation routine in the graphing utility). If the environments were truly symmetric then the LDEF data would **also** be symmetric, regardless of the orientation of the rows and intercostals. The experimental data imply that the environment is **not** simply symmetric. We cannot explain this at present.

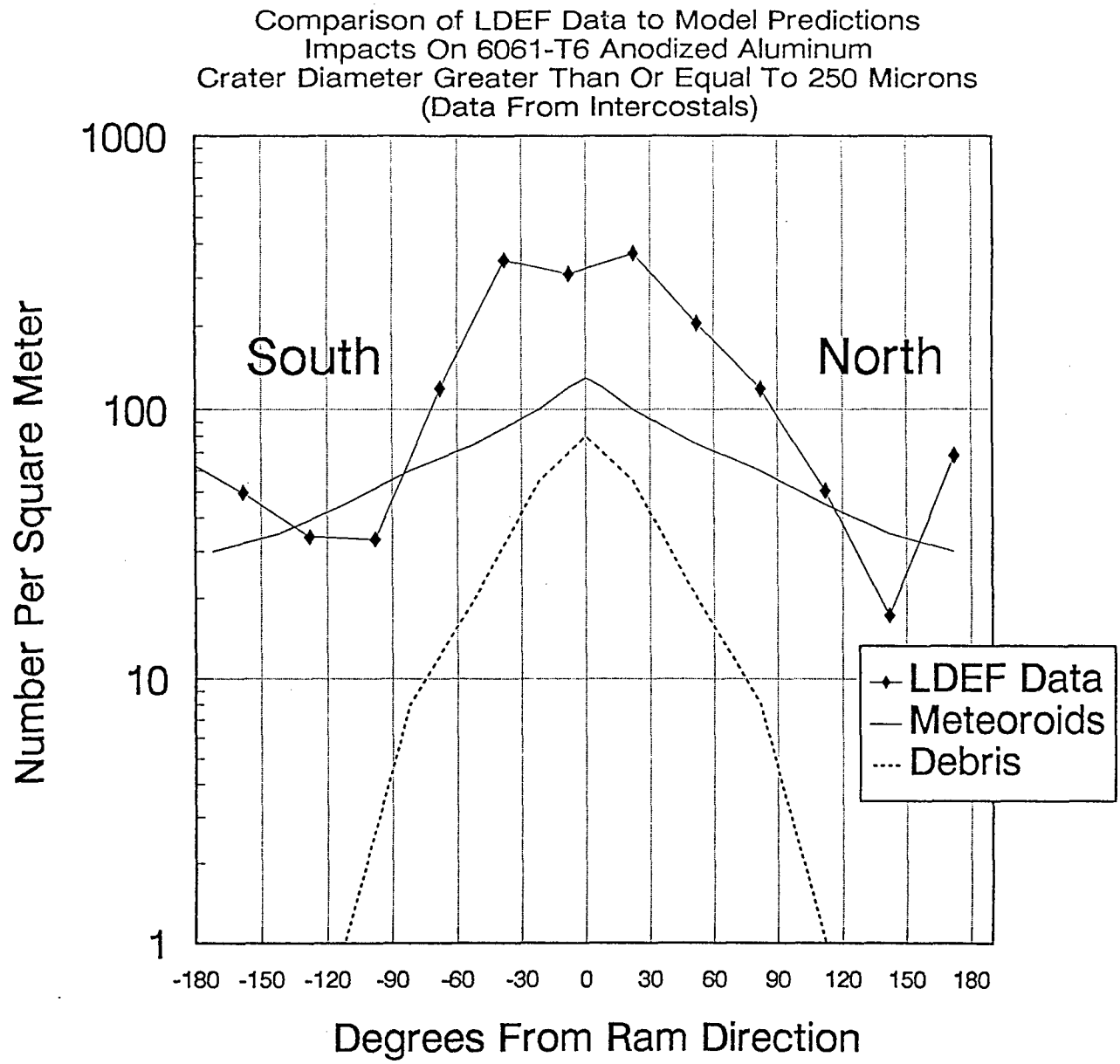
A caution should be raised with regard to measurements of the smallest craters: the target material is not pure aluminum alloy, but has an anodized surface (*i.e.*, an effective coating of alumina). For the larger craters this coating has negligible effect, but for the smallest craters the coating may constitute the "target". Since alumina has both a higher density and is tougher than



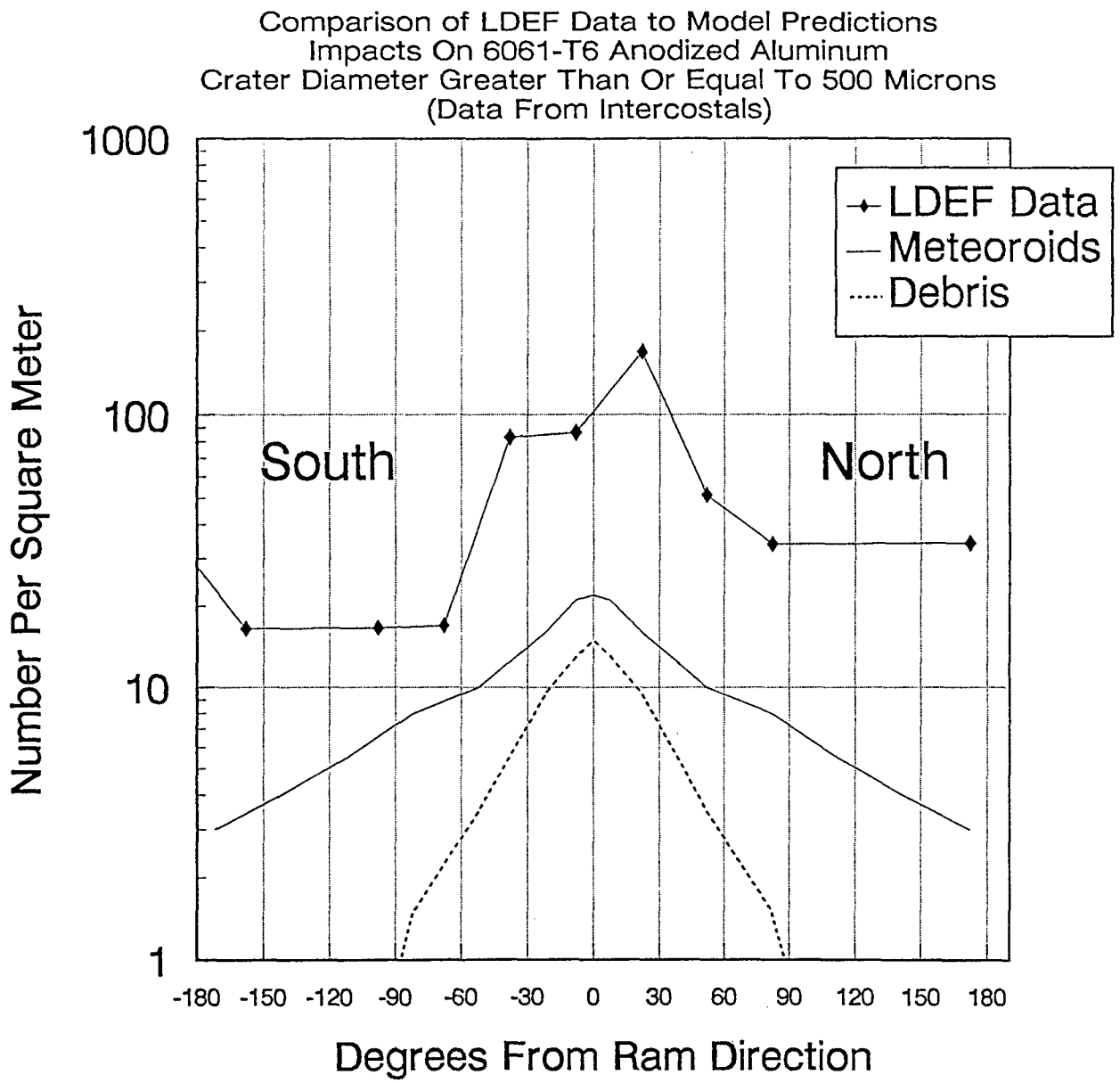
Figures 10a: Comparison between LDEF data and the M&D model predictions discussed in the text as a function of row location on the satellite.



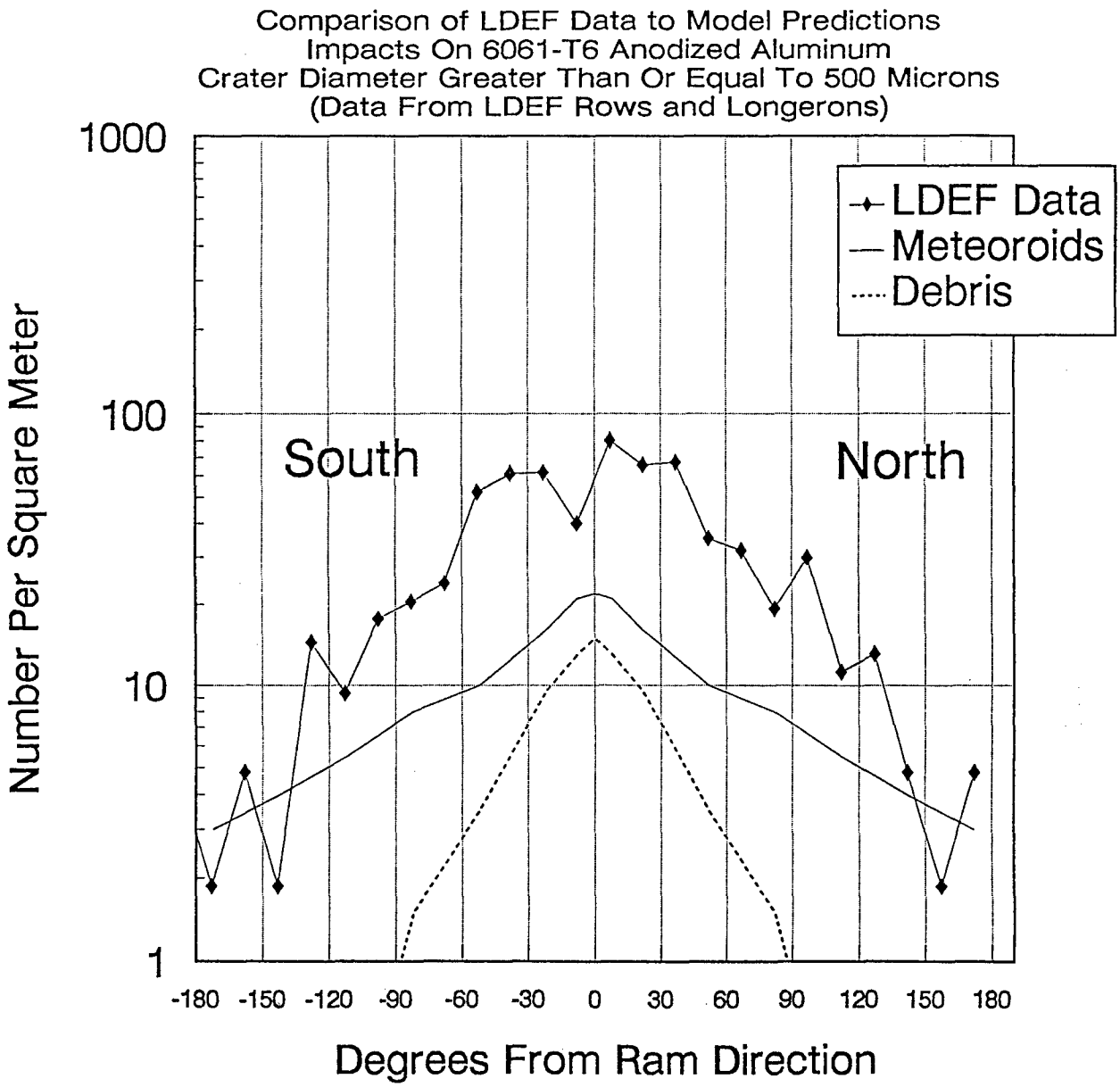
Figures 10b: Comparison between LDEF data and the M&D model predictions discussed in the text as a function of row location on the satellite.



Figures 10c: Comparison between LDEF data and the M&D model predictions discussed in the text as a function of row location on the satellite.



Figures 10d: Comparison between LDEF data and the M&D model predictions discussed in the text as a function of row location on the satellite.



Figures 10e: Comparison between LDEF data and the M&D model predictions discussed in the text as a function of row location on the satellite.

Table 1: Statistical Information For LDEF Intercostal Data

Impacts On Aluminum Surfaces, Crater Diameters ≥ 10 μm

LDEF Row #	Degrees From Ram Direction	Intercostal Number	Surface Area Examined (m^2)	n = Number of Impacts Found	Impacts/m^2 (n/Area)	Error $\pm\sqrt{n}$	Scaled Error $\pm(\sqrt{n}/Area)$	Scaled Error %
1	112	B01F02	0.0594708	31	521.26	5.56	93.49	17.9%
2	142	B02F02	0.057873	41	708.45	6.4	110.59	15.6%
3	172	C03F02	0.0586895	30	511.16	5.48	93.37	18.3%
4	202	F04F02	0.0603608	18	298.21	4.24	70.25	23.6%
5	232	E05F02	0.0587443	97	1651.23	9.85	167.69	10.2%
6	262	B06F02	0.0600495	65	1082.43	8.06	134.22	12.4%
7	292	F07F02	0.058855	539	9158.1	23.22	394.56	4.3%
8	322	F08F02	0.0602198	172	2856.19	13.11	217.7	7.6%
9	352	F09F02	0.0579995	384	6620.69	19.6	337.93	5.1%
10	22	E10F02	0.059526	248	4166.25	15.75	264.62	6.4%
11	52	B11F02	0.0584148	158	2704.79	12.57	215.2	7.9%
12	82	C12F02	0.0590156	60	1016.67	7.75	129.71	12.8%

Table 2: Statistical Information For LDEF Row Data

Impacts On Aluminum Surfaces, Crater Diameters ≥ 500 μm

LDEF Row #	Degrees From Ram Direction	Surface Area Examined (m^2)	n = Number of Impacts Found	Impacts/m^2 (n/Area)	Error $\pm\sqrt{n}$	Scaled Error $\pm(\sqrt{n}/Area)$	Scaled Error %
1	112	0.6231	7	11.23	2.65	4.25	37.8%
2	142	0.6231	3	4.82	1.73	2.78	57.7%
3	172	0.6231	3	4.82	1.73	2.78	57.7%
4	202	0.6231	3	4.82	1.73	2.78	57.7%
5	232	0.6231	9	14.44	3	4.81	33.3%
6	262	0.6231	11	17.65	3.32	5.33	30.2%
7	292	0.6231	15	24.07	3.87	6.21	25.8%
8	322	0.6231	38	60.99	6.16	10.6	17.4%
9	352	0.6231	25	40.12	5	8.02	19.9%
10	22	0.6231	41	65.8	6.4	10.27	15.6%
11	52	0.6231	22	35.31	4.69	7.53	21.3%
12	82	0.6231	12	19.26	3.46	5.55	28.8%

the underlying aluminum, the result can be to reduce the crater sizes. This effect will produce a "skew" to the data, such that the plot of cumulative cratering artificially "flattens off" at the smaller sizes. Presently, we do not know the exact thickness of the anodized layer. However, we do know that if it is about 1 mil, then all craters below about 100 microns in diameter are affected.

Since impact events are assumed to be random it is appropriate to apply Poisson statistics to establish the appropriate standard deviations for the data. Thus, if the number of hits on a given area is N, the standard deviation is +/- $N^{0.5}$. Table I summarizes the data for the intercostals, giving the raw hit counts, the corresponding areas, and the resulting standard deviations, while Table II summarizes similar data for the rows. Since the investigated areas were usually considerably less than 1 square meter each, the error must be scaled up by the same ratio as the count rate in order to be consistent for quotes on a per meter squared basis. In Figures 9a-l there are overlapping data at some common crater sizes for the intercostals and the rows. Sometimes these data differ by more than a standard deviation of the **individual** data points. This more accurately indicates the true degree of uncertainty in the measured data. Such variations are to be expected, since Poisson statistics only apply for a truly random flux of impactors. As a simple example, if debris were really in circular orbits they would exist in striated orbits, since launches have not been made randomly into every possible altitude. It is the combination of (a) random collisional breakup, (b) air drag and, (c) initial elliptical launched orbits, that tend to give a randomization of the debris particles. Likewise, there is no *a priori* reason to believe that the micrometeoroids are truly randomly distributed. Data from the IDE[16] experiment on LDEF certainly indicate a degree of non-randomness *in time* showing apparent clustering behavior, and the integrated data from the F07F02 intercostal indicate similar effects with regard to *location.*

CONCLUSIONS

The comparisons provided herein demonstrate a good measure of the relative applicability of the environment models for first-order engineering design purposes, but illustrate the need for higher fidelity in the small impactor - spacecraft degradation - regime. One should be cautious in utilizing these comparisons to validate the micrometeoroid and debris models. The assumptions underlying these analyses are necessarily simplistic. For example, time-dependent variations associated with toroids or clouds of debris impactors (as inferred from the IDE experimental data) are not taken into consideration, nor is the fact that many of the debris impactors are in elliptical orbits around the Earth. The models and collected data do agree on several points however. Space debris does exist in all sizes, and has the possibility of growing into a potentially catastrophic problem, particularly since self-collisions between particles can rapidly escalate the numbers of small impactors. Kessler has deduced that a "runaway" escalation (which grows with the square of the population of particles) may already be occurring at an altitude of about 1000 km, where there is a local peak in the debris population.[2]

With regard to statistical errors, the data suggest that the true impact fluence, or flux, is rarely defined any better than one standard deviation (*s.d.*, Poisson logic) and is frequently only good to about three standard deviations, as evidenced by the "overlap" data taken on the intercostals versus the rows. Clearly, an updated model of the debris environment is required which incorporates elliptical orbits. Kessler[7] is presently addressing this issue, while an independent study is underway by Divine[18] at the Jet Propulsion Laboratory based on first-principles of orbital dynamics.

Updates in the scaling laws used to predict cratering are also needed. While this present study concentrated on the aluminum structure, there are many other target materials which suffered from cratering and/or perforations. Scaling laws are required to relate these various data. Presently, based on our own independent CTH computer modelling, we conclude that the

perforation limit equation of McDonnell[8,12] is credible, at least for symmetric impacts (*e.g.*, Al/Al). The McDonnell equation is cited **only** because it is one that we have been recently exercising. Other equations, such as those by Cour-Palais or Christiansen may be equally credible, we simply have not yet performed the necessary comparisons. However, more data and modelling are needed to establish generalized rules which account for both cratering and perforations for **any** combination of impactor/target and for wide ranges of impact speeds and angles of incidence.

Based on limited attempts to model impact events with the CTH code, we conclude that this hydrocode has the capability to realistically simulate many experimentally observed phenomena. A virtue of such a code is the ability to map out the sensitivities to assumed parameter changes, such as yield strengths, fracture strengths and interlayer bond strengths. Accordingly, we recommend further such computer studies in order to allow better understanding of impact events and correlations with experimental data.

REFERENCES

1. Cour-Palais B.G. *et. al.*: Meteoroid Environment Model - 1969 (Near Earth to Lunar Surface). *NASA SP-8013,* 1969.
2. Kessler D.J.; Reynolds R.C.; Anz-Meador P.D.: Orbital Debris Environment for Spacecraft Designed to Operate in Low Earth Orbit. *NASA TM-100471,* 1988. Also: D.J. Kessler, Orbital Debris Technical Interchange Meeting, Phillips Laboratory presentation, 2-3 April, 1991.
3. Bell R.L. *et al.*: *The CTH Code* (Version 1.024), Structural and Solid Mechanics Department, Sandia National Laboratory, Albuquerque, NM, October, 1991.
4. Atkinson D.A.; Watts A.; Crowell L.: *Final Report: Spacecraft Microparticle Impact Flux Definition.* Prepared for: LLNL, Univ. of Calif. by POD Associates, Inc., 1991.
5. Berhard R.P., See T.H., Horz F., Projectile Compositions and Modal Frequencies on the "Chemistry of Micrometeoroids" LDEF Experiment, Second LDEF Post-Retrieval Symposium, *NASA Conf. Pub.,* 1992.
6. Simon C.G. *et al.*: Elemental Analyses of Hypervelocity Micro-Particle Impact Sites on Interplanetary Dust Experiment Sensor Surfaces (abstract). Second LDEF Post-Retrieval Symposium, *NASA Conf. Pub. 10097,* 1992.
7. Kessler D.J.: Origin of LDEF Debris Impacts on LDEF's Trailing Surfaces. *Second LDEF Post-Retrieval Symposium,* 11 pp, NASA CP-3194, 1993.
8. Watts A.J.; Atkinson D.R.; Rieco S.F.: *LDEF Penetration Assessment: Final Report.* Prepared for Nichols Research Corporation, Dayton, OH by POD Associates, Inc., 1992.
9. Zook H.A.: Meteoroid Directionality on LDEF and Asteroidal Versus Cometary Surfaces (abstract). *In Lunar and Planet. Sci. Conf. XXII,* Lunar and Planetary Institute, Houston, TX, pp. 1385-1386, 1990.
10. Cour-Palais B.G., Hypervelocity Impacts in Metals, Glass and Composites, *Proceedings of the 1986 Symposium, Hypervelocity Impact,* Pergamon Press, 1986.

11. Christiansen E.L., Investigation of Hypervelocity Impact Damage to Space Station Truss Tubes, *International Journal of Impact Engineering, Proceedings of the 1989 Symposium*, Vol. 10, 1990, p. 125.
12. McDonnell J.A.M. *et al.*: An Empirical Penetration Equation for Thin Metallic Films Used in Capture Cell Techniques. *Nature, 309*, pp. 237-240, 1984. Updates with K. Sullivan, private communication, 1991.
13. Miriam Gersten: Maxwell Laboratory, Personal Communication, March 1992.
14. See T.H. et al.: Meteoroid and Debris Impact Features on the Long Duration Exposure Facility: A Preliminary Report. *NASA JSC #24608*, 1990.
15. See T.H. et al.: Detailed examination of LDEF's Frame and the A0178 Thermal Blankets by the Meteoroid and Debris Special Investigation Group (abstract). *Second LDEF Post-Retrieval Symposium*, 1992.
16. Mullholland J.D., and 8 co-authors (1991), IDE Spatio-Temporal Fluxes and High Time-Resolution Studies of Multi-Impact Events and Long-Lived Debris Clouds, *LDEF - 69 Months in Space, First Post-Retrieval Symposium, NASA CP-3134*, p. 517-528.
17. Grün E. *et al.*: Collision Balance of the Meteoritic Complex. *Icarus, 62*, 244-272, 1985.
18. Divine N. and Agüero R. C.: New Meteoroid Model Predictions for Directional Impacts On LDEF (abstract), Second LDEF Post-Retrieval Symposium, *NASA C.P. - 10097*, p. 56, 1992 .

Appendix

CTH Code Validation

APPENDIX

CTH CODE VALIDATION

The first task with the CTH code was to perform some type of validation between experimental results and reproducible computer simulations. The data and results from a series of gas gun experiments were provided by Dr. Fred Hörz of NASA Johnson Space Center.

The data provided by NASA contained many combinations of materials that were used for the impactor and the projectile. In order to get reasonably accurate results with the CTH code the materials chosen had to have material properties that were readily available and well characterized. Complex compound materials were ruled out, leading to a choice of an aluminum target and an impactor made of soda-lime glass. Results from the runs are illustrated below in Table A-1.

Table A-1: Data Comparison from CTH Run and Hörz et al. (1992)

Shot Number	Projectile Diameter (mm)	Aluminum Thickness (mm)	Velocity (km/sec)	Hole Diameter (mm) HÖRZ (1992)	Hole Diameter (mm) CTH
785	3.18	9.53	5.91	2.24	9.8
786	3.18	9.02	5.8	3.62	10
787	3.18	8.64	5.81	7.31	12.5
788	3.18	7.62	5.79	10.19	12.5
789	3.18	1.6	5.87	8.77	10
791	3.18	19.94	5.84	13.73*	11.000*

*These values are for crater diameters; they were not penetrations.

Several models were available in the CTH code, however, the one chosen was the Mie-Grüneisen. The variables used in the CTH runs are shown in Table A-2.

Table A-2: Variables used in CTH Calculations

Material	Density (g/cm^3)	Sound Speed (cm/sec)	Grüneisen	Heat Capacity ($erg/cm^3/eV$)	Constant in Linear Hugoniot
Aluminum	2.7	5.31×10^5	2.25	1.049×10^{11}	1.34
Soda-Lime	2.2	5.91×10^5	0.4	8.744×10^{10}	1.5

The aluminum alloy that was used in the experiments was Al-1100 variety, but the temper was not known. The temper of the metal can result in large changes in the tensile strength and the yield strength. In order to match the experimental results, it was necessary to run several calculations that used a range of yield and tensile strengths. The final values that were arrived at are listed in Table A-3:

Table A-3: Yield and Tensile Strengths Used in CTH Calculations

Material	Yield Strength (kbar)	Poisson Ratio	Fracture Stress (kbar)
Aluminum	1.3	0.35	1.6
Soda-Lime Glass	10	0.16	1.2

The primary goal of this series of runs was to replicate the wall penetration limit that was seen in the experimental results. The final values listed above successfully simulated this experimental limit. Exact replication of the hole diameters for penetration was not expected, since only small changes in velocity or material properties produce rapid changes in the perforation. The aluminum alloy that best matched the NASA-JSC data was identified as Al-1100-H16. The data chosen for the soda-lime glass were based on quotes from manufacturers and reference data for various glasses. The CTH calculations indicated only a moderate sensitivity to parameter changes for the glass impactor, but large sensitivity to the

values for the aluminum target. No attempt has yet been made to model other experimental data, such as that for the Al foils used by McDonnell.

NEW METEOROID MODEL PREDICTIONS FOR DIRECTIONAL IMPACTS ON LDEF

Neil Divine and Rene C. Agüero
Jet Propulsion Laboratory
California Institute of Technology
Pasadena, California 91109

ABSTRACT

An extensive body of data, from meteors, zodiacal light, spacecraft-borne impact detectors (Helios, Pioneer, Galileo, Ulysses), and other sources, forms the basis of a new numerical model for the distributions of interplanetary meteoroids. For each of the five populations in this model it is possible to evaluate meteoroid concentration and flux for oriented surfaces or detectors having arbitrary position and velocity in interplanetary space (Divine, 1992, in preparation). For a spacecraft in geocentric orbit the effects of gravitational focussing and shielding by the Earth have been newly derived with full attention to the directionality of the particles, both on approach (i.e., relative to a massless Earth) and at the target. This modeling approach has been exercised to provide an estimate of meteoroid fluence for each of several oriented surfaces on LDEF.

This research was performed at the Jet Propulsion Laboratory, California Institute of Technology, under contract with the National Aeronautics and Space Administration.

LONG DURATION EXPOSURE FACILITY (LDEF) ATTITUDE MEASUREMENTS OF THE INTERPLANETARY DUST EXPERIMENT

Philip C. Kassel, Jr., William R. Motley III
NASA Langley Research Center
Hampton, VA 23681-0001
Phone: 804/864-4621, Fax: 804/864-7607

S. Fred Singer, J. Derral Mulholland, John P. Oliver,
Jerry L. Weinberg, William J. Cooke
Institute for Space Science and Technology
Gainesville, FL 32609

Jim J. Wortman
North Carolina State University
Raleigh, NC 27695

ABSTRACT

Analysis of the data from the Long Duration Exposure Facility (LDEF) Interplanetary Dust Experiment (IDE) sun sensors has allowed a confirmation of the attitude of LDEF during its first year in orbit. Eight observations of the yaw angle at specific times were made and are tabulated in this paper. These values range from 4.3 to 12.4 degrees with maximum uncertainty of ±2.0 degrees and an average of 7.9 degrees. No specific measurements of pitch or roll were made but the data indicates that LDEF had an average pitch down attitude of less than 0.7 degrees.

INTRODUCTION

The LDEF IDE was unique in providing a time history of impacts of micron-sized particles on six orthogonal faces of LDEF during the first year in orbit.[1] The value of this time resolved data depended on and was enhanced by the proper operation of some basic LDEF systems. Thus the value of the data is greatly enhanced when the location and orientation of LDEF is known for each time of impact. The location and velocity of LDEF as a function of time can be calculated from the "two-line elements" published by NASA Goddard Space Flight Center during the first year of the LDEF mission. The attitude of LDEF was passively stabilized in a gravity-gradient mode and a magnetically anchored viscous damper was used to dissipate roll, pitch, and yaw motions.[2,3] Finally the IDE used a standard LDEF Experiment Power and Data System (EPDS) to collect and store data and also to provide a crystal derived clock pulse (1 count every 13.1 seconds) for all IDE time measurements. All that remained for the IDE was to provide a system to calibrate the clock, eliminating accumulative errors, and also to verify the attitude of LDEF. The typical steady-state motion of LDEF was expected to be less than 2 degrees for pitch and roll oscillations but there was greater uncertainty about the yaw attitude.[4]

The IDE used solar cells on six orthogonal faces to observe the LDEF sunrise and provide data about the LDEF attitude. The data were recorded by the EPDS about 10 times per day for the first 346 days of the LDEF mission. These data consist of the number of IDE counts since the last LDEF sunrise and the status of the six solar cells (light or dark) at

the time of the last IDE pulse. The EPDS determined the time that the data were recorded and includes with each record the master EPDS clock counter (1 count every 1.638 seconds) that provided the range and resolution for time measurements. The IDE solar cells provided data for an excellent clock calibration, meeting their primary purpose, and this paper will present the time resolved LDEF attitude measurements that can be gleaned from this data.

THE EPDS/IDE CLOCK

All of the timing measurements of the IDE are derived from the EPDS crystal controlled clock which had a design frequency of 1.280 MHz. The EPDS circuitry used a 26 stage divider chain to provide a large selection of clock rates. The IDE used the twenty-first stage of this divider (a period of 1.638 seconds) as the master clock rate. The EPDS also had a 24 bit counter that was used to store the accumulated counts since the experiment was turned on and the value stored in this counter was written to the data tape as part of every IDE record. The master clock rate and the count in the 24 bit counter are referred to as the EPDS clock or count.

The IDE also used the twenty-fourth stage of the EPDS divider chain as a secondary clock rate with a period of 13.1 seconds. This clock rate and its related counts are referred to as the IDE clock or count and is used to provide 12 bit measurements of time relative to the 24 bit EPDS count. This clock rate is used to sample and hold the sun sensor status, and to measure the time since sunrise. The phase between the IDE and the EPDS clock counts was fixed such that when the EPDS count changed from 3 to 4 counts the first IDE clock pulse was generated. Thus the integer relationship between IDE and EPDS counts can be expressed as:

$$EPDS + 4 = IDE * 8$$

SENSITIVITY OF THE SOLAR CELL CIRCUIT

Since the primary purpose of the sun sensors was to detect the sunrise event independent of the LDEF orientation at the time of sunrise, the sensitivity of the light sensing circuit was intentionally high. Each sun sensor circuit consists of four solar cells in series. The photo-current was amplified by a single transistor and the output of the transistor was clocked by the IDE clock pulses into a storage register for use by the other digital circuits of the IDE.

THE CLOCK CALIBRATION

The IDE clock calibration datum is essentially the count in a 12 bit counter which continually counts IDE clock pulses and is reset whenever a sunrise has been observed. The reset pulse for this counter is derived in the following manner. All sun sensors data are combined in a logic OR gate so that each IDE clock pulse can be considered as a light or dark pulse depending on whether LDEF is in sunlight or not. After 46 dark pulses (10 minutes) a circuit is armed so that the next light pulse will cause the desired reset (note that this reset is synchronized to the IDE clock pulses). The most precise piece of information that can be calculated from this counter is the EPDS count that marks, not the

sunrise event, but the end of an IDE interval during which the sunrise occurred. This EPDS count can be calculated by converting the EPDS (24 bit counter) count, that marks the time of the record, to an IDE count (Integer) subtracting the sunrise count value, then converting back to an EPDS count. Four more counts were subtracted to obtain the EPDS count associated with the center of the IDE interval in which the sunrise occurred.

The clock calibration used for this paper was obtained in the following manner:

(1) The geometry of the LDEF sunrise is defined as LDEF being on a line that is tangent to the earth and sun; the line bent at the earth surface by some small constant angle of deviation. The sense of this angle is in the direction of atmospheric refraction but it also accounts for the height of the sun's upper limb above the horizon to provide sufficient light for the IDE sun sensors.

(2) The time of sunrise was calculated with a precision of 0.1 seconds using the LDEF orbital elements (NASA Goddard "two-line elements") reported during the first year in orbit and matched to the EPDS sunrise count as indicated above.[5,6]

(3) Since the IDE was turned on about 3 hours before the LDEF was released and the first data was recorded while the LDEF was still attached to the shuttle, the first IDE record is not used in this analysis.

(4) The EPDS time zero and a constant EPDS period was determined using a linear least squares method.

(5) The deviation angle defined in (1) was varied to minimize the standard deviation of the total error of the least squares process.

The clock calibration constants that were determined and used in this report are as follows:

Average EPDS Time Zero:	98.594187 ±2.8E-6 Day of Year 1984
Average EPDS Period:	1.63770501 ±2.3E-8 Seconds
Deviation Angle:	0.00376 radians
Standard Deviation of Total Error:	3.63 √(count * second)

LDEF POSITION AND ORIENTATION RELATIVE TO THE SUN

With the above clock calibration the position and velocity vectors of LDEF were calculated for the time when the sun sensor status was clocked into storage for each of the IDE data records. Also for these times the XYZ coordinates of the sun (in the same coordinate system) were calculated. This positional data of LDEF and the sun were then combined to form the following three parameters for each IDE record:

(1) The angle between the LDEF position vector and the sun. This angle has its vertex at the center of the earth and is in a plane that contains the centers of LDEF, the earth and the sun.

(2) The Beta angle, which is the angle between the plane of LDEF's orbit and the direction to the sun. The plane of LDEF's orbit is that plane which contains LDEF's position and velocity vectors. For LDEF the Beta angle is positive when the sun is on the north side of the orbital plane and negative on the south side.

(3) A light level parameter which indicates whether LDEF is expected to be in sunlight or the earth's shadow based on the sunrise condition defined in the clock calibration procedure.

These three parameters form the essential data that indicate the position and orientation of LDEF relative to the sun and sunlit earth. By comparing this data with the corresponding observed sun sensor status data some conclusions about the LDEF yaw and pitch angles can be made.

Figure 1 is a plot of the number of sun sensors illuminated as a function of the angle between LDEF and the sun. The way this angle was defined, it can vary from 0 to 180 degrees and does not indicate whether LDEF is approaching a sunset or leaving a sunrise. The complete IDE data set consists of 3,413 data points randomly distributed over the range of 0 to 180 degrees; however, the figure plots only the data (642 points) between 85 and 115 degrees with the morning and evening data indicated by different symbols. When the LDEF is greater than 115 degrees from the sun, all sensors are dark as LDEF is in the earth's shadow. When the angle is less than 85 degrees, all sensors are illuminated either by the sun or by sunlight reflected by the earth.

The first conclusion that was made about this data was that the sunlit earth was very significant in determining the light or dark status of the sun sensors. The method of determining the attitude of LDEF used in this investigation depends only on light coming directly from the sun, and it was expected that when the sunlight was parallel to a sun sensor surface that sensor would be dark. The determination of yaw depended on LDEF being totally out of the earth's shadow and the sun sensors on both row 12 and row 6 being dark. A similar determination of pitch using the sensors on the space and earth end was not possible because the earth end sensor is illuminated by light reflected from the earth.

Some observations about the pitch attitude can be made by looking at the angle at which the sun sensor on the space end of LDEF changed from light to dark near sunset as compared to the dark-to-light angle near sunrise. It was expected that both these angles would be less than 90 degrees and on average would be an indication of the resolution by which the yaw measurement was made; also the difference between the angles would indicate twice the average pitch angle. How well the IDE sun sensor status can be used to define these angles can be a measure of the variability of the pitch. If the pitch is constant, the angles will be well defined within the expected errors for determining an angle between the LDEF and the sun.

To determine how well the sun sensor data and a linear clock calibration can be used to indicate an angle between LDEF and the sun, the data of figure 1 was used to determine the sunrise/sunset angle. The data between 111 and 113 degrees was replotted in figure 2 with the observed sun sensor status indicating whether LDEF is in sunlight or shadow and the symbols indicating the expected lighting based on the sunrise condition defined in the clock calibration. For this analysis the exact angle of sunrise or sunset is not as important as the

spread of the observed lighting, identified as sunrise or sunset data scatter, and the symmetry of the two intervals. If the standard deviation of total error from the clock calibration is used to calculate error bars for this data the range of errors for angles near 112 degrees would be from ±0.16 to ±0.30 degrees with the maximum error at minimum beta angle (for the clock calibration the maximum residuals occurred at maximum beta angle). The interval identified as "sunrise data scatter" is only slightly greater than the maximum error bar for a single data point and includes five sunrise data points: two points have the expected lighting and three have lighting that is the opposite of expected. The greater interval identified as "sunset data scatter" includes 13 sunset data points: 8 have the expected lighting and 5 have opposite lighting. Of the total eight points that have lighting that is opposite to the expected lighting, five are less than 112 degrees and indicate LDEF in darkness when it should have been in sunlight, and three points above 112 degrees indicate sunlight when LDEF was expected to be in the earth's shadow. The symmetry of these intervals about the sunrise/sunset angle is a good indication that the linear clock calibration's starting time is probably correct since any error in the starting time would shift the sunrise and sunset points in opposite directions destroying the symmetry. The length of the total data scatter interval (0.9 degrees) can be used as a measure of the precision with which the angle between LDEF and the sun can be determined using this clock calibration.

LDEF PITCH ATTITUDE

The sun sensor data of IDE cannot measure the pitch of LDEF directly but can put some limits on what the pitch may have been during the first year in orbit. Figure 3 presents the sun sensor data for the space end of LDEF. The first obvious feature of this data is that the morning and evening data is offset from 0.5 to 1.4 degrees. This would indicate that for the first year in orbit LDEF had a slight pitch down that, on average, was at least 0.25 degrees but not more than 0.7 degrees. The scatter in this data is slightly greater than that in figure 2 and can be attributed to variations in attitude as well as variations due to the precision of the clock calibration. Both pitch and roll variations can cause scatter in this data. Either a constant or a varying roll would cause scatter in this data but probably would not effect the morning to evening offset. If the pitch was oscillating the amplitude of the oscillation would be reflected in the amplitude of the scatter. Even if all of the scatter is attributed to variations in pitch, then the pitch oscillations were less than 2.0 degrees.

LDEF YAW ANGLE

The LDEF yaw angle can be defined as the angle between two planes. One plane referred to as the LDEF body axes plane contains the LDEF long axis and the normal to rows three and nine. The second plane is the LDEF orbital plane. It is assumed that the LDEF position vector is coincident with the LDEF long axis which is defined as the yaw axis. The traditional definition of yaw is a clockwise rotation of a body about its vertical axis when viewed from above; thus when the velocity vector and orbital plane is in the quadrant between the normal to row nine and twelve, LDEF has experienced a positive yaw. Early observations of LDEF and the results of the pinhole camera experiment indicated a yaw of about +8.0 degrees.[7]

The IDE measurement of the yaw angle is time dependent though not too sensitive to clock errors. It depends on observing an alignment of the yaw angle with the beta angle. Figure 4 indicates the alignment of a positive yaw angle with a negative beta angle at a time near sunrise. In this figure the IDE sun sensors would indicate that the sun was in the LDEF body axes plane and the yaw angle would be equal to the beta angle (except for sign). A similar alignment near sunset would be a positive yaw angle with a positive beta angle. Because the orbit of LDEF regresses, the beta angle oscillates with a period of about 45 days and has a maximum rate of changes of 0.4 degrees per IDE record. For a constant yaw angle of 8.0 degrees there would have been about 12 morning alignments and 13 evening alignments during LDEF's first year in orbit.

In figure 1 there are eight points between 103 and 112 degrees where only two sun sensors are illuminated. In each case the sun sensor on the earth end was illuminated along with either the leading edge or the trailing edge. These points indicate yaw angle aligned with beta angle to at least ±2 degrees if we consider the sensitivity of the sensor near grazing incidence to be like that of the space end (figure 3). These points account for two of the expected morning alignments and six evening alignments. The yaw angle measurements from these points is presented in table 1.

There are two possible explanations for why only one third of the expected alignments were observed by the IDE sun sensors. The most likely cause is that alignments that would be observed when LDEF is less than 103 degrees from the sun are not observed because the light reflected by the earth illuminates both the north and south sensors. There is some evidence to support this explanation in the data of figure 1 between 99 and 101 degrees. Most of the points in this interval have only three sun sensors illuminated. Where four sun sensors are illuminated (11 points), the yaw and beta angles are near an expected alignment. The second explanation is that the yaw angle was oscillating. The data in table 1 show that the yaw was definitely not constant during the first 100 days of LDEF. If the yaw angle was oscillating, the time of some alignments would be prolonged and others shortened because of the relative phase of the beta and yaw angles; thus, some alignments would more likely be observed than others.

CONCLUSIONS

The sun sensors of the IDE were used to make eight measurements of the LDEF yaw angle at discrete times during the first year of its mission. These measurements indicate that the LDEF yaw angle was not constant but was oscillating about some average value. There is evidence that the oscillations were dampening but there is insufficient data to indicate the period of the oscillations or the dampening coefficient.

The determination of the LDEF pitch attitude was qualitative and indicates that LDEF had an average pitch down attitude of not more then 0.7 degrees with time variations less than ±1 degree during the first year.

REFERENCES

1. J. D. Mulholland, S. F. Singer, J. P. Oliver, J. L. Weinberg, W. J. Cooke, P. C. Kassel, J. J. Wortman, N. L. Montague, and W. H. Kinard: IDE Spatio-Temporal Impact Fluxes and High Time-Resolution Studies of Multi-Impact Events and

Long-Lived Debris Clouds. First LDEF Post-Retrieval Symposium. NASA CP-3134, 1992.

2. R. L. O'Neal and E. B. Lightner: Long Duration Exposure Facility--A General Overview. First LDEF Post-Retrieval Symposium. NASA CP-3134, 1992.

3. W. H. Kinard and G. D. Martin: Long Duration Exposure Facility (LDEF) Space Environments Overview. First LDEF Post-Retrieval Symposium. NASA CP-3134, 1992.

4. LDEF 840-2: Long Duration Exposure Facility (LDEF) Experiment Users Handbook, Prepared by Staff, LDEF Project Office. January 15, 1978.

5. F. R. Hoots and R. L. Roehrich: Models for Propagation of NORAD Element Sets. Project Space Track. ADA 093554, 1980.

6. J. Meeus: *Astronomical Formulae for Calculators, Second ed.* Willmann-Bell, Inc. 1982.

7. P. N. Peters and J. C. Gregory: Pinhole Cameras as Sensors for Atomic Oxygen in Orbit; Application to Attitude Determination of the LDEF. First LDEF Post-Retrieval Symposium. NASA CP-3134, 1992.

Table 1. LDEF Yaw Angle at Days in Orbit

Day	Yaw Angle
4.15	6.9
75.77	12.4
91.77	4.3
163.69	9.8
167.44	5.2
205.43	9.5
238.04	9.2
288.69	5.9
Average	7.9

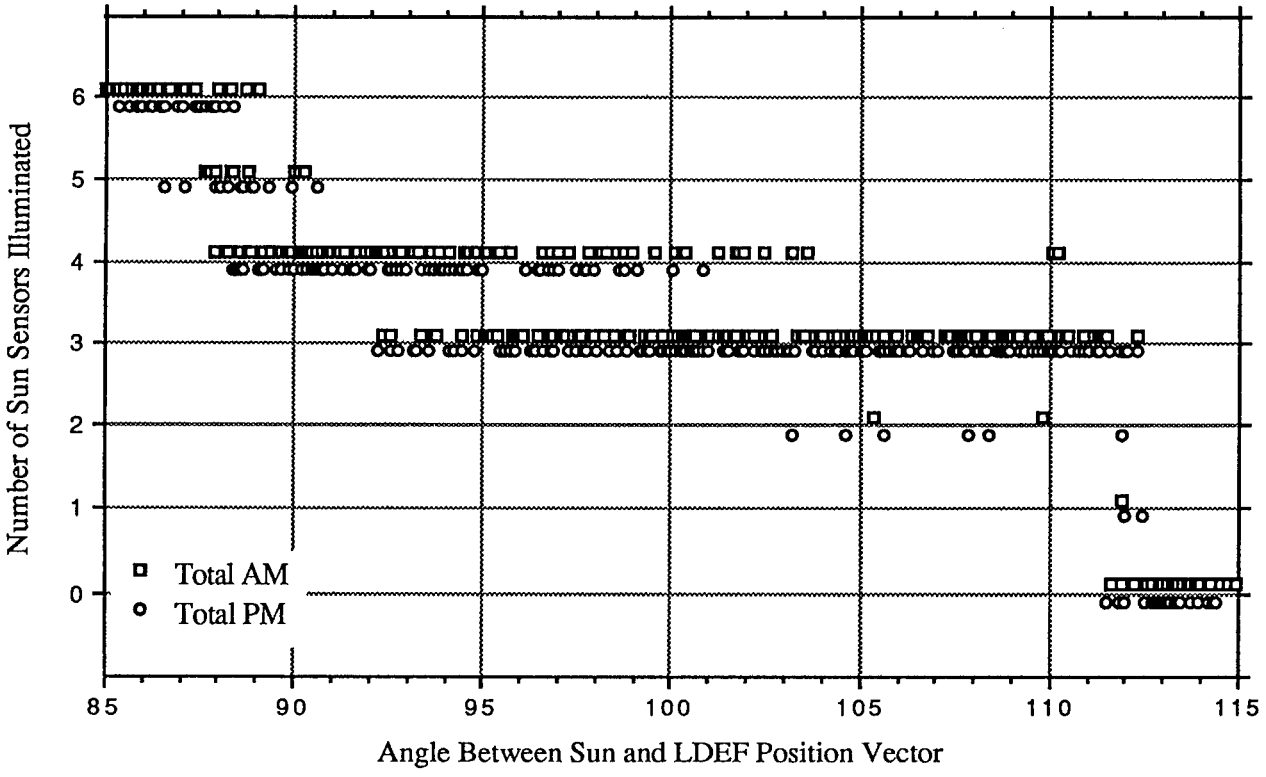


Figure 1. IDE sun sensor data at morning and evening for six orthogonal faces of LDEF.

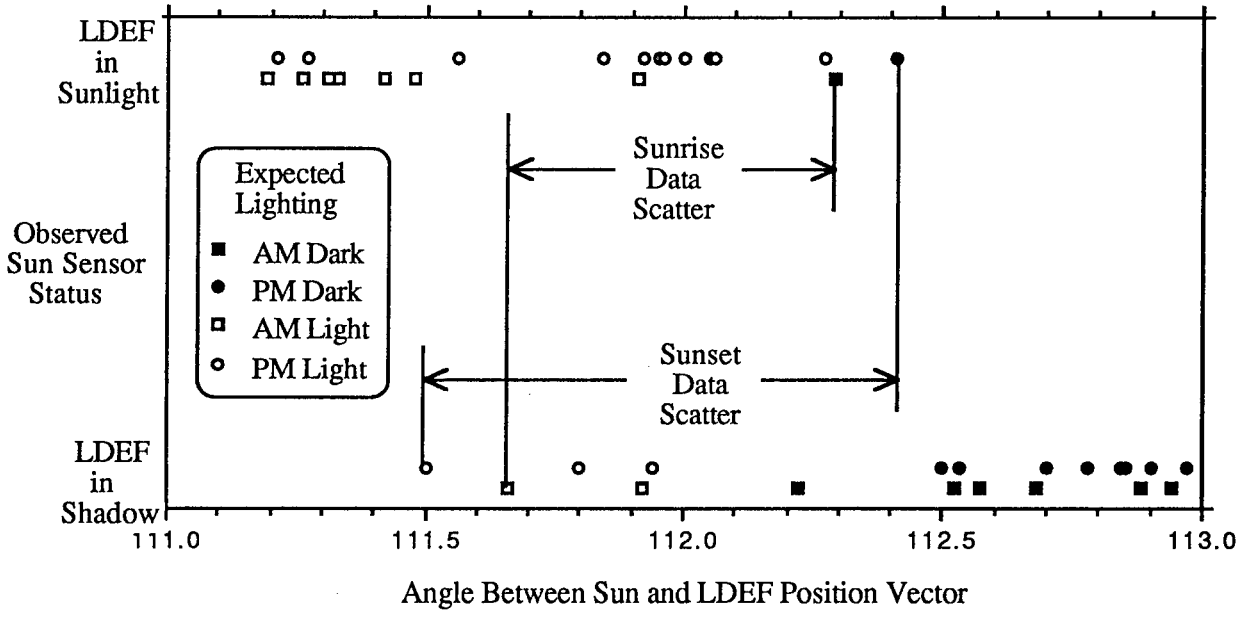


Figure 2. Sun sensor data at sunrise and sunset geometry.

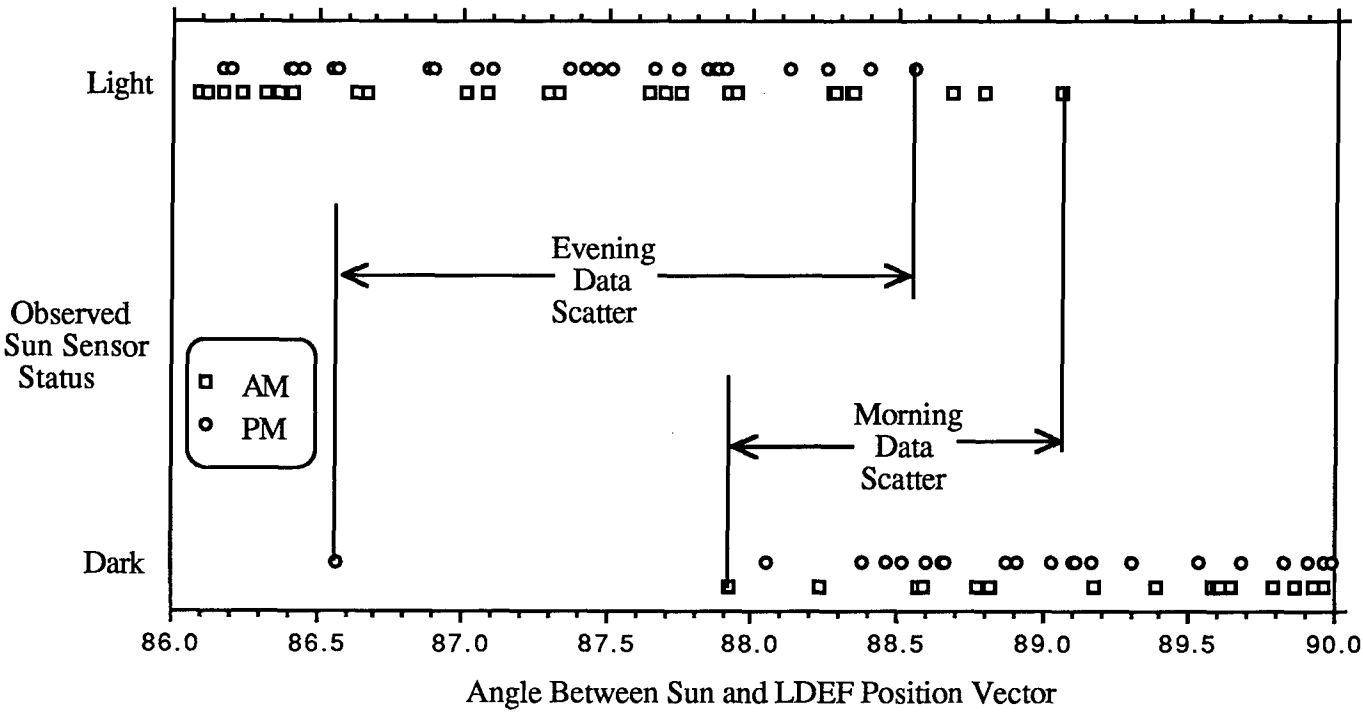


Figure 3. Sunlight on the Space End of LDEF.

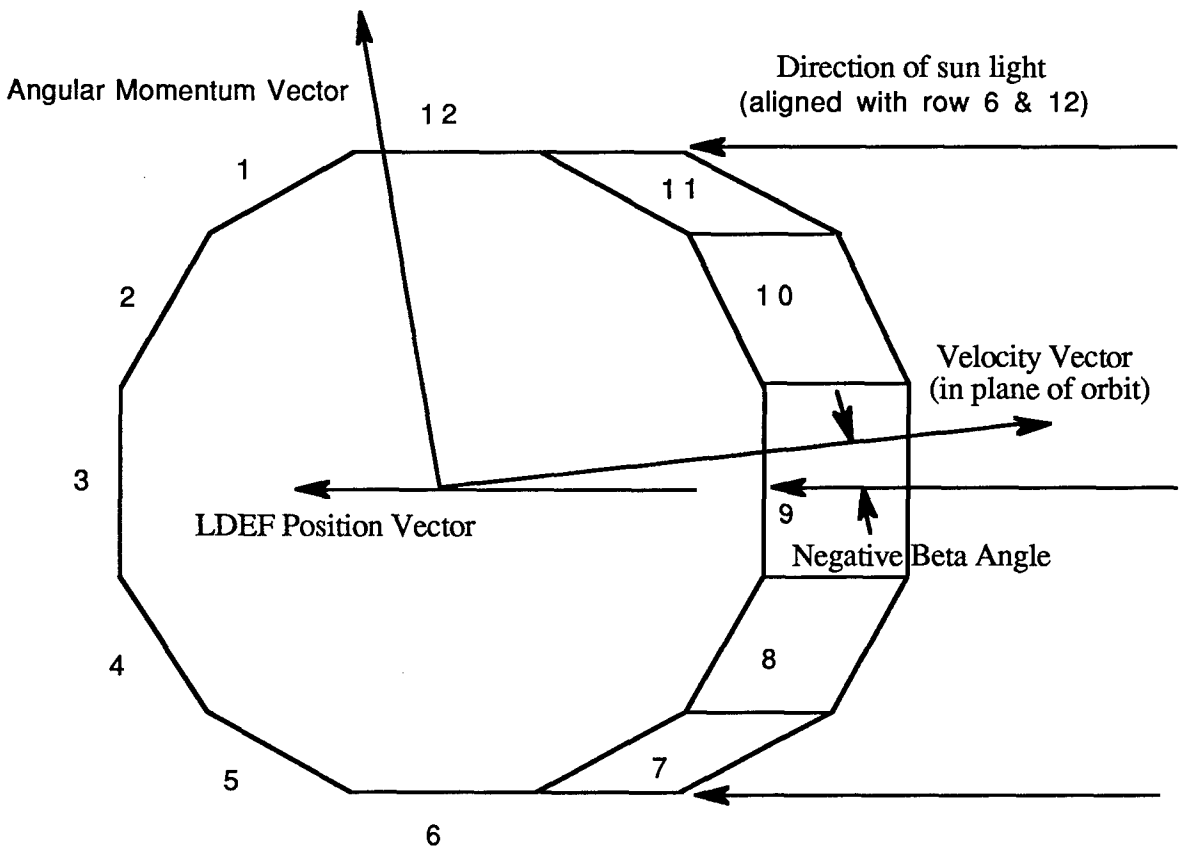


Figure 4. Alignment of yaw and beta angles near sunrise.

ELEMENTAL ANALYSES OF HYPERVELOCITY MICROPARTICLE IMPACT SITES ON INTERPLANETARY DUST EXPERIMENT SENSOR SURFACES

C. G. Simon
Institute for Space Science and Technology
Gainesville, FL 32609

J.L. Hunter, D.P. Griffis, V. Misra, D.A. Ricks, J.J. Wortman
Analytical Instrumentation Facility, North Carolina State University
Raleigh, NC 27695

D.E. Brownlee,
Astronomy Department, University of Washington
Seattle, WA 98195

ABSTRACT

The Interplanetary Dust Experiment (IDE) had over 450 electrically active ultra-high purity metal-oxide-silicon impact detectors located on the six primary sides of the Long Duration Exposure Facility (LDEF). Hypervelocity microparticles (~0.2 to ~100 μm diameter) that struck the active sensors with enough energy to breakdown the 0.4 or 1.0 μm thick SiO_2 insulator layer separating the silicon base (the negative electrode), and the 1000Å thick surface layer of aluminum (the positive electrode) caused electrical discharges that were recorded for the first year of orbit. The high purity Al-SiO_2-Si substrates allowed detection of trace (ppm) amounts of hypervelocity impactor residues.

After sputtering through a layer of surface contamination, secondary ion mass spectrometry (SIMS) was used to create two-dimensional elemental ion intensity maps of microparticle impact sites on the IDE sensors. The element intensities in the central craters of the impacts were corrected for relative ion yields and instrumental conditions and then normalized to silicon. The results were used to classify the particles' origins as "manmade", "natural" or "indeterminate". The last classification resulted from the presence of too little impactor residue, analytical interference from high background contamination, the lack of information on silicon and aluminum residues, or a combination of these circumstances.

Several analytical "blank" discharges were induced on flight sensors by pressing down on the sensor surface with a pure silicon shard. Analyses of these blank discharges showed that the discharge energy blasts away the layer of surface contamination. Only Si and Al were detected inside the discharge zones, including the central craters, of these features.

Thus far a total of 79 randomly selected microparticle impact sites from the six primary sides of the LDEF have been analyzed: 36 from tray C-9 (Leading [ram], or East, side), 18 from tray C-3 (Trailing [wake], or West, side), 12 from tray B-12 (North side), 4 from tray D-6 (South side), 3 from tray H-11 (Space end), and 6 from tray G-10 (Earth end). Residue from manmade debris has been identified in craters on all trays. (Aluminum oxide particle residues were not detectable on the Al/Si substrates.)

These results were consistent with the IDE impact record which showed highly variable long term microparticle impact flux rates on the West, Space and Earth sides of the LDEF which could not be ascribed to astronomical variability of micrometeorite density. The IDE record also showed episodic bursts of microparticle impacts on the East, North and South sides of the satellite, denoting passage through orbital debris clouds or rings.

INTRODUCTION

The Interplanetary Dust Experiment (IDE) had approximately 450 high purity MOS type detectors mounted on the six primary sides of the stabilized spacecraft. The sensors were constructed from 2 inch diameter, 250 μm thick, boron-doped ultra high-purity silicon wafers covered with either a 0.4 or a 1.0 μm thick layer of thermally grown SiO_2 insulator, and coated with ~1000Å of high-purity aluminum. The location and identification of microparticle hypervelocity impacts on the formerly active detectors was facilitated by the presence of 50 μm wide "discharge zones" in the Al top layer surrounding each impact (see Figs. 1-3). It is also suspected that the negatively biased Si electrode surface exposed in the impact cratering event enhanced the collection efficiency of positive ions formed from impactor materials in the impact plasma.

The objective of the chemical analysis study is to empirically determine the manmade-to-natural microparticle population ratio of impactors that struck the LDEF satellite while in orbit. The study takes advantage of the purity of the IDE substrates and their location on all six primary sides of the satellite. Data from this study will be added to the growing pool of orbital hypervelocity impact site analyses produced from studies of the Solar Max, Palapa B and LDEF satellites.

EXPERIMENTAL

The detailed analysis protocol developed specifically for the IDE samples is described elsewhere (ref. 1). Optical microscopy and field-emission scanning electron microscopy (SEM) were used to locate and record the morphology of microparticle impact sites. Energy dispersive x-ray spectroscopy (EDS) and secondary ion mass spectrometry (SIMS) were used to look for and map the distributions of residual impactor debris in and around the impact craters. The presence and relative abundances of elements found in the craters were used to classify impactors as "manmade", "natural" or "indeterminate". Examples are presented in the following section.

EDS analyses of microparticle impact sites on the IDE sensor were limited in scope due to the concentrations of residue (~1%) required to produce detectable signals using EDS compared to the (ppm) concentrations needed to yield semi-quantitative results using the far more sensitive SIMS techniques. EDS and Auger electron spectroscopy (AES) were used to further analyze high concentration deposits of material (residues and contaminants) that were identified in and around impact sites with SIMS.

As previously described (ref. 1), all SIMS data was collected with a Cameca IMS 3F using $^{16}O^+$ or $^{16}O^-$ ion beams. The instrument was used in the ion microscope mode and data was recorded as two-dimensional elemental positive ion maps with lateral resolution of 1-2 μm. Pixel intensities were used to calculate relative element abundances. Briefly, the SIMS analytical protocol involves the following steps:

1.) Each impact site was first sputtered with the oxygen beam while monitoring the concentrations of C, Na and Mg in order to assure removal of the bulk of the surface contamination layer ubiquitous to LDEF.

2.) Next, an energy filtered bargraph type mass spectrum was recorded.

3.) Then, a dual channel-plate/ccd-digital-camera detector system was used to record high resolution ($M/\Delta M$= 3,000-4,000) elemental positive ion maps for C, O, Na, Mg, Si, Al, K, Ca, Ti, Cr, Fe, Ni, Cu, Zn, Ag and Au, and molecular ion maps for $^{56}Si_2$ and $^{58}Si_2$. (Images were not recorded if there were less than ~4 ion counts/min at the observed mass.)

4.) If there was enough of the IDE sensor's 1000Å Al top layer remaining around the impact site to prevent sample charging, negative elemental ion maps were recorded for H, C, O, F, Si, Al, S, Cl and Au.

Analysis of impacts on Ge witness plates flown on tray B-12 as part of the IDE experiment has been suspended. A summary of the work done to date on two of the Ge wafers, including crater counts and dimensions, description of contamination problems, and SIMS and/or EDS analyses for 13 impact sites, was presented in the LDEF First Post-Retrieval Symposium Proceedings (ref. 1). Contamination feature counts, crater counts, and representative photographs were recorded for all other witness plates mounted on LDEF tray B-12 along with the Ge plates. These included three 1" square Si plates from Washington University (Expt AO187) and ten zirconia, quartz and sapphire plates from NCSU with a total surface area of ~4 in^2. Results from these other witness plates showed clearly that the Ge witness plates were exposed to a major pre-flight contamination event.

The IDE Microparticle Impact Sample Set

The sample set for the study was composed of impacts selected from the 215 IDE sensors that have 1.0 μm thick insulator layers. These sensors were selected over the ones with thinner insulators because their electronically sturdier structure resulted in the majority of them remaining active for the entire 5.77 year LDEF orbital lifetime. Thus, no time bias was introduced into the sample set. The only selection criterion used was size. Impact craters with spall dimensions less than 30 μm were the focus of the study, but a few larger craters were also analyzed.

In order to gather data from a statistically significant fraction of this microparticle impact sample set, the total number of these impacts on each sensor group located on the six primary sides of LDEF was determined. Then, using 10% statistics, the total number of analyses required to achieve a significant fraction was calculated. This technique assumes that the statistics of a randomly selected group of 10% of the samples in a large, random sample set will, to first order, represent the statistics of the entire sample set.

The microparticle impact sample sets on the West, Space and Earth end IDE sensors are comprised of 290, 600 and 330 impact sites, respectively. Analyses of 122 impacts would provide 10% statistics for these three sample sets.

The above logic was iterated a second time for the extremely large sample sets represented by the impacts on IDE sensors that were located on the East, North and South sides of LDEF. Optical scanning of 3 out of 32 sensors from each of these groups provided estimates of the sample set sizes of 10,000, 4,600 and 4,400 impact sites, respectively. Clearly, the resources were not available to analyze 2,000 samples. However, since the sample sets were so large, it seemed logical to select 10% of the sensors from each location and analyze 10% of the samples on each sensor. This yielded the more practical goal of 200 analyses. Thus, analyses of a total of ~320 impact sites on IDE sensors would provide a first order statistical look at the manmade/natural microparticle population ratio.

To date 79 impact sites on IDE sensors have been analyzed with SEM/EDS and SIMS. Manmade or natural classifications have been assigned to 40 of the residues, or ~ 50%. An extensive background and blank discharge study required to establish the level of contamination and other analytical interferences has been conducted, but more work is required in this area. Although there are significant analytical interferences associated with elemental analyses of impact sites on the ultra high-purity IDE detector surfaces, most of these can be mitigated through recognition. The details and results from the contamination study will be the subject of a future paper.

Impactor Classification

The impactor classifications listed in Table 2 were assigned after reviewing all available data and are subject to the described limitations. Decisions were based on:

1) the element distributions depicted in the two dimensional ion maps described above,

2) the relative (to Si) ion abundance values calculated for each species in the central craters of the impact features, and

3) the local contamination environment in and around the impact feature.

Because the IDE detectors were constructed from silicon and aluminum, these two important elements could not be identified in impactor residues. Thus, aluminum oxide particle residues were undetectable, and the Si in natural impactor residues was also undetectable.

Identification of natural meteoroid residues followed the guidelines of the Meteoroid and Debris SIG. Residues were labeled natural if they had elemental compositions that were similar to common components of chondritic meteorites or interplanetary dust particles (IDP's). Most IDP's of micron size have solar elemental abundance ratios for Mg, Si, Fe, S, Ca, Ni and Na in decreasing order of abundance. The atomic abundances of Mg, Si and Fe are roughly equal in most IDP's and are an order of magnitude more abundant than Ca, Ni and Na. In practice, residues were labeled as natural meteoroids if they had high Mg and Fe abundances and either lacked or contained low abundances of elements not common in primitive meteoritic materials. Relative ion sensitivity factors ,"RSF" (see below) were taken into account when estimating compositions from ion intensity maps.

Manmade particle residues were identified by the presence of relatively high concentrations (>100 ppm in most cases) of metals such as Ti, Zn, Cr, Cu or Ag. Manmade classifications were also assigned to 4 residues (out of the 79) containing only Na, K and Mg under the assumption that these were the remains of impacts with paint particles that used silicate or magnesium oxide pigments. This assumption is subject to change as more insight into possible Na, K and Mg contamination is gained. All 4 of the impacts were located on leading edge sensors.

Indeterminate classifications were assigned to 39 residues that did not fall into either of the above categories. These included sites that contained only traces of Na and/or K. A subset of the indeterminate classification, labeled "clean", was composed of impact sites with no detectable residues. These may be the result of aluminum oxide particle impacts, a likelihood for impacts on the leading (East) and the North and South sides, or the result of impacts from very high velocity submicron interplanetary dust particles that completely vaporize, a statistical likelihood for impacts on the trailing (West) and Space end trays. As the study progresses, some of the indeterminate classifications may change.

Consideration of all the analytical data was complex and subject to interpretation. As a result, some impactor classifications may change as further insight into the analytical contamination and background issues is gained. For example, H, F and Cl were present in all central craters. This has been traced to ppm level contamination from HF and HCl during sensor fabrication. Na, K, and Mg to a lesser extent were present in the majority of impacts and may be from residual background contamination. The presence of these elements is reported since there is no verification of background contamination at this time, and there were many impact sites with little or no detectable Na, K or Mg. The Cameca instrument has been retrofitted with an electron flood gun that will permit depth profile studies of the IDE sensor surfaces through the insulating SiO_2 layer. These depth profiles should reveal the presence of bulk and interfacial contaminants in the SiO_2 and Si.

Depth profiles through the conductive aluminum layer have already shown that this material is contaminated with ~10-100 ppm of Ca. This severely limits the ability to identify Ca in impact sites. Calcium was detected all around the areas surrounding nearly all impact discharges, but was absent from

most central craters, or present at concentrations much lower than the background. The few instances where Ca was found in the impact craters at higher than background levels are reported.

Differential sputtering of the contamination layer from the highly textured impact sites was unavoidable and was considered when interpreting the SIMS data. The phenomenon results from beam shadowing effects caused by the craters, ridges, and even the smaller "hills and valleys " of the vapor deposited Al surface layer. In practice, ion images of control areas in the vicinity of the impacts, both before and after oxygen beam sputter cleaning, provided an estimate of the level of "background" concentrations for these areas. Images of impact areas (after sputter cleaning) were interpreted with these values in mind, and only after all sites on a given sensor were examined.

In order to gain insight into the distribution of the material in the surface contamination layer after an impact induced discharge occurred, a series of "blank discharges" were induced on a flight sensor using an ultrapure Si shard. SIMS analyses of these "blanks" showed that the C, Na, Mg, K, Ca bearing contamination layer was blown away from the central craters and surrounding zone of vaporized Al by the discharge energy. Only Si and Al were detected within the discharge craters and vaporization zones of these analytical blank discharges.

SIMS Data Reduction Method

Besides the obvious visual information, each pixel of the element ion maps contains digitized intensity information that can be reduced to a semi-quantitative number relative to the Si signal. The following steps were employed in this process:

1.) Ion maps were displayed on a computer screen individually and a rectangular box was electronically scribed around the same area of interest on each map.

2.) The cumulative pixel intensity data within the box was summed.

3.) Relative ion sensitivity factors (RSF) for species implanted in Si were used to correct the intensity values (see Table 1, refs. 2 and3).

4.) The corrected ion intensity values were normalized to the Si ion signal recorded for the same area.

5.) Data from individual craters were normalized for the number of pixels summed, the beam intensity during data collection, and the detector conditions during data collection.

Table 1 Relative Sensitivity Factors (RSF's) for species implanted in silicon (ref. 2 and 3). In general the values are applicable for elemental concentrations up to ~1%.

Ion	RSF	Ion	RSF
C^+	0.007	Cu^+	1.61
Na^+	139	Zn^+	0.054
Mg^+	18.0	Ag^+	0.694
Al^+	36.0		
Si^+	1.00	H^-	0.602
K^+	125	C^-	0.161
Ca^+	38.5	F^-	102
Ti^+	13.9	Al^-	0.250
Cr^+	7.69	S^-	5.10
Fe^+	1.85	Cl^-	26.3
Ni^+	1.35	Au^-	0.658

The reduced data have several limitations. First, RSF values for species implanted in Si were not appropriate for species deposited in or on aluminum or for deposits that were massive enough to form their own matrix. They are valid only for elements implanted in Si up to concentrations of ~1%. The assumption that the negative Si electrode exposed in the central crater region of impacts on the IDE sensors acted as an ion trap was the reason for selecting these RSF values. This assumption was based on the knowledge that positive ion pairs act as the charge carriers in the IDE discharge event and would theoretically be implanted in the Si. It should be noted that, in general, the RSF values for species in other matrices follow the same relative trend.

The second major limitation of the semi-quantitative data was the result of an artifact of the Cameca 3f operational protocol. This instrument could only collect data for one mass at a time. Up to ~50Å of material was sputtered away during each ion imaging step. Thus, the data for each element was from a different layer within the residue. For example, several hundred angstroms of material was removed between the imaging of Mg and Fe. This is a significant limitation on the ability to deduce impactor chemical composition from the scant residues.

Examples of semi-quantitatively reduced SIMS data are included in this report. More detailed interpretations will be presented in a future report after analysis of several ground based hypervelocity microparticle impact induced discharge features on retrieved IDE sensors is completed, and a more thorough understanding of contamination issues is gained.

RESULTS AND DISCUSSION

Overview

To date, 79 impacts on IDE sensors have been analyzed with SIMS. These include 36 impacts on two IDE sensors from LDEF tray C-9 (leading, or east side), 18 impacts on four different sensors from tray C-3 (trailing, or west side), 12 impacts on one sensor from tray B-12 (north side), 4 impacts on one sensor from tray D-6 (south side), 6 impacts on one sensor from the earth end tray G-10, and 3 impacts on one sensor from the space end tray H-11. Of the 79 impacts, 57 were formed from particles estimated to have been <3 μm in size, 18 were formed from particles estimated to have been 5-20 μm in size, and 3 were formed from particles estimated to have been 30-50 μm in size.

Microimpactor residue classifications are listed in Table 2. Elements identified at concentrations significantly higher than the background are listed for each impact site. The term "trace" refers to less than 10 ppm concentration, relative to Si, for all elements except Na and K, where the term refers to <100 ppm. Examples of impact feature morphologies, SIMS elemental ion maps, and quantitatively reduced SIMS data are presented in Figs. 1-3.

Minimum crater size of IDE impact features is ~10 μm due to the electrical discharge damage caused when the capacitor sensor was triggered (ref. 1). The sensors responded to hypervelocity particles ~0.5 μm or larger (assumed density of ~3 g/cm^3). Observed spall zone sizes for small particle impacts into the crystalline IDE sensor surfaces were typically ~3X the size of the central craters (Table 2, ref. 1). The central crater size of microimpacts in crystalline materials typically approximate the impactor size (ref. 4). Thus, it was impossible to estimate impactor size in the range of 0.5 to ~3 μm from the crater morphology on active IDE sensors.

The formation mechanism for craters ~10-25 μm in size on active IDE sensors was dominated by the impactor's kinetic energy (KE) transfer, but the discharge energy caused the entire crater and spall area to melt and fuse. "Crater" dimensions listed are for this fused area, but are more representative of spall zone size. Impactor size for these features was estimated to have been ~1/3 of the fused crater/spall size.

Formation of larger impact craters (>30 μm) was totally dominated by the impactor ΔKE and there were frequently shock induced spall zones around the craters. These larger impact sites had the typical morphology of hypervelocity impacts in crystalline material and impactor size was estimated to have been slightly less than the central crater size. The spall sizes listed in Table 2 are for the maximum dimension of the associated spall zones.

Impact identification Nos. in Table 2 refer to the IDE sensor number followed by a crater number (i.e. 1176-C3). Locations of all impacts were recorded for future reference. Craters were not always sequentially numbered since SIMS analyses were not performed on all craters that were labeled for further study in the initial optical scan. This was primarily due to the inability of the SIMS beam to reach every crater on a given surface without venting and reloading the sample in a different orientation, and in no way affected the randomness of the micro-impact site selections.

Considering all of the limitations described above, the impactor classifications cannot be taken as absolute, but there is moderate confidence in their accuracy within the described limitations of the study. Limits can be ascribed to the manmade/natural ratios based on the results to date. ***Future adjustments, resulting from better understandings of contamination issues and impactor residue deposition mechanisms, and from additional analyses of orbital impact sites, may alter the statistical distribution of manmade and natural impactor classifications deduced from currently available data.*** Additionally, the combination of this data set with data from other LDEF investigators should provide a more accurate assessment of the microparticle population ratio in LEO.

Tray C-3 (Trailing [wake], or West side)

There was an average of 10 impacts per sensor on tray C-3. Impactor residues in 18 impact sites on four different sensors were classified as: 5 manmade, 3 natural and 10 indeterminate. Four of the manmade residues had Ti and/or Zn in high concentrations and were assumed to be from paint particles. Two of these particles were <~3 μm in size, and the other two were ~20 and ~40 μm in size. Residue from a fifth manmade impactor (<~3 μm in size) was identified by the presence of significant amounts of Cr along with Mg and Fe.

Figure 1a shows a SEM micrograph of impact No. 1382-C2 from tray C-3 with its 22 μm wide central crater and its 65 μm wide spall zone. SIMS ion maps for Na^+, Mg^+, Si^+, K^+, Ti^+ and Zn^+ are shown in Fig. 1b. The black box in these images outlines the image area that was selected for quantitative data reduction. A bar graph of the calculated concentrations, relative to Si=1.0, is shown in Fig. 1c and provides an example of the type of data that can be evaluated further as the study progresses. It should be possible to derive significant information about the chemical composition of the non-volatile components of many impactors from these types of data after contamination interferences are better understood.

The three natural micrometeorite residues on tray C-3 sensors were all identified by the presence of Mg and Fe. Two of the impacts were made by small (<~3 μm) particles and had Na, Mg, K, Fe and Mg, and Ca, Fe, Ni present in residues. The third impact (No. 1336-C4)had a 23 x28 μm central crater (as described above) with no additional spall zone. A residue containing Na, Mg, K, Ca and Fe was found in the crater. Probable impactor size was estimated to have been ~10 μm. Figure 2a is an optical micrograph of this impact. SIMS ion maps are shown in Fig. 2b, and Fig. 2c shows a bar graph plot of the reduced image data for the central crater region.

Ten of the 18 impact sites had insufficient debris remaining to be positively identified above the background levels. This situation could be the result of natural microimpactors that had very high encounter velocities (>>10 km/s), or impacts from aluminum oxide particles which were not detectable in the Al/Si substrate. Central craters in these impacts ranged in size from 10-25 μm. Figure 3a shows an example of a medium size impact in the "clean" category, No. 1359-C6. Probable impactor size was estimated at ~10 μm. Figures 3b shows some of the ion maps associated with this impact, and Fig. 3c

shows a bar graph of the reduced SIMS data for the central crater. It is anticipated that further analysis of this type of data in "clean" impact sites will lead to quantitation of background contamination levels and allow more accurate assessment of chemical compositions of the non-volatile impactor components.

If all 10 of the "clean" impact sites are assumed to have been caused by small, high speed natural particles, the manmade/natural ratio equals 5/13=0.38. This microparticle value is significantly higher than the assumed ratio of 0.1 for all impactors striking the trailing edge of satellites in low earth orbit (LEO) and could be the result of contamination interferences. However, the IDE data showed that the long term average flux of particles >0.5 μm in size varied drastically during the nearly 6 year long mission (ref. 5). Of the total of 290 impacts on these sensors, 186, or 64% occurred during the first year. The overall mission flux rate measured by the sensors matched that measured by other investigators (ref. 6). It is possible that orbital debris impacts caused the enhanced rate during the first year. (This topic is discussed in more detail in ref. 5.) The chemical analysis data collected thus far, subject to the stated limitations, seem to support this scenario.

Tray C-9 (Leading [ram], or East side)

There was an average of 311 impacts/sensor on tray C-9. Using the same criteria described above, impactor residues in 36 impact sites on 2 different sensors were classified as: 11 manmade, 5 natural and 20 indeterminate. If 19 of the 20 "indeterminate" impactors (those that were "clean" or had only Na and K present in the craters) are assumed to have been Al_2O_3 particles, then the manmade/natural ratio would equal 30/5=6.0. This micorparticle ratio is somewhat lower than the assumed ratio of 10 for all impactors on the leading edge of satellites in LEO, but considering the limitations of the current study, this preliminary result is reasonable. It should be noted that the long term impact flux measured by these leading edge sensors did not vary substantially and matched the flux rates measured by other LDEF investigators (ref. 6).

Of the 11 manmade impactors, 9 were particles that were <~3 μm in size and 2 were particles estimated to have been 30-40 μm in size. Of the 9 small particle residues, one had only Ti and a trace of Na and K, three residues contained Cu in addition to Na, K and Mg, one contained Cu along with Na, K, Mg, Fe and traces of Ti and Cr, and four residues contained only Na, K and Mg.

The two largest manmade debris impacts examined have significant amounts of impactor residue. Residue from an ~30 μm particle contained Na, Mg, Ti, Cr, Fe, Cu, Zn and Ag and could be from a small piece of electrical component with paint. Residue from a 40 μm particle contained high concentrations of H, C, Ti, Cr and Fe and could have been a piece of painted plastic or a paint particle with an organic binder. (This was the only high concentration H, C residue found in the 79 impact sites.)

All 5 of the natural impactors were identified by the presence of Mg and Fe. Only one residue had Ca above background. One particle was estimated to have been <~3μm in size, and the other 4 were estimated to have been ~5-10 μm in size.

Of the 20 "indeterminate" impactors, 16 were <~3 μm in size, and 4 were ~4-8 μm in size. This could support the assumption that most of these impactors were small aluminum oxide spheres (from solid rocket motor exhaust). Zinner, et al., have reported that 8 out of 11 small particle impact craters examined on Ge capture cells from LDEF tray E-8 (near leading edge) contained only Al and O residues (ref. 7).

Tray D-6 (South side)

There was an average of 137 impacts/sensor on tray D-6. Impactor residues in 4 craters examined on one sensor were classified as : 1 manmade (Na, K, Mg, Cu) and 3 indeterminate. All craters were

formed by particles <~3 μm in size. These results are too preliminary to draw any conclusion other than the obvious, expected result that orbital debris did strike the North side of the satellite. Cu was the indicator for the manmade impactor residue. Al_2O_3 particles, or small high speed natural particles could have caused the other impacts.

Tray B-12 (North side)

There was an average of 143 impacts/sensor on tray B-12. Impactor residues in 12 craters examined on one sensor were classified as: 4 manmade, 6 natural and 2 indeterminate (clean). Natural impactors were all identified by the presence of Mg and Fe. Only one of these had significant Ca. Three of the 6 natural impactors were <~3 μm in size, and three were ~5 μm in size. The two indeterminate impactors were both <~3 μm in size.

Three of the 4 manmade impactors were <~3 μm in size and the fourth was ~6 μm in size. Residue from the largest impactor contained Fe, Cu and Zn along with Na, K, and Mg. One of the 3 smaller impacts contained Na, Mg, K and traces of Cu and Ag, one contained Na, Mg, K, Ti and Zn, and one contained Na, Mg, Fe and Cu.

Tray G-10 (Earth end)

There was an average of 10 impacts/sensor on tray G-10. Two out of 6 small particle(<~3 μm) impactor residues analyzed on one sensor were classified as manmade based on the presence of Fe and Ti in one and Ti and Cr in the other. The other four impactors were classified as indeterminate since only traces of Na and K were found in the craters. The only conclusion that can be drawn from these data is the expected result that orbital debris did strike the Earth end of the satellite. It is interesting to note that the entire impact set on the Earth end sensors was formed by particles <4 μm in size. (The sensors were shielded from highly oblique (<4°) grazing impacts.)

Tray H-11 (Space end)

There was an average of 21 impacts/sensor on tray H-11. Three impacts on one sensor were analyzed and classified as: 2 manmade and 1 natural. The natural impactor, estimated to have been ~8 μm in size, left a residue containing Na, Mg, K, Ca and Fe. Only Ti and Zn were detected in the residue from one small manmade particle (<~3 μm). The second manmade particle, estimated to have been ~6 μm in size, also left a residue containing Ti and Zn, but traces of Na and K were detected in the crater. Both particles were probably pieces of paint. No conclusions can be drawn from this small sample set on the Space end tray, but the early results indicate that there may have been more orbital debris strikes on the Space end than expected.

Comments

The presence of Cu in 5 of the 11 manmade impactor residues on sensors from the East panel, and 4 of the 5 manmade impactor residues found on sensors from the North and South sides of LDEF, is unexpected. This may be due to higher than normal, heterogeneously distributed background levels of Cu, or some other unidentified mass interferent. However, a review of all residue compositions shows that Cu was only detected in impact sites on the East, North and South sides of the satellite. The IDE impact record shows that the LDEF passed through several orbital debris clouds during its first year in

orbit that affected only these three sides of the spacecraft. Thus, it is possible that Cu bearing debris may be a significant component of these debris clouds. If the Cu is shown not to be a contaminant in future work, this could point to a specific source type for this debris. The other manmade impactors were presumably paint particles as discussed above.

Remaining resources for this study will be utilized for the following tasks:

1) continued analysis and interpretation of data collected to date in order to further define the nonvolatile chemical composition of impactors,

2) continued contamination studies including depth profiles down to the Si substrate that will address background contamination levels for Na, Mg, K and Cu.

3) EDS and Auger spectroscopic studies of heavy deposits of impactor residues and surface contamination features in order to determine the composition and possible cross interference of these species

4) analyses of several simulated (Fe hypervelocity particles) impact sites on an active flight sensor, and

5) analysis of as many flight impact sites as possible until the optimum number of 320 is reached.

SUMMARY

To date, 79 impacts on IDE sensors have been analyzed with SIMS. These include 36 impacts on two IDE sensors from LDEF tray C-9 (leading, or east side), 18 impacts on four different sensors from tray C-3 (trailing, or west side), 12 impacts on one sensor from tray B-12 (north side), 4 impacts on one sensor from tray D-6 (south side), 6 impacts on one sensor from the earth end tray G-10, and 3 impacts on one sensor from the space end tray H-11. Of the 79 impacts, 57 were formed from particles estimated to have been <3 μm in size, 18 were formed from particles estimated to have been 5-20 μm in size, and 3 were formed from particles estimated to have been 30-50 μm in size. Residue from manmade debris, mostly paint particles and metal bits, has been identified in craters on all trays. (Aluminum oxide particle residues were not detectable on the Al/Si substrates.)

Preliminary estimates of the manmade/natural microimpactor population ratio for the East and the West sides of LDEF were calculated assuming that unknown impactor residues were all manmade or all natural, respectively. The calculated ratios were 6.0 for the East and 0.38 for the West. These values are subject to change as more information on contamination interferences, and more analyses impact sites is collected. Additionally, the combination of this data set with data from other LDEF investigators should provide a more accurate assessment of the microparticle population ratio in LEO.

Quantitative analyses of impactor residue chemical composition is underway, but results will not be reported until a better understanding of contamination issues is gained.

Cu was detected in 9 out of 16 "manmade" impacts on sensors from the East, North and South sides of LDEF, but was not detected in any of the 9 "manmade" impacts on sensors from the West, Space and Earth ends of the satellite. If, after further investigation, the Cu is shown not to be a contaminant, this could point to a specific source type for this debris.

The results to date are generally consistent with the IDE impact record which showed highly variable long term microparticle impact flux rates on the West, Space and Earth sides of the LDEF which could not be ascribed to astronomical variability of micrometeorite density. The IDE record also showed episodic bursts of microparticle impacts on the East, North and South sides of the satellite, denoting passage through orbital debris clouds or rings.

REFERENCES

1. C.G. Simon, J.L.Hunter, D.P. Griffis and J.J. Wortman, "Ion Microprobe Elemental Analyses of Impact Features on Interplanetary Dust Experiment Sensor Surfaces", NASA CP 3134, pp. 529-548 (1991).

2. R.G. Wilson, F.A. Stevie and C.W. Magee, Secondary Ion Mass Spectrometry - A Practical Handbook for Depth Profiling and Bulk Impurity Analysis, J. Wiley & Sons, p. E-17 (1989).

3. Ibid, p. E-22.

4. B.G. Cour-Palais, "The Current Micrometeoroid Flux at the Moon for Masses $\leq 10^{-7}$ g from the Apollo Window Surveyor 3 TV Camera Results", Geochimica et Cosmochemica Acta, Vol. 3, pp. 2451-2462 (1974).

5. C.G. Simon, J.D. Mulholland, J.P. Oliver, W.J. Cooke and P.C. Kassel, "Long-Term Microparticle Flux Variability Indicated by Comparison of Interplanetary Dust Experiment (IDE) Timed Impacts for LDEF's First Year in Orbit with Impact Data for the Entire 5.77 year Orbital Lifetime",

6. C.G. Simon, J.C. Mandeville, J.A.M. McDonnell, M. Mirtich and R.W. Walker, "M&DSIG Microcrater Committee Report", in NASA CP-3194, (1993).

7. S. Amari, J. Foote, C. Simon, P. Swan, R. Walker and E. Zinner, "SIMS Chemical Analysis of Extended Impacs on the Leading and Trailing Edges of LDEF Experiment AO187-2", in NASA CP-3194, (1993).

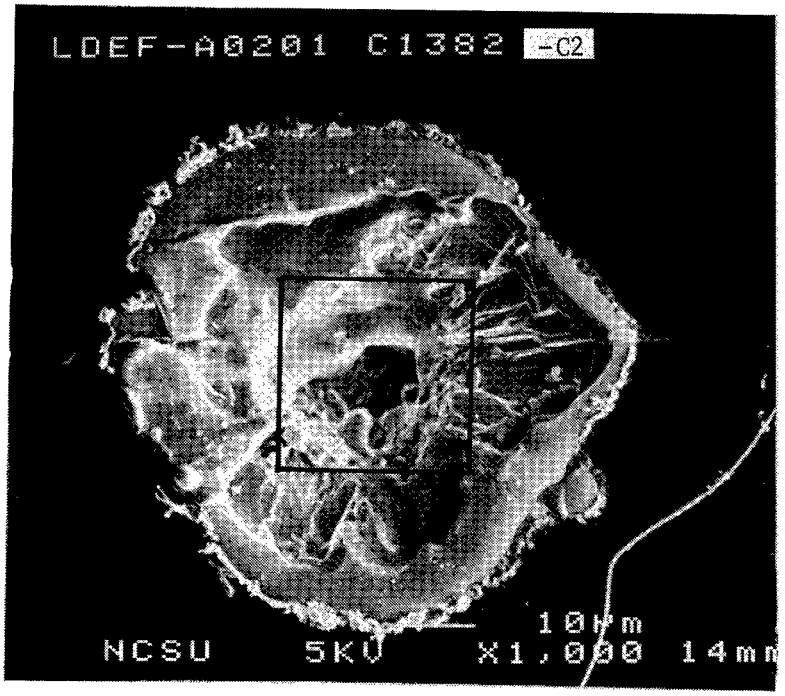
Table 2. Microparticle residue classifications for 79 impacts on IDE sensor surfaces based on SIMS analyses. (See text for explanation of crater and spall zone sizes.) *Na not looked for in all sites.

Impact No.	Size (μm) Crater	Spall	Elements Detected with SIMS	Impactor Classificaton manmade	natural	indeterminate
LDEF Tray C-3 (Trailing [wake], or West side)						
1300-C1	36x54	138	(Na, Mg, K, Ca)--(Ti, Fe)	X		
1300-C2	13x18	-	clean (trace Na)			X
1300-C3	12	-	Na, Mg, K, Fe		X	
1300-C4	13	-	clean			X
1300-C5	11	-	Na, K, Mg, Cr, Fe	X		
1300-C6	10	-	clean			X
1300-C7	12	-	Na, K, Ti	X		
1300-C8	12	-	Na, Mg, K, Ti	X		
1336-C1	10	-	clean (trace Na)			X
1336-C4	23x28	-	Na, Mg, K, Ca, Fe		X	
1359-C4	10	-	clean			X
1359-C5	9x12	-	clean (trace Na, Mg)			X
1359-C6	18x25	42	clean			X
1359-C7	12	-	clean			X
1382-C2	22	65	Na, Mg, K, Ti, Zn	X		
1382-C4	9	-	(trace Mg, Ca, Fe, Ni)		X	
1382-C5	10	-	clean			X
1382-C9	15x20	-	clean (trace Mg)			X
LDEF Tray C-9 (Leading [ram], or East side)						
1176-C1	23	-	Na, Mg, K, Fe		X	
1176-C2	9	-	clean (trace Na, K)			X
1176-C3	9	-	Na, K			X
1176-C4	11	-	Na, K, Cu	X		
1176-C5	32	212	Na, Mg, Ti, Cr, Fe, Cu, Zn, Ag	X		
1176-C6	23x37	-	Na, K			X
1176-C7	50	138	H, C, Ti, Cr, Fe	X		
1176-C8	9	-	Na, Mg, K	X		
1176-C9	12x16	-	Na, Mg, K--(Fe)			X
1176-C10	9	-	Na, Mg, K, Cu	X		
1176-C11	9	-	Na, K			X
1176-C12	10	-	Na, Mg, K	X		
1176-C13	9	-	Na, Mg, K, Cu	X		
1176-C14	9	-	Na, K			X
1176-C15	9	-	Na, K			X
1176-C16	10	-	Na, K			X
1176-C17	11	-	Na, Mg, K, Fe, Cu (trace Ti, Cr)	X		
1176-C18	22x25	-	Na, Mg, K, Fe		X	
1176-C19	11	-	Na, Mg, K	X		
1176-C20	11	-	Na, Mg, K	X		
1293-C1	13x17	-	*clean			X
1293-C2	24x31	-	*Mg, K, Fe		X	
1293-C3	18	-	*Mg, K, Ca, Fe		X	
1293-C4	12	-	*Mg, Fe		X	

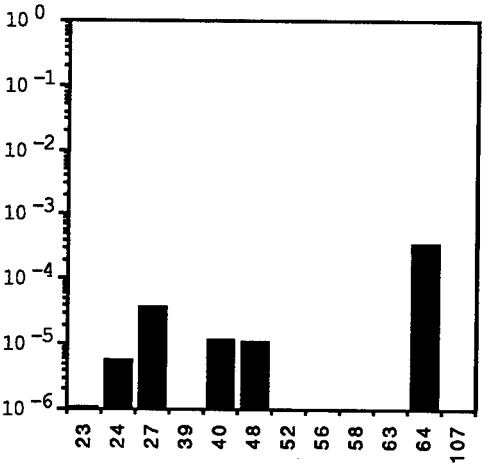
Table 2. [continued] Microparticle residue classifications for 79 impacts on IDE sensor surfaces based on SIMS analyses. (See text for explanation of crater and spall zone sizes.) *Na not looked for in all sites.

Impact No.	Size (μm) Crater	Spall	Elements Detected with SIMS	Impactor Classificaton manmade	natural	indeterminate
LDEF Tray C-9 (Leading [ram], or East side) {continued}						
1293-C5	22x28	-	*clean			X
1293-C7	12	-	*clean			X
1293-C8	10	-	*clean			X
1293-C12	12	-	Ti (trace Na, K)	X		
1293-C13	9	-	clean			X
1293-C14	9	-	clean			X
1293-C15	11	-	clean			X
1293-C16	11	-	clean			X
1293-C17	9	-	clean			X
1293-C18	11	-	clean			X
1293-C19	13	-	clean			X
1293-C20	11	-	clean			X
LDEF Tray D-6 (South side)						
1252-C3	10x13	-	Na, Mg, K, Cu	X		
1252-C4	10	-	clean (trace K)			X
1252-C5	10	-	clean (trace K)			X
1252-C9	10	-	clean (trace K)			X
LDEF Tray B-12 (North side)						
1298-C1	11x19	34	Na, Mg, K, Fe		X	
1298-C2	10	-	clean			X
1298-C6	15x20	38	Na, Mg, K, Fe		X	
1298-C7	10	-	Na, Mg, K, Ca, Fe		X	
1298-C8	16x20	30	Na, Mg, K, Fe, Cu, Zn	X		
1298-C9	15	-	Mg, Fe		X	
1298-C10a	10	-	Na, Mg, K (trace Cu, Ag)	X		
1298-C10b	10	-	Na, Mg, K, Ti, Zn	X		
1298-C11	11	-	clean			X
1298-C12	9x13	-	Na, Mg, Fe		X	
1298-C13	10	-	Na, Mg, Fe		X	
1298-C14	10	-	Na, Mg, Fe, Cu	X		
LDEF Tray G-10 (Earth end)						
1172-C5	9	-	Na, Mg,Ti,Fe	X		
1172-C6	9	-	clean (trace Na, K)			X
1172-C7	11	-	Na, K			X
1172-C8	10	-	clean (trace Na, K)			X
1172-C10	9	-	clean (trace Na, K)			X
1172-C11	10	-	Na, K, Ti, Cr	X		
LDEF Tray H-11 (Space end)						
1255-C1	20	32	Ti, Zn (trace Na, Mg)	X		
1255-C2	23x27	-	Na, Mg, K, Ca, Fe		X	
1255-C4	11	-	Ti, Zn	X		

(A)



(C)



(B)

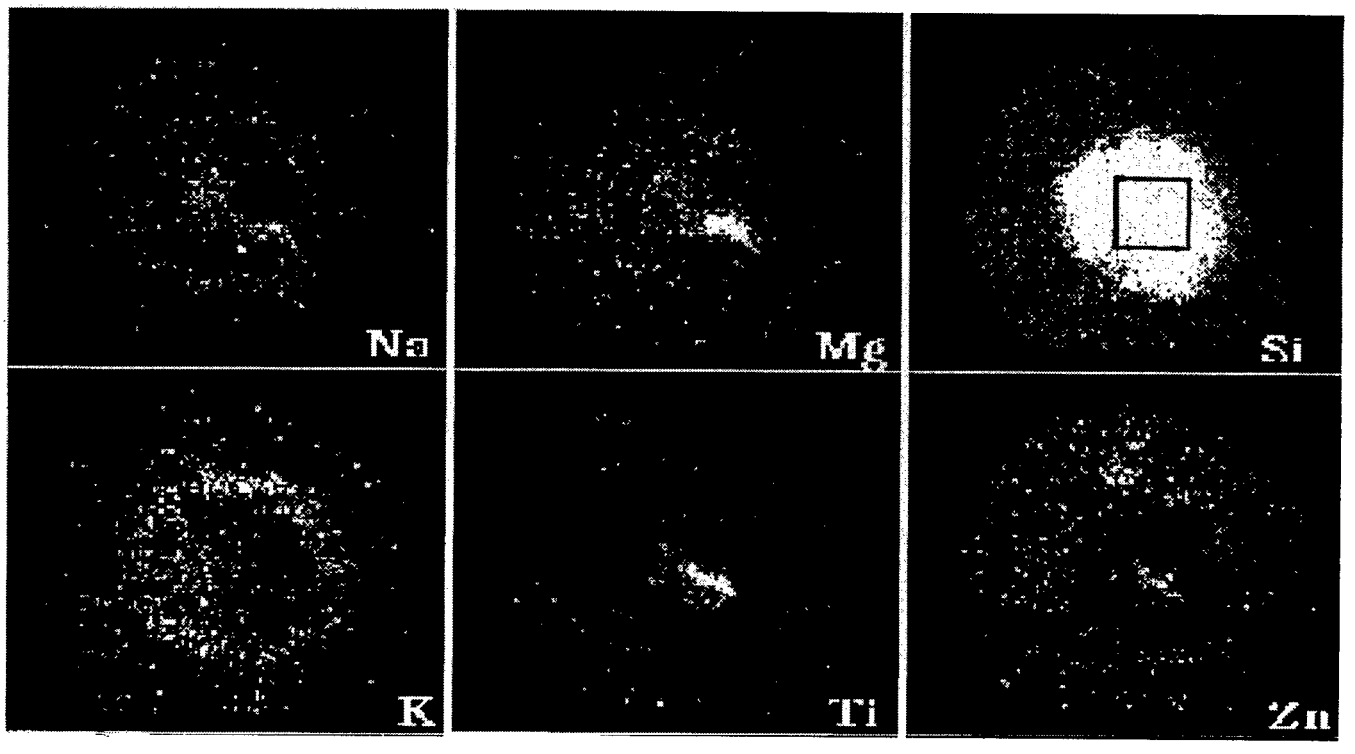
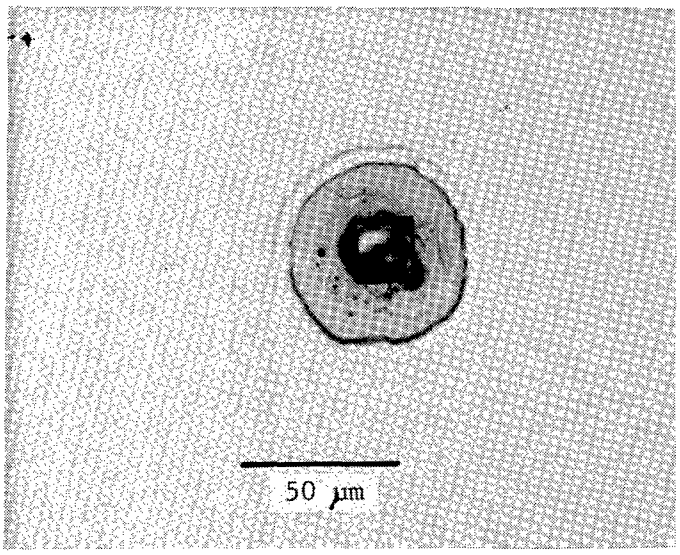
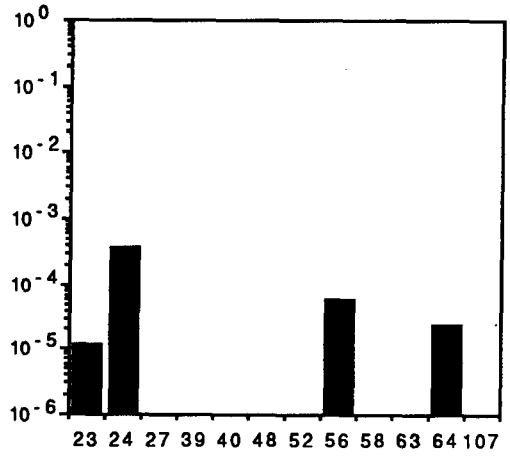


Figure 1. Example of a manmade debris impact (1382-C2) on an IDE sensor mounted on LDEF tray C-3 (Trailing or West side). (A) SEM micrograph. (B) Secondary positive ion images of impact area. Imaged area is 150 μm in diameter. Intensities are uncorrected for relative ion yields. Note exposed area of Si and SiO_2 defined by the Si^+ map. (C) Bar graph plot of corrected ion intensity data for boxed area.

(A)



(C)



(B)

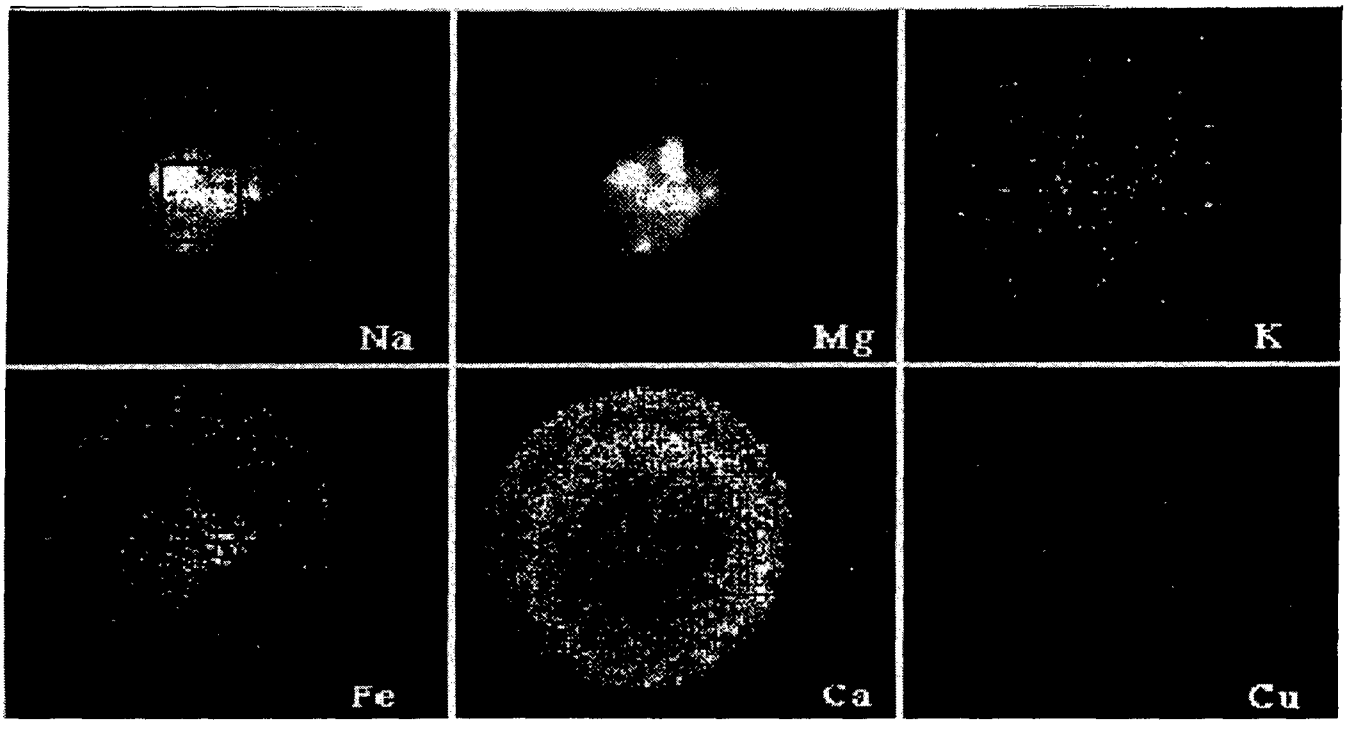
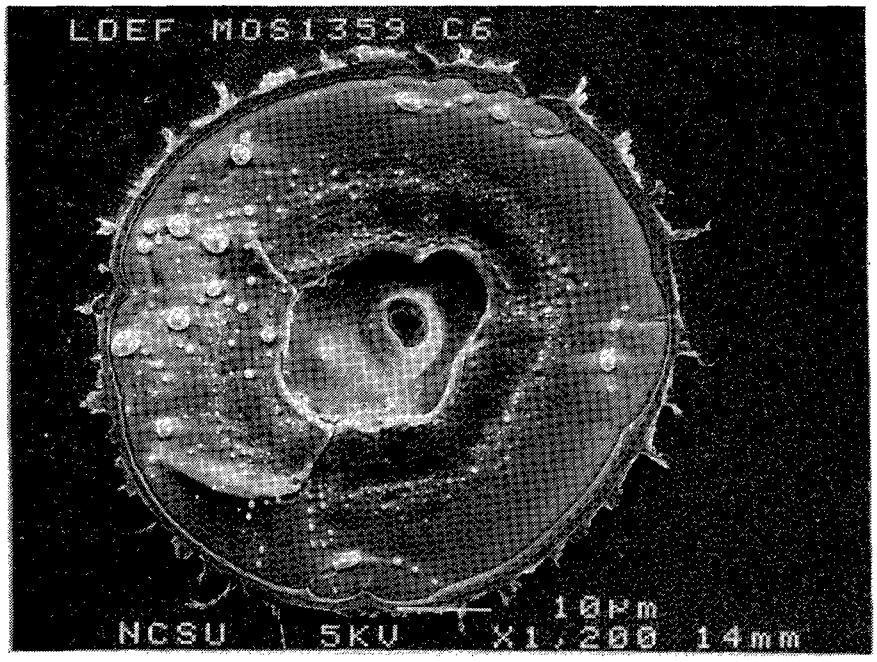


Figure 2. Example of a natural micrometeorite impact (1336-C4) on an IDE sensor mounted on LDEF tray C-3 (Trailing or West side). (A) Optical micrograph. (B) Secondary positive ion images of impact area. Imaged area is 150 µm in diameter. Intensities are uncorrected for relative ion yields. (C) Bar graph plot of corrected ion intensity data for boxed area. Note the low intensity for mass 64 (Cu+) in the ion image and the relatively high concentration value displayed in the bar graph. This methodological artifact raises the minimum detectable Cu level to the 100 ppm range. The high Ca+ background intensity surrounding the impact has been traced to contamination in the top layer of aluminum on the substrate.

(A)



(B)

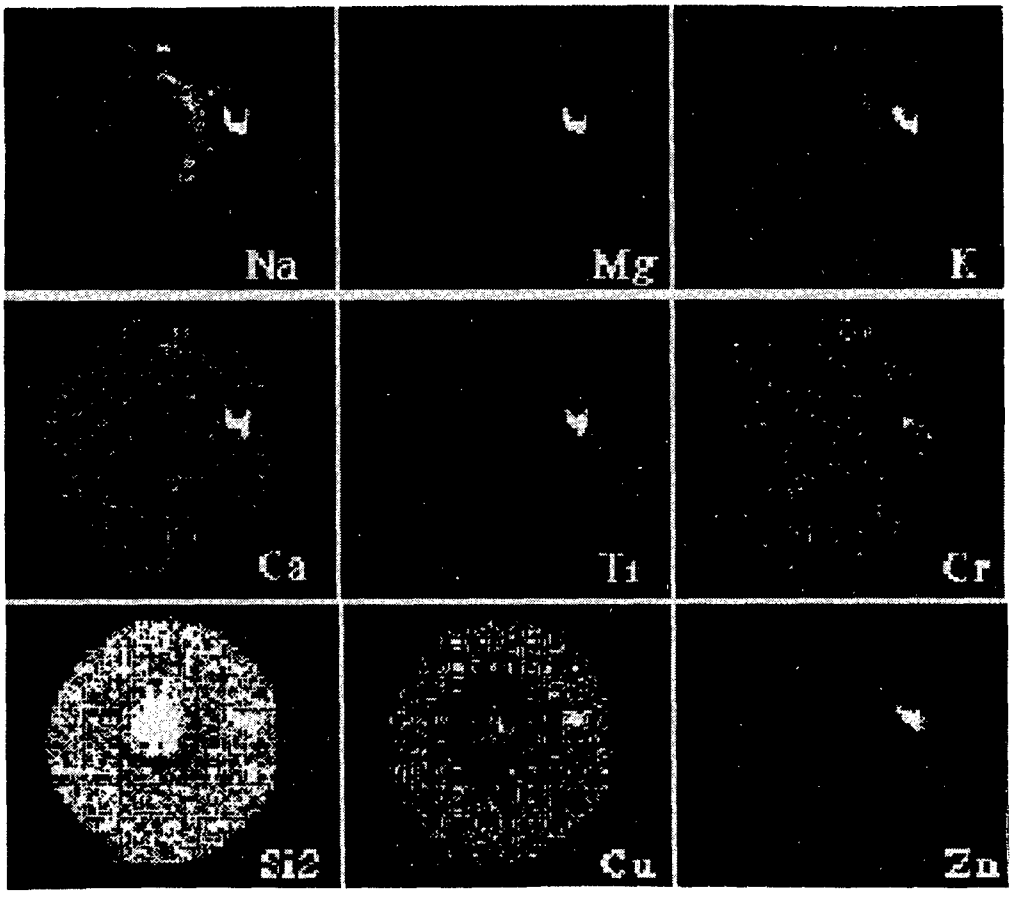


Figure 3. Example of an indeterminate impact (1359-C6) on an IDE sensor mounted on LDEF tray C-3 (Trailing or West side). (A) SEM micrograph. (B) Secondary positive ion images of impact area. Imaged area is 150 μm in diameter. Intensities are uncorrected for relative ion yields. Note central crater area defined by the Si_2^+ map. Bright spot of Na, Mg, K, Ca, Ti, Zn is a contaminate well outside of the impact crater.

LONG-TERM MICROPARTICLE FLUX VARIABILITY INDICATED BY COMPARISON OF INTERPLANETARY DUST EXPERIMENT (IDE) TIMED IMPACTS FOR LDEF'S FIRST YEAR IN ORBIT WITH IMPACT DATA FOR THE ENTIRE 5.77-YEAR ORBITAL LIFETIME

C. G. Simon, J. D. Mulholland[1], J. P. Oliver[2], W. J. Cooke
Institute for Space Science & Technology, Gainesville FL 32609

P. C. Kassel
NASA Langley Research Center, Hampton VA 23665

[1]Also Observatoire de la Cote d'Azur, 06304 Nice, France
[2]Also University of Florida, Gainesville FL 32611

ABSTRACT

The electronic sensors of the Interplanetary Dust Experiment (IDE) recorded precise impact times and approximate directions for submicron to ~100-micron size particles on all six primary sides of the spacecraft for the first 346 days of the LDEF orbital mission. Previously-reported analyses of the timed impact data have established their spatio-temporal features, including the demonstration that a preponderance of the particles in this regime are orbital debris and that a large fraction of the debris particles are encountered in megameter-size clouds. Short-term fluxes within such clouds can rise several orders of magnitude above the long-term average. These unexpectedly large short-term variations in debris flux raise the question of how representative an indication of the multi-year average flux is given by the nearly one year of timed data. One of the goals of the IDE was to conduct an optical survey of impact sites on detectors that remained active during the entire LDEF mission, to obtain full-mission fluxes.

We present here the comparisons and contrasts among the new IDE optical survey impact data, the IDE first-year timed impact data, and impact data from other LDEF micrometeoroid and debris experiments. The following observations are reported.

1) The 5.77 year long-term integrated microparticle impact fluxes recorded by IDE detectors matched the integrated impact fluxes measured by other LDEF investigators for the same period.

2) IDE integrated microparticle impact fluxes varied by factors from 0.5 to 8.3 for LDEF days 1-346, 347-2106 and 1-2106 (5.77 years) on rows 3 (trailing edge, or West), 6 (South side), 12 (North side), and the Earth and Space ends.

3) IDE integrated microparticle impact fluxes varied less than 3% for LDEF days 1-346, 347-2106 and 1-2106 (5.77 years) on row 9 (leading edge, or East).

These results give further evidence of the accuracy and internal consistency of the recorded IDE impact data. This leads to the further conclusion that the utility of long-term flux ratios for impacts on various sides of a stabilized satellite in low Earth orbit (LEO) is extremely limited. These observations, and their consequences, highlight the need for continuous, real time monitoring of the dynamic microparticle environment in LEO.

INTRODUCTION AND BACKGROUND

The electronic sensors of the Interplanetary Dust Experiment (IDE) recorded precise impact times and approximate directions for submicron to ~100-micron size particles on all six primary sides of the spacecraft for the first 346 days of the LDEF orbital mission. The resulting data set of over 15,000 impacts represents perhaps the most extensive record ever gathered of the number, locations, and times of small particle impacts on a spacecraft in Earth orbit. The fact that the involuntarily "extended mission" of LDEF assured that the IDE detectors would be exposed to the LEO environment for a much longer time than the duration of their data recording system made it clear from the moment of recovery that it would be desirable to perform impact counts on detectors that remained active during the entire mission in order to compare the IDE 5.77-year integrated fluxes with the 346-day integrated fluxes from the IDE timed data. In this paper we report on that comparison, and on the comparison with full mission integrated microparticle fluxes from other LDEF experiments.

The IDE detectors are constructed from 2 inch diameter, 250 μm thick, boron-doped ultra high-purity silicon wafers covered with either a 0.4 or a 1.0 μm thick layer of thermally grown SiO_2 insulator, and coated with ~1000Å of high-purity aluminum. The detectors are divided into two sensitivity levels based on the insulator thickness. (The reader is directed to ref. 1, Singer *et al.*, for details of the hardware design.)

Extensive hypervelocity impact testing of the detectors was performed at Langley Research Center by Kassel (ref. 2) prior to LDEF launch. The two different sensitivity detectors were subjected to hundreds of impacts from 0.5 to 5 μm diameter carbonyl iron projectiles (density = 7.86 g/cm^3, mass range = 5×10^{-13} to 5×10^{-10} g) at velocities of 4 to 10 km/s and incident angles from 0 to 75° from normal. The applied voltage across the detectors ranged from -60 to -20 volts. These tests indicated that a 0.5 μm particle impacting at 3 km/s (or faster) would trigger the low sensitivity detectors, and a 0.5 μm particle impacting at 2 km/s (or faster) would trigger the high sensitivity detectors. While the tests did not establish an absolute calibration for the detectors, they did demonstrate several important features:

1) the detector operation is reliable (stable and reproducible) when the bias voltage is greater than 30V;
2) after an impact the detector returns to its original condition with an insignificant loss of active area;
3) the sensitivity of the detectors is inversely proportional to the insulator layer thickness;
4) the sensitivity of the detectors is strongly dependent on the bias voltage below 40V;
5) submicron hypervelocity particles will trigger the detectors.

(A more extensive study of the detectors, which involved an expanded operational parameter set and several thousand hypervelocity microparticle impacts, is the topic of a paper currently under preparation by the IDE team.)

While the IDE detector sensitivities could be related to each other, and they were very stable under stable bias conditions, their absolute sensitivities were not known. When LDEF was retrieved at the end of its 5.77 year mission, nearly all of the low sensitivity IDE detectors were still functional and were operating at a bias voltage of 62V, compared to an initial bias voltage of 71V. Based on observations during impact testing, this difference is not considered significant at this high voltage level. In order to empirically evaluate the extent of this effect, the IDE detector array from the South side of LDEF (tray D-6) was powered up to 71V and monitored for 28 days. Any impact damaged sites that did not cause an active detector to discharge while on orbit under a bias of 62V should have triggered the detector within a few minutes under a bias voltage of 71V. Twenty-two of the 32 low sensitivity IDE detectors on this tray were found to still be active on retrieval. Post flight optical scanning showed an average of ~140 impact induced discharges on each detector. When the 22 detectors were powered up, only one discharge occurred within the first two minutes. A total of 6 discharges occurred within 4 hours, and an additional 3 discharges occurred over the next 28 days. It was apparent that there was not a significant amount of impact damage on the sensors that had not already caused the detectors to discharge while on orbit.

(It should be noted that two similar pre-flight tests of the same detectors showed 1 discharge over 22 days and 0 discharges over 34 days.)

The power-up test of the IDE tray D-6 detectors also provided further evidence that anomalous sensor status readings periodically recorded during the active portion of the mission were unrelated to detector performance. Sensor status readings were designed to give instantaneous checks of the recharge state on the capacitor detectors. The anomalies appear to be the result of the circuit's interaction with the local spacecraft plasma (ref. 3). A detailed report on the IDE system behavior is currently in preparation by the experiment team.

Examination of the impact records on all arrays showed that impact counting rates were not related to the "sensor status" record. There were, in fact, several instances where impacts were recorded immediately prior to, just after, and even *during* a status check that indicated all sensors were uncharged. If the detectors had actually been functioning under a reduced charge state, the impact sensitivity, and thus the counting rates, would be biased negatively. It is also noted that these anomalous status readings were indicated <5% of the time for the low sensitivity IDE detectors on the South panel, and this was the worst case. Overall impact counting rates for tray D-6 (South) and tray B-12 (North), which experienced very few sensor status anomalies during the first year were similar, with the South panel recording ~10% more impacts than the North panel. This was another indication that the anomalous sensor status readings were not related to detector functionality.

Considering this evidence, it appeared practical to count the impact induced discharge sites on the IDE low sensitivity detectors that remained active during the entire orbital mission, and derive impact flux values for all 6 orthogonal sides of LDEF. These values could then be compared to the flux values observed by other LDEF investigators, resulting in an empirical calibration of the IDE detector sensitivity with respect to a standard measure of impact damage, such as equivalent crater size in aluminum. (This is a particularly useful standard, since there was a large amount of aluminum surface area exposed on LDEF.) The long term flux values could also be contrasted to the fluxes recorded electronically by the same detectors during their first year of operation. This permits a determination of microparticle impact flux values for 3 long-term time periods: days 1-346, days 1-2106, and days 347-2106 (by subtraction).

DESCRIPTION OF IDE DATA SETS

It is important to distinguish among the various impact data sets (IDE and others) and to constantly be aware of which sets are being compared or contrasted. The timed data from the two different sensitivity IDE detectors represent two distinct data sets, labelled "A" and "B" below. The impact-induced discharge record on the low sensitivity detectors that remained active during the entire orbital mission represents a third, distinct data set labelled "C" below. A fourth data set can be derived by subtracting the electronically-recorded impact data on the low sensitivity IDE detectors (data set "B") from the optical record of impact discharges during the entire mission (data set "C"). This data set is labelled "D". To summarize, we have assigned the following labels to the four distinguishable long-term IDE impact data sets:

A = electronically timed impacts for particles that triggered the high sensitivity IDE detectors during LDEF's first year in orbit (days 1-346),

B = electronically timed impacts for particles that triggered the low sensitivity IDE detectors during LDEF's first year in orbit (days 1-346),

C = all impacts that triggered low sensitivity IDE detectors that remained active during the entire LDEF orbital mission (days 1-2106),

D = all impacts that triggered low sensitivity IDE detectors that remained active during the entire LDEF orbital mission on days 347-2106 (i.e., C-B=D).

The first two data sets, "A" and "B", contain the 15,000 electronically timed impacts recorded by IDE detectors mounted on the six orthogonal sides of LDEF. The impact times are known with a resolution of 13s and an accuracy of 20s (ft. note 1). Even though the recording tape ran out after 346 days, the IDE detectors continued to function. Housekeeping data on the tape indicated that bias voltages on the arrays of both sensitivities of IDE detectors had dropped <1% during the first 346 days. Most of the low sensitivity detectors were active and performing nominally (as described above) on retrieval. Some had suffered catastrophic impact damage. All of the high sensitivity detectors arrays had drained their batteries sometime after the first year (because of higher operational leakage currents) and were inactive upon retrieval.

The third IDE data set , "C", includes over 10,000 impacts and is contained in the optical record of impact discharges on low sensitivity IDE detectors that remained active during the entire LDEF 5.77 year mission. This record has been extracted by optical microscopic examination of these detectors (discussed below) and represents the impact fluxes for the entire mission. Data set "D" contains approximately 6,000 impacts and represents the impact fluxes during the 4.8 years after the IDE recording tape ran out.

It is imperative that readers keep in mind the differences in these three data sets. **Direct comparisons of LDEF flux numbers are valid only when the spatial, temporal and physical impact criteria on which the flux values are based are identical.** For example, it **is** valid to directly compare long term IDE flux values (data set "C") with other LDEF long term flux values for the equivalent impact feature sizes on surfaces from equivalent LDEF locations. These values should be essentially identical if there are no problems with the associated data sets.

However, it is **not** valid to directly compare IDE first year flux values (data sets "A" and "B") with IDE data sets "C" and "D" or other LDEF 5.77 year long term flux values for equivalent impact feature sizes and locations. These values are not necessarily identical. *Indeed, it is the differences (contrasts) between the 5.77 year long-term fluxes measured by IDE and other LDEF experiments and the one year "long-term" fluxes measured by IDE (and FRECOPA on the West side of LDEF) that constitute a significant discovery and are the bases of the following discussions.*

Comparisons and contrasts of flux values among IDE data sets B, C and D and other LDEF dust experiments will be discussed in this paper. Results from non-temporally-resolved LDEF impact experiments were extracted from the LDEF Meteoroid and Debris Special Investigation Group's Interim Report (ref. 4), which was based on LDEF investigator supplied and reviewed data.

IDE data set A is not included in these discussions since almost no LDEF impact flux data has been generated to date that can be directly compared or contrasted to this data set. Some temporal resolution is available from impacts that occurred on surfaces contained within experiment exposure control canisters (EECC) located on LDEF rows 2, 3, 4, 8 and 9. These canisters were open during the same time period that the IDE experiment was recording impact events. The difficulty is in securing samples from these experiments that have smooth enough surface textures to allow accurate assessment of the 1 μm crater population. This comparison is left to a future study after more information has been reported by other LDEF investigators.

Previously reported analyses of the IDE timed microparticle impact data established their basic spatio-temporal features, including the demonstration that a preponderance of the particles in this size regime are orbital debris (a finding that is consistent with the results of the first catastrophic hypervelocity laboratory impacts on a real satellite, OSCAR-22, recently reported in the press [ref. 5]), and that a large fraction of the debris particles are encountered in megameter-size clouds (refs. 1, 6 and 7; ft. notes 2 and 3). Higher than expected impact fluxes detected by IDE on the West (trailing) edge of LDEF provided the first evidence of a far greater population of debris in highly elliptic orbits (>0.07 eccentricity) than previously known, a conclusion now supported by additional LDEF experiment results (*e.g.* ref. 8). Short-term fluxes within such clouds increased several orders of magnitude above the long-term average. A discussion of the sizes, densities and orbital parameters of several of these orbital debris clouds is presented in footnote 3.

We present here comparisons and contrasts among the IDE optical survey impact data, the IDE first-year timed impact data, and integrated impact data from other LDEF micrometeoroid and debris experiments. There are undoubtedly more observations and conclusions remaining to be discovered from investigation of these impact data. However, in this paper we will limit our discussion to the details of the data collection procedures and the gross conclusions that are immediately apparent from these data.

OPTICAL SCANNING OF IDE DETECTORS

Flux data from low sensitivity IDE detectors that were active during the entire LDEF mission and were selected for optical counting of impact induced discharges were considered valid when the following criteria were met:

1) the detector suffered no significant down time based on interpretation of sensor status check data recorded during the first 346 days on orbit;

2) the detector's post-flight capacitance value was within 3% of the pre-flight value;

3) no impact craters without associated discharges were noted on the detector in the 125x optical scan.

Hypervelocity impacts that triggered an electrical discharge of the IDE capacitor-type detectors could be readily distinguished from impacts with sub-threshhold kinetic energy, and from impacts that occurred on an inactive detector, by the fact that the discharge energy vaporizes the thin aluminum top layer on the detector in an ~50 μm diameter zone around the impact site. The underlying SiO_2 layer is shockingly pink and is therefore easily identifiable under optical examination. An optical scan at 125x was undertaken to count the on-orbit impact-induced discharges on those sensors that are known to have remained active during the entire 5.77-yr LDEF mission (i.e., met the 3 criteria listed above).

A post-flight photographic catalogue of the entire set of flight detectors has been made with the same optical setup used in 1983 for a pre-flight catalogue. (Both catalogues will eventually be deposited in the LDEF Program data archive.) Comparison of the pre- and post-flight images while conducting optical microscopic examination of detectors permitted segregation of fabrication flaws and pre-flight discharges (caused during ground testing) from orbital impact-induced discharges. Contamination or defect caused discharges, also called "spurious" discharges, that occurred on orbit were identified by the presence of the associated contaminant or defect site in the pre-flight photo. These discharges often have unusual morphologies as well. Thus far, there appears to be an average of <1 of these spurious discharges per detector.

Optical scanning of at least a representative sample of the active IDE detectors from each LDEF location is complete. Each of the detectors has ~20 cm^2 of active surface area. The results discussed below are based on optical scans of 29 detectors from the West (trailing, row 3) side of LDEF, 18 detectors from the Earth (down) end, 8 detectors from the Space (up) end, and three detectors each from East (leading, row 9), North (row 12), and South (row 6) sides of LDEF. The first three locations (West, Earth and Space) experienced low impact activity, with an average of 10-20 impacts per detector. The latter three locations (East, North and South) experienced high impact activity, with an average of 130-310 impacts per detector.

DISCUSSION

Calculated impact flux values for IDE surfaces are listed in Table 1 along with flux values reported by two other LDEF experiment teams for indicated impact feature sizes, LDEF locations, and orbital time periods. The additional data are from the Micro Abrasion Package (MAP), experiment AO023 reported by

McDonnell and Stevenson (ref. 9), and from the FRECOPA experiments AO138-1 and AO138-2 reported by Mandeville and Borg (ref. 10,ftn4). Interested readers are referred to ref. 4 for details on the counting statistics and surface areas used to derive the flux values.

Table 1. Selected cumulative microparticle impact fluxes observed on LDEF surfaces. IDE data is for impacts that would produce craters in aluminum ≥~3 μm in dia. FRECOPA data are for impacts into Al foils or plates with indicated crater sizes counted in SEM scans. MAP data are optical transmission counts of penetrations in thin foils with indicated equivalent crater sizes. Values in [ ] are subject to confirmation. Error estimates, s, are calculated from Poisson statistics, $s = (n^{-1/2})(f)$ where n is the number of impacts in the data set and f is the flux.

Cumulative LDEF impact flux values for indicated equiv. crater diameters in aluminum (x 10^{-4} $m^{-2}s^{-1}$)

LDEF location	time res. IDE (≥3 μm) days 1-346	foil FRECOPA (≥2 μm) days 10-280	inte-grated IDE (≥3 μm) days 347-2106	inte-grated IDE (≥3 μm)	plate FRECOPA (≥3 μm)	2.0 μm foil MAP (≥3 μm)	3.1 μm foil MAP (≥4 μm)	3.7 μm foil MAP (≥5 μm)	4.8 μm foil MAP (≥7 μm)
				{----------days 1-2106, (5.77 years)----------}					
North (row 12)	6.1 ±0.18		3.5 ±0.20	3.9 ±0.17		[3.7] [±0.19]		[1.5] [±0.087]	1.3 ±0.060
South (row 6)	6.6 ±0.19		3.2 ±0.19	3.8 ±0.19		[6.0] [±0.18]	[2.2] [±0.15]	[1.9] [±0.14]	1.5 ±0.063
East leading (row 9)	8.5 ±0.22		8.7 ±0.31	8.7 ±0.28					2.3 ±0.22
West trailing (row 3)	0.99 ±0.073	0.86 ±0.38	0.12 ±0.013	0.26 ±0.016	0.22 ±0.11		[0.23] [±0.049]	[0.062] [±0.025]	0.070 ±0.014
Space (up)	1.1 ±0.090		0.48 ±0.039	0.59 ±0.045					0.34 ±0.024
Earth (down)	0.16 ±0.030		0.30 ±0.023	0.28 ±0.022					

The MAP data listed in Table 1 are based on optical transmission scanning of recovered foils. In this technique, the opaque Al foils are back lighted and all points that transmit light are counted. The method is subject to positive bias from secondary impacts and newly formed pinholes (since post flight background counts were made) that are not the result of orbital impacts. At the time of this writing, the MAP impact counts on foils <4.8 μm thick (equiv. to craters in Al with diameters <~7 μm) are considered preliminary and subject to verification by high magnification microscopic examination of significant areas of the foils. The MAP sensitivities listed in Table 1 in terms of crater diameter in Al were supplied by the experiment team after extensive calibration tests (see ref. 9).

The MAP experiment is particularly useful in supplying the IDE with an on-orbit empirical calibration since the impact fluxes are based on penetration damage to thin Al foils. While the IDE detector substrates are composed of SiO_2, the shock-induced impact damage mechanism responsible for triggering the detectors at their minimum threshold is the same mechanism that is responsible for marginal penetration of the MAP Al foils. It should be noted that orbital debris and natural micrometeoroids are expected to

have vastly different encounter velocities on LDEF surfaces. In general, orbital debris particles strike satellite surfaces at much lower velocities than micrometeoroids. This means that for a given mass impactor, more damage will result from natural particles than from manmade debris particles. This results in enhanced detection of natural micrometeoroids versus equal mass manmade debris particles for experiments that depend on impact damage for counting rates, such as IDE and MAP (see ref. 11 for a detailed discussion of this subject). However, both experiments should accurately predict the level and flux of impact-induced damage to spacecraft surfaces by all microparticles in the LEO environment.

FRECOPA data presented in Table 1 were derived from high magnification SEM scans of Al foils and ultrasmooth plates and are not subject to bias at the indicated crater sizes. These values are based on careful counts but are somewhat limited by low counting statistics. As more area is scanned by this research team, the FRECOPA integrated flux numbers may change slightly.

It should also be noted that shielding effects were not considered in this first-order comparison of measured impact fluxes. Shielding can introduce negative bias in perceived impact fluxes due to geometric constraints, but these effects are expected to be minimal for the particular LDEF surfaces under discussion. (The MAP foils are recessed ~10 cm below the tray lips, the IDE detector surfaces were recessed 0.3 cm, and the FRECOPA targets were recessed 0 to ~5 cm.) In general, the more a surface is recessed below the surrounding spacecraft structure, the greater is the degree of shielding from impacts, and the greater is the potential for secondary impacts from material ejected out of impacts in the surrounding structures. Some secondary debris sprays from impacts into IDE Al frames (especially on the space end tray) were noted in optical scanning. While the splatters of melted Al ejected from theses frame impacts did not cause the IDE detectors to discharge in any instance, this same material could puncture the thin foils used in the MAP experiment. It is anticipated that the MAP and FRECOPA teams will report on the effects of shielding and secondary impacts on their respective experiments in the future.

Consistency Among LDEF Experiments

Figure 1 depicts in bar graph format the impact flux data presented in Table 1. The IDE data are segregated into three distinct time periods, one corresponding to the electronically timed impacts recorded on magnetic tape for the first 346 days in orbit, a second corresponding to the visually scanned impact results which refer to the entire 5.77 year orbital mission, and a third time period corresponding to the difference between the first two time periods. These are compared to the Canterbury MAP experiment, which had no time resolution and can only be presented as 5.77-yr averages, and to the French FRECOPA experiment. The latter had two experiment modes, a 5 μm foil mounted in a drawer which was exposed for 0.74 years, starting a few days after LDEF deployment, and a smooth aluminum plate which was exposed for the full 5.77 year mission. These experiments are ideally suited for such a comparison.

Overall, the data show that the low sensitivity IDE detectors responded to impacts that would produce ~3 μm diameter craters in aluminum. Scaling from this result indicates that the high sensitivity detectors were sensitive to impacts that would produce ~1.2 μm diameter craters in Al. These results are consistent with the pre-flight calibration tests by Kassel (ref. 2). The major conclusion from this is that the IDE detectors did, in fact, work as expected, and an on-orbit empirical calibration can be derived from impact damage assessment on adjacent LDEF surfaces.

The most important aspect of Figure 1 is that the IDE 5.77-yr average flux data are consistent with flux data from both of the other experiments on all locations (with one exception). It is particularly gratifying that the results of the *only* other dust experiment which gave data specifically for the first year on LDEF's West panel (FRECOPA) are also consistent with IDE. These are important points since they indicate that **the overall flux rates measured by the IDE matched those measured by other LDEF experiments.** With this knowledge, the temporal history of the flux measured by IDE can be assumed to be accurate with high confidence.

The highly variable microparticle impact flux on the West , or trailing edge (row 3) of LDEF observed by IDE is confirmed by the 0.74 year and 5.77 year FRECOPA data. IDE and FRECOPA recorded first year microparticle impact fluxes (for craters in Al that are 2-3 μm in diameter and larger) on the West side of 0.99 and 0.86 x 10^{-4} $m^{-2}s^{-1}$, respectively, and 5.77 year (full mission) fluxes of 0.26 and 0.22 x 10^{-4} $m^{-2}s^{-1}$, respectively. (The MAP experiment also showed a full mission integrated flux of 0.23 x 10^{-4} $m^{-2}s^{-1}$ for craters in Al $\geq$~4μm.) The calculated flux for the time period after the IDE recording tape ran out (days 347-2106) is 0.12 x 10^{-4} $m^{-2}s^{-1}$, or a factor of 8.3 times lower than the first year flux. The consequences of this high variability are discussed further in the next section.

The one point of apparent inconsistency among the IDE, MAP and FRECOPA data occurs on the South side (row 6). The MAP data for penetrations in a 2.0 μm thick Al foil (equivalent to craters ≥~3 μm in dia.) yield a 5.77-year integrated flux of 6.0 x 10^{-4} $m^{-2}s^{-1}$, which is 1.6 times higher than the IDE 5.77-year integrated flux of 3.8 x 10^{-4} $m^{-2}s^{-1}$ on the South side. Penetration counts in a slightly thicker (3.1 μm) MAP foil (equiv. to craters ≥~4 μm in dia) yield an integrated flux of 2.2 x 10^{-4} $m^{-2}s^{-1}$. Additionally, 4.8 μm thick MAP foils mounted on both the South and North (row 12) sides of LDEF yield verified integrated fluxes of 1.5 and 1.3 x 10^{-4} $m^{-2}s^{-1}$, respectively. Also, the North side MAP and IDE data showed fluxes of 3.7 and 3.9 x 10^{-4} $m^{-2}s^{-1}$, respectively. Thus, it appears that the penetration counts in the thinnest MAP foil mounted on the South side are positively biased by secondary impacts or by non-impact induced penetrations or ruptures.

This apparent positive bias to one point of the South side MAP data is also supported by the self-consistency of the IDE data, which showed similar fluxes for all long-term time periods on the North and South sides, as would be expected by their near equivalent positions on LDEF. Thus far there is no indication that the IDE data were negatively biased due to loss of detector sensitivity (as described in the previous section), and McDonnell and Stevenson have been careful to point out the possibility of positive bias in the thinnest MAP foils (ref. 9). Therefore, at this time we must assume that it is the MAP data that is biased. However, this issue can be readdressed after the MAP team has examined the suspect foil microscopically.

Evidence for Temporal Structure at All Finite Averaging Times

Figure 1 puts into striking relief the fact of extreme temporal variation in the orbital debris environment over long time periods. This is the first evidence that this variability exists at all averaging intervals. We have already shown (see refs. 6 and 7; ft. notes 2 and 3) important variation from minute to minute and from week to week. This is further illustrated in Figures 2a and 2b where the East and West fluxes and East/West flux ratios for the high and low sensitivity IDE detectors are shown as a function of time. The points plotted are the result of a 5-day running average smoothing function.

Figure 1 shows the same effect from year to year for the low sensitivity IDE detectors. East has comparable values for 0.95 yr and 5.77 yr, while North, South, and Space show an excess factor of 1.6 to 1.9 for the first year, whereas Earth shows a deficit factor of 1.9 for the first year. The first year on West shows 3.7 times the flux of the full mission. These values can be compared to the IDE flux values calculated for days 347-2106 and listed in Table 1.

Although there is no microparticle impact flux reported to date that can be directly compared to the IDE data from the East, or leading, edge of LDEF (row 9), the IDE data show that there was essentially no long-term change in the measured fluxes on this location (see Table 1 and Fig. 1). The MAP team reported an East/West ratio (leading/trailing) of 33 for somewhat larger impacts (equivalent to ≥~7 μm diameter craters in Al) for the entire mission. The IDE low sensitivity detectors also measured an East/West ratio of 33 for the same time period for impacts that would form craters in Al ≥~3 μm.

Although these ratios are consistent, the East/West microparticle impact flux ratios measured by the same IDE detectors during days 1-346, and days 347-2106 are 8.5 and 73, respectively.

The extreme range for the long-term integrated flux ratio measured by the IDE low sensitivity detectors is due entirely to the variability in impact flux on the trailing edge of LDEF (Fig. 1), whereas the short term variability in the ratio is due to activity on both sides, as shown in Fig. 2. The relative activity levels on the IDE detectors can provide information on the mass distribution of microparticles, and the variabilities of the short-term impact flux ratios among the various sides of LDEF can yield important information on the characteristics of orbital debris clouds and natural dust sources. **However, for theoretical and practical applications, the extreme variability of long-term East/West microparticle impact flux ratios must be taken into account.** For some applications, it may be more appropriate to use impact flux values, and respective ratios, for the 4.82 year period represented by LDEF orbital days 347-2106. These values represent the modal ratio (that was prevalent during ~85% of the LDEF mission), whereas the 5.77 year integrated values represent the mean ratio for the entire mission. We are continuing our investigation of these observed variabilities of impact flux ratios.

In an effort to understand the high variability of impact flux recorded by the IDE detectors on the trailing edge (West), we have investigated the effect of spurious discharge activity. As described above, this activity is most notable just after IDE activation. We have looked at this question in several ways. Such discharges can occur, as described above, but in large measure only within the first few hours after activation -- much less than a day. From optical scans of all West panel low sensitivity IDE detectors we found an average of <1 contaminant- or defect-caused inflight spurious discharge per sensor on this panel. If all of these discharges had occurred during the first year, the total number of recorded impacts would have to be adjusted from 186 to 156, for an average first-year East/West flux ratio of 9.7. Even this does not account for the large variation in ratios.

We also looked at whether the East/West ratio is "front-loaded" by high activity associated with the deployment and activation of the IDE. Figure 2b shows that 5-day means of the ratio vary by two orders of magnitude about the mean value of 8.5 for essentially the entire year. These data, and additional data in preparation, are a striking reminder of the variability and episodic nature of microparticle impacts in low Earth orbit.

The Earth Side Mystery

One of the more puzzling aspects of the IDE data comes from the LDEF side that was originally considered the least interesting -- the Earth end. We remind the reader that, since this face was only 0.07 Earth radii from the surface, it was expected on kinematic grounds to be largely shielded from both natural and artificial particles (ref. 1). In reality, the 5.77-year flux on the Earth end was comparable to that on West, which itself was higher than expected. Here also, as on several other faces, there was a significant difference between the first-year flux and the full-mission flux. The long-term microparticle impact flux was roughly double the first-year flux. In addition, the optical survey gives no evidence of large particles and no evidence of highly-oblique impacts.

Could the averages be skewed by a single event after day 346? We cannot answer this question directly, but there are some intriguing coincidences. For example, in a 1986 SDI-sponsored test a Delta rocket vehicle launched its third stage into such an orbit as to collide with its own second stage at 3 km/s (ref. 12). The collision was at about 200 km altitude. The resulting debris cloud is known to have had a large outward component, and the recent ground-based Oscar-22 disruption test suggests strongly that that cloud had a very high number density of micron-sized particles (ft. note 5). An ASAT weapon test on September 13, 1985 resulted in a 7 km/s collision between the weapon and an 850 kg P78-1 satellite at about 500 km altitude, the same altitude as LDEF (ref. 12). We repeat: we can draw no conclusions from the information now available to us. Had the IDE magnetic tape been longer, or had there been downlink telemetry on LDEF-1, explicit answers could be given to the questions raised by the Earth side IDE panel.

SUMMARY

The Interplanetary Dust Experiment continues to yield new discoveries about the microparticle population in low Earth orbit. The latest findings indicate that the long term (multi-year) average microparticle impact fluxes on all sides of LDEF, except East (ram) varied widely during the mission. Measured long-term microparticle impact fluxes on the North, South, West, Space and Earth sides of LDEF during the first year were 0.5 to 3.7 times the 5.77 year fluxes. We have presented the comparisons and contrasts among the IDE optical survey impact data, the IDE first-year timed impact data, and impact data from other LDEF micrometeoroid and debris experiments.

The following observations were reported.

1) The 5.77 year long-term integrated microparticle impact fluxes recorded by IDE detectors matched the integrated impact fluxes measured by other LDEF investigators for the same period.

2) IDE integrated microparticle impact fluxes varied by factors from 0.5 to 8.3 for LDEF days 1-346, 347-2106 and 1-2106 (5.77 years) on rows 3 (trailing edge, or West), 6 (South side), 12 (North side), and the Earth and Space ends.

3) IDE integrated microparticle impact fluxes varied less than 3% for LDEF days 1-346, 347-2106 and 1-2106 (5.77 years) on row 9 (leading edge, or East).

These results give further evidence of the accuracy and internal consistency of the recorded IDE impact data. This leads to the further conclusion that the utility of long-term flux ratios for impacts on various sides of a stabilized satellite in low Earth orbit (LEO) is extremely limited. These observations, and their consequences, highlight the need for continuous, real time monitoring of the dynamic microparticle environment in LEO.

ACKNOWLEDGEMENTS

The authors wish to thank all of the members of the LDEF IDE experiment team, and the NASA/Langley LDEF Project and Science offices for their support throughout the duration of this 10 year long effort. We also wish to thank the members of the M&D SIG Microcrater Committee (A. McDonnell, J.C. Mandeville, M. Mirtich and R. Walker) for their timely transfer of data pertinent to this study. This work is supported under NASA grant NAG 1-1218.

REFERENCES

1. S.F. Singer, J.E. Stanley, P.C. Kassel, W.H. Kinard, J.J. Wortman, J.L. Weinberg, J.D. Mulholland, G. Eichorn, W.J. Cooke and N.L. Montague, "First Spatio-Temporal Results from the LDEF Interplanetary Dust Experiment", *Adv. Space Res.*, Vol. 11, No. 12, pp. 115-122 (1991).

2. P.C. Kassel, "Characteristics of Capacitor-Type Micrometeoroid Flux Detectors When Impacted With Simulated Micrometeoroids", *NASA TN D-7359* (1973).

3. E. Friebele, "Plasma: LDEF Adds to the Equation", LDEF Spacecraft Environmental Effects Newsletter, Vol. III, No. 4 , pp.11-13 (1992).

4. M. Zolensky,H. Zook, F. Horz, D. Atkinson, C. Coombs, A. Watts, C. Dardano, T. See, C. Simon and W. Kinard, "Interim Report of the LDEF Meteoroid and Debris Special Investigation Group", NASA CP- 3194, (1993).

5. L.David, "Satellite Dust Experiment Produces Surprising Results", Space News, Feb. 24-Mar. 1, p. 15 (1992).

6. J.D. Mulholland, S.F. Singer, J.L. Weinberg, J.P. Oliver, W.J. Cooke, N.L. Montague, J.J. Wortman, P.C. Kassel, and W.H. Kinard, J.E. Stanley, in *NASA CP-3134,* pp 517-527 (1991).

7. J.P. Oliver, J.D. Mulholland, S.F. Singer, W.J. Cooke, N.L. Montague, J.L. Weinberg, P.C. Kassel and J.J. Wortman, "Results from the Interplanetary Dust Experiment:", *Bull. AAS,* Vol 23, p. 940 (abstract), presented at the 178th AAS Meeting, Seattle, WA, May, (1991).

8. D. Kessler, "Origins of Orbital Debris Impacts on Long Duration Exposure Facility (LDEF) Trailing Surfaces", NASA CP-3194 (1993).

9. J.A.M. McDonnell. and T.J. Stevenson, "Hypervelocity Impact Microfoil Perforations in the LEO Space Environment (LDEF MAP AO023 Experiment)", *NASA CP 3134*, pp. 443-4357, (1991).

10. J.C. Mandeville and J. Borg, "Study of Cosmic Dust Particles On Board LDEF: The Frecopa Experiments AO138-1 and AO138-2", in *NASA CP 3134,* pp. 529-548, (1991).

11. R.P. Bernhard, T.H. See and F. Horz, "Projectile Compositions and Modal Frequencies on the 'Chemistry of Micrometeoroids' LDEF Experiment", *NASA CP-3194* (1993).

12. V.A. Chobotov and D.B.Spencer, "A Review of Orbital Debris Modelling at The Aerospace Corporation", *AIAA Conference Paper* 90-1356, American Institute of Aeronautics and Astronautics, Washington D.C. (1990).

FOOTNOTES

1. W.J. Cooke, J.D. Mulholland, J.P. Oliver, P.C. Kassel, "Calibration of the IDE Clock and Determination of LDEF Attitude Using Sun Sensors", (in preparation for submission to *JSR*, 1992).

2. J.D. Mulholland, S.F. Singer, J.P. Oliver, J.L. Weinberg, W.J. Cooke, P.C. Kassel, J.J. Wortman, N.L. Montague and W.H. Kinard, "LDEF Interplanetary Dust Experiment: A High Time-Resoluton Snapshot of the Near-Earth Particulate Environment", in Proceedings *Hypervelocity Impacts in Space*, U Kent Canterbury, in press (1992).

3. J.P. Oliver, J.D. Mulholland, S.F. Singer, C.G. Simon, J.L. Weinberg, W.J. Cooke, P.C. Kassel, J. J. Wortman, N. L. Montague and W. H. Kinard, "Estimation of Debris Cloud Temporal Characteristics and Orbital Elements", presented at the 29th meeting of COSPAR, in press (1992).

4. Mandeville, J.C. *personal communications*, April/May (1992).

5. W. Tedeschi and D. McKnight, "Implications of Satellite Impact Test Data to Debris Environment Estimates", presented at the 29th meeting of COSPAR, in press (1992).

THE INTERSTELLAR GAS EXPERIMENT: ANALYSIS IN PROGRESS

F. Bühler[1], D.L. Lind[2], J. Geiss[1], and O. Eugster[1]

[1] Physikalisches Institut, Universität Bern, Switzerland
[2] Utah State University, Logan UT

SUMMARY

The interstellar gas experiment (IGE) exposed thin metallic foils aboard the LDEF spacecraft in low earth orbit in order to collect neutral interstellar particles which penetrate the solar system due to their motion relative to the sun. By mechanical penetration these atoms were imbedded in the collecting foils along with precipitating magnetospheric ions and, possibly, with ambient atmospheric atoms. During the entire LDEF mission, seven of these foils collected particles arriving from seven different directions as seen from the spacecraft. After the foils were returned to earth, a mass spectrometric analysis of the noble gas component of the trapped particles was begun. The isotopes of ^{3}He, ^{4}He, ^{20}Ne and ^{22}Ne have been detected. We have given a first account of the experiment in ref. 1.

In order to infer the isotopic ratios in the interstellar medium from the concentrations found in the foils, several lines of investigation had to be initiated. The flux of ambient atmospheric noble gas atoms moving toward the foils due to the orbital motion of LDEF was estimated by detailed calculations. Any of these particles which evaded the baffles in the IGE collector could be entrapped in the foils as a background flux. However, the calculations have shown that this flux is negligible, which was the intent of the experiment hardware design. This conclusion is supported by the measurements.

However, both the concentration of trapped helium and its impact energy indicate that the flux of magnetospheric ions which was captured was larger than had been expected. In fact, it appears that the magnetospheric particles constitute the largest fraction of the particles in the foils. Since little is known about this particle flux, their presence in the IGE foils appears fortunate. The analysis of these particles provides information about their isotopic composition and average flux.

Foil and machine backgrounds for the four measured isotopes had to be assessed individually. While this was easy for ^{4}He, spurious foil background of ^{3}He had to be monitored carefully by systematically analyzing unflown foil pieces. Concentrations of trapped neon are not far above background even for the larger pieces.

During the flight, the foil trays did not sequentially expose several foils as designed, because of a stuck electrical relay. Therefore, we could not use the seasonal variation of the angular distribution of the incoming interstellar atoms to distinguish them from the magnetospheric component of the trapped particles. However,

the interstellar helium impacts the foils at much lower energies than most of the magnetospheric helium. Thus we could use the method of stepwise heating to extract from the foils the interstellar component at lower temperatures than are used to release the bulk of the magnetospheric component. However, the high voltage for the shielding grids was not commanded to switch on; thus, separation of the two sources was more difficult because the energies of magnetospheric ions and interstellar atoms overlapped.

The analysis of entrapped gases in the IGE foils is still proceeding. Thus far, we have concluded that we are able to give a reliable figure for the $^4He/^3He$ ratio of the more energetic magnetospheric component of the trapped flux.

INTRODUCTION

The isotopic composition of the present-day interstellar gas of our galaxy is not well known. Spectroscopic methods are limited, practically, to determinations of elemental frequencies. Space-borne mass spectrometers of the AMPTE and Ulysses missions did observe interstellar $^4He^+$ ionized near the Sun and carried away with the solar wind, but they are not sufficiently sensitive for $^3He^+$, and they are not detecting neutral species. Our knowledge of the local interstellar neutrals is derived mainly from systematic observation of the scattering, by ^4He atoms, of the Sun's He I 58.4-nm resonance line (refs. 2, 3, 4).

Isotopic abundances of helium and neon in the interstellar gas are highly significant: both elements, being noble gases, are completely contained in the gas phase. Isotopic ratios do not suffer from fractionation, nor does any gas chemistry alter them. The isotopes of helium were produced in the Big Bang. Fusion in stars has produced ^3He ever since. Whenever stars explode, they enrich the interstellar gas by ^3He. The $^3He/^4He$ ratio of the presolar material is known from meteoritic and solar wind data. Today, we expect a higher $^3He/^4He$ ratio in the interstellar medium than when the Sun formed 4.6 billion years ago.

The differences in the $^{20}Ne/^{22}Ne$ ratios found in different sources (meteorites, solar flares, solar wind, cosmic rays) are as yet unexplained. A known ratio in the interstellar medium would serve as a baseline datum.

Finally, a direct measurement of the interstellar ^3He influx into the atmosphere would shed light on the old problem of the mass balance of ^3He in the atmosphere. One other important source of the atmospheric ^3He is the precipitation from the magnetosphere of solar wind ^3He that previously penetrated through the magnetopause.

In-situ collection of neutral atoms from the local interstellar medium opens a new source of material from outside the solar system. Sufficient concentrations of trapped noble gases are building up

during few months in the metal foils to allow mass-spectrometric measurement of ^{3}He, ^{4}He, ^{20}Ne, and ^{22}Ne in returned foil samples.

The technique of using foils to entrap particles for later laboratory mass spectrometric analysis was first developed for the Apollo missions to the moon by the Bern group. In this application, noble gas isotopes were measured in the solar wind (refs. 5, 6). Later, on the Skylab missions, this technique was used to analyze the isotopes of precipitating magnetospheric particles (ref. 7). This same procedure has been utilized on a sounding rocket to investigate auroral particles (refs. 8, 9). Although it is a relatively new experimental technique, considerable experience has been accumulated in this method of collecting samples of extraterrestrial particles.

For the interstellar gas experiment, the collecting foils consisted of 15 μm thick beryllium-copper (2% Be by weight). On the surface of these foils a thin Be oxide layer was formed in a procedure especially adapted for large foils. The foils were positioned at the bottom of seven rectangular IGE collectors (shown in Figure 1) which were mounted on four trays at different LDEF locations. The open end of each box-like collector established the field of view from which particles could reach the foils. The center line of the collector, standing orthogonally on the center of the foil, defined the orientation of the field of view relative to LDEF and, ultimately, to the celestial sphere.

Each collector contained six foils mounted on separate plates. It was planned to expose the foils to the particle flux in sequence for periods of roughly two months. The varying concentrations in the sequence of foils should reflect the seasonal variation of the flux of the interstellar neutrals in the vicinity of the sun. However, because of a stuck relay in the initiation circuit, the foil trays were not repositioned as intended. Thus the entire particle flux was directed to a single foil in each collector for the entire 69 months of the LDEF mission. During each orbit of LDEF, the center line of any collector was scanning along a parallel of latitude of the celestial sphere. Particles coming into its sweeping field of view were trapped by the exposed foil.

One axis of LDEF pointed radially outward from the earth and one axis pointed forward along the velocity vector. The collectors were oriented so as to optimize the collection of interstellar particles and to reduce the collection of particles from other sources. They were positioned roughly perpendicular to the direction of orbital motion. This was because the LDEF velocity would have been sufficient to ram ambient atmospheric atoms into the foils as a background flux, if they could reach the foils. The orientation of the collectors prevented that. In addition, a series of knife-edge baffles near the opening of the collectors, and serrations along the inner walls of the collectors prevented atmospheric particles from striking the walls and from reaching the foils in a single bounce. The view directions of the five collectors oriented orthogonal to the velocity vector were designated by the angle which their center line makes with the LDEF radial vector, i.e., 24°N, 24°S, 70°N, 70°S, and 110°N. The 110°N

collector looked 20° below the horizon with the intention of measuring only background particles. In the event that, after deployment, LDEF had stabilized with the space and earth-pointing ends reversed, it could have performed a minimal experiment by itself. The center lines of the two remaining collectors, designated "0° forward" and "0° backward", lay in the orbital plane and were tilted 24° forward or backward of the radial vector. The collector tipped forward into the flux of ambient atmospheric particles was to check the effectiveness of the system of baffles described above. The one tipped backward was shielded further from this possible atmospheric particle flux. Fig. 1 in reference 1 shows the fields of view for the seven foil cassettes.

A model calculation, starting from a set of fairly well known parameters for the interstellar ^{4}He far from the Sun, predicts different concentrations in each IGE foil. These parameters are (ref. 1): velocity 24 km/s, temperature 12'000 K, density 0.0124/cm^3, right ascension 252°, declination -17.5°, ionization rate at 1 a.u. $1/1.5 \cdot 10^7$s. As the neutral interstellar particles enter the heliosphere and approach the sun, their velocity distribution is significantly altered by the gravitational focussing of the sun. Thus, during the spring and summer months when the earth is in the upwind portion of interstellar flux, the angular distribution of interstellar particles approaching the earth, and hence approaching LDEF and the IGE foils, is radically different from the angular distribution observed in the wintertime (see details in ref. 1, figure 3).

The seasonal rate of particle entrapment is complicated further as the trapping efficiency changes by more than an order of magnitude as the earth moves upstream, then across the stream, and finally downstream in the interstellar particle flow. As the earth moves upstream, the orbital velocity of the earth adds to the on-coming interstellar particle velocity, increasing the impact velocities of the particles as they strike the foil, thus increasing the trapping probability (ref. 10). The opposite, reduction in trapping probability, occurs on the downstream side of the orbit as the earth moves away from the overtaking interstellar particles. A full calculation was performed (ref. 1) to determine how many helium atoms were entrapped in each foil as each collector swept a precessing path across this seasonally changing angular distribution on the celestial sphere, with the seasonally varying trapping probability, for the length of the entire LDEF mission. The result is shown in Figure 2. The model, of course, predicts equal concentrations of particles in both 0° collectors, and no particles being captured in the +110° collector (not shown). For a collector which points in a direction where, throughout the entire earth orbit, particles arrive predominantly from an off-axis part of this particular field of view, a collector wall partially shadows one side of the foil and there is a pronounced north-south gradient in the predicted interstellar particle concentration across the foil. It is remarkable that even though the IGE foils contain the particles accumulated in almost six years, it is expected that a characteristic pattern of concentrations is still recognizable.

PARTICLE SOURCES

As we analyze the recovered IGE foils in a mass spectrometer, we would expect to find noble gas atoms from several different sources.

1. The interstellar atoms which originate in the local interstellar medium and travel as neutrals into the inner solar system should be distributed among the various foils as we have outlined above. It is a goal of IGE to infer, from the measurements of the particle concentration in the foils, the helium and neon isotopic ratios in the local interstellar medium.

2. Magnetospheric ions which come from the trapped particle region around the earth and precipitate at low latitudes down to the LDEF altitude should also appear in the IGE foils. We assume that these particles reach the lower altitudes through a double charge-exchange process. They are originally geomagnetically trapped in the ring current as ions. Then they loose their charge by charge exchange and escape to lower altitudes. As neutrals they can cross the earth's magnetic field lines. The flux of these particles would be insignificant if a fraction of them did not undergo a second charge exchange, regaining their charge, and again become trapped by the geomagnetic field at the LDEF orbital altitude. To accumulate a significant flux at this low altitude, they must remain trapped for a relatively long time. Ions with a low pitch-angle are quickly lost; therefore, large pitch-angles are expected to dominate. The gyroradius (in the order of 1 km) is small compared to a reasonable scale height for these magneto-spheric particles. We expect a rather isotropic distribution in the east/west - up/down plane and a marked decrease in the north/south direction. Relatively little is known about the flux and composi-tion of magnetospheric precipitation at these low latitudes, so another goal of IGE is to attempt to separate and analyze this particle component trapped in the foils.

3. Neutral ambient atmospheric atoms do not appear to give a significant contribution to the entrapped foil particles. As indicated earlier, the sidewalls of the IGE collectors and the baffling system eliminate the vast majority of these potential background particles. The measurements support this conclusion.

4. He and Ne either already present in the untreated metal foils or introduced as contamination during foil preparation constitute foil background and must be accounted for in our data analysis. This is accomplished by analyzing portions of prepared foil material which was not flown on IGE.

5. Similarly, the He and Ne background of the gas extraction system and of the mass spectrometer has to be subtracted.

SEPARATION OF PARTICLE SOURCES

The flux of interstellar particles integrated over the extended LDEF mission should show the characteristic pattern indicated in Figure 2. This is one characteristic which we can use to separate these particles from the other significant foil particle component - the magnetospheric ions. However, there is a second characteristic which should also be useful in separating these two major particle sources. That is the impact energy of the arriving particles. As previously mentioned, the energy of the interstellar particles varies according to the position of the earth in its orbit. In the spring time this energy reaches almost 120 eV for ^{4}He. By summer it drops to about 70 eV and in the fall it drops to around 10 eV. In contrast, most of the magnetospheric particles have higher energies, up to 50 keV. This difference in energy has the consequence that the magnetospheric particles are much more firmly imbedded in the collecting foils. By using the technique of stepwise heating, we can extract most of the interstellar atoms at lower temperatures than are used to liberate the more tightly bound magnetospheric particles. Calibrations on pretreated foils (ref. 11) showed how two particle populations with significantly different impact energies are released from foils in a series of different heating steps. The squares and fine curves in Figures 3 and 4, starting at a temperature of 210°C, show the integrated fraction of gas released in the calibrations.

MASS-SPECTROMETRIC ANALYSIS

Concentrations of the helium and neon isotopes were measured in 20 rectangular pieces cut from the seven foils which had been exposed in space. Each foil piece is identified by a label (first column in the tables). Its history including formation process, location during exposure, and analysis can be traced throughout the documentation by means of this label. Its position on the backing plate during exposure was mapped. The coordinates of its four corners were determined taking as a reference the coordinate system defined during the survey for impacts by the M&D SIG inspectors (ref. 12). After cutting, the pieces were weighed (absolute error < 0.1 mg) and their length and width measured to ± 0.2 mm. The area was calculated by using the calibration factor between foil mass and area of 12.0 mg/cm^2 (±3%). The result was checked for gross errors by comparison with the area calculated from length and width. Because the calibration error was small and constant for all pieces, it was not included in the errors given in the tables.

After weighing, the foil pieces were rinsed with clean ethanole, then rolled and filled into a cup made of 15 µm thick Al foil. The cup made it possible to handle the CuBe foil pieces and to insert them into the noble gas extraction system of the mass spectrometer. The small amount (33 mg) of Al foil did not contain measurable quantities of neon or helium. However, when pieces of unexposed foil are analyzed, the neon background is perceptively higher than when the extraction procedure is run without foils. The difference, called "foil blank" here, is not proportional to the area. Therefore, care was taken to make the unexposed foil pieces of comparable size with

the exposed ones. A total of 17 unexposed pieces with a total area of 310 cm^2 was analyzed, compared to the 20 exposed pieces analyzed which had a total area of 550 cm^2. (The total exposed area is approximately 7 x 22 x 21 cm^2 or 3200 cm^2.)

Analysis was performed routinely in a mass spectrometer dedicated to helium and neon measurements. The spectrometer is connected directly to the extraction system. After considerable conditioning of the extraction line and doing frequent machine blank checks, samples were dropped into a molybdenum crucible and heated in steps by HF induction. The crucible reached a specified temperature (between 150 and 1800°C) after 10 to 20 minutes and was kept at this temperature for 12 minutes. After each step, released gases were cleaned from reactive components by titanium getters and active charcoal cooled with liquid nitrogen, then pumped into the mass spectrometer. Five spectra were sequentially measured by peak-jumping. The error of their average intensities was calculated from the variation of the individual mass peaks. Interferences and background were subtracted. Background and its reproducibility were carefully assessed, separately for each temperature step.

The "foil blank", estimated from measurements of unexposed foil pieces, was negligible for ^4He. For neon, however, it was of the same order of magnitude as the released amount of trapped gas, especially for the high-temperature steps. For a few unexposed foil pieces, the ^3He released in the 450°C and 600°C steps was of the same order of magnitude as for the exposed pieces. For the foils in the cassettes with almost vertical view directions (24°N to 24°S), the ^3He foil blank never amounted to more than 15 percent of the trapped ^3He, while for the cassettes with almost horizontal view directions (110°N, 70°N, and 70°S) the foil blank renders the $^3He/^4He$ ratio more unreliable, possibly up to ±50%. The uncertainty of the blank estimates is reflected in the errors given.

RESULTS

The results are presented in Tables 1 and 2. In order to get a first estimate of the concentrations, five small pieces (4 to 10 cm^2), one each for the view directions 110°N (view below the horizon), 70°N, 24°N, 24°S, and 70°S, were heated to 1400°C for total extraction. These measurements are marked [1] in Table 1. Obviously, even these small pieces allowed good helium measurements, while larger areas are needed for more precise neon measurements. Concentrations were higher by a factor of about three than expected from the model of Fig. 2. The average ratio of the concentrations for ^4He and ^3He was 7400. With the correction for different trapping probabilities for ^4He and ^3He (Fig. 2), this ratio would reflect a $^4He/^3He$ ratio in the flux of approximately 4500. Of course, no interstellar particles at all should have hit L249-2-1 which was exposed on the cassette pointing 20° below the horizon.

With these results, it seemed possible that a fraction of the ^4He could be atmospheric atoms that had hit the foil directly or after collisions with the inner walls of the collectors. Their energies

would be of the order of 30% of $^1/_2mv^2$ (m = atomic mass of ^{4}He, v = satellite orbital velocity), i.e., 0.4 eV. The trapping probability was never measured for atoms with such a low energy. On the other hand, only an extremely low fraction (approx. 1 ppm) of the flux n·v (n = atmospheric ^{4}He density at spacecraft altitude) hits the foils directly, and the baffles and serrations on the inner walls practically prevent any atom to hit the foil after only one collision.

We assumed that, if atmospheric ^{4}He atoms are trapped in the foils, heating to 150°C should at least release part of them, while calibration experiments done by Michel in the Bern laboratory (ref. 11) showed that only approximately 15 percent of 75 eV ^{4}He (the incidence energy of interstellar particles) were released at 210°C (see Fig. 3). Four pieces from the two collectors with 0° view angle were heated to 150°C, then to 450°C, finally to 1400°C, in order to check for the presence of trapped atmospheric atoms (see pieces marked with [2] in Tables 1 and 2). The fraction of ^{4}He released at 150°C was 3% of the amount released at 450°C for L290-2-1 on the 0° collector tilted backward. For L296-1-1 to -3 (on the 0° collectors tilted forward) which could be expected to see more incoming atmospherics, the fractions were between 1.2 and 2.2% only. At 150°C ^{3}He and the neon isotopes could not be detected on any of the pieces. Atmospheric particles, therefore, certainly contribute unimportant quantities to the 450°C releases as given in Table 2. This conclusion is strengthened by the arguments that the ratios ^{4}He/^{3}He found on the two 0° collectors are not different from each other (both are about 6000) while one would expect a higher ratio for the forward-looking ones (L296-1-..) as the atmospheric ^{4}He/^{3}He ratio is very high, approximately 100'000, at 300 km.

The atmospheric particles thus excluded from being responsible for the deviation of the measurements from the model calculations, we had to take into account a possible contribution of magnetospheric precipitation. As the magnetic field is approximately horizontal and south-north at low latitudes, we expect the 0° view collectors to see the highest fluxes of particles gyrating about these field lines, the 24°N and 24°S collectors slightly smaller fluxes, and the 110°N, 70°N, and 70°S much smaller fluxes because of the loss cone. The ^{4}He concentrations in Table 1 do show this tendency which is, unfortunately, similar to the signature of interstellar particles in Fig. 2. Finer models of the expected distribution have not been worked out yet. The magnetospheric particles are assumed to cover a wide energy spectrum, with a considerable part of the flux down to energies characteristic for interstellar particles. Note that the experiment was designed to protect the foils from the infall of ions with energies below 1 keV. One of the three grids in Fig. 1, at +1200 V relative to the spacecraft, should have rejected low-energy magnetospheric ions, while neutral interstellar particles (energies for ^{4}He below 140 eV, for ^{20}Ne below 700 eV) would not have been affected. Because, as mentioned above, a system relay malfunctioned, the grids never were connected to a high potential; thus, the spectra of the two particle populations were superposed. Still, we hoped that a difference between low-temperature and high-temperature releases could be seen in the isotopic ratios. We did not, however, do the fine-step release

from 210° to 450° of Michel's calibrations, because of the small amounts expected to be released in each step. Instead, we chose steps 450, 600 and 800°C in the hope to sufficiently separate low energies from high energies. An additional step at 1700°C made sure that the 1400°C step had extracted the trapped gases completely. The results of the stepwise extractions are given in Figures 3 and 4. For both ^{4}He and ^{20}Ne, the release patterns were very similar to each other for 7 pieces (the darker shaded region contains all their release curves) and only two pieces showed greater, irregular deviations (brighter region).

Losses by thermal diffusion are much more dependent on temperature than on time. Therefore, comparison with the calibration experiments indicates that a large part of the trapped particles impacted the foil with high (magnetospheric) energies, but that a considerable part of the 450°C release are interstellar particles which arrive with low energies. It could, however, be argued that the influence of the diffusion time can not be neglected, and that the comparison gives an impression of too high energies for the trapped particles in the exposed foils. Fine-resolution heating steps and more direct calibrations, including ^{3}He, will be necessary to resolve the question.

The stepwise heating method should not only give clues as to the energies with which particles have hit the foil. Its potential to separate low-energy from high-energy components also allows to determine, independently, isotopic and elemental ratios for low-energy and for high-energy populations. We have to take into account, however, that even if helium has hit the foils with the same energy as neon, it is released at lower temperatures, owing to its higher mobility. The effect can give the illusion of a difference in elemental ratios for low- and for high-energy components; thus, careful calibration is necessary. The effect gets worse if energies are proportional to mass, such as for interstellars which impact with equal velocities. Even for isotopic ratios, it may not be neglected.

From Table 2, the isotopic and elemental ratios can be calculated for the trapped gas components which are released at 450°C.

Their weighted averages are:

$$^{4}He/^{3}He = 6300\pm300$$
$$^{20}Ne/^{22}Ne = 14.4\pm1.4$$
$$^{4}He/^{20}Ne = 10'600\pm1'000$$

The errors (one sigma) of the averages are estimated from the variation of the 15 measurements. They are only little higher than expected from the errors given for the individual measurements of the isotopic ratios. They are three times as large, however, for $^{4}He/^{20}Ne$, reflecting a poorer reproducibility for the elemental ratio than for the isotopic ratios.

Isotopic and elemental ratios for trapped gases released in four temperature steps and for the total release (all steps summed) are in the following ranges for over half the number of the measured pieces:

Temperature	Pieces	$^4He/^3He$	$^{20}Ne/^{22}Ne$	$^4He/^{20}Ne$
450°C	15	5500-7300	11-22	7800-17000
600°C	11	5000-7500	13-56	7100-12000
800°C	11	6200-7500	14-18	2300-3600
1400°C	11	6300-10500	15-18	340-670
total	20	6000-7100	13.9-17.5	2300-4200

$^4He/^3He$ ratios do not differ from step to step. Actually, if we assume that most of the 450°C step is of interstellar and the bulk of the other steps of magnetospheric origin, the average ratio for the trapped magnetospheric helium, 6600, is not far from the ratio 6300 for the trapped interstellar particles.

$^{20}Ne/^{22}Ne$ is 14.4 for the 450°C step, 15.5 for the total release. Even though the range of measured ratios is large, these numbers are definitely above 9.8, the terrestrial ratio, and are also above 13.7, the value in the solar wind. If the magnetosphere is mainly supplied by atoms escaping from the atmosphere, a ratio higher by up to a factor of 2 than the terrestrial value may be expected, because the two neon isotopes have different scale heights in the exosphere, and the lighter isotope is enriched.

The $^4He/^{20}Ne$ ratio, finally, clearly shifts from high to low values with higher temperature. This trend merely reflects the fact that helium of any energy is released at lower temperatures than neon of the same energy (compare Fig. 3 with Fig. 4). The average $^4He/^{20}Ne$ ratio for the total release is 3000, and 10 out of the 20 pieces show ratios between 2300 and 4200. This is much higher than expected for interstellar particles, but may be explained for magnetospheric ions.

DISCUSSION

The results show that atmospheric contamination of the trapped helium and neon is negligible.

The bulk of the particles is magnetospheric, while an appreciable part of the 450°C release is probably of interstellar origin. If release curves from Michel's calibrations (ref. 11) are taken at face value, postulating complete independence of diffusion times, it may be that 30 percent of the trapped ^4He are interstellar atoms (energies around 100 eV), 40 percent are 3 keV and 30 percent are 30 keV magnetospheric particles. This estimate is very crude, and different combinations of percentages and energies are possible, considering the limited applicability of the available calibrations. It is clear from the difficulties with the analysis of the components that methods like high-voltage protection grids and protection of the foils from particle infall when the collector is not directed toward the arrival direction of interstellar particles would be highly useful for separating particle sources.

Taking as an example L199-2-2 (from the collector looking 24°N), with $133 \cdot 10^9$ ^4He atoms trapped per cm^2, the suggested 30 percent

interstellar particles would almost exactly correspond to the concentration proposed by the calculations (Fig. 2) where we assumed an interstellar ^4He density far from the sun of $0.0124/cm^3$.

The average $^4He/^3He$ ratio of the 450°C release is 6300, not far from the average for the total trapped helium of 6500. After correction for the lower trapping probability of ^3He compared to ^4He (approximately 60 percent according to Fig. 2), an estimate of the interstellar $^4He/^3He$ density ratio of 3800 would result. This value falls in the range of possible values for the present interstellar medium. It is too early to speculate, however, whether it is different from the value at the time of formation of the solar system.

For the magnetospheric contribution to the ^4He trapped in L199-2-2, a concentration of $0.7 \cdot 133 \cdot 10^9/cm^2$, after an approximate correction for the trapping probability, results in a fluence of about $1.5 \cdot 10^{11}$ atoms/cm^2. Other foils contain 30-50 percent more or less particles, thus a crude average over the 69 months of exposure would be 800 $^4He/s\ cm^2$, arriving from 0.34 sterad (the solid angle of directions seen by a foil piece through the open end of the collector box). The resulting figure for the average magnetospheric flux along the LDEF orbit, for approximately vertical infall, is a rather brave guess. It suffers from the fact that the energy spectrum is not known and, therefore, the trapping probabilities must be guessed. Moreover, no detailed model of the flux was worked out. Also, the concentrations on different pieces seem not to follow an obvious pattern as yet.

The magnetospheric $^4He/^3He$ flux ratio is 6600 and corresponds, practically, to the ratio of concentrations for the total trapped helium. This ratio is clearly much higher than the solar-wind ratio of 2350 (ref. 6), but very much lower from the atmospheric ratio at high altitudes which is near 100'000. The ratio of 6600 would clearly indicate a mixture of particles in the magnetospheric regions from which they originate. Similar contributions from escaped atmospheric atoms and from solar-wind ions which have penetrated the magnetosphere can be assumed. A foil experiment flown in 1973 on Skylab (ref. 7) collected precipitating particles. Because of varying contamination by ambient atmospheric atoms, the $^4He/^3He$ ratios fluctuated widely, from <3'000 to >50'000. It was not sure whether the low values found were representative of the low-latitude magnetospheric precipitation. The Skylab orbital inclination was 50° (for LDEF, 18.5°), thus Skylab eventually approached auroral latitudes. In another foil experiment, Bühler et al. (ref. 9) had found that auroras can contain almost pure solar-wind helium ($^4He/^3He$ = 3'000). Thus the low-latitude magnetospheric trapped component on the Skylab foils could have been contaminated by direct auroral precipitation.

For neon, assessing fluxes from the stepwise releases is more difficult than for helium, as the calibration curves contradict each other for 3 keV and for 30 keV (see Fig. 4). Moreover, interstellar neon has a five times higher energy than ^4He, i.e., about 500 eV, and its release pattern is similar above 600°C to that of neon of higher energies. It is difficult, even based on the low-temperature steps alone, to suggest that more than ten percent of the trapped neon could

be interstellar. Because the averaged $^{20}Ne/^{4}He$ ratio for the trapped gases is 1/3000 in the foils analyzed so far, this would mean that neon is much rarer in the interstellar medium than predicted by models (e.g., ref. 13).

Even for the magnetospheric neon, the measured ratio is lower than expected when compared to ratios estimated for the upper atmosphere, or if a considerable admixture of solar-wind neon is assumed as in the case of helium. Certainly, measurements of neon are less conclusive than those of helium because they depend more critically on assumptions on foil blanks and trapping probabilities. For interstellar particles ionization losses near one astronomical unit may have been underestimated; moreover, losses for neon are higher than those for helium.

CONCLUSIONS

About a third of the helium trapped in our foils seems to be of interstellar origin, two thirds being precipitated magnetospheric particles. This agrees with our model calculations and is consistent with our preliminary calibrations of the release curves for stepwise heating. The $^{4}He/^{3}He$ density ratio of the interstellar medium is tentatively estimated as 3800, with wide error limits. The $^{4}He/^{3}He$ ratio for the flux of magnetospheric ions must be around 6600. The averaged flux of magnetospheric ^{4}He ions is, for large pitch angles, of the order of 2000/s cm^2 sterad.

We expect that the reliability of the interstellar $^{4}He/^{3}He$ ratio can be improved by more detailed calibrations.

To estimate the interstellar and magnetospheric contributions to the trapped neon is more difficult. We found about 3000 times less trapped neon than trapped helium in the exposed foils. This low Ne concentration is difficult to understand. We hope to improve the measurements of neon by performing heating steps at lower temperatures, with lower background, and with calibrations in parallel.

The method of collecting interstellar and magnetospheric helium and neon has proved to be successful, even though the reliability of the results suffered from the superposition of trapped particles from the two sources. Superposition of interstellar atoms and magnetospheric ions can be prevented successfully on future missions. Based on our experience with IGE, we propose: 1) to shield off magnetospheric ions of low energies with high-voltage grids, 2) to open a cover on top of each collector only at times when the arrival direction of the interstellar particles is in the field of view, and, most effectively, 3) to fly an inertially stabilized platform with collectors continuously pointed at the direction of the most intense interstellar flux.

ACKNOWLEDGEMENT

This work is supported by NASA grant NAG N-2066 and by the Swiss National Science Foundation.

REFERENCES

1. Lind, D.L., J. Geiss and W. Stettler: Solar and Terrestrial Noble Gases in Magnetospheric Precipitation. J. Geophys. Res., 84, 6435, 1979.

2. Paresce, F. and S. Bowyer: Resonance Scattering from Interstellar and Interplanetary Helium. Astron. Astrophys., 27, 399-406, 1973.

3. Weller, C.S. and R.R. Meier: Observations of Helium in the Interplanetary/Interstellar Wind: the Solar-Wake Effect. The Astrophys. J., 193, 471-476, 1974.

4. Dalaudier, F., J.L. Bertaux, V.G. Kurt, and E.N. Mironova: Characteristics of Interstellar Helium Observed with Prognoz 6 58.4-nm Photometers. Astron. Astrophys., 134, 171-184, 1984.

5. Geiss, J., P. Eberhardt, F. Bühler, J. Meister, and P. Signer: Apollo 11 and 12 Solar Wind Composition Experiments: Fluxes of He and Ne Isotopes. J. Geophys. Res., 75, 5972, 1970.

6. Geiss, J., F. Bühler, H. Cerruti, P. Eberhardt, and Ch. Filleux: Solar-Wind Composition Experiment. Apollo 16 Preliminary Science Report, NASA SP-315, Section 14, 1972.

7. Lind, D.L., J. Geiss, F. Bühler, and O. Eugster: The Interstellar Gas Experiment. LDEF-69-Months in Space. First Post-Retrieval Symposium, NASA Conference Publication 3134, Part 1, 585, 1991.

8. Axford, W.I., F. Bühler, H.J.A. Chivers, P. Eberhardt, and J. Geiss: Auroral Helium Precipitation. J. Geophys. Res., 77, 6724, 1972.

9. Bühler, F., W.I. Axford, H.J.A. Chivers, and K. Marti: Helium Isotopes in an Aurora. J. Geophys. Res., 81, 111, 1976.

10. Filleux, C., M. Mörgeli, W. Stettler, P. Eberhardt and J. Geiss: Trapping of Low-Energy Helium Ions in Polycrystalline Al and Pt and in BeO and Anodic Al_2O_3 Films at Room Temperature. Radiation Effects, 46, 1-6, 1980.

11. Th. Michel: I Temperaturaufgelöste Extraktion von Helium und Neon aus BeO-Schichten, II Auswertprogramme für Messungen kleiner Proben. Lizentiatsarbeit, Universität Bern, 1986.

12. See, T., M. Allbrooks, D. Atkinson, C. Simon, and M. Zolensky: Meteoroid and Debris Impact Features Documented on the Long Duration Exposure Facility: A Preliminary Report. NASA JSC, 1990.

13. Bürgi, A.: Ueber die Nukleosynthese der Isotope von Helium und Neon. Lizentiatsarbeit, Universität Bern, 1980.

Table 1: Concentrations [in 10^6 atoms/cm^2] of trapped gases in exposed foils: total amount of gases released in all heating steps up to 1400°C. Corrections were applied for foil and machine blanks.

Foil piece	Area [cm^2]	^{3}He	^{4}He	^{20}Ne	^{22}Ne
Cassette 9, 110°N					
L249-2-1[1]	9.6	2.34 ±0.36	17300 ± 400	6.2 ± 2.7	0.35 ±0.35
L249-2-2	56.9	3.36 ±0.86	18600 ± 300	6.0 ± 0.6	0.35 ±0.13
Cassette 8, 70°N					
L275-1-1[1]	9.6	3.79 ±0.47	27400 ± 700	15.3 ± 2.8	1.42 ±0.27
L275-1-2	57.7	3.28 ±0.30	26000 ± 400	6.6 ± 0.5	0.36 ±0.06
Cassette 5, 24°N					
L199-2-1[1]	3.8	18.08 ±0.64	135000 ±3400	76.8 ±10.7	6.53 ±0.67
L199-2-2	38.4	21.33 ±0.73	133300 ±1900	34.4 ± 1.2	2.26 ±0.24
L199-2-3	9.7	17.17 ±1.27	98600 ±1300	32.3 ± 2.7	1.99 ±0.38
L199-2-4	9.7	19.08 ±1.09	110600 ±1300	37.5 ± 1.7	2.18 ±0.39
L199-2-5	49.0	11.96 ±0.46	74800 ±1100	13.7 ± 0.8	0.78 ±0.14
Cassette 4, 0° bwd.					
L290-2-1[2]	19.9	12.63 ±0.43	85300 ±1700	48.4 ± 2.4	3.47 ±0.39
L290-2-2	57.8	14.29 ±0.63	89100 ±1400	40.1 ± 1.2	2.71 ±0.16
L290-2-3	49.3	16.60 ±0.51	98500 ±1400	34.9 ± 0.8	2.28 ±0.18
Cassette 3, 0° fwd.					
L296-1-1[2]	19.0	30.23 ±0.76	197600 ±3100	69.0 ± 2.3	4.38 ±0.23
L296-1-2[2]	3.8	30.12 ±1.61	190000 ±3100	72.5 ±10.6	4.94 ±1.47
L296-1-3[2]	3.7	30.01 ±1.90	186100 ±3000	87.9 ± 8.2	5.29 ±1.03
L296-1-4	38.2	32.16 ±0.92	199000 ±2700	63.4 ± 1.4	3.25 ±0.37
Cassette 6, 24°S					
L273-1-1[1]	3.9	12.68 ±0.64	92400 ±1900	69.6 ± 8.1	6.37 ±1.34
L273-1-3	44.6	14.45 ±0.91	98800 ±1400	45.0 ± 0.9	3.12 ±0.28
Cassette 7, 70°S					
L255-1-1[1]	9.4	3.92 ±0.40	30600 ± 800	20.7 ± 4.0	1.85 ±0.40
L255-1-2	56.8	5.86 ±0.86	35000 ±1000	21.2 ± 0.9	1.48 ±0.24

[1] Total extraction at 1400°C.
[2] Heating step sequence was 150°, 450°, 1400°C.
All others: heating step sequence was 450°, 600°, 800°, 1400°C.

Table 2: Amount [in 10^6 atoms/cm^2] of trapped gases released at 450°C. Corrections were applied for foil blank and machine background.

Foil piece	Area [cm^2]	^3He	^4He	^{20}Ne	^{22}Ne
Cassette 9, 110°N					
L249-2-2	56.9	<0.4	8500 ± 300	0.6 ±0.3	<0.07
Cassette 8, 70°N					
L275-1-2	57.7	1.8 ±0.2	9200 ± 200	1.5 ±0.1	0.15 ±0.04
Cassette 5, 24°N					
L199-2-2	38.4	6.7 ±0.4	40900 ±1100	3.4 ±0.4	0.27 ±0.09
L199-2-3	9.7	3.5 ±0.4	22000 ± 500	3.0 ±1.3	0.13 ±0.11
L199-2-4	9.7	6.0 ±0.5	33100 ± 700	4.2 ±1.3	0.19 ±0.08
L199-2-5	49.0	4.4 ±0.2	25600 ± 700	1.5 ±0.2	<0.12
Cassette 4, 0°, backward					
L290-2-1[2]	19.9	2.6 ±0.3	20100 ± 500	5.6 ±1.7	0.43 ±0.17
L290-2-2	57.8	3.2 ±0.2	18000 ± 500	1.6 ±0.3	0.16 ±0.03
L290-2-3	49.3	4.5 ±0.3	27200 ± 700	2.9 ±0.3	0.24 ±0.08
Cassette 3, 0°, forward					
L296-1-1[2]	19.0	7.2 ±0.4	48200 ± 900	6.1 ±0.4	0.30 ±0.15
L296-1-2[2]	3.8	7.9 ±1.1	54900 ±1600	<7.0	<0.6
L296-1-3[2]	3.7	9.8 ±1.0	51900 ±1300	8.3 ±1.4	<0.4
L296-1-4	38.2	8.1 ±0.5	52100 ±1300	4.3 ±0.3	<0.3
Cassette 6, 24°S					
L273-1-3	44.6	4.0 ±0.8	24800 ± 500	2.4 ±0.3	0.16 ±0.05
Cassette 7, 70°S					
L255-1-2	56.8	2.3 ±0.8	9200 ± 900	7.3 ±0.8	0.62 ±0.16

[2] Heating step sequence was 150°, 450°, 1400°C.
All others: heating step sequence was 450°, 600°, 800°, 1400°C.

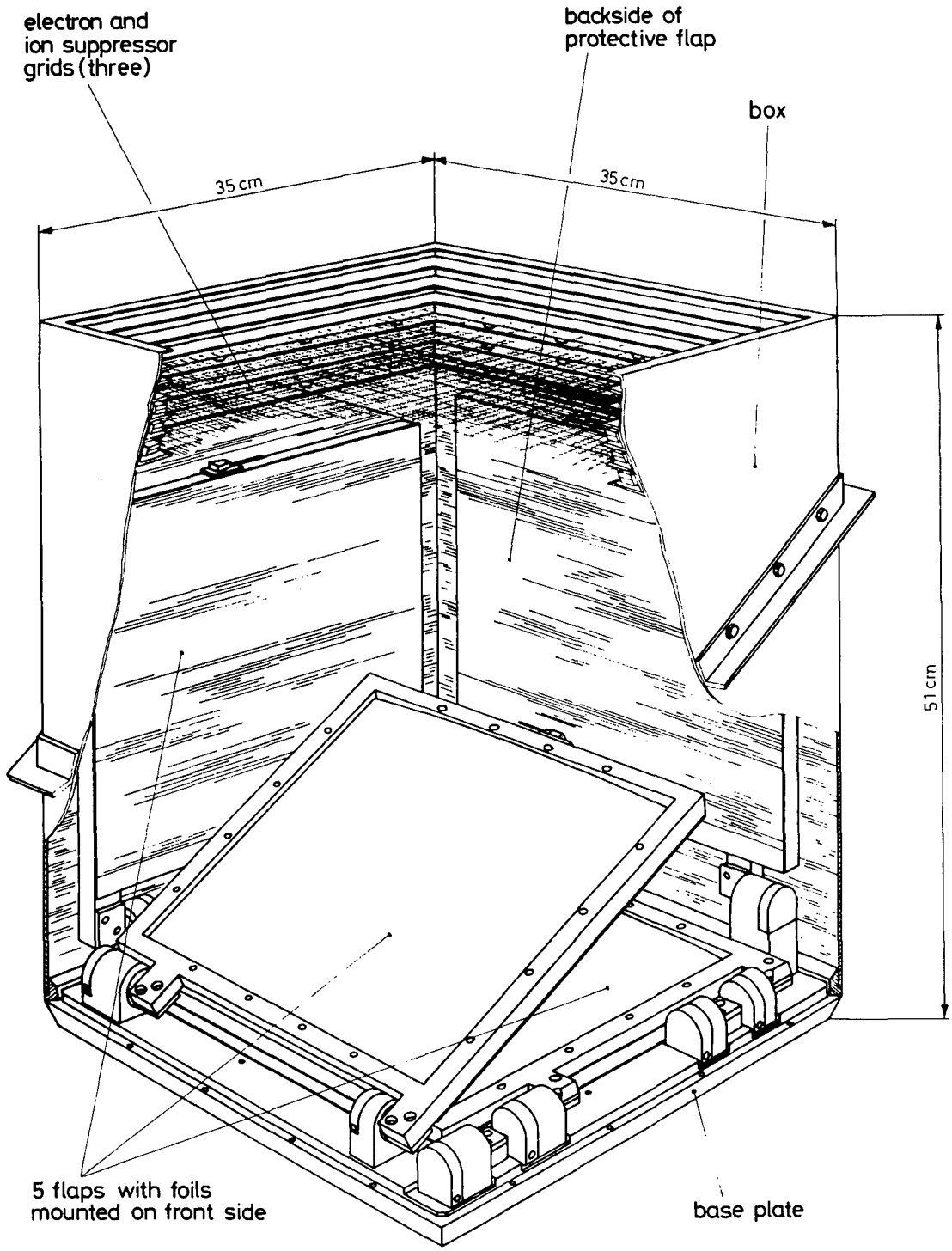


Fig. 1 One of seven collectors, containing a cassette with six plates (5 moveable, one fixed) holding one foil each. The third plate is shown turning up to expose the fourth foil.

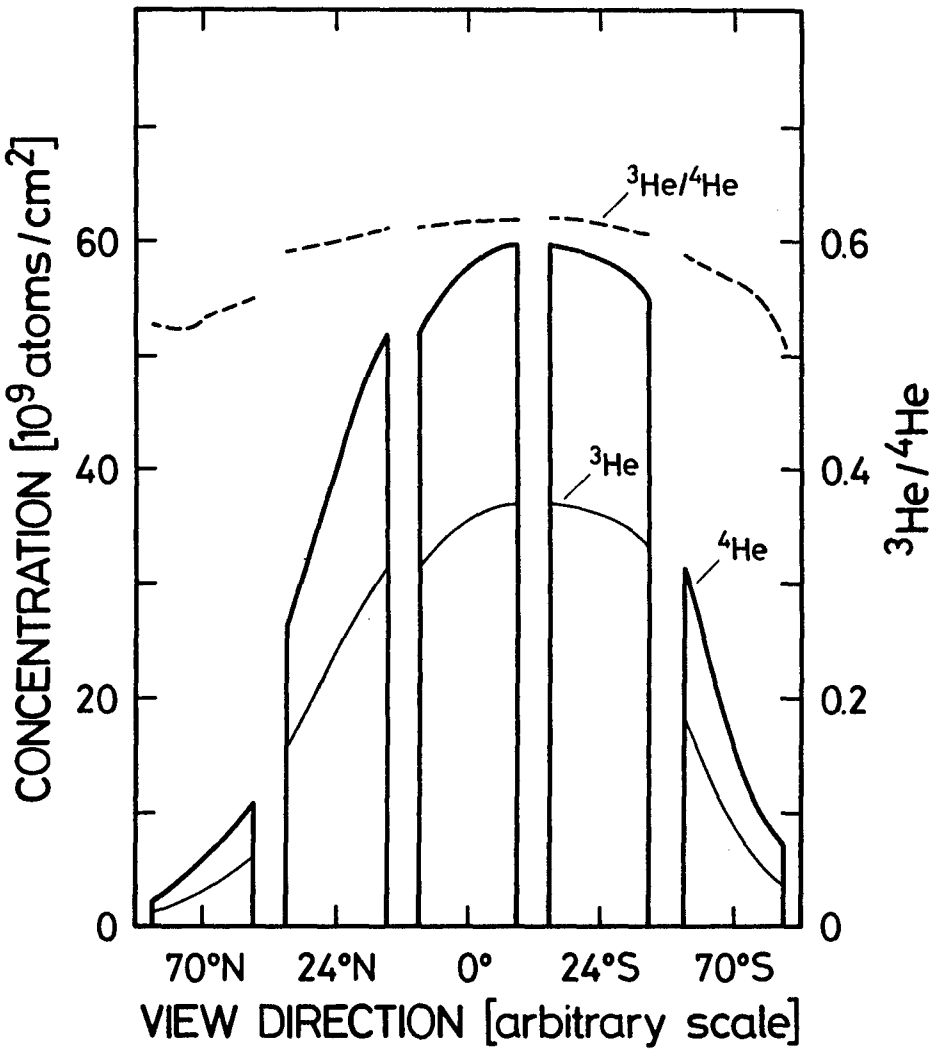


Fig. 2 Model calculation for interstellar neutral helium trapped in the IGE foils of different collectors (see ref. 1).

Interstellar ^{4}He density was assumed for both isotopes in order to show the discrimination of ^{3}He by its lower trapping probability.

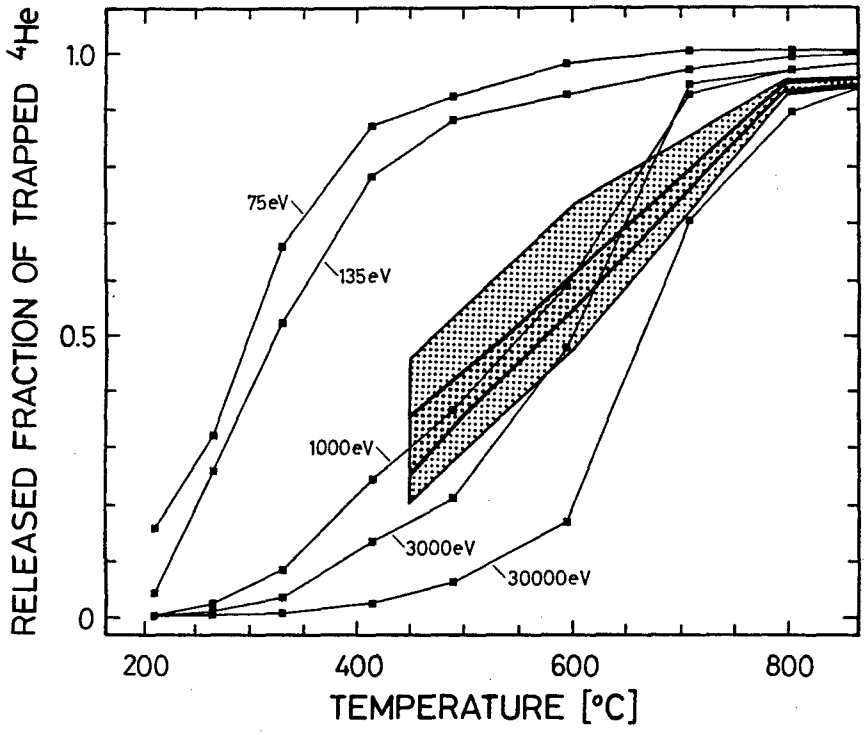


Fig. 3 ^{4}He released from IGE foils by stepwise heating. Squares connected by thin lines are from calibrations (ref. 11). Heating steps for exposed pieces were 450°, 600°, 800° and 1400°C, and release curves (not drawn) are within shaded regions.

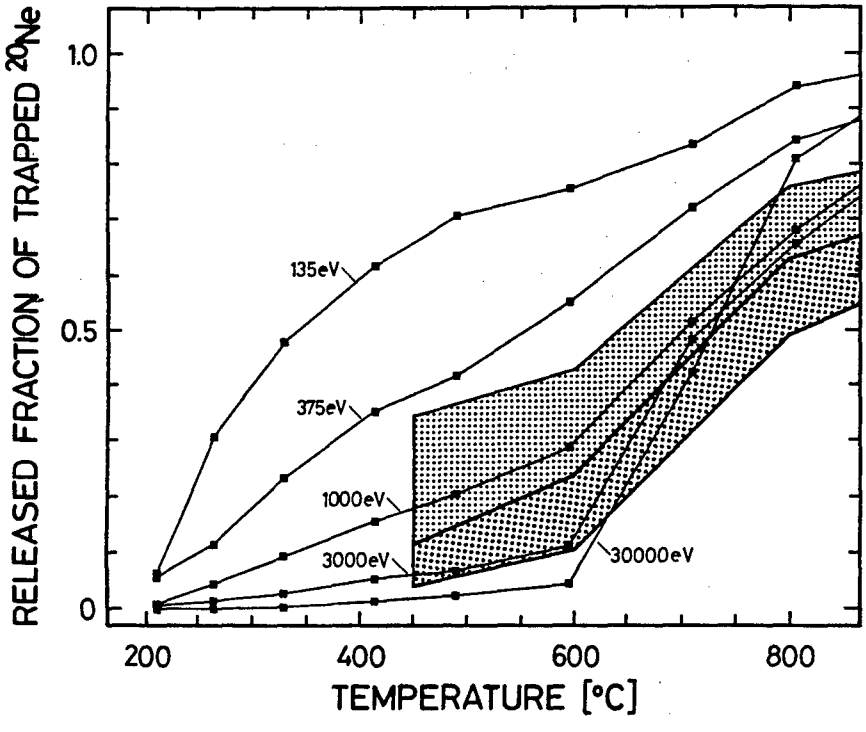
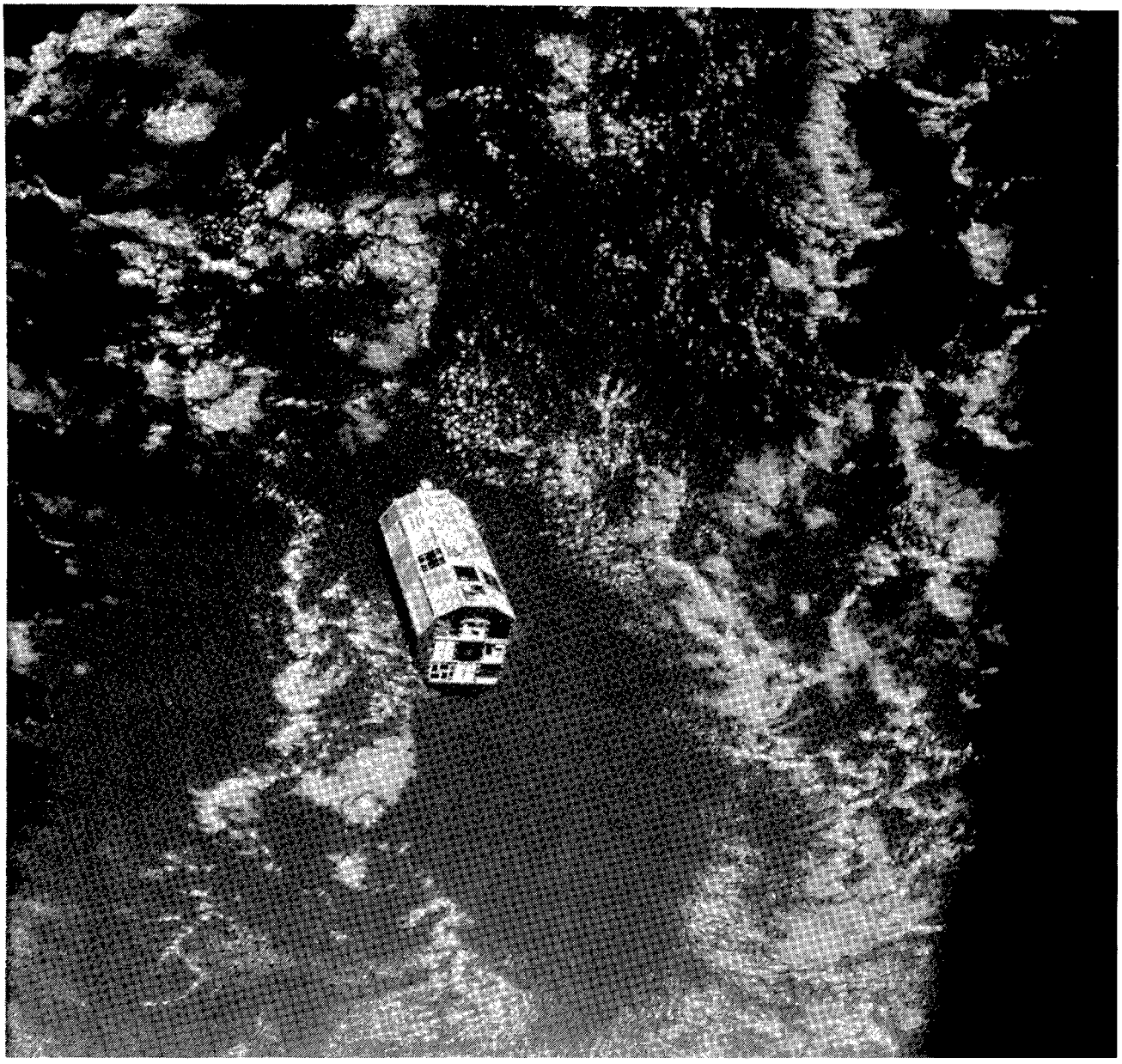


Fig. 4 ^{20}Ne released from IGE foils in calibrations (ref. 11) and from exposed pieces (shaded regions).

SPACE ENVIRONMENTS

MICROGRAVITY



L-84-4337

FOLLOW UP ON THE CRYSTAL GROWTH EXPERIMENTS OF THE LDEF

K. F. Nielsen
Technical University of Denmark, Physics Laboratory III
DK-2800 Lyngby, Denmark.

M. D. Lind
Rockwell International Science Center
Thousand Oaks, California 91360.

The results of the 4 solution growth experiments on the LDEF have been published elsewhere (1),(2). Both the crystals of $CaCO_3$, which were large and well shaped, and the much smaller TTF-TCNQ crystals showed unusual morphological behaviour.

The follow up on these experiments (planned in 1979) was started already in 1981, when ESA initiated a "Concept Definition Study" on a large, 150 kg, Solution Growth Facility (SGF) to be included in the payload of EURECA-1, the European Retrievable Carrier. This carrier was a continuation of the European Spacelab and at that time planned for launch in 1987.

The long delay of the LDEF retrieval and of subsequent missions brought about reflections both on the concept of crystal growth in space and on the choice of crystallization materials, that had been made for the LDEF. As explained in (1) under "Historical Background" events on earth, during the flight of LDEF, caused a dramatic decline in the demand for TTF-TCNQ crystals. Already before the LDEF retrieval, research on TTF-TCNQ had been stopped, and a planned growth experiment with TTF-TCNQ on the SGF/EURECA had been cancelled.

The target of the SGF investigation is now more fundamental in nature. None of the crystals to be grown here are, like TTF-TCNQ, in particular demand by science or industry, and the crystals only serve the purpose of model crystals. The real purpose of the investigation is to study the growth behaviour. One of the experiments, the Soret Coefficient Measurement experiment is not growing crystals at all, but has it as its sole purpose to obtain accurate information on thermal diffusion, a process of importance in crystal growth from solution.

The 4 LDEF growth reactors had all approximately the same size and were packed together in a thermostated container. The implication of this was that all the experiments had to be run at the same temperature. This temperature was determined by simple design (no cooling water) and the minimum consumption of electrical energy to the heating elements. 35^{o} C was used.

The 4 SGF/EURECA experiments (fig. 1) may be of different sizes, and they are each individually thermostated. The volumes of the reactors are increased up to 5 times the LDEF volumes, but still the simple design is maintained (no cooling water). Experiment temperatures may range from 35^{o} C to 70^{o} C, and the temperature-time profile as well as the temperature-position profile is monitored for each experiment throughout the mission.

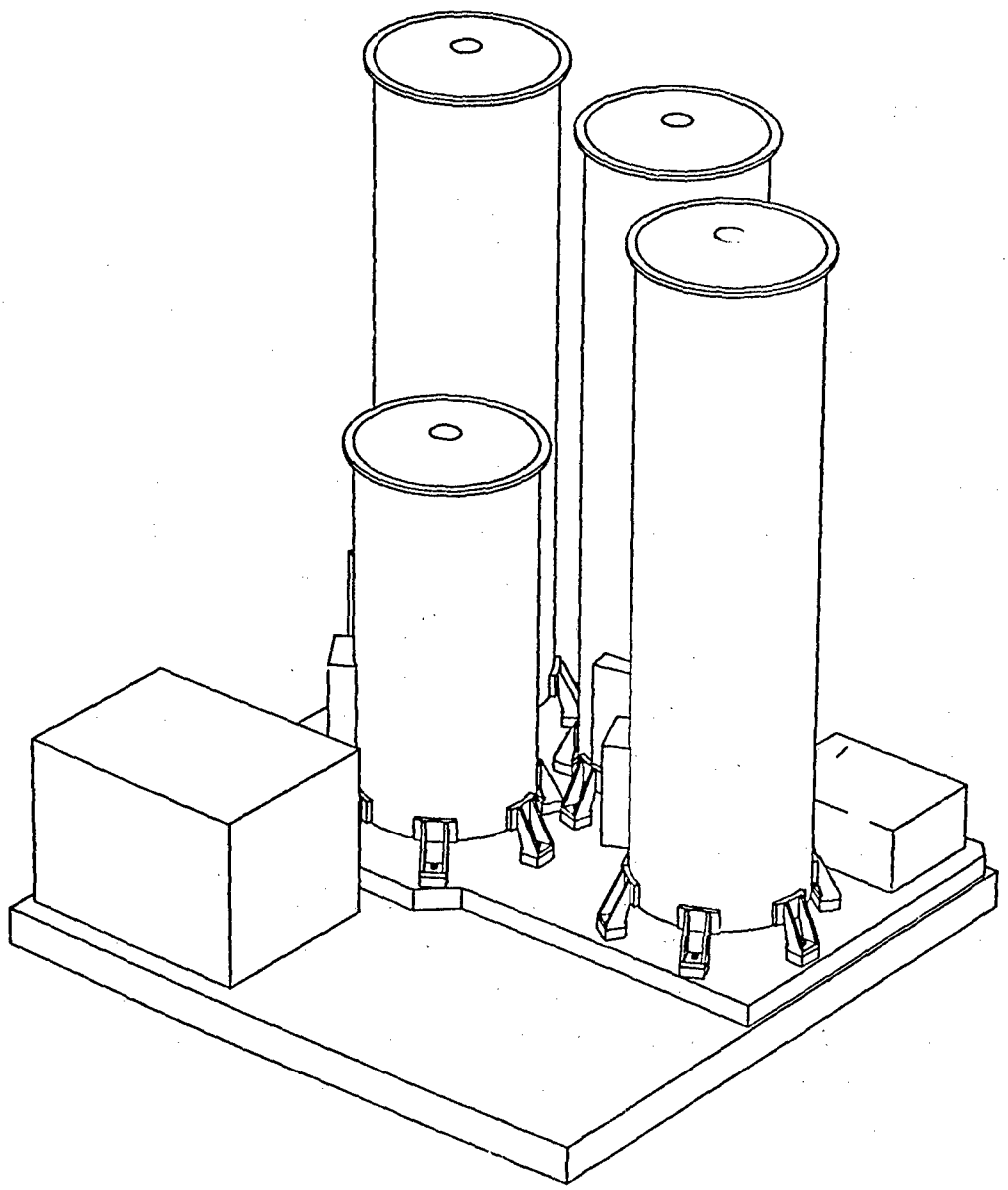


Fig. 1.

Fig. 2 is a construction drawing of a growth reactor. Basically they follow the same design principles as the LDEF reactors (2). A major improvement has been introduced in the pressure equallizing system with the bellows, designed and constructed by A.G. Contraves in Switzerland.

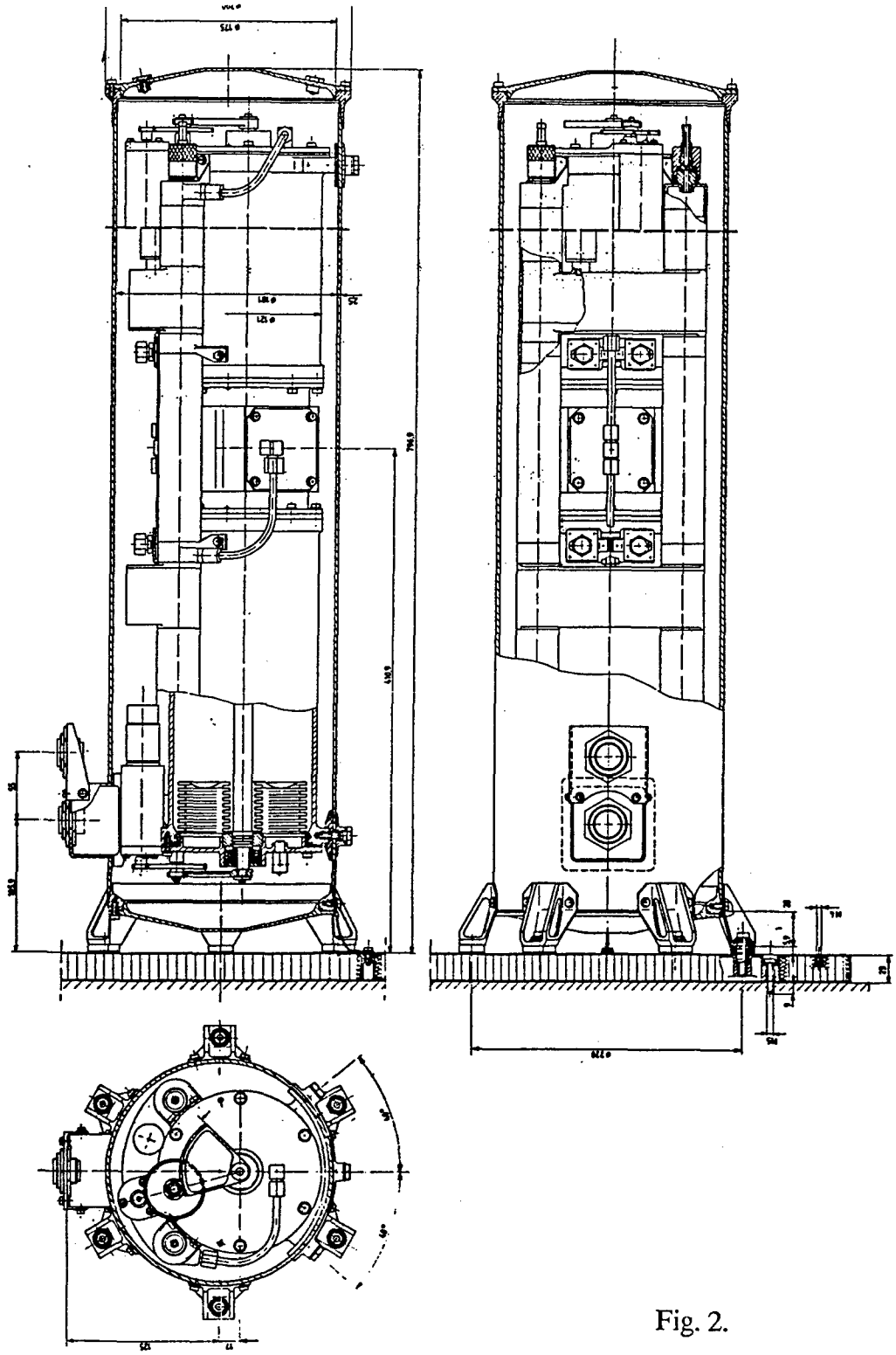


Fig. 2.

The SGF reactors and the total integrated EURECA under testing are shown in figures 3 and 4.

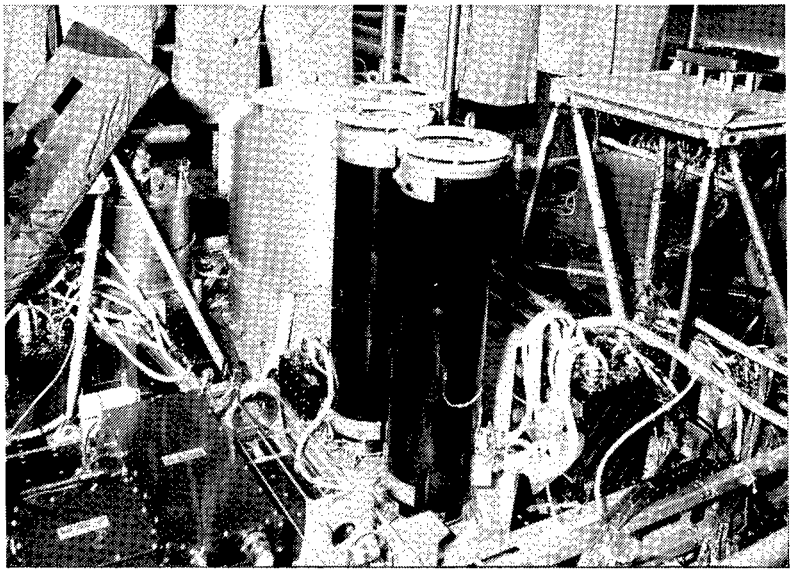


Fig. 3. The SGF reactors mounted on the EURECA.

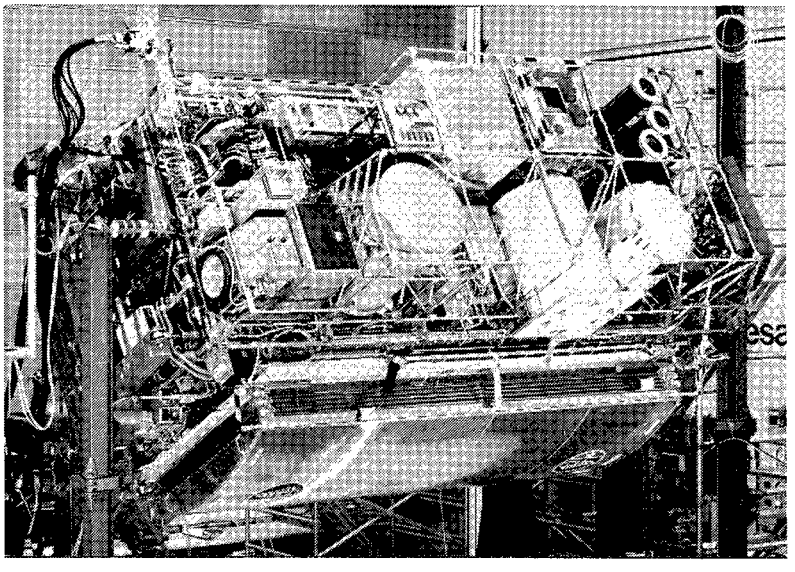


Fig. 4. Total integrated EURECA under testing.

The 4 SGF experiments have been described in detail elsewhere (3). Here only a schematic summary of the scientific background for the experiments will be given.

1. Growth of Calcium-Carbonate Crystals.

P.I. M. David Lind
Rockwell Int. Science Center
Thousand Oaks, California.

Co. P.I. Kjeld Flemming Nielsen
Technical University of Denmark
Lyngby, Denmark.

This experiment is a reproduction of the successful growth experiment on the LDEF. The unexpected and unintended long duration of LDEF prevented us from observing free $CaCO_3$-crystals obtained via homogeneous nucleation in the bulk of the solution, followed by growth of freely suspended crystals. Apart from this we are interested in a further study of the habit formation under microgravity conditions, which is unusual.

2. Formation and Transformation of Tri-Calcium-Phosphate.

P.I. H.E. Lundager Madsen
Royal Veterinary and Agricultural University
Frederiksberg, Denmark.

Nucleation and crystallization of Calcium-Phosphate takes place with an even stronger participation of water molecules than in the case of Calcium-Carbonate. Tri-Calcium-Phosphate can be described as an intermediate gel structure, from which further crystallization takes place. The study of the influence of gravitation on this gel structure and its further crystallization into 3 or 4 new crystal structures is the background for this experiment. Morphology, nucleation, and aggregation of the various structures in microgravity will be studied.

In living organisms the calcified tissues, known to be influenced by the lack of gravitation, consist mainly of Phosphates and Carbonates. Thereby the above two experiments may be viewed in a broader perspective than only that of basic science in the growth of crystals.

3. Growth of Zeolite Crystals.

P.I. Michael Stoecker
Center for Industrial Research
Blindern, Oslo, Norway.

Zeolites are crystalline Alumino-Silicates with well defined pore structures containing open channels, pockets, and pores in the same range of kinetic diameters as small molecules (3-12 Å). They are used for catalysis and ion exchange. Also here water molecules are active in the crystallization that takes place via an aqueous gel. With these crystals accurate knowledge of pore diameters is important for their application, and the material in question is Offretite, of which large, well shaped crystals are wanted. The objective is to produce channels with pore size diameters 6.4 Å and 4.3 Å (12 and 8 membered ring channels). Thus the study of morphology here is somewhat specialized.

4. Soret Coefficient Measurements (Diffusion).

P.I. J. C. Legros
Chimie Physique E.P. (CP.165)
Universite Libre de Bruxelles, Belgium.

The Soret Coefficient is the ratio of the thermal to the isothermal diffusion coefficient and is defined positive, if the denser component migrates towards the cold side. This investigation aims at the determination of the Soret coefficient in various binary organic mixtures and aqueous electrolyte solutions. The interior of this experiment is therefore totally different from the other 3 experiments. It contains an arrangement with 20 tubes with a volume of 10 ml each, and a temperature gradient of about $10^{o}C$ is placed over each tube.

The relation to crystal growth in this experiment is that the value of the Soret coefficient is an important parameter in the growth from solution. If the growth process involves exchange of heat, which it normally does, extra liquid flows will be generated under gravitation.

During the past year, a number of EWG's (Expert Working Groups) havebeen set up by ESA, the European Space Agency. The group on solution growth has come up with a

number of ideas for further investigations under microgravity, which may be summarized as follows:

Morphological Studies	Mass Transfer Studies	Nucleation Studies	Aggregation Studies
Available theories may only be experimentally verified in micro-g environments.	Diffusion profiles may be steeper without convection.	Induction time is increased in micro-g. Early stages may be found.	Cluster formation & behaviour greatly influenced by gravitation.

The morphological, nucleation, and aggreation studies have been dealt with. Studies of mass transfer have until now only been in "natural" concentration gradients, i.e. gradients that are isothermal and where the gradient is maintained by removing solute from one side. The Soret coefficient experiment is now studying thermal gradients as well.

By removing solvent from the other side of a concentration gradient, f.inst. by evaporation, gradients may be steeper. Under microgravity conditions, gradients may become almost arbitrarily steep without convection. Thereby diffusive mass transfer may be enhanced.

One of the EWG members, Rafael Rodriguez-Clemente, has proposed a microgravity experiment to this effect. It is based on earth experiments on crystal growth from boiling solutions (4).

References:

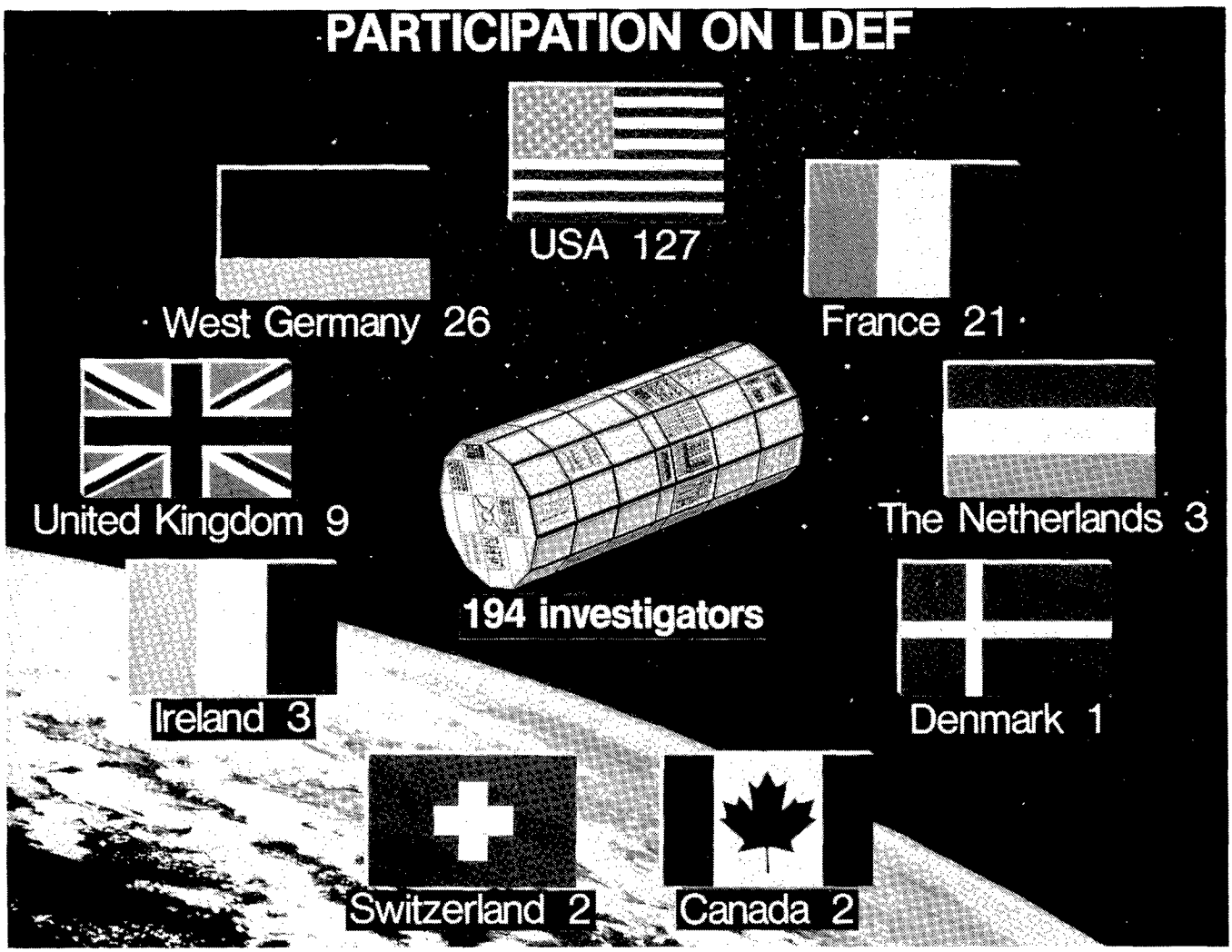
1) K.F.Nielsen & M.D.Lind: "Results of the TTF-TCNQ and the $CaCO_3$ Crystallization on the LDEF", NASA Conf. Publ. 3134, part 3, p. 1675, Kissimmee FL, 1991.

2) M.D.Lind & K.F.Nielsen: "Crystal Growth by Diffusion in Earth-Orbit", SPIE Vol. 1557, p. 259, San Diego CA, 1991.

3) EURECA-1 Experiment Book, ESA Ref: MU/132/LI, Noordwijk, 1989.

4) R.Rodriguez-Clemente et al: "Crystal Growth from Boiling Solutions", Prog. Crystal Growth and Charact., Great Britain, Vol. 17, pp 1-40, 1988.

AUTHOR INDEX



L-84-2986

Author Index

Index Guide

Part 1, pages 1–274; Part 2, pages 275–738

Part 3, pages 739–1254; Part 4, pages 1255–1570

Adams, J.H., Jr. 247, 1551

Agüero, R.C. 665

Ahearn , J.S. 1285

Albrecht, A. 231

Allbrooks, M.K. 595

Alston, J.A. 1493

Amari, S. 513

Armstrong, T.W. 137, 163, 187, 195, 207, 221

Arthur, R.J. 79

Atkinson, D.R. 277, 595, 619, 1399

Auer, B.M. 1137

Bada, J. 453

Banks, B.A. 431, 1137

Beahm , L.P. 247

Beaujean , R. 239

Becker, L. 453

Benton, E.R., 171, 181

Benton, E.V. 163, 171, 181, 187

Bergman, L.A. 1439

Bernhard, R.P. 541, 551

Berry, J.N. 1425

Best, S. 479

Blake, J.B. 147

Blakkolb, B.K. 1035, 1343

Blue, M.D., 1333

Boberg, P.R. 247

Bobias, S.G. 87

Bohnhoff-Hlavacek, G. 1223

Bonnemason, F. 1401

Borg, J. 347

Borson, E.N. 1033

Bosch, J. 261

Bourassa, R.J. 13

Bourrieau, J. 157

Bowen, H.S. 1035

Bradley, J. 577

Brennan, P.J. 1455

Brinker, D.J. 1291, 1375

Brodzinski, R.L. 79

Brownlee, D.E. 577, 677

Bühler, F. 705

Bunch, T.E. 347, 453

Burns, F. 107

Cagle, J.A. 1511

Callen, W.R. 1403

Carabétian, Ch. 1355

Chaloupka, T. 479

Champetier, R.J. 1399

Chang, A.C. 827

Chapman, S.P. 1425

Chatzitheodoridis, E. 791

Coggi, J.M. 357, 1075, 1235

Christl, L.C. 1169

Colborn, B.L. 137, 163, 187, 195, 207, 221

Cooke, W.J. 667, 693

Coombs, C.R. 277, 595, 619

Crawford, G. 479

Cromer, T.F. 1015

Cromwell, B.K. 1001

Crutcher, E.R. 1023, 1187

Csige, I. 171, 181, 187
Dardano, C.B. 277
Davis, J.M. 1201
de Groh, K.K. 1137
DeHainaut, L.L. 1361
Delaboudinère, J.P. 1355
Derrickson, J.H. 171
Deshpande, S.P. 417
De Vries, C. 431
DeWalt , S.A. 1413
Dezfouly-Arjomandy, B. 231
Divine, N. 665
Domingo, C. 261
Drolshagen, G. 325
Durin, C. 541, 1315
Dursch, H.W. 923, 1041, 1257
Edelman, Joel 1257
Edwards, J.L. 1137
Enge, W. 239
Erlichman, J. 453
Eugster, O. 705
Farrow, A. 849
Felbeck, D.K. 889
Finckenor, M.M. 1125
Fishman, G.J. 111, 125
Fleming, R.H. 453
Foote, J. 513
Ford, D.I. 811
Frank, A.L. 163, 171
Frigo, L.A. 171, 187
Funk, J.G. 1201
Gaylord, T.K. 1403
Gebauer, L. 1137
Geiss, J. 705
George, G.A. 867
George, P.E. 923
Gillis, J.R. 13
Gilmour, J.D. 791
Golden, J.L. 1099
Grammer, H.L. 1015
Green, S.F. 417
Gregory, J.C. 3, 231, 1111, 1169
Griffis, D.P. 677
Grigsby, D.K. 1479
Gursky, H. 1535
Gyetvay, S.R. 357, 1235
Harmon, B.A. 111, 125, 231
Hartmayer, R. 1439
Harvey, G.A. 797
Havey, K. 1389
Hemminger, C.S. 963
Hennessy, C.J. 595
Henke, R.P. 171
Herzog, G. 231
Hickey, J.R. 1291, 1375
Hill, D.J.T. 867
Hill, S.G. 923
Hochedez, J.F. 1355
Hörz, F. 277, 551, 577
Hunter, J.L. 677
Hurley, D.L. 97
Imamoto, S.S. 147
Jaggers, C.H. 1075
Jansen, F. 261
Jenkins, P. 1375
Johnson, R.E. 811
Johnston, A.R. 1439
Jonathal, D. 239
Joswiak, D. 577
Kamenetzy, R.R. 1125, 1151
Kassel, Jr., P.C. 667, 693
Keegan, R. 261

Kemp, W.T. 1399
Kenemuth, J.R. 1361
Keough, B. 1041
Kessler, D.J. 585
Kinard, W.H. 277
Kinser , D.L. 529
Klein, J. 231
Kosic, T.J. 1035
Laird, C.E. 111, 125
Lange, G. 513
Lauriente, M. 51
Le, T.D. 977
Lee, M. 957
Letton, A. 849
Lind, D.L. 705
Lind, M.D. 725
Linton, R.C. 1151
Lyon, I.C. 791
Mack, K.S. 313
Mackay, N. 417
Macklin, J. 453
Mallon, J.J. 963
Mandeville, J.-C. 303, 347
Manuelpillai, G. 493
Masarik, J. 87
Mason, J.B. 1257
Matthews, R. 877
McCreight, C. 1455
McDonnell, J.A.M. 417
McKibben, R.B. 1535
McIntosh, R. 1455
Mell, R.J. 1061, 1111
Merrow, J.E. 431
Meshishnek, M.J. 357, 1075, 1235
Middleton, R. 231
Miglionico, C.J. 905
Miller, E.R. 1061, 1111
Mirtich, M.J. 431
Misra, V. 677
Monarski, T.W. 1425
Moss, C.E. 87
Motley, W.R. III 667
Mulholland, J.D. 667, 693
Murr, L.E. 905
Mustico, A. 1389
Newman, P.J. 417
Newman, S.C. 1511
Nielsen, K.F. 725
Norwood, J.K. 1125
Oda, K. 171
O'Donnell, J.H. 867
Oliver, J.P. 667, 693
Olmez, I. 107
O'Sullivan, D. 261
Padden, R.J. 1425
Parnell, T.A. 69, 111, 125, 171, 187
Paschen, K.W. 357
Pender, C.W. 1001
Perry, A.T. 1511
Peters, P.N. 3, 1111, 1169
Pippin, H.G. 13, 1023, 1041, 1187
Pomery, P.J. 867
Radhakrishnan, G. 1269
Radicati di Brozolo, F. 347, 453
Raikar, G.N. 1169
Rasoul, F.A. 867
Reedy, R.C. 87
Reeves, J.H. 79
Ricks, D.A. 677
Rooney, W. 957
Rose, M.F. 479
Roybal, R.E. 905

Rutledge, S.K. 431
Ryan, L.E. 1035, 1343
Sagalyn, P. 107
Sampair, T.R. 27, 51
Sanchez, A.D. 1425
Sapp, C.A. 339
Saxton, J.M. 791
Scheiman, D.A. 1291
Schurig, H.J. 1343
See, T.H. 277, 313, 339, 551
Seegmiller, D.W. 1361
Shepherd, S.D. 1001
Simon, C.G. 277, 677, 693
Simpson, J.A. 1535
Sinsheimer, F.B. 1033
Singer, S.F. 667
Slemp, W.S. 827, 1015, 1093
Smith, A.R. 97
Soundararajan, S. 181
Steckel, G.L. 977
Stein, B.A. 741
Stein, C. 905
Stella, P.M. 1303
Stephens, B. 479
Strganac, T. 849
Strickland, J.W. 1201
Stuckey, W.K. 1269
Swan, P. 513
Taylor, E.W. 1413, 1425
Taylor, W.W.L. 1343
Tennyson, R.C. 493, 877
Thompson, A. 261
Tidler, C.E. 1361
Turner, G. 791
Tuzzolino, A.J. 1535
Tylka, A.J. 247
Uht, J.C. 963
Vallimont, J. 1389
Van Lierde, P. 791
Venables, J.D. 1285
Voss, H.D. 1535
Vyhnal, R.F. 941
Wagner, J.D. 595, 619
Walker, R.M. 513
Wallace, D. 1269
Warren, J.L. 313
Watts, A.J. 277, 595, 619
Watts, J.W., Jr. 137, 171, 187
Weinberg, J.L. 667
Wenzel, K.-P. 261
Whitaker, A.F. 1125
Whitehouse, P.L. 3
Whiteside, J. 957
Wiedlocher, D.E. 529
Wightman, J.P. 1015
Wilkes, D.R. 1061, 1111, 1521
Wilson, B.K. 1499
Wong, W.C. 1343
Wood, B.E. 1001
Wortman, J.J. 667, 677
Yaung, J.Y. 1343
Young, P.R. 827, 1015, 1093
Zinner, E. 513
Zolensky, M.E. 277, 313, 339, 541
Zook, H.A. 277, 313, 339, 575
Zwiener, J.M. 1061, 1111

REPORT DOCUMENTATION PAGE

Form Approved
OMB No. 0704-0188

Public reporting burden for this collection of information is estimated to average 1 hour per response, including the time for reviewing instructions, searching existing data sources, gathering and maintaining the data needed, and completing and reviewing the collection of information. Send comments regarding this burden estimate or any other aspect of this collection of information, including suggestions for reducing this burden, to Washington Headquarters Services, Directorate for Information Operations and Reports, 1215 Jefferson Davis Highway, Suite 1204, Arlington, VA 22202-4302, and to the Office of Management and Budget, Paperwork Reduction Project (0704-0188), Washington, DC 20503.

1. AGENCY USE ONLY *(Leave blank)*	2. REPORT DATE	3. REPORT TYPE AND DATES COVERED
	April 1993	Conference Publication

4. TITLE AND SUBTITLE
69 Months In Space—Second LDEF Post-Retrieval Symposium

5. FUNDING NUMBERS
506-48-91-11

6. AUTHOR(S)
Arlene S. Levine, Editor

7. PERFORMING ORGANIZATION NAME(S) AND ADDRESS(ES)
NASA Langley Research Center
Hampton, VA 23681-0001

8. PERFORMING ORGANIZATION REPORT NUMBER
L-17196

9. SPONSORING/MONITORING AGENCY NAME(S) AND ADDRESS(ES)
National Aeronautics and Space Administration
Washington, DC 20546-0001

10. SPONSORING/MONITORING AGENCY REPORT NUMBER
NASA CP-3194, Part 2

11. SUPPLEMENTARY NOTES

12a. DISTRIBUTION/AVAILABILITY STATEMENT
Unclassified–Unlimited

Subject Category 99

12b. DISTRIBUTION CODE

13. ABSTRACT *(Maximum 200 words)*
This document is a compilation of papers presented at the Second Long Duration Exposure Facility (LDEF) Post-Retrieval Symposium. The papers represent the data analysis of the 57 experiments flown on the LDEF. The experiments include materials, coatings, thermal systems, power and propulsion, science (cosmic ray, interstellar gas, heavy ions, micrometeoroid, etc.), electronics, optics, and life science.

14. SUBJECT TERMS
Space experiment

15. NUMBER OF PAGES
476

16. PRICE CODE
A21

17. SECURITY CLASSIFICATION OF REPORT	18. SECURITY CLASSIFICATION OF THIS PAGE	19. SECURITY CLASSIFICATION OF ABSTRACT	20. LIMITATION OF ABSTRACT
Unclassified	Unclassified	Unclassified	

NSN 7540-01-280-5500

Standard Form 298(Rev. 2-89)
Prescribed by ANSI Std. Z39-18
298-102

NASA-Langley, 1993